AD-A106 548 NATIONAL BUREAU OF STANDARDS WASHINGTON DC F/G 20/5
LASER INDUCED DAMAGE IN OPTICAL MATERIALS: 1980,(U)
OCT 81 H E BENNETT, A J GLASS, A H GUENTHER
UNCLASSIFIED NBS-SP-620 NL

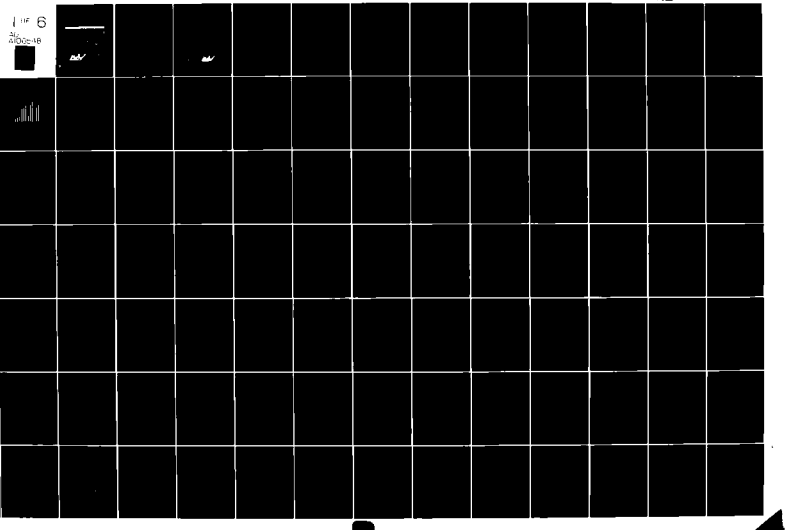

LEVEL II

12

NBS SPECIAL PUBLICATION 620

U.S. DEPARTMENT OF COMMERCE / National Bureau of Standards

Laser Induced Damage in Optical Materials: 1980

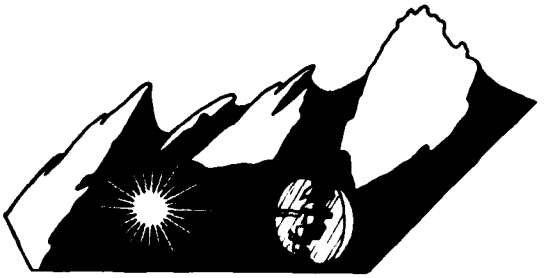

BOULDER DAMAGE SYMPOSIUM

ASTM

STP 759

NATIONAL BUREAU OF STANDARDS

The National Bureau of Standards[1] was established by an act of Congress on March 3, 1901. The Bureau's overall goal is to strengthen and advance the Nation's science and technology and facilitate their effective application for public benefit. To this end, the Bureau conducts research and provides: (1) a basis for the Nation's physical measurement system, (2) scientific and technological services for industry and government, (3) a technical basis for equity in trade, and (4) technical services to promote public safety. The Bureau's technical work is performed by the National Measurement Laboratory, the National Engineering Laboratory, and the Institute for Computer Sciences and Technology.

THE NATIONAL MEASUREMENT LABORATORY provides the national system of physical and chemical and materials measurement; coordinates the system with measurement systems of other nations and furnishes essential services leading to accurate and uniform physical and chemical measurement throughout the Nation's scientific community, industry, and commerce; conducts materials research leading to improved methods of measurement, standards, and data on the properties of materials needed by industry, commerce, educational institutions, and Government; provides advisory and research services to other Government agencies; develops, produces, and distributes Standard Reference Materials; and provides calibration services. The Laboratory consists of the following centers:

Absolute Physical Quantities[2] — Radiation Research — Thermodynamics and Molecular Science — Analytical Chemistry — Materials Science.

THE NATIONAL ENGINEERING LABORATORY provides technology and technical services to the public and private sectors to address national needs and to solve national problems; conducts research in engineering and applied science in support of these efforts; builds and maintains competence in the necessary disciplines required to carry out this research and technical service; develops engineering data and measurement capabilities; provides engineering measurement traceability services; develops test methods and proposes engineering standards and code changes; develops and proposes new engineering practices; and develops and improves mechanisms to transfer results of its research to the ultimate user. The Laboratory consists of the following centers:

Applied Mathematics — Electronics and Electrical Engineering[2] — Mechanical Engineering and Process Technology[2] — Building Technology — Fire Research — Consumer Product Technology — Field Methods.

THE INSTITUTE FOR COMPUTER SCIENCES AND TECHNOLOGY conducts research and provides scientific and technical services to aid Federal agencies in the selection, acquisition, application, and use of computer technology to improve effectiveness and economy in Government operations in accordance with Public Law 89-306 (40 U.S.C. 759), relevant Executive Orders, and other directives; carries out this mission by managing the Federal Information Processing Standards Program, developing Federal ADP standards guidelines, and managing Federal participation in ADP voluntary standardization activities; provides scientific and technological advisory services and assistance to Federal agencies; and provides the technical foundation for computer-related policies of the Federal Government. The Institute consists of the following centers:

Programming Science and Technology — Computer Systems Engineering.

[1]Headquarters and Laboratories at Gaithersburg, MD, unless otherwise noted; mailing address Washington, DC 20234.
[2]Some divisions within the center are located at Boulder, CO 80303.

Laser Induced Damage In Optical Materials: 1980

Proceedings of a Symposium Sponsored by:
National Bureau of Standards
American Society for Testing and Materials
Office of Naval Research
Department of Energy
Defense Advanced Research Project Agency
Air Force Office of Scientific Research

September 30–October 1, 1980
NBS, Boulder, Colorado 80303

Edited by:

Harold E. Bennett
Naval Weapons Center
China Lake, California 93555

Alexander J. Glass
Lawrence Livermore Laboratories
Livermore, California 94550

Arthur H. Guenther
Air Force Weapons Laboratory
Kirtland Air Force Base, New Mexico 87117

Brian E. Newnam
Los Alamos Scientific Laboratory
Los Alamos, New Mexico 87545

U.S. DEPARTMENT OF COMMERCE, Malcolm Baldrige, Secretary
NATIONAL BUREAU OF STANDARDS, Ernest Ambler, Director

Issued October 1981

Library of Congress Catalog Card Number: 81-600110

National Bureau of Standards Special Publication 620
Nat. Bur. Stand. (U.S.), Spec. Publ. 620, 483 pages (Oct. 1981)
CODEN: XNBSAV

U.S. GOVERNMENT PRINTING OFFICE
WASHINGTON: 1981

For sale by the Superintendent of Documents, U.S. Government Printing Office, Washington, DC 20402
Price $9.50
(Add 25 percent for other than U.S. mailing).

Foreword

The Proceedings contain the papers presented at the Twelfth Symposium on Optical Materials for High Power Lasers held at the National Bureau of Standards in Boulder, Colorado, on September 30 - October 1, 1980. The Symposium was jointly sponsored by the National Bureau of Standards, the American Society for Testing and Materials, the Office of Naval Research, the Defense Advanced Research Projects Agency, the Department of Energy, and the Air Force Office of Scientific Research. The Symposium was attended by over 150 scientists from the United States, the United Kingdom, Japan, France, and West Germany. It was divided into sessions devoted to the following topics: Materials and Measurements, Mirrors and Surfaces, Thin Films, and finally Fundamental Mechanisms. The Symposium Co-Chairmen were Dr. Harold E. Bennett of the Naval Weapons Center, Dr. Alexander J. Glass of the Lawrence Livermore Laboratories, Dr. Arthur H. Guenther of the Air Force Weapons Laboratory, and Dr. Brian E. Newnam of the Los Alamos Scientific Laboratory. They also served as editors of this report.

The editors assume full responsibility for the summary, conclusions, and recommendations contained in the report, and for the summaries of discussion found at the end of each paper. The manuscripts of the papers presented at the Symposium have been prepared by the designated authors, and questions pertaining to their content should be addressed to those authors. The interested reader is referred to the bibliography at the end of the summary article for general references to the literature of laser damage studies. The Thirteenth Annual Symposium on this topic will be held in Boulder, Colorado, November 17-18, 1981. A concerted effort will be made to ensure closer liaison between the practitioners of high peak power and the high average power community.

The principal topics to be considered as contributed papers in 1981 do not differ drastically from those enumerated above. We expect to hear more about improved scaling relations as a function of pulse duration, area, and wavelength, and to see a continuing transfer of information from research activities to industrial practice. New sources at shorter wavelengths continue to be developed, and a corresponding shift in emphasis to short wavelength and repetitively-pulsed damage problems is anticipated. Fabrication and test procedures will continue to be developed, particularly in the diamond-turned optics and thin film areas.

The purpose of these symposia is to exchange information about optical materials for high power lasers. The editors will welcome comment and criticism from all interested readers relevant to this purpose, and particularly relative to our plans for the Thirteenth Annual Symposium.

H. E. Bennett, A. J. Glass
A. H. Guenther and B. E. Newnam
Co-Chairmen

DISCLAIMER

Certain papers contributed to this publication have been prepared by other than NBS authors. These papers have not been reviewed or edited by NBS; therefore, the National Bureau of Standards accepts no responsibility for comments or recommendations contained therein.

Certain commercial equipment, instruments, and materials are identified in this publication in order to explain the experimental procedure adequately. Such identification in no way implies approval, recommendation, or endorsement by the National Bureau of Standards, nor does it imply that the equipment, instruments, or materials identified are necessarily the best available for the purpose.

CONTENTS

Materials and Measurements

Mirrors and Surfaces

Thin Films

Fundamental Mechanisms

SYMPOSIUM WELCOME

Brian E. Newnam
Los Alamos National Laboratory
Los Alamos, New Mexico 87545

On behalf of my fellow co-chairmen, Hal Bennett, Alex Glass, Art Guenther, and myself, Brian Newnam, I welcome you to the Twelfth Annual Symposium on Optical Materials for High Power Lasers. This ongoing series of meetings continues to be of importance to and attracts participants from the laser community around the world. To our foreign guests from the British Isles, Canada, England, France, Japan, Scotland, and West Germany, we extend our special greetings.

Once again we are indebted to our gracious hosts here at the National Bureau of Standards in Boulder. In particular, we acknowledge the overall support of Robert A. Kamper, Chief, of the Electromagnetic Technology Division, the coordination activity of Aaron A. Sanders, Group Leader of the Optical Electronic Metrology Group, and the helpful assistance of his secretary, Pat Rice. In addition, this year Art and Alex brought their secretarial staff from Kirtland and Livermore, namely Pat Whited and Mary Ann George, to conduct the registration. The services of Giovanni Fiorenza and Allan Stewart of the Air Force Weapons Laboratory are also appreciated. I should also mention that David Milam of Lawrence Livermore Laboratory, a well-known veteran of these meetings, served us well in the pre-conference organization.

As many of you have experienced, the printed proceedings of these Laser Damage Symposia in our personal libraries are frequently borrowed by interested colleagues. These valuable volumes have become hard-to-replace collector's items. So, I am pleased to report that the ASTM has recently republished, and offers for sale, the proceedings for the years 1977, 1978, and 1979 under their publication numbers STP 655, STP 689, and STP 726, respectively.

Further good news comes from Art Guenther who told me that the library staff at the Air Force Weapons Lab is preparing a bound compilation of the first 10 year's proceedings from 1969 to 1978. It will include listings by author, co-author, title, subject, and materials. The published abstracts will also be included. Art expects it to be ready in 1981, and it will be distributed to registrants at this year's symposium as well as the past contributors not presently in attendance.

Since the first Laser Damage Symposium in 1969, interest in this area of research has shown a large increase. As indicated by both the number of papers presented and the number of registered participants, shown in the bar graph (Fig. 1), the level of activity peaked in 1977. Since that time, participation in these symposia has been consistent at the level of approximately 45 contributed papers and 150 registrants. Although one might consider that this is a maturing field, it is apparent to most of us that there is a substantial amount of work yet to be done.

Each year's damage symposium has a different character - either some new understanding, or a concentration of papers on a particular aspect by a number of researchers, or even a controversial paper. In the early seventies, self-focusing and plasma formation at window surfaces received great attention. In 1978, we celebrated our Tenth Annual Symposium by devoting a portion of the proceedings to invited review papers summarizing the state-of-the-art in the primary topics. Last year, the characterization of thin films and their impurities received special emphasis.

I will not hazard suggesting which subjects at this year's symposium will, in retrospect, appear as having received the most significant advances in our knowledge and understanding. One can observe, however, that the papers are fairly well divided among the four major headings of bulk materials and measurements, mirrors and surfaces, thin films, and breakdown theory.

What have we learned over the past decade or so? We have made certain progress in a number of areas. Let me cite some examples. First, we came to understand the phenomena of self-focusing. Second, we learned how standing-wave electric fields are responsible for the once mysterious asymmetry of front- and rear-surface thresholds of windows. Third, we developed experimental methods to separate the surface- and bulk-absorption components of laser windows. Fourth, we determined, but yet do not understand, that a half-wave thick SiO_2 barrier layer, deposited between an AR coating and substrate, increases, on the average, the laser damage resistance. Likewise, for half-wave SiO_2 overcoats on multilayer reflectors. Fifth, we found that testing of a statistically significant number of samples is necessary to determine a dependence reliably, especially with thin-film optics which have so many materials parameters in the mix. As a last example, we learned that for the most damage-resistant materials there is generally no correlation of the average linear absorption properties and the damage threshold. It is apparent that localized impurities of even sub-micron dimensions are the limitation.

What areas now deserve our special attention or continued emphasis? For particular laser systems operating at high-repetition rates, we need to know if and how our experiments with 1-on-1 irradiation can be related to multi-shot survival. Perhaps, single-shot-per-site tests can be used for identifying superior materials and designs, but supplemental N-on-1 tests may be necessary. Next, we need to further examine how large a test laser beam must be to provide threshold data applicable to large laser systems. In the past year, damage tests with large-diameter (~1 cm) beams produced some disappointing surprises when contrasted to tests with very small beams (0.1-mm diameter). Still yet another need is for development of rugged optical components for the ultraviolet wavelengths from 190 to 350 nm. Research in this spectral region is still in its infancy, and large projects such as laser fusion, laser isotope separation, as well as military applications, have needs here.

To solve the existing damage problems, we need to bring to bear the well-developed talents from outside as well as within the laser community. For timely progress in

understanding surface- and thin-film damage resistance, for example, there is need for close collaboration of 1) the producers of optical components, 2) researchers who have perfected diagnostic techniques for measuring spatially-resolved optical properties, e.g., absorption, 3) surface physicists, and 4) experts in the measurement of damage thresholds. Recognizing that such diverse talents focused on particular problems might well identify solutions, the Department of Energy, the Air Force and Navy laboratories, within the past year, did convene special groups of materials and laser experts to consider difficult optics problems in the ultraviolet and infrared.

In conclusion, I wish to acknowledge the sponsorship and financial support of this meeting by six organizations. These include the American Society for Testing and Materials, the National Bureau of Standards, the Department of Energy (in particular, Lawrence Livermore Laboratory), the Office of Naval Research, the Defense Advanced Research Projects Agency, and a new sponsor, the Air Force Office of Scientific Research. Sponsorship by so many prominent organizations underlines the need for continued progress in developing and testing optical materials for high-power lasers.

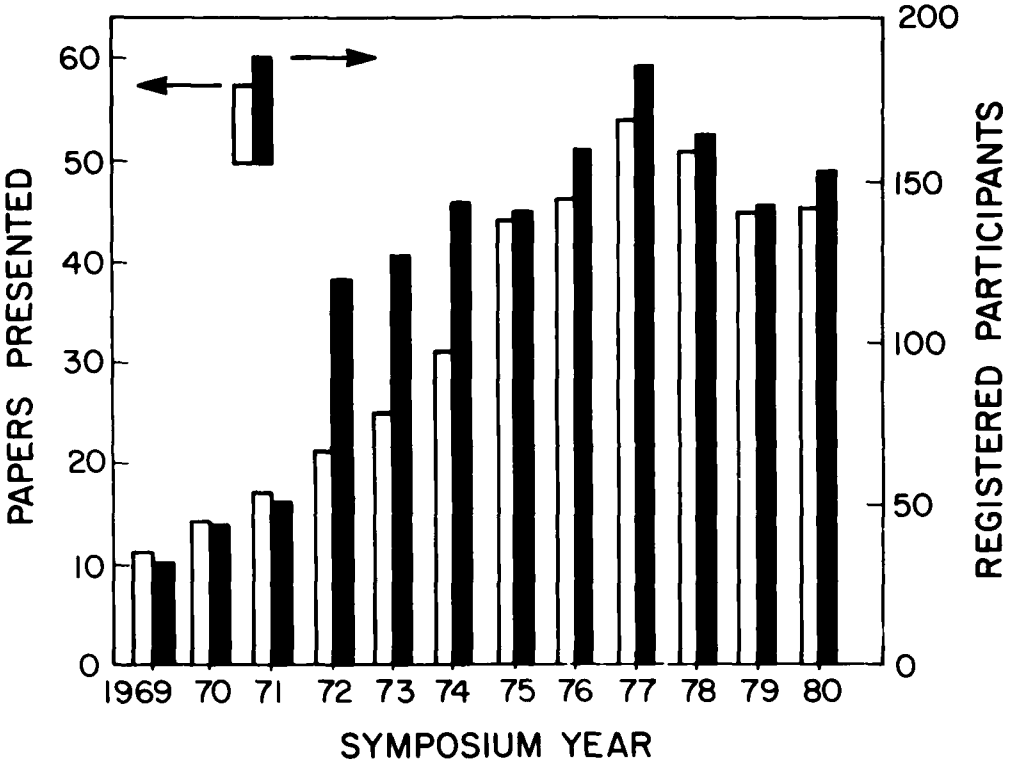
PAPERS PRESENTED
REGISTERED PARTICIPANTS
SYMPOSIUM YEAR
0
10
20
30
40
50
60
0
50
100
150
200
1969
70
71
72
73
74
75
76
77
78
79
80

REMARKS TO THE 12TH ANNUAL SYMPOSIUM ON
OPTICAL MATERIALS FOR HIGH-POWER LASERS
Boulder Damage Symposium
30 September 1980

Major Harry Winsor
AFOSR/NE
Bolling AFB, D. C. 20332

I am pleased to once again address my remarks to this symposium. As many of you have noted, I have transferred to a new job. Effective 26 September 80, I left the Defense Advanced Research Projects Agency (DARPA) and assumed my new duties as a Program Manager in the Electronic and Material Sciences Directorate (NE) of the Air Force Office of Scientific Research (AFOSR).

This change has raised two topics which I wish to address: First, what is the status at DARPA/MSD and who has taken responsibility for the programs I managed at DARPA and second, what are my new responsibilities at AFOSR?

Both organizational and managerial changes have occurred at DARPA since I last addressed this gathering. The old Materials Science Office (MSO) has become the Materials Sciences Division (MSD) of the new office called the Defense Sciences Office (DSO). The director designate of DSO is Dr. Elliot Leventhal, who is coming to DARPA from Stanford University. The deputy director of DSO is Dr. Richard Reynolds formerly of MSD. Dr. Edward Van Reuth has assumed the position of acting director of MSO, which now has "three and a half" program managers: Dr. Michael Buckley, Dr. Sven Roosild, Lt. Col. Lauren Jacobson (USAF), and Dr. Joseph Friebele (half-time). The programs I managed have been distributed to three of these program managers, Drs. Buckley, Jacobson, and Friebele's. Those attending this symposium are primarily interested in Dr. Friebele programs, since he has assumed responsibility for all the electro-optical and optical materials efforts I formerly managed. Dr. Buckley has assumed the Laser Aided Machining effort into his Advanced High Speed Machining program, and the Autoreplication program. He has also taken responsibility for two new programs I may be contributing to from AFOSR: Ultimate Ablator and Propellant Science.

The status of the major programs Dr. Friebele has assumed is as follows: the Laser Windows, Coatings and Mirrors program has been narrowed down and concentrated on the development of thin films suitable for HF laser mirrors and windows in a space environment. This program has demonstrated almost complete success, as you will hear later. The UV-Visible Laser Components program has taken a turn toward the basic research direction with the expansion of a thrust to understand the growth habits of high quality thin films in intense ultra-violet and visible pulses, and the beginning of a university

effort to understand the growth habits of high quality thin films. The Large Optics Materials Program is funding a 60 cm diameter carbon-carbon composite mirror substrate, and has expanded into the area of particulate composites in its search for zero coefficient of thermal expansion (CTE). We are currently demonstrating a fist order zero in the CTE of a composite consisting of niobia spheres in a nickel matrix. The amounts of nickel and niobia can be adjusted to position the zero in the CTE anywhere in the region OK-300K.

Other programs of interest to the people attending this conference are proceeding normally. A new program to study highly efficient laser host materials has just started. New ideas in this area should be referred to Dr. Friebele, as should new directions for research on Fiber Optic Sensor Systems (FOSS). FOSS is discussed extensively elsewhere, so all I will say here is that the program has a very successful record to date and has attracted a high degree of attention in Navy and Defense circles.

The Forged Flir Optics program is nearing a major decision point. The program has produced forged potassium bromide lenses which have at times nearly met the required specifications for the Army's MOD FLIR system. If a moisture protection coating can successfully protect the KBr in the military environment, forged lenses will be able to successfully fill a number of potential roles in military systems, as well as scientific applications. Forged lens technology looks very promising at this point.

I will also discuss one program Dr. Buckley has taken over: The Laser Aided Machining Program has been renewed for a 3 year period to complete the definition of the technology of combining machining with laser irradiation. Materials successfully machined to date include superalloys, hardened tool steel, silicon carbide, silicon nitride, lithium aluminum silicate, alumnia, mild steel, and many others.

At this time, I would like to thank all of you who have worked with me while I have been at DARPA, especially those of you who have been responding to my requests for completion report preparation so that my programs can be properly documented as I leave, and those of you who have helped me manage the 15 program areas in which I have worked. I could not have done anything without you.

Let me now say a few words about some potential new research area on the horizon. The area of laser damage is a good place to start. I notice a striking fact that I hope only seems to be little appreciated: Laser damage prevention is very closely related to research the electronics industry is performing on laser processing of semiconductors. In fact, semiconductor processing research may provide the best diagnostics possible on impurity migration, phase changes, and micro-yield under laser loading. I hope laser damage people make full use of the rapidly growing body of these "controlled laser damage" results to understand the materials mechanisms responsible for the laser damage they are trying to avoid. This interaction appears strikingly fertile from my perspective.

The area of "controlled damage" to materials needs to be studied from the materials side for another purpose: the development of materials which can handle very high laser fluxes without prohibitive damage, for use as beam dumps for example. Beam dumps for a

space based laser will require good ablation resistance and very high mass efficiency, requirements not particularly important for ground based systems.

I could mention other programs at this point, but the above examples will serve very well. DARPA and AFOSR need more good ideas and welcome them from any source.

Speaking of AFOSR, let me now say a few words about my new job. My duties at AFOSR may include some of the new programs I was investigating while at DARPA, notably the Gun Propellent Science program and the Ultimate Ablator program. My new AFOSR responsibilities include microlithography, surface acoustic wave spectroscopy of semiconductors, dielectrics, and metals.

The new DARPA programs are envisioned to start during FY 81(Oct 80-Sep 81) and increase to approximately $1.2M/yr and $800K/yr expenditure rates, respectively. The AFOSR program has some room for new starts in either the sub-micron lithography area, the definition of electronic and physical properties at very small sizes, and improved microwave and millimeter wave signals processing materials. The program's expenditure rate is currently about $1.2M/yr.

Should you have any ideas for new programs in these areas, or know a colleague who does, I may be phoned at (202) 767-4931 (Autovon 297-4931), telecopied at (202) 767-4977 (6 minute automatic telecopy machine), or contacted at the following address:

AFOSR/NE
ATTN: Major H. Winsor
Bolling AFB, DC 20332

Should you have any further questions, or ideas which do not fall under my listed program responsibilities, I will try to direct you to the responsible person or agency. I look forward to our continued relationship.

Finally, let me thank the organizers of this Symposium. They have done a superlative job for 11 years and are still going strong and getting better. I have especially enjoyed working with them and hope my new job allows me to continue attending this annual gathering. It has a very special place in my heart, largely due to the solid repeat performers the organizers have assembled. I also wish to thank them for the opportunity to present these remarks, and all of you for listening.

Boulder Damage Symposium 1980

ASTM Welcome

John A. Detrio
University of Dayton
Dayton, Ohio 45469

On behalf of the American Society for Testing and Materials I welcome you to the 12th Annual Symposium on Optical Materials for High Power Lasers - The Boulder Damage Symposium.

The conference organizers, Hal Bennett, Alex Glass, Art Guenther, and Brian Newnam, have put together a fine program with 25 presented papers and 20 poster papers. The next two days should be filled with stimulating papers and opportunities for discussions.

I would like to depart from the usual platitudes that you might expect from the very first welcome speaker and extend a challenge to you. I extend the challenge because the ASTM is charged with developing consensus standards; standard definitions, standard test methods, standard practices, and even standard materials. This is a voluntary effort requiring the cooperation of users and producers in the development of standards and specifications.

In the 12 years that this conference has been held, starting with the ASTM sponsorship of the very first meeting, we in the subcommittee "on Lasers" have yet to develop and adopt a single standard document. We have one in draft form but nothing published.

I challenge you to participate in the development of damage standards for these reasons:

1. Better agreement on definitions and test methods would improve communication and eliminate many of the disagreements over measured values of damage threshold.
2. The availability of standard test methods would simplify the procurement of laser components. Producers and users would be talking the same language.
3. To develop good standard test methods you would have to perform interlaboratory exchange of specimens. These Round Robins would permit the precision and accuracy of test methods to be specified. Round Robin participation can also be a humbling experience--maybe you're not as good as you think you are.
4. This hard close look at the test methods will improve the understanding of the measuring processes. You would have to consider factors such as
   Scaling with pulse duration,
   Scaling with area,
   Scaling with wavelength,
   Sampling practices, and
   Statistical analysis.

Plus all of the measurement practices already required (power, beam profile, and pulse shape).

These remarks only briefly summarize the challenges and rewards of working on standards. It's hard work with limited, apparent short-term reward. In the long run, better quality optics and better quality measurements will repay the costs.

I will end with another invitation. We will meet tonight in an informal rump session to assess the needs for standards and to solicit your ideas on that subject. Producers, coaters, polishers, and materials suppliers should attend. If you are concerned with quality assurance - or just interested in better science - if you think you're up to it, join me.

Enjoy the conference!

Laser Induced Damage in Optical Materials

Twelfth ASTM Symposium

September 30 -- October 1, 1980

The Twelfth Annual Symposium on Optical Materials for High Power Lasers (Boulder Damage Symposium) was held at the National Bureau of Standards in Boulder, Colorado, September 30 -October 1,1980. The Symposium was held under the auspices of ASTM Committee F-1, Subcommittee on Laser Standards, with the joint sponsorship of NBS, the Defense Advanced Research Project Agency, the Department of Energy, the Office of Naval Research, and the Air Force Office of Scientific Research. Over 150 scientists attended the Symposium, including representatives of the United Kingdom, France, Japan, and West Germany. The Symposium was divided into sessions concerning Materials and Measurements, Mirrors and Surfaces, Thin Films, and finally Fundamental Mechanisms. As in previous years, the emphasis of the papers presented at the Symposium was directed toward new frontiers and new developments. Particular emphasis was given to materials for high power systems. The wavelength range of prime interest was from 10.6 μm to the uv region. Highlights included surface characterization, thin film-substrate boundaries, and advances in fundamental laser-matter threshold interactions and mechanisms. The scaling of damage thresholds with pulse duration, focal area, and wavelength was discussed in detail. Harold E. Bennett of the Naval Weapons Center, Alexander J. Glass of the Lawrence Livermore Laboratories, Arthur H. Guenther of the Air Force Weapons Laboratory, and Brian E. Newnam of the Los Alamos Scientific Laboratory were co-chairmen of the Symposium. The Thirteenth Annual Symposium is scheduled for November 17-18, 1981 at the National Bureau of Standards, Boulder, Colorado.

Key words: laser damage; laser interaction; optical components; optical fabrication; optical materials and properties; thin film coatings.

1. Introduction

The Twelfth Annual Symposium on Optical Materials for High Power Lasers (Boulder Damage Symposium) was held, as in previous years, at the National Bureau of Standards in Boulder, Colorado, September 30 - October 1, 1980. The Symposium was held under the auspices of the ASTM Committee F-1, Subcommittee on Laser Standards, with the joint sponsorship of NBS, the Defense Advanced Research Projects Agency, the Department of Energy, the Office of Naval Research, and the Air Force Office of Scientific Research. Working sessions of the Committee F-1 Subcommittee on Lasers were held on Monday, September 29. Over 150 scientists attended the Symposium, including representatives of the United Kingdom, France, Japan, and West Germany. The Symposium was divided into sessions concerning materials and Measurements, Mirrors and Surfaces, Thin Films, and finally Fundamental Mechanisms. As in previous years, several poster sessions were held. The general consensus of those presenting poster papers and those viewing them was highly favorable. In all, over forty technical presentations were made. Harold E. Bennett of the Naval Weapons Center, Alexander J. Glass of the Lawrence Livermore Laboratories, Arthur H. Guenther of the Air Force Weapons Laboratory, and Brian E. Newnam of the Los Alamos Scientific Laboratory, were co-chairmen of the Symposium.

The purpose of these symposia is to exchange information about optical materials for high power lasers. The authors will welcome comments and criticism from all interested readers relevant to this purpose and particularly relative to our plans for the Thirteenth Annual Symposium, scheduled for November 17-18, 1981, at the National Bureau of Standards, Boulder, Colorado.

2. Principal Conclusions

The importance of surface as well as volume absorption in evaluating the performance of laser window materials was reemphasized this year, and the usefulness and validity of relatively new techniques such as photoacoustic spectroscopy, infrared wavelength modulation spectroscopy, and pulsed calorimetry for separating and measuring these small absorption levels were demonstrated. Flux dependent absorption coefficients caused either by two photon absorption or other high intensity effects were reported both for some alkali halides and for semiconductors. Large spot size laser damage results on NaCl and KCl were reported and the validity, in this case, of scaling the results of small spot size measurements was demonstrated. A new glass family, the hafnium fluorides, was reported. They have low absorption coefficients in the 3 to 5 μm region, low indices of refraction, and good chemical properties. Press-forged LiF with increased resistance to micro-creep and good optical properties was achieved and a simplified theory for predicting the thermally induced distortion of infrared windows was described. Finally a preliminary survey of window materials for iodine lasers and a general survey of properties available for most potential laser window materials were given.

It was most gratifying to note that the major topics discussed in the area of mirrors and surfaces centered on new fabrication procedures for the polishing of metallic elements. This is not surprising considering the growing utility of metal optics and the improvements that are continually being made in single point diamond turning of such elements.

Advances were reported in both classical polishing techniques and more innovative, recently developed techniques. In particular, the report of a float polishing technique developed in Japan for processing defect-free metallic surfaces was a highlight of the meeting. In the procedure employed, a slurry of abrasive compound is passed across the surface to be polished which is suspended above a diamond turned lap but not in direct contact with the lap. This technique offers great promise for commercial application. It has already gained wide acceptance for finishing precision electronic elements such as tape recording heads. Other advances in metal optics concern the electron beam processing of bulk copper substrates after having been diamond turned. This is also a new procedure and offers great promise when combined with "hard" diamond tuning (negative rake angle). Single point diamond turned surfaces continue to perform better than conventionally polished metals. However, multishot damage thresholds are considerably below those exhibited in single snot threshold experiments.

Concerning the interaction between laser irradiation and metal surfaces, considerable discussion of fundamental mechanisms of pulsed lasers was held concentrating on the differences observed for various crystalline orientations. To this was added the revelation that the surface plasma produced under repetitively pulsed laser irradiation leads to enhanced thermal and mechanical coupling between the laser and the metal surface. An extension of this work concerned the subject of laser working of metals in various environments. Finally, realizing the wide acceptance of this type of optical element, excellent reflectivity, change in reflectivity with temperture and basic thermal data for copper, silver, and aluminum was presented. As a result, damage thresholds in many cases now approach the theoretical limit, albeit only over small areas. It was pointed out that dust and defects present on optical surfaces do not play anywhere near the important role demonstrated for pulsed irradiation when the laser is operated CW or with long pulses.

Concerning dielectric surfaces, continual progress in the utility of CO_2 laser-treated fused silica was evidenced although this technique does not appear to be as near transfer to the industrial community as the float polishing technique previously described. In the crystalline area, there was a correlation shown between grain size and absorption in CVD ZnSe.

In the area of thin films, the principal developments heard at the Symposium fell into the category of characterization instrumentation, deposition technique development, and improved coating performance. This conference has always stressed the need for advances in technique to characterize thin films such that correlations between film structure and optical property as a function of deposition techniques could be identified. This year the use of multiple-reflection spectroscopy to measure the complex refractive index, as a measure of impurity concentration and location, was heard. New ellipsometers have been developed and measurements in the 3.4 and 4 μm and 1 to 12 μm spectral region were reported together with a description of the capabilities of various polarizers for the infrared region. New optical techniques such as two beam interference, to obtain fringe spacing of from 5 to 105 μm at variable wavelengths, revealed no difference in threshold versus beam size as compared to single large beam irradiation. That conclusion, however, may be misleading because of the pulse lengths employed. Impurities smaller than 1 micron are apparently responsible for damage initiation in all cases.

Concerning deposition development, DC magnetron sputtering demonstrated greatly increased damage thresholds for silicon films as compared to other processes such as UHV or E-gun produced films. The lower reported absorption being a direct result of higher packing density and correspondingly lower defect density. It was pointed out that ion beam deposition, particularly when coupled with ion surface cleaning offers great advantages in producing stress-free, low loss optical coatings. Thick coatings of $Ge_{33}As_{12}Se_{55}$ have been developed which afford an environmental shield for hygroscopically sensitive elements employed at 10.6 μm. A most exciting discussion at this year's Symposium concerned diamond-like carbon films deposited on silicon surfaces by ion beam deposition. The films appear to be pinhole free. The high quality of these films may result from the large mobility of energetic carbon atoms and the tendency to minimize free energy resulting in a very smooth film surface.

While a large number of data were heard on the damage thresholds of films of different designs at various wavelengths, pulse lengths, spot sizes, etc., the major conclusion again indicated decreased damage thresholds at the shorter wavelengths, e.g., 532 nm compared to 1064 nm. Some films composed of SiO_2 and BK-7 glass indicated variations in performance as a result of the process-dependent variation in the deposition of titania. Of more immediate practical importance to the commercial sector was some recent work on damage resistance coatings for $LiNbO_2$.

A quantitative model for the fundamental mechanisms under which optical materials fail under intense irradiation is still incomplete. Pulsed laser damage, in particular, is inadequately understood. Questions about intrinsic damage include the relative importance of multiphoton absorption as compared to avalanche ionization and the relative importance of self-focusing and self-defocusing in the damage process. The importance of impurities and localized defects in the damage process under various conditions is also incompletely understood. Progress was made this year both in reporting carefully controlled damage measurements and in identifying cases where the experimental results did agree with theoretical predictions. In other cases, NaCl for example, evidence was presented that what had previously been thought to be an intrinsic process was actually defect-dominated and that defects, besides directly absorbing radiation, contribute to the modification of free carrier concentrations through the efficient removal of electron hole pairs. Electron concentration is also invoked in analyzing the electron-avalanche theory and an argument was given that the relaxation time should be dependent both on optical freuency and on instantaneous field strength. Solid state theory was also invoked in calculating the two-photon absorption in solids more accurately. The large disparities found between the predictions of earlier more approximate calculations and experiment have now been reduced by these more detailed band structure calculations to a factor of two or less, a very encouraging achievement. The simplistic initial assumption widely held 10 or 12 years ago that pulsed laser damage to materials was a simple thermal process has thus now been largely superseded by attempts to apply the powerful tools of solid state physics to resolve this complicated problem.

3. Summary of Papers

The subject matter of the Twelfth Annual Symposium covered four broad areas of interest to the high power laser community. These are (1) Materials and Measurements, (2) Mirrors and Surfaces, (3) Thin Films, and finally (4) Fundamental Mechanisms. These Conference Proceedings are organized accordingly. In this Section, a concise summary of each paper is provided. Closely related papers are discussed together, whenever possible. The interested reader is referred to the complete manuscript of any paper for further details. Our intention here is to provide the reader with an overview of the Symposium and to identify the topics of current interest, and the authors and their organizations. Each topical area is introduced with a brief statement of the underlying problems and the status of understanding within the area of interest as well as to highlight this year's presented papers.

3.1 Materials and Measurements

A key factor in the performance of laser window materials concerns their absorption of energy. This absorption can take place at the surface or in the volume of the window material and can either be independent of flux density or, in some cases, can increase with increasing flux. The opposite effect, thermal bleaching by the laser flux, is only infrequently seen. Since the absorption coefficients of good laser window materials are typically in the 10^{-3} to 10^{-5} cm^{-1} range and surface absorption gives comparable absorption levels, measurements on conventional spectrophotometers are too inaccurate and special techniques have to be devised to detect and identify the absorption of interest. Among these have been calorimetry, emittance measurement, photoacoustic spectroscopy, internal reflectance spectroscopy, and most recently infrared wavelength modulation spectroscopy. The promise of these various techniques is now being fulfilled and several papers this year at the Boulder Damage Conference report their utilization to clarify our understanding of the absorption process.

One of the most pressing needs has been the development of a technique for scanning the absorption spectrum of the various window materials as a function of wavelength. Several of the above mentioned techniques can, with varying degrees of difficulty, be applied to this problem. One of the most promising of these, infrared wavelength modulation combined with calorimetry, was reported last year by R. Braunstein, et al. This year he and R. Kim of the University of California, Los Angeles, in collaboration with M. Braunstein of Hughes Research Laboratories have reported the results of measurements of the spectral distribution of absorption in the 2.5 to 12 μm wavelength region for CaF_2, LiF, NaCl, LaF_3, BaF_2, MgF_2, SrF_2, and MgO. KBr and KCl were reported last year. Total absorption/cm of these samples, which includes both volume and surface absorption, were all roughly in the 10^{-3} cm^{-1} range. The data showed considerable richness in spectral detail. Certain dominant bands tended to appear in many of the samples. Among these were the 2.8 μm band, identified as physisorbed OH^-, the 3.0 μm band, identified as bulk or chemisorbed OH^-, the hydrocarbon overlap bands in the 3 to 4 μm region, the CO_2 band at 4.2 μm, liquid water at 4 to 6 μm, and carbonates in the 6 to 8 μm region. A major contribution to the observed absorption was made by physisorption at the surface of the samples and significant reductions in absorption were observed when the samples were in a dry nitrogen atmosphere. An exception was LiF, which appeared to be the least surface active of any of the materials studied.

The data obtained by the infrared wavelength modulation system complement data on surface absorption obtained at discrete wavelengths by techniques such as calorimetry and photoacoustic spectroscopy (PAS). Since PAS probes only to depths below the test specimen surface of the order of the thermal diffusion depth and since it has a sensitivity of ~ 10^{-6}, it is a good tool for studying surface absorption of adsorbed species such as water. Recall that in absorbing regions, a monolayer of water can cause surface absorption levels of ~ 10^{-4}. J. McDavid and S. Yee of the University of Washington have reported PAS measurements on KCl and NaCl at 10.6 μm. Results on both materials were similar. The samples were first etched to reduce surface absorption to a minimum. Upon initial exposure to nitrogen passed through an NaCl saturated water solution the absorption of KCl increased

by 3.0×10^{-4}. A "second layer" slow-rate additional adsorption process resulted, after 7 days of exposure, in an increase in absorption of a factor of 8 over the value for KCl prior to exposure.

PAS was also used by E. Van Stryland and M. Woodall of North Texas University to study 2 photon absorption in CdS at 1.06 μm wavelength. The sensitivity gain was as much as 10^3 times compared to transmission measurements for low absorption samples. Since the fractional change in PAS caused by two photon absorption is independent of sample thickness, it may be possible to use this technique to observe non-linear absorption even in optical coatings. The transmission decreased, for the bulk CdSe tested here, by about a factor of two as the incident intensity increased from zero to 400 MW/cm^2. For CdTe the increase was even larger.

The validity of results obtained using PAS was checked by N. Fernelius, D. Dempsey, and D. O'Quinn of the University of Dayton Research Institute. Results obtained on samples cut from one CaF_2 single crystal boule at 1.3 μm for surface and bulk absorption are reported. Three methods were used, (1) laser rate calorimetry on samples of various thicknesses, (2) the long bar calorimetric technique, and (3) photoacoustic spectroscopy. An upper limit of 0.3 cm was established for the ratio $r = \beta_S/\beta_B$ by the long bar technique, where β_S is the surface absorption and β_B the volume absorption/cm. Using samples of varying thickness, a value of $r = 0.14$ cm was obtained, and using photoacoustic calorimetry a value of 0.07 was measured. The latter measurements are within a factor of two of each other and in agreement with the results of the long bar technique. Considering the experimental uncertainty, the results of all three independent measuring techniques are consistent, e.g. The volume absorption was measured to be 0.61×10^{-3} cm^{-1} using calorimetry and 0.68×10^{-3} cm^{-1} from photoacoustic measurements.

In calculating absorption coefficients and damage thresholds for alkali halides, it is usually assumed that the absorption coefficient is independent of flux density. Data obtained by S. Wu and M. Bass of the Center for Laser Studies at the University of Southern California on NaCl, KCl, and KBr at a wavelength of 10.6 μm indicate that this assumption is valid only for flux densities below about 100 MW/cm^2. At higher flux densities (110 MW/cm^2 for KBr, 140 MW/cm^2 for NaCl and KCl), the absorption coefficient increases abruptly by as much as 70 percent and reaches a new plateau. An additional marked increase in absorption is observed at the damage threshold for KBr which may have been associated with plasma formation. Possible models suggested to explain the increase in absorption with flux density are (1) a single photon process in a three level energy level system, (2) a multiphoton process, or (3) high field induced primary defects and electron avalanche. More data is required to evaluate these possibilities. To obtain the measurements just discussed, Wu and Bass developed a repetatively pulsed laser calorimetric technique with low repetition rate (5 to 8 Hz). The theory required to analyze this data is presented in their paper and its measurement technique is described.

There is always a danger in scaling the results of small spot size tests of laser damage threshold to the large areas required for engineering applications. J. Detrio and D. Dempsey of the University of Dayton Research Institute, Dayton, Ohio, have remedied this

problem for KCl and NaCl at 10.6 μm by reporting large spot size (1.6 cm diam.) long pulse length (10 μsec) tests on NaCl and KCl which should be useful for system design. In addition, there is surprisingly good agreement for NaCl with the thresholds scaled from the short pulse length (1.6 n sec) small spot size (0.18 cm diam.) results reported earlier by Soileau and Bass. The observed large spot size NaCl threshold, 12.0 J/cm^2, was doubled by etching the surface, whereas the unetched, etched,and coated KCl samples all had damage thresholds of about 10 J/cm^2.

Development of new and better infrared materials is a key to progress in several areas of infrared laser development as well as to other infrared activities. M. Drexhage, B. Bendow and H. Lipson of Rome Air Development Center, in collaboration with C. Moynihan of the Vitreous State Laboratory, Catholic University of America, have continued their exploration of new infrared glasses for the 3 to 5 μm wavelength regions and shorter wavelengths. Last year they reported on fluorozirconate glasses. Now they report on several new hafnium fluoride glasses. The intrinsic multiphonon absorption edges of these glasses are at slightly longer wavelengths than the Zr-based glasses. Absorption coefficients as low as 10^{-2} cm^{-1} have been achieved at a wavelength of 5 μm for some of these new glasses and the range of transparency extends into the ultraviolet. Intrinsic levels as low as 10^{-7} cm^{-1} at 3 μm are predicted from analysis of the multiphonon edges. Since their indices of refraction are ~ 1.5 and they have good chemical stability and low hygroscopicity, they offer considerable promise for a variety of infrared applications provided internal scattering can be reduced.

The theory and measurement of bulk damage in optical glasses has been the subject of many papers presented at these symposia, especially during the early 1970s. This year the topic was revisited by H. Hack and N. Neuroth of Jenaer Glaswerk Schott and Gen. of Mainz, West Germany who tested 39 types of Schott glasses using 3-ns laser pulses at 1.06 μm. They placed each sample (20 mm thick) in a gradually converging beam at a position 10 cm in front of the focus produced by a 1.1-m f.l. lens. At this plane the beam diameter was ~ 2 mm. The thresholds ranged from a low of 10 J/cm^2 to greater than 70 J/cm^2. Damage was observed to occur either at random points along the beam or in threadlike structures extending from the exit surface to some interior point. The pointlike damage associated with internal defects was not correlated with any other physical property of the glasses. The threadlike damage was interpreted as arising from self-focusing as quantified by a nonlinear index n_2. A plot of damage threshold versus n_2 was derived. The authors correctly pointed out that the absolute values of their internal damage thresholds could well have been influenced by concurrent surface damage. The proceedings of these symposia since 1969 have included consistent reports that, except for early damage on bulk inclusions, surface damage always occurs prior to bulk damage in a collimated or gently converging beam such as used in the present tests. Unfortunately, this complication renders the magnitude of these bulk damage thresholds and their correlation with nonlinear index of marginal value.

Lithium fluoride possesses a combination of optical properties which make it an attractive candidate material for use as windows in high-power, short-pulse ultraviolet and visible lasers. Press-forged samples can be made in sizes adequate for proposed

applications, but they often contain veils which induce unacceptable scattering and absorption at short wavelengths. Lithium fluoride is also susceptible to micro-creep, which can destroy the precise mechanical tolerances required in stringent optical appications. H. Vora and J. Ready of Honeywell Corporate Technology Center have now demonstrated that two-stage press-forging of lithium fluoride at the 90 percent deformation level can be achieved without introducing significant internal cloudiness and without increasing the optical absorption coefficient by more than about a factor of two in the visible and ultraviolet. Press forging also increases the microyield point by a factor of between three and ten. Significant micro-creep does not occur in LiF stressed below the microyield point.

The prediction of thermal lensing in high-average-power laser windows is a difficult challenge, particularly for polycrystalline material whose elastic and photoelastic coefficients are not well known. C. Klein, Research Division, Raytheon Company, has analyzed this question and shown that thermal lensing can be expressed in terms of two parameters, one of which reflects stress birefringence, and the other all other temperature induced effects. Photoelastic and elastic coefficients for polycrystalline CaF_2 and KCl and for ZnSe are calculated. It is shown that of these only CaF_2 can exhibit significant stress-birefringent effects. It can be negated by using single crystal windows oriented in the <111> direction. Windows made of KCl exhibit isotropic distortion patterns perhaps an order of magnitude larger than CaF_2 but an order of magnitude smaller than ZnSe and of opposite sign.

Iodine lasers present a new challenge to the laser materials community. N. Fernelius, D. Dempsey, D. Walsh, and D. O'Quinn of the University of Dayton Research Institute, in collaboration with W. Knecht of the Materials Laboratory of the Air Force Wright-Aeronautical Laboratories have now reported an initial survey of optical materials useful for iodine lasers. Since no iodine laser was available to them, the material survey was based on calorimetric measurements made using a Nd:YAG laser operating at 1.319 μm. There is some uncertainty in the quantitative application of these results to iodine lasers, which operate at ~ 1.315 μm, since the 1.3 μm water band is rich in spectral lines in this region. However, even if some discrepancies are found, the ranking of materials by the 1.319 μm absorption coefficient reported in this paper will prove helpful. The lowest absorption materials found were NaCl and KCl with $\beta \sim 3 \times 10^{-4}$ cm^{-1}. KBr, which was not measured, may have an even lower absorption coefficient. Fused silica, in contrast, ranged from 8×10^{-4} cm^{-1} and other glasses ranged as high as 1861×10^{-4} cm^{-1}. Glasses used in fiber optics in this range have absorption coefficients as low as 10^{-6} cm^{-1}, so there appears to be the possibility of improvement in windows for iodine lasers.

A survey of the available data on various materials of interest for laser windows was reported by Ann Glassman of the Avionics Laboratory, Wright-Patterson AFB, Ohio. A table summarizes the data found on various materials. There are significant gaps for several materials which should give direction for future experimental work. Key properties of CaF_2, KCl, NaCl, and ZnS, and the best bulk absorption coefficients of a variety of infrared materials at wavelengths of 1.3 μm, 2.7 μm, and 3.8 μm are also reported in the paper.

Damage thresholds of materials may result either from intrinsic or extrinsic

behavior. In the case of silicate or fluorophosphate laser glasses and KDP crystals tested at 1064 nm discrete damage sites are often generated within the bulk of the material. N. Thomas, J. Sonderman, S. Stokowski, and D. Walmer of the Lawrence Livermore National Laboratory have developed a camera to record the onset of bulk laser damage in such materials. In order to achieve good focus over the entire thickness of the sample they employ the Scheimflug condition, tilting the focal plane of the camera to bring amplifier disk samples, which because of experimental constraints are necessarily at an oblique orientation to the camera axis, into sharp focus at all points. Disk thicknesses up to 5 cm have been evaluated in this way. Damage sites found at threshold vary in density from 10^7/cc to less than 10/cc and damage volumes are small, from 1 to 5 μm in diameter. The authors attribute these sites to small foreign inclusions less than 1μm in diameter and suggest that they may be platinum particles introduced during the melting process.

3.2 Mirrors and Surfaces

The key to increasing the performance of metal mirrors and optical surfaces lies primarily in developing improved surface finishing techniques. This year we heard two most intersting presentations, one dealing with innovative advances in rather standard abrasive techniques and the other in employing lasers to anneal ground fused silica surfaces. Both techniques lead to measurable increases in laser damage thresholds, although only the first technique appears ready for wide spread industrial application at this time.

One of the highlights of this years symposium was a presentation by Y. Namba and H. Isura of the Department of Precision Engineering, Osaka University on the ultra smooth polishing of ceramics, dielectrics, ferrites, semiconductors and metals by float polishing techniques. This technique is not routinely employed in this country. However if the results on metal surfaces displayed by the Osaka group are any indication of the efficacy of this finishing method, there will be considerable interest to recommend this procedure. In this technique the samples are ultimately finished by suspending them above a diamond turned tin lap but not in direct contact, polishing particles suspended in a liquid vehicle gently pass by the surface of the material to be polished. Surprisingly adequate removal rates are achieved. However besides the <10 A° rms surface roughness achievable on metals or saphire, only a very thin disturbed or damaged laser is produced on the sample surface which is essentially stress free, compared to normal or bowl-feed polishing. When poly-crystalline materials are polished, various crystalline orientations exhibit different stock removal rates. In these cases recourse is made to chemical agents to afford uniform chemo-mechanical polishing rates for all crystallographical orientations. The specific agents vary depending on the material being polished and crystalline orientation involved.

Continuing studies initiated last year on the efficacy of CO_2 laser polishing of fused silica as a finishing technique to improve the damage sensitivity of silica substrates to pulsed 1.06 μm radiation, P. A. Temple and M. J. Soileau of the Michelson Laboratory at the Naval Weapons Center found that a reasonably sharp transition from damage prone to damage resistant surfaces takes place over a small CO_2 laser power range where material flow begins to take place. Preliminary data indicates that the damage threshold over small areas for

these processed surfaces can be as high as impurity free bulk damage thresholds. The surface of these processed parts still exhibits high strain attributed to microcrack healing, but this year use of a new multipass CO_2-laser polishing techniques resulted in less, albeit still generally unacceptable, disruption to the optical figure of the part; a reduction in surface stress was also noted. One thought immediately comes to mind, Is this technique now ready for the finishing of areas small dimension, such as fiber optic waveguide ends?"

A subject which always exhibits high interest at the damage symposium is metal optics and the interaction of lasers with metals. This year was no exception. The span of topics covered, attests not only to the utility of metal optics but the growing interest in lasers for metal working (e.g., rapid heat treatment, etc.). Papers reported on the fundamental properties of metals, damage threshold scaling with laser parameters, regrowth of laser irradiated metal and the micro and macro mechanical response of metal mirrors subjected to repetitively pulsed laser irradiation.

As one gains understanding into the vagaries of laser induced damage to metallic optical elements, the need for accurate fundamental physical properties becomes evident. To this end D. L. Decker and V. A. Hodgkin of the Michelson Laboratory of the Naval Weapons Center have determined the wavelength and temperature dependence of the absolute reflectance of Ag, Cu and Al from the visible (400 nm) to the infrared (10.6 μm) over the temperature range 270 to 450°K. Sample surfaces were prepared by as diverse techniques as vacuum evaporation and single point diamond turning. They conclude that the near infrared behavior in aluminum includes electron interband effects which yield non-Drude values of reflectance and dR/dT. Aluminum films appear more stable to temperature cycling than SPDT samples of Ag or Cu. In contrast to Al, the near-infrared behavior of Ag and Cu includes extrinsic surface and perhaps volume absorption which are both temperature and time dependent. In the far infrared the Drude theory quite adequately predicts the observed behavior for all metals studied.

Continuing their parametric assessment of damage thresholds to metal optics, J. O. Porteus, D. L. Decker, S. C. Seitel, and M. J. Soileau of the Michelson Laboratory at the Naval Weapons Center evaluated the threshold as a function of wavelength (1.06 μm to 10.6 μm); material (Cu, Ag and Au); pulse length (9 nsec to 2 μsec) and sample preparation method (SPDT, evaporation, etc.). The correlation of this experimental work with previously reported analytical models show quite good, if not excellent, agreement for melt threshold prediction over a portion of the range of parameter space studied. Agreement at 10.6 μm is to ±15 percent for all metals while only Ag agrees well at 3.8 μm and 2.7 μm. Low thresholds for Au and Cu at 3.8 μm suggest a roughness enhanced absorption. At 1.06 μm agreement between theory and experiment must be considered poor, probably implying failure of the Drude theory. Damage thresholds, melt, slip, flash, etc. but not crater formation scale nearly as the square root of pulse length at 10.6 μm.

In one of a pair of papers on regrowth in laser irradiated elemental metals and alloys, C. W. Draper of the Western Electric Engineering Research Center discussed the role of surface non-uniformities on coupling phenomena. The principal thrust of this presentation

concerned coupling effects as it relates to the uniformity in laser surface melting and laser surface alloying. The four principal causes of nonuniformities were identified as topographical, structural, compositional, chemical or impurity related and those arising from interference. It is these factors which are presently limiting the utility of uniform high quality laser surface processing. Furthermore these nonuniformities may act as sites for corrosion initiation or accelerated wear points from tribological factors.

In a companion paper C. W. Draper together with L. Buene, D. C. Jacobson, J. M. Poate and S. Nakahara of Bell Laboratories looked at epitaxial regrowth and defects in laser irradiated single crystal Ni in an attempt to address, from a fundamental standpoint, regrowth resulting from the interaction of pulsed lasers with pure metals. Epitaxially regrown layers were probed using Rutherford backscattering and channeling as well as by TEM. The later technique revealed a large number of extended defects such as dislocations. Considerable differences in surface character was noted where different crystal orientation (<100> and <111>) were irradiated even from the same boule. This difference was explained by fact that slip occurs more easily in the <111> plane of fcc structures resulting in a preponderance of defect nucleation centers (for regrowth).

Continuing his excellent work on pulsed laser effects on metal mirrors H. M. Musal, Jr. of Lockheed Palo Alto Research Laboratory contributed a paper this year on the initiation of surface plasmas from the interaction of pulsed lasers on metals. The primary issues covered in his work concerned the enhanced thermal and mechanical coupling resulting from the presence of a surface plasma. The plasmas are thought to be initiated by exo-electron emission associated with plastic micro-yielding of the metal surface under thermo-mechanical stress, induced by a sudden temperature rise on the surface. In a second consecutive step, plasma growth ensues via non-equilibruim ionization. From an analytical treatment, the critical temperture rise, threshold flux, and asympotic fluence required ror surface plasma formation are defined in terms of pertinent radiation, material and enviornmental parameters. The model is then employed to treat the response of copper mirrors subject to pulsed CO_2 lasers of various duration in various environments.

Because of the important role that reflecting metal optics play in CO_2 laser ICF systems at the Los Alamos National Laboratories, S. J. Thomas, C. R. Phipps, Jr. and R. F. Harrison of that organization have performed a study on pulsed optical damage limitations for coppper mirrors finished by different techniques. For the first time reports of the relative decrease in 1.06 μm damage thresholds corresponding to multiple shots and the loss of reflected beam brightness at high levels of irridation are given. Performance variation from operation in vacuum or ambient atmoshpere were also noted where complications in damage threshold evaluation due to air breakdown at the mirror surface was evident. The finding of greatest import relating to the operation of conventional polished metal mirrors in ambient air at high fluence (considerably above the $5J/cm^2$ in 1.7 nsec pulse length for air breakdown) is the onset of losses due to absorption, scattering etc. of the tail of the laser pulse by the breakdown plasma proper. The most obvious conclusion was drawn "don't use single shot damage thresholds when designing a sytem for multi-shot operation." If you must operate metal mirrors in air, single point diamond turned optical elements are preferred.

The session on mirrors and surfaces drew to a close with discussions on the importance or lack of importance in the cleaning of optical surfaces. The papers concerned themselves with very special situations regarding the interplay between laser parameters and specific material properties.

Continuing in their longstanding tradition of support to this meeting, the group at GEC Hirst Research Centre, England namely J. Foley, S. K. Sharma and R. M. Wood reported on carefully performed laser induced damage measurements to coated and uncoated Ge and CVD ZnSe substrates. They also measured the variations in absorptance of the samples under vacuum and ambient atmospheric conditions. For germanium, absorption was up to 50 percent higher after exposure to the atmosphere. The absorption was shown to be due to both a hydrocarbon and water layer, their exact character being related to previous cleaning and ambient conditions, while residual surface absorption depended in the large on the polishing technique employed. For the CVD grown ZnSe substrates, a correlation between grain size and bulk absorption coefficient was reported.

A presentation by H. L. Bennett of the Michelson Laboratory at the Naval Weapons Centers was suspiciously entitled "Insensitivity of the catastrophic damage threshold of laser optics to dust and other surface defects". However, the initial surprise rapidly dissipated when it became obvious that the paper dealt with a thermal response associated with either cw or long pulse length lasers. In this case, the role of surface defects should be predictable from an analysis of standing wave patterns, material properties and geometry of defects and simple heat transfer calculations. It was shown that while dust or other surface defects may cause small isolated damage sites to occur, these sites do not grow or produce catastropic damage unless of a critical dimension or density. The conclusions drawn in this paper should not be applied to laser optics intended for pulsed applications without further study!

3.3 Thin Films

Thin film optical coatings are the least damage resistant of the three classes of materials (bulk, surfaces and thin films) and are also the most complicated. To make permanent progress in our understanding of the complex phenomena affecting the damage resistance, coating research must be conducted in a careful and disciplined manner. A number of this year's papers exhibited such care. Among these were two papers devoted to the characterization of the optical properties, including the complex refractive index and localized absorbing impurities.

In support of the U.S. Air Force high-energy laser program, three infrared ellipsometers for thin-film research were described by T. Leonard, J. Loomis, K. Harding and M. Scott of the University of Dayton Research Institute. The first is a conventional null type for operation in the 3.39 to 4.00 μm range. Ellipsometric parameters (Δ and ψ), repeatability and absolute accuracy can be measured with a precision of 0.01°, yielding optical constants accurate to 0.1 percent in some cases. The second instrument, also a null-type ellipsometer capable of similar precision and accuracy, was built for in situ monitoring of thin film coatings at the fixed wavelength of 3.39 μm. The third type, an

automated rotating polarizer design to be completed in 1981 was designed for the extended wavelength range of 1 to 12 μm with 0.5 percent accuracy in n and k. Much attention was given to proper polarizer selection as relates to extinction ratio, beam deviation and wavelength coverage. In the 3.39 to 4.00 range, their measurements of various polarizers gave the following extinction ratios and beam deviations (half angle): 1) CdTe in reflection (10,000; 2 mr); 2) ZnSe, stacked plates; (6) (800; 0.3 mr); 3) rutile Glan prism (10,000; 0.2 mr); (4) grid on BaF_2 prism (43; < 0.1 mr); (5) ion-beam etched grid on ZnSe (5000; < 0.1 mr) and (6) dichroic calcite (6000 at 3.39 μm to as low as 5 at 3.60 μm; < 0.1 mr). The associated software was described and examples of measurement capabilities with the null instruments were presented.

Using multiple-reflection techniques (both internal and external) described at the 1979 Laser Damage Symposium, W. Anderson of the U. S. Air Force Academy and W. Hansen of Utah State University measured the infrared reflection spectra of several optical coatings from 2.5 to 15 μm. Single-and two-layer coatings of ZnS, ThF_4 and SiO on Ge, Ag and ZnSe substrates were tested. Impurities were identified from the reflection spectra followed by calculation of the complex refractive index and, thus, the absorption coefficient. The authors were also able to predict the position of impurities by varying the angle of incidence and polarization in the reflection measurements so as to maximize the square of the electric field in the region of interest. All of the films studied were determined to contain significant absorbing species e.g. ThF_4 contained large amounts of water, especially at the film-substrate interface, of the order of 5-10 percent of the total film mass. SiO films were anisotropic near the absorption band at 1100 cm^{-1}, and the ZnS film was contaminated with water and by hydrocarbon impurities, again of the order of one to two monolayers at the film-substrate interface. As suggested by the authors, their spectroscopic method could well be used as a routine diagnositic in optical deposition laboratories.

The next five papers were studies of the damage resistance of state-of-the-art coatings for laser wavelengths ranging from the ultraviolet (248 nm) to the near infrared (1.06 um).

A primary limitation for excimer lasers operating in the ultraviolet is the availability of adequate optics. The situation is particularly difficult at wavelengths shorter than 0.3 μm where multiphoton effects are expected to limit the performance of virtually all materials. In a paper published in an earlier Boulder Damage Conference Proceedings Newnam and Gill reported some initial measurements on the performance of multilayer dielectric coating at 0.266 μm. This year S. Foltyn and B. Newnam of the Los Alamos National Laboratory reported on more extensive tests of 20 multilayer samples from five different sources, most of them deposited on Suprasil 2 substrates having a microroughness of about 12A RMS. Five different material combinations were tested using a multigas excimer laser having a pulse length of 10-12 ns FWHM and a repetition rae of 35 Hz operated with KrF (248 nm) and Xe Cl (308 nm). The mean spot diameter was 0.62 mm at the shorter wavelength and 0.66 mm at the longer one. In all but one case more than one sample containing a given choice of materials was evaluated. Results were (1) the damage thresholds observed ranged between 1.0 and 3.0 J/cm^2 at both ThF_4 wavelengths with

ThF_4/Na_3AlF_6 being the best (at least at 248 nm), (2) wide variations were found in site to site damage thresholds (each sample was irradiated at 10 different sites) but an estimate could be made of potential coating performance, which was less than 4 J/cm^2 in all cases, (3) a subthreshold preirradiation treatment results in a 20-25 percent improvement in damage threshold in most (but not all) cases, (4) no evidence of a lowered damage threshold for multiple shots was found, (5) damage generally initiated at visible defects, but not all visible defects damaged, (6) near threshold damage sites did not grow with successive shots and (7) evidence for a $t^{1/2}$ and a λ^4 scaling law was found.

One of the most controversial topics considered at these symposia is whether or not the damage threshold of surfaces, especially optical coatings, is dependent on the spot size of the laser beam irradiation. As early as 1972, Newnam and DeShazer at the University of Southern California observed a monotonically increasing threshold with decreasing spot-size radius for radi less than 0.25 mm. Later, in 1975 Bettis and Coworkers at the Air Force Weapons Laboratory proposed a 1/d scaling of the energy density (J/cm^2) threshold primarily supported by measurements reported in the Soviet literature. However, several American colleagues, including Newnam at Los Alamos and Milam at Lawrence Livermore National Laboratories have reported numerous instances (particularly with pulsewidths shorter than 2 ns) where no spot-size effects were discernable.

It is important in the design of large laser systems (having diameters (~1 cm or larger) that the damage thresholds of optical components, ordinarilly measured with millimeter and smaller-size test beams, be relevant or at least scalable. Thus, continued investigation of the spot-size effect is merited and welcome. At this symposium, T. Wiggins, T. Walker and A. Guenther of the Air Force Weapons Laboratory reported the application of a novel interference technique to examine possible beam-size effects in optical coatings of ZnS, ZrO_2 and ThF_4/ZnS.

By overlapping two beams from a frequency doubled Nd-YAG laser (pulsewidth of 5 ns), interference fringes of spacing 5 to 125 μm were systematically produced on test coatings. Damage as a function of fringe spacing was then compared to that produced by a single beam hundreds of times larger. The primary finding of this study was that no significant difference in threshold was measured between the single-beam and two-beam cases. Also microscopic examination of the damaged areas revealed no differences for small- and large-beam irradiation. From the damage morphology and the absence of a spot-size dependence, these authors concluded that the source of damage initiation for their 5-ns pulses was impurities smaller than 1μm. It is hoped that further work of a similar definitive nature for different coating materials, wavelengths and pulsewidths will be pursued.

Bichromatic optical coatings are required for the conduct of dual-wavelength laser irradiation of inertial-confinement fusion targets. To address this need, G. Wirtenson and J. Willis of Lawrence Livermore National Laboratory and E. Enemark of Optical Coating Laboratory, Inc. performed a study entitled, "Evaluation of Bichromatic Coatings Designed for Pulsed Laser Fusion Applications at 0.53 and 1.06 Micrometers." Two designs each of AR coatings, partially transmitting reflectors (R=97%) and total reflectors using titania and silica layers were deposited on BK-7 glass substrates. Narrow-band and broadband AR designs

(R < 0.25% at both wavelengths) were used. For the reflectors, one design was a "two-to-one" stack using quarter-wave TiO_2 layers and halfwave SiO_2 layers at the intermediate wavelength of 0.71 μm. The second "ensemble" design employed a quarter-wave reflector stack for 0.53 μm deposited on top of a similar stack for 1.06 μm.

Damage tests were conducted at 1.06 μm using 1-ns pulses and at 0.53 μm using 0.7-ns pulses according to a single-shot-per-site comparative technique with a previously calibrated TiO_2/SiO_2 AR coating as the reference. The damage thresholds of the two AR-coat designs were identical with mean values of 2.5 and 5.5 J/cm^2 at the green and ir wavelengths, respectively. Likewise, no consistent differences between the damage resistance of the two reflector designs were measured. The partial reflectors had mean thresholds of 3 and 8 J/cm^2, respectively, at the two wavelengths. Those for the maximum reflectors were slightly higher at 4 and 9 J/cm^2, respectively.

Overall, the 1.06 μm thresholds were of similar magnitude as those for previous monochromatic production coatings However, the 0.53 μm thresholds of the broad-band AR coatings were considerably lower than a similar set reported by Deaton, et al. below, which had a mean value of nearly 5 J/cm^2. The authors speculated that increased absorption in the titania layers at 0.53 μm might have been responsible for the depressed damage resistance of their samples.

As laser fusion experiments shift to shorter wavelengths the need for characterization of the damage resistance of the associated optics follows naturally. In support of the current target irradiation experiments at 532 nm by Lawrence Livermore National Laboratory (LLNL), T. Denton, F. Rainer, D. Milam and W. L. Smith of that institution performed a survey of the damage thresholds of current production run optical components . The array of optics included multidielectric reflectors, AR coatings, multilayer beam dumps, graded-index (leaced) AR glass surfaces, uncoated surfaces and dual-wavelength (1064 and 532 nm) coatings. Testing at 532 nm was conducted in the same manner as previously reported for 1064 nm tests at LLNL. Single shot persite irradiations was conducted with 0.7 ns pulses focused to a spot diameter of 2mm.

High reflectors for use at normal incidence had thresholds of about 5 J/cm^2. For reference, the average threshold of many reflectors previously tested at 1064-nm, but with a much shorter 150-ps pulsewidth, was also 5 J/cm^2. Anti reflection coatings for 532 nm damaged at thresholds from 1.3 to 6.2 J/cm^2 with a median value of 3-4 J/cm^2. This range is similar to the 3.9 J/cm^2 average found during 150-ps, 1064 nm tests. Partially-reflecting (R= 50%) coatings had thresholds of 3 to 3.5 J/cm^2, and the graded-index AR surfaces had higher thresholds of 12 to 13 J/cm^2 similar to the levels determined at 1064 nm. As expected, greater values (18 and 24 J/cm^2) were measured for uncoated, polished fused silica and BK-7 glass, respectively. In general, the 532-nm thresholds fell slightly below the 1064-nm average of previous tests, but since only a few samples of each type were evaluated in this survey and at a different pulse length, general conclusions on the spectral dependence of the damage resistance must be considered preliminary at this time.

An important objective of performing careful damage threshold measurements on optical coatings is the improvement in the state-of-the-art of coating deposition. By communicating

the numerical results and interpretations of the cause of failure to the coating producer, the deposition procedures can be modified in an iterative manner to attain improved laser damage resistance. M. J. Soileau of the Naval Weapons Center reported an order-of-magnitude increase in the threshold of AR-coated $LiNbO_3$ by using such a cooperative procedure. (Regrettably, the identity of the single layer AR coating material was withheld by the coating vendor.)

Initial tests with small spot-size (41μm), 30-ns pulses at 1.06 μm indicated that the damage initiated at sites of absorbing defects at the coating/substrate interface at a level of 2 GW/cm^2. In response, the coating vendor modified the substrate preparation and deposition procedures which yielded thresholds of 5 GW/cm^2 as limited by linear absorption in the coatings. Further improvements resulted in coatings with thresholds of 5 to 20 GW/cm^2. Microscopic inspection of these improved coatings showed that damage was associated with defects (e.g., dust) on the outer surface of the coating. Although cleaning with a lens tissue saturated with acetone produced no effect, vigorous rubbing with a saturated tissue did remove the surface particles and increased damage thresholds of 15 to 20 GW/cm^2 resulted. Abrupt termination at the peak of the transmitted waveforms indicated failure by avalanche breakdown.

An order-of-magnitude increase in the relative damage threshold is very impressive. However, the editors must caution prospective laser designers that the small-spot 20 GW/cm^2 (30-ns pulses) thresholds are not necessarily applicable to larger, millimeter size laser beams.

Although thermal deposition methods (resistive heating and electron-gun) are currently standard, other methods are being actively evaluated for their ability to produce coatings with fewer defects. This year properties of sputtered and ion-beam-deposited films were emphasized.

One of the important coating materials for HF laser applications is silicon. However, compared with low-index materials, the relatively high absorption and low damage thresholds of Si have limited its performance. Presumably, the high absorption at 2.8 μm in evaporated Si layers is related to porous film structure, defects and water contamination. To improve on these deficiencies, T. Donovan, J Porteus and S. Seitel of the Naval Weapons Center and P. Kratz of Northrop Research and Technology Center have evaluated sputtering, both dc and rf, as alternate techniques for obtaining high packing density, low defect and, thus, damage-resistant silicon films. Direct comparison was made with evaporated films produced in high ($3x10^{-7}$ torr) vaccum. From resonant nuclear resonance analysis (RNRA) and secondary-ion mass spectroscopy (SIMS) they found the water impurity content of dc magnetron-sputtered films (deposited at $3x10^{-3}$ torr) to be one-half that of UHV-evaporated films,(100 ppm vs 200 ppm). Not suprisingly, the absorption (at 2.8 μm) of the magnetron films was correspondingly less (20 cm^{-1} vs 40 cm^{-1}).

Damage thresholds measurements at 2.7 μm (100-ns pulses) indicated dc magnetron sputtering to be the superior method over all others evaluated (dc reactive, rf reactive, rf diode as well as UHV evaporated). The threshold of a dc magnetron-produced half-wave Si film on a Si substrate was approximately 45 J/cm^2, respectively, in contrast to the 15 J/cm^2

threshold measured for the corresponding UHV-evaporated film. Similar damage tests at 3.8 μm, where absorption by OH^- is greatly reduced (10 cm^{-1} or less for sputtered films) yielded thresholds of approximately 170 J/cm^2 and 50 J/cm^2, respectively, in favor of the magnetron-produced Si film. Furthermore, no tendency for cracking or delamination was observed for the magnetron films, indicating excellent adhesion. In general , the failure made of the films was thermal, e.g., the melt threshold was reached. Clearly, application of magnetron sputtering to commercial production of optical films is suggested.

In recent years, deposition of optical coatings with ion beams has been found to have important advantages over thermal deposition and sputtering techniques. Generally, the flexibility of geometric arrangement of ion source, sputter target and optical substrate (to provide uniform coatings) is cited along with capability of operation in a high vacuum environment. This year W. C. Hermann, Jr., of Optic-Electronic Corp. and J. R. McNeil of New Mexico State University described their use of a novel ion-beam arrangement to deposit films of $Ge_{33}Ae_{12}Se_{55}$ glass on a variety of substrates for protective coating applications in the infrared region. Unique to their deposition arrangement was use of two separate Kaufman-type ion beam sources: one to sputter-etch the optical substrate prior to coating and the other for bombarding the coating target. Films in excess of 100 μm thickness were deposited without cracking, providing evidence of low stress. Optical analysis indicated low absorption from 1 to 16 μm and an amorphous, homogeneous structure. Although the reported magnitudes of their laser damage thresholds for 20-ns pulsed, 1.06 μm radiation appeared quite low, both pulsed and cw thresholds at 10.6 μm were moderately high. For example, a 100 μm thick film on NaCl had a threshold of 2.3 GW/cm^2 for 1.2-ns pulses and ~ 0.2 MW/cm^2 for 5 second exposure to a cw CO_2 laser. Thick films of this chalcogenide glass material may well find good use as moisture barriers for alkalai halide windows in humid environments.

The many favorable mechanical and optical properties of diamond windows have prompted several groups to attempt to deposit diamond optical thin films. S. Aisenberg and M. Stein of Applied Science Laboratories described their ion-beam deposition technique to form films of what they called diamond-like carbon. In their device, argon ions sputter atoms from a carbon cathode which, by aid of an axial magnetic field, are directed onto a substrate within a vacuum of 10^{-4} to 10^{-5} torr. Deposition rates between 3 and 10 angstroms/sec were achieved, and quite thick films (up to 10μm) were grown. These diamond-like films on Si substrates were described as being pinhole free, and low optical absorption was apparent from transmission measurements between 2.5 to 50μm. From scanning electron micrographs of coated and uncoated surfaces, the authors observed that the coated surfaces appeared, qualitatively, much smoother. This was assumed to result from the high mobility of the energetic (~50 eV) carbon atoms on the surface of the growing film. Further explanations involving the very high free surface energy of the carbon atoms and the tendency toward minimum area by minimization of surface irregularities were offered.

The capability of a laser reflector to perform its primary function, e.g., to focus the beam to a near diffraction-limited spot, precedes consideration if its damage resistance. In a multi-element optical train of a laser system, severe optical figure tolerances are

required for individual mirrors, even for use at infrared wavelenths. The error in mirror figure is caused not only by the geometrical shape attained by the polisher, but also by overcoatings. The coating contribution from thin metal films can be dismissed as negligible, but multilayer dielectric films (MLD) pose special problems. H. Bennett and D. Burge of the Naval Weapons Center reviewed the origin of coating figure errors, their measurement and practical methods to mimimize them in a paper entitled, "Multilayer Thickness Uniformities Required to Meet Wavefront Error Tolerances in Laser Mirrors."

Both the nonuniform coating thickness and the resulting phase change differences across the mirror diameter contribute to figure error. To meet typical mirror figure specifications in infrared systems, e.g., for 3.8 and 10.6 μm, the authors calculated that the thickness nonuniformity of MLD films must not exceed 1 percent. Such uniformity becomes increasingly difficult to achieve as the mirror diameter becomes larger. To even measure the figure nonuniformity is problematic. The author convincingly demonstrated that optical figure measurements with the conventional interferometric techniques with visible wavelengths does not provide an accurate value of the figure error at ir wavelengths. For example, tested in the visible, a coating can make a mirror appear convex, whereas it can actually be concave in the infrared. The obvious solution is to make interferometric measurements at the design wavelength, but the particular cw laser source and data reduction apparatus must be available. Two other methods, reflectance measurements around the ir design wavelength as a function of position on the mirror surface and direct measure of the Optical Transfer Function were also recommended by the authors to discern coating thickness nonuniformities. To attain the desired coating uniformity, careful coating chamber design (double-planetary motion, proper substrate orientation and distance from the source) and masking elements between the source and substrate were determined as essential.

3.4 Fundamental Mechanisms

The fundamental mechanisms whereby optical materials fail under intense illumination have been investigated intensively over the past decade. Although significant progress has been made in understanding these processes, a quantitative model is still lacking. Outstanding issues include the relative importance of multiphoton absorption vs. avalanche ionization and the importance of impurities and defects in mediating the damage process.

Scaling laws for the variation of bulk and surface damage in optical materials have been obtained empirically for several years, and provide useful comparison with theory. Some, like the $t^{1/2}$ scaling of damage fluence, are generally validated for a wide range of experimental conditions. Others, such as scaling with spot size, are applicable only under certain circumstances.

In a paper read by title only Yu. K. Danileiko, A. A. Manenkov and V. S. Nechitailo of the Lebedev Physical institute in Moscow reviewed their research into the role of absorbing defects in laser damage, primarily as it relates to bulk and surface failure. Considerable emphasis on the potential of thermal treatment and preconditioning for elevating damage resistance is just given. After this ground work is laid to indicate the dominant role played by absorbing defects in laser induced damage, physical mechanisms are proposed for

the catastrophic nature of a damaging event, namely - thermal explosion followed by photo ionization of the surrounding medium. Scaling relations based on the proposed are model are given in terms of size and properties of defects and wavelength and pulse duration of the incident laser radiation.

A careful comparison of damage thresholds in SiO_2, NaCl, and air, as a function of spot size and pulse duration, was reported by E. Van Stryland, M. Soileau, A. Smirl, and W. Williams of North Texas State University. Experiments were carried out with a Nd: YAG laser operating in the TEM_{00} mode with a variable pulsewidth between 30 and 200 ps, and a Q-switched Nd: glass laser pulsing at 31 ns. Intensity was varied by adjusting crossed Glan polarizers, for two lenses of different focal lengths. Damage was identified by the appearance of a visible flash or the observation of scattered light from a co-axial He-Ne laser beam.

The data were fit to an emphirical expression of the form $E_B = (A/V + C_1)\ t_p^{-1/4} + C_2$, where E_B is the breakdown field strength, t_p is the pulse duration and V is the focal volume, which was assumed to be proportional to the fourth power of the Gaussian radius of the beam at the focus. The authors argue that for their experimental conditions, self-focusing and lens aberrations are negligible. For NaCl and SiO_2, they found that $C_1 = 0$, while for gas breakdown, $C_2 = 0$. They conclude that the observed expressions were consistent with the model of multiphoton-induced avalanche breakdown, but not with the scaling law advanced by Bettis et al., or with Spark's theory. They note that in large focal volumes, the breakdown process is dominated by impurities or defects, while Spark's theory applies to intrinsic breakdown.

The qualitative features of the data are worth noting. The pulse duration dependence is more pronouced for small spot size (5 μm) than at a larger spot size (10-20 μm). Noticeable differences are seen between thresholds at 5 μm spot size and those at 6 μm spot size, implying that damage initiation sites occur with a spacing of about 5 μm. A very striking feature of the data presented is the fact that the breakdown fields in SiO_2 are approximately 3 to 4 times the values in NaCl for the same pulse duration and spot size, for all cases reported. This ratio greatly exceeds the expected ratio of (n^2-1) previoulsy reported in the literature.

An illuminating contrast to the previous investigation is provided by the work of M. Soileau of North Texas State University and J. Franck and T. Veatch of the Naval Weapons Center. They compared the dependence of the observed breakdown threshold on focusing conditions for several Kerr liquids (high n_2), low-nonlinearity liquids, and NaCl, a low-nonlinearity solid. Different dependences were seen for each class of materials. In the experiment, a 9 ns pulse from a Nd: YAG laser operating in the TEM_{00} mode was focused in the sample with lenses of two different focal lengths. Increased scattering of He-Ne laser beams was taken to be indicative of damage. Microscopic observations of damage sites was used as the criterion for the solid samples.

In the Kerr liquids, the breakdown power level was inversely proportional to the index nonlinearity n_2, and independent of focal spot size, as expected for whole-beam self-focusing. In CS_2-ethanol mixtures, however, the breakdown power was found to increase for

small spot sizes, as might be expected if the breakdown were initiated at microscopic impurities. The authors also propose that defocusing might be occurring due to free-carrier generation, but offer no definitive evidence. In NaCl, their observations are consistent with those of the preceeding paper. Again, the breakdown field is seen to increase with decreasing spot size. The authors caution against naively assuming that whole-beam self-focusing is the dominant mechanism in bulk damage.

As part of a continuing study of the basic process of dielectric breakdown under intense illumination, P. Kelly and D. Ritchie of the National Research Council, and P. Braunlich, A. Schmid, and G. W. Bryant, of Washington State University, have developed a detailed computer code ("Pulse") to model the breakdown process. Both avalanche ionization and multiphoton absorption are included in the model, along with the refraction of the incident beam by the evolving concentration of free carriers. The authors have compared their calculations with experimental observations of damage in NaCl. They find that neither the avalanche nor multiphoton model agrees with the observed values of breakdown threshold. In either case, refractive defocusing of the incident light by the free carriers reduces the local intensity well below the computed threshold, for incident intensities at which damage was observed. The damage threshold in this calculation was taken to correspond to local lattice heating to the melting temperature.

The apparent disparity between the calculations and experimental observation may be due to one of several factors:

1) The formation of primary defects may reduce the electron concentration and increase the lattice heating, as is discussed in a companion paper by these authors,

2) The observed damage may be due to the presence of impurities in the medium, which are not accounted for in the calculation. (The importance of impurities in mediating damage in real materials has been stressed in the past by A. Manenkov.) Further work on the role of primary defect formation is proposed by the authors.

If bulk damage experiments are carried out with sub-nanosecond pulses, the distribtuion of observed damage sites can be taken as indicative of the points at which breakdown was initiated. If the damage is impurity-mediated, these might be taken as the location of impurities. However, a certain regularity observed in the breakdown patterns has let to the suggestion that the location of the damage sites may correspond to the maximum of the focused beam induced along the Z-axis through spherical aberration in the lens.

P. Braunlich, G. Bryant and A. Schmid of Washington State University have investigated this hypothesis. They have calculated the positions of the maxima induced for varying degrees of spherical aberration. The results obtained are somewhat ambiguous. For calculations carried out at 1.06 μm, for focusing parameters corresponding to experimental conditions, the maxima induced by spherical aberration are more widely spaced than the observed damage sites. However, some gross features are reproduced. For example, no damage is predicted beyond the focus, and none is observed. This could also be due to absorption at breakdown sites before the focus. The authors point out that nonlinear effects, such as plasma refraction or self-focusing are not taken into account.

It is well known that under the influence of intense illumination, various "primary" defects, such as V_k, F and H centers and self-trapped excitons, can be formed in alkali halide crystals. P. Braunlich, G. Brost and A. Schmid of Washington State University, and P. Kelly of the National Research Council, discuss the role of primary defect formation in the optical breakdown of NaCl. Defect formation affects the breakdown process in two competing ways. The free carrier concentration is reduced in the process of primary defect formation by the efficient removal of electron-hole pairs, while new channels of absorption are created through absorption of incident light by the defect structure. The authors assess the net effect of these two competing processes. The model used to evaluate these processes was multiphoton absorption, although the authors maintain that since both multiphoton absorption and avalanche ionization are sensitive to carrier concentration, the net effect should be the same in either model. The authors find that at visible wavelengths, free carrier formation is strongly reduced by primary defect formation, but that the net effect on the damage threshold is small, due to the offsetting increase in primary defect absorption. They propose that effects which probe free carrier concentration directly like carrier-induced beam deformation should be sensitive to primary defect formation.

In theoretical modeling of the electron avalanche process, the effective collision time for electron scattering, τ, plays an important role. B. Jensen, of Boston University, discussed corrections to the Drude theory which become important at high frequency and high intensity. The collision time is no longer a constant, in Jensen's model, but becomes a function of frequency at low intensities in the infrared, and of intensity or applied field at high intensity even at low frequency. She carries out explicit quantum mechanical calculations to obtain the dependence of τ on both frequency and applied field strength. Comparison with previous calculations and with experiment are given for InP, GaAs, and InAs. Both the polar optical mode and impurity scattering are considered. Agreement with experiment is excellent for electron concentrations up to $10^{19}cm^{-3}$.

It has been observed that bulk damage in germanium requires a very high incident fluence. G. Bryant, A. Schmid, and P. Braunlich of Washington State University, along with P. Kelly and D. Ritchie of the National Research Council, have initiated a computational study of the interaction of 2.7 μm light with germanium. Their model tracks the generation of free carriers by two-photon absorption, subsequent relaxation processes leading to phonon excitation, and the phonon temperature rise. Separate account is maintained for optical and acoustical phonon temperatures.

Beam refraction due to carrier-induced index changes is not taken into account. However, preliminary conclusions indicate interesting features of the interaction. In particular, the optical and acoustical phonon temperatures rise together, with the two temperatures remaining in agreement to within one percent during the entire pulse. In future, both Auger recombination of free carriers and refractive effects will be added to the model.

The question of calculating two-photon absorption in solids has been of concern for almost two decades. Calculations based on simple models were put forward in the early

1960's by Braunstein, Basov, and Keldysh, and subsequently revisited by several authors. Disparities among these calculations were noted to be large and agreement with experimental data has been unsatisfactory.

A. Vaidyanathan and A. Guenther of the Air Force Weapons Laboratory, and S. Mitra of the University of Rhode Island, have carried out a detailed calculation of the two-photon absorption coefficient in several direct-gap semiconductors, including GaAs, InP, CdTe and ZnSe, for the case in which the photon energy is less than the band gap, but twice the photon energy exceeds the gap energy. The calculation was carried out using an empirical pseudo- potential method. Bloch wave functions were constructed for the highest four valence bands and lowest 31 conduction bands, for all k-values in the first Brillouin zone. The results were compared to those obtained using the models of Braunstein and Basov, and with available experimental data. This more accurate calculation yielded values of two photon absorption coefficients more than an order of magnitude larger than the more approximate models. The calculated values agreed with experimental values to within a factor of two.

The greater accuracy of these calculations arises from use of detailed band structure calculations, rather than assuming parabolic bands and from the use of an extensive basis set. The authors conclude that of the range of values measured for two-photon absorption in GaAs, the most likely value is about one cm/MW.

In a short note, the same authors find agreement between the Basov formula and Keldysh's expression for two-photon absorption. They find that non-parabolicity and band degeneracy have a strong effect on the results of these calculations. However, from the preceeding paper, it is clear that the simpler models are only qualitative, even in an approximate sense, and that detailed band structure calculations are required for quantitative

Carrying their theoretical investigation one step further N. Judell and S. S. Mitra of the University of Rhode Island and V. Vaidyanathan and A. H. Guenther of the Air Force Weapons Laboratory made estimates of the three - photon absorption coefficient in direct-gap crystals (CdS, GaAs, InSb, ZnSe and KCl) through the use of third order time dependent perturbation theory. They conclude that, initially the absorption coefficients increase with increasing photon energy until a maximum is reached at relatively low energy at which time they decrease significantly.

The effect of the nonlinearity of the refractive index on propagation in optical waveguides was analyzed in a paper by B. Bendow and P. Gianino of the Rome Air Development Center, and N. Tzoar of City University of New York. They considered two problems, the effect of the nonlinearity on mode mixing in CW propagation and the formation of solitons in pulse propagtion. For the CW case, they found that above the Talanov critical power, the beam self-focuses within the waveguide, while below the critical power, non-singular, oscillatory, trapped solutions are found. The critical power for glass or silica waveguides at 1 μm is in excess of 10 kW.

Solitons arise in wave propagtion when nonlinear effects counteract dispersive effects to provide stable pulse propagtion. A "bright" solution corresponds to a single isolated

pulse of a specified form. In a homogeneous medium, it only can exist in the presence of anomalous dispersion. In a waveguide, however, bright soliton solutions exist even for normal dispersion. The power density required for soliton propagation for a 1 ns pulse is about 10^5 W/cm^2.

4. Recommendations

Work reported this year emphasized the importance of separating bulk and surface absorption and understanding the scientific basis for these effects. New measurement tools are now available, which together with those reported previously, give encouragement that these absorption processes are beginning to be understood in detail. Further work both on developing and using these techniques and an emphasis on corrective procedures made possible by our deeper understanding of the fundamental processes could result in a significant additional reduction in window absorption and hence an increased power handling capability. Hydrophobic surface treatments, for example, seem a definite possibility for reducing surface absorption. Further work on new materials and new fabrication techniques for old materials continue to be called for. Several examples of the usefulness of such work in overcoming longstanding problems were seen this year. Finally, additional work using the new tools now becoming available on an exploration of intensity dependent absorption in laser window materials is obviously required.

The presentation at this year's meeting of the new finishing techniques and CO_2 laser polishing demands increased attention to transfer these procedures to industrial practice. In the case of float polishing, further testing is needed and other materials besides those already studied need to be investigated, particularly those aspects where chemical aided polishing would allow one to account for differences in removal rate of various crystalline orientations. In the case of CO_2 laser polishing, this technique offers the promise of such advantage that it should be pursued to determine if it can be used to fabricate larger sized elements to the tolerances required for high performance lasers. The use of this technique to polish fiber optic ends is immediately suggested. Continuing in the area of finishing, more work is needed on the electron beam treatment of bulk metallic materials particularly that aspect of negative rake angle diamond turning. As we progress toward increased laser applications in the ultraviolet, it was brought out that cerium oxide should not be used in the polishing of ultraviolet optics but rather diamond or other nonultraviolet absorbing abrasives should be employed.

Much additional work needs to be done in the area of laser interaction with metals. To name one requiring further studying is the importance of laser annealing, e.g., melting and alloying the surfaces including surface hardness. The fundamentals of the interaction must be studied and understood better. Experiments need to be performed to verify the predictions of the mechanical responses of polycrystalline metal surfaces to lasers. All of this work should be performed in such a manner that spot size effects, if any, can be evaluated to suggest bounds or generate scaling relations. Finally, one must always call for improvements in the measurement of optical properties of these materials, particularly the metals and their properties as a function of polishing procedure, e.g., one needs to investigate the origin of the abnormal behavior (probably extrinsic) of the nonideal reflection of silver and copper surfaces reported at this year's Symposium.

Realizing that optical materials in thin film form still are the weakest form of any element, a major effort in improving coatings is dictated. From this year's meeting, several opportunities for a more immediate payoff were suggested together with the identification of the need for continued basic research in understanding why thin films do not perform as well as surfaces or materials in bulk form. While this need for basic research continues unabated, there is much potential benefit to be accured from extensive developments heard at the conference. Most notable is an increased activity in the development of deposition techniques for large sized elements. In addition, ion beam deposition/ion beam cleaning should be widely explored for optical coatings since the reports of low-loss, stress-free films are very encouraging. Scaling to a reliable size with requisite uniformity also needs to be demonstrated. In the area of deposition, the community needs to pursue magneto-sputtering to check on its scalability as well.

Of course, one should document the pedigree of a coating from conception to application. In this regard, more data to improve statistics are needed to reconcile differences in regard to such things as the spectral dependence of damage in thin films. This requires the development and application of improved characterization techniques and instrumentation. In fact, multiple-reflection spectroscopy would be a good candidate for incorporation in coating laboratories as a routine tool in evaluation of deposition processes.

We must conclude with a recommendation for quality damage testing of thin films. Due to the present controversy over spot size effects one should use relatively large laser beams for the evaluation of test coatings to be employed on full size optical elements. However, further spot size studies similar to those presented at the meeting are obviously needed particularly as a function of pulse width, film material and wavelength such that we can scale our laboratory experiments to real world scenarios.

Theoretically speaking the spot size dependence of the pulsed laser damage mechanism is still incompletely understood and further careful experimental work similar to that reported this year should be pursued to answer this question quantitatively. Two photon and multiphoton effects need to be understood more clearly, particularly in view of the increased interest in the ultraviolet region of the spectrum. Detailed band structure calculations involving the higher energy levels reported this year are very encouraging and more work of this type is needed. The more approximate calculations reported in past years are clearly inadequate in many cases for quantitative results. The increased application of solid state theory to the laser damage problem is a recent development which will surely yield more good results in future years. The theoretical results need to verified experimentaly, however, and should not be applied outside the range in which experimental verification is available. Finally, the importance of localized defects on laser damage is becoming increasingly clear both from the standpoint of direct absorption and because they modify both the free carrier concentration and the mean free path at high irradiation levels. The effect of defects needs to be modeled more accurately and the possibility of engineering materials to improve damage thresholds through reduced concentration of key defect types needs to be explored.

5. Acknowledgment

The editors would like to acknowledge the invaluable assistance of Mr. Aaron A. Sanders and Ms. Pat Rice as well as the other involved staff members of the National Bureau of Standards in Boulder, Colorado, for their interest, support, and untiring efforts in the professional operation of the Symposium and Ms. Susie Rivera and Ms. Sheila Aaker for their part in the preparation and publication of the Proceedings. The continued success of the Damage Symposium would not have been possible without the enthusiastic support of those named above.

This year the conference co-chairmen and attendees were please to have the assistance and presence at the Symposium of Ms. Pat Whited of the Air Force Weapons Laboratory and Ms. Mary Ann George of the Lawrence Livermore National Laboratory. Giovanni Fiorenza and Dr. Alan Stewart of the Air Force Weapons Laboratory also participated effectively in the conference operation.

For primarily technical assistance, we are grateful to Dr. D. Milam of Lawrence Livermore National Laboratory for sharing with us his expertise in paper selection and to Dr. Jim Stanford of the Michelson Laboratory and Russ Austin for very effectively serving as a rapporteurs for the poster sessions.

Thanks to all!

6. References

[1] Glass, A. J.; Guenther, A. H., eds. Damage in laser glass, ASTM Special Technical Publication 469, ASTM, Philadelphia, PA; 1969.

[2] Glass, A. J; Guenther, A. H., eds. Damage in laser materials. Nat. Bur. Stand. (U.S.) Spec. Publ. 341; 1970.

[3] Bloembergen, N. Fundamentals of damage in laser glass, National Materials Advisory Board Publication NMAB-271, National Academy of Sciences; 1970.

[4] Bloembergen, N. High power infrared laser windows, National Materials Advisory Board Publication 356; 1971.

[5] Glass, A. J.; Guenther, A. H., eds. Laser induced damage of optical materials: 1972," Nat. Bur. Stand. (U.S.) Spec. Publ. 372; 1972.

[6] Glass, A. J.; Guenther, A. H., eds. Laser induced damage in optical materials: 1973, Nat. Bur. Stand. (U.S.) Spec. Publ. 387; 1973.

[7] A. J. Glass and A. H. Guenther, "Laser Induced Damage in Optical Materials, 1973: A Conference Report," Aplied Optics 14, 74-88 (1974).

[8] A. J. Glass and A. H. Guenther, Editors, "Laser Induced Damage in Optical Material: 1974," NBS Special Publication 414 (1974).

[9] A. J. Glass and A. H. Guenther, "Laser Induced Damage in Optical Materials: 6th ASTM Symposium," Applied Optics 14, 698-715 (1975).

[10] A. J. Glass and A. H. Guenther, Editors, "Laser Induced Damage in Optical Materials: 1975," NBS Special Publication 435 (1975).

[11] A. J. Glass and A. H. Guenther, "Laser Induced Damage in Optical Materials: 7th ASTM Symposium," Applied Optics 15, No. 6, 1510-1529 (1976).

[12] A. J. Glass and A. H. Guenther, Editors, "Laser Induced Damage in Optical Materials" 1976," NBS Special Publication 462 (1976).

[13] A. J. Glass and A. H. Guenther, "Laser Induced Damage in Optical Materials: 8th ASTM Symposium," Applied Optics 16, No. 5, 1214-1231 (1977).

[14] A. J. Glass and A. H. Guenther, Editors, "Laser Induced Damage in Optical Materials: 1977," NBS Special Publication 509 (1977).

[15] A. J. Glass and A. H. Guenther, "Laser Induced Damage in Optical Materials: 9th ASTM Symposium," Applied Optics 17, No. 15, 2386-2411 (1978).

[16] A. J. Glass and A. H. Guenther, Editors, "Laser Induced Damage in Optical Materials: 1978," NBS Special Publication 541 (1978).

[17] A. J. Glass and A. H. Guenther, Editors, "Laser Induced Damage in Optical Materials; 10th ASTM Symposium," Applied Optics 18, No. 13, 2212-2129 (1979).

[18] H. E. Bennett, A. J. Glass, A. H. Guenther and B. E. Newnam, "Laser Induced Damage in Optical Materials: 1979" NBS Special Publication 568 (1979).

[19] H. E. Bennett, A. J. Glass, A. H. Guenther and B. E. Newnam "Laser Induced Damage in Optical Materials: 11th ASTM Symposium," Applied Optics 19, No. 14, 2375-2397 (1980).

INFRARED WAVELENGTH MODULATION SPECTROSCOPY OF LASER WINDOW MATERIALS*

Rubin Braunstein, Ryu K. Kim
Department of Physics
University of California
Los Angeles, California 90024

and

Morris Braunstein
Hughes Research Laboratories
Malibu, California 90265

We have previously shown that the infrared wavelength modulation system that we have developed is capable of measuring the complete spectral distribution of the extrinsic absorption in highly transparent solids at levels of 10^{-5} cm^{-1} in the spectral range from 2.5 to 12 microns [1].[1] The previous measurement techniques that were employed for KBr and KCℓ have been extended to other crystalline systems which are of interest in light guiding applications, namely: CaF_2, LiF, NaCℓ, NaF, LaF_3, BaF_2, MgF_2, SrF_2, and MgO. Rich and varied absorption structures were observed in all of these crystals enabling an identification of volume and surface absorption. Similar dominant bands are observed in many of these substances indicating the presence of common impurities regardless of the crystal and the origin of its growth. However, varied fine structures are observed in different crystals which are indicative of the individual characteristics of the chemistry of the crystal preparation. These measurements were performed in laboratory and dry N_2 ambients and readily show the physisorption and desorption of surface contaminants. In appropriate materials, measurements were extended into the intrinsic multiphonon region.

Key words: Extrinsic and intrinsic infrared absorption; volume and surface impurities; infrared wavelength modulation; CaF_2; LiF; NaCℓ; NaF; LaF_3; BaF_2; MgF_2; SrF_2; MgO; laser windows.

1. Introduction

The requirements for high power laser and light guiding systems continue to generate a need for extremely low absorption levels in infrared transmitting materials. These interests continue to stimulate efforts at material growth and surface preparation techniques to produce materials that approach intrinsic absorption levels in appropriate spectral regions. In practice, in the highly transparent regions, absorption coefficients are observed to vary greatly from sample to sample indicating the extrinsic nature of the absorption processes. To assess progress in improvements in material preparation, sensitive techniques are required to measure low levels of absorption.

To determine the sources and nature of the extrinsic light absorptions, we have employed the technique of infrared wavelength modulation in the spectral region from 2.5 to 12.0 μm. We have previously employed this technique [1] in a study of KBr and KCℓ prepared by different crystal growth techniques and were able to identify possible surface and volume impurities. In the present work, we have extended these studies to survey a number of optical materials commonly used in laser window applications, namely: CaF_2, LiF, NaCℓ, NaF, LaF_3, BaF_2, MgF_2, SrF_2, and MgO. The continuous spectral distribution of the absorption obtainable by wavelength modulation techniques at levels of 10^{-5} cm^{-1} facilitates identification of volume and surface absorption centers. Although rich and varied absorption structures are observed in all of these crystals, similar dominant bands are observed in many of these substances indicating the presence of common impurities regardless of the crystal origin and the concomitant growth techniques used to prepare the materials.

2. Experimental Techniques

The infrared wavelength modulation spectrometer was previously described [1]. It consists of a system for sweeping the output wavelength of a monochromator across the exit slit by a vibrating output diagonal mirror whose depth of modulation can be continuously controlled. Careful consideration is given to the subtraction of the background of the transfer function of the monochromator which can include atmospheric absorption, the spectral response of the optics as well as the detector. To accomplish this, a sample-in-sample-out procedure is used to obtain the background intensity without the sample, the derivative of this background, the transmitted intensity with the sample present and its derivative. The above operations are performed under microprocessor control. The computation of the energy derivative of the absorption as well as its integration to display absorption peaks are performed on-line using a PDP 11/20 computer. Although the primary data in the form of the energy derivative of the sample absorption is adequate to reveal absorption structures, as an aid for comparison with the conventional literature, the integrated results are reported in this paper.

3. Experimental Results and Analysis

The crystals used in this study are indicated in table 1, together with suppliers of the materials. Standard procedures were used to prepare the surfaces of the samples; these consisted of surface grinding, polishing with a slurry of Linde A in ethanol or propanol, and then drying under a heat lamp. Prior to the optical measurements the samples were stored in a vacuum desiccator. The optical measurements were performed with the samples in the laboratory ambient as well as in a dry N_2 atmosphere. The data for the various materials studied are shown in figures 1, 3, 4, 5, 6, 7, 8, 9, 10.

*Supported by the Air Force Office of Scientific Research.
[1]Figures in brackets indicate literature references at the end of this paper.

The laboratory ambient and dry N_2 atmosphere runs for a given sample are displayed on the same page to facilitate comparison. The absorption coefficients at the upper left hand of the figures are the beginning of the intrinsic multiphonon tails and are shown when they fall within the spectral range of the spectrometer.

When the absorption coefficient is sufficiently high, as in the multiphonon region it is possible to measure the transmission directly as well as its derivative. In this case, it is possible to determine the constant of integration which is necessary to obtain the absolute value of the absorption when integrating derivative data; this constant can be used to calculate the absorption coefficient in the extrinsic region well below the multiphonon tail. The constant of integration can also be obtained from a laser calorimetric measurement at a given frequency. The integration is performed by a standard trapezoidal integration; in this computation the depth of modulation, which in the present work is 10 cm^{-1}, is inserted as a parameter. The integrated derivative data without the constant of integration is shown to the right of the figures. The zero of ΔK is obtained by a computer correlation procedure to deconvolute the background derivative [2]. The zero of the ΔK wavelength modulation result is subsequently normalized to an absorption coefficient determined by laser calorimetry shown in each figure, which effectively supplies the constant of integration. To read the actual absorption coefficient at a given wavelength, one merely adds or subtracts the value of ΔK at that wavelength to the calorimetive value.

The absolute value of the absorption coefficient can be slightly ambiguous in providing the baseline data using multi-mode laser calorimetry since the mode structure of the laser can straddle some line features in the absorption spectrum of the sample. Obtaining the constant of integration, i.e., the baseline correction by a direct absorption measurement in the same wavelength modulation apparatus would be a more direct procedure as when the derivative measurements span the spectral range into the multiphonon region. This was not done in this work since this procedure would be more precise if the direct absorption measurement were performed above and below the region where the baseline is to be obtained. However, since the main thrust of the present work is to reveal the spectral features of the absorption, the laser calorimetric normalization was used and the values of ΔK from the integrated wavelength modulation data displays the fine structure excursions above and below the calorimetric point.

Figure 1a and figure 1b show the absorption spectra of BaF_2 taken in the laboratory ambient and in a dry N_2 atmosphere, respectively. The richness of the spectra should be noted; previous laser calorimetric measurements using a few discrete lines show only a broad peak between 1-5 μm peaking at 3.4 μm. Comparing the spectra in figures 1a and 1b; it should be noted that the absorption within the spectral region from 1600 to 4000 cm^{-1} decreases after the sample has been initially in the laboratory atmosphere and is subsequently placed in a dry N_2 atmosphere for two hours. When the sample is returned to the laboratory ambient for several hours the original structure in figure 1a is recovered. The fact that the magnitude and the linewidths of some of the bands change in a dry N_2 atmosphere indicates that a portion of the absorption is due to surface physisorption. The structures that persist even when the samples are flushed in dry N_2 may be due to surface chemisorption species or volume impurities. The absorption edge starting at 1000 cm^{-1} and increasing to lower energy is the multiphonon absorption tail.

Crystals containing substitutional molecular anion impurities typically exhibit a number of sharp infrared absorption bands corresponding to various internal modes of polyatomic ions. There may be small shifts in frequency and increase in linewidths depending on the particular host; however, because of the relatively small interaction with the crystal host, the vibrational frequencies can be used to identify a particular chemical impurity and the nature of its bonding. In addition to bulk absorption there is the possibility of surface absorption which can be comparable to bulk absorption which can be due to crystal growth techniques, mechanical or chemical polishes and chemical cleaners. In addition, exposure to the atmosphere can lead to a deposition of a conglomeration of impurities.

Correlation-type charts have been published which tabulate molecular-ion vibrational frequencies as a means of identification of possible surface and volume impurities in laser windows [3]. If one considers a complete frequency overlay of all possible impurities that can be present in concentrations of 0.1 ppm, one would expect a quasi-continuum absorption throughout the 2.5 to 12.0 μm region due to the overlap of the Lorentzian tails of the various absorption bands. However, the distinct absorption bands observed in the present work indicates the presence of dominant impurities. Consequently, rather than dwelling on the multiplicity of possible impurities, we shall consider the common molecular anion impurities such as the metaborates, nitrides, hydrocarbons, carbonates, and OH^- ions that are revealed by conventional absorption spectroscopy of pure commercial crystals since it is reasonable to expect that they may still be present at lower levels in purified materials.

The vibrational frequencies of common bonds of some polyatomic anions are shown in figures 2a and 2b which display the OH^-, C-H and carbonate groups and the metaborates and nitrides, respectively; figure 2a will be used primarily in the following analysis since these impurities seem to be dominant; however, bands in figure 2b may also be present.

If we examine figure 1a for the laboratory atmosphere data in conjunction with figures 2a and 2b, it is possible to identify some possible impurities. A prominent band at 4.2 μm can be associated with the physisorption of atmospheric CO_2. The bands in the 4 to 6 μm and 2.8 μm regions can be due to atmospheric water, while the bands in the 3 to 4 μm region can be assigned to an overlap of hydrocarbon bands. The bands in the 6 to 8 μm region seem to be associated with carbonates. The fact that the bands in the 4 to 6, 2.8 μm and 3 to 4 μm regions are largely due to physisorbed species is confirmed by the decrease in absorption in the dry N_2 atmosphere data shown in figure 1b.

The region between 6 and 8 μm in BaF_2 shows considerable structure whose magnitude varies only slightly with dry N_2 flushing. As we have previously indicated by the examination of figures 1a and 1b in conjunction with figures 2a and 2b these structures can be associated with the chemisorption of carbonates. Photoacoustic measurements on BaF_2 and SrF_2 using a CO laser that was tunable to discrete lines in the 6 to 8 μm region [4] have revealed step-like structures in the surface adsorption, while our measurements reveal distinct bands.

The MgF_2 laboratory atmosphere data shown in figure 3a reveal a cluster of bands similar to those observed in BaF_2. Again the ubiquitous CO_2 at 4.2 μm is evident. The 2.8 and 4 to 6 μm regions reveal the "liquid" water and OH^- bands, while the 3 to 4 μm region reveals the possible overlap of C-H bands. The 6 to 8 μm bands seen in BaF_2 seem to be absent or are obscured by the strong water band in the 4 to 6 μm region. The dry N_2 data in figure 3b shows a dramatic suppression of all the above bands. The remaining structure can be due to volume or chemisorbed species; the rise in the neighborhood of 2.8 and 4.8 can be due to OH^- and "liquid" water, respectively.

The SrF_2 sample in laboratory atmosphere shown in figure 4a is very similar to the structure seen in BaF_2 and the identifications of the bands are similar to the BaF_2 discussion. However, it should be noted that the dry N_2 atmosphere run in figure 4b shows a much greater decrease in the structure compared to the BaF_2 dry N_2 run. The remaining structures in figure 4b can be due to bulk or chemisorption with the possible identifications: 6 to 8 μm (carbonates), 3 to 4 μm (C-H bands), 2.8 μm (OH^-).

The CaF_2 laboratory data in figure 5a again shows a similar distribution of bands as exhibited by the BaF_2 and SaF_2 sample with a possible similar identifications of the bands. The marked decrease in height of these bands in the dry N_2 is again evident as shown in figure 5b.

The distribution of the bands in NaF in figure 6a exhibits the familiar pattern previously discussed for BaF_2, SrF_2, and CaF_2. However, figure 6b shows a large decrease in the band heights in the 2.5 to 4.0 μm region.

The LaF_3 sample in the laboratory atmosphere shown in figure 7b reveals the 4.2 μm CO_2 band, the 6 to 8 μm possible carbonates and the OH^- band near 2.8 μm. However, it should be noted that the bands in the 3 to 4 μm region due to C-H vibrations which have been prominent in BaF_2, MgF_2, SrF_2, CaF_2 and NaF seem to be absent or greatly suppressed. In the dry N_2 data in figure 7b the peak near 2.8 μm possibly due to OH^- is about the same height as in figure 7a. One should note the decrease in the overall absorption in the 4 to 8 μm region as indicated by the large negative values of the ΔK.

The NaCℓ data in both the laboratory and dry N_2 atmosphere data in figure 8a and 8b, respectively, show prominent structures. Although the spectral distribution is different in detail in both of these figures one can still identify the: 6 to 12 μm (carbonates), 4.8 μm ("liquid" water), the 4.2 μm (CO_2), 3 to 4 μm (C-H) and the 2.8 μm (OH^-) bands. The prominence of the bands in both ambients is consistent with the greater surface activity expected for NaCℓ as compared to the above substances. Although there is a large decrease in the height of the bands in figure 8b, as shown by the large negative values of ΔK, most of the bands are still evident that were present in figure 8a.

The LiF data in figures 9a and 9b show little structure indicating that LiF is the least surface active of all the substances studied. The absence of the 4.2 μm CO_2 band which was visible in all the previous substances studied including KBr and KCℓ which was previously published [1] should be noted. The only band which seems to be noticeable is 4.5 μm band in both ambients possibly due to water.

The data for MgO are shown in figures 10a and 10b. The most prominent features seen in the laboratory ambient are: a doublet in the 2.8 to 3.0 μm region (water and OH^-), some aspects of a possible 4.2 μm (CO_2), structure in the 4 to 6 μm region (liquid H_2O) and very slight structure in the 3 to 4 μm region (hydrocarbons). It is interesting to note that of the doublet in the laboratory ambient it is only the 3.0 μm band which survives dry N_2 flushing with a noticeable suppression of the 2.8 μm band. In a previous study of MgO [5] impurity bands were observed between the 3.8 μm and 2.7 μm. Our study clearly shows that the 3.0 μm band is due to bulk or chemisorbed OH^- while the 2.8 μm band is due to physisorbed OH^-.

The region of intrinsic absorption in MgO shows some fluted structures in the multiphonon absorption tail. The rise around 1600 cm^{-1} (6.3 μm) agrees with the shoulder previously studied in the multiphonon spectra of MgO [6] and was attributed to 4TO phonons by suitably averaging over the disperson curves.

4. Summary

Figure 11 shows a "schematic" representation of the typical spectra seen in most of the samples in the laboratory atmosphere; this "free-hand" drawing essentially summarizes the dominant bands that are observed! An examination of all of the samples studied except LiF show many features in common despite the fact that a cursory glance would emphasize the differences in detail. The 6 to 8 μm (carbonates), the 4-6 μm (liquid water), the 4.2 μm (CO_2), the overlap of bands in the 3 to 4 μm region (hydrocarbons) and the 3 and 2.8 μm bands (OH^- bound to water and free OH^-) are seen in most of the samples. In general, the physisorbed surface character of these bands is confirmed by their marked suppression in a dry N_2 atmosphere.

5. Conclusion

We have measured the continuous spectral distribution of the absorption in a number of materials of interest for laser window applications in the spectral region from 2.5 to 12.0 μm. This work has enabled an identification of volume and surface contaminants where their existence could only be conjectured from previous discrete thermocouple laser calorimetry and photoacoustic calorimetry measurements. It is interesting to note that although the diverse chemistry and crystal growth techniques were employed in the preparation of these materials, similar dominant bands are observed in most samples which are due to physisorption, volume, and surface chemisorption. It has been possible to identify the type of bonding of the particular constituents present. The surface character of some of the absorption at levels of 10^{-4} to 10^{-5} cm^{-1} indicates the importance of performing measurements in the same ambient when comparing low level absorption measurements by various sensitive techniques. The sensitivity of the infrared wavelength modulation technique indicates that a fraction of a monolayer of surface adsorbed species can be detected. Experiments in controlled ambients and on well characterized surfaces using this technique can be rewarding for the study of the physics and chemistry of surfaces. The dramatic changes in the physisorbed spectra in the substances studied indicate that

a continuous flow of dry N_2 along the outer surfaces of optics may have some rewards in high power laser systems.

6. Acknowledgments

The authors wish to thank Robert Curran for performing the laser calorimetric measurements, Rick Pastor and Mort Robinson for supplying several of the samples for this work, and James A. Harrington, Bradley Bobbs and Michael Burd for helpful discussions.

References

[1] Braunstein, R., Kim, R.K., and Braunstein, M., Wavelength modulation spectroscopy of highly transparent solids; Laser Damage in Optical Materials; 1979, 30-31 October 1979, NBS Boulder Co., ed. by H.E. Bennett, A.J. Glass and A.H. Guenther, NBS Special Publication 568, U.S. Government Printing Office, Washington, D.C. 1970, p. 99.

[2] To be published.

[3] Flannery, M. and Sparks, M., Extrinsic absorption in infrared laser-window materials; Laser Damage in Optical Materials; 1977, 4-6 October 1977, Boulder, Colo., ed by A.J. Glass and A.J. Guenther, NBS Special Publication 509, U.S. Government Printing Office, Washington, D.C. 1977, p. 5.

[4] Hordvik, A., Measurement techniques for small absorption coefficients: recent advances, Appl. Opt. 16, 2827 (1977).

[5] Harrington, J.A., Gregory, D.A., and Otto, Jr., W.F., Infrared absorption in chemical laser window materials, Appl. Opt. 15, 1953 (1976).

[6] Gourley, J.T., and Runciman, W.A., Multiphonon absorption spectra of MgO and CaO, J. Phys. C. Solid State Phys. 6, 583 (1973).

Table 1. Origins of the samples used in this work.

BaF_2	HARSHAW
MgF_2	OPTOVAC
SrF_2	Hughes Research Laboratories – Press-forged from RAP Boule
CaF_2	HARSHAW
NaF	OPTOVAC
LaF_3	Hughes Research Laboratories – He+HF cast
NaCℓ	Hughes Research Laboratories
LiF	MELLER
MgO	OPTOVAC

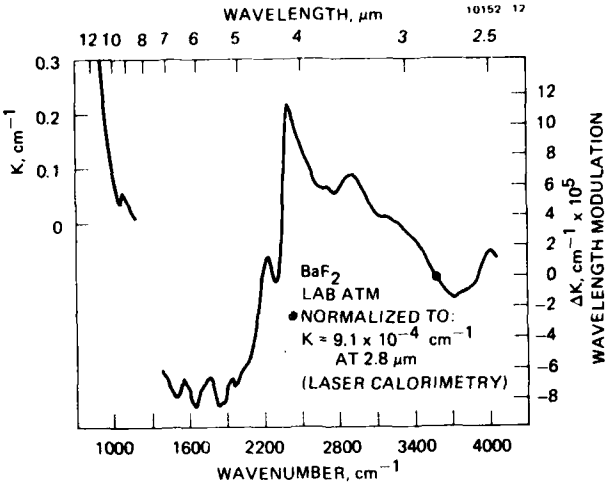

Figure 1a. Wavelength modulation spectra of BaF_2 in the laboratory atmosphere.

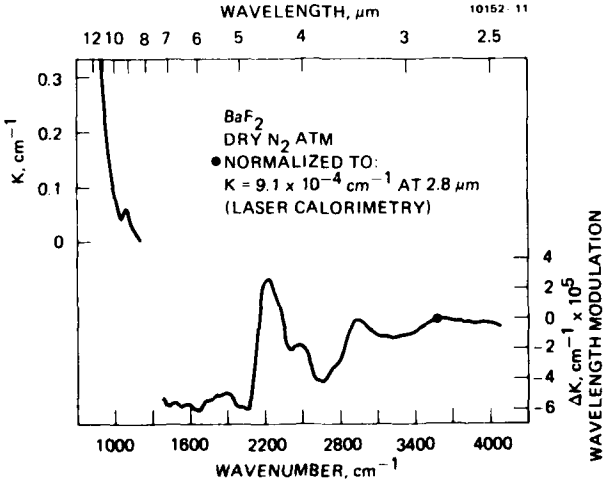

Figure 1b. Wavelength modulation spectra of BaF_2 in a dry N_2 atmosphere.

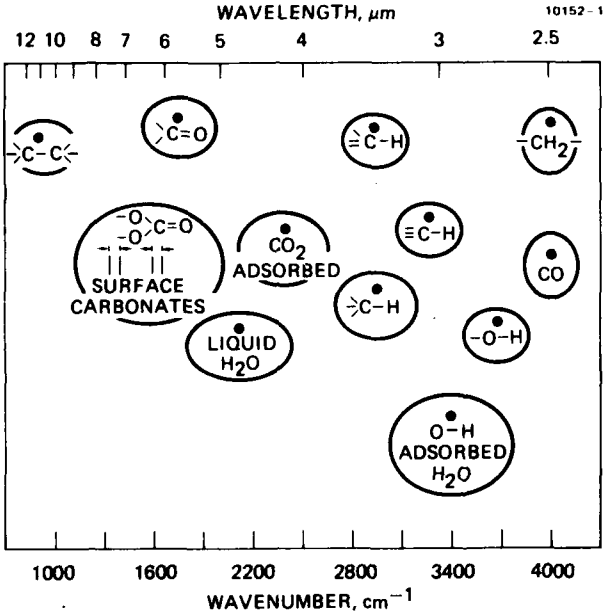

Figure 2a. Correlation chart of carbonates, C-H, O-H and water frequencies.

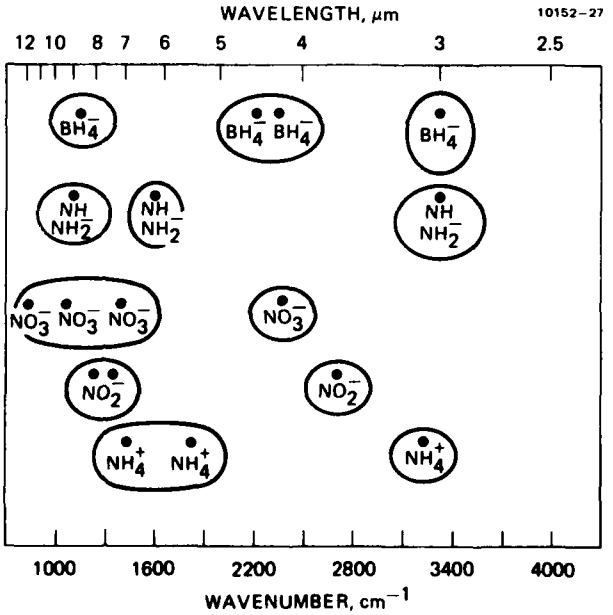

Figure 2b. Correlation chart of metaborate and nitride frequencies.

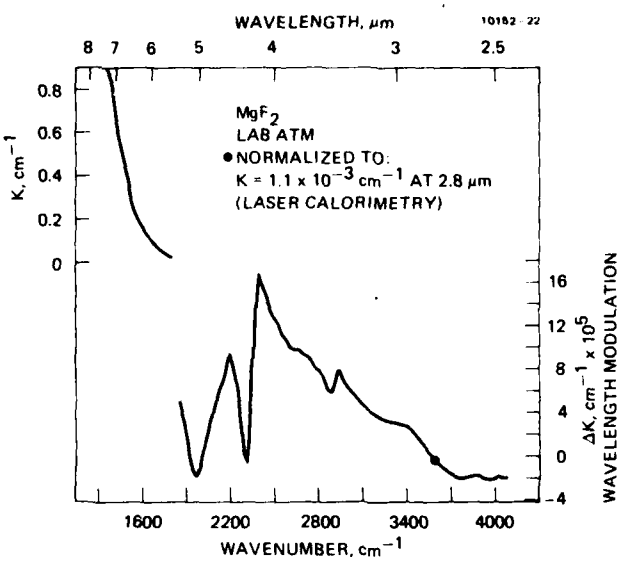

Figure 3a. Wavelength modulation spectra of MgF_2 in the laboratory atmosphere.

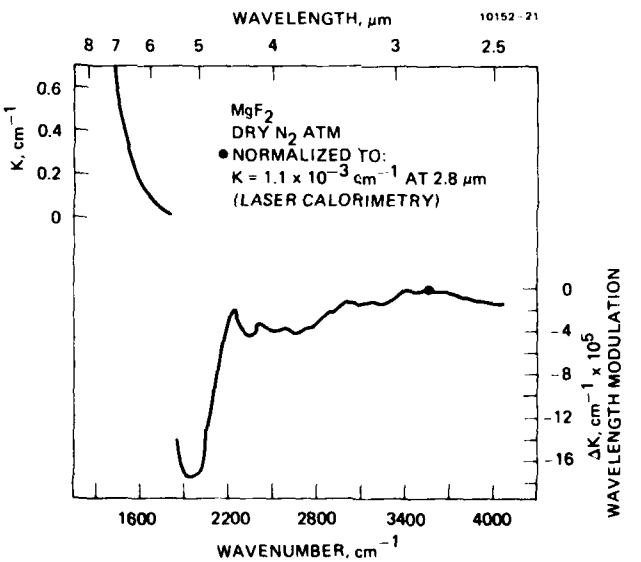

Figure 3b. Wavelength modulation spectra of MgF_2 in a dry N_2 atmosphere.

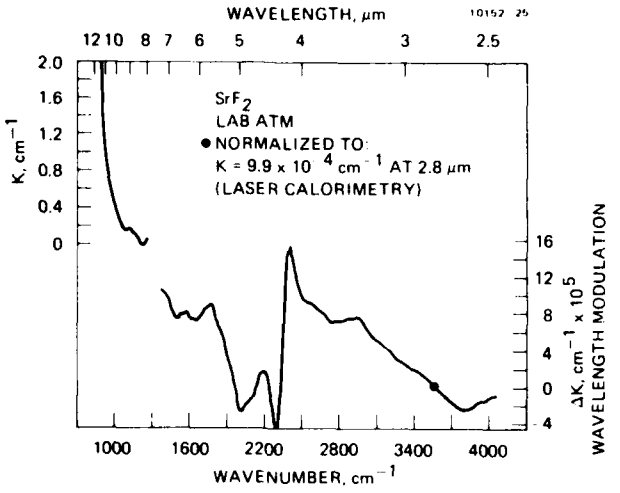

Figure 4a. Wavelength modulation spectra of SrF_2 in the laboratory atmosphere.

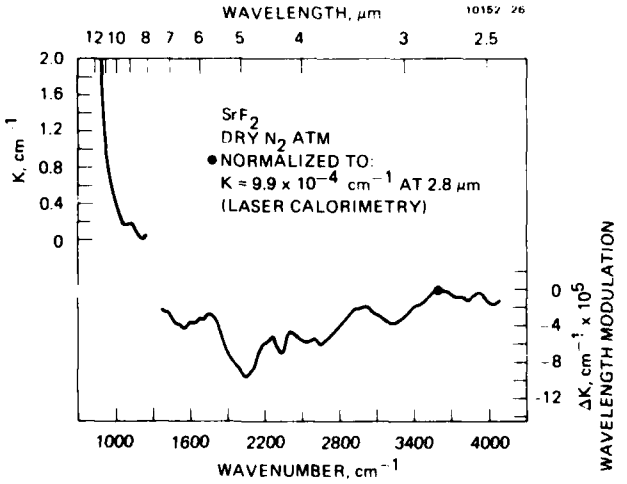

Figure 4b. Wavelength modulation spectra of SrF_2 in a dry N_2 atmosphere.

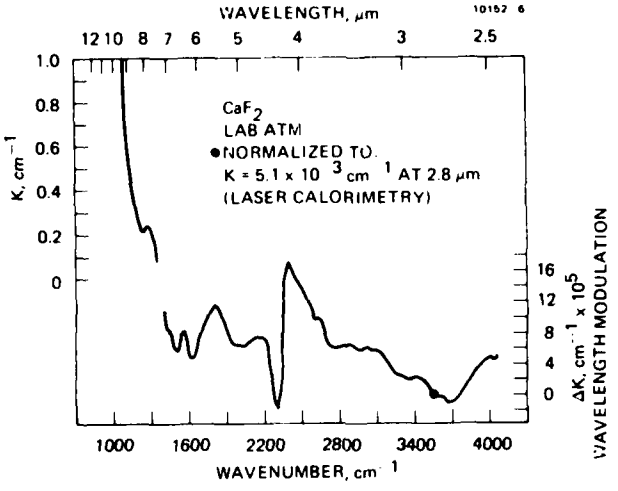

Figure 5a. Wavelength modulation spectra of CaF_2 in the laboratory atmosphere.

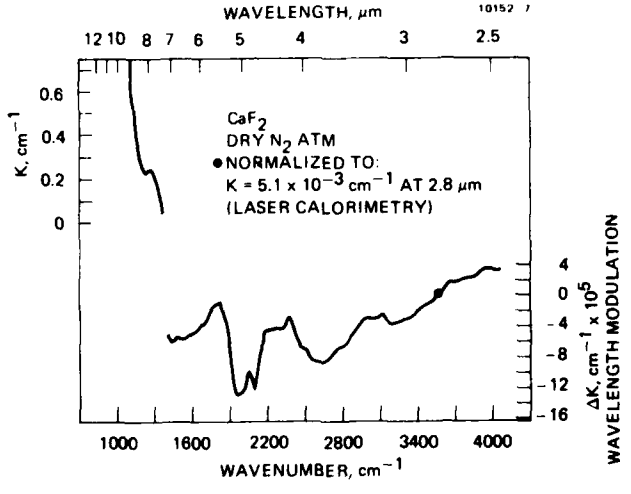

Figure 5b. Wavelength modulation spectra of CaF_2 in a dry N_2 atmosphere.

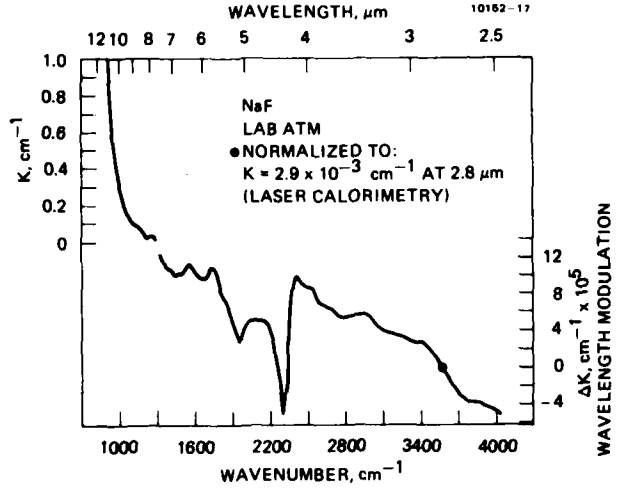

Figure 6a. Wavelength modulation spectra of NaF_2 in the laboratory atmosphere.

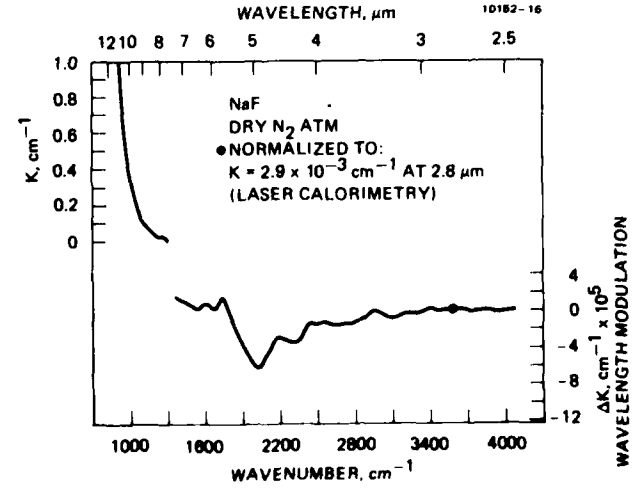

Figure 6b. Wavelength modulation spectra of NaF_2 in a dry N_2 atmosphere.

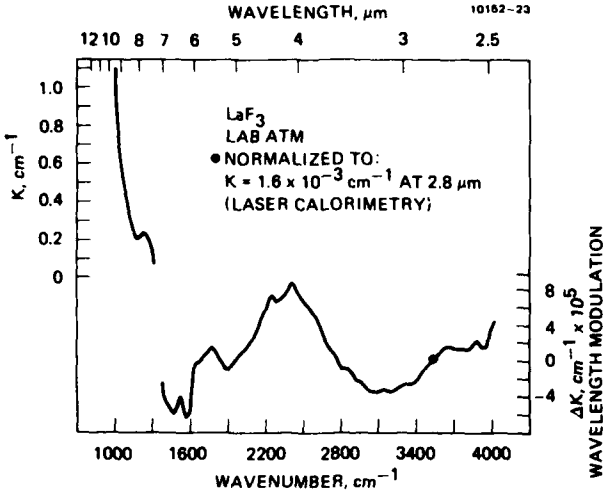

Figure 7a. Wavelength modulation spectra of LaF_3 in the laboratory atmosphere.

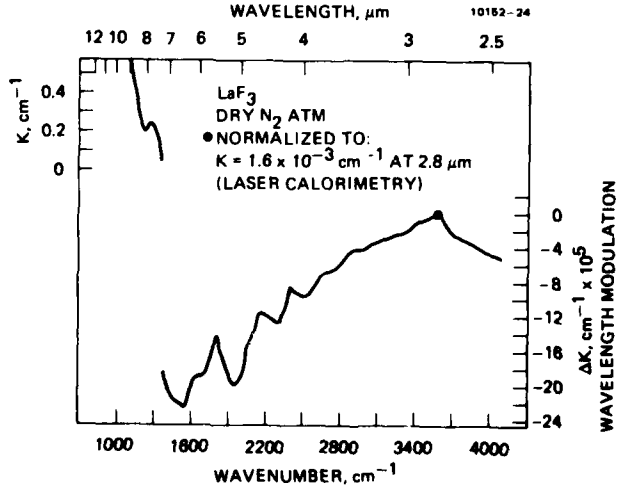

Figure 7b. Wavelength modulation spectra of LaF_3 in a dry N_2 atmosphere.

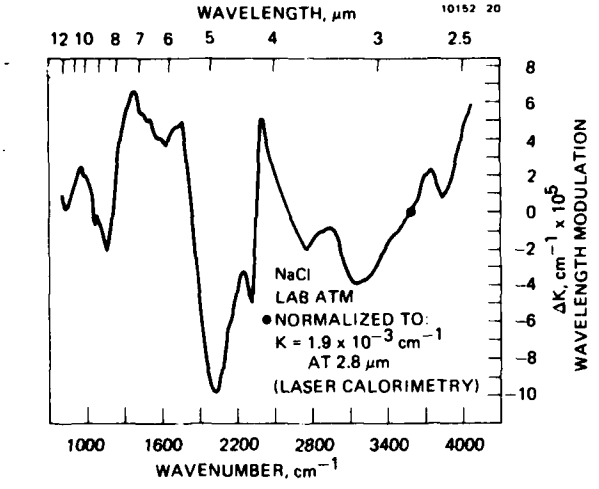

Figure 8a. Wavelength modulation spectra of NaCℓ in the laboratory atmosphere.

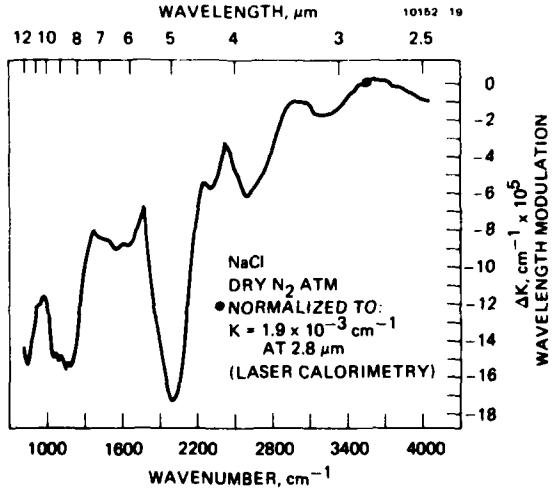

Figure 8b. Wavelength modulation spectra of NaCℓ in a dry N_2 atmosphere.

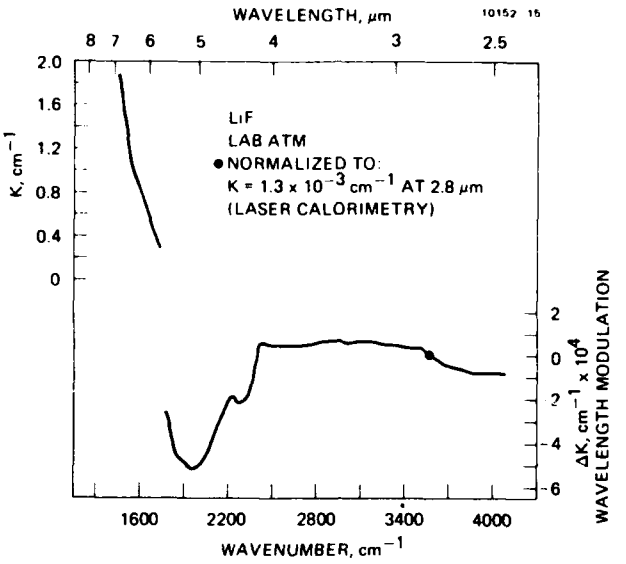

Figure 9a. Wavelength modulation spectra of LiF in the laboratory atmosphere.

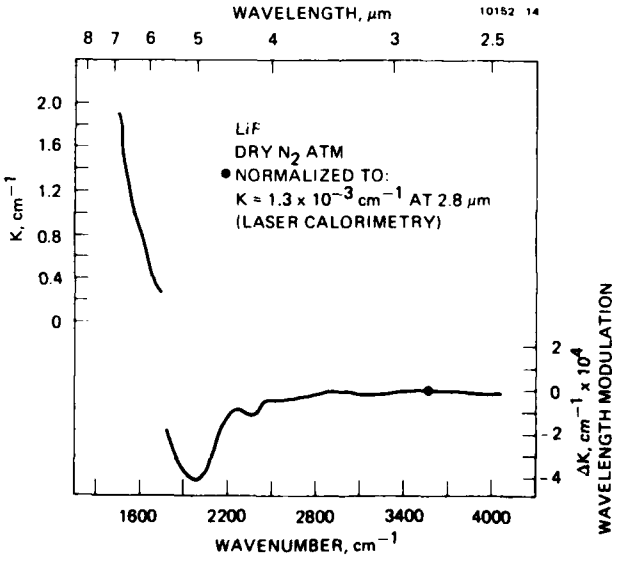

Figure 9b. Wavelength modulation spectra of LiF in a dry N_2 atmosphere.

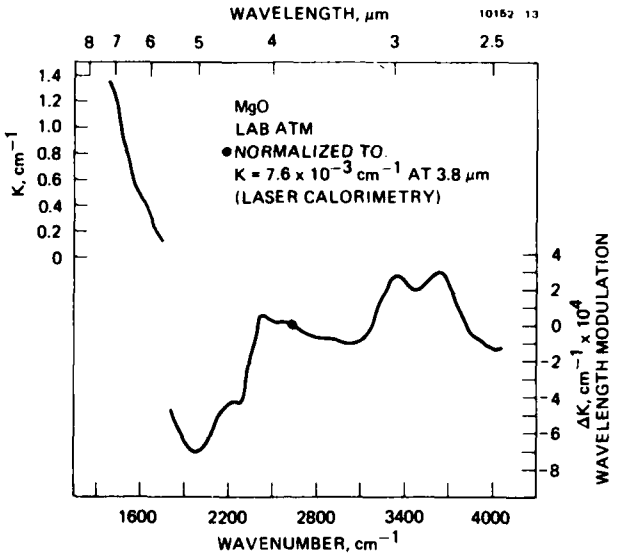

Figure 10a. Wavelength modulation spectra of MgO in the laboratory atmosphere.

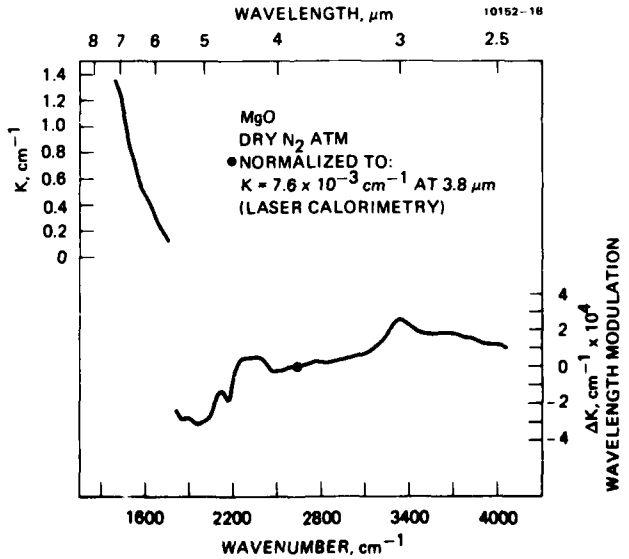

Figure 10b. Wavelength modulation spectra of MgO in a dry N_2 atmosphere.

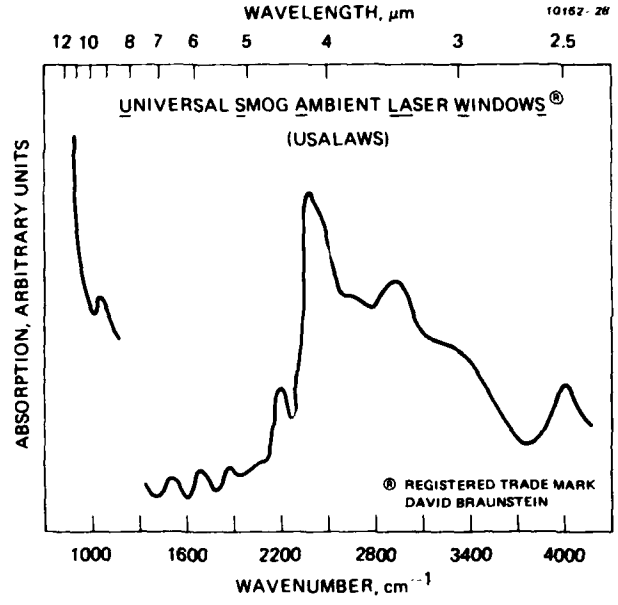

Figure 11. "Schematic" representation of the typical spectra seen in most samples in the laboratory atmosphere.

The speaker reported that purging of the sample system for two hours was required before the observed bands stopped changing. The changes were also reversible. Breaks in the Urbach tail could be seen by using modulation spectroscopy. It was suggested that the second derivative could be taken to display this structure better and that other techniques such as PAS or TIR spectroscopy be used to verify the results obtained. The speaker agreed.

PHOTOACOUSTIC SPECTROSCOPY OF ADSORBED SURFACE IMPURITIES ON ALKALI-HALIDE LASER WINDOWS[†]

J. M. McDavid and S. S. Yee
Department of Electrical Engineering
University of Washington
Seattle, WA 98195

Significant infrared absorption can arise from vapors adsorbed on laser window surfaces during exposure to the atmosphere, during exposure to low-vapor-pressure system components, and during surface passivation or stabilization treatments. The photoacoustic effect has proved to be useful quantitative technique for the measurement of surface optical absorption and, when using a carbon dioxide laser source, provides a sensitivity of a few percent of one monolayer for vapor molecules chemisorbed on highly transparent substrates.

The work reported here involves an application of photoacoustic spectroscopy to surface absorption studies of high power laser window materials. Results are presented for the time dependence of surface absorption during controlled vapor exposure and for the wavelength dependence of surface absorption, in the 9-11 μm range, following atmospheric contamination. The application of these techniques to the determination of adsorption rate constants, activation energies, and the chemical identification of surface impurities is discussed.

Key words: Alkali-halide laser windows; KCl; NaCl; optoacoustic spectroscopy; photoacoustic spectroscopy; surface impurities.

1. Introduction

The photoacoustic effect involves the irradiation, using a modulated light source, of a material in a closed cell. Incident photons which are absorbed and which convert to heat in the sample by nonradiative processes result in temperature and pressure fluctuations in the coupling gas in the cell. These gas pressure fluctuations are synchronous with the modulated source and can be detected using a sensitive microphone. A thermal wave associated with optical absorption at a distance L inside a solid is attenuated by a factor

$$q = \exp[-(j\frac{2\pi fc}{\kappa})^{1/2} L]$$

with the result that contributions to the photoacoustic signal from absorption significantly deeper in the sample than a thermal diffusion length are negligible [1][1], where the thermal diffusion length is defined by

$$L_{th} = (\frac{K}{\pi fc})^{1/2}$$

and where K, c, and f, are the thermal conductivity, the specific heat per unit volume, and the chopping frequency, respectively. The photoacoustic technique, when using gas coupling between the sample and the microphone, is relatively more sensitive to surface absorption due to the lack of attenuation during heat transport through the solid.

An early application of photoacoustic spectroscopy to surface analysis was reported by Rosencwaig [2]. The procedure involved the use of a conventional lamp source and monochromator to obtain spectra of highly polished copper electrodes passivated with benzotriazole. Sensitivity with this type of apparatus is better than 1 monolayer at the surface. Since the photoacoustic signal is directly related to the amount of heat produced, improvement in sensitivity can be obtained by increasing the power in the source from the few milliwatts available from the lamp source to the much higher powers available from tunable laser sources. A laser-excited photoacoustic apparatus can detect fractional surface absorption at levels of 10^{-6} and below, while a monolayer of a surface absorber yields a fractional absorption on the order of 10^{-4}.

This paper is concerned with infrared absorption at the surfaces of high power laser window materials, as detected by photoacoustic spectroscopy using fixed-wavelength and tunable CO_2 laser sources operated at power levels of a few watts in the 9-11 μm wavelength range.

2. Experiment

A block diagram of the experiment apparatus is shown in figure 1. The CO_2 laser used in the fixed

[†]Supported in part by the Air Force Office of Scientific Research.

[1]Figures in brackets indicate the literature references at the end of this paper.

wavelength measurement of the time dependence of the photoacoustic signal during a controlled vapor exposure is an Apollo Laser, Inc. Model 500 operating at 10.6 μm with a maximum output of 50 W cw. This fixed wavelength laser has been modified by replacement of the extraction mirror with a specially coated mirror to avoid the possibility of oscillation near 9.6 μm. The CO_2 laser used in wavelength dependence studies is an Advanced Kinetics, Inc. Model MIRL-50-SL operating in range of 9.2 to 10.9 μm with a maximum output of 35 W cw averaged over all lines. This tunable laser is equiped with a Sargent-Welch Model 8821 mechanical pump for high gas throughput in order to reach higher cw power levels. The power meter is a Coherent Radiation, Inc. Model 201. The condenser microphone is a Brüel and Kjaer Model 4134 followed by a Model 2619 preamplifier. The lock-in amplifier is a Princeton Applied Research Corp. Model 129A modified to accept a Model 189 selective amplifier stage.

The aluminum photoacoustic cell has a cavity of approximately 0.5 cm thickness and 1.3 cm diameter. The cavity is enclosed by two samples (laser windows) clamped against gaskets. The acoustic signal in the cell is coupled to the microphone through a 13-gauge hypodermic needle. The cell has valves which permit purging or filling with gases other than air when necessary. The absolute absorption calibration of the photoacoustic cell was accomplished by use of an electrically heated thin film resistor mounted on the cell, to which a known electrical power was supplied, and for which the acoustic response was measured [3]. The wavelength calibration of the tunable laser was obtained using an Optical Engineering, Inc. Model 16-A spectrum analyzer, for which the calibration was verified using a HeNe laser. The photoacoustic cell was operated with a slight rotation away from normal incidence to bring reflections away from the laser cavity and to eliminate some possible interference effects [3]. The chopping frequency for the data presented here was 33 Hz.

The controlled vapor source consists of a three stage gas dispersion apparatus constructed from 500 ml Erlenmeyer flasks having medium and coarse porosity gas dispersion tubes submerged in the first and second stages, respectively, and a straight glass tube submerged in the final stage. Ultra pure nitrogen carrier gas was passed through each of the partially filled flasks, which contained saturated solutions of NaCl in deionized water, with approximately a 20% excess of NaCl. The flow rate was typically set at a few cubic centimeters per minute to provide a constant replacement of gas in the cell from the constant relative humidity source above the saturated solutions. The technique is related to that recently reported for a higher flow rate apparatus [4].

The polished KCl and NaCl crystals discussed in this report were purchased from The Harshaw Chemical Company, Part Number L-02505, and further selected for low total absorption.

3. Results

An example of results obtained for the time dependence of the photoacoustic signal during a controlled vapor exposure following a chemical etch is given in figure 2. The etching procedure is a standard one consisting of two minutes in HCl followed by 10 sec rinses in ethanol and two isopopanol rinses followed by drying with a hot air blower. The procedure was to expose the etched KCl crystals to the vapor derived from the saturated NaCl solution continuously, except during the actual photoacoustic measurement, when the valves of the cell were closed. Similar results have been obtained with NaCl crystals. The initial portion of the curve, represented by the dashed line, includes laser beam exposure-time effects, as discussed below, in addition to effects from elasped-time or vapor exposure-time, as plotted on the horizontal axis.

In general, in experiments involving both KCl and NaCl laser windows, effects were observed which were separately associated with desorption of contaminants (having a beam exposure-time dependence), gas adsorption (having a vapor exposure-time dependence), and local heating (having a laser power-level dependence). The choice of only a few watts for the laser output power in the experiments reported here was to eliminate any significant contribution from the latter effect above, which can be important at higher power levels on crystals having localized, highly absorbing defects which can produce temperature dependent absorption.

Some initial results for the wavelength dependence of the photoacoustic signal during a controlled vapor exposure is given in figures 3(a) through 3(c). These data are for KCl crystals (a) 1 day after etching and mounting in cell filled with ultra pure nitrogen, (b) after 4 days exposure to vapor derived from the saturated NaCl solution in deionized water, and (c) the difference spectrum for data obtained after and before vapor exposure.

Finally, in figure 4 are shown results for the wavelength dependence of the photoacoustic signal for a pair of etched crystals, which were first stored mounted in the cell filled with ultra pure nitrogen for 1 day, then exposed to atmospheric contamination for 7 days by storing in a glass cover dish with desiccant. The contribution to the signal shown in figure 4 from the background signal (existing prior to atmospheric exposure) is approximately 12% of the total signal.

4. Discussion

The contributions to the total photoacoustic signal, as shown in figure 2, and as inferred from

that data and additional measurements on NaCl and KCl crystals, can be viewed as (1) a background signal arising from bulk and surface impurities and defects, (2) a "first layer" fast-rate surface adsorption which occurs during, and just after, etching, and (3) a "second-layer" slow-rate adsorption process occurring during the vapor exposure. This latter process is the time dependent portion of the signal represented by the solid line in the figure. The consideration of the surface adsorption effects as two processes has been put forth previously by Bennett during a discussion of water contamination of thin films in connection with the work of Sparks [5].

The data of figure 3 show general trends for absorption after etching consistent with that observed previously by other workers [6]. The difference spectrum in figure 3(c) demonstrates the capability of this technique to provide optical absorption spectra of chemisorbed species of value in chemical identification of adsorbates. The tentative association, by the design of the experiment, which involved the water vapor exposure of a hygroscopic substrate, is with adsorbed water. This identification is, of course, subject to further measurements and calculations. Internal molecular vibration modes for water would not correspond to peaks in the 9-11 μm range, but quite possibly vibrations of the molecule associated with the (weaker) chemisorption bonds would. The character of the etched surface, the adsorption site heterogeniety, and the various possible adsorption orientations combine to make this a relatively complex problem, however.

The data of figure 4 are primarily of interest for the demonstration of the relatively large surface absorption change that occurs with atmospheric contamination and also its relatively broad wavelength dependence. The application of this type of measurement (which employs uncontrolled exposure conditions) would be primarily in the testing of handling or assembly environments for laser or optical systems.

For a precisely characterized substrate and adsorbing-molecule system, the analysis of data such as that shown in figure 2 will yield an effective rate constant for the adsorption process (or the actual rate constant for a less heterogeneous system). Extension to the analysis of the temperature dependence for such a system would yield the effective activation energy of the process and, in turn, provide information on useful operating or exposure parameters for optical systems.

For the purpose of comparison with other work, it should be noted that the conversion from photoacoustic signal expressed as μV/watt (root-mean-square photoacoustic signal per average optical power transmitted) to the fractional absorption per surface for pure surface absorption or for surface absorption changes for KCl windows is made by multiplying by a factor of 2.0×10^{-5}. This yields, for example, a change in surface absorptance in the difference spectrum of figure 3 amounting to 3.0×10^{-4} at a wavelength of 10.6 μm.

5. Conclusion

A photoacoustic technique has been applied to the study of adsorbed surface impurities on alkali-halide materials of interest in high power laser systems. The sensitivity of the method corresponds to a few percent of a single monolayer for a chemisorbed species such as water vapor. The technique could be extended, with the addition of ultra high vacuum processing techniques, precisely characterized substrate crystals, and detailed monitoring of exposure-gas composition, to provide fundamental information on particular substrate-adsorbate systems. However, many practical applications in the development of high power laser systems, such as the investigation of surface absorption due to vapors adsorbed on laser window surfaces during exposure to the atmosphere, during exposure to low-vapor-pressure system components, and during surface passivation treatments, correspond to less stringent experimental conditions such as those used for the initial investigations described here.

6. References

[1] McClelland, J. F., and Kniseley, R. N., Signal saturation effects in photoacoustic spectroscopy with applicability to solid and liquid samples, Appl. Phys. Lett. 28, 467 (1976).

[2] Rosencwaig, A., Solid state photoacoustic spectroscopy, in Optoacoustic Spectroscopy and Detection, Y.-H. Pao, ed. (Academic Press, New York, 1977), p. 193.

[3] McDavid, J. M., Lee, K. L., Yee, S. S., and Afromowitz, M. A., Photoacoustic determination of the optical absorptance of highly transparent solids, J. Appl. Phys. 49, 6112 (1978).

[4] Nakamura, O., Ogino, I., and Kodama, T., Simple humidity control system, Rev. Sci. Instrum. 50, 1313 (1979).

[5] Sparks, M., Materials for high-power window and mirror coatings and multilayer-dielectric reflectors, in Laser Induced Damage in Optical Materials: 1976, NBS Spec. Publ. 462, A. J. Glass and A. H. Guenther, eds. (U.S. GPO, Washington, D.C., 1976), p. 203.

[6] Davisson, J. W., Hass, M., Klein, P. H., and Krulfeld, M., Growth, finishing, and optical absorption of pure potassium chloride single crystals, in Third Conference on High Power Infrared Laser Window Materials, November 12-14, 1973, Volume I: Optical Properties, C. A. Pitha and B. Bendow, eds., 1974, p. 31.

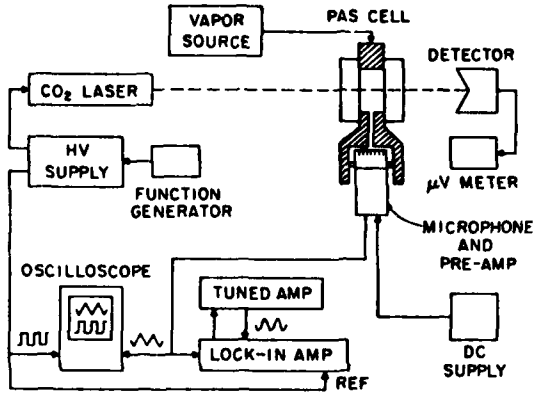

Figure 1. Block diagram of the photoacoustic apparatus.

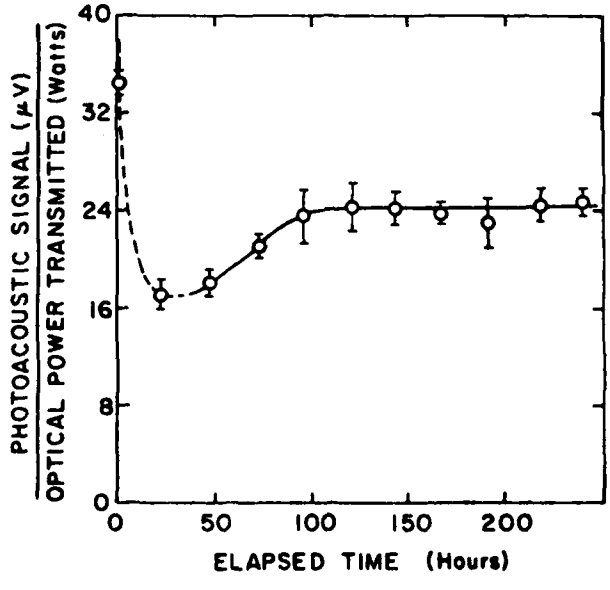

Figure 2. Time dependence of the photoacoustic signal during water vapor exposure of potassium chloride crystals.

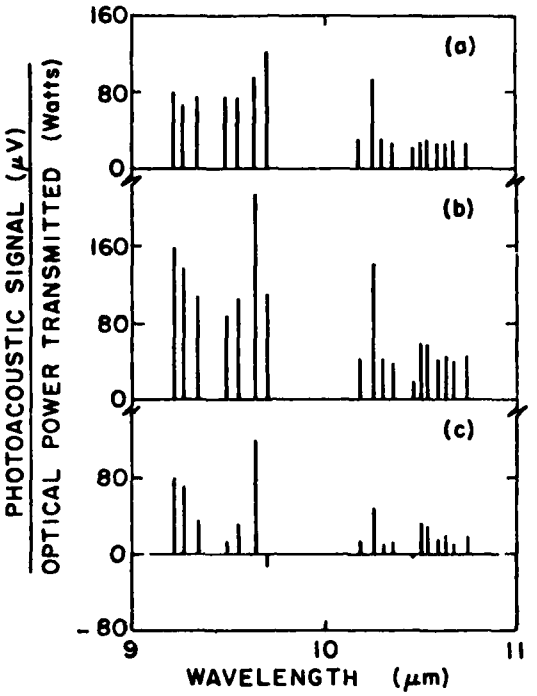

Figure 3. Photoacoustic spectra for potassium chloride crystals (a) before vapor exposure, (b) after vapor exposure, and (c) difference spectrum.

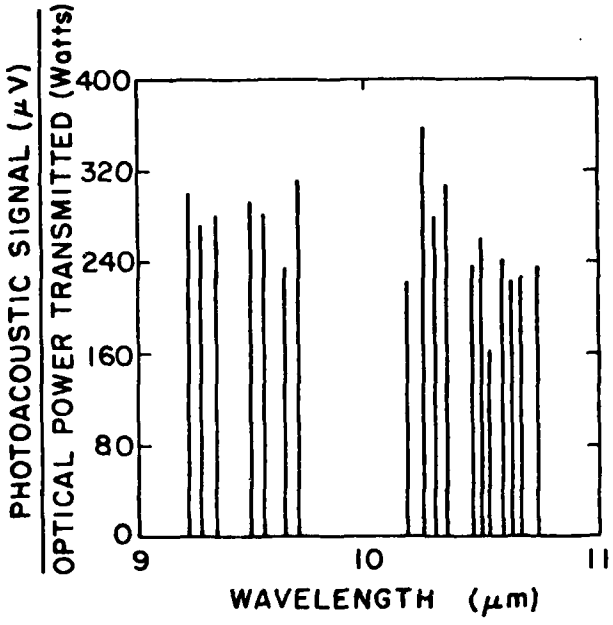

Figure 4. Photoacoustic spectrum following atmospheric contamination of potassium chloride crystals.

In response to a question on the importance of scattered light the speaker pointed out that its only effect is to raise the background level by a few microvolts. To his knowledge PAS has not been used in the ultraviolet wavelength region, although it could be.

PHOTOACOUSTIC MEASUREMENT OF NONLINEAR ABSORPTION IN SOLIDS

E. W. Van Stryland and M. A. Woodall
North Texas State University
Denton, Texas 76203

The photoacoustic technique, using a piezoelectric transducer to detect acoustic signals induced in semiconductors by the absorption of light, has been used to measure two-photon absorption. The transducer signal amplitude is directly proportional to the absorbed energy from all absorption processes, nonlinear as well as linear. This signal was monitored as a function of the intensity of single, picosecond, 1.06 μm, pulses. At high intensities, beam depletion was observed, and a direct comparison was made with the sample transmission. The sensitivity of this technique allows nonlinear absorption to be measured at intensities significantly lower than when using transmission. In addition, the advantage of the nonlinear photoacoustic technique over the recently described calorimetric technique is that powerful signal averaging techniques can be used. This is because the absorption at a given intensity can be determined by a single pulse in a few microseconds while calorimetry requires at the least several seconds.

We describe the use of the photoacoustic absorption measurement technique for the determination of nonlinear absorption in solids. Advantages and disadvantages of this method (using a piezoelectric transducer to detect acoustic signals induced in solids by the absorption of light) are discussed, as well as suggestions for future uses where the particular advantages of the nonlinear photoacoustic technique should prove valuable [1,2]. The photoacoustic signals, using a piezoelectric transducer to detect the acoustic signals induced in CdTe and CdSe by two-photon absorption of light, are directly compared to transmission measurements made simultaneously on the samples.

We show that the photoacoustic measurement of two-photon absorption on samples whose linear absorptivity is small offers significant increases in sensitivity over conventional measurements such as transmission. Similar advantages occur for higher order nonlinearities. The increased sensitivity is directly related to the increased sensitivity of the recently developed nonlinear laser calorimetric method while offering the additional advantage that an absorption measurement can be made rapidly (μsec) [3]. Calorimetry measures a rate of change in sample temperature as determined by a thermocouple output and thus requires considerably longer experimental times. On the other hand calorimetry absolutely calibrates the measured absorption coefficient while the photoacoustic signals need to be calibrated.

Figure 1 shows the photoacoustic experiment modified to observe nonlinear absorption. The usual chopped cw laser is replaced by a pulsed laser anticipating the need for higher intensities. If the laser is repetitively pulsed the acoustic signals can be signal averaged using lock-in amplifiers or box-car integrators. The sample cell shown is a liquid filled cell where the acoustic wave is coupled to the piezo-electric via the liquid as was done in the experiments presented here [4]. Alternatively the transducer can be directly attached to the sample [1].

The increased sensitivity of photoacoustic spectroscopy (PAS) over transmission experiments for observing two photon absorption in transparent materials (i.e. small linear absorption) is shown by the following analysis. Two photon absorption (2PA) is proportional to the square of the intensity, I, such that

$$\frac{dI}{dZ} = -(\alpha + \beta I) I \qquad \text{(Eq. 1)}$$

where α is the linear absorption coefficient and β is the 2PA coefficient. For a sample of length L with a surface reflectivity r this equation can be solved yielding for the inverse of the transmission T, a linear function of the incident intensity I_0, given by

$$\frac{1}{T} = \frac{e^{\alpha L}}{(1 - r)^2} + \frac{\beta I_0}{(1 - r)} \frac{(1 - e^{-\alpha L})}{\alpha} \qquad \text{(Eq. 2)}$$

where the effects of light reflected into the sample at the rear surface are ignored. If the index mismatch is large this approximation can lead to significant errors as discussed in Ref. 3. Using liquid filled samples cells reduces this index mismatch. Within this approximation the ratio of absorbed energy, E_a, to incident energy, E_i, is given by

$$\frac{E_a}{E_i} = 1 - r - \frac{T}{1 - r} \qquad \text{(Eq. 3)}$$

We are now in a position to compare the two methods of PAS and transmission. Assume that the total absorption is small i.e., $(\alpha + \beta I)L \ll 1$, then eq. 2 reduces to

$$\frac{1}{T} = \frac{1}{(1 - r)^2} [1 + \alpha L + \beta I_0 L(1 - r)] \qquad \text{(Eq. 4)}$$

and eq. 3 reduces to

$$\frac{E_a}{E_i} = (1 - r)\,[\alpha L + \beta I_0 L(1 - r)] \qquad \text{(Eq. 5)}$$

In order to get the same percentage change in the transmission experiment due to 2PA, as in the photoacoustic experiment, we compare the 2PA term (third term in eq. 4, second term in eq. 5) to the other terms. For transmission we find that to observe a 10% change in the signal

$$\beta I_0 L(1 - r) \cong (.10)\,(1 + \alpha L) \cong (.10) \qquad \text{(Eq. 6)}$$

while for PAS we find

$$I_0 L(1 - r) \cong (.10)\,\alpha L \qquad \text{(Eq. 7)}$$

Using samples of low linear loss the PAS method has a clear advantage. For example, using a sample of 1 cm length having a linear absorption coefficient of 10^{-3} cm^{-1} would allow the 2PA term using PAS to be 10^{-3} as large as when using transmission. Thus, to measure the same 2PA coefficient, intensities using PAS can be 10^{-3} as large as intensities using transmission; or 2PA coefficients 10^{-3} as large can be measured using the same intensity. Clearly to take advantage of the PAS method samples having small linear absorption must be used. In addition, in eq. 7 for PAS, the length L cancels. The fractional change in the PAS due to 2PA is independent of the sample length. It may, therefore, be possible to use the PAS technique to observe nonlinear absorption in optical coatings.

The experiments presented here directly compare the PAS signal to the transmission on a single shot basis. Signal averaging is not used nor do the samples have particularly low linear absorptivities. Thus, these experiments do not demonstrate the ultimate sensitivity of nonlinear PAS but do show the feasability of the technique for observing nonlinear absorption and how the PAS signals compare to the standard nonlinear transmission measurements. Similar work to that presented here using a tunable repetitively pulsed nanosecond dye laser is being performed in Austria [5].

The laser source for the studies was a passively mode-locked microprocessor-controlled, Nd:YAG system operating at 1.06 μm. A single pulse of measured Gaussian spatial and temporal intensity distribution was switched from the mode-locked train and amplified. The temporal pulsewidth was approximately 40 picoseconds. The width of each pulse was monitored by measuring the ratio, R, of the square of the energy in the fundamental (1.06 μm) to the energy in the second harmonic, produced in a $LiIO_3$ crystal. This ratio is directly proportional to the laser pulsewidth as long as the spatial profile remains unchanged. The ratio was calibrated by measuring the pulsewidth using Type I secord harmonic autocorrelation scans.

The spatial beam distribution was determined by pinhole beam scans and by vidicon scans of single laser shots. The beam was thus determined to be Gaussian and stable from pulse to pulse. The energy on target was varied by changing the angle between a calibrated pair of Glan polarizers that were arranged to keep the direction of polarization at the sample surface constant. The output energy of the laser and the energy transmitted through the sample were continuously monitored by sensitive photodiode peak-and-hold detectors. These detectors were determined to be linear over their range of use and were absolutely calibrated with respect to a pyroelectric energy monitor. The pyroelectric detector was in turn checked with a thermopile calorimeter.

The samples were placed in a water filled photoacoustic cell similar in design to that of Patel and Tam [4]. The acoustic signal generated in the solid travels through the solid, is transmitted through the liquid and then to a stainless steel plug in contact with the piezoelectric transducer. Since the acoustic wave travels fastest in the solid it is detected before the signal produced by the linear absorption in water [6]. Using the liquid filled cell has the advantage that the Fresnel reflections are reduced, and samples are readily interchanged. The amplitudes of the first acoustic spike for both samples as read directly off an oscilloscope constituted the PAS signal. This signal has been shown to be directly proportional to the total absorbed energy [4]. By monitoring this signal as a function of intensity, the contributions from nonlinear as well as linear absorption are determined.

If the solid sample is placed at one extreme end of the sample cell it is observed that the first spike in the acoustic signal varies linearly with intensity. Many microseconds later a spike that grows nonlinearly with intensity is observed that is due to absorption in the sample. The delay is the time it takes sound to travel the extra distance through the liquid. Thus, the response of the system is shown to be linear.

Figures 2 and 3 show inverse transmission as a function of intensity of picosecond pulses for CdSe and CdTe respectively. The intensity distribution of the pulses incident on the sample was

$$I(r,t) = I_0\, e^{-\left(\frac{r}{w_0}\right)^2} e^{-\left(\frac{t}{\tau}\right)^2} \qquad \text{(Eq. 8)}$$

after taking into account reflections from the windows in the sample cell and the absorption in water. Here τ was 25 ± 5 psec and w_0 was .17 cm for CdSe and .15 cm for CdTe. Thus, rather than using eq. 2, eq. 1 was integrated over space and time to yield

$$T = \frac{2\alpha e^{-\alpha L}(1-r)}{\sqrt{\pi}\beta I_0(1-e^{-\alpha L})} \int_0^\infty dx \ell n[1 + \frac{\beta}{\alpha} I_0(1-r)(1-e^{-\alpha L}) e^{-x^2}] \qquad \text{(Eq. 9)}$$

Using for CdSe $\alpha = 1.01\ cm^{-1}$ and $\beta = 0.035$ cm/MW and for CdTe $\alpha = 0.45\ cm^{-1}$ and $\beta = 0.050$ cm/MW gave the fits shown in Figs. 2 and 3. The CdSe sample was 2 mm thick and the CdTe was 2.13 mm thick. The deviation at high intensities has been observed previously and has been explained as being due to the linear absorption of free carriers created by 2PA [7]. The value of β for CdSe is consistent with Ref. 7 while β for CdTe is a factor of two larger. By using the values for T obtained from Figs. 2 and 3 we calculate what the expected PAS signal divided by incident energy should be from eq. 3. These are plotted in Figs. 4a and 5a. Figure 4b and 5b show the actual PAS signal divided by incident energy. Since the PAS signal voltage is not absolutely calibrated the vertical axis was scaled to coincide with the low intensity data of Fig. 4a and 5a. For CdSe there is a 1 to 1 correspondence of the data from the transmission and PAS experiments. The apparent deviation at the very lowest intensities is not understood but may be an electronic noise problem and is not considered significant. For CdTe at very high intensities (greater than 500 MW/cm^2) there is a clear deviation of the PAS signal below what is expected from the transmission data. At these high intensities it is possible that stimulated emission processes become appreciable. CdTe has been made to lase at .79 μm. Energy reemitted at another wavelength does not increase the PAS signal but it does lower the transmission at 1.06 μm. A 1.06 μm filter was used in front of the detectors. In order to account for the observed difference between Fig. 5a and 5b the fraction of energy absorbed that contributed to reradiation at .79 μm would need to be nearly 20%. This appears somewhat unlikely in which case we may be seeing a saturation the acoustic signal. The voltages obtained from the piezoelectric at these intensities were millivolts. However, the voltages using the CdSe sample were comparable and no such deviation was observed. This should pose little problem for future experiments using lower intensities.

The authors wish to thank M. Bass for the loan of samples and gratefully acknowledge the support of the Naval Weapons Center, the Office of Naval Research, the Research Corporation, and the North Texas State Faculty Research Fund.

References

[1] Hordvik, A., and Schlossberg, H., Appl. Opt. 16, 101 (1977).

[2] See for example Alan Rosencwaig in "Optoacoustic Spectroscopy and Detection", ed. Y. H. Pao, Academic Press, N.Y., p. 193, (1977).

[3] Bass, M., Van Stryland, E. W., and Stewart, A. F., Appl. Phys. Ltrs. 34(a), 142 (1979).

[4] Patel, C. K. N., and Tam, A. C., Appl. Phys. Lett. 34(7), 1 (1979).

[5] Schmidt, A., Technische Universitat, Vienna Austria, private communication.

[6] Sam, C. L., and Shank, M. L., PHOTOACOUSTIC SPECTROSCOPY, Technical Digest, Paper THA7, Ames, Iowa, 1979.

[7] Bechtel, J. H. and Smith, W. L., Phys. Rev. B8, 3515 (1976).

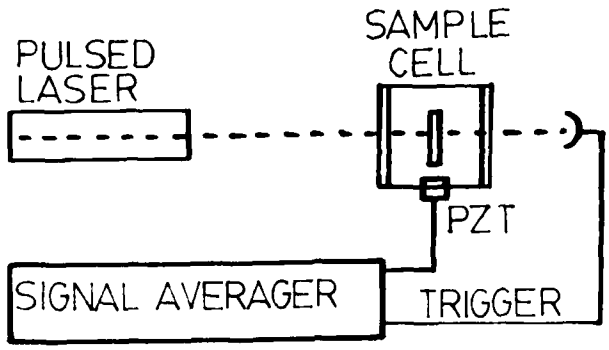

Figure 1. Nonlinear photoacoustic experiment.

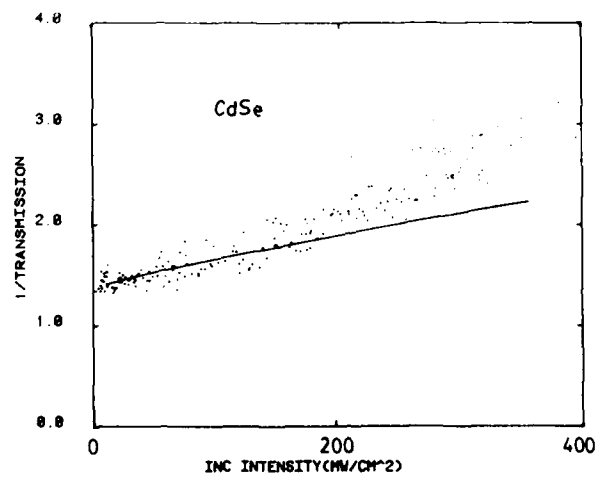

Figure 2. Inverse transmission as a function of the intensity of picosecond pulses in CdSe. The line is a fit for low intensities using $\alpha = 1.1\ cm^{-1}$ and $\beta = 0.35$ cm/MW.

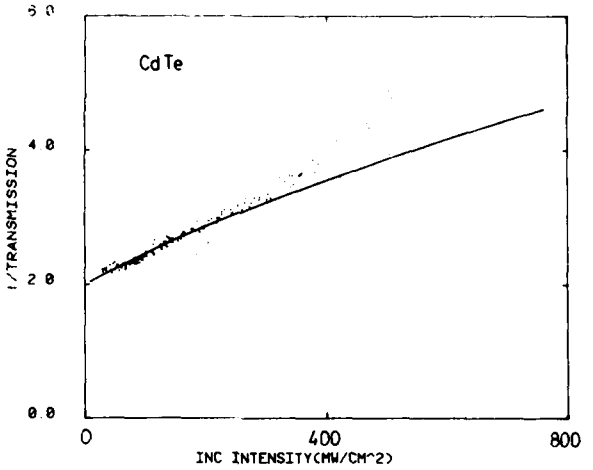

Figure 3. Inverse transmission as a function of the intensity of picosecond pulses in CdTe. The line is a fit for low intensities using $\alpha = 0.45\ cm^{-1}$ and $\beta = 0.51$ cm/MW.

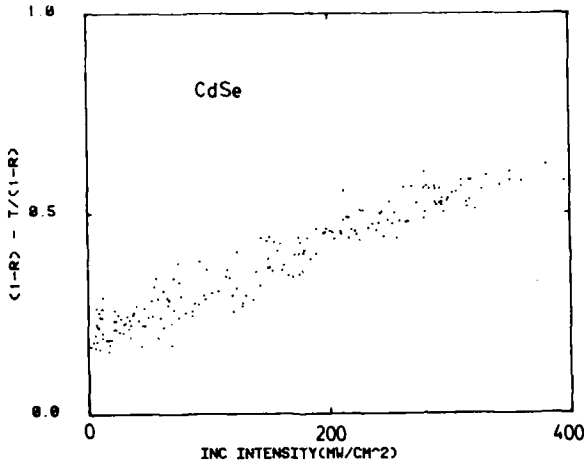

Figure 4(a). The expected PAS signal divided by incident energy as a function of incident intensity as calculated from the observed transmission of CdSe.

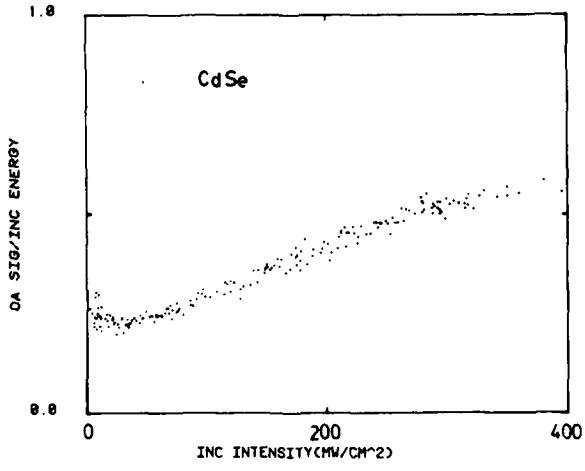

Figure 4(b). The observed PAS signal divided by incident energy as a function of incident intensity for CdSe.

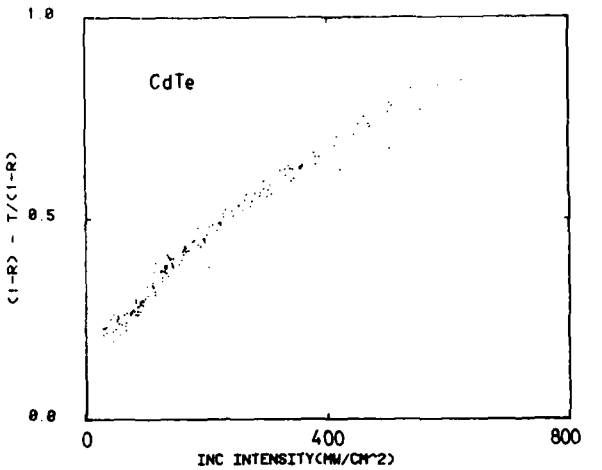

Figure 5(a). The expected PAS signal divided by incident energy as a function of incident intensity as calculated from the observed transmission of CdTe.

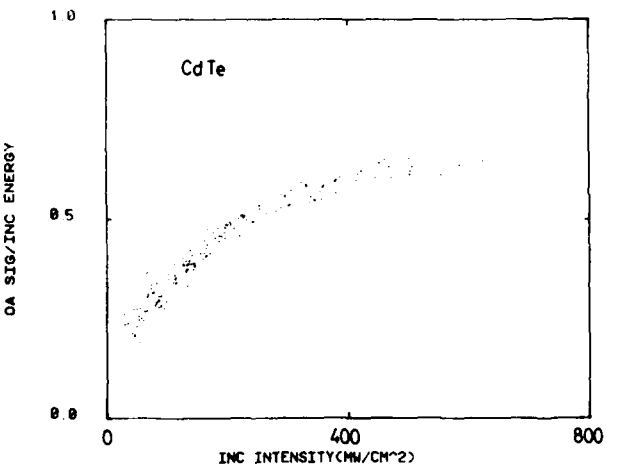

Figure 5(b). The observed PAS signal divided by incident energy as a function of incident intensity for CdTe.

It was pointed out that saturation effects are sometimes seen in PAS for strongly absorbing liquids. Nonlinear affects in liquids as well as solids can thus be seen using PAS. Surface and bulk absorption can also be separated using PAS, as has been demonstrated at the University of California, Berkeley, and also at the University of Michigan. Transient absorption can also be studied using PAS up to the 100 MHz limit of the detector.

1.3 μm LASER RATE CALORIMETRY AND PHOTOACOUSTIC STUDIES OF THE SURFACE AND BULK OPTICAL ABSORPTION IN CaF_2 SINGLE CRYSTAL SAMPLES

Nils C. Fernelius, David V. Dempsey and David B. O'Quinn
University of Dayton Research Institute
Dayton, Ohio 45469

There are a variety of techniques for measuring the surface-to-bulk optical absorption ratio most of which require specially prepared samples. In most works only one technique was employed on a given sample. In this work we tried three different techniques to measure the surface-to-bulk optical absorption ratio, r, at 1.3 μm on a group of similar CaF_2 single crystal samples. Laser rate calorimetry results on a series of samples of varying thickness gave $r = \beta_S/\beta_B = 0.14$ cm where β_S is the surface absorption and β_B is the bulk optical absorption in cm^{-1}. A second slope was not seen on the long bar samples which implies that r is less than 0.3 cm. Analysis of photoacoustic chopping frequency variation studies using the Bennett-Forman theory gave r = 0.07 cm about half the multithickness result. Considering the experimental uncertainties all three techniques yielded consistent results.

Key words: CaF_2; laser calorimetry; laser windows; optoacoustic; photoacoustic; surface-to-bulk optical absorption.

1. Introduction

In the design of laser windows it is desirable to know the ratio of the surface optical absorption to bulk optical absorption of a given window. When this ratio is known, then the designer knows where to concentrate his efforts to obtain a lower absorbing window. If the bulk absorption predominates, then the emphasis will be on improving purification of starting materials, crystal growth techniques, forging methods, and variation of strengthening additives. If the surface is the major contributor, then the emphasis will be placed on improving polishing and cleaning techniques or use of different protective coatings.

The measurement of optical absorptance in highly transparent materials requires special measurement techniques. The status of various useful techniques has been covered in several review articles [1,2].[1] Probably the most commonly used technique is laser rate calorimetry [3,4,5]. Figure 1 shows an experimental arrangement. The window of interest is mounted in a thermally isolated condition with a thermocouple embedded in an indium bead pressed against the side. In practice two thermocouples in series are used in a bridge circuit. The output of the thermocouples is recorded on an X-Y recorder with the x axis controlled by a timer. The laser is turned on (or shutter opened) and the change in temperature versus time dT_2/dt is recorded where T refers to temperature and t refers to time. The laser is turned off and the cooling slope dT_3/dt is recorded. To a good approximation the conductive and radiative losses can be approximated by being proportional to $T-T_{ambient}$. From these recorded slopes the quantity $\Delta T/\Delta t = |dT_2/dt| + |dT_3/dt|$ is obtained. The optical power absorbed in the sample is $P_A = mC_p(\Delta T/\Delta t)$ where m is the sample mass and C_p is its specific heat.

For transparent window materials with small absorption and identical reflectance, R, and absorption, β_S, at each surface, the following relation exists

$$P_A/P_T = [(1+x)\beta_S+\beta_B\ell][(1+R)/(1-R) \qquad (1)$$

where P_T is the transmitted power, β_B is the bulk optical absorption coefficient and ℓ is the sample thickness. This is Case 8 of Fernelius and Johnston [6]. Depending on various theoretical assumptions x lies between 1 and n, the index of refraction of the material. On a single sample of thin thickness dimensions one cannot separate the surface and bulk magnitude not to mention x and one generally reports a

$$\beta_{eff} \equiv \beta_B + (1+x)\beta_S/\ell \ . \qquad (2)$$

There are a variety of ways for obtaining the surface-to-bulk absorption ratio. Most of these require specially prepared or shaped samples. The most recent review of this subject is by Temple [7]. Here we shall discuss several methods readily obtainable in the laboratory.

The most commonly used calorimetric method is the multithickness sample technique [8]. This technique assumes one has a number of samples with varying thicknesses grown from the same boule and given identical surface polish and other treatments. By plotting $\beta_{eff}\ell$ versus ℓ for the samples, in theory, one obtains a number of points which can be fit by a straight line whose slope is β_B and whose intercept at ℓ=0 gives $(1+x)\beta_S$. In practice these conditions are hard to obtain especially for for polycrystalline forged samples. Thus often the points are not too close to the straight line and often a negative surface absorption is obtained. Here we shall give results on some single crystal CaF_2 samples obtained from Harshaw which were supposedly cut from the same boule and given the same surface treatments.

[1] Figures in brackets indicate the literature references at the end of this paper.

The second calorimetric method is the so-called two-slope method [9]. If a long bar sample is irradiated along its length and thermocouples are attached at the midpoint along the sides, then the thermal rise curve may exhibit two slopes. The first slope is identified with bulk absorption and the second with total (surface plus bulk) absorption. So far results using this method have only been reported on KCl and NaCl both of which undergo surface attack by the atmosphere. In these reports the ratio of the surface to bulk absorption was 0.3 cm or higher. Thus numbers are attainable using this method only with long bar geometry samples in which the surface and bulk absorption values are of comparable magnitude.

The third technique we shall discuss here is that of the chopping frequency dependence of a photoacoustic (PA) signal. Photoacoustic spectroscopy [10,11] is a recently revived technique whose full potential is being developed. In the photoacoustic effect a sample is illuminated by periodically modulated light. The light undergoes optical absorption and the sample is heated by nonradiative transitions. There is a concomitant stress wave generated. Thus periodic stress and thermal waves propagate through the sample. The stress wave can be detected directly by attaching a transducer to the sample [12]. Indirectly these effects can be detected by having the sample in an enclosed cell with a sensitive microphone and measuring the sound wave generated in the gas by the periodic heating of the sample surface. Figure 2 shows the experimental arrangement for chopping frequency studies.

Several theoretical treatments have been developed to describe the photoacoustic signal observed from solids. A discussion of their scope has been given elsewhere [13]. Here we shall consider the most widely used theory, that of Rosencwaig and Gersho [14] which assumes that the PA signal is generated solely by periodic heat flow from the sample to the gas. The other theory we shall treat is that of Bennett and Forman [15] developed for nearly transparent samples which includes both acoustic and thermal diffusion terms.

In both of these theories there are regimes in which the amplitude of the photoacoustic signal S has the form $S = A f^{-n}$, where f is the modulating frequency and A is a constant. For predominately surface absorption contributions to the PA signal, n=1 and for predominately bulk absorption n=3/2. The surface contribution can dominate if the sample has a large optical absorption coefficient, β, which does not allow light to penetrate deeply into the sample, or due to a high modulating frequency, which does not allow the heat generated to be transported to the surface before another heat pulse begins. For the samples treated here we are working with small β values.

While the theoretical analysis of the PA signal is rather involved, with more experience it may be developed into a more straightforward method. One big advantage of the PA method is that it is applicable to windows of conventional dimensions. Also theoretical treatments on ZnSe indicate that the PA technique is sensitive in regions where the suface to bulk absorption ratio is 0.1 cm or less. Presumably this is the situation obtained for good quality windows.

In previously reported work, the researcher has used one of the above mentioned suface-to-bulk techniques to obtain the experimental ratio. The main purpose of this work was to apply three techniques—multithickness sample method, long bar two-slope analysis, and analysis of photoacoustic chopping frequency dependence—to compare the results of each for consistency.

2. Experimental Results

In an attempt to obtain good quality results a number of single crystal CaF_2 samples were ordered from Harshaw Chemical Company. All were presumably made from the same boule. They are all cylindrical shaped rods, 38 mm in diameter, with varying thickness. All faces were supposed to receive the same polishing treatment. Thus it was hoped that the systematic errors inherent in taking data through different directions in a parallelepiped would be eliminated. All samples were used in the multithickness study. Only a long bar sample was used for the two-slope study. The photoacoustic study used the two 1 cm thick samples to enclose the PA cell.

All data were taken with a Quantronix 114 Nd:YAG laser fitted with special mirrors to operate at 1.3 μm. This approximates the wavelength of the iodine (I_2) laser now undergoing development for scaling up to high power levels.

2.1. Laser Rate Calorimetry Results

The experimental arrangement was as shown in figure 1. Two sets of thermocouples were used to record the temperature changes. One pair of thermocouples was attached to the Teflon® mounting blocks holding the samples. These thermocouples measure temperatures about 3 to 4 mm from the laser entrance face of the samples. Thus for conventional thickness samples 5 to 10 mm thick, they measure temperatures roughly at the midpoint along a side. In addition we often place a piece of polystryrene between the thermocouple bead (copper-constantan in an indium bead) and the mounting blocks for further thermal insulation. A second set of thermocouples were mounted on Teflon® rods supported by an aluminum ring painted black. These thermocouples could touch a variety of locations along the edge of the thick samples above the mounting blocks. However they were unable to get closer than about 2 cm from the entrance face. For the 1 cm thick samples, the windows were supported by the two Teflon pads which hold the thermocouple beads. For the thicker samples two additional blocks with Teflon pads provided support but also provided an additional path for conduction heat losses.

In laser calorimetry, samples with appreciable scattering show a temperature rise jump when the cw laser is turned on and a drop when it is shut off. These jumps were not observed with these samples, so scattering effects were neglected.

Table 1 lists the results of 1.3 μm laser calorimetry experiments measured with the thermocouples near the entrance face. The average value of the 1 cm samples is $\beta_{eff} = 0.769 \times 10^{-3} cm^{-1}$. The results on the 2 cm thick sample seem anomalously low, yet repeated experiments verified the number.

Table 1. 1.3 μm Laser Calorimetry Results on CaF_2.
Temperature Measured Near Entrance Face.

AFML Sample Number	Thickness in cm	$A_s \div 10^{-3}$ or $\beta_{eff}\ell \div 10^{-3}$	$\beta_{eff_{slope}} \div 10^{-3} cm^{-1}$
2894	1	0.7505	0.7505
2895	1	0.7870±0.0333	0.7870±0.0333
2896	2	0.6463±0.0405	0.3232±0.0203
2897	4	1.648±0.2160	0.4120±0.0135
2898	6	2.7696±0.0558	0.4616±0.0093

Table 2 gives the values measured with the movable thermocouples. The values in these tables are plotted in figure 3. Considering the β_{eff} values of the 1 cm and 2 cm samples as both entrance face and center of length measurements, several analyses of these data can be made, although it is understood that this is not a good assumption for the 2 cm thick sample. For lack of better information the value of x in eq. (1) is taken to be 1.0. Thus the y intercept of the straight line fit is taken to be $2\beta_s$. Linear regression analysis was made on various combinations of points. The results

Table 2. 1.3 μm Laser Calorimetry Results on CaF_2.
Values Measured with Movable Thermocouples.

AFML Sample Number	Thickness in cm	Location	$\beta_{eff_{slope}}\ell \div 10^{-3}$	$\beta_{slope} \div 10^{-3}$
2897	4	Near Front	2.48	0.621
		Center	2.655	0.664
		Exit	2.18	0.545
2898	6	Center	3.833±0.0208	0.6389±0.0035
		Exit	3.81	0.6355

are summarized in table 3. In the first column data at the entrance face are used. The correlation of the best fit with the data points is only fairly good, R = 0.967. The ratio $\beta_s/\beta_B = 0.078$ cm. The curve drawn from the results is the solid line in figure 3. In the second column the entrance data on the 1 and 2 cm thick samples are now treated as center of sample data. The 2 cm results are obviously low. Even so a slightly better correlation is obtained, R = 0.974, than in the preceding case. However this case leads to a negative surface absorption which is an unphysical result. The results are drawn as a dashed curve in figure 3. Omitting the 2 cm value, the analysis was repeated in the third column. The best correlation, R = 0.9998, of the three cases was obtained. In this case $\beta_B = 0.614 \times 10^{-3} cm^{-1}$, $\beta_s = 0.000084$ and $\beta_s/\beta_B = 0.136$ cm were obtained.

Inspection of the rate calorimetry traces taken by the thermocouples located at the mid position along the side did not reveal any second slope. Thus a two slope analysis could not be made. No reported value using the slope technique has been smaller than $\beta_s/\beta_B = 0.3$ cm. In the results of Vora et al. [16] on KCl and NaCl gave values of β_s/β_B between 0.5 and 3 cm. Thus we conclude that the lack of a second slope implies that β_s/β_B is smaller than 0.3 cm. This is consistent with our linear regression analysis giving $\beta_s/\beta_B = 0.14$.

Table 3. Linear Regression Analysis of Data

Data Used

ℓ in cm	$\beta\ell \div 10^{-3}cm^{-1}$		
	entrance —	Center ----	center - — -
1	0.7688	0.7688	0.7688
2	0.6463	0.6463	-
4	1.6480	2.655	2.655
6	2.7696	3.8333	3.8333
Linear Regression Results			
Y intercept $= 2\beta_s$	0.06679	-0.22647	0.16715
β_s	0.03340	-0.11324	0.08358
slope $= \beta_B$	0.42812	0.67764	0.61415
β_s/β_B in cm	0.0780	-0.1671	0.136
R	0.96714	0.97424	0.9984

2.2. Photoacoustic Experimental Results

The photoacoustic experimental arrangement is shown in figure 2. The chopper was a Princeton Applied Research (PAR) variable frequency light chopper Model 192 with a 20 blade chopper wheel. The chopping frequency was measured by a Hewlett Packard Model 5304A electronic timer-counter. The detector microphone was a Gen-Rad type 1961-9601 random incidence 1-inch Electret-Condenser microphone. The signal from this was fed into an Ithaco Model 167 pre-amplifier and a PAR model 5204 lock-in amplifier operated in the flat mode.

The shutter in front of the laser was opened and after the initial transients died down, the lock-in phase was adjusted to give zero quadrature signal. The lock-in signal amplitude and phase setting were recorded. The shutter was closed. If any in phase or quadrature signals existed, they were recorded on the second run. Thus coherent noise corrections could be made as in the appendix of Fernelius and Walsh [17]. The chopper frequency was changed and the process was repeated. Amplitude and phase plots are shown in figures 4 through 7. The circular points were taken as the chopper frequency was increasing; triangular points as the frequency was decreasing. On the second run the coherent noise corrections [17] were made and indicated by open points. The amplitude plots gave an $S = A\ f^{-n}$ dependence of n=1.01 and 0.99 thus indicating a largely surface type absorption. Due to an arbitrary zero in the phase setting, in fact to agree with the theoretical calculations a phase angle of 360°-ϕ should be plotted, phase angle differences are considered. As in ref. [13] values of $\Delta\phi = \phi_{f_1} - \phi_{f_2}$ were obtained where f_1 = 1000 Hz and 500 Hz, f_2 = 100 Hz and 50 Hz. In the first day's run values of $\Delta\phi_{\substack{1000\\500}-50} = 13°$ and $\Delta\phi = \phi_{\substack{500\\1000}} - \phi_{100} = 4°$ were obtained; on the second day, $\Delta\phi = \phi_{\substack{1000\\500}} - \phi_{50} = 10°$ and $\Delta\phi = \phi_{\substack{1000\\500}} - \phi_{100} = 2°$.

The average β_{eff} value of the two samples (AFML 2894-5) from table 1 is $\beta = 0.77 \times 10^{-3} cm^{-1}$. Since a number of quantities in the photoacoustic expressions are not known with great precision, as a first approximation we use for β the β_{eff} obtained from laser rate calorimetry. Standard values for various CaF_2 parameters are: density, ρ = 3.18 g/cc; heat capacity, C = 0.812 J/g°K and thermal conductivity, κ = 0.080 W/cm°K. These values were inserted into FORTRAN IV complex number computer programs written to compute the PA signal amplitude and phase for various PA theories. Details of these programs are given elsewhere [13]. The Rosencwaig-Gersho (R-G) theory yields plots (figs. 8 and 9) showing n=3/2 for values of between 0.001 cm^{-1} and 0.0001 cm^{-1}, and a phase angle change between 1 Hz and 10kHz of less than 0.003°. Thus the R-G theory fails to approximate the experimental results.

Next a series of calculations using the Bennett-Forman theory for various r values were made using $\beta_{bulk} = 0.00077\ cm^{-1}$. As discussed by Fernelius [13], this bulk value only enters in the scale of the amplitude plots thus no other values were tried. From the results of these calculations $\Delta\phi$ for f_1 = 1000 Hz and f_2 = 100 and 50 Hz were made obtained with f_1 = 500 Hz and f_2 = 100 Hz and plotted in figure 10. $\Delta\phi = \phi_{1000} - \phi_{100} = 4°$ for r = 0.035 cm; 2° for r = 0.07 cm. $\Delta\phi = \phi_{500} - \phi_{100} = 4°$ for r = 0.028; 2° for r = 0.055 cm. $\Delta\phi = \phi_{1000} - \phi_{50} = 13°$ for r = 0.011; 10° for r = 0.018.

Amplitude and phase plots using r = 0.01, 0.02, 0.03 and 0.07 in the Bennett-Forman theory are shown in figures 11 and 12. In the amplitude plot $\sim$1.5 for r = 0.01 and $\sim$1.0 for r = 0.07. Thus we conclude that r = 0.07 is in better agreement with experiment on the amplitudes. Again in the angular plots, the r = 0.07 again most closely fits the mirror image of the experimental results. Hence we conclude that an r value of 0.07 cm is the value obtained from analysis of the PA experiments.

The above analysis used the experimentally measured β_{eff} as β_{bulk} in making its estimates. As in ref. [13] a slightly better value can be obtained. Since $\beta_B = \beta_{eff}/(1+2r/\ell)$; we have using r = 0.07 cm, $\beta_{bulk} = 0.00077/1.14 = 0.00068\ cm^{-1}$ and $\beta_s = 0.000048$.

3. Conclusions

Measurements of the surface-to-bulk optical absorption coefficient ratio, r, were made by three different methods. Laser rate calorimetry results on multithickness samples gave $r = \beta_s/\beta_B = 0.136$ cm. Since two slopes were not seen in long bar samples, we conclude that r is less than 0.3 cm. Analysis of photoacoustic experiments using the Bennett-Forman theory gives r = 0.07 cm about half the multithickness result. Considering the somewhat arbitrary choice of points used in the linear regression analysis of the multithickness samples, this agreement is quite good.

4. Acknowledgments

We wish to thank Mr. Jeffrey A. Fox for making the computer plots for the photoacoustic theories. This work was supported by the AFWAL Materials Laboratory, Wright-Patterson Air Force Base, Ohio 45433.

References

[1] Skolnik, L., in *Optical Properties of Highly Transparent Solids*, Eds. S.S. Mitra and B. Bendow (Plenum, NY, 1975) pp. 405-433.

[2] Hordvik, A., Appl. Opt. 16, 2827 (1977).

[3] Kushida, T. and Geusic, J.E., Phys. Rev. Lett. 21, 1172 (1968).

[4] Pinnow, D.A. and Rich, T.C., Appl. Opt. 12, 984 (1973).

[5] Hass, M., Davisson, J.W., Klein, P.H., and Boyer, L.L., J. Appl. Phys. 45, 3959 (1974).

[6] Fernelius, N.C. and Johnston, G.T., in NBS Spec. Publ. 541: *Laser Induced Damage in Optical Materials: 1978* edited by A.J. Glass and A.H. Guenther, pp. 7-12.

[7] Temple, Paul in NBS Spec. Publ. 547: *Basic Optical Properties of Materials—Summaries of Papers*, Ed. Albert Feldman, May 1980, pp. 194-200.

[8] Deutsch, T.F., J. Electron Mater. 4, 663 (1974).

[9] Rosenstock, H.B., Hass, M., Gregory, D.A. and Harrington, J.A., Appl. Opt. 16, 2837 (1977).

[10] Rosencwaig, A., in *Optoacoustic Spectroscopy and Detection*, Ed. Yuh-Han Pao (Academic Press, NY, 1977) p. 193ff.

[11] Rosencwaig, A., in *Advances in Electronics and Electron Physics*, Ed. L. Marton (Academic Press, NY, 1978) p. 207ff.

[12] Hordvik, A. and Schlossberg, H., Appl. Opt. 16, 101, 2919 (1977).

[13] Fernelius, N.C., J. Appl. Phys. 51, 1756 (1980).

[14] Rosencwaig, A. and Gersho, A., J. Appl. Phys. 47, 64 (1976).

[15] Bennett, H.S. and Forman, R.A., J. Appl. Phys. 48, 1432 (1977) and references therein.

[16] Vora, H., Ohmer, M.C. and Stoebe, T.G., J. Appl. Phys. 50, 4936 (1979).

[17] Fernelius, N.C. and Walsh, D.A., in NBS Spec. Publ. 541: *Laser Induced Damage in Optical Materials-1978*, Eds. A.J. Glass and A.H. Guenther, pp. 43-49.

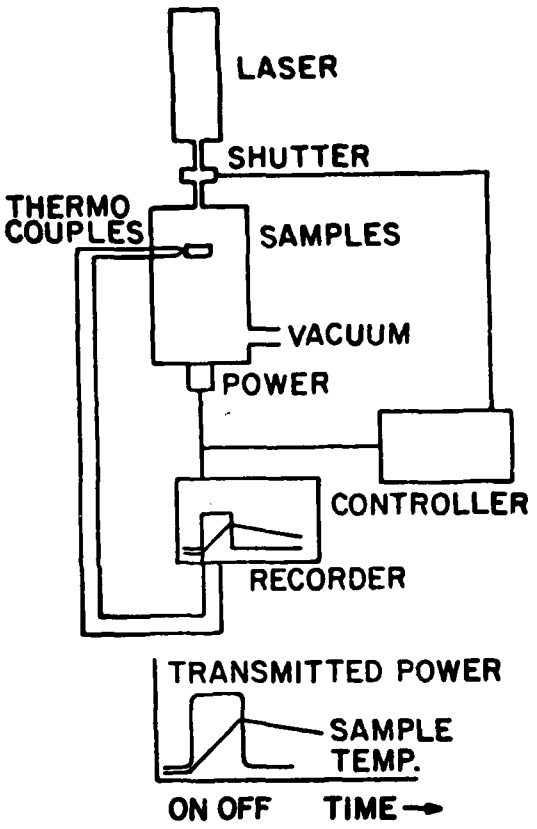

Figure 1. Diagram of laser rate calorimetry apparatus.

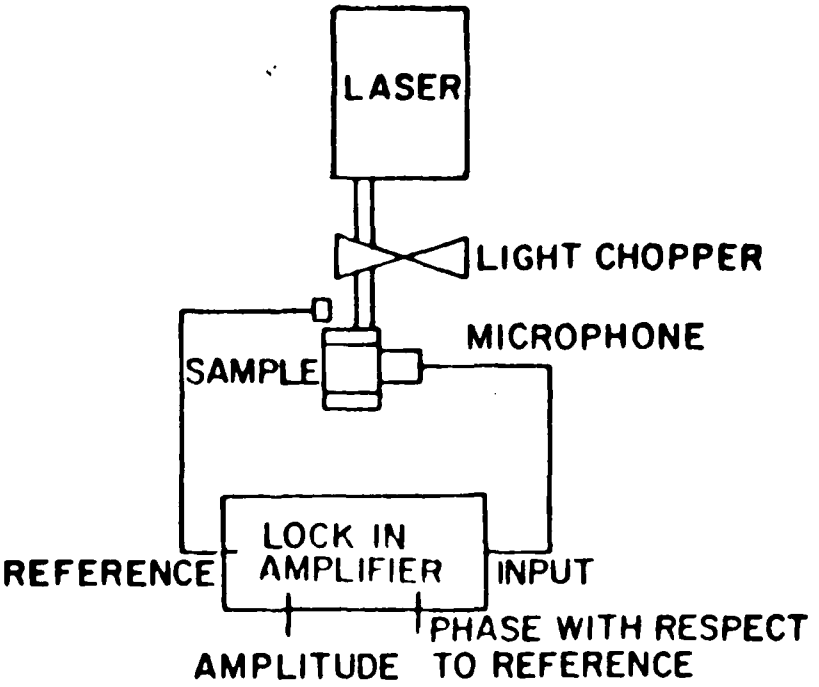

Figure 2. Diagram of photoacoustic chopping frequency apparatus.

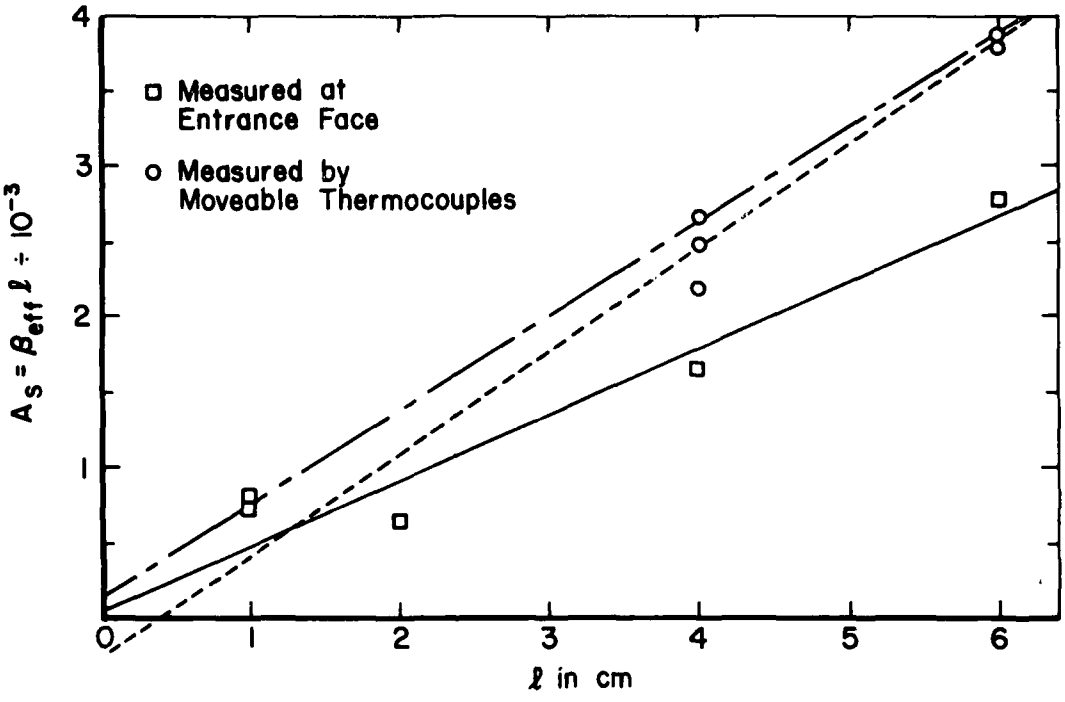

Figure 3. Fractional absorptance, $A_s = \beta_{eff}\ell$ versus sample thickness ℓ. — , thermocouples at entrance face; ---- , thermocouples at center of side; — - — , thermocouples at center, 2 cm thick sample ignored.

AFML 2894-5 CaF_2 WINDOWS
1.3 μm QUANTRONIX 114 Nd: YAG LASER 37 amp
ITHACO 167 PREAMPLIFIER
PARC 5204 LOCK-IN FLAT MODE, FLOAT A
INPUT x 10 OUTPUT x 100
D.C. PREFILTER 1 sec, τ = 1 sec

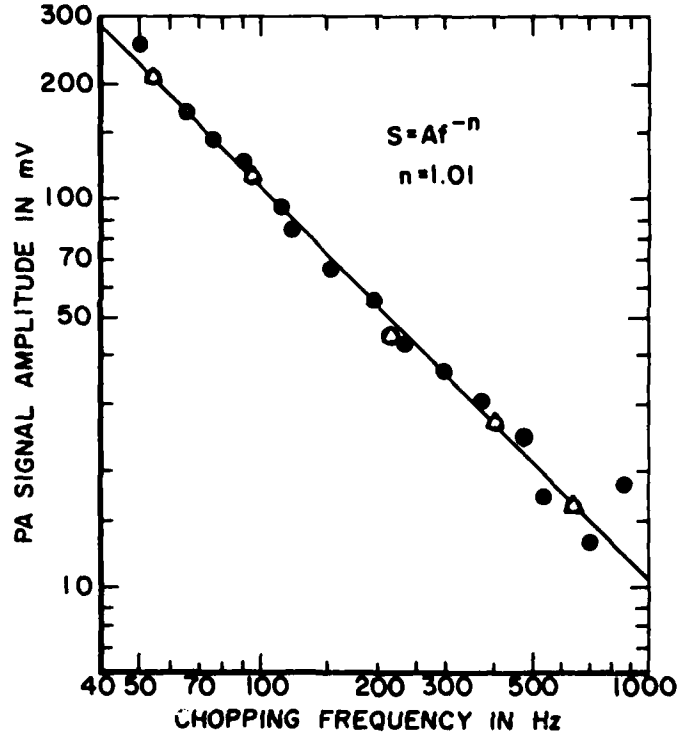

Figure 4. Experimental photoacoustic signal amplitude versus chopping frequency on 1 cm thick single crystal CaF_2 discs. Solid points taken while increasing frequency; hollow points while decreasing frequency.

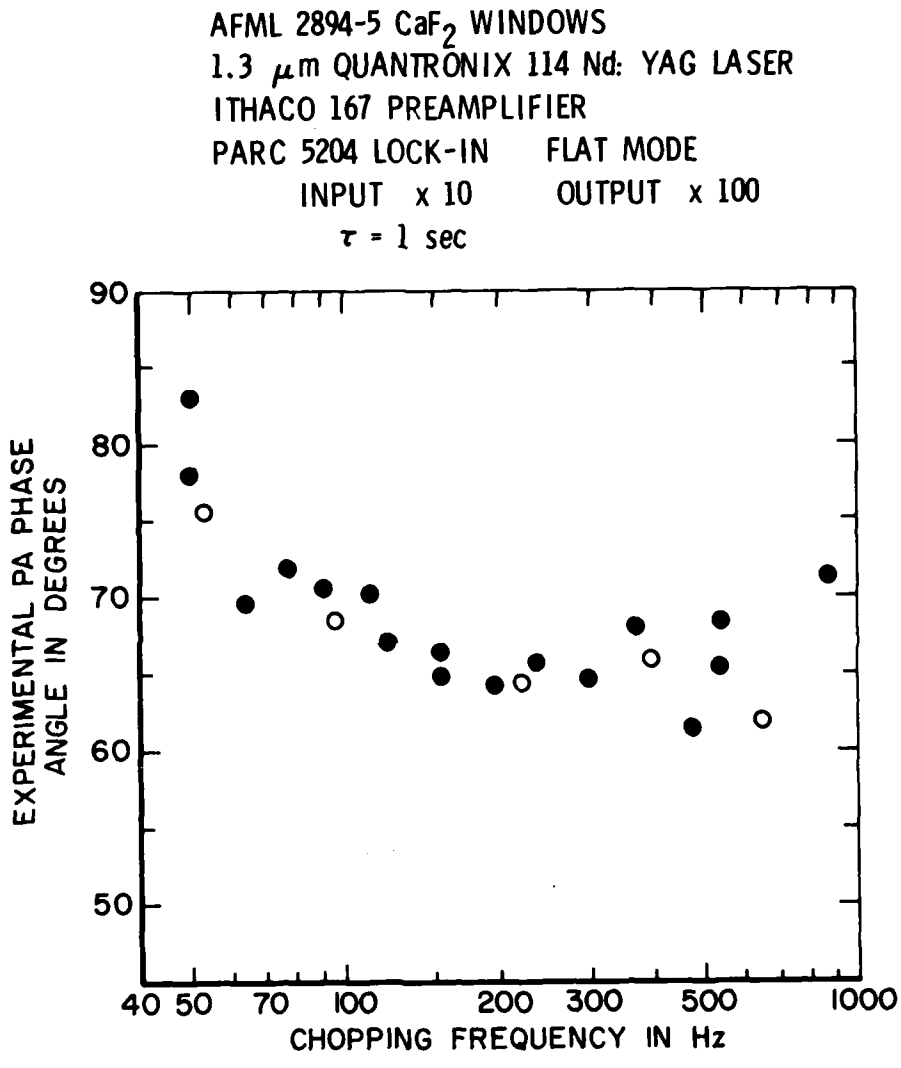

Figure 5. Experimental photoacoustic phase angle versus chopping frequency on 1 cm thick single crystal CaF_2 discs. Solid points taken while increasing frequency; hollow points while decreasing.

AFML 2894-5 CaF_2 WINDOWS
1.3 μm QUANTRONIX 114 Nd: YAG LASER
35 amp
ITHACO 167 PREAMPLIFIER
PARC 5204 LOCK-IN FLAT MODE, FLOAT A
INPUT x 10 , OUTPUT x 100
D.C. PREFILTER 1 sec, τ = 1 sec

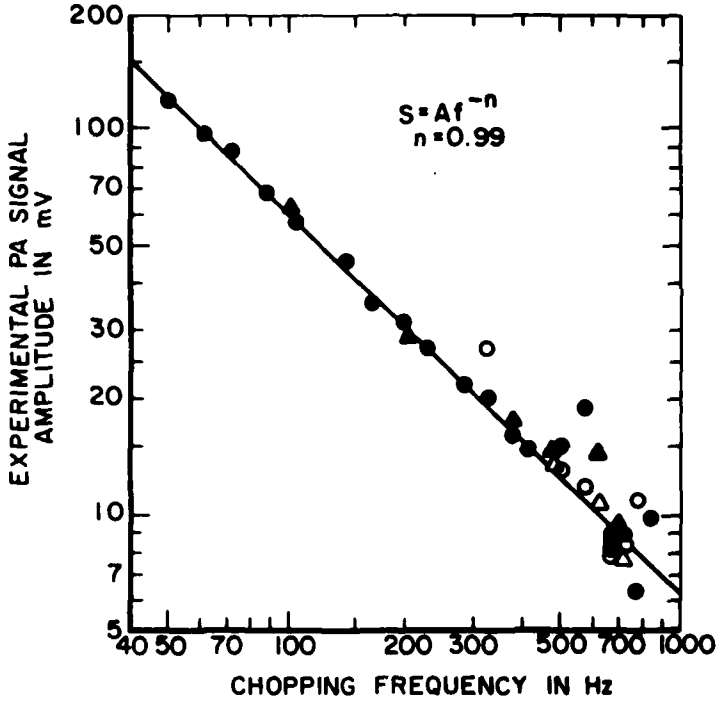

Figure 6. Experimental photoacoustic signal amplitude versus chopping frequency of 1 cm thick single crystal CaF_2 discs. Solid circles while increasing frequency; solid triangles while decreasing frequency. Hollow points include coherent noise corrections.

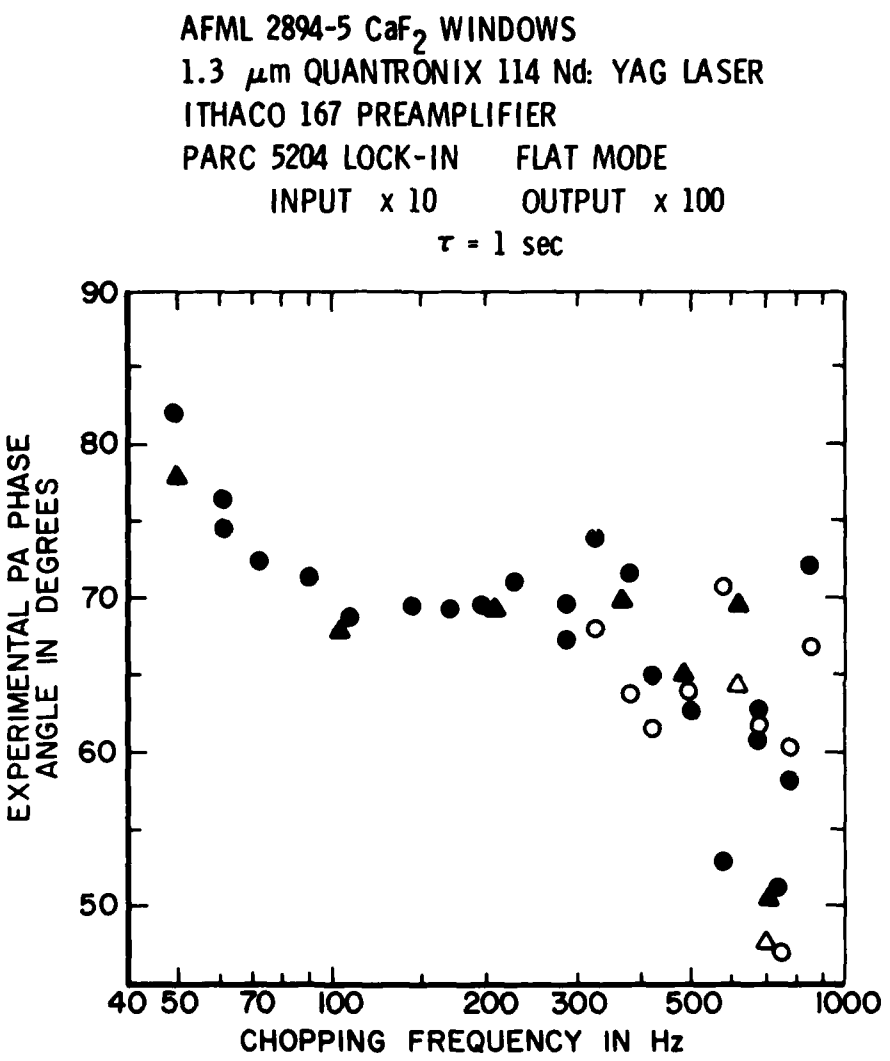

Figure 7. Experimental photoacoustic phase angle versus chopping frequency of 1 cm thick single crystal CaF_2 discs. Solid circles while increasing frequency; solid triangles while decreasing frequency. Hollow points include coherent noise corrections.

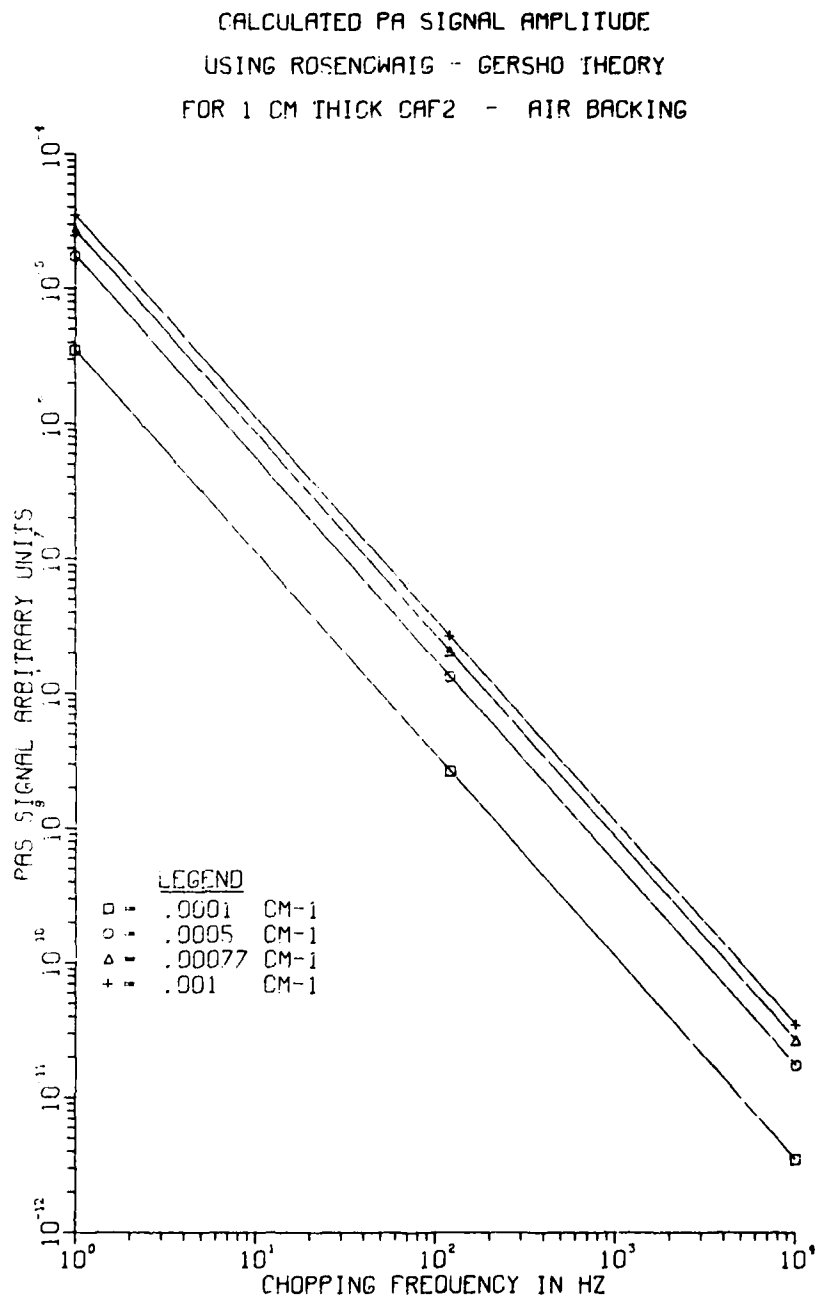

Figure 8. Calculated photoacoustic signal amplitude versus chopping frequency using Rosencwaig-Gersho theory for 1 cm thick CaF_2 with air backing. Various bulk optical absorption values were used.

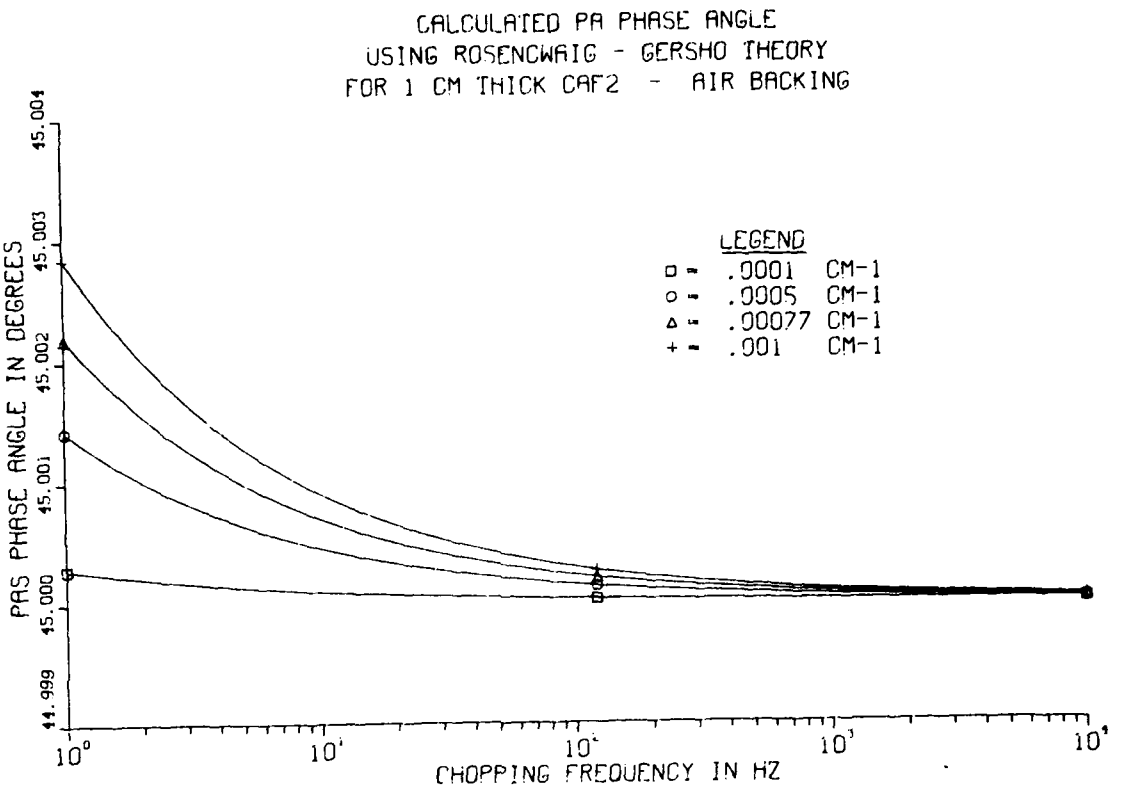

Figure 9. Calculated photoacoustic phase angle versus chopping frequency using the Rosencwaig-Gersho theory on a 1 cm thick CaF_2 sample with air backing. Several bulk optical absorption values were used.

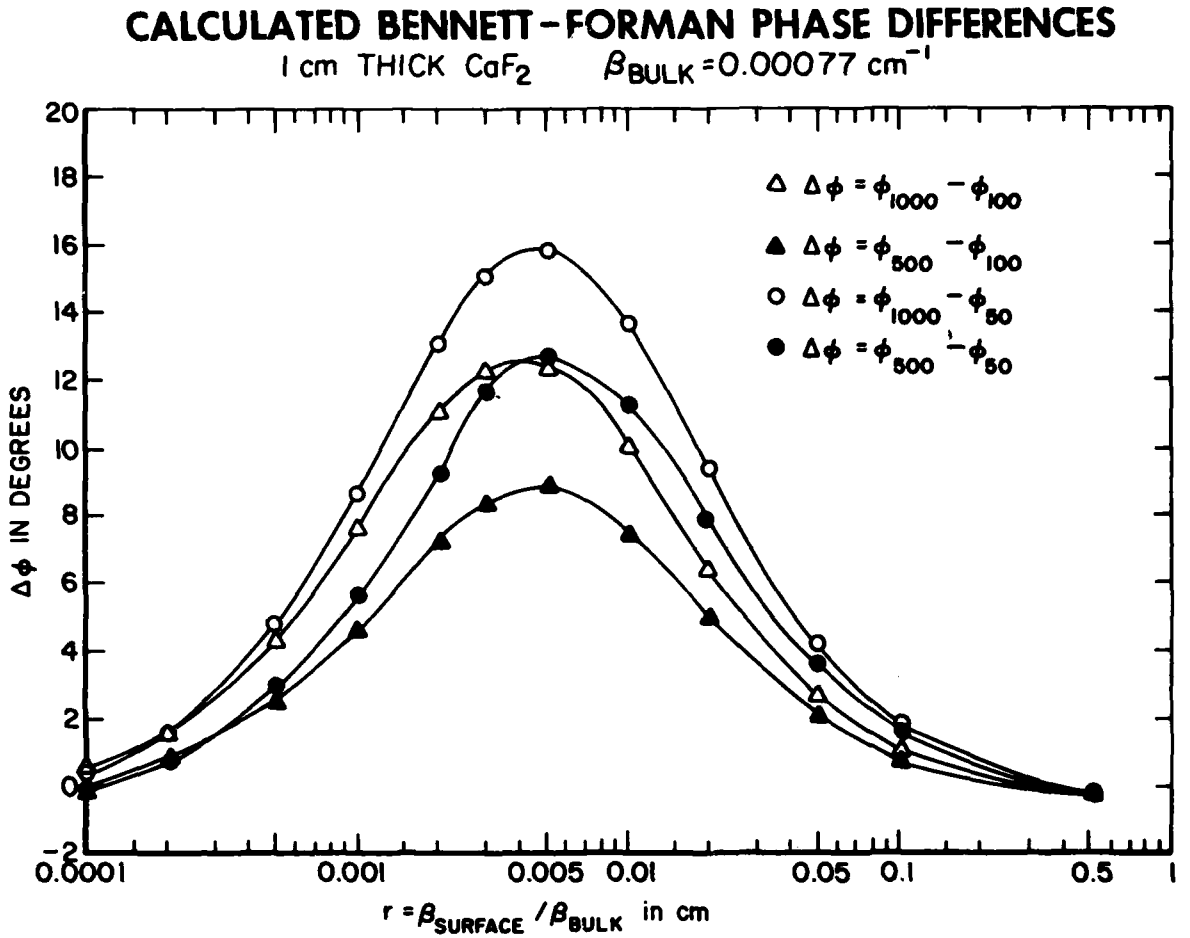

Figure 10. Calculated values of $\Delta\phi$ versus the surface-to-bulk optical absorption ratio, r, using the Bennett-Forman theory on a 1 cm thick CaF_2 sample with $\beta_{bulk} = 0.00077\ cm^{-1}$.

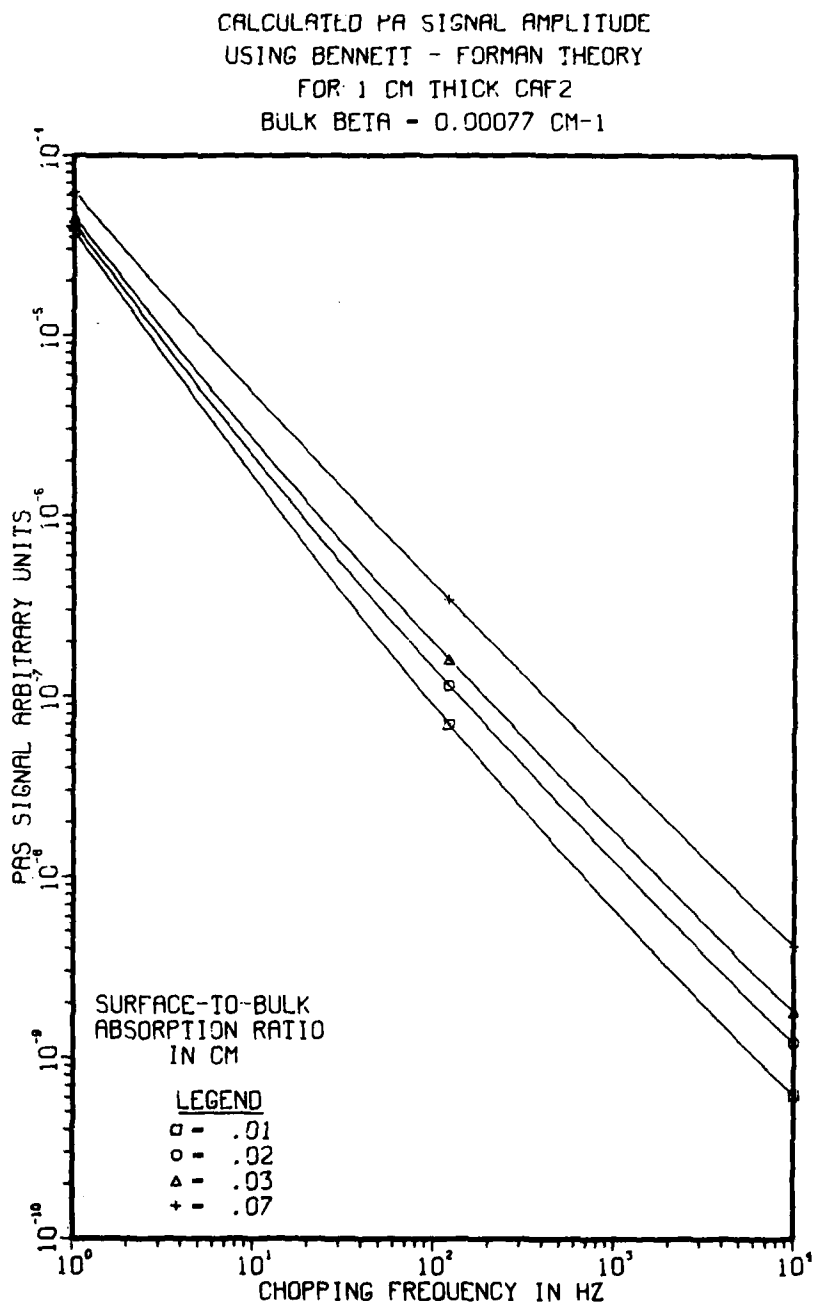

Figure 11. Calculated photoacoustic amplitude versus chopping frequency for a 1 cm thick CaF_2 sample. $\beta_{bulk} = 0.00077\ cm^{-1}$. Several surface-to-bulk optical absorption ratios, $r = \beta_{surface}/\beta_{bulk}$, were used.

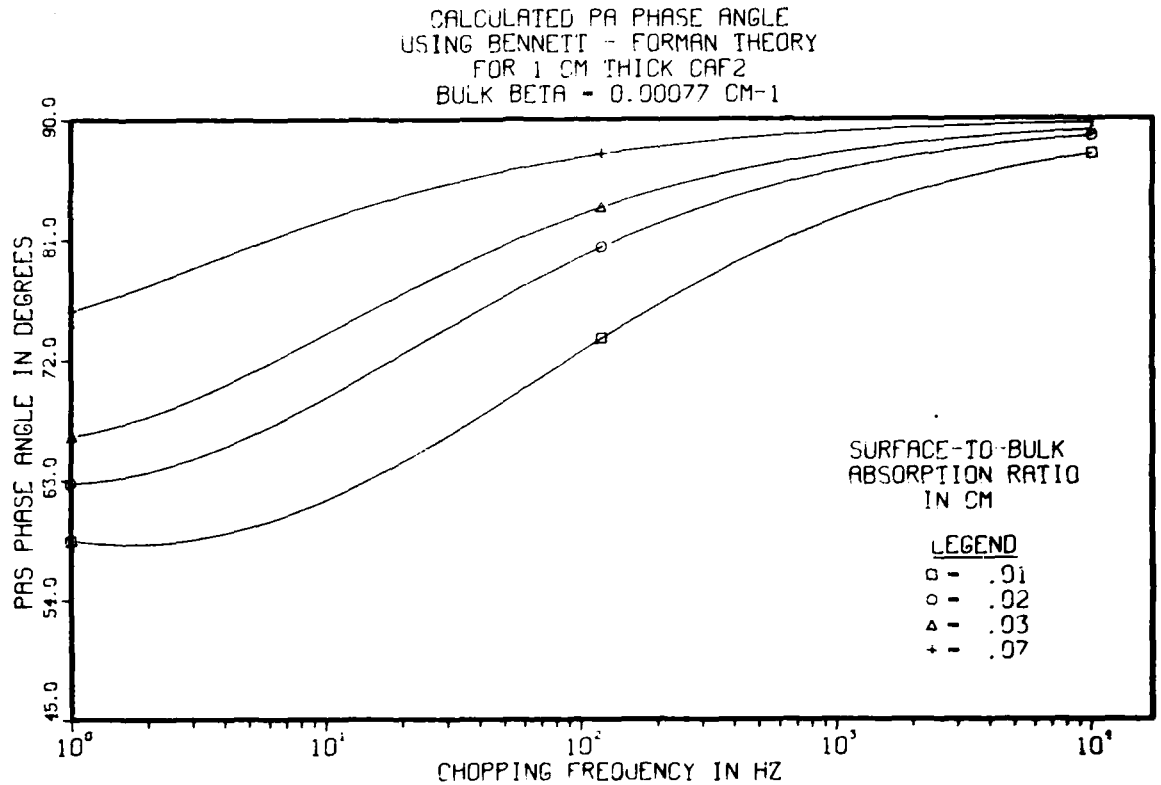

Figure 12. Calculated photoacoustic phase angle versus chopping frequency for a 1 cm thick CaF_2 sample. β_{bulk} = 0.00077 cm^{-1}. Several surface-to-bulk optical absorption ratios, r, were used.

The author pointed out that most of the complexity in PAS analysis is in the theoretical interpretation, not in the experiment.

INTENSITY DEPENDENT ABSORPTION OF ALKALI-HALIDES AT 10.6 μm

S.-T. Wu and M. Bass
Center for Laser Studies
University of Southern California
University Park
Los Angeles, California 90007

Repetitively pulsed laser calorimetry has been developed and applied to measure the intensity dependent absorption of NaCl, KCl and KBr at 10.6 μm. The absorption increases as much as 70% at high laser intensity. Furthermore, multipulse damage data was obtained for KBr which indicates that the absorption increases very rapidly at intensities just below the single pulse damage threshold. The functional form of this phenomenon is still not well characterized. A simple model is suggested and the course of necessary additional investigations is discussed in this paper.

Key words: Calorimetry; intensity dependent absorption; alakali-halides; multipulse damage; damage mechanisms.

1. INTRODUCTION

With the wide development of high power lasers in scientific, industrial and military communities, optical transparent materials are often damaged. The mechanism of laser induced damage in optical materials has been studied for more than ten years, and is still not completely understood. alakali-halides, such as NaCl, KCl, KBr, are transparent at CO_2 laser wavelength. So they are reasonably good optics. However, in order to damage as they are observed to do, they must absorb an amount of energy greater than that which can result from the absorbtivity measured at low intensities.

Most of the previous experimental studies focused on measuring the single pulse damage threshold as a function of frequency, temperature, pulse width and focal volume [1-5]. Some theoretical efforts tried to model the possible damage mechanisms and predict the damage threshold [6-9]. However, the explanation of the damage phenomenon is still not completely satisfactory. In order to clarify the damage process, we have studied intensity dependent absorption of NaCl, KCl and KBr at 10.6 μm by the method of repetitively pulsed laser calorimetry [10]. We describe our experiments and initial results in the following sections. In addition, a simple model for the observed intensity dependent absorption is suggested.

2. EXPERIMENT

In an intensity dependent absorption experiment, reliable results depend upon having a single longitudinal mode high power laser with a Gaussian spatial distribution. For this purpose, we built an unstable resonator CO_2 TEA pulsed laser with an intracavity cw discharge (Fig. 1). The 100% reflector was a convex copper mirror with a 10m radius of curvature. The output coupler was a flat germanium plate with a 7.6 mm diameter spot on center surrounded by a 10.6 μm antireflection coating. The cavity length was 2 meters and so $g_1g_2 = -1.2$ as required for an unstable resonator [11]. Both the TEA and cw discharges contained a mixture of CO_2, N_2, and He with ratios 1:1:2. The laser output was donut shaped in the near field, but on propagation into the far field (≈7m away) the central part of the beam was found to have a nearly Gaussian shape. An apperture was placed before the attenuator (Fig. 1) to remove any energy outside this central region. The alignment of the attenuator was very critical since misalignment would cause displacement of the transmitted beam when we rotated the attenuator.

In order to reduce the interference from the TEA laser's electrical discharge noise, the whole calorimeter was set in a screen room. The laser beam was focused on the sample by a 63 mm focal length ZnSe lens and temperature rise due to absorption at 10.6 μm was detected by the thermocouple, nanovoltmeter and chart recorder sketched in Fig. 1. The transmitted energy was measured with a Scientech model 362 energy meter. To assure the quality of the sample surface, every sample was etched properly prior to the experiment. The calorimeter chamber was filled with dry N_2 gas to prevent fogging of the surfaces.

The beam spatial distribution at the focal plane was measured by scanning a slit and correcting for the convolution of the slit with the circular focal spot. The beam shape was Gaussian and the corrected beam diameter was 150 μm at $1/e^2$ points in intensity. Figure 2 shows the waveform of the laser output (pulse width ≈120 ns at 1/e in intensity). The pulse to pulse energy stability was ±5%.

Some attention must be paid to the waveform. Since the gas mixture contained N_2, each pulse contained a low intensity N_2 pumped trailing component. This trailing pulse contained 1/3 of total energy but was at too low an intensity to contribute to the nonlinearity. However, it could contribute to the total absorption and so it can not be ignored in the analysis of the data that follows.

3. REPETITIVELY PULSED LASER CALORIMETRY

Unlike the case of high repetition rate pulsed laser calorimetry in which the rate of heat flow into the material can be accurately approximated by the analysis of cw calorimetry, our TEA laser was fired at the slow rate of 5/8 Hz. With such a low repetition rate interpulse cooling was apparent and an analysis of calorimetry was developed which accounts for this.

Consider the temperature and time history in a general heating and cooling curve, Fig. (3). The temperature rises steeply when the laser pulse is in the material and falls exponentially between successive pulses. Assume ΔT_0 is the temperature rise for each pulse, then according to Pinnow and Rich[12], the temperature of the sample at time t after first pulse is

$$\Delta T_1 = \Delta T_0 \, e^{-t/\tau} \tag{1}$$

where τ is the cooling time constant.

The laser fires again after time Δt so that the temperature of the sample at time t after the second pulse is

$$\Delta T_2 = \Delta T_0 \, (1 + e^{-\Delta t/\tau}) e^{-t/\tau} \tag{2}$$

Thus, the temperature rise after the N^{th} pulse is

$$\Delta T = \Delta T_0 \, \{1 + e^{-\Delta t/\tau} + e^{-2\Delta t/\tau} + \ldots e^{-(N-1)\Delta t/\tau}\} e^{-t/\tau}$$

$$= \Delta T_0 \, \frac{1 - e^{-N\Delta t/\tau}}{1 - e^{-\Delta t/\tau}} \, e^{-t/\tau} \tag{3}$$

$$= \Delta T_0 \, N_{eff} \, e^{-t/\tau}$$

where N_{eff} is defined as $\dfrac{1 - e^{-N\Delta t/\tau}}{1 - e^{-\Delta t/\tau}}$

In an experiment, we measure the net temperature rise $\Delta T = (\Delta T_0)N_{eff}$, but the desired temperature rise is $(\Delta T_0)N$. The difference here is due to interpulse cooling. For example, in our NaCl, where τ = 100 sec., for Δt = 1.6 sec. and N = 50, N_{eff} is only 34. This indicates that interpulse cooling can not be neglected. From the relation between absorbed heat energy and temperature change, we have

$$MC_p\Delta T = \alpha \ell E_t \, \frac{n^2 + 1}{2n} \tag{4}$$

where M = mass of the sample
C_p = heat capacity
ΔT = temperature rise of the sample
α = absorption coefficient
ℓ = length of the sample
E_t = total transmitted energy
n = index of refraction

Substituting $\Delta T = \dfrac{N}{N_{eff}} \Delta T$ into Eq. (4), we find

$$\alpha = \frac{MC_p(N/N_{eff}) \, T}{\ell E_t (n^2 + 1/2n)} \tag{5}$$

We recall now that E_t contains the N_2 pumped trailing pulse which contributes only to the low intensity absorption and so we have to make a correction to α in order to obtain the high intensity absorption.

In Fig. 2 let e_H stand for the energy of the gain switched high intensity part of the pulse and e_L be the energy of the N_2 pumped low intensity part. For each laser pulse the sample absorbs heat Δq_0.

$$\Delta q_0 = \Delta q_H + \Delta q_L$$

$$= MC_p(\Delta T_H + \Delta T_L)$$

We want ΔT_H, but ΔT_L is not measured separately. Thus, we must calculate the temperature rise due to the N_2 pumped trailing pulse as

$$\Delta T_L = \frac{\alpha_L e_L}{MC_p}$$

where the absorption coefficient α_L is that measured for low total pulse intensity. We use this result to rewrite the equation for Δq_0 as

$$\Delta q_H = MC_p \Delta T_0 - \alpha_L e_L$$

and for N pulses at repetition frequency $1/\Delta t$ we then have

$$\alpha_H = \frac{MC_p (N/N_{eff}) \Delta T}{\ell R E_t \frac{n^2+1}{2n}} - \frac{1-R}{R} \alpha_L \qquad (6)$$

where

$$R = \frac{e_H}{e_H + e_L}$$

It is obvious that if we take the N_2 out from the gas mixture then R = 1 and Eq. (6) is exactly the same as Eq. (5). The intensity of the high intensity part of the pulse is calculated using

$$I_H = \frac{RE_i}{\sqrt{\pi} A \tau_p} \qquad (7)$$

where E_i = input energy per pulse, A = beam spot area in the focal plane at the $1/e^2$ points in spatial intensity, and τ_p = pulse width at 1/e intensity.

5. RESULTS

The experimental raw data was as shown in Fig. (4). Figure 4a is the typical heating and cooling curve as expected from the preceding analysis. Figure 4b shows the temperature-time history when single pulse bulk damage occurred. When the sample is damaged, a bright flash of light can be seen in the chamber, and the transmitted energy is greatly reduced possibly because of the large plasma absorption. More interesting damage data is shown in Fig. 4c. Here damage occurred after several pulses. Upon examining this heating curve more carefully we see that during the first 5 pulses the absorption coefficient was 2 times larger than that when no damage occurred. During the following 3 pulses the absorption is still higher. However, at present we can not be sure that this latter increase in absorption is due to plasma scattering onto the thermocouple or to truely higher absorption.

The absorption coefficient is plotted versus intensity for KBr in Fig. 5, for NaCl in Fig. 6 and for KCl in Fig. 7. In each case the absorption stays constant at low intensity then increases gradually and saturates at a higher level until damage occurs. In the case of KBr we had sufficient intensity to reach the level where the absorption increased abruptly prior to damage. The absorption measured with a cw CO_2 laser agrees with the low intensity pulsed measurement to within experimental error of $\pm$ 10%. It is important to note here that the curve was reversible if no catastrophic damage occurred. We have obtained the same results while increasing or decreasing the intensity.

6. THE SUGGESTED MODEL

Laser induced damage to materials had been studied for more than a decade and most studies concentrated on damage threshold measurement and prediction. Since this is the first investigation of the interactions at low intensities, it may lead to a better understanding of the damage process.

Constant absorption at low intensity is to be expected. However, no intensity dependent absorption at 10.6 μm has been considered. Multiphoton excitation from the valence band to the conduction band requires at least 60 photons. The probability for such an event is exceedingly small. Also a thermal effect on absorption can be excluded because of the low (<1°C) local temperature change. The observed increased absorption suggests that impurity levels are involved. There are several possible processes to explain the observed phenomenon. Let us consider them individually as follows:

6.1 A One Photon Process in a 3-level system

The rate equation governing the states in Fig. 8 gives the absorption as

$$\alpha = \alpha_0 \left[1 + \frac{CI}{I_s + I} \right] \qquad (8)$$

where $C = (\sigma_2 - \sigma_1)/2\sigma_1$ and $I_s = A_{21}/2\sigma_1$ is the saturation intensity.

These 3 levels can result from any or all of the following possibilities:

a. 1 and 2 are shallow donors, and 3 is in the conduction band.

b. 1 is a shallow donor and 2 and 3 are in the conduction bands.

c. 1, 2 and 3 are all deep impurity levels.

d. Excitonic levls may be involved.

e. 1 is in the valence band and 2 and 3 are shallow acceptors.

The general form of Eq. 8 is similar to the observed results but the slope is too shallow to fit the data.

6.2 Multiphoton Process

Since the absorption starts to increase at such a high intensity, it is very possible that it causes multiphoton excitation. In this process

$$\alpha = \alpha_0 + \beta I + \gamma I^2 + \ldots.$$

where α_0 is the linear absorption coefficient, β is the two photon absorption coefficient and γ may represent two photon excited free carrier absorption. As shown in Fig. 9, the shallow trapped electrons can be excited to the conduction band by light through free carrier absorption. The reason for the saturation of the absorption may result from finite impurity concentration and short free carrier lifetime.

6.3 High Field Induced Primary Defects and Electron Avalanche

It seems premature to discuss these two processes from our limited data, so we just mention these possibilities very briefly. As an extrinsic damage process, the accumulation of primary defects had been proposed [13]. If the damage process is intrinsic, then the functional form of $\alpha(I)$ in the pre-damage region must be measured and compared with the electron avalanche theory.

7. CONCLUSION

We have observed intensity dependent absorption in KBr, KCl and NaCl at 10.6 μm. The absorption increases as much as 70% then saturates. Furthermore, the absorption increased very rapidly just prior to the occurrence of damage. This initial evidence of pre-damage changes may provide valuable information about the damage mechanism. In order to identify the actual damage mechanism, future efforts will concentrate on pre-damage intensities to work out the functional form of $\alpha(I)$. In addition we will extend this research to shorter wavelengths since the free carrier absorption is proportional to λ^2 and multiphoton absorption from valence band to conduction band will be more likely. Energy level shifting (Franz-Keldysh effect) may have to be taken into account at such a high intensities. Also the suggestion by Brawer [9] of a phenomenological theory for increased absorption can be tested.

8. ACKNOWLEDGEMENT

We would like to thank Drs. S. D. Allen, R. Swimm, R. Quimby, N. Koumvakalis and M. J. Soileau for useful discussions and suggestions. Also we are indebted to Mr. C.-S. Lee and Miss Y.-C. Liu for helping with taking the data and with computer analysis.

REFERENCES

[1] Fradin, D.W., Yablonovich, E. and Bass, M., Appl. Opt., 12, 700 (1973).

[2] Bloembergen, N., IEEE J. Quantum Electron. QE-10, 375 (1974).

[3] Yasojima, Y., Ohmori, Y., Okumura, N., and Inuishi, Y., J. Appl. Phys. 14, 815 (1975)

[4] Manenkov, A. A., Laser-Induced Damage in Optical Materials: 1976, N.B.S. Spec. Pub. 509, pp. 455, (1977).

[5] Soileau, M. J., Bass, M., and Klein, P. H., Laser-Induced Damage in Optical Materials: 1978, N.B.S. Spec. Pub. 568, pp. 497 (1979).

[6] Holway, L. H., and Fradin, D. W., J. Appl. Phys. 46, 279 (1975).

[7] Schmid, A., Kelly, P., and Bräunlich, P., Phys. Rev. B 16 4569 (1977).

[8] Sparks, M. et.al., Laser-Induced Damage in Optical Materials: 1978, N.B.S. Spec. Pub. 568, pp. 467 (1979).

[9] Brawer, S., Phys. Rev. B 20 3422 (1979).

[10] Bass, M., Van Stryland, E. W., and Stewart, A. F., Appl. Phys. Lett. 34, 142 (1979).

[11] Siegman, A. E., Proceeding Of The IEEE, 277 (1965).

[12] Pinnow, D. A., and Rich, T. C., Appl. Optics, 12, 984 (1973).

[13] Danileiko, Yu, K., Manenkov, A. A., and Nechitailo, V. S., Sov. J. Quant. Electron. 6, 236 (1976).

9. FIGURES

AD-A106 548 NATIONAL BUREAU OF STANDARDS WASHINGTON DC F/G 20/5
LASER INDUCED DAMAGE IN OPTICAL MATERIALS: 1980,(U)
OCT 81 H E BENNETT, A J GLASS, A H GUENTHER
UNCLASSIFIED NBS-SP-620 NL

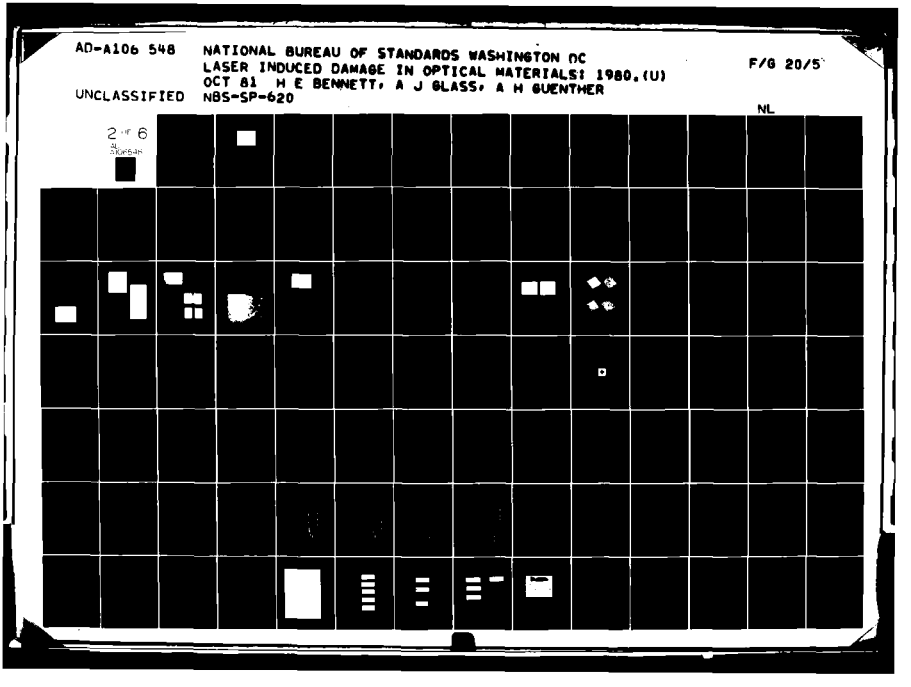

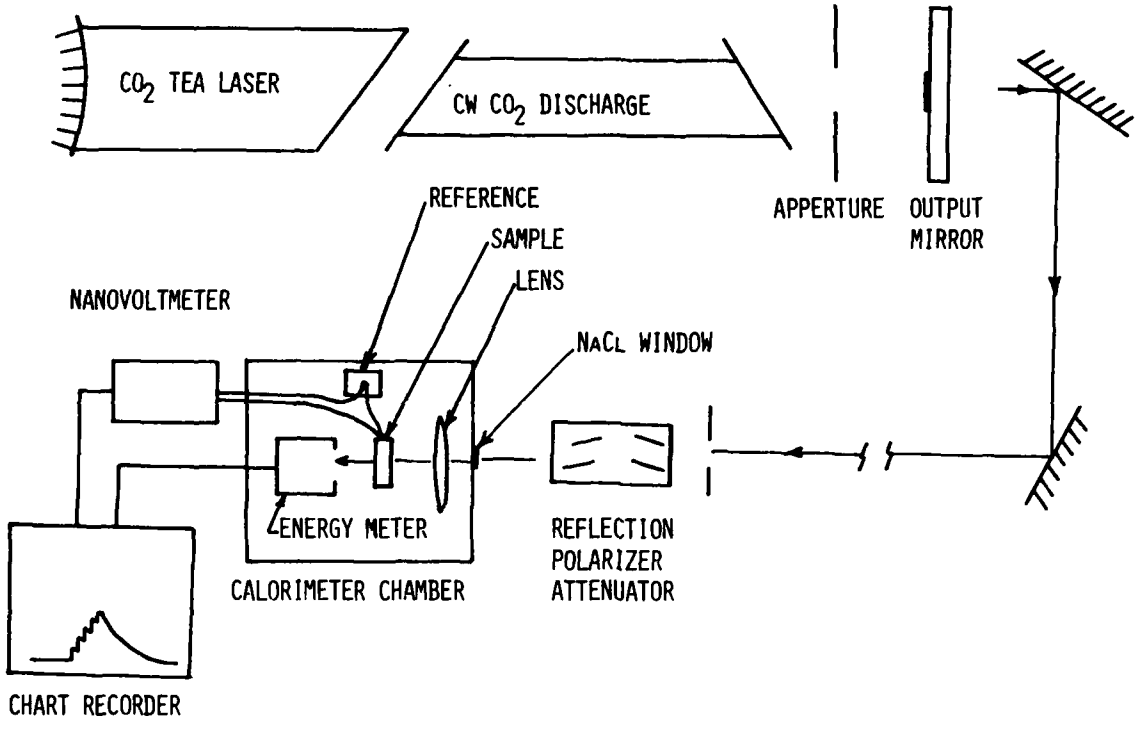

Figure 1. Sketch of the experiment.

TYPICAL CO_2 TEA LASER WAVEFORM WITH
INTRACAVITY cw DISCHARGE ON

200 NSEC/DIV

Figure 2. Typical CO_2 TEA laser waveform with intracavity cw discharge on, 200 ns/div.

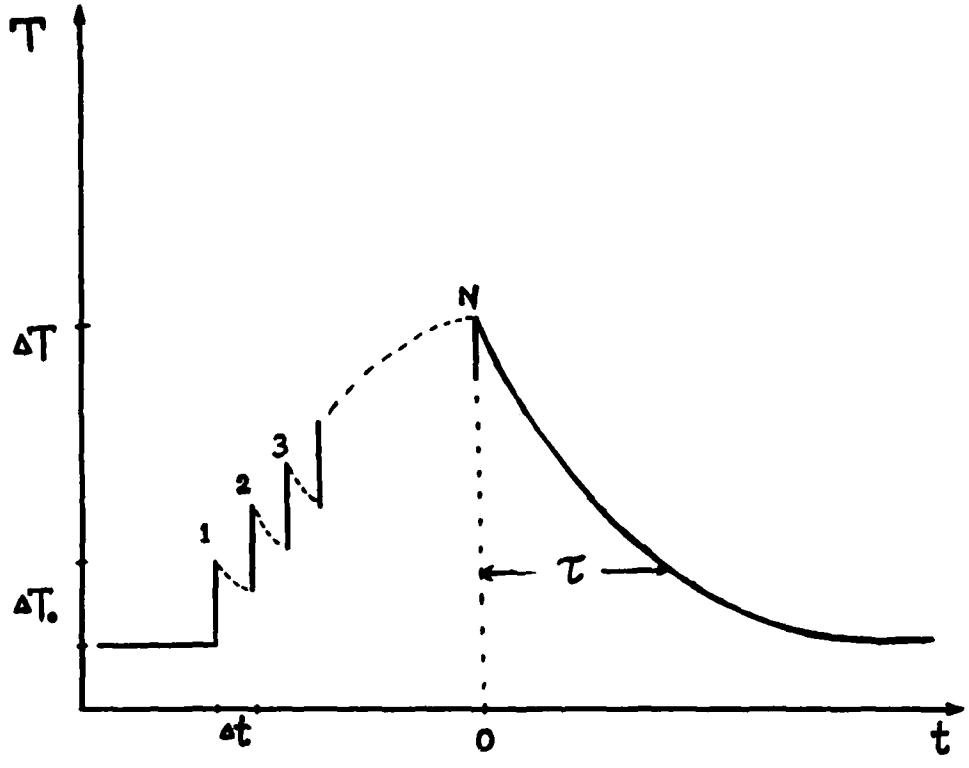

Figure 3. Temperature-time history in pulsed laser calorimetry.

TEMPERATURE-TIME HISTORY IN
PULSED LASER CALORIMETRY

A. TYPICAL HEATING AND COOLING CURVE

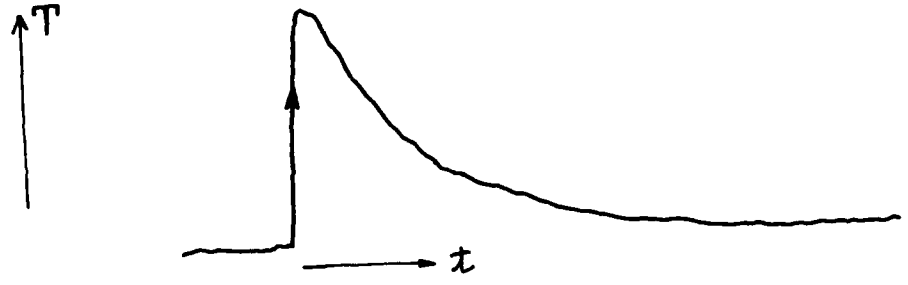

B. SINGLE PULSE DAMAGE

C. MULTIPULSE DAMAGE

Figure 4. Experimental raw data.

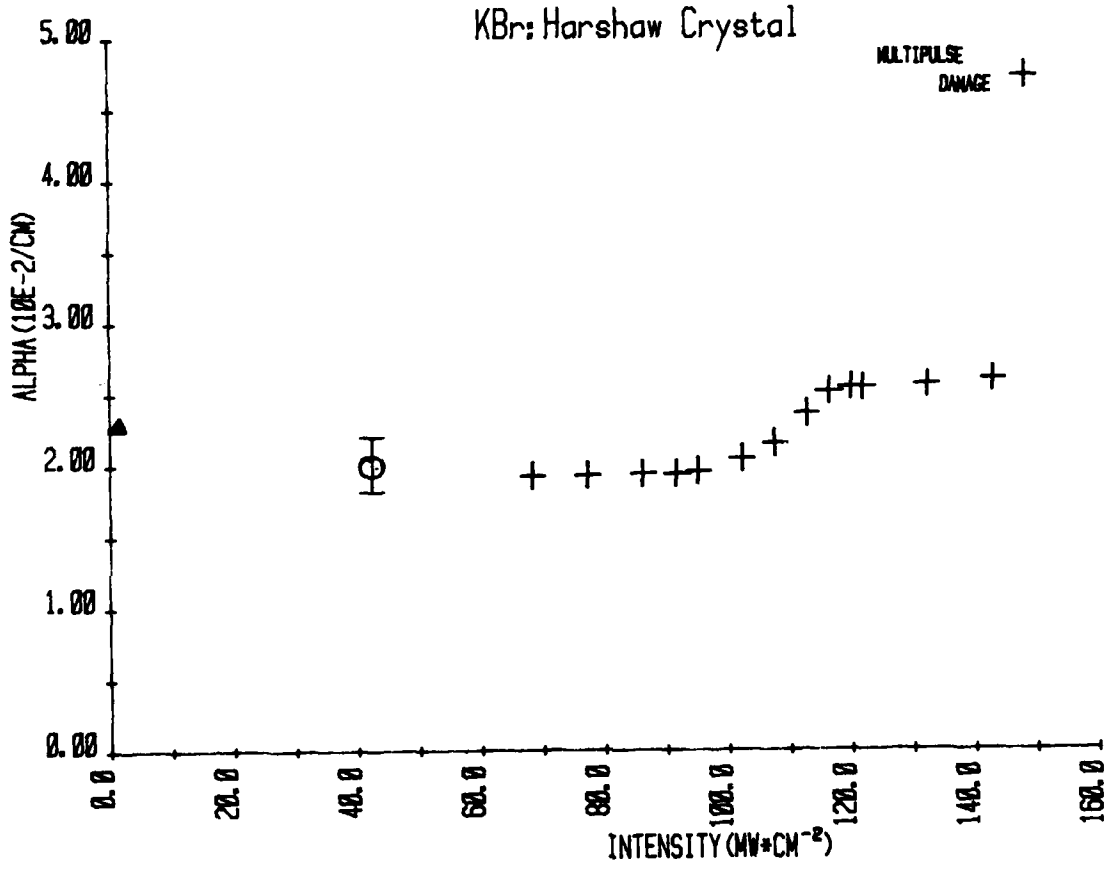

Figure 5. Experimental data for KBr: Harshaw crystal.

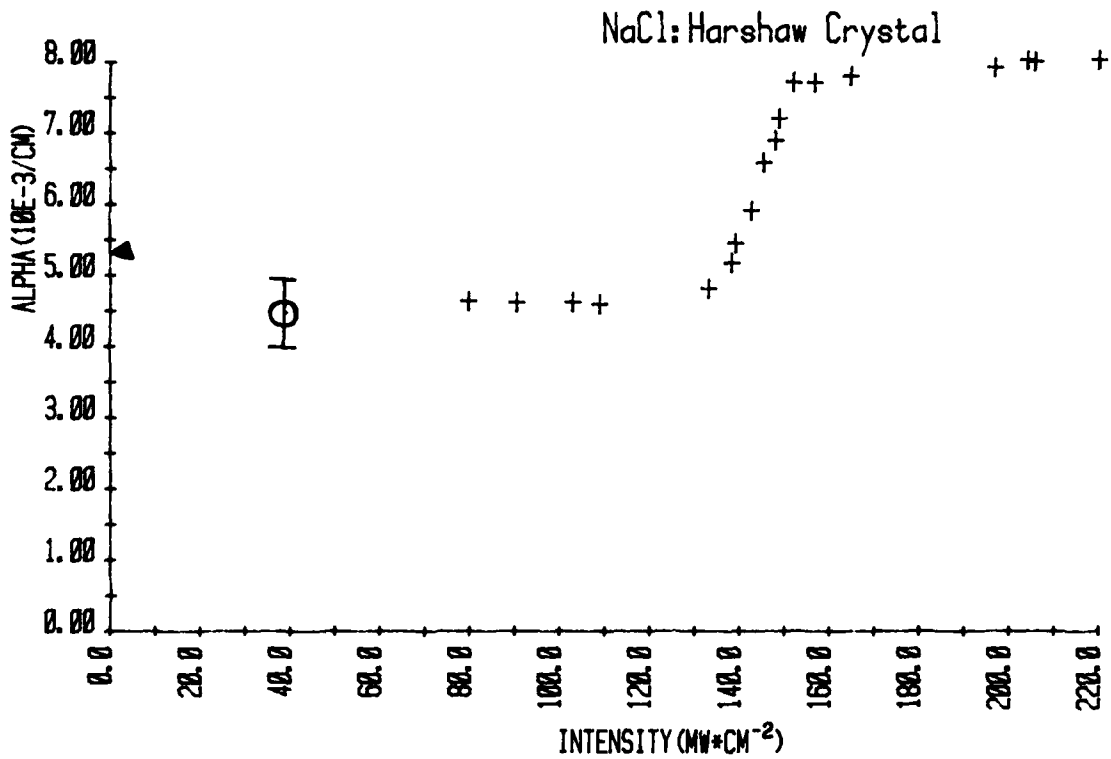

Figure 6. Experimental data for NaCl: Harshaw crystal.

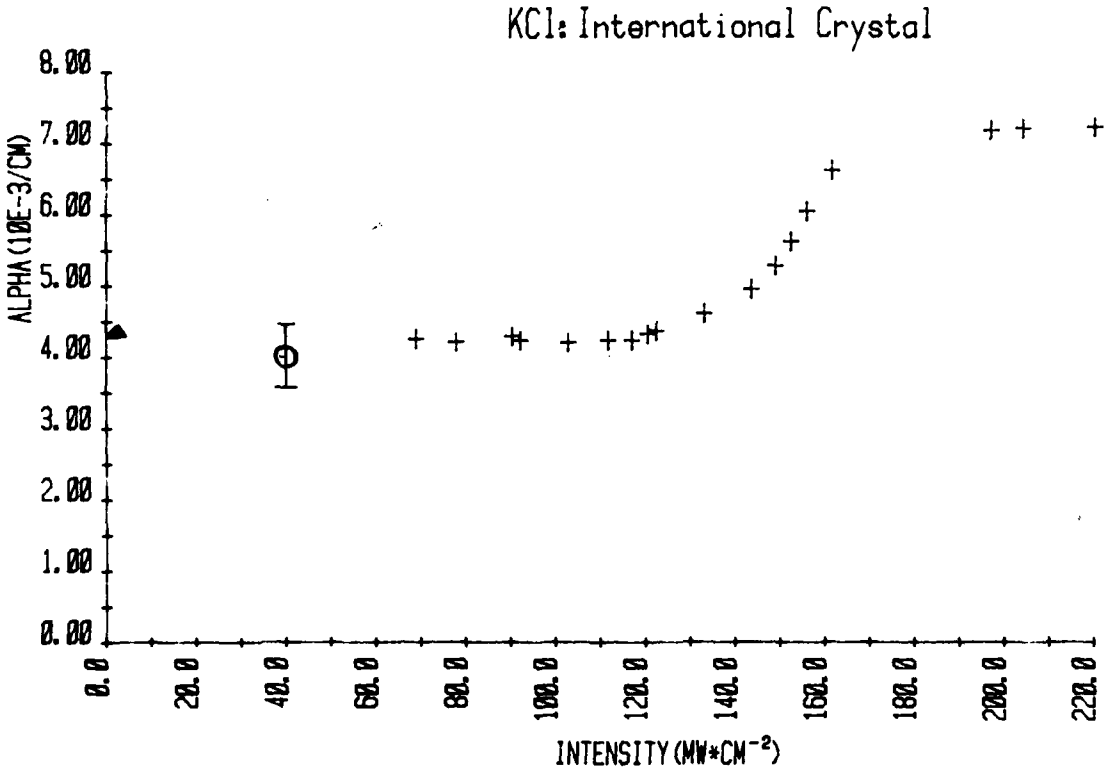

Figure 7. Experimental data for KCl: International crystal.

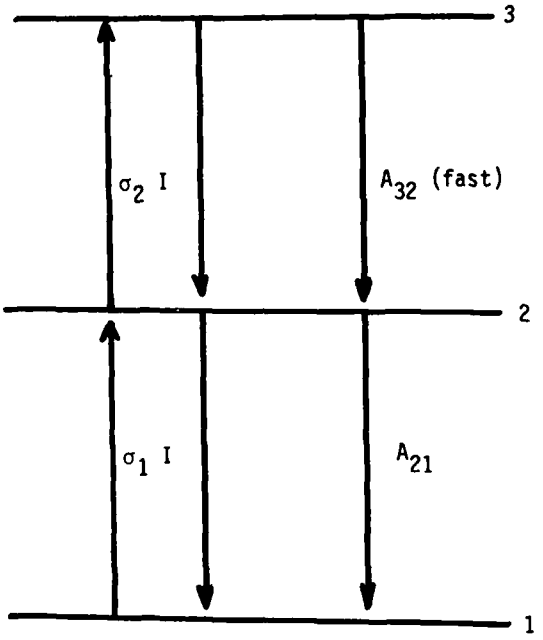

Figure 8. Energy levels and transitions for a one photon process.

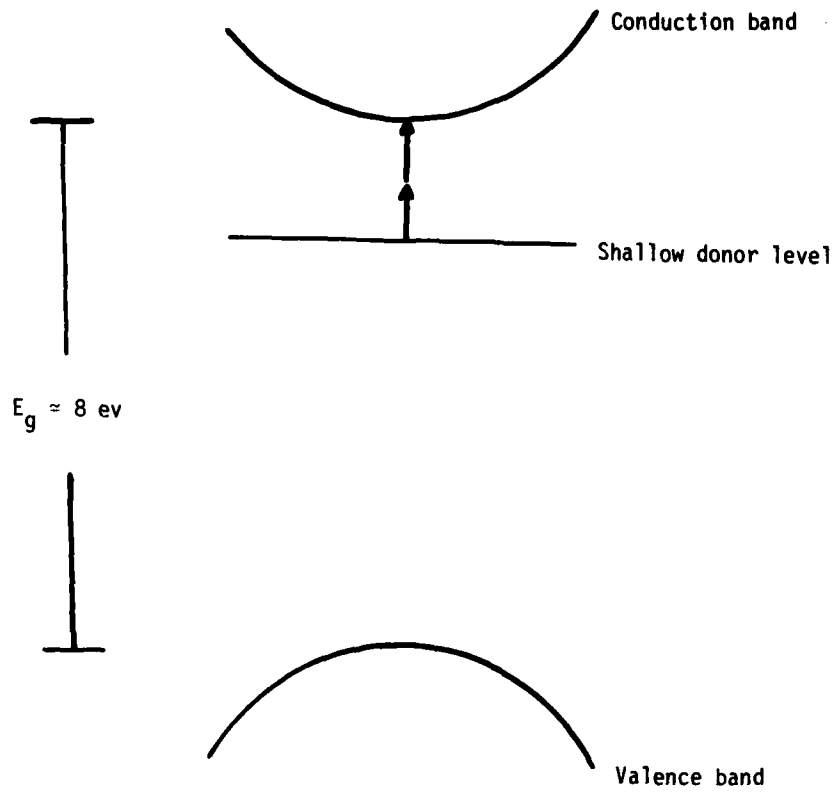

Figure 9. Energy levels and transitions for a multiphoton process.

In response to a question the authors pointed out that the temperature rise observed during absorption was less than $1^{\circ}C$. *However, they have not measured at different temperatures. The absorptivity observed was found to be reversible in the sense that low to high and high to low intensity gave the same results.*

PULSED CO_2 DAMAGE THRESHOLD MEASUREMENTS OF Rb:KCl AND NaCl

John A. Detrio and David A. Dempsey
University of Dayton Research Institute
Dayton, Ohio 45469

The 1-on-N damage threshold of specimens of forged NaCl, Rb:KCl and antireflection coated KCl were measured at 10.6 μm with a pulse duration of 10 μ sec. An acid etch significantly improved the survivability of the NaCl specimens which normally received surface damage while the response of KCl was not influenced by the etch treatment. The coated KCl survived about as well as the uncoated specimens. The measured damage thresholds were: etched NaCl, 24.2 J/cm^2; NaCl, 12.0 J/cm^2; etched KCl, unetched KCl, and coated KCl, 10 J/cm^2.

The damage morphology included entrance and exit surface damage on all types of specimens and bulk damage in the KCl specimens. The surface damage observed in some cases was an artifact produced by a plasma which formed at the specimen entrance face.

Key words: Alkali halides; bulk damage; CO_2 laser; coating damage; laser damage; microsecond pulses; NaCl; surface damage.

1. Introduction

Damage threshold measurements of alkali halide materials have been of continuing interest to the laser damage community [1,2,3][1] The data we present herein extend the available pulsed CO_2 laser damage results to large spot sizes (1.6 cm dia.) using long pulse durations (10 μ sec.). In addition, we explored the role of surface finish on damage resistance by comparing the damage resistance of specimens which were polished, freshly etched, and coated. The scope of this work included forged KCl:Rb and Polytran (forged) NaCl. The damage threshold data for fracture failure of the specimens studied are given in table 1.

The sodium chloride was found to have a higher damage threshold than potassium chloride as expected. The influence of the surface treatment was quite dramatic only for the NaCl; increasing the threshold by 100%. The coated KCl held up about as well as the polished but uncoated material and almost as well as the etched specimens. The damage morphology for each material was also distinctly different. Sodium chloride always exhibited surface crazing. The etched KCl showed internal star tracks, internal fractures associated with point imperfections or inclusions. The coated materials failed by coating removal. In those cases where a plasma formed at the specimen surface, damage artifacts associated with this violent event were frequently observed.

2. Test Design

The large laser spot size (1.6 cm dia.) relative to the specimens (3.8 cm dia.) and the high cost of each laser shot caused us to follow a test procedure which is a little different from that customarily reported. The unique features of the test plan are the spacing of the test levels and the damage threshold definition. Our approach follows the methods developed for CW testing which has similar constraints on laser test exposures and specimen limitations.

The test strategy that is most economical in the use of laser test time, which also provides threshold data at approximately the 90% confidence level, is the multilevel Bayesian approach [4]. This method is best applied to specimens that do not exhibit "conditioning," if a given specimen is tested at one fluence level its probability of failure is not influenced by previous test exposures. (In the jargon of the testing literature the results of 1 on N and n on 1 tests are equivalent. That is, one test at each level on each of N different specimens is equivalent to separately testing each specimen at each of the n levels.)

The damage threshold values are obtained, in accordance with our definition of damage threshold:

$$P_{TH} = \frac{P_{i+1} + P_i}{2}$$

where P_{i+1} is the fluence level at which at least 3 of 4 specimens fail. The uncertainty in the threshold is defined as:

$$P_{TH} = \frac{P_{i+1} - P_i}{2} .$$

For this experiment the uncertainty was designed to be no less than ±15%. That is the test levels are set as follows:

$$P_{i-1} = P_i[(1-a)/(1+a)] = 0.74\ P_i$$

with a = 0.15. For a 7-level test designed to produce a 50% probability of failure [(LD50) at the 4th level (i.e., 20 J cm^{-2})] the fluences should be those found in table 2. The fluence levels

[1]Figures in brackets indicate the literature references at the end of this paper.

Table 1. Pulsed CO_2 laser damage data for NaCl, KCl, and TlI/KCl/TlI/KCl specimens. Pulse length 10 μ sec, area 2 cm^{-2}, modified 1 on N format

Substrate Material	Surface Treatment	Fluence at Which no Failures Occurred (J cm^{-2})	Fluence Above Threshold (J cm^{-2})	No. Failed No. Tested	Threshold (J cm^{-2})	Uncertainty ±(J cm^{-2})	%	Avg. Abs., β_e $\div 10^{-3}(cm^{-1})$
NaCl	Etched	21.9	26.4	3/4	24.2	2.3	10	3.3
NaCl	Unetched	8.3	15.7	3/4	12.0	3.7	31	3.2
KCl	Etched	8.3	11.6	3/4	10.0	1.7	17	0.5
KCl	Unetched	8.3	11.6	3/4	10.0	1.7	17	0.9
KCl	Coated TlI/KCl/TlI	8.3	11.6	3/3	10.0	1.7	17	3.1

achieved during the tests were not precisely those specified in the design and, therefore, the uncertainty of the results varied between ±10% and ±17%. This is in extremely good conformity to the plan considering the difficulties of pulsed laser testing and the difficulty of precisely establishing the fluence levels. The damage testing is graphically summarized in figure 1. A complete tabulation of the specimens' measured absorption is given in table 3.

3. Beam Diagnostics

The primary beam diagnostics data of interest in this test is the pulse energy. This quantity is monitored on each pulse using a scraper mirror which spatially samples a portion of the beam. The relationship between the sampled portion and the transmitted portion was established in a series of calibration test shots. The calibration data are summarized in table 4. The fluences are obtained from the energy incident on a measured spot size of 2 cm^2. The spot size was obtained from the beam diagnostics measurement made at the specimen position.

Table 2. Test level fluences and laser energies for a ±15% precision in the test level and a dynamic range of 6.25:1.

Test Level (Relative)	Fluence (J cm^{-2})	Energy (J) A(1.92) 3 cm^2	Estimated Number of Shots	Comments
1.0	49.4	143	1	Certain failure
0.74	36.5	106	3	
0.55	27.0	78	5	
0.41	20.0	58	10	Expected LD 50 Level
0.30	14.8	43	10	
0.22	11.0	32	10	
0.16	8.1	23	10	Expected Survival
		TOTAL	49	

The shot history of the test series is summarized in figure 2. The laser is remarkably stable. The sampled beam varies by approximately ±2% at all levels. The correlation between the sampled portion of the beam and the total energy was determined to only about ±15%. Therefore, the energy levels are probably established to no better than ±15% in these experiments. The relative values or ratios are established more precisely, perhaps ±5% but this is only an estimate.

The beam transmitted by the window specimens was monitored with a thermal sensitive plastic material. The beam profile data provide an interesting insight into the optical quality of the transmitted wavefront. The NaCl specimens had good optical quality—even when etched. The KCl specimens generally gave a very poor far field spot.

4. *Damage Morphology*

Post-mortem examinations of the irradiated specimens were made with several techniques: During the testing Nomarski micrographs were made immediately before and after each irradiation. Following the testing micro- and macroscopic examinations were made. The specimens will be

Table 3. Window test specimens. The AFML specimen number identifies the specific samples. Effective absorption values are tabulated.

Surface Treatment	Substrate Material			
	KCl		NaCl	
	AFML No.	Abs·10^{-3}	AFML No.	Abs·10^{-3}
	2178	0.476	2872	2.9
	2183	0.549	2825	3.8
As-Is	2180	0.923	2830	3.74
	2184	0.912	2829	3.06
	2188	1.47	2824	2.3
		0.8±0.4		
	2176	0.276	2826	3.2
	2186	0.684	2831	2.3
Etched	2177	0.382	2832	3.77
	2187	0.818	2823	4.15
	2182	0.264	2828	2.9
		0.48±0.3		
	2068	3.51		
	2071	2.56		
Coated	2072	3.04		
	2075	2.3		
	2070	4.14		
		3.11±0.7		

discussed in groups by material in order of decreasing damage resistance.

The entrance face of the etched NaCl specimens generally showed an extensive area that was involved with the beam—an area that appears larger than the beam footprint. Intergranular craze cracks are observed over much of the central portion of this area. One specimen exhibited a square pattern of fine craze cracks. Only one specimen exhibited cracks on the exit face and then only over the apparent beam footprint. The remaining specimens showed no obvious exit surface damage.

Table 4. Pulse energy calibration data

Test Level	Mean Energy on Specimen (J cm^{-2})
1	6.42
2	8.33
3	11.58
4	15.86
5	21.78
6	26.46

All unetched NaCl specimens had extensive craze cracking over the exposed entrance surface. The involved area is greater than the apparent footprint on the entrance face. The cracking is judged more severe for the etched specimens. The exit surface of two of the specimens exhibited cracking while the remaining specimens were undamaged on the exit face.

The etched KCl specimens exhibited extensive fracturing and small internal fractures—star tracks along the beam path within the bulk of the specimen. The entrance surface of two specimens also had a whitish residue that has the appearance of smoke damage. One specimen did not have any apparent exit surface damage; the remainder of the specimens showed rear surface damage.

The polished KCl specimens showed the smoke damage on the entrance face and extensive fracture pattern. The star tracks were also observed within the bulk. Exit surface damage was also observed in the form of surface cracks and pitting.

The TlI/KCl coating was removed over an extensive area apparently larger than the footprint. The exit face had a granular appearance over the beam footprint and the usual surface cracking.

5. Discussion of results

The surface cracks observed in these tests appears to follow crystallographic planes and to be influenced by grain boundaries. The failures appear similar to those observed in CW laser testing of alkali halides. The bulk damage in the form of star tracks appears to be the result of small, isolated fractures probably associated with inclusions. In some cases the small defects are arrayed in planes; in some cases they are uniformly dispersed. The smoke damage may be an artifact of the LSD or plasma observed on the entrance surfaces. This type of damage has a white appearance and looks a little like water spotting in its spatial distribution. In fact we suspect an interaction between residual microcrystals on the surface and the plasma. The area covered by the smoke damage extends beyond the apparent beam footprint.

The damage to these specimens does not correlate with the measured absorption but is probably more strongly correlated with the bulk material properties. Sodium chloride is predicted to be a better pulsed CO_2 material [2] and this test confirms this prediction. Previous pulsed damage measurements are also supported by these results [1,2,3]. In these tests we observed more extensive entrance surface damage relative to the exit surface; this observation is contrary to the usual results of the short-pulsed damage studies. For a given substrate the surface treatment does influence survival. Etching significantly improved the performance of NaCl but only provided a slight improvement in KCl. The coated specimens held up about as well as the etched KCl specimens in these tests.

The relative performance of the two alkali halides were as expected with the NaCl a significantly better pulsed laser window material. The effect of etching the specimens in HCl for 2 minutes at room temperature did significantly improve the response of NaCl but had a statistically insignificant effect on the damage resistance of the KCl. It appears that the damage resistance of the KCl is limited by intrinsic properties that are essentially independent of the surface absorption or conditions. On the other hand, etching of the NaCl surface greatly improved its damage resistance. The NaCl still failed due to surface heating and subsequent fracture failure but at much higher fluence levels.

The scaling of NaCl damage data for smaller spot sizes (0.18 cm dia.) and short pulse duration [3] (1.6 n sec.) predicted a damage threshold approximately equal to that observed in these experiments. The scaling was obeyed surprisingly well considering the significant differences between the test conditions and the possible differences in quality between the materials tested.

6. Acknowledgments

This work was supported by the AFWAL Materials Laboratory, Wright-Patterson Air Force Base, Ohio 45433.

References

[1] Hayden, J.J. and Liberman, I., in NBS Spec. Publ. 462: *Laser Induced Damage in Optical Materials-1976*, Eds. A.J. Glass and A.H. Guenther, pp. 173-180.

[2] Newman,, B.E., Nowak, A.V. and Gill, D.H., in NBS Spec. Publ. 568: *Laser Induced Damage in Optical Materials-1979*, Eds. H.E. Bennett, A.J. Glass, A.H. Guenther and B.E. Newman, pp. 209-227.

[3] Soileau, M.J. and Bass, Michael, "Optical breakdown in NaCl and KCl from 0.53 to 10.6 μm," Appl. Phys. Lett. *35*, 370-1 (1 Sept. 1979).

[4] Detrio, J.A. and Berens, A.P., in NBS Spec Publ. 509: *Laser Induced Damage in Optical Materials-1977*, Eds. A.J. Glass and A.H. Guenther, pp. 496-506.

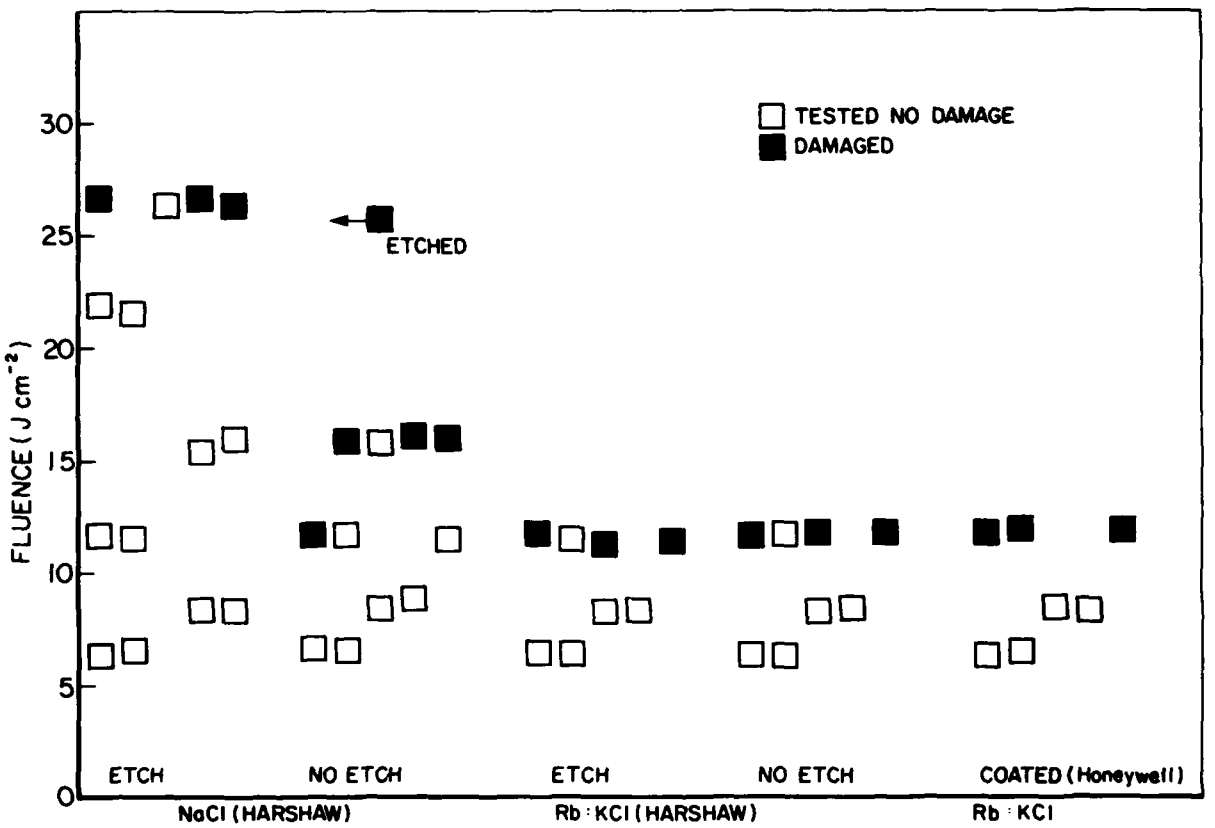

Figure 1. Graphical summary of pulsed CO_2 damage test of alkali halides. Four specimens of each type were tested. One spare specimen was available for testing if required to establish the test level at which at least 3 of 4 failed.

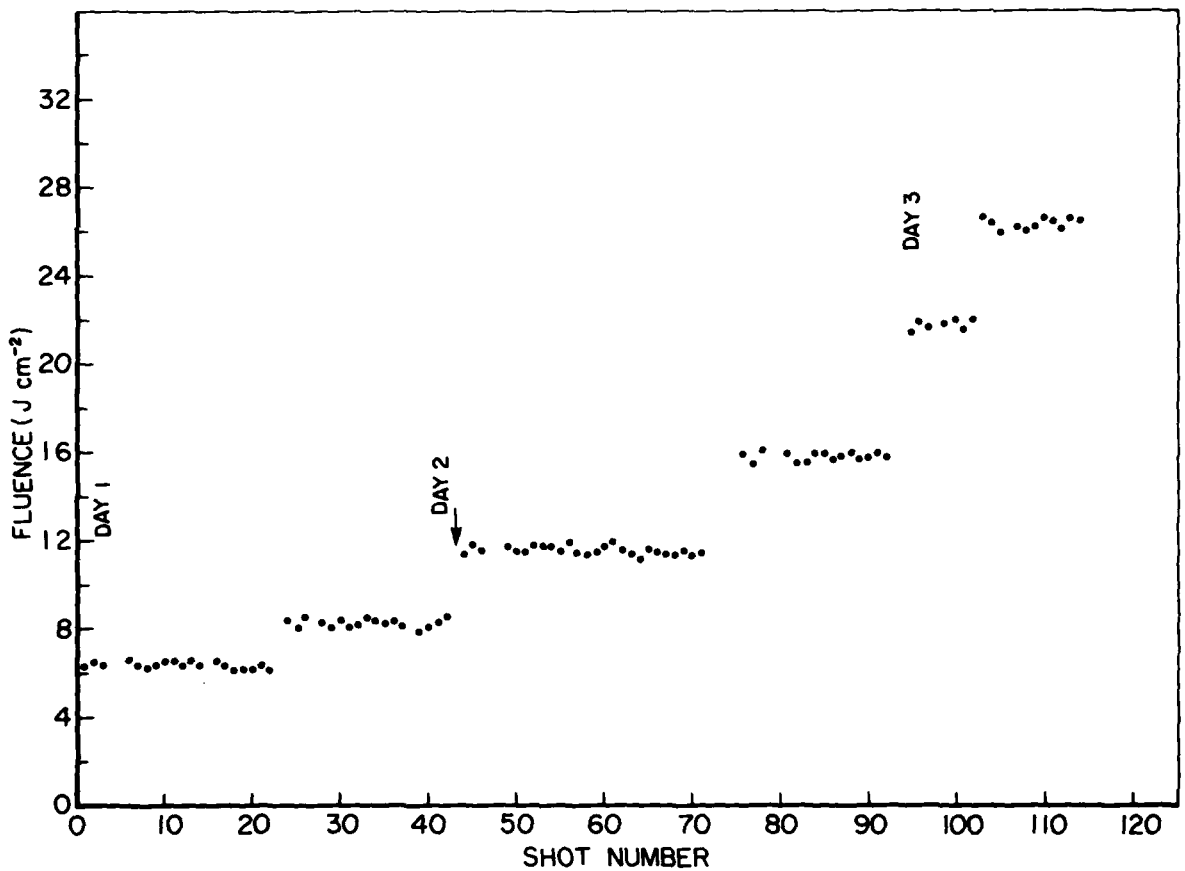

Figure 2. Test shot history.

INFRARED ABSORPTION IN HIGHLY TRANSPARENT GLASSES BASED ON HAFNIUM FLUORIDE

Martin G. Drexhage, Bernard Bendow and Herbert G. Lipson
Solid State Sciences Division, Rome Air Development Center
Hanscom AFB, MA 01731

and

Cornelius T. Moynihan*
Vitreous State Laboratory, Catholic University of America
Washington, D.C. 20064

There has been considerable research activity recently in the preparation and characterization of multicomponent glasses based on heavy metal fluorides. These glasses offer excellent prospects for multispectral transmission (from 5-7μm to 0.2-0.3μm), are amenable to the incorporation of a wide variety of atomic species, possess a moderately low refractive index (~1.5), and are readily forged into optical components. In previous work we reported investigations of the infrared edge of fluorozirconate glass. In this paper, we report investigations of the infrared absorption in the transparent regime of several new hafnium fluoride glasses developed recently at our laboratories. We find, as expected, that the infrared edge is shifted to longer wavelengths compared to Zr-based glass, but with most other spectral features remaining similar for both families of glasses. One interesting feature, for example, is a shoulder in the vicinity of 1300-1400 cm^{-1} in the infrared edge spectrum of these glasses. We discuss the influence of processing conditions on the mid-IR absorption; it appears that at this time that RAP processing utilizing CCl_4 yields the best glasses, with somewhat steeper IR edges and reduced absorption in the 3μm regime. An analysis of the infrared edge data in terms of multiphonon theory is utilized to estimate the intrinsic limiting absorption in the 3-5μm regime. Finally, the infrared edge measurements are correlated with the fundamental vibrational spectra of the glasses deduced from Raman and reflectivity studies.

Key words: Infrared glasses, infrared absorption, fluorozirconates, fluorohafnates, fluoride glasses, infrared materials, multispectral materials.

1. Introduction

Multicomponent fluoride glasses have attracted considerable interest recently as prospective materials for multispectral optics [1-6].[1] Available compositions possess continuous transparency over a very wide frequency range, spanning the mid-IR to near-UV (a typical transmission spectrum is indicated in fig. 1). One particular potential application of special interest for these glasses is mid-IR fiber optics [4]. In addition to enabling transmission over an extended range of IR frequencies, operation in the mid-IR offers potential for lower ultimate losses than in current-day silicate fibers, and the likelihood of reduced susceptibility to nuclear radiation effects. Listed in table 1 are some of the pertinant attributes of, and in table 2 some of the potential applications for, the multicomponent fluoride glasses under investigation here.

Table 1. Prospective Advantages of Multicomponent Fluoride Glasses

Very broad range of high transparency, UV to mid-IR
Excellent potential for ultra-low loss
Good chemical stability, low hygroscopicity
Fabrication using standard glass making techniques
Very wide range of compositions available
Relatively low refractive index (~1.5)
Most compositions free of toxic materials

Table 2. Potential Applications for Multicomponent Fluoride Glasses

UV to mid-IR multispectral optics
IR-domes and FLIR windows
Laser windows
Forged or stamped optical components
Millimeter waveguides
Long distance repeaterless fiber optics links
IR fibers for focal plane remoting
Laser host glasses

*Research supported by Solid State Sciences Division, Rome Air Development Center (AFSC) Under Contract No. F19628-79-C-0061.

[1]Figures in brackets indicate the literature references at the end of this paper.

In this work we are concerned specifically with fluorozirconate or fluorohafnate type glasses in which ZrF_4 or HfF_4 are the glass formers, BaF_2 is generally used as the primary network modifier, and one or more other fluorides are used as secondary modifiers (see table 3 for typical compositions).

Table 3. Composition of some typical multicomponent fluoride glasses

Designation	Composition, Mole percent								
	HfF_4	ZrF_4	BaF_2	ThF_4	LaF_3	NaF	KF	RbF	CsF
ZBT		58	33	9					
HBT	58		33	9					
HBL	58		33		9				
HZBT	29	29	33	9					
HBLC	62		23		5				10
HBTLNRC	53		22	8	4.2	4.2		4.2	4.2
ZBTKLRC		53	22	8	4.2		4.2	4.2	4.2

The latter may include fluorides of the inner transition metals (e.g., ThF_4 or NdF_3), group III elements (e.g., LaF_3 or GaF_3), or alkalis (e.g. KF or CsF). Such glass systems appear to be the best-suited for the mid-IR applications referred to above and have thus received the most attention. For the most part, only a small portion of a ternary composition field such as HfF_4-BaF_2-LaF_3 is glass forming, although it is possible to enlarge the glass formation region by adding further components to the melt. Some glass forming binary compositions exist, but these require rapid quenching and are hence much more difficult to prepare than the ternary compositions. The present glasses may be obtained by directly fusing the anhydrous fluorides of the desired composition (typical fusion temperature 800°C), or by converting the oxide to fluoride prior to fusion (conversion may be accomplished utilizing ammonium bifluoride). The melting is generally carried out in platinum crucibles or, preferably, vitreous carbon to prevent contamination. To ensure good glass formation and high purity, melting is performed under an inert atmosphere (e.g., N_2,He,Ar) or a reactive atmosphere (e.g.,CCl_4). Typically, one may obtain the glass by casting the melt into a mold, annealing briefly and cooling slowly to ambient temperatures. For further details of the glass preparation the reader is directed to Refs. [1-5]. As might be expected, the successful preparation of high quality specimens requires both high-purity starting materials as well as careful preparation procedure.

In Table 4 we list various physical properties for selected fluoride glasses. Note that while the refractive index and dispersion are similar to that of silicate glasses, the densities and thermal expansions are much greater, while the glass transition temperatures are much lower. Note also the proximity of glass transition and crystallization temperatures for the fluoride glasses; a consequent tendency toward devitrification is one reason that special care must be exercised during glass fabrication.

Table 4. Selected properties of fluoride glasses

Glass		Refr. Index N_D	Abbe No. ν	Density (g/cm^3)	Therm. Exp. $\alpha \times 10^7/°C$	Trans. Temp T_G(°C)	Cryst. Temp. T_C(°C)
HBL	*	1.522	---	5.87	191.2	315	389
HBLC	†	1.506	---	5.82	174.8	306	391
HBLPC	†	1.525	75	6.12	---	---	---
HBLAPC	†	1.526	---	6.18	---	---	---
HBTKLRC	*	1.504	72	5.87	---	312	389
ZBTNLRC	*	1.517	86	4.68	---	---	---
HBTKLLi	#	1.508	---	5.90	155.7	---	---
ZBTLLi	#	1.518	---	4.66	213.6	---	---
Fused silica		1.458	68	2.20	5.5	1100	~1675

H=Hafnium, Z=Zirconium, B=Barium, L=Lanthanum, Li=Lithium, C=Cesium, T=Thorium, K=Potassium, P=Lead, N=Sodium, A=Aluminum, R=Rubidium
*RADC, †Catholic U., #Galileo E-O

In the present work we report investigations of infrared absorption in several hafnium-based fluoride glasses, and utilize the results to predict the intrinsic limiting absorption in the ultra-transparent regime. Moreover, we discuss the effect of processing conditions and of compositional variation on the infrared transparency. The measurements reported here were carried out using samples prepared at RADC and Catholic Univ.

2. Infrared Absorption Studies

Our earlier investigations of infrared absorption in fluorozirconates and fluorohafnates [3,4,7] were aimed at establishing certain general characteristics of the infrared edge, such as the dependence on frequency, temperature and base glass composition. The principal indications suggested by

these studies were:

a. The frequency dependence of the infrared edge absorption is very similar to that of many crystalline ionic materials, displaying an overall exponential-like decrease with increasing frequency, with only weak structure superimposed. The rate of decrease is roughly similar to that of other mid-IR crystalline materials.

b. The temperature dependence is well-fitted over a wide range of frequencies and temperatures by a theoretical formula for multiphonon absorption.

c. On the basis of a. and b. the observed IR edge absorption may be attributed to multiphonon processes.

d. There is a definite shift of the IR edge to longer wavelength for hafnium-based glasses as compared to zirconium-based glasses.

In recent work, which will be reported in detail elsewhere [8], we have assesed the potential contribution of additional components to IR edge absorption in zirconium-based glasses. The possibility of being able to incorporate such additions is very important from a glass-forming and physical properties standpoint. For example, the ability to tailor viscosity through composition could well be crucial for successful drawing of transmission-quality optical fiber. Guidelines for selecting or altering components were derived from analogy with general trends displayed in the IR edge absorption of various crystalline materials (see table 5) and verified by measurements taken on a large number of glass samples of varying compositions. These guidelines are summarized in table 6, and should be viewed as "worst case" prescriptions which provide a margin of safety in preserving the optimum infrared absorption range. It is possible, of course, that other effects which we have not accounted for explicitly (such as modifications in coordination number induced in the vitreous state) may allow the guidelines to be relaxed in some instances.

Table 5. IR edge absorption: semi-empirical rules

Dependence on mass for isostructural series:

(1) $\alpha_{AX_n} > \alpha_{BX_n}$ if $m_A < m_B$

Dependence on valence for species with similar cation masses:

(2) $\alpha_{AX_n} > \alpha_{BX_{n-1}}$ if $m_A \approx m_B$

Additivity rule for ternary compounds $AX_n \cdot BX_p$:

(3) $\alpha \approx c_A \alpha_{AX_n} + c_B \alpha_{BX_p}$, (c = contentration):

Table 6. Components XF_N which retain IR transparency of fluorozirconate and fluorohafnate glasses

N	X not lighter than
1	Na
2	Ca
3	La
4	Th

The composition studies indicated above lead to the conclusion that the IR edge absorption is determined exclusively by the HfF_4 or ZrF_4 component in glasses conforming to the rules in table 6. This conclusion is bolstered by recent studies of fundamental infrared reflectivity and polarized Raman scattering in these glasses, which will be presented in detail elsewhere [9]. The principal result of significance in this connection is the observation of a set of prominent high frequency peaks in the spectra of the present glasses attributed to the ZrF_4 or HfF_4 component. Approximate values for the corresponding TO, LO and Raman frequencies, for HBT glass, e.g., are found to be ω_{TO} ~425 cm^{-1}, ω_{LO} ~625 cm^{-1} and ω_R ~575 cm^{-1}. These values are consistent with an analysis of the corresponding infrared edge data, which imply an average vibrational frequency for multiphonon absorption of approximately 500 cm^{-1} [7].

The absorption spectra in figures 2 and 3, for example, which were obtained utilizing Fourier spectrocopy, illustrate some of the above points. Note the distinct separation of the edges in the hafnium and zirconium glasses. On the other hand, note the close coincidence of the spectra for HB (HfF_4-BaF_2) and HBL(HfF_4-BaF_2-LaF_3) glasses (the HB data above 1500 cm^{-1} are somewhat uncertain due to the thinness of the sample). Observe also the overall exponential-like frequency dependence over four decades in absorption in HBL, and the broad structure superimposed on the spectrum. The shoulder in the 1300-1400 cm^{-1} region is a persistent feature manifested in varying degrees of prominence in virtually all the glasses we have measured.

Finally, we present a brief discussion of the effect of preparation method and processing conditions on the infrared absorption of these glasses. As in low-loss silicate glasses, the major factors affecting the optical transparency of fluoride glasses are contamination of the material by transition metal (and/or rare earth impurities), hydroxyl groups (OH^-) and oxide species.

Our first hafnium fluoride glasses, made from HfO_2 of 97% purity, exhibited numerous absorption bands throughout the near UV to the near IR and gave the glass a pale green color. Analysis indicated

large amounts of iron and other transition metals in the raw materials. Use of 99.9% purity (or better) starting materials resulted in clear glasses with a featureless transmission curve between ~0.3 to 6.0 μm (fig. 1). Along the IR edge, from ~1000 to ~1500 cm^{-1}, such impurities appear to have a minimal effect; the absorption coefficients of the clear and green glasses are identical.

Oxide and hydroxyl contamination is a more serious problem, affecting both the mid-IR transparency of the fluoride glasses and the glass forming ability of many compositions. Glasses melted and cast in ambient atmosphere have a high tendency towards devitrification; those prepared under inert or reactive atmospheres have a greater probability of success.

The effects of hydroxyl/oxide contamination on the IR edge may be seen in figures 4 and 5. The three HBL glasses of figure 5, while of identical composition, were melted under inert atmosphere at two different laboratories (CUA and RADC), in different furnaces under slightly different time-temperature conditions, and cast in air. The high frequency "spread" in their absorption coefficients is most likely due to variations in their hydroxyl/oxide content resulting from incomplete fluorination of the oxide raw materials by the ammonium bifluoride and/or atmospheric attack during casting.

Figure 4 clearly shows a broad absorption band centered at 2.9 μm which may be identified with OH vibrations. Spectroscopic examination of samples thinned repeatedly have thus far been inconclusive. In some specimens, the intensity of the band is invariant with sample thickness, indicating that the OH^- is only on the surface of the glass; in others a thickness dependence is observed, suggesting the presence of hydroxyl groups within the glass. (The bands marked "?" in figure 4 are associated with C-H surface vibrations due to oils used in cutting or polishing the samples).

An effective approach to eliminating or greatly reducing hydroxyl/oxide contamination in the fluorozirconate type glasses has recently been suggested by Robinson et. al.[5]. The technique involves melting and fabrication of the glass under a reactive atmosphere of CCl_4. The CCl_4 reacts to eliminate both OH^- and outgassed water from the furnace and melt below 400°C; above 400°C it cracks to yield chlorine gas which can compensate for fluorine deficiencies in the glass. Our preliminary experiments indicate that this approach is very effective; "difficult", i.e., high devitrification tendency compositions are easier to fabricate into thicker castings and yield samples with consistently lower high frequency absorption coefficients than non-CCl_4 treated glasses. Additionally, the 2.9 μm OH^- band is substantially reduced in intensity or eliminated entirely.

3. Prospects for ultralow absorption

The data base which has been built up from the measurements reported here and elsewhere now allows us to speculate with a reasonable degree of confidence on a range of values for the intrinsic limiting absorption in the ultra-transparent regime. One such projection for HBL is indicated in figure 5. One primary source of uncertainty in this projection is differences from sample to sample at absorption levels less than 10^{-1} cm^{-1}. These may be due to oxide or hydroxyl impurities in the samples themselves, as well as uncertainties in the measurement for thin samples(~2-3 mm in the present case). In any case,one may utilize the extreme values to bracket the predictions,as indicated in figure 5. For example, we predict that an intrinsic absorption of 10^{-6} cm^{-1} occurs in the range 2700-3000 cm^{-1}.

In order to contrast the potential of HBL glass as a fiber optic transmission medium with that of silicate-based glasses, note that the intrinsic limiting absorption of the silicates (which occurs in the 1.4-1.6 μm regime) is about 0.2 dB/km. Although it is apparent that the fluoride glasses are potentially capable of much lower intrinsic absorptions, the ultimate intrinsic loss in fibers is given by a sum of absorption and scattering losses. Definitive values of the scattering losses in fluoride glasses are not yet available, although it is believed likely that they will be larger than for fused silica.

From a practical standpoint there are a variety of factors which affect the potential of achieving intrinsic limiting absorption in these glasses. Figure 4 indicates the transmission spectra of several early samples of fluoride glass, which display various peaks in the 2500-4000 cm^{-1} region. As discussed above, there are indications that these are at least due in part to surface absorptions, so that they might have a less critical effect on fibers than in bulk glass applications. Fortunately, current work suggests that the absorptions in this regime may be reduced by appropriate changes in processing conditions. An obvious consideration related to fabrication of ultratransparent glass is the availability of ultrapure starting materials, and the effects of various trace impurities on the absorption in the regimes of interest. Such effects have yet to be studied in a systematic fashion. Finally, many of the glasses produced to date appear to possess small crystallites (typically ten to fifty microns across) distributed more or less randomly throughout the volume of glass. Although these crystallites make up a small fraction of the glass volume, they may contribute undesirably to scattering losses in the ultra-transparent regime. Further studies are required to quantify their effect on transparency, if any, and to determine their origin and relation to processing conditions.

4. Concluding remarks

In this paper we have described various measurements of infrared edge absorption in fluorohafnate and fluorozicronate glasses and discussed some of their implications. Our observations indicate that these glasses possess infrared edges, attributable to multiphonon absorption, that are very similar to those of crystalline fluorides. Their multiphonon absorption spectra display broad structural features, as opposed to the narrower, more distinct peaks evident in chalcogenide glass spectra. We have established the existence of a broad range of additional components that may be incorporated into the present fluoride glasses without degrading their IR absorption characteristics. Our glass processing studies suggest that reactive atmosphere processing produces the best quality glass for infrared applications. Finally, predictions based on our IR edge studies indicate intrinsic limiting absorption less than 0.1 dB/km for the 3-3.5 μm regime in these glasses. In combination with the results of other studies, these observations suggest that fluorohafnate and fluorozirconate glasses are highly promising candidates for a wide variety of mid-IR applications.

5. Acknowledgements

The authors acknowledge the contributions of co-workers at RADC (R. N. Brown, K. P. Quinlan) and Catholic Univ. (M. Saleh Boulos, K. H. Chung, E. Gbogi) in preparation of the glasses and in assisting with some of the measurements. We would also like to thank T. Loretz and co-workers of Galileo E-O Corp. for performing refractive index and thermal expansion measurements; and P. K. Banerjee, J. Goltman and S. S. Mitra of University of R.I. for IR reflectivity and Raman scattering measurements.

References

[1] Poulain, M. and Lucas, J., A new class of materials: Fluoride glasses made with zirconium tetrafluoride, Verres Refract. 32 (4) 505-13 (1978).

[2] Lecoq. A., Poulain, M. and Lucas, J., Lanthanum fluorozirconate glasses, J. Non-Cryst. Solids, 34 (1) 101-10 (1979)

[3] Drexhage, M. G., Moynihan, C. T., and Saleh, M., Infrared transmitting glasses based on hafnium fluoride, Mat. Res. Bull. 15, 213-19 (1980).

[4] Drexhage, M.G., Moynihan, C.T., Saleh Boulos, M., Quinlan, K.P., Fluoride glasses for visible to mid-IR guided wave optics, in Physics of Fiber Optics, B. Bendow and S. S. Mitra, eds, American Ceramic Society, 1980, in press.

[5] Robinson, M., Pastor, R.C., Turk, R. R., Braunstein, M. and Braunstein, R., Infrared transparent glasses derived from the fluorides of Zr, Th, and Ba, Mat. Res. Bull 15 (6), 735-42 (1980).

[6] Drexhage, M. G., Bendow, B., Moynihan, C.T., IR transmitting fluoride glasses, Laser Focus (Oct., 1980).

[7] Lipson, H. G., Bendow, B., Drexhage, M. G., Multiphonon Absorption in IR glasses based on Zr and HF fluorides, in Basic Opt. Props. Mats., NBS Spec. Pub. 574 (NBS, Wash., D.C. 1980).

[8] Moynihan, C.T., Drexhage, M.G., Bendow, B., Saleh Boulos, M., Quinlan, K. P., Chung, K. H., Gbogi, E., Composition dependence of IR edge absorption in ZrF_4 based glasses, Mats. Res. Bull. (1980, in press).

[9] Bendow, B., Drexhage, M.G., Banerjee, D. K., Goltman, J., Mitra, S. S., Moynihan, C.T., Vibrational spectra of fluorohafnate and fluorozirconate glasses, to be published.

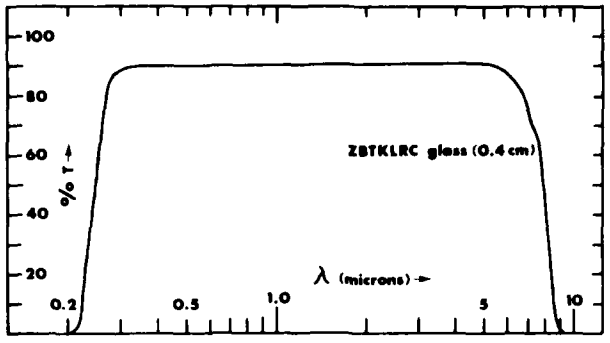

Figure 1. Transmission vs. wavelength for ZBTKLRC (ZrF_4-BaF_2-ThF_4-KF-LaF_3-RbF-CsF) glass.

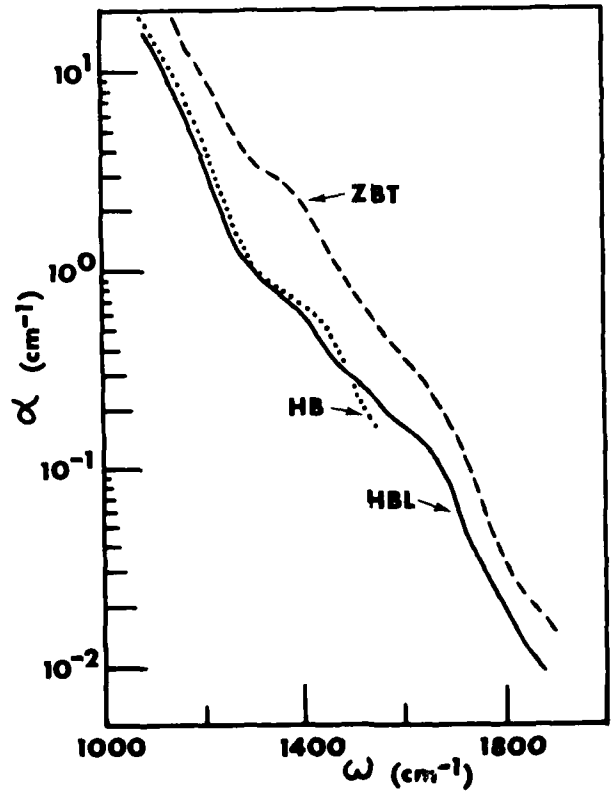

Figure 2. Absorption coefficient vs frequency for selected fluoride glasses. ZBT = $58ZrF_4$-$33BaF_2$-$9ThF_4$; HB=$62HfF_4$-$38BaF_2$; HBL=$62HfF_4$-$33BaF_2$-$5LaF_3$.

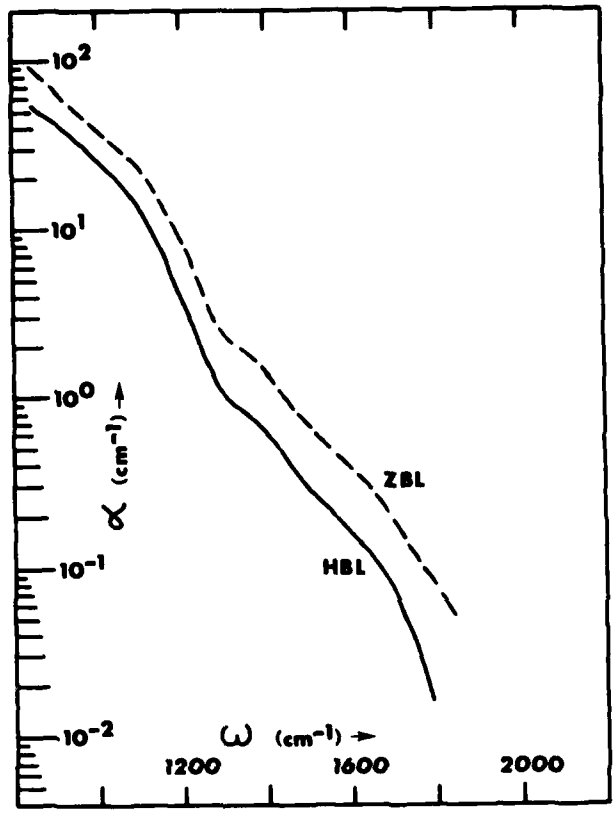

Figure 3. Absorption coefficient vs frequency for HBL (see fig. 2) and ZBL ($62ZrF_4$-$33BaF_2$-$5LaF_3$).

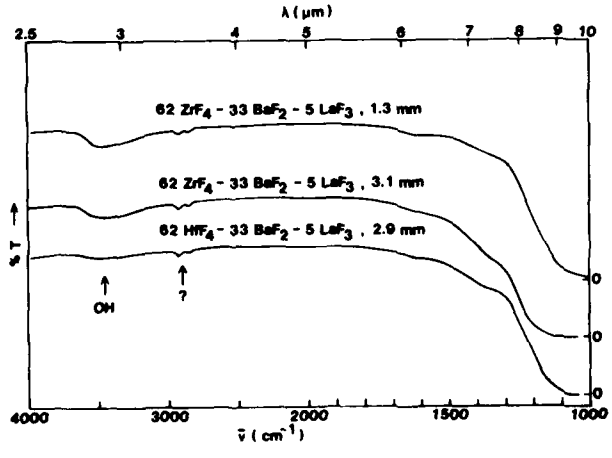

Figure 4. Transmission vs wavelength for three unpolished specimens of fluoride glass.

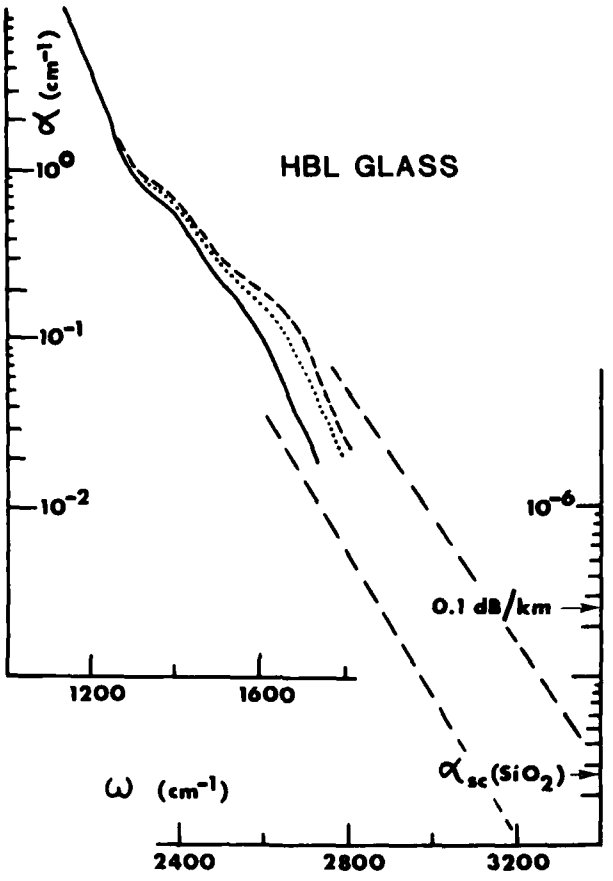

Figure 5. Absorption coefficient vs wavelength for HBL glass (see fig. 2). Top left: Measured absorption coefficients for three different samples. Lower right: Extrapolated bounds on intrinsic absorption coefficient in 3 μm regime. Intrinsic scattering of fused silica at 3300 cm^{-1} is indicated for reference.

No comments on this paper.

INTERNAL DAMAGE TO OPTICAL GLASSES WITH 3 ns-PULSE LASER

H. Hack and N. Neuroth
Jenaer Glaswerk Schott & Gen., Zentrale Forschung
und Entwicklung, 6500 Mainz, West-Germany

The beam of a 3 ns pulse laser (1060 nm) is focussed with a convex lense with 1,1 m focal length. The glass sample to be tested is 20 mm thick: its rear surface has a distance of 100 mm from the focus. The part of the sample which will be shot is illuminated with a Xenon lamp and inspected with a microscope with four fold magnification before and after the shot. In each case a photo is taken.

Two types of internal damage are to be recognized: pointlike damage and threadlike damage. Some glass types show only pointlike damage, even at higher energies (applied energy densities up to 65 J/cm²); other glass types show only threadlike damage caused by self-focussing (dependent to the n_2-value). In the most cases both damage types occur but at different levels of energy densities. In BK 1 and BK 7 glass no internal damage is to be seen when applying energy densities up to 65 J/cm².

Key Words: Damage types; non linear effect; optical glass; threshold values.

Apparatus

We measured the internal damage in glasses by laser pulses with the apparatus described in figure 1. The laser pulse is generated by a Nd-YAG oscillator. The pulse shape is formed by a Pockels cell. The laser pulse coming from the oscillator is amplified by two amplifiers, one with a Nd-YAG crystal, one with a Nd-glass rod (Quantel laser type NG 24, without polarex system). The beam diameter is 18 mm. The beam is attenuated by neutral density filters. Then the beam is focussed by a convex lense with a focal length of 1,10 m. About 10 cm off the focus the sample is placed into the beam. In this region the beam diameter is about 2 mm; the most intense region has a diameter of 0,6 mm. The size of the sample to be tested is 20 x 20 x 40 mm. The beam transverses 20 mm of the sample. Its surface has a declination of 10° from the normal incidence in order to prevent a feedback of the reflected light with the laser. A beam splitter reflects 8 % of the beam energy to an energy meter (Laser Precision Instruments). The sample is mounted on a z-y-carriage. Above the sample, a microscope is mounted to inspect the damage sites. A photo is taken from the region to be shot before and after each pulse. The beam energy is increased step by step. The damage sites are detected looking through a microscope with four fold magnification. For this inspection the sample is illuminated by a Xenon lamp.

Determination of the beam profile

The intensity profile of the laser beam is measured by exposing infrared sensitive film (type 1-Z spectroscopic by Kodak). Figure 2 shows the intensity distribution of the parallel laser beam; figure 3 shows the densitometric measurement along a diameter of the cross section. The beam diameter is 18 mm. There is an outer annular part with low energy density and an inner part of approximate 5 mm diameter with high intensity (caused by the different cross section of the first and the second laser amplifier); figure 4 gives the intensity profile of the focussed beam in the plane where the sample is. The most intense part has now a diameter of approximate 0,6 mm.

We determined the energy density by another way. Instead of the sample we put diaphragms of different diameters into the beam. We took care for an exact adjustment in the beam axis. Laser pulses of constant energy were directed onto the diaphragm, and the energy of the transmitted part of the beam was measured. In figure 5, the ratio of transmitted energy to the incident energy is given as a function of the diaphragm area. In a region of a diameter of 0,6 mm, the energy density is nearly constant and decreases in the outer region of the beam. The energy density in the near of the beam axis is responsible for our threshold values. The reproducibility of the peak on axis energy density from shot to shot is $\pm$ 5 %. The absolute value of the energy density is uncertain about 20 %.

Decision of damage

There are different possibilities of decision of internal damage in transparent material:

- light emission during the radiation
- visible defects detected with the microscope
- visible defects detected with the unaided eye.

We used a microscope with a four fold magnification. The magnification is relatively low, because we want to be sure that one can see the damage occurring along the whole beam trail (20 mm long) in the sample. The area of the sample to be shot is photographed before and after the shot. Both pictures are compared carefully. If there is only one small point more, or a small point before the shot has become larger by the shot, this is defined as damage. At least four shots with energies a bit lower than the threshold must cause no damage.

Results

We measured a selection of optical glasses situated in different parts of the Abbe diagram. There are

two types of internal damage:

pointlike (example figure 6 above)
threadlike (example figure 6 below).

The pointlike sites occur at any place along the beam. Sometimes, already existing particles are enlarged, sometimes defects were generated, which have not been seen before. A threadlike damage starts at any place along the beam and runs always to the exit surface. When the energy density is enlarged, the thread damage starts nearer to the entrance surface, but always runs through out to the exit surface. The damage size is increasing towards the exit surface.

Some glasses show a simple statistical distribution of damage with the energy density: there is no damage up to a certain energy density; all shots with higher energy density cause a damage (fig. 7 left side). Other glass types have a more complex behaviour: there is a range of energy density above the threshold where a damage may occur or not (fig. 7 right side).

The thresholds for pointlike damage and threadlike damage are individually different (fig. 8). The glasses with low n_2-values have mostly low pointlike damage thresholds and high threadlike damage thresholds. The glasses with high n_2-values have low threadlike damage thresholds and mostly higher thresholds for the pointlike damage. In the medium range of n_2-values, there is a mixed behaviour.

The threadlike damage is correlated with the n_2-value as is shown in figure 9. It is caused by self-focussing in the sample. The higher the n_2-value, the lower the threadlike damage threshold, if the samples have all the same thickness. From 39 glass types investigated six glass types with n_2-values between 0,7 and 1,4 $\cdot$ 10^{-13} e.s.u. show no threadlike damage when irradiated with 65 J/cm^2 (the highest energy density we are getting with the apparatus). But four of them show pointlike damage at lower energy density. The glasses BK 1 and BK 7 are not damaged by energy densities up to 65 J/cm^2. In cases where the pointlike damage is low it is mostly impossible to look for the threadlike damage because the pointlike damage are so strong that one cannot detect the threads.

We found no property which is correlated with the pointlike damage. In each glass there is an amount of particles already without being irradiated with laser pulses. The nature of the particles can be crystals, undissolved parts of the melt, platinum. These elements may have different sensitivities to damage. There are also small bubbles, which don't absorb and therefore are less sensitive to damage than for instance platinum.

The intense part of the beam hits a volume of about 6 mm^3 in the sample. When we irradiate the sample 10 times, a volume of 60 mm^3 is tested. That is very little, compared with the volume of optical components used in laser apparatus. This work is only an information about the behaviour of the different glass types when irradiated with laser pulses. In order to qualify much greater volumes of glass - for instance 1 l, that is 2 $\cdot$ 10^{+4} times greater - a greater volume should be tested.

Comments on the absolute values of the damage threshold: they are defined by a) the accuracy of the measurement of the beam energy density; we think this is accurate within 20 % (apparative contribution); b) the magnification of the microscope; we had a four fold magnification; if one uses higher magnification, one may get lower damage thresholds (sensitivity of damage detection); c) we only have tested about 60 mm^3 of the sample; when the test volume is increased, it is to be expected that the damage threshold will become smaller (statistical base); d) in these measurements we looked only for the internal damage and not for the surface damage. Normally the surface damage occurs at lower energy densities than internal damage. When the surface is irradiated a plasma may be generated and/or scattering may occur. These effects absorb or deviate a part of the beam. That means the values here given for the damage threshold are possibly adulterated by these effects. The true energy density causing the internal damage is possibly smaller.

Acknowledgement

We thank Mr. H. Schwartz for performing the extensive measurements.

Literature

Glass, A. J., Guenther, A. H., Laser induced damage in optical materials: tenth ASTM symposium, Appl. Opt. 18, 2112 (1979)

Stokowski, S. E., Milam, D., Weber, M. J., Laser induced damage in fluoride glasses: a status report, NBS Special Publication 541, 1978

Milam, D., Measurement and identification of laser-damage thresholds in thin films, presented at the S.P.I.E. Technical Symposium East, Washington, DC (March 28-30, 1978)

Milam, D., Lowdermilk, W. H., Wirtenson, G. R., Laser damage testing at LLL an overview and an update, Proceedings of Electro-Optics/Laser 78

Table 1. n_2-value and damage threshold (3 ns)

glass type	n_2 (10^{-13} e.s.u.)	pointlike (J/cm²)	threadlike (J/cm²)
FK51	0,69	10	>66,5
FK52	0,73	15	>36
PK51	0,86	12	>37
FK5	0,91	10	>66,5
PSK50	1,03	>66	66
BK3	1,06	42	51
PK2	1,13	20	>68,5
BK1	1,14	>63	>63
BK7	1,15	>70	>70
TiK1	1,16	>64	64
BaLK3	1,27	>59	59
K5	1,31	48	34
BaK2	1,37	62	>63
ZK1	1,40	56	66
PSK52	1,44	20	41
KF6	1,56	28	>37
PSK53	1,58	31	37
KzF2	1,65	>53	46
SK16	1,71	54	61
LaK21	1,82	50	59
LaKN7	1,95	15	51
SSK2	2,07	58	59
LLF1	2,09	48	58
LaK8	2,59	15	27
BaF4	2,63	59	59
LF5	2,73	>60	43
LaFN3	3,11	21	26
TiF4	3,18	>33	33
BaSF1	3,33	>42	32
F3	3,45	>44	38
BaSF52	3,77	11	>39
LaF21	3,78	12	37
F7	3,80	>60	34
LaF22	5,35	27	31
LaSF5	5,80	12	26
TiSF1	5,89	>35	35
SF6	9,90	>10	10
SF57	12,02	>34	12
SF59	19,2	10	13

Figures

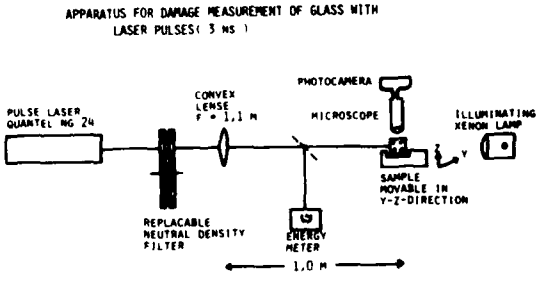

Figure 1. Apparatus for damage measurement of glass with laser pulses (3 ns).

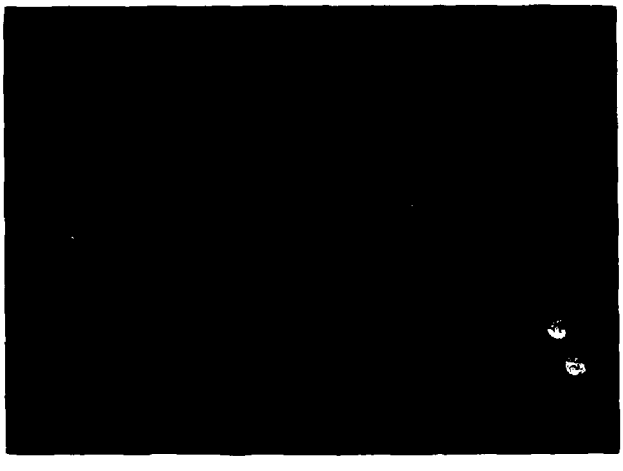

Figure 2. Intensity distribution of the unfocussed laser beam.

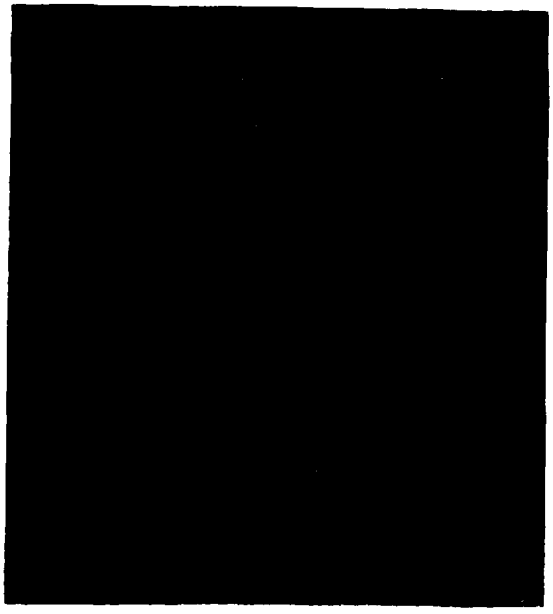

Figure 3. Laser beam intensity profile.

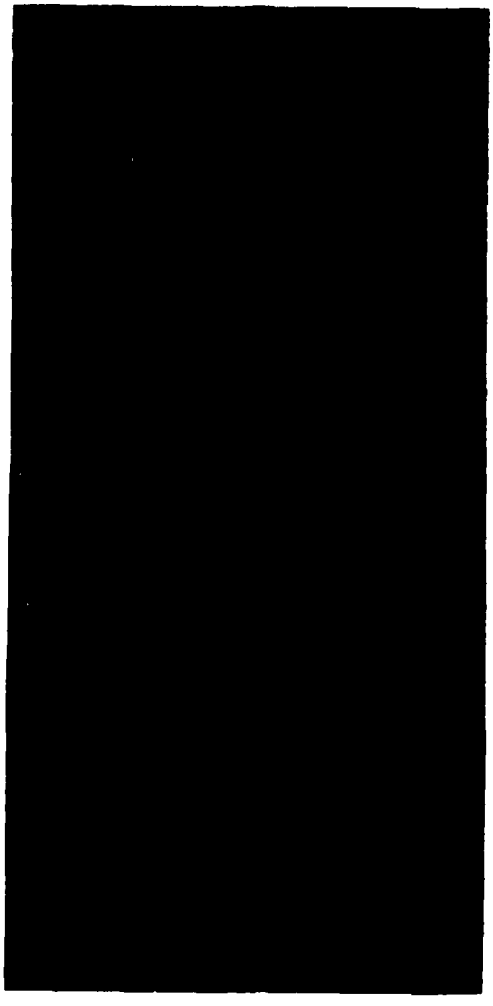

Figure 4. Intensity profile of the focussed laser beam in the sample plane.

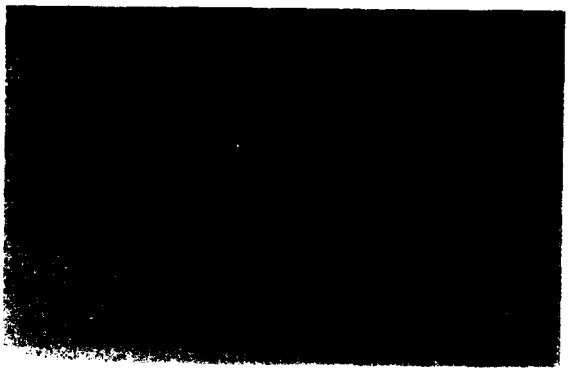

Figure 5. Distribution of energy density across the beam (measurement with diaphragm).

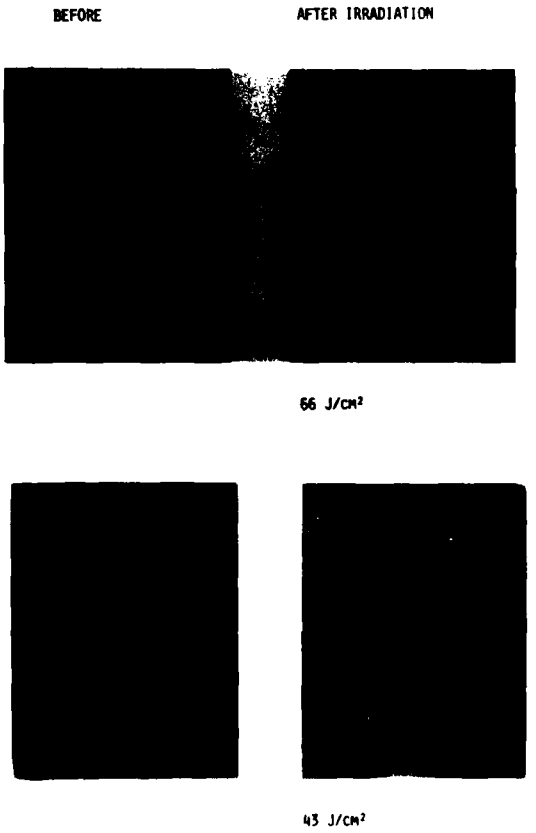

Figure 6. Types of damage in glass (above: pointlike; below: threadlike).

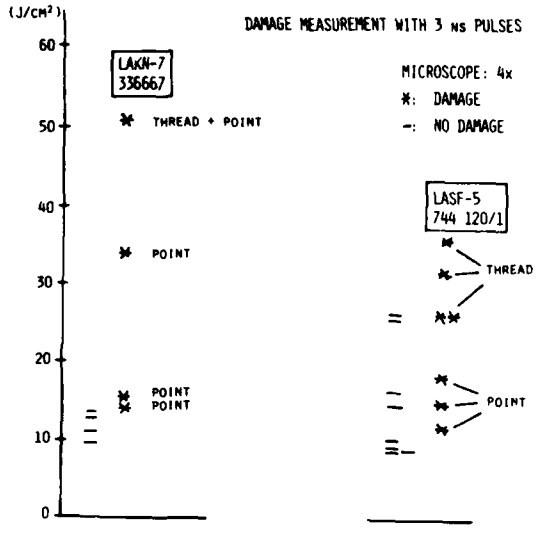

Figure 7. Statistical distribution of the damage measurement.

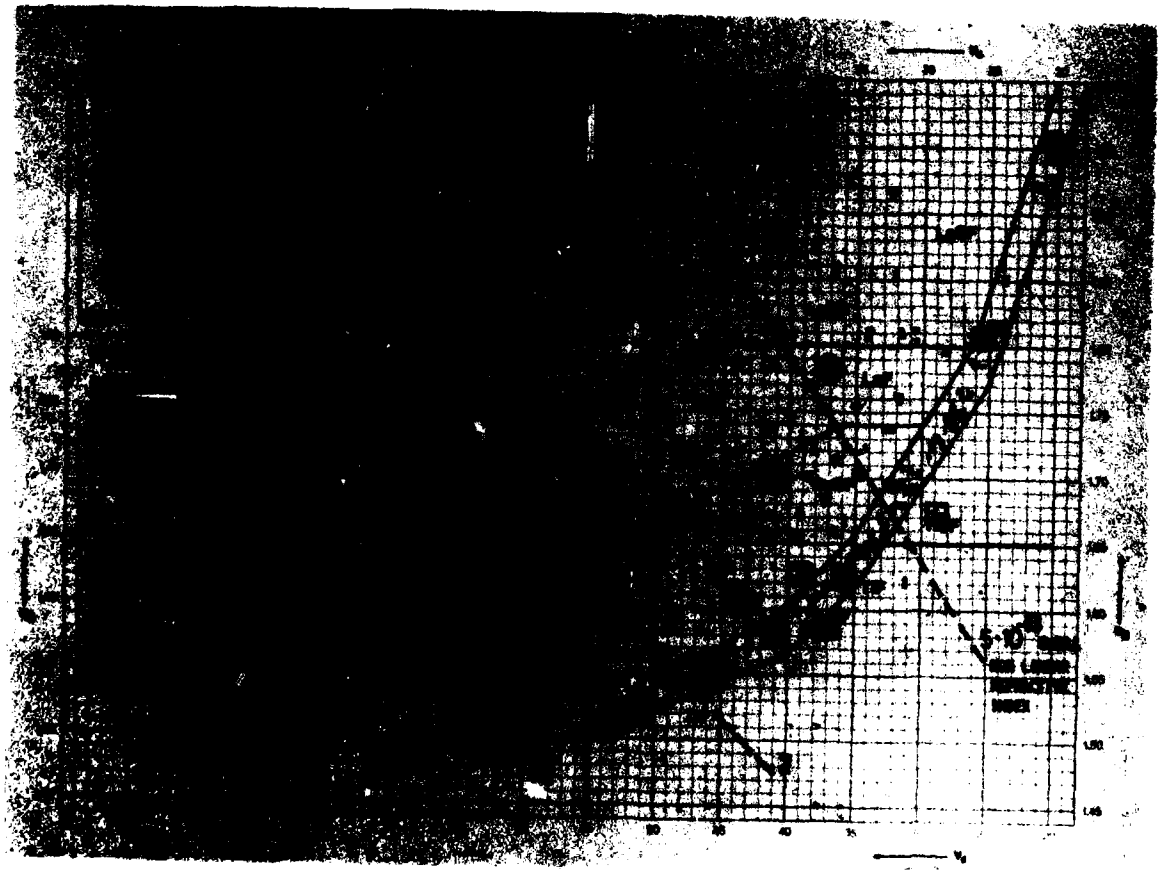

Figure 8. Abbe-diagram with damage thresholds.

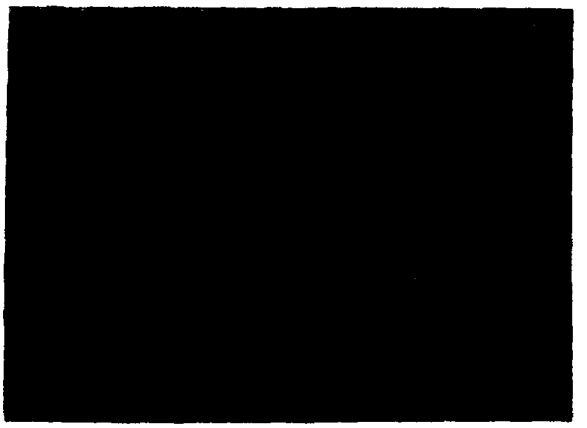

Figure 9. Threadlike damage in correlation with the n_2-value.

It was pointed out that one should monitor pulse width and energy density of the laser beam on every shot since every pulse may be somewhat different. The speaker stated that this was not done on these measurements. It was also pointed out that variations from melt to melt make it dangerous to make broad statements about unusual glasses. Variations of up to two times are sometimes seen in the results. The speaker agreed.

DEVELOPMENT OF FORGING PROCESSES FOR LARGE-SCALE DEFORMATION OF LITHIUM FLUORIDE*

H. Vora and J. F. Ready
Honeywell Corporate Technology Center
10701 Lyndale Avenue South
Bloomington, Minnesota 55420

Development of forging processes that would permit large-scale deformation of LiF without degradation of its optical properties is required for potential application of this material as an optical element in laser systems generating short intense pulses in the ultraviolet to heat targets for laser fusion. This paper describes forging processes that permit deformation of nearly 90% without introducing internal cloudiness in LiF. Mechanical and optical properties of LiF forged using these processes are also discussed, including the microyield and microcreep at room temperature and the residual absorption in the visible and ultraviolet.

Key words: Fluorides; forging; laser windows; lithium fluoride; mechanical properties, optical properties; ultraviolet transmission.

1. Introduction

Lithium fluoride possesses a combination of optical properties that qualifies it as an important candidate material for windows on high-power, short-pulse ultraviolet and visible lasers. This combination includes large band-gap, low residual absorption in the ultraviolet and visible, low refractive index, low nonlinear refractive index coefficient [1][1] and high damage threshold [2]. The relatively low mechanical strength and the limited size of the commercially available LiF single crystals could restrict the potential application of this material in high-power lasers operating at short wavelengths in the visible or ultraviolet. For this reason, we have been studying the feasibility of press forging LiF. The objective of this study is to introduce grain boundaries in LiF and thus improve its mechanical properties without degrading its good optical properties. The forging also increases the diameter of the sample.

2. Isostatic press forging

All LiF crystals were press forged isostatically in a helium atmosphere at 13.8 MN/m^2 (2000 psi) using a forging system that has been described elsewhere [3,4]. In an earlier paper it was shown that if an LiF crystal of <100> orientation is forged in one step at a displacement rate of 0.013 cm/min, the maximum deformation that can be given to it is limited to approximately 40% at 300°C. The maximum deformation increases with increasing forging temperature to approximately 65% at 600°C [4]. When deformation exceeded these limits, scattering centers (veils) were observed in LiF. Metallographic examinations of LiF crystals forged at 600°C indicated that their grain size was not uniform and that they contained several large grains a few mm in size. Thus the forging temperature could not be increased above 600°C.

It was further shown that veiling in LiF could be suppressed by forging in two steps over the temperatures in the range 300-525°C, with an intermediate annealing at 700°C for 1-4 hrs. With this process, we could deform LiF crystals by as much as 75% without veiling. LiF crystals forged using this two-step process contained fairly uniform grains of size in the range 15-30μm.

We have recently developed a forging process that permits a still higher deformation of LiF. This is also a two-step forging process and is based on the observation that the ductility of LiF single crystal increases significantly from 65% to more than 88% as the forging temperature is raised from 600°C to 700°C. (The ductility is defined as the maximum deformation that can be given to an LiF single crystal without veiling.) The problem of nonuniform and coarse grain size associated with the employment of high forging temperature was overcome by additional (a second-step) deformation at a lower temperature. Several LiF crystals which were first forged 80% at 700°C were forged again to determine their ductility at temperatures in the range 400-550°C. The examinations of these forgings indicated that the ductility of the previously forged LiF was severely restricted (<15%) at a temperature of 500°C or lower, but became significant (>40%) at 550°C. The second-step deformation of 40% at 550°C significantly refines the grain size and also makes it more uniform, as illustrated in Figure 1. The two-step deformation of 80% at 700°C and 40% at 550°C amounts to an overall deformation of 88%, which corresponds to nearly a factor of three increase in the initial diameter of the forging billet.

Figure 2 illustrates the scattering profiles of various LiF samples. The scattering profile is a very sensitive method of detecting veils in press-forged materials. It defines areas of high scattering due to the presence of internal defects. The scattering profile is obtained with a laser flying point scanner, which uses a helium-neon laser as a light source, galvanometer deflectors, and a photodiode positioned such that it detects scattered light at 90° from the forward direction. In Figure 2, only the scattering profile of LiF sample forged 80% at 700°C plus an additional 25% at 500°C shows the presence of a significant quantity of scattering centers. The formation of these scattering centers during the second-step deformation at 500°C can be prevented by restricting the deformation to 15%.

3. Optical absorption

In order to determine the effects of press forging on the ultraviolet and visible transparency of LiF, we made calorimetric absorption measurements on a series of single-crystal and press-forged LiF samples using a line-tunable argon ion laser. The results of these measurements are summarized in table 1. These data indicate that the press forging increases the residual ultraviolet and visible absorption in LiF, but that the observed increase is nominal (less than a factor of two) in at least

*Work supported by the Lawrence Livermore Laboratory under Subcontract #9354409.

[1]Figures in brackets indicate the literature references at the end of this paper.

four out of six samples.

Table 1. Summary of Ar-ion laser calorimetric data on single-crystal and press-forged LiF.

Sample		Absorption Coefficient, (cm^{-1}) X 10^{-3}						
		514.5 nm	488 nm	457.9 nm	Multi-Line Ultraviolet	Single - line Ultraviolet 364 nm	351 nm	339 nm
H-30	Single Crystal	1.0	1.1	1.2	2.4			
	Forged 350C-30%, 550C-50%	1.7	2.0	2.3	3.9			
H-31	Single Crystal	1.5	1.7	2.5	7.2			
	Forged 525C-61%	2.2	2.3	2.3	18	12	14	45
H-38	Single Crystal	1.1	1.1	1.3	2.1			
	Forged 350C-50%, 500C-50%	1.8	2.0	2.6	4.4			
H-41	Single Crystal				2.7	1.5	1.9	
	Forged 500C-50%, 400C-15%	5.5	5.7	6.5	8.6			
H-42	Single Crystal	0.71	0.64	0.80	5.4			
	Forged 400C-61%	2.7	2.7	3.0	4.6			
H-<110>-4	Single Crystal	0.30	0.30	0.36		0.97	0.96	1.41
	Forged 500C-50%	0.65	0.69	0.72	2.1	1.35	1.77	2.68

4. Mechanical properties

Strengths of alkali halides are often measured in 4-point bending. In this context, proportional limit corresponds to the stress at which the stress-strain curve is observed to deviate from linearity. The fact that many materials can undergo plastic deformation at a fraction of their conventionally measured proportional limit is of concern in the design of precision optical systems. In this connection, the term microyield behavior is used to describe microplastic strain resulting from short duration loading, and the term microcreep refers to time dependent strains of small magnitude occurring at temperatures near room temperature and under stresses that are low relative to conventional proportional limit.

We have made a detailed study of the microyield behavior of LiF. Dimensions of the specimens used in this study were: thickness ≈ 2.5mm, width >5mm, and length ≥30mm. The specimens were mechanically polished and subjected to a series of load-unload cycles in 4-point bending using a distance of 1.91cm between the supporting pins and 0.79cm between the loading pins. The load on the specimen was increased incrementally in successive cycles using a crosshead speed of 0.0025 cm/min to load the sample. The sample was unloaded as quickly as possible. After each cycle the permanent strain was measured by a bonded wire resistance strain gage which was attached to the specimen face subjected to the maximum tensile stresses.

Microyield behavior of single-crystal and press-forged samples H-41 are shown in figure 3. It is apparent that the microyeild behavior is improved by forging. In order to quantify the improvement, these data are replotted over a wide strain range on a log-log plot, as shown in figure 4. The straight lines represented by these plots were extrapolated to obtain σ_y (10^{-6}), the yield stress corresponding to an offset strain of 10^{-6}. Estimated σ_y (10^{-6}) values for various LiF samples are summarized in table 2 along with the proportional limit and fracture strength determined by conventional loading in 4-point bending at a crosshead speed of 0.0025cm/min to failure. These data indicate that the ratio of σ_y (10^{-6}) to the conventional proportional limit for LiF lies in the range 0.1 - 0.3 and that the press forging can increase σ_y (10^{-6}) of LiF by a factor of three to as much as a factor of ten (samples H-31 and H-41).

Microcreep behavior of LiF was also studied in this program. Specimens of two forgings, H-43-H1 and H-46-H2, were dead-weight loaded in 4-point bending at room temperature to σ_y (10^{-6}) for a period of five hours; no microcreep was detected in samples of either forging. Fig. 5 illustrates the microcreep behavior of samples of forging H-43-H1 at several stresses between the microyield point and the proportional limit. These preliminary data indicate that the microcreep in LiF can be prevented by keeping the design stresses below the microyield point.

5. Conclusions

It has been shown that two-step forging processes involving a first-step deformation at 700°C and a second-step deformation at 550°C permits large-scale deformation of LiF, leading to nearly a factor of three increase in the initial diameter of the forging billet. Press forging increases the microyield point of LiF by a factor between three and ten without significantly degrading its ultraviolet and visible transparency. Microcreep data indicate that significant microcreep does not occur in press-forged LiF when it is stressed at or below the microyield point.

Table 2. Microyield, macroyield and fracture characteristics of LiF.

	SAMPLE	σ_y (10^{-6}) (MN/m^2)	Conventional Proportional Limit (MN/m^2)	Fracture Strength (MN/m^2)
H-30	Press-Forged*	2.9	25.1	40.2
H-31	Single-Crystal	0.83	-	-
	Press-Forged	8.27	-	-
H-38	Press-Forged	3.72	34.01	51.92
H-41	Single-Crystal	1.17	12.48	18.31
	Press-Forged	10.34	40.91	51.82
H-42	Press-Forged	10.34	58.85	64.48
H-<110>-4	Single-Crystal	2.28	25.68	40.02
	Press-Forged	16.54	56.04	63.15
H-43-H1	Press-Forged	4.48	29.33	40.79
H-46-H2	Press-Forged	4.48	26.89	32.06

*Forging parameters of all samples except H-43-H1 and H-46-H2 are listed in table 1. H-43-H1 was forged 80% at 700°C and additional 15% at 550°C. H-46-H2 was forged 80% at 700°C.

6. Acknowledgments

The authors gratefully acknowledge the capable technical assistance of R. J. Brinda, K. A. Esaklul, E. V. Kiff, C. D. Olson and J. G. Satnik.

References

[1] Milam D., Weber, M. J., and Glass, A. J., Appl. Phys. Lett. 31, 822 (1977).

[2] Deaton, T. F. and Smith, W. L., in Laser Induced Damage in Optical Materials: 1979 (NBS Special Publication 568), Bennett, H. E., Glass, A. J., Guenther, A. H., and Newnam, B. E., Eds., p. 417 (1980).

[3] Ready, J. F., Vora, H., Skogman, R. A., Leung, K. M., and Bernal G., E., in Laser Induced Damage in Optical Materials: 1978 (NBS Special Publication 541), Glass, A. J. and Guenther, A. H., Eds., p. 59 (1978).

[4] Ready, J. F. and Vora, H., in Laser Induced Damage in Optical Materials: 1979 (NBS Special Publication 568), Bennett, H. E., Glass, A. J., Guenther, A. H., and Newnam, B. E., Eds., p. 39 (1980).

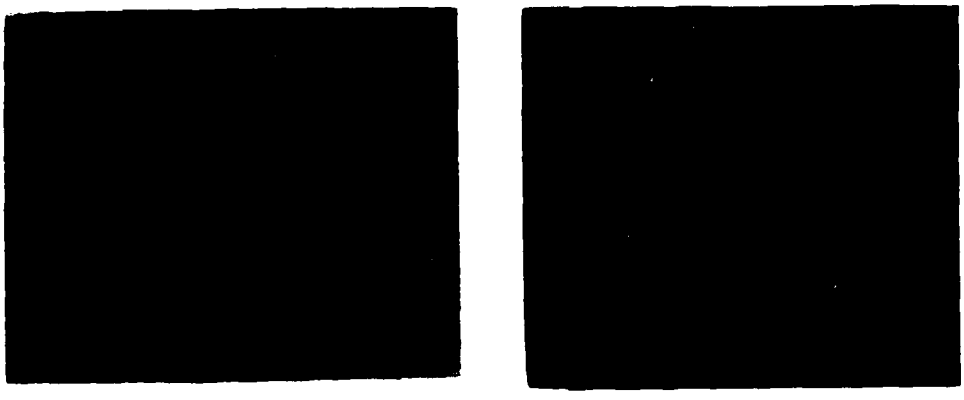

Figure 1. Microstructures of press-forged LiF single crystals. (A) Forged 80% at 700°C. (B) Forged 80% at 700°C and additional 40% at 550°C.

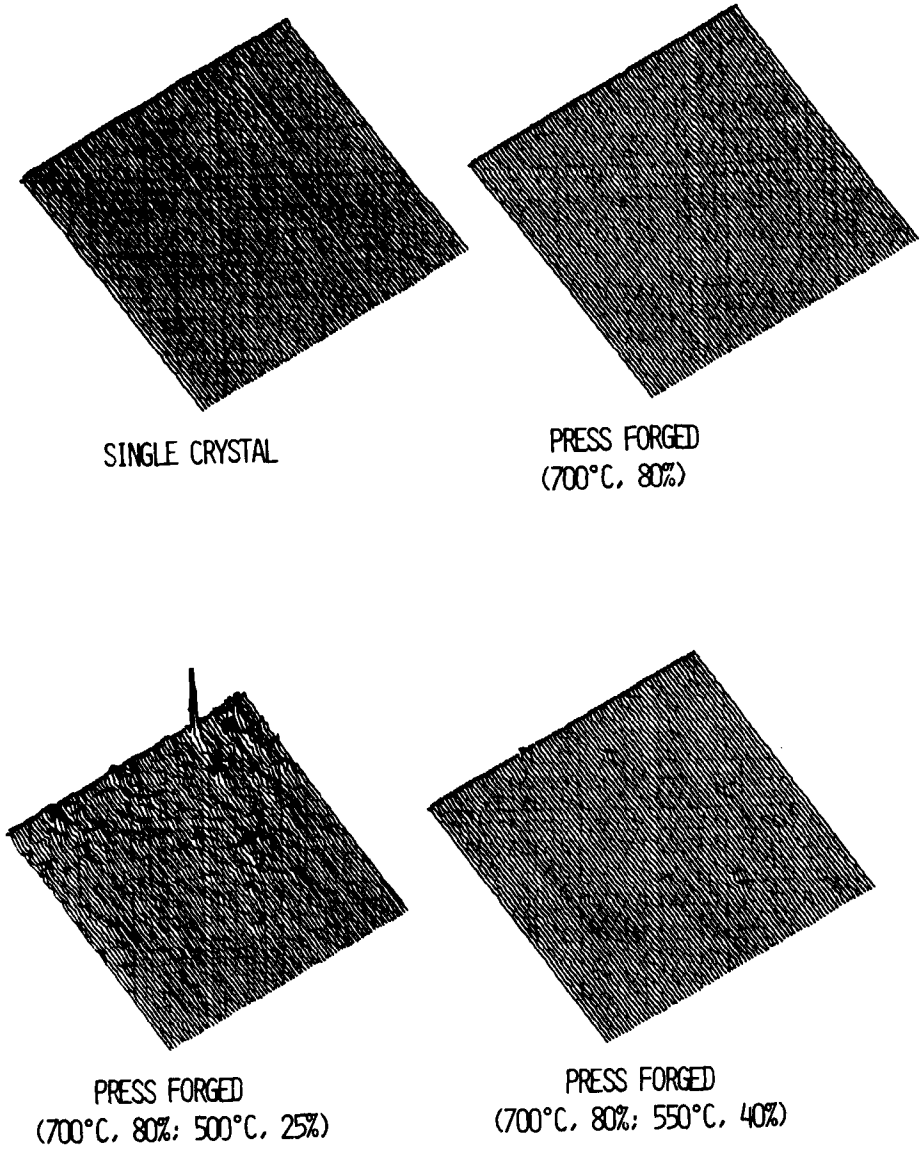

Figure 2. Scattering profiles of various LiF Samples.

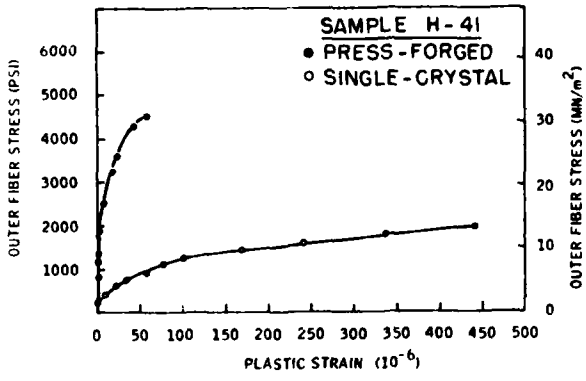

Figure 3. Microyield behavior of single-crystal and press-forged samples H-41,

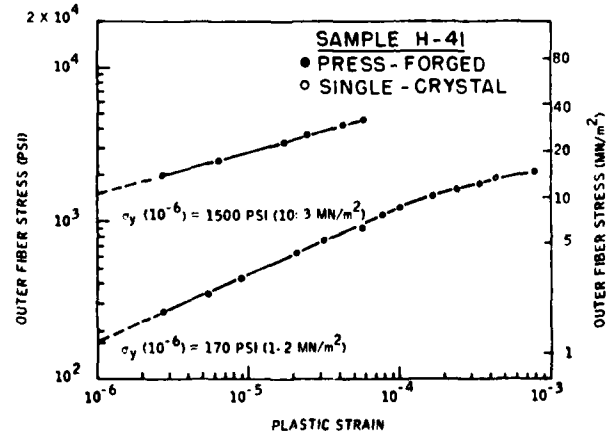

Figure 4. Log-log plot of the microyield data shown in figure 3.

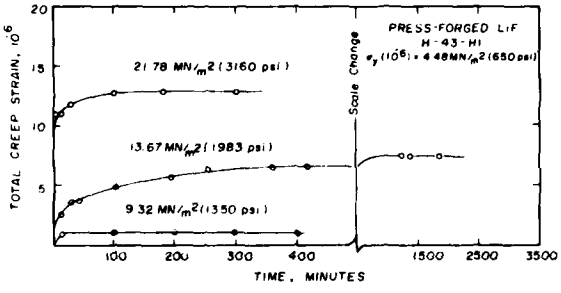

Figure 5. Microcreep of a press-forged LiF sample at room temperature.

STRESS INDUCED BIREFRINGENCE, CRITICAL WINDOW ORIENTATION, AND THERMAL LENSING EXPERIMENTS

Claude A. Klein
Research Division, Raytheon Company
Waltham, Massachusetts 02254

A proper assessment of thermal lensing phenomena in high-average-power laser windows involves an evaluation of two optical distortion coefficients: (a) the coefficient χ_+, which combines the effects of temperature-induced change in refractive index, surface bulging through constrained expansion, and photoelasticity averaged over the principal stress directions, and (b) the coefficient χ_-, which exists only if there is stress birefringence. This evaluation can be performed for <111>-oriented and for randomly-oriented aggregates of cubic single crystals. It is emphasized that the calculations require correct inputs in terms of elastic and photo-elastic coefficients. Among presently contemplated key laser-window material candidates, only CaF_2 can exhibit significant stress birefringence effects. this is not so in the <111> orientation, which reflects a critical situation in the sense of Joiner, Marburger, and Steier. Windows made of KCl exhibit isotropic distortion patterns because the magnitude of the thermo-optic coefficient is such that the "small-birefringence condition," $\chi_-/\chi_+ << 1$, is satisfied. The results of interferometric testing substantiate these considerations.

Key words: Elastic coefficients; high-energy laser; interferometric testing; optical distortion; photo-elastic coefficients; polycrystalline aggregate; stress birefringence; thermal lensing; window materials.

1. Introduction

Wavefront distortions caused by "thermal lensing" of optical components can have a major impact on the operation of high-energy laser (HEL) systems [1].[1] Windows, in particular, can distort an incident beam in a complex manner because laser-induced phaseshifts reflect changes in the optical pathlength arising from position-dependent variations in window thickness as well as from position- and polarization-dependent variations in refractive index [2]. This problem is now well understood in the sense that a theory of thermal lensing has been developed and shown to be amenable to practical calculations for relatively simple configurations in terms of both material characteristics and beam geometry [3]. In its present form, the theory applies only if the following assumptions are verified: (a) The window is subjected to axially symmetric thermal loadings; (b) The elastic and photo-elastic properties are isotropic in the plane of the window; and (c) The stress distribution obeys classical thin plate theory. Under these conditions, and in the absence of mechanical loadings, unconstrained laser windows are subjected to stress distributions characterized by cylindrically symmetric radial and azimuthal components, σ_ρ and σ_θ, which relate to the temperature profile in a fairly simple manner. Furthermore, the distortion of the beam can be described by means of two principal phaseshifts, $\delta\Phi_\rho$ and $\delta\Phi_\theta$, that is, the phaseshifts experienced by a normally incident light-ray polarized either in the radial or the azimuthal direction. These phaseshifts involve contributions stemming from the change in pathlength as the heated portion of the window expands and bulges outward, from the temperature dependence of the refractive index, and from photo-elastic effects associated with non-uniform heating patterns. Considering that σ_ρ and σ_θ differ everywhere except at the origin, it follows that for windows made of stress-birefringent material, the two principal phaseshifts are also different, which may have troublesome consequences. The emergence of stress-induced birefringence generates two distorted phase surfaces, one for each polarization, thus altering the polarization state of the incident beam; in this connection, we emphasize that presently available adaptive optical techniques cannot correct for this type of situation.

Recently, however, it was discovered that in windows made of certain single-crystalline materials, stress birefringence can be eliminated simply by properly orienting the window [4]. Specifically, Joiner, Marburger, and Steier (JMS) discovered that, if the piezo-optic constants that characterize birefringence in a solid possessing cubic symmetry are opposite in sign, there exists a direction along which incident radiation may preserve its polarization, even in the presence of stress perpendicular to the direction of incidence. In the case of CaF_2, for instance, this critical direction practically coincides with the [111] axis, which indicates that <111>-oriented CaF_2 laser windows cannot exhibit substantial birefringence, and this independently of the polarization of the incident beam since (111) planes in cubic material are known to be isotropic [5]. Keeping in mind that, of all the standard crystallographic planes, only the <111> configuration exhibits isotropic features, it would appear that calcium fluoride represents a unique situation in the sense that a JMS-oriented CaF_2 window is amenable to a proper evaluation of thermally induced optical distortions. This is not the case with other window materials of interest, such as KCl, which possess a cubic structure but exhibit strong elastic anisotropy in the critical orientation. Previously, if I have chosen to carry out an analysis of thermal lensing in KCl on assuming that the window consists of single-crystalline <111>-oriented material, this was done for convenience only [3]. At this time, hot-forging of KCl and fusion-casting of CaF_2 are being pursued as the most promising techniques for the production of large window blanks [6]. While it is not anticipated that these polycrystalline structures can be truly representative of macroscopically isotropic fine grained aggregates of cubic material, it should be desirable to obtain optical distortion coefficients on that basis because their availability does provide useful information for the design of HEL systems. In this context, I wish to point out that related calculations in the published literature always use single crystal values for the elastic and photo-elastic parameters that enter thermal lensing equations; this is incorrect because the corresponding quantities for polycrystalline aggregates can be quite different.

[1] Figures in brackets indicate the literature references at the end of this paper.

In this paper, I will briefly review the theory of thermal lensing in laser-heated windows, specify the role of stress-induced birefringence effects, and apply the concept of a critical window orientation to key window-material candidates (sec. 2). In section 3, I will address the problem of obtaining Young's modulus, Poisson's ratio, and the photo-elastic coefficients of a window blank made of either <111>-oriented cubic crystals or randomly oriented polycrystalline material. On that basis, I will derive relevant optical distortion coefficients for CaF_2, KCl, and ZnSe over a broad wavelength range (sec. 4). The discussion in section 5 concerns thermal lensing experiments performed at the Honeywell Corporate Material Sciences Center [7-9]; its purpose is to validate our evaluation of the distortion coefficients and to provide an interpretation of polarization-dependent phenomena in laser windows.

2. Theory of Thermal Lensing

Consider a thin circular window consisting of isotropic material or material that responds with cylindrical symmetry when exposed to a cylindrically symmetric heat load. If it is assumed that the optical path through the "cold" window gives rise to a phase[2]

$$\phi = k(n-1)L \tag{1}$$

at all positions of incidence, any disturbance resulting in a variation of the window thickness and/or a variation of the refractive index generates wavefront deformations, or phaseshifts.

$$\delta\phi = k[(n-1)\delta L + L\,\delta n] \ . \tag{2}$$

The change in thickness follows immediately from Hooke's law and is given by

$$\delta L = L[\alpha\,\delta T - (\nu/Y)(\sigma_\rho + \sigma_\theta)] \tag{3}$$

in the context of a thin-plate approximation. The change in index also involves two processes, the temperature dependence of the index at zero stress and the stress-induced photo-elastic contribution; since the principal directions of the dielectric tensor coincide with those of the stress, we may simply consider the index change for radially and azimuthally polarized light:

$$\delta n_\rho = (\partial n/\partial T)\,\delta T - (n^3/2)(q_{\parallel}\sigma_\rho + q_{\perp}\sigma_\theta) \tag{4a}$$

$$\delta n_\theta = (\partial n/\partial T)\,\delta T - (n^3/2)(q_{\parallel}\sigma_\theta + q_{\perp}\sigma_\rho) \ . \tag{4b}$$

Note that $q_{\parallel}$ and $q_{\perp}$ are the *stress-optic coefficients* for polarizations parallel and perpendicular to the stress direction and are defined in accord with Nye's convention [10]. Hence, if there is birefringence ($q_{\parallel} \neq q_{\perp}$), it is readily seen that the two principal phaseshifts can be expressed in the following manner:

$$\delta\phi_{\rho,\theta} = kL\left\{(n-1)[\alpha\,\delta T - (\nu/Y)(\sigma_\rho+\sigma_\theta)] + (\partial n/\partial T)\,\delta T - (n^3/2)(q_{\parallel}\sigma_{\rho,\theta} + q_{\perp}\sigma_{\theta,\rho})\right\} \ , \tag{5}$$

where the first subscript is for radial and the second is for azimuthal polarization.

In this model, the principal stresses are [11]:

$$\sigma_\rho = \alpha Y\left[\int_0^1 \delta T r\,dr' - (1/r^2)\int_0^r \delta T\, r'dr'\right] \tag{6a}$$

$$\sigma_\theta = \alpha Y\left[\int_0^1 \delta T r\,dr' + (1/r^2)\int_0^r \delta T\, r'dr' - \delta T\right] \tag{6b}$$

if $\underline{r}$ refers to radial distances measured in units of the window radius. Returning now to eq. (5), and since $\underline{r}$-independent terms do not contribute to the lensing process, the two principal phaseshifts are best expressed as follows [3]:

$$\delta\phi_\rho = \delta\phi_+ + \delta\phi_- \tag{7a}$$

$$\delta\phi_\theta = \delta\phi_+ - \delta\phi_- \ . \tag{7b}$$

Here, $\delta\phi_+$ and $\delta\phi_-$ represent two aberration functions, which can be specified in a very compact manner,

$$\delta\phi_+ = (k\,\chi_+ L)\,\delta T \tag{8a}$$

$$\delta\phi_- = (k\,\chi_- L)(\overline{\delta T} - \delta T) \ , \tag{8b}$$

on using the symbol $\overline{\delta T}$ to designate the mean temperature increase from the origin to the radial distance $\underline{r}$, i.e.,

---

[2]The symbols are identified in Appendix.

$$\overline{\delta T} = (2/r^2) \int_0^r \delta T \; r'dr' \quad . \tag{9}$$

Equation (8) defines two optical distortion coefficients,

$$\chi_+ = (\partial n/\partial T)_{\sigma=0} + (n-1)\alpha(1+\nu) + (n^3 \alpha Y/4)(q_{\parallel} + q_{\perp}) \tag{10a}$$

$$\chi_- = (n^3 \alpha Y/4)(q_{\parallel} - q_{\perp}) \; , \tag{10b}$$

which regroup all material properties required to assess the susceptibility to thermal lensing of stress-birefringent laser windows. The coefficient χ_+ reflects the temperature-induced isotropic change in index, the contribution due to surface bulging through constrained expansion, and the photo-elastic effect averaged over the two principal stress directions; the χ_- coefficient involves only the stress-induced birefringence. The advantage of this formulation is that it separates out the effects of birefringence on wavefront distortions, which makes it feasible to describe the situation in terms of only two lumped constants once the temperature distribution is known. In this regard, we note that birefringence-independent distortions reflect the temperature profile as created by the incident beam, whereas birefringence-dependent contributions are always minimal in the central region but may become substantial at larger radial positions. From eq. (7) it follows immediately that the relative importance of birefringence-dependent effects will be determined by the ratio $\delta\phi_-/\delta\phi_+$, or

$$\frac{\delta\phi_-}{\delta\phi_+} = \frac{\chi_-}{\chi_+} * \frac{\overline{\delta T} - \delta T}{\delta T} \quad . \tag{11}$$

which demonstrates that it is the combination of the factor χ_-/χ_+ and the function $(\overline{\delta T} - \delta T)/\delta T$ that controls the impact of stress birefringence. In this light, we conclude that an evaluation of the two distortion coefficients not only allows one to map out the wavefront surfaces and, thus, to derive far-field patterns, but also to provide the designer with highly relevant information on the relative "weight" of stress birefringence compared to all other sources of optical distortion in a given window-material candidate.

In this regard, we recall that in cubic crystals for which the piezo-optic anisotropy, $A = q_{44}/(q_{11}-q_{12})$, is negative, there are planes where the principal axes of the dielectric tensor are independent of the stress situation, as long as the stresses are confined to that plane [4]. It follows that a beam propagating in a direction normal to this plane and possessing linear polarization along one of the principal dielectric axes cannot experience self-induced depolarization. The critical direction is in a (110) plane at an angle θ_c from the [001] axis given by

$$\tan^2(\theta_c) = -A \; , \tag{12}$$

which suggests that in single-crystalline windows (or highly-textured cubic aggregates) that verify eq. (12), stress-birefringence effects can be eliminated for properly polarized beams. We now examine the applicability of this important result to three key window materials.

Table 1. Wavelength-dependent optical-distortion related properties of three laser-window material candidates, at room temperature. Unless specified, the data are as given in ref. [12].

	Laser wavelength	λ(μm)	0.458	0.633	1.15	3.39	10.6
CaF_2	Refractive index	n(I)	1.438	1.433	1.428	1.415	
	Thermo-optic coefficient	$dn/dT(10^{-5}K^{-1})$	-1.10±.01	-1.13±.02	-1.15±.02	-1.12±.03	
	Piezo-optic constants[a]	$q_{11}(10^{-12}Pa^{-1})$		-0.38±.03	0.40±.06	0.46±.11	
		$q_{12}(10^{-12}Pa^{-1})$		1.08±.03	1.09±.06	0.94±.11	
		$q_{44}(10^{-12}Pa^{-1})$		0.71±.01	0.72±.01	0.66±.06	
KCl	Refractive index	n(I)	1.502	1.488	1.478	1.473	1.455
	Thermo-optic coefficient	$dn/dT(10^{-5}K^{-1})$	-3.49±.02	-3.58±.02	-3.62±.02	-3.62±.02	-3.48±.04
	Piezo-optic constants[b]	$q_{11}(10^{-12}Pa^{-1})$		4.6±.2			4.3±.3
		$q_{12}(10^{-12}Pa^{-1})$		2.7±.8			2.8±.3
		$q_{44}(10^{-12}Pa^{-1})$		-3.9±.8			-3.4±.4
ZnSe	Refractive index	n(I)		2.591	2.475	2.436	2.403
	Thermo-optic coefficient	$dn/dT(10^{-5}K^{-1})$		10.6±.1	7.0±.1	6.2±.1	6.1±.1
	Piezo-optic constants[c]	$q_{11}(10^{-12}Pa^{-1})$		-1.44±.04			1.46±.07
		$q_{12}(10^{-12}Pa^{-1})$		0.17±.05			0.51±.07
		$q_{44}(10^{-12}Pa^{-1})$		-1.60±.01			1.97±.02

(a) The 3.39-μm data are corrected results (R. Waxler, private communication, 1980).
(b) Also applicable to KCl nominally doped with 1.5% KI.
(c) For chemically vapor-deposited (CVD) ZnSe; note that $q_{44} = q_{11}-q_{12}$.

1. The case of CaF_2. As seen in table 1, which is based on data generated by Feldman and his collaborators [12], the measured piezo-optic constants are essentially independent of wavelength. Since $q_{11} - q_{12} = 1.45 \times 10^{-12}$ Pa^{-1} and $q_{44} = 0.70 \times 10^{-12}$ Pa^{-1}, it follows that the critical angle θ_c is close to 55.2 deg and, thus, should be within 0.5 deg off the [111] direction. In this light, we surmise that <111>-oriented CaF_2 laser windows cannot exhibit much birefringence, and this irrespective of the polarization of the incident beam because (111) planes in cubic material are known to be isotropic.

2. The case of KCl. With $q_{11} - q_{12} = 1.7 \times 10^{-12}$ Pa^{-1} and $q_{44} = 3.65 \times 10^{-12}$ Pa^{-1}, over the whole wavelength range of interest (see table 1), we have $\theta_c = 34.3$ deg, which is 20.4 deg off the [111] direction. In principle, therefore, it would appear that <111>-oriented KCl windows can be depolarizing.

3. The case of ZnSe. The concept of a critical window orientation does not apply to chemically vapor deposited (CVD) ZnSe, which is macroscopically isotropic, as can be readily established by referring to table 1.

3. Elastic and Photo-Elastic Properties

The elastic properties of relevance in a thermal lensing situation [see eq. (10)] include Young's modulus, Y, and Poisson's ratio, ν. In cubic material, both Y and ν may assume a wide range of values depending on orientation, but (111) planes always exhibit isotropic features. Specifically, if one makes use of standard directionality equations, it is seen that [3]

$$Y_{(111)} = \frac{2}{s_{11}+s_{12}+(1/2)s_{44}} \tag{13}$$

and

$$\nu^{[111]}_{(111)} = -\frac{2}{3} \cdot \frac{s_{11}+2s_{12}-(1/2)s_{44}}{s_{11}+s_{12}+(1/2)s_{44}} \tag{14}$$

in the geometry of interest here; note that, while a single value of Poisson's ratio is normally associated with isotropic material, this does not apply to (111) planes. Similarly, directionality equations for the photo-elasticity tensor show that, in the (111) plane, the two stress-optic parameters of eq. (10) become

$$q_{\parallel} + q_{\perp} = (1/3)[3(q_{11}+q_{12}) + q_{44} - (q_{11}-q_{12})] \tag{15a}$$

$$q_{\parallel} - q_{\perp} = (1/3)[2q_{44} - (q_{11}-q_{12})] \ , \tag{15b}$$

where the q_{ij}'s are as measured in the laboratory.[3] Elastic compliances and piezo-optic constants of single crystalline CaF_2, single-crystalline KCl, and chemically vapor-deposited ZnSe are listed in table 1 and table 2; Young's modulus, Poisson's ratio, and the two stress-optic coefficients that apply to <111>-oriented windows then are as given in table 3. Regarding <111> CaF_2, we note that, in effect, there is no birefringence, which is as expected considering that a direct evaluation of $q_{\parallel} - q_{\perp}$ can be made from $(q_{11}-q_{12})\cos^2\theta + q_{44}\sin^2\theta$, with $\theta = 54.74$ deg, thus yielding $q_{\parallel} - q_{\perp} = -0.016 \times 10^{-12}$ Pa^{-1}.

Table 2. Wavelength-independent optical-distortion related properties of three laser-window material candidates, at room temperature.

Item	Symbol (units)	CaF_2	KCl	ZnSe
Expansion coefficient	$\alpha(10^{-6}K^{-1})$	18.7[a]	37.1[a]	7.3[a]
Elastic compliances	$s_{11}(10^{-12}$Pa$^{-1})$	6.87[b]	26.2[c]	13.9[d]
	$s_{12}(10^{-12}$Pa$^{-1})$	-1.45[b]	-3.5[c]	-4.4[d]
	$s_{44}(10^{-12}$Pa$^{-1})$	29.67[b]	160[c]	
Bulk modulus	$K(10^9$Pa)	84.0[e]	17.4[e]	
Shear modulus	$G(10^9$Pa)	43[f]	9.4[f]	

(a) A. Feldman, et al., reference [12].
(b) C. Wong and D. Schuele, J. Phys. Chem. Solids 28, 1225 (1967).
(c) R. F. Hearmon, Adv. Phys. 5, 323 (1956).
(d) Chemically vapor-deposited isotropic material (ref. [12]).
(e) Derived from elastic compliances.
(f) Average value for a polycrystalline aggregate (ref. [14]).

[3] The stress-optic tensor elements q_{ij}, which are usually identified as piezo-optic constants, refer to standard crystallographic directions (see ref. [10]).

Table 3. Elastic and photo-elastic coefficients of isotropically configured laser-window material candidates.

Item	Symbol (units)	<111>CaF_2[a]	PCA-CaF_2[b]	<111>KCl[a]	PCA-KCl[b]	CVD-ZnSe[c]
Young's modulus	$Y(10^9$ Pa)	98.8	110	19.5	23.9	79.9
Poisson's ratio	$\nu(1)$	0.36	0.28	0.395	0.27	0.32
Stress-optic coefficient	$q_{\parallel}+q_{\perp}(10^{-12}Pa^{-1})$	1.35[d]	1.01[d]	5.42[d]	6.35[d]	-1.28[e]
Stress-birefringence coefficient	$q_{\parallel}-q_{\perp}(10^{-12}Pa^{-1})$	-0.02[d]	-0.32[d]	-1.87[d]	-0.85[d]	-1.60[f]

(a) The window normal coincides with the [111] crystal axis.
(b) PCA = polycrystalline aggregate, macroscopically isotropic.
(c) CVD = chemically vapor-deposited, macroscopically isotropic.
(d) Assumes that the piezo-optic constants are wavelength independent.
(e) At 0.633 μm; increases to -0.95 at 10.6 μm.
(f) At 0.633 μm; decreases to -1.97 at 10.6 μm.

Turning now our attention to macroscopically isotropic solids, we have

$$Y^* = 1/s_{11}^* \quad , \tag{16}$$

and

$$\nu^* = -s_{12}^*/s_{11}^* \tag{17}$$

because the elastic isotropy criterion $[s_{44}^* = 2(s_{11}^*-s_{12}^*)]$ applies. These simple formulas yield "good" values for Young's modulus and Poisson's ratio of CVD ZnSe (see table 3), but the compliances of randomly oriented polycrystalline aggregates of CaF_2 or KCl are not yet available. It is known, however, that the bulk modulus of single-phase aggregates of cubic material, i.e.,

$$K = 1/[3(s_{11}^* + 2s_{12}^*)] = (1/3)(c_{11}^*+2c_{12}^*), \tag{18a}$$

is unambiguously equal to

$$K = 1/[3(s_{11} + 2s_{12})] = (1/3)(c_{11} + 2c_{12}), \tag{18b}$$

where s_{ij} and c_{ij} are the usual single-crystal compliances and stiffnesses. Furthermore, the shear modulus,

$$G = 1/[2(s_{11}^* - s_{12}^*)] = (1/2)(c_{11}^* - c_{12}^*), \tag{19}$$

falls between narrow bounds as established by Hashin and Shtrikman [13] and tabulated in reference [14]. Since these two properties (K and G) suffice to completely characterize the elastic features of a solid, they appear in table 2 with other wavelength-independent property data for CaF_2 and KCl. It is then a straightforward matter to calculate Young's modulus and Poisson's ratio by means of the relations

$$Y^* = \frac{9KG}{G + 3K} \tag{20}$$

and

$$\nu^* = \frac{3K-2G}{2(G+3K)} \quad , \tag{21}$$

which derive from eqs. (16-19). In conjunction with CaF_2, it is worth noting that, recently, Young's modulus and Poisson's ratio were determined on four specimens of Raytheon-made fusion-cast CaF_2[6]. The averages, $\bar{E} = 111 \times 10^9$Pa (16.1Mpsi) and $\bar{\nu} = 0.28$, were almost identical to the values predicted for polycrystalline aggregates (see table 3). This may imply that, on a macroscopic scale, CaF_2 window blanks fabricated by this technique do have properties that are effectively those of randomly oriented aggregates, even though the process does not result in fine-grained material. Similar measurements on hot-forged KCl [15] yielded overall averages of 22 ±6 GPa (3.2 ± .9Mpsi) and 0.26 ± .10, respectively, which is not incompatible with our calculations but suggests that much of the single-crystal anisotropy of the starting material was retained in the hot-forged product.

According to Flannery and Marburger [16], the strain-optic coefficients of a randomly oriented polycrystalline aggregate of cubic material relate to single-crystal parameters in the following manner:

$$p_{\parallel} + 2p_{\perp} = p_{11} + 2p_{12} \tag{22}$$

$$\frac{p_{\parallel} - p_{\perp}}{2G} = \frac{p_{11} - p_{12}}{c_{11} - c_{12}} + \frac{3}{5} j_3\left(\frac{p_{44}}{c_{44}} - \frac{p_{11}-p_{12}}{c_{11}-c_{12}}\right), \tag{23}$$

where the factor j_3 is as given by Hershey [17],

$$j_3 = \frac{5c_{44}(3K+4G)}{G(9K+8G) + 8c_{44}(K+2G)} \quad . \tag{24}$$

Since we work with stresses, we are using the matrix equation $p_{mn} = q_{mr}c_{rn}$ [10] to write down relations such as

$$p_{11}+2p_{12} = (q_{11}+2q_{12})(c_{11}+2c_{12}) \quad (25a)$$

$$p_{11}-p_{12} = (q_{11}-q_{12})(c_{11}-c_{12}) \ . \quad (26a)$$

and since the matrix equation also holds for polycrystalline solids,

$$p_{\parallel}+2p_{\perp} = (q_{\parallel}+2q_{\perp})3K \quad (25b)$$

$$p_{\parallel}-p_{\perp} = (q_{\parallel}-q_{\perp})2G \ . \quad (26b)$$

Keeping in mind that the bulk modulus is an invariant [eq. (18)], it is easily shown that the Flannery-Marburger equations then lead to

$$q_{\parallel}+q_{\perp} = q_{11}+q_{12}+(j_3/5)[q_{44}-(q_{11}-q_{12})] \quad (27a)$$

$$q_{\parallel}-q_{\perp} = q_{11}-q_{12}+(3j_3/5)[q_{44}-(q_{11}-q_{12})] \ . \quad (27b)$$

In an isotropic medium such as CVD ZnSe, for which $q_{44}^* = q_{11}^*-q_{12}^*$, eq. (27) boils down to $q_{\parallel}+q_{\perp} = q_{11}^*+q_{12}^*$ and $q_{\parallel}-q_{\perp} = q_{11}^*-q_{12}^*$, thus demonstrating self-consistency. The stress-optic coefficients of polycrystalline CaF_2 and polycrystalline KCl are listed in table 3 as obtained from eq. (27) in conjunction with single-crystal data. The calculated stress birefringence of polycrystalline CaF_2 is -0.32 in the usual units, which is less than the measured (but unconfirmed) value of -0.51 reported for Kodak-made Irtran-3 at 10.6 μm [18].

4. Optical Distortion Coefficients

Returning now to eq. (10), and on inserting previously tabulated property values, it is a simple matter to derive optical distortion coefficients as a function of wavelength, and to generate the plots that are displayed in figure 1. By the same token, these plots summarize the substance of this paper, as they provide essential information for assessing the optical performance of HEL window materials; for a more graphic presentation of the situation at the He-Ne laser wavelength, the reader may refer to figure 2. Since optical distortion in <111>-oriented windows has been the subject of earlier publications [3,5], I will focus here on thermal lensing processes in polycrystalline window materials, at the 3.39-μm laser wavelength, which should be of interest in connection with HF/DF chemical lasers.

1. Polycrystalline CaF_2. The wavelength dependence of the birefringence-free coefficient χ_+ reflects mainly the trend towards less negative values exhibited by the thermo-optic coefficient, in the visible, and the same observation holds for KCl. At 3.39 μm, the arithmetic boils down to this:

$$\chi_+ = \underset{-1.12\pm.03}{dn/dT} + \underset{0.99}{(n-1)\alpha(1+\nu)} + \underset{0.15}{(n^3\alpha Y/4)(q_{\parallel}+q_{\perp})} = (\ 0.02\pm.03)\times 10^{-5}K^{-1}$$

$$\chi_- = (n^3\alpha Y/4)(q_{\parallel}-q_{\perp}) = -0.05\times 10^{-5}K^{-1} \ ,$$

which demonstrates that, in randomly oriented CaF_2, χ_+ should be practically insignificant due to the suppression of the positive optical path differences (OPDs) associated with thermal expansion and isotropic photoelasticity by the negative dn/dT contribution. Consequently, the thermal lensing process will be dominated by stress-birefringence effects, which explains why depolarization can become highly apparent with CaF_2 windows that are not "JMS oriented"[8].

2. Polycrystalline KCl. As shown in fig. 1, randomly oriented KCl windows behave essentially in the same manner as <111>-oriented structures, which suggests that thermal lensing in KCl does not critically depend on crystalline order or preferred orientation. At 3.39 μm, the optical distortion coefficients are as follows:

$$\chi_+ = \underset{-3.62}{dn/dT} + \underset{2.23}{(n-1)\alpha(1+\nu)} + \underset{0.45}{(n^3\alpha Y/4)(q_{\parallel}+q_{\perp})} = -0.94\times 10^{-5}K^{-1}$$

$$\chi_- = (n^3\alpha Y/4)(q_{\parallel}-q_{\perp}) = -0.06\times 10^{-5}K^{-1} \ ,$$

thus implying that the "small-birefringence condition," $\chi_-/\chi_+ << 1$, is satisfied. Thin windows exhibit circular distortion patterns [7] not because the birefringence is smaller than in CaF_2, as some authors seem to believe [8], but because the magnitude of dn/dT is such that the isotropic contribution to OPDs dominates in spite of some degree of cancellation. In this regard, we note that, in reference [9] the thermo-optic coefficient of KCl was assumed equal to $-2.46\times 10^{-5}K^{-1}$, which is incorrect and leads to a "distorted" interpretation of thermal lensing in KCl. Actually, the coefficient χ_+ takes on negative values, which is in accord with the observation that KCl windows behave in the manner of a negative lens [19].

3. Polycrystalline ZnSe. At 3.39 μm, the contributions to optical distortion add up as follows:

$$\beta_+ = \underset{6.2}{dn/dT} + \underset{1.4}{(n-1)\alpha(1+\nu)} + \underset{-0.2}{(n^3\alpha Y/4)(q_\parallel + q_\perp)} = 7.4 \times 10^{-5} K^{-1}$$

$$\beta_- = (n^3\alpha Y/4)(q_\parallel - q_\perp) = -0.35 \times 10^{-5} K^{-1} .$$

It is immediately seen that the thermo-optic coefficient controls the process and, thus, insures polarization-independent lensing in this material. There is, nevertheless, a substantial stress-birefringence contribution (see fig. 2), primarily because of the comparatively large refractive index of ZnSe, but this does not affect the thermal lensing situation. We note that the level of wavefront deformation referred to the dissipated power should be almost an order of magnitude greater than in KCl, and perhaps even two orders of magnitude greater than in CaF_2, in accord with much experimental evidence.

5. *Thermal Lensing Experiments*

An investigation of wavefront-distortion phenomena associated with thermal lensing in laser windows requires some interferometric testing, which is best performed on a real-time basis, by means of holographic techniques [7-9]. The effect of the window on the interferogram can be understood in simple terms if the incident linearly polarized field has cylindrical symmetry,

$$\vec{E}_{in} = e_{in}\vec{E}(r) , \tag{28}$$

and if the window response is also cylindrically symmetric. In that case, the theory described in section 2 applies, and since the incident polarization can be split into components along the principal axes, the transmitted field becomes

$$\vec{E}_{out} = E(r)[\cos(\psi)\exp(i\delta\phi_\theta) + \sin(\psi)\exp(i\delta\phi_\eta)] , \tag{29a}$$

which can be rewritten as follows:

$$\vec{E}_{out} = E(r)\Big\{e_{in}[\cos^2(\psi)\exp(i\delta\phi_\theta) + \sin^2(\psi)\exp(i\delta\phi_\eta)] + e_{orth}\cos(\psi)\sin(\psi)[\exp(i\delta\phi_\theta) - \exp(i\delta\phi_\eta)]\Big\} \tag{29b}$$

if the unit vectors θ and η are reexpressed in terms of the polarization vector e_{in} *and its orthogonal complement* e_{orth}. Depolarization effects reflect the emergence of an orthogonal field, $E(r)\cos(\psi)\sin(\psi)[\exp(i\delta\phi_\theta) - \exp(i\delta\phi_\eta)]$, which exists only if there is birefringence, that is if the two principal phaseshifts differ ($\delta\phi_\theta \neq \delta\phi_\eta$). As we have seen earlier, this cannot happen on axis, thus implying that the axial field always preserves its polarization. Off the beam axis, and in the presence of stress birefringence, the aberration function $\delta\phi_-$ takes on non-zero values; in a first-order approximation, therefore, eq. (29) demonstrates that the window impresses a phase retardation [7],

$$\delta\phi = \delta\phi_+ + \delta\phi_- \cos(2\psi) = \delta\phi_+[1 + (\delta\phi_-/\delta\phi_+)\cos(2\psi)] , \tag{30}$$

on the incident polarization. On this basis, it becomes a simple matter to predict the effects of window distortion on circular bias interference fringes. For instance, it is immediately seen that: (a) The interferometric pattern of laser-heated windows always assumes a fourfold symmetry; (b) Circular bias fringes evolve into ellipse-like, or *more complex shapes, whose "eccentricity" increases with the* ratio $\delta\phi_-/\delta\phi_+$; and (c) Fringe motion is controlled via the symmetric aberration function $\delta\phi_+$, that is, by the temperature rise at the local radial position.

Figure 3 displays some of the significant results of Honeywell's interferometric testing of CO_2 laser heated windows [7-9]. The contour maps that are reproduced here illustrate laser-induced OPDs measured in fractions of "wave" (0.6328 μm), thus providing a vivid picture of the nature and the magnitude of the optical distortion. Unfortunately, they were obtained under widely differing conditions of beam power and beam spot-size, which renders them unsuitable for comparative evaluations; even a cursory examination, however, affords some highly revealing insights.

1. Single-Crystalline CaF_2. The contour maps in Fig. 4 (step size = 0.1λ) refer to three specimens cut perpendicular to the [111], the [110], and the [100] axes, respectively. The ‹111› disk exhibits azimuthally symmetric distortions, which are quite weak per watt of absorbed power and *independent of the polarization of the "viewing" beam; this is in accord with theory (see table 3)* and also confirms Detrio's observation [20] that, viewed between crossed polarizers, ‹111›-oriented CaF_2 does not "rotate" any beam power. The strongly anisotropic (and polarization-dependent) effects observed with ‹110› and ‹100› cut disks indirectly substantiate our calculation for polycrystalline material in the sense that they point to a situation dominated by stress birefringence for all crystal orientations that do not conform to the JMS requirement.

2. Single Crystal/Hot Forged KCl. The circular fringes displayed in figure 3 are for ‹100›-oriented KCl and illustrate this material's response to a 5-sec laser exposure at a beam-power level of 200 W. There is no evidence of anisotropic effects in this inteferogram, which demonstrates that, even in a geometry that is not amenable to the simple theory of thermal lensing, stress birefringence has little impact on wavefront distortions in KCl and, hence, causes no reduction in far-field intensity [3]. At much higher power levels (8 kW) and longer exposure times (30 sec), hot-forged KCl

exhibits partly elliptical equal-OPD contours beyond the beam-impacted area (see fig. 3). Since the inner contours (step size = 0.8λ) retain circular symmetry, we can attribute this effect to the behavior of the ratio $\delta\phi_-/\delta\phi_+$ [see eq. (30)], which may reach "detectable" levels at large radial positions, where the function $(\overline{\delta T}-\delta T)/\delta T$ reaches peak values [see sec. 2].

3. Chemically Vapor-Deposited ZnSe. The contours shown in figure 3 are for OPD steps of 0.3λ and illustrate the situation in this material after 30 seconds of irradiation at a beam-power level of 2 kW. In appearance, these contours resemble concentric circles centered on the beam axis, which emphasizes that birefringence effects are negligible in CVD ZnSe; they also demonstrate that the optical path distortion is fairly severe, as may have been anticipated from the χ_+ evaluation [see table 3], and will require some form of passive or active correction to permit operation at the power levels presently contemplated for HEL applications.

6. Conclusion

It has long been recognized that, in principle, stress-birefringence effects associated with thermal lensing processes that occur in infrared-transmitting windows can have a highly deleterious impact on the operation of high-energy laser systems. The theory and the calculations presented in this paper should provide the designer with simple analytical tools for predicting the performance of a given window material in a specific system environment. Perhaps the most important conclusion of this work is that calcium fluoride windows represent a unique situation in the sense that birefringence-independent contributions to optical distortion essentially cancel, which leads to strongly anisotropic lensing at high fluences, for crystalline configurations that do not conform to the critical orientation requirement of Joiner, Marburger, and Steier.

References

[1] Klein, C.A., in Laser-Induced Damage in Optical Materials: 1979 (NBS-SP-568, Washington, 1980), p. 425.

[2] Sparks, M., J. Appl. Phys. 42, 5029 (1971).

[3] Klein, C.A., Infrared Phys. 17, 343 (1977) and 18, 251 (1978).

[4] Joiner, R., Marburger, J., and Steier, W., in Laser-Induced Damage in Optical Materials: 1977 (NBS-SP-509, Washington, 1977), p. 89.

[5] Klein, C.A., Appl. Phys. Letters 35, 52 (1979).

[6] Graves, J.A., Wimmer, J.M., and McCullum, D.E., Exploratory Development on Multidisciplinary Characterization of Infrared-Transmitting Materials (AFML-TR-79-4152, Wright-Patterson Air Force Base, 1979).

[7] Bernal, E.G., and Loomis, J.S., in Laser-Induced Damage in Optical Materials: 1976 (NBS-SP-462, Washington, 1976, p. 36.

[8] Leung, K., Bernal, E., and Loomis, J., in Proc. High-Power Laser Optical Components and Component Materials Meeting (AFML, Wright-Patterson Air Force Base, 1977), p. 461.

[9] Leung, K.M., Ready, J.F., and Bernal, E.G., in Proc. High-Power Laser Optical Components Meeting (NWC-TP-6111-1, Naval Weapons Center, China Lake, 1979), p. 88.

[10] Nye, J.F., Physical Properties of Crystals (Oxford U. Press, Oxford, 1957).

[11] Boley, B.A., and Weiner, J.H., Theory of Thermal Stresses (J. Wiley, New York, 1960).

[12] Feldman, A., Horowitz, D., Waxler, R., and Dodge, M., Optical Materials Characterization: Final Report (NBS-TN-993, Washington, 1979).

[13] Hashin, Z., and Shtrikman, S., J. Mech. and Phys. Solids 10, 335 (1962) and 10, 343 (1962).

[14] Simmons, G., and Wang, H., Single-Crystal Elastic Constants and Calculated Aggregate Properties (MIT Press, Cambridge, 1971).

[15] Wurst, J.C., Graves, G.A., and Fenter, J.R., in Proc. Fifth Annual Conf. Infrared Laser Window Materials (AFML, Wright-Patterson Air Force Base, 1976), p. 576.

[16] Flannery, M., and Marburger, J., Appl. Phys. Letters 28, 600 (1976).

[17] Hershey, A.V., J. Appl. Mech. 21, 236 (1954).

[18] Pitha, C.A., and Friedman, J.D., in Proc. Fourth Annual Conf. Infrared Laser Window Materials (AFML, Wright-Patterson Air Force Base, 1975), p. 150.

[19] Loomis, J.S., and Bernal, E.G., in Laser-Induced Damage in Optical Materials: 1975 (NBS-SP-435, Washington, 1976), p. 126.

[20] Detrio, J.A., and Petty, R.D., in Laser-Induced Damage in Optical Materials: 1978 (NBS-SP-541, Washington, 1978), p. 78.

Appendix

List of Symbols

A	:	Anisotropy ratio	$q_{\parallel,\perp}$	:	Stress-optic coefficients
c_{ij}	:	Elastic stiffnesses	r	:	Radial coordinate
$\vec{E}_{in}$	:	Incident field	s_{ij}	:	Elastic compliances
$\vec{E}_{out}$	:	Transmitted field	T	:	Local temperature
$E(r)$	:	Beam amplitude	Y	:	Young's modulus
$\hat{e}_{in}$	:	Polarization vector	α	:	Expansion coefficient
$\hat{e}_{orth}$	:	Orthogonal vector	δT	:	Temperature increase
G	:	Shear modulus	$\delta\phi$	:	Phase retardation
K	:	Bulk modulus	$\delta\phi_{+,-}$	:	Aberration functions
k	:	Propagation constant	$\delta\phi_{\rho,\theta}$	:	Principal phaseshifts
L	:	Window thickness	θ_c	:	Critical angle
n	:	Refractive index	ν	:	Poisson's ratio
p_{ij}	:	Electro-optic constants	$\sigma_{\rho,\theta}$	:	Stress components
$p_{\parallel,\perp}$	:	Strain-optic coefficients	ψ	:	Directional angle
q_{ij}	:	Piezo-optic constants	$\chi_{+,-}$	:	Distortion coefficients

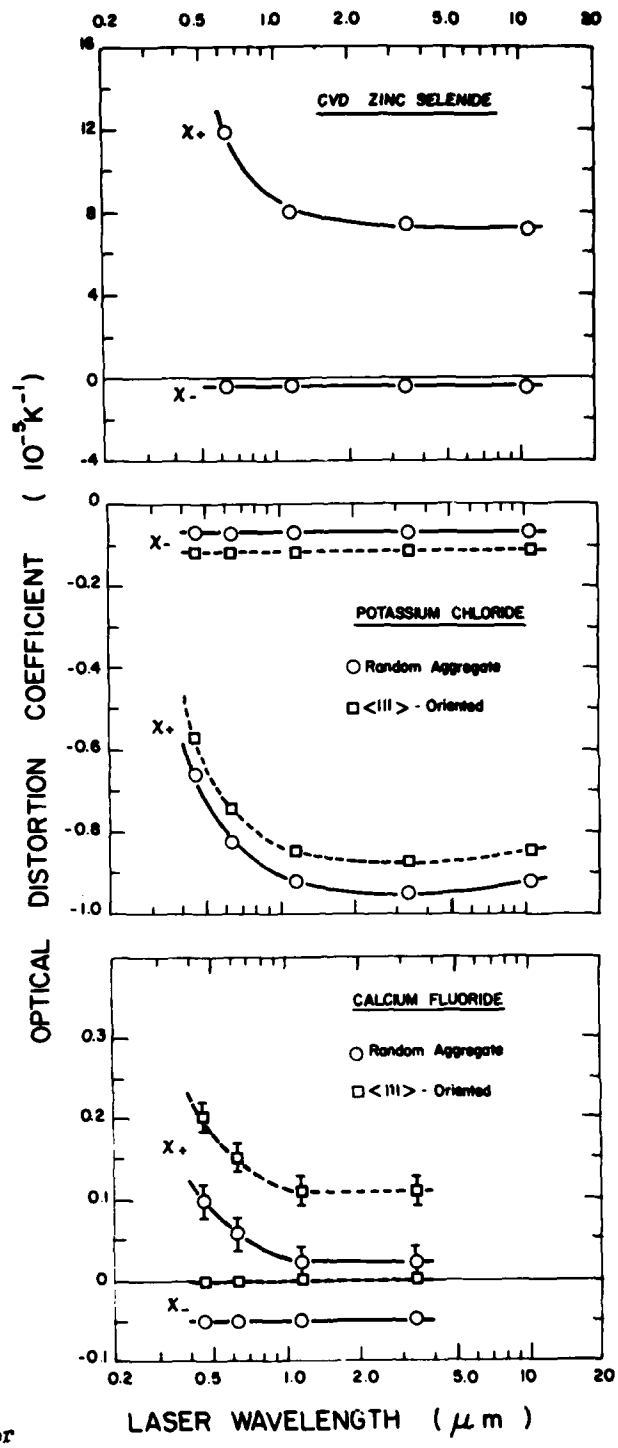

Figure 1. Optical distortion coefficients for CaF_2, KCl, and ZnSe laser windows. The coefficients χ_+ and χ_- refer to polarization-independent and polarization-dependent contributions, respectively. These calculations are based on property data listed in tables 1, 2, and 3.

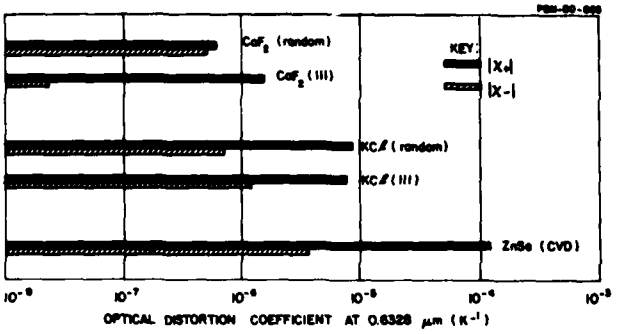

Figure 2. A comparison of optical distortion coefficients for CaF_2, KCl, and ZnSe, at the He-Ne laser wavelength. These are magnitudes plotted on a log scale. Note that, in randomly oriented polycrystalline CaF_2, the stress-birefringence contribution (X_-) matches that of all other sources of distortion combined.

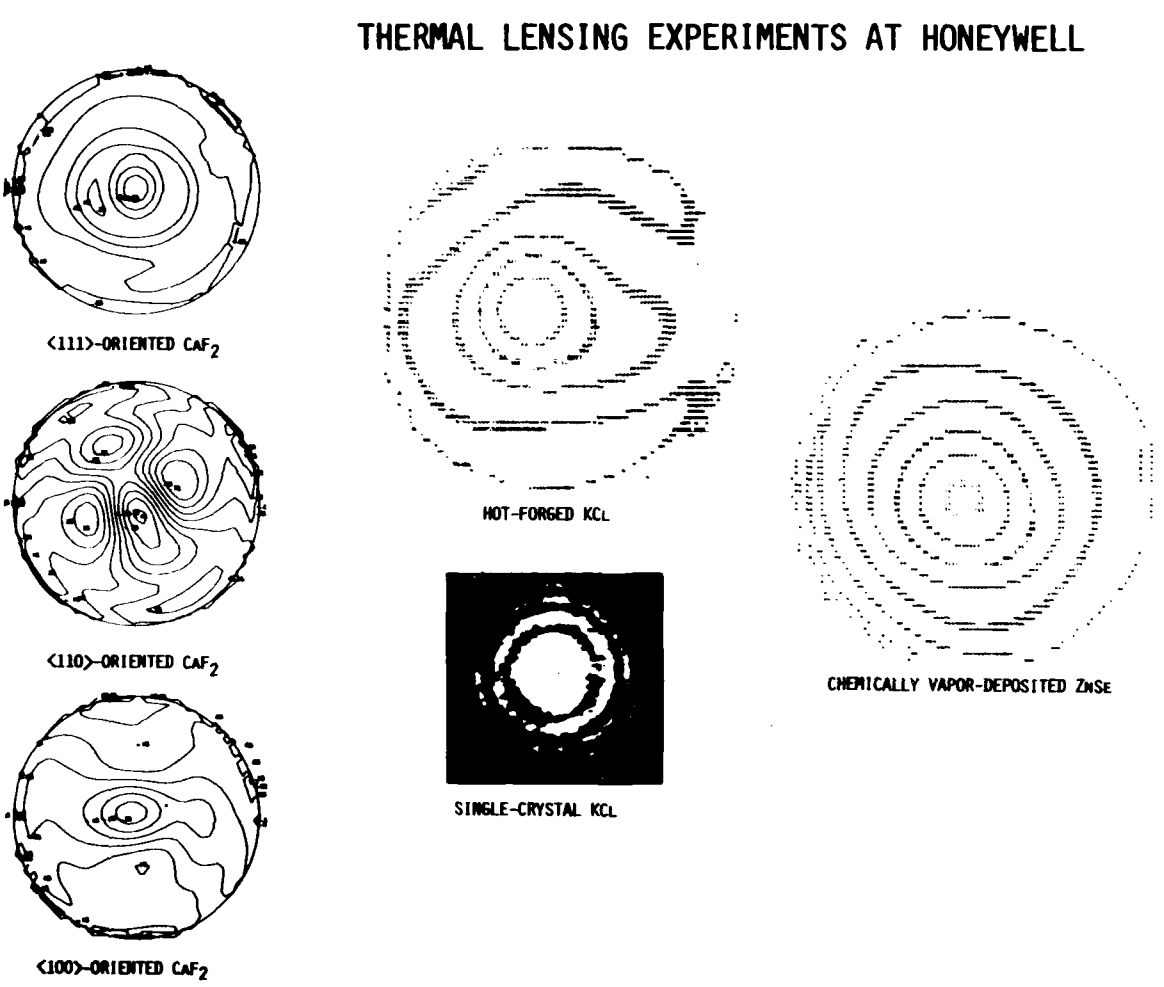

Figure 3. Equal optical-path-difference contours derived from interferometric measurements on CO_2-laser heated window materials. Data taken from reference 8 (CaF_2) and reference 9 (KCl and ZnSe). The single-crystal KCl interferogram (ref. 7) shows that circular bias fringes retain their symmetry during irradiation.

SURVEY OF 1.3 μm WINDOW MATERIALS

Nils C. Fernelius, David V. Dempsey, David A. Walsh and
David B. O'Quinn
University of Dayton Research Institute
Dayton, Ohio 45469

and

Walter L. Knecht
Air Force Wright-Aeronautical Laboratories, Materials Laboratory
Wright-Patterson Air Force Base, Ohio 45433

The purpose of this work is to screen candidate materials for use in the iodine laser which operates at 1.315 μm. Most of the results presented here are the effective optical absorption, β_{eff}, measured by laser rate calorimetry using a Quantronix Nd:YAG laser modified to operate at 1.319 μm. Spectral transmission scans using the Beckman UV 5270 and Perkin-Elmer 180 spectrophotometers are presented on the less common materials. In the beginning we measured β on materials obtained for CO_2, CO and HF-DF laser studies. These included NaCl, KCl, LiF, CaF_2, SrF_2, Al_2O_3 (sapphire), ZnSe, Si and GGG ($Gd_3Ga_5O_{12}$). At 1.3 μm a number of oxides which were too absorbing to use at the longer wavelengths can be considered. We present results on a variety of commercially available fused silicas, SiO_2. Additional results on BaF_2, Raytran ZnS, spinels ($xMgO{\cdot}Al_2O_3$), MgO, Barr and Stroud BS37A and BS39B calcium aluminate glasses, CORTRAN 9753 and 9754 glasses, ZBT glass, undoped YLF ($LiYF_4$) and As_2S_3 will be presented.

Key words: Infrared materials; iodine laser; laser calorimetry; optical absorption coefficients.

1. Introduction

The purpose of this work is to screen candidate materials for use in the development of the iodine (I_2) laser which operates at 1.315 μm. This wavelength is short enough so that a number of materials which were not usable in the HF-DF, CO and CO_2 lasers can now be considered. Many of these new materials are oxides. For a start we measured samples which were on hand and had been used in studies for the other previously mentioned lasers [1].[1] In addition samples which were purchased for this work were measured.

The results reported here were obtained using laser rate calorimetry [2,3]. The light source was a Quantronix 114 Nd:YAG laser fitted with special mirrors to operate at 1.319 μm. The data reported are effective optical absorption coefficients, β_{eff}, obtained from the equation

$$\beta_{eff} = \frac{(1-R_b)}{(1+R_b)} \frac{P_A}{P_T} = \frac{2n}{1+n^2} \frac{mC_p}{\ell} \frac{1}{P_T} \frac{\Delta T}{\Delta t} \qquad (1)$$

where P_A is the power absorbed in the sample, P_T is the power transmitted, R_b is the reflection coefficient at the exit face, n is the index of refraction, m is the mass of the sample, C_p is the heat capacity, ℓ is the sample thickness and $(\Delta T)/(\Delta t)$ is the sum of the magnitudes of the heat rise and cooling slopes. In reality

$$\beta_{eff} \equiv \beta_B + (1+x)\beta_s/\ell \qquad (2)$$

where β_B is the bulk optical absorption coefficient and β_s is the surface absorption. Depending upon various theoretical assumptions x lies between 1 and n. This is discussed in Case 8 of Fernelius and Johnston [4]. So far the only surface-to-bulk absorption study at 1.3 μm has been on single crystal CaF_2 [5].

[1] Figures in brackets indicate the literature references at the end of this paper.

2. Experimental Results

The NaCl samples studied were grown by Harshaw Chemical. They were all single crystal samples. All reported values were taken after etching the samples. Three samples were from the cone end of a boule grown by the Stockbarger technique and had an average $\beta_{eff} = 0.328 \times 10^{-3} cm^{-1}$. The other samples were from a Kyropoulous grown boule. The sample from the seed end had a $\beta_{eff} = 0.353 \times 10^{-3} cm^{-1}$; from the cone end, $0.326 \times 10^{-3} cm^{-1}$.

YLF ($LiYF_4$) is a material developed by Sanders Associates, Inc., Nashua, NH as a laser host material for various rare earth dopants. We obtained an undoped sample 32 mm thick. The sample was rotated 90° between measurements and the initial orientation repeated. Since we did not know the orientation of the sample, the reflection correction was made using n_e and n_o. Less than 0.1% difference in the resulting β_{eff} was obtained between the two values. A transmittance versus wavelength trace taken on the Perkin-Elmer 180 is shown in figure 1.

Raytheon fabricated ingot CF 3-9 from remelted CaF_2 castings into a six-inch ingot in a large furnace. The four samples taken from this ingot formed a homogeneity study of optical test samples. A related study was done on single crystal CaF_2 samples of varying thickness obtained from Harshaw to determine the surface-to-bulk optical absorption coefficient [5]. The average of ten runs with the thermocouples located at the midpoint of thickness of several samples was 0.711±0.071. Multithickness laser rate calorimetry gave a surface-to-bulk optical absorption coefficient ratio, $r \equiv \beta_s/\beta_B =$ 0.136 cm. Photoacoustic chopping frequency studies interpreted using the Bennett-Forman theory [6] gave r = 0.07 cm.

Two KCl samples were obtained from the University of Utah. They were reported to be ultrapure. Both samples were irregular in shape with fairly rough surfaces. These samples gave very low β_{eff} values at 2.7 μm indicating that they were relatively free of the OH^- radical which is prevalent in most KCl samples. All samples were etched before taking measurements. One sample was obtained from Harshaw. Two RAP-grown (Reactive Atmospheric Processed) Rb-doped KCl samples prepared by Hughes were obtained from the Naval Weapons Center at China Lake, California. The temperature versus time traces showed considerable scattering effects. These samples had been etched at least six times in measurements made at other wavelengths. Since etching tends to pit the surface, this could enhance scattering which due to the $1/\lambda^4$ dependence for Rayleigh scattering is particularly prominent at 1.3 μm. In addition the Rb dopants provide additional scattering centers.

Harshaw prepared some LiF crystals to be forged in the DOE-Lawrence Livermore Laboratory Laser Fusion Program. One sample was a single crystal and the other a forged sample. Surprisingly the forged sample was some 20% lower in value than the single crystal.

Sapphire (Al_2O_3) appears to be an excellent candidate for practical laser components at 1.3 μm. Its strength and environmental resistance are favorable factors. One drawback in certain applications is that it is birefringent with the index of the extraordinary ray approximately 0.008 less than that for the ordinary ray. We have measured a number of samples from Crystal Systems, Inc., Salem, MA. Most, if not all, of these samples have 0° orientation, i.e. the c axis is perpendicular to the plane of the window.

Another promising good window candidate is fused silica, SiO_2. We studied samples obtained from a variety of sources. In the initial part of the study we evaluated General Electric 125 and Heraus-Amersil Suprasil II fused silica plus Schott BK-7 glass. Spectral traces taken on a Beckman 5270 Spectrophotometer are shown in figure 2; on a Perkin-Elmer 180 in figure 3. Note that the Suprasil II and BK-7 exhibit strong water absorption bands at 1.38 μm while GE 125 shows none. A similar situation occurs around 2.2 μm. The BK-7 sample cuts off at 2.7 μm and Suprasil II has an exceedingly strong absorption band at 2.7 μm. The GE 125 does show a weak absorption dip at 2.7 μm. Laser calorimetry on these samples showed that the GE 125 was the least absorbing while BK-7 was the highest. Homogeneity of these samples was checked by Schlieren and Zygo evaluation. The BK-7 sample showed the best homogeneity while the GE 125 was the worst.

From conversations with manufacturers some information was gathered on the processes used to make the fused silica melts. Heraus-Amersil in Germany produces Suprasil II by melting in a natural gas flame which introduces water into the material. This type of silica is usually used in the vacuum uv. Suprasil W or Infrasil 1 is fused in a moisture free plasma arc and used in the infrared. GE 125 was formerly made by General Electric in Cleveland but production was discontinued in 1975. This material, which exhibits no water band at 1.385 μm, was fused in an electric-arc furnace, a process which was hard to control and thus resulted in a nonhomogeneous structure.

Heraus-Amersil Suprasil W-1 and Corning Grade 7940 were some samples obtained later which were free of the 1.385 μm absorption band (see fig. 4). Later a variety of fused silicas were obtained from Heraus-Amersil. T-08 Commercial, T-12 Optosil, T-15 Homosil and T-16 Ultrasil all exhibited a weak absorption band at 1.385 μm. Only T-17 Infrasil showed no dip. Laser rate calorimetry was performed on all samples. In general these samples with no dip at 1.385 μm had lower optical absorption values at 1.3 μm.

Barium fluoride, BaF_2, is one of the few candidate windows at 1.3 μm which also has 8-12 μm multispectral capability. Nine samples from Optovac, Inc., North Brookfield, MA were measured. Between measurements the sample was rotated about 90°. Thus thermocouple contact variations were averaged out. An IR spectral trace is shown in figure 5.

Two Optovac SrF_2 samples were used in an interlaboratory comparison with the University of Alabama-Huntsville at other wavelengths. These were measured at 1.3 μm also.

A French subsidiary of Corning Glass Works makes two infrared glasses. One of them is CORTRAN® Code 9753, calcium alumina silicate, $CaO{\cdot}Al_2O_3{\cdot}SiO_2$. We had the blanks polished by John Unertle Optical Company, Pittsburgh, PA. Results on three of our ten samples are presented. The samples were rotated 90° between measurements for a total of five runs on each.

A ZBT sample was obtained from Hughes Research Laboratory, Malibu, CA. It is presumably a $0.60ZrF_4{:}0.07ThF_4{:}0.33BaF_2$ glass prepared by the RAP process using a CCl_4 atmosphere [7]. Spectral scans show the glass to be highly transparent from 0.3 to 5.5 μm. The sample studied was a parallelepiped 32.2 mm x 10.65mmx6.85mm. Two measurements each were made passing the laser beam through the two smaller dimensions.

Gadolinium gallium garnet (GGG), $Gd_3Ga_5O_{12}$, is a material which was developed as a substrate for magnetic bubble devices. Thus the vendors were not accustomed to giving the surfaces an optical finish. The Allied Chemical samples had a particularly poor finish and the temperature traces exhibited scattering effects. The samples were run as-is. Thus the values presented here should be considered as an upper bracket on this material. Spectral traces on an Allied Chemical Company sample are shown in figures 6 and 7.

Two spinel, $xMgO{\cdot}Al_2O_3$, were obtained. The Coors sample was hot pressed and the Raytheon was fusion cast. Transmittance curves of them are shown in figure 8. There is considerable opportunity for improvement in these materials by varying the composition and preparation procedures.

We had five CVD ZnSe samples prepared by Raytheon which we had measured at other laser wavelengths, thus they were used in this study. These samples were part of the MT-11 project. The samples were run as-received at 1.3 μm. Later a few samples were cleaned by wiping the sample with a Liquinox® soaked Q-tip, followed by an ethanol rinse, then an acetone rinse. Since the cleaning procedure did not significantly reduce the β value and in a few cases increased it, we quote only the initial values on all samples.

We had difficulty in obtaining magnesium oxide samples. Eastman Kodak has discontinued manufacturing IRTRAN 5. Semi-Elements has gone out of business. We obtained two disc samples from Adolph Meller Company, Providence, RI who bought blanks at two different times from Norton Research Corporation then polished them. One window was colorless while the other had a slight yellow-greenish tinge. The samples were rotated 90° between measurements. The clear sample had a $\beta = 9.33{\pm}0.10x10^{-3}cm^{-1}$; while the greenish sample had $\beta = 6.79{\pm}0.16x10^{-3}cm^{-1}$. Norton Research Corporation, Niagara Falls, Canada was able to supply square single crystal samples. The faces are as-cleaved. They contain small scratches and imperfections. After our initial measurements we plan to have them polished and we shall remeasure them.

An ultrahigh-purity state-of-the-art silicon sample was obtained from a boule grown by Texas Instruments. Here we present the results of two measurements run at different power levels.

Unique Optical Company, Farmingdale, NY lists As_2S_3 windows, 38.1 mm diameter x 12.5 mm thick, in its catalog. Here we present results on three of its windows.

The second Corning infrared glass is CORTRAN® 9754 a germinate glass whose composition may be $CaO{\cdot}Al_2O_3{\cdot}GeO_2$. Here we present results on three of our ten samples.

We obtained six standard RAYTRAN® ZnS 1.5 inch squares x 0.5 thick from Raytheon. The material has a dark orange-yellow milky appearance. The surface had some scratches. We present the results on one sample here. A spectral trace is shown in figure 9. Raytheon is currently developing a water clear ZnS material which is colorless and should be a much improved material.

Barr & Stroud Ltd., Glasgow, Scotland makes two types of calcium aluminate glasses - BS37A and BS39B. We obtained five disc samples of each type. The surface had a nice polish. The material had a light blue tinge with no bubbles or veils. These materials have a very low thermal diffusivity which causes a long delay time between the time the laser is turned on and a temperature rise is observed. Thus the results might be off by a factor of two. Spectral traces in the visible and infrared of both types of material are shown in figures 10-13.

3. Conclusions

The effective optical absorption coefficient of a number of materials has been measured at 1.3 μm. Some of the results presented are preliminary values. So far surface-to-bulk absorption studies at this wavelength have only been done at 1.3 μm on CaF_2.

4. Acknowledgments

This work was supported by the AFWAL Materials Laboratory, Wright-Patterson Air Force Base, Ohio 45433.

References

[1] Coble, G.S., Dempsey, D.V., Detrio, J.A., Fernelius, N.C., Fox, J.A., Greason, P.R., Johnston, G.T., and O'Quinn, D.B., in NBS Special Publication 574: *Basic Optical Properties of Materials - Summaries of Papers*, edited by Albert Feldman, pp. 122-125.

[2] Pinnow, D.A. and Rich, T.C., Appl. Opt. *12*, 984 (1973).

[3] Hass, M.,Davisson, J.W., Klein, P.H. and Boyer, L.L., J. Appl. Phys. *45*, 3959 (1974).

[4] Fernelius, N.C. and Johnston, G.T., in NBS Special Publication 541: *Laser Induced Damage in Optical Materials: 1978* edited by A.J. Glass and A.H. Guenther, pp. 7-12.

[5] Fernelius, N.C., Dempsey, D.V. and O'Quinn, D.B., this volume.

[6] Bennett, H.S. and Forman, R.A., J. Appl. Phys. *48*, 1432 (1977).

[7] Robinson, M., Pastor, R.C., Turk, R.R., Devor, D.P., Braunstein, M. and Braunstein, R., Mat. Res. Bull. *15*, 735 (1980).

Table 1. List of 1.3 μm Materials by Increasing Optical Absorption

Material	$\beta_{slope} : 10^{-3}cm^{-1}$ @1.3 μm	n @ 1.3 μm	High Transmission Range in μm
NaCl Harshaw single xtal	0.333±0.016	1.53	0.4-13
YLF ($LiYF_4$) Sanders Assoc.	0.343±0.009 0.345±0.009	n_e=1.47 n_o=1.45	0.22-5
CaF_2 Raytheon	0.393±0.049	1.427	0.25-7
CaF_2 Harshaw single xtal	0.711±0.071		
KCl Univ. of Utah	0.351	1.48	0.4-15
KCl Harshaw	0.471±0.023		
RAP Rb:KCl Hughes	0.527		
LiF Harshaw	0.520±0.061	1.385	0.18?-4.5
Al_2O_3, Sapphire Crystal Systems	0.818±0.156	n_o=1.7505	0.24-4
SiO_2, Fused Silica		1.447	0.2-2.5
Suprasil W-1	0.83		
GE 124 (125?)	1.08		
Heraus-Amersil, T-16 Ultrasil	1.12		
H-A,T-17 Infrasil	1.22		
H-A,T-12 Optosil	1.33		
H-A,T-15 Homosil	1.39		
H-A, T-08 Comm.	1.46		
Suprasil II	2.83		
Corning 7940	3.18		
BK-7	3.19		
BaF_2 Optovac	1.285±0.043	1.4670	0.22-9
SrF_2 Optovac	1.56	1.43	0.3-9
CORTRAN 9753 $CaO{\cdot}Al_2O_3{\cdot}SiO$ glass	2.369±0.064	1.588	0.6-3.8
ZBT glass Hughes	3.270±0.202	1.53	0.4-5.5
GGG, $Gd_3Ga_5O_{12}$ Lambda/Airtron Allied Chem.	5.26 11.6±2.7	1.944	0.42-4.8
Spinel $MgO{\cdot}Al_2O_3$ Raytheon Coors	6.55 18.63	1.703	0.5-5

Table 1. List of 1.3 μm Materials by Increasing Optical Absorption (Cont'd.)

Material	$\beta_{slope} \div 10^{-3}cm^{-1}$ @ 1.3 μm	n @ 1.3 μm	High Transmission Range in μm
CVD ZnSe Raytheon	7.38±0.96	2.44	0.65-18
MgO Adolph Meller Norton Res. Corp	8.06±1.35 10.02±0.87	1.662 (1.719?)	0.4-6
Silicon Texas Inst.	11.1	3.505	1.1-8
As_2S_3 glass Unique Optical Co.	17.88±1.57	2.449	1-8
CORTRAN 9754 Germinate glass	19.19±1.79	1.644	0.4-4.2
Raytran® ZnS Raytheon	19.9	2.289	0.9-13
Calcium aluminate glasses Barr & Stroud BS39B BS37A	 154.7±7.6 186.1±15.6	 1.658 1.649	 0.45-4 0.4-4

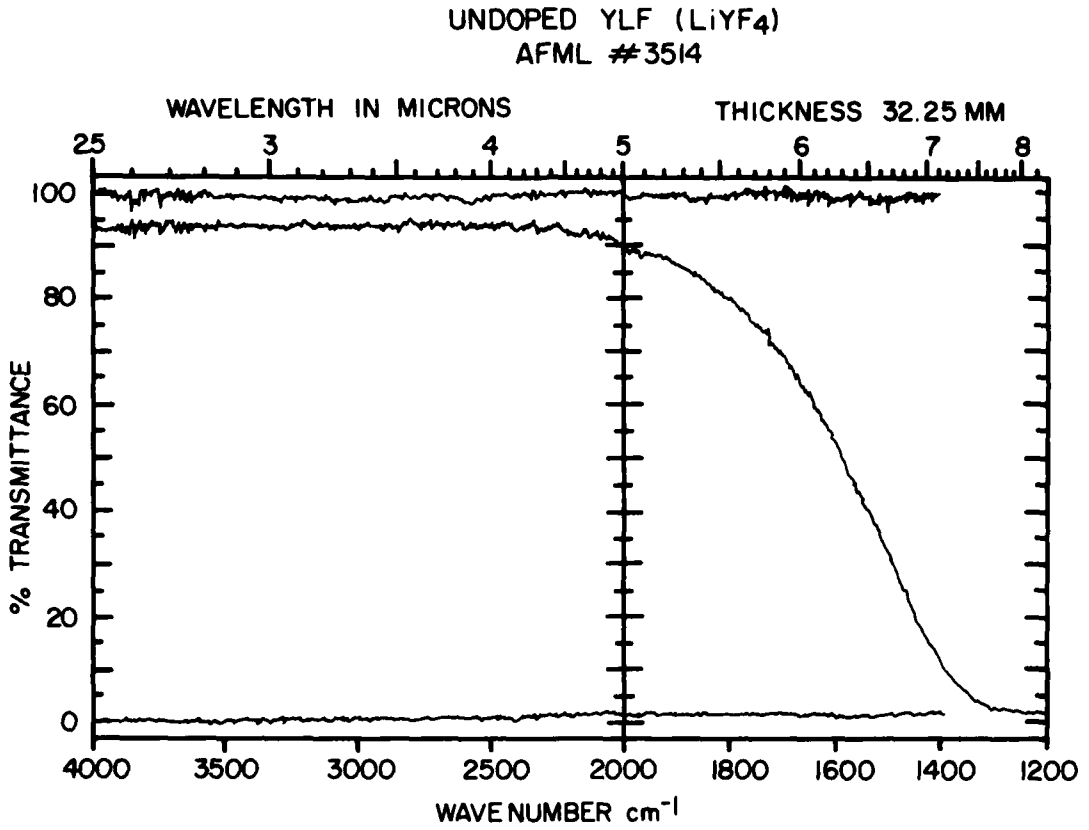

Figure 1. Transmittance of undoped YLF ($LiYF_4$) versus wavelength from 2.5 μm to 8.5 μm taken on a Perkin-Elmer 180 spectrophotometer.

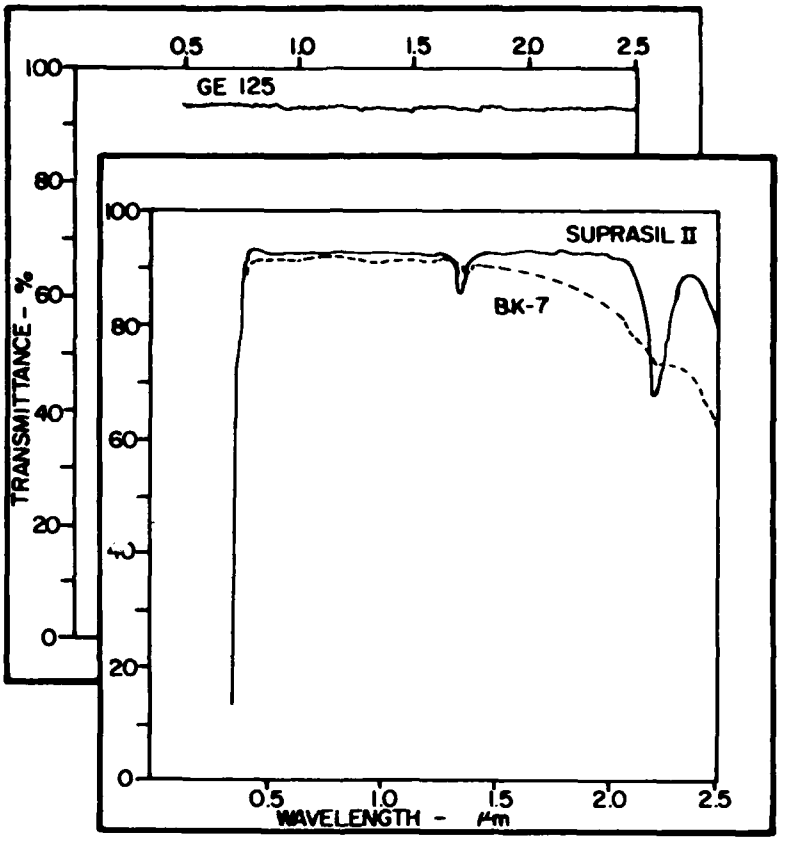

Figure 2. Visible and near infrared transmittance trace for Suprasil II and GE 125 fused silica and BK-7 glass samples.

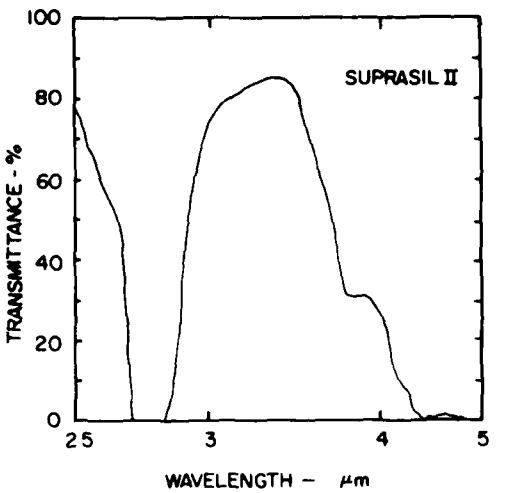

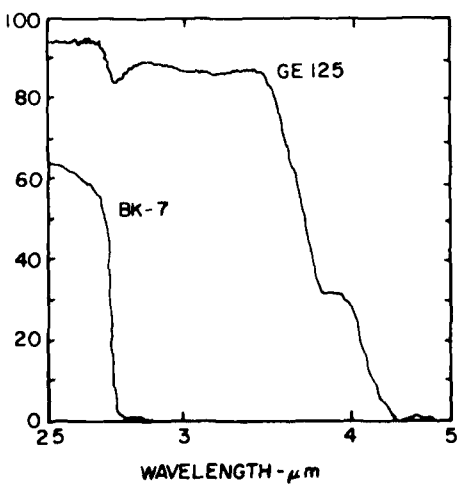

Figure 3. Infrared transmittance plot showing 2.7 μm water band and IR cut-off for (A) Suprasil II fused silica and (B) GE 125 fused silica and BK-7 glass samples.

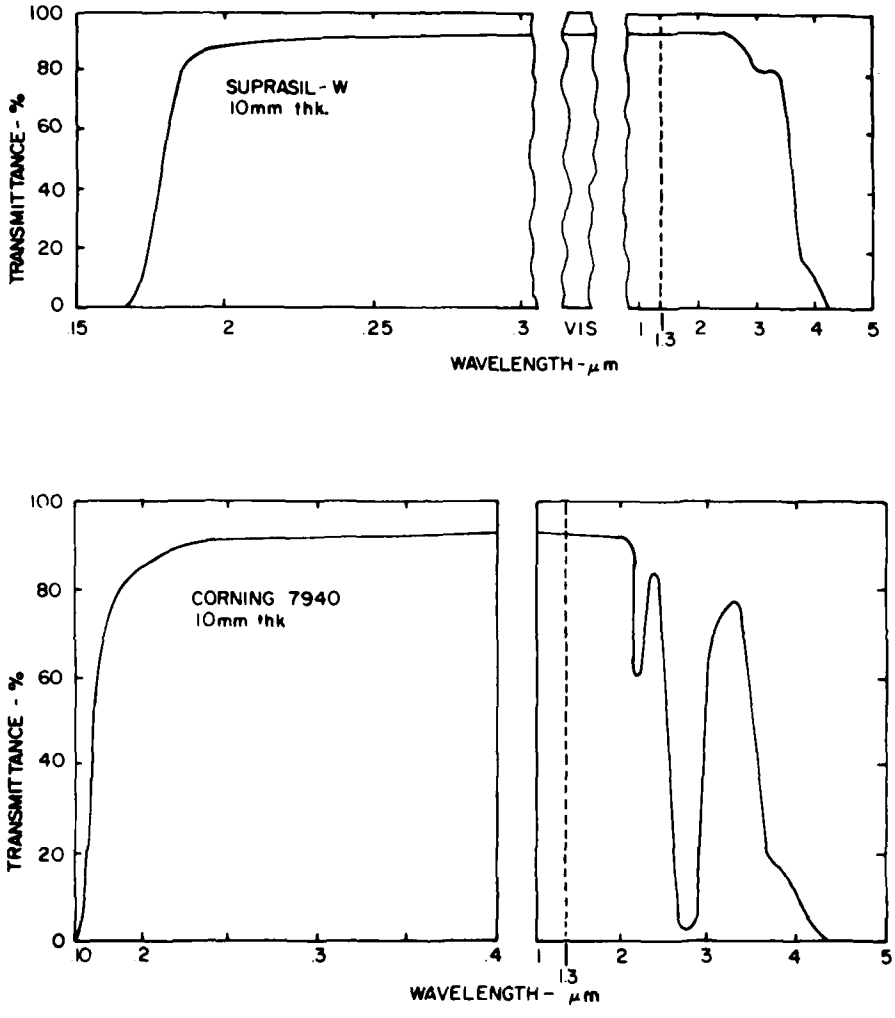

Figure 4. Transmittance traces of Suprasil-W and Corning 7940 fused silica materials showing absence of water band absorption in the 1.3 μm region.

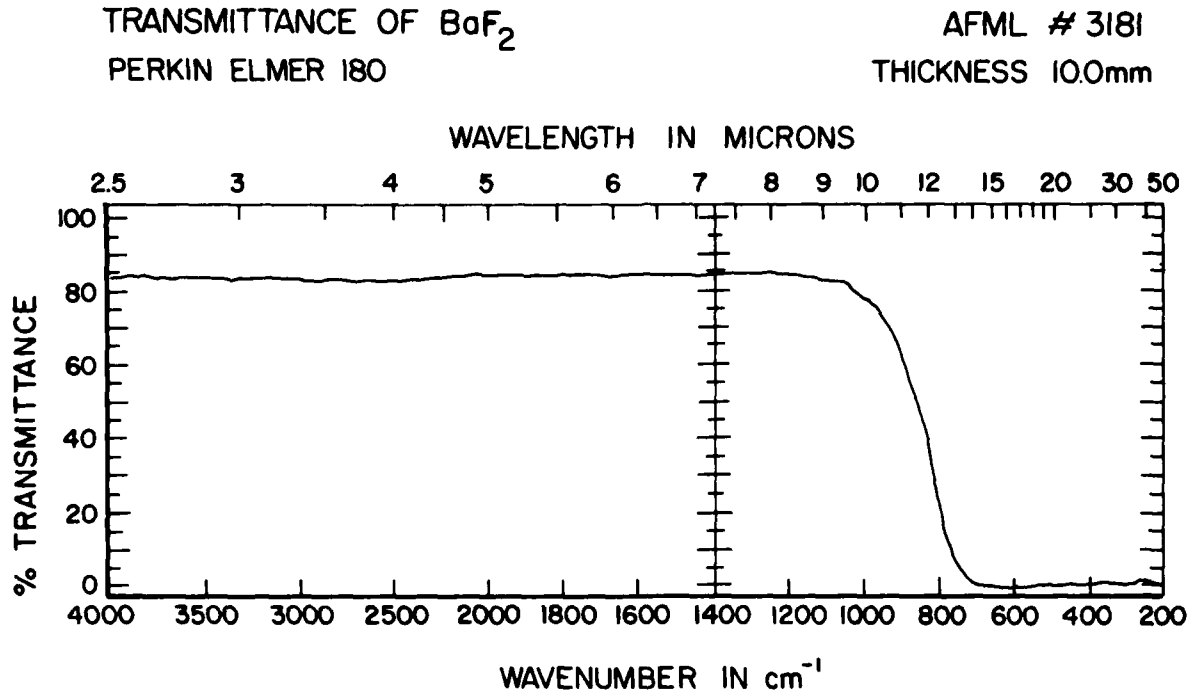

Figure 5. Transmittance of BaF_2 versus wavelength from 2.5 to 50 μm taken on a Perkin-Elmer 180.

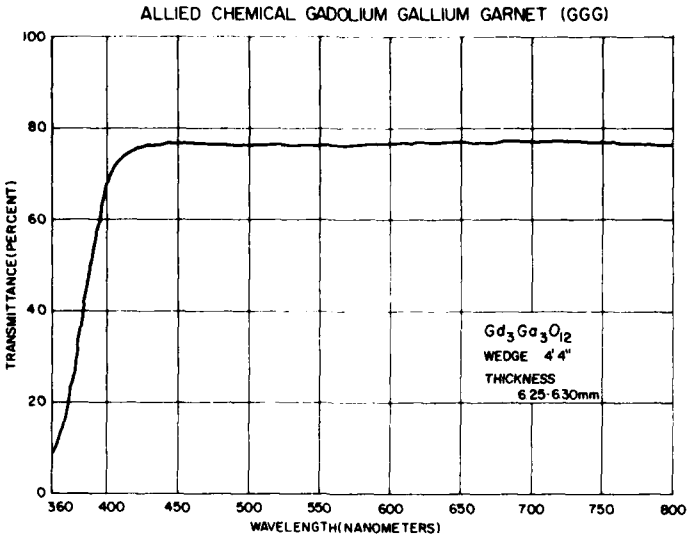

Figure 6. Transmittance of gadolinium gallium garnet (GGG) versus wavelength from 360 to 800 nm.

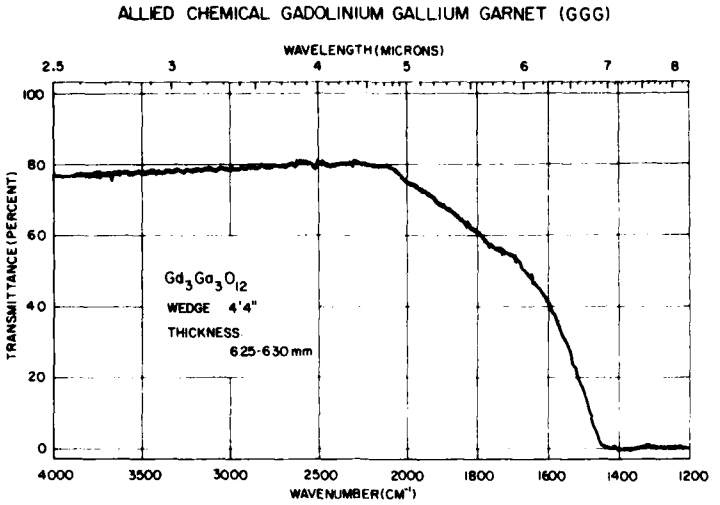

Figure 7. Transmittance of gadolinium gallium garnet (GGG) versus wavelength from 2.5 μm to 8.5 μm.

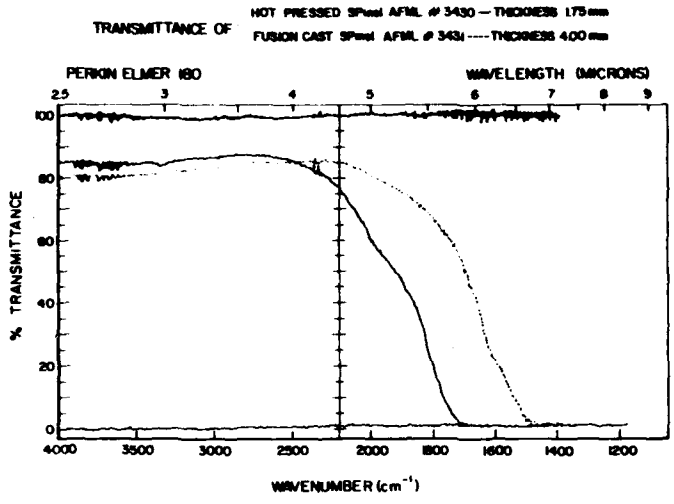

Figure 8. Transmittance of spinel samples versus wavelength from 2.5 μm to 9 μm.

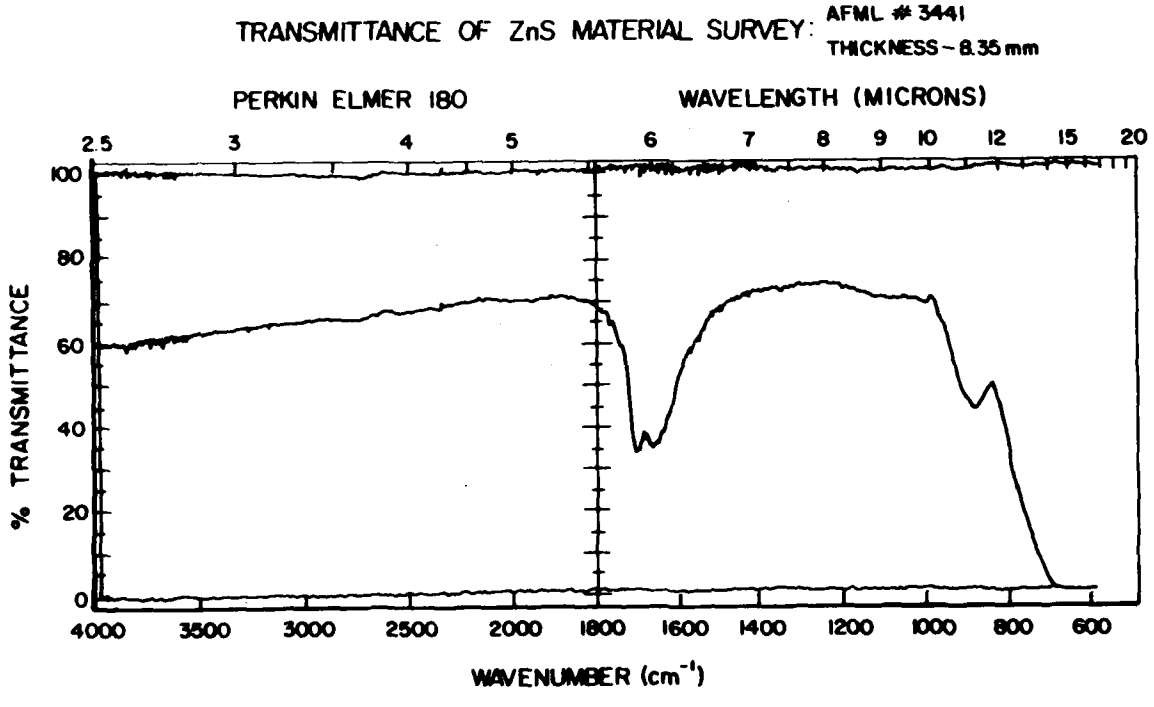

Figure 9. Transmittance of Raytran® ZnS versus wavelength from 2.5 to 20 μm.

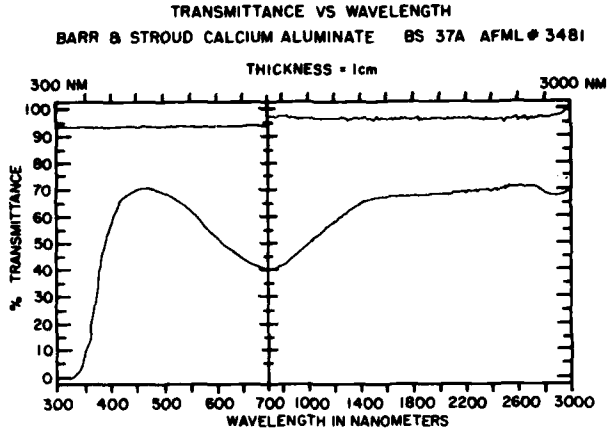

Figure 10. Transmittance of Barr & Stroud calcium aluminate glass BS37A versus wavelength from 0.3 μm to 3 μm.

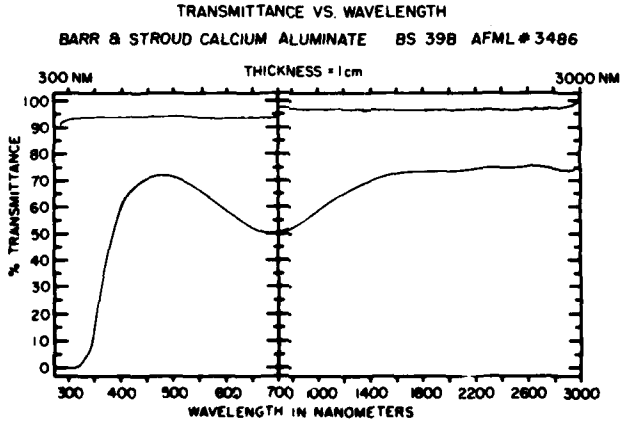

Figure 11. Transmittance of Barr & Stroud calcium aluminate glass BS39B versus wavelength from 0.3 μm to 3 μm.

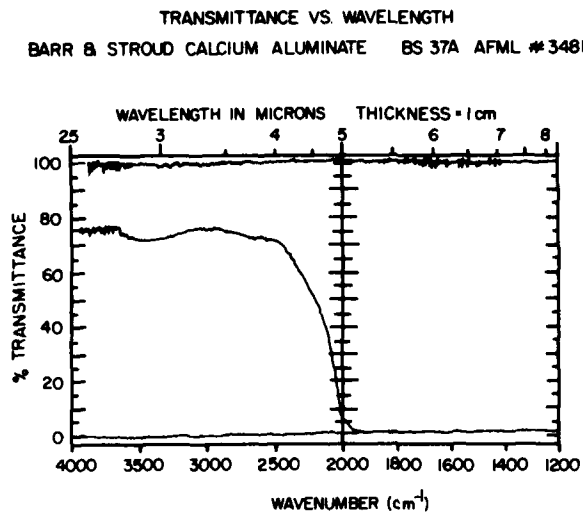

Figure 12. Transmittance of Barr & Stroud calcium aluminate glass BS37A versus wavelength from 2.5 μm to 8 μm.

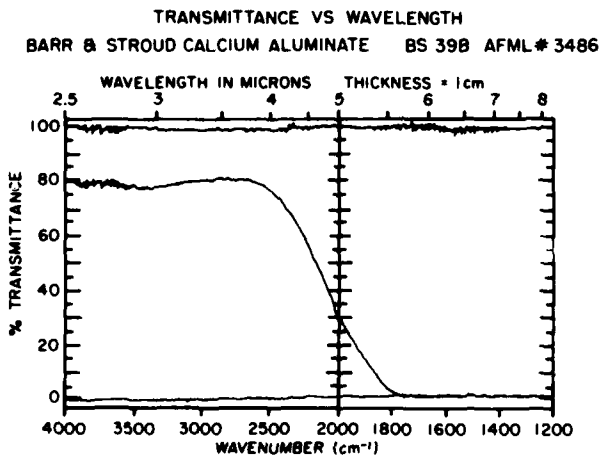

Figure 13. Transmittance of Barr & Stroud calcium aluminate glass BS39B versus wavelength from 2.5 μm to 8 μm.

MATERIAL PROPERTY REQUIREMENTS FOR LASER WINDOWS*+

ANN TOBY GLASSMAN
AVIONICS LABORATORY
WRIGHT-PATTERSON AIR FORCE BASE, OHIO 45433

Systems designers and theoreticians require reliable material properties--the designer to make informed selections of window materials, and the theoretician as input to his performance models and figure of merit calculations. The information is not always available, however, because (a) some measurements are difficult to make and exist for only a few selected materials; (b) stable lasers have not been readily available for use in making measurements, etc. at all wavelengths of interest. This paper indicates some gaps in material properties relevant to windows and gives directions for future experimental work, based on a literature search to compile data on candidate materials for infrared windows.

The types of gaps in material properties are illustrated by constructing a three-dimensional matrix of values, pointing out areas for future work. Data availability for many materials of interest is given.

Material properties for materials of interest are tabulated.

Key Words: Absorption; laser windows; transmission; material properties

1. Introduction

The Systems designers and the theoreticians require reliable material properties--the designer to make informed selections of window materials, and the theoretician as input to his performance models and figure-of-merit calculations. The information is not always available, however, because (a) some measurements are difficult to make and exist for only a few selected materials; (b) stable lasers have not been readily available for use in making measurements, etc., at all wavelengths of interest. This paper indicates some gaps in material properties relevant to windows and gives directions for figure experimental work, based on a literature search to compile data on candidate materials for infrared windows.

2. Uses of Material Data

For each laser system requiring a window, the designer chooses the best possible material, based on constraints of particular wavelength transmission, beam intensity, size, and harshness of environment. A wise choice requires up-to-date property information on available materials. Of special importance are transmission, absorption, and refractive index at the wavelengths of interest to judge the passive optical properties; piezo-optic coefficients and birefrigence to judge changes expected with irradiation; mechanical properties such as hardness, Young's modulus, thermal conductivity, yield strength, and mass density to gauge survivability

Another constraint is availability of blanks of sufficient sizes. In some cases, size requirements cannot immediately be met and the designer must select materials for the fabricators to scale up. Information is needed on fabrication properties such as susceptibility to thermal shock, phase transition temperatures, present production methods, melting point, and crystal structures.

Theoreticians develop models to predict the performance of windows in actual use, before they are made. Examples of needed data are thermal expansion coefficient; absorption, bulk and surface; and heat capacity.

3. Literature Search

The author conducted a literature search to determine optical and mechanical properties of materials for infrared laser windows. These materials included: $AgCl_2$, Al_2O_3, As_2S_3, BeO, CaF_2, CdTe, GaAs, GGG, Ge, KBr, BaF_2, KCl, LiF, MgF_2, NaCl, NaF, Si, SrF_2, ThF_4, ZnS and ZnSe. References consulted can be classified as manufacturer's literature; technical reports by government contractors dealing with materials research, damage testing, and components fabrication; proceedings of Damage Symposia and Window Symposia; earlier compendia, and government laboratory reports including the useful Optical Materials Characterization, by Feldman, Horowitz, Waxler, and Dodge, National Bureau of Standards Technical Note 993, 1979. Texts on infrared materials were also consulted.

* The work was done while the author was with the University of Dayton Research Institute.

+ This work was supported by the Air Force Weapons Laboratory, Kirtland AFB, NM under Contract F29601-79-C-0027 and by the Air Force Materials Laboratory.

4. Data Availability

Based on the literature search, the author compiled a material handbook, and in so doing, found many gaps. The types of gaps and their relation to available data can be illustrated by constructing a three-dimensional matrix of values. See figure 1. On the x dimension, property names are listed. The y dimension is a scale of wavelength in microns, and each z represents a different material. Entries in the matrix, therefore, represent a value for a particular property, at a specific wavelength for one material. For example, if the bulk absorption of NaCl at 1.06um is known, but no information on bulk absorption is known at 3.39um there would be a number at x = bulk absorption, y = 1.06um but not at x = bulk absorption, y = 3.39um at the z level designated for NaCl. Laid out in this fashion, the gaps are revealed in rows, columns, or planes.

The most serious gaps are those of property, which lie in the y-z plane. These occur when no measurements exist for a particular property at any wavelength for any material, or, less severely, at only a few wavelengths or materials. See figure 2. Less severe in this hierarchy are gaps along a column, i.e., no information for a particular wavelength. Presumably, once a suitable light source and detector are available, the measurement could be made, as it has been at other wavelengths. See figure 3.

Least severe is the situation where a material level is blank or nearly blank; a measurement has not been made on a particular material because it is not available. See figure 4.

Properties not found include piezo-optic and stress-optic coefficients, shear modulus, Weibull parameters, and Poisson's ratio. The levels for several materials had few if any entries. These were CdF_2, SrO_2, ThF_4, and more exotic materials.

The data availability can be summarized by graphing the y-z plane, property versus material. Properties at several wavelengths have been added for completeness. See table 1.

Each measurement reported in the literature was made at a particular time, using a particular method on a specific sample or group of samples and, as such, must be scrutinized for interferences before being accepted as typical of a certain material and applicable to all samples of that material. Surface absorption is affected by sample preparation, history, coating, and aging, while bulk absorption is affected by purity and inclusions. Sample information is not always given with the measurements. Brittle materials are a special problem as it is not possible to characterize their strength with one number.

Statistical data based on measurements of multiple samples is more meaningful.

5. Data

The data were compiled on individual data sheets by material, an example is given as table 2. To facilitate comparisons, several summaries of data were made. Selected properties of engineering materials, those that are presently commercially available in reasonable sizes, are compiled in table 3. Absorption and transmission of the investigated materials are given in tables 4,5 grouped by chemical family.

The full compilation has not yet been published as a handbook.

6. Recommendation

In the future, requirements for material properties information will increase and extend to more materials. Work needs to be done to improve and standardize measurement techniques for absorption, scattering, piezo-optic and stress-optic coefficients and birefrigence of materials. Standardization of the more common tests by a working group of the American Society for Testing and Materials would simplify comparisons of data from different laboratories. The work being done by the National Bureau of Standards should be extended to wavelengths which are of interest for military and commercial systems, especially nonvisible wavelengths, such as those of chemical and iodine lasers. Materials, if transparent at these wavelengths, should be evaluated as windows, whether used for this purpose before or not.

Systematic studies should be undertaken to determine the effects of surface preparation, inclusion, and fabrication methods on individual material properties. This would be a long term effort, but a very useful one from the practical viewpoint of the system designer who must specify fabrication and finishing techniques for his chosen window material.

As more material properties are measured, the data should be published with full information as to sample preparation and history.

7. Acknowledgment

Dr Nils Fernelius of the University of Dayton Research Institute supplied some of the reference material for the more exotic materials. John Detrio also of the University of Dayton Research Institute supplied absorption measurements as they were taken in his laboratories at the Air Force Materials Laboratory.

References

[1] Feldman, A., Horowitz, D., Waxler, R.M., and Dodge, M.J., Optical Materials Characterization (Final Technical Report), NBS, February 1979, NBS Technical Note 993.

[2] Austerman, S., Thermal and Optical Properties of BeO, Compared to Other High Power Laser Mirror and Window Materials, Rockwell International.

[3] Gadolinium Gallium Garnet (GGG), Substrates for Bubble Domain Technology, Lambda/Airtron, 1973.

[4] Detrio, J., Window Materials Properties (CaF_2, SrF_2, KCl, NaCl, ZnSe), UDRI.

[5] Wolfe, W.L., Zissis, G.J., Eds., The Infrared Handbook, The Infrared Information and Analysis Center, 1978.

[6] Connolly, J., diBenedetto, B., Donadio, R., Specifications of Raytran Material, Raytheon Co., 181-24.

[7] Crystan Crystal Products, Crystan.

[8] Detrio, J.A., Iden, D.J., Space Chamber Window Feasibility Study, UDRI, 1 March 1978, UDR-TR-78-48.

[9] Proceedings of the High Power Laser Optical Components Meeting, NWC, 1978 Meeting.

[10] Detrio, J., Compendium of Laser Window Material Properties, UDRI.

[11] Detrio, J.A., Harris, R.J., Walsh, D.A., Fernelius, N.C., Optical Evaluation and Characterization of IR Transmitting and Laser Window Materials, UDRI, November 1978, AFML-TR-78-172.

[12] Smakula, A., Swinehart, C.F., Whitaker, G., O'Dell, E.W., Johnson, R.N., Harshaw Optical Crystals, Harshaw, 1967.

[13] High Power Laser Optics, Harshaw Chemical Co., TP0403772M.

[14] Benbow, Fundamental Optical Phenomena in Infrared Window Materials, 1977.

[15] Deutsch, Laser Window Materials - An Overview, Raytheon Co., Journal of Electronic Materials, 4, 4, 1975.

[16] Sapphire, Tyco Saphikon Division.

[17] Donald, I.W., McMillan, P.W., Review: Infrared Transmitting Materials, Part I Crystalline Materials, Journal Of Materials Science 13, 1151-1176, 1978.

[18] Fernelius, N.C., Optical Absorption at 1.3um Materials Survey Study, 1979.

[19] Johnston, G.T., Harris, R.J., Coble, G., Optical Properties of $Gd_3Ga_5O_{12}$, UDRI.

[20] Strecker, C., Andrews, R., Proceedings of the Fourth Annual Conference on Infrared Laser Window Materials, AFML, 1974.

[21] Leung, K.M., Ready, J.F., E. Bernal, G., Analysis of Interferometric Data Obtained from Low - Power Laser Tests of IR Window Materials at 10.6um, Honeywell Inc., 15 August 1978, HR-77-255:5-45.

[22] E. Bernal, G., Leung, K.M., Loomis, J.S., Interferometric Testing and Analysis of Windows Exposed to CO_2 Laser Irradiation, Honeywell Inc., 20 May 1977, HR-77-255:5-45.

[23] Willingham, C.B., Fusion Cast Calcium Fluoride and Strontium Fluoride Optical Blanks, Raytheon Co., 15 June 1978, Final Technical Report 7/76 to 1/78.

[24] Zar, J.L., Investigations into the Feasibility of High Power Laser Window Materials, Avco Everett Research Lab, 15 April 1975, AFCRL-TR-75-0264.

[25] Detrio, J.A., Optical Characterization of IR Transmitting and Laser Window Materials, UDRI, November 1979, #15 Monthly R&D Status Report.

[26] Raytran Infrared Materials, Raytheon Co.

[27] Unique Optical Co., Catalog #105, 1979.

[28] Coble, G.S., Dempsey, D.V., Detrio, J.A., Fernelius, N.C., Fox, J.A. Greason, P.R., Johnston, G.T., O'Quinn, D.B., Multiwavelength Laser Rate Calorimetry on Various Infrared Window Materials, UDRI.

[29] Wyckoff, R.W.G., Crystal Structures Interscience Publishers Inc., New York 1960.

[30] Harrington, J.A., New Materials for Chemical Laser Windows, Laser Induced Damage in Optical Materials: 1976 National Bureau of Standards, NBS special publication 462.

TABLE 1. DATA AVAILABILITY
(★ data found)

	AgCl	Al_2O_3	As_2S_3 glass	BaF_2	BeO	CaF_2	CdF_2	CdTe	GaAs	GGG	Ge	KBr	KCl	LiF	MgF_2	NaCl	NaF	Si	SrF_2	SrO_2	ThF_4	ZnS	ZnSe
REFRACTIVE INDEX (3.8μ)		★	★	★		★					★		★	★		★			★			★	★
REFRACTIVE INDEX (1.3μ)	★	★	★	★		★				★		★	★	★	★	★	★	★	★			★	★
TRANSMISSION 3-5μ	★	★	★	★	★	★			★		★	★	★	★	★	★	★	★	★			★	★
TRANSMISSION 8-12μ	★	★	★	★	★	★			★		★	★	★	★	★	★	★	★	★			★	★
ABSORPTION COEFF (3.8μ)		★		★		★				★	★	★	★	★	★	★	★	★	★			★	★
ABSORPTION COEFF (2.7μ)		★		·		★				★	★	★	★	★	★	★	★	★	★				★
ABSORPTION COEFF (1.3μ)		★				★				★	★		★	★		★		★	★				★
BIREFRINGENCE																							
REFLECTION COEFF																							
IMPACT ENERGY													★										★
HARDNESS	★	★	★	★		★		★	★	★	★	★	★	★	★	★	★	★	★			★	★
SHEAR MODULUS																							★
YOUNG'S MODULUS	★	★	★	★	★	★		★	★		★	★	★	★	★	★		★	★			★	★
YIELD STRENGTH				★		★						★	★	★		★			·				★
RUPTURE STRENGTH		★	★	★		★		★	★		★	★	★	★	★	★		★	·			★	★
ULTIMATE STRENGTH																							★
THERMAL EXPAN. COEFF.	★	★	★	★	★	★	★	★	★	★	★	★	★	★	★	★	★	★	★			★	★
CRYSTAL STRUCTURE	★			★		★				★		★	★	★	★	★	★	★	★				
THERMAL CONDUCTIVITY	★	★	★	★	★	★		★	★	★	★	★	★	★	★	★	★	★	★			★	★
SPECIFIC HEAT	★	★		★	★	★		★		★	★	★	★	★	★	★	★	★	★			★	★
MASS DENSITY	★	★		★	★	★				★		★	★	★	★	★	★	★	★			★	★
POISSON'S RATIO						★							★			★			★				★
BULK MODULUS	★	★				★					★	★	★	★		★		★					★
BRITTLE-DUCTILE TRANSITION TEMP.													★										★
dn/dt	★	★	★	★	★	★	★	★	★	★	★	★	★	★	★	★	★	★	★			★	★
PLEZO-OPTIC COEFF Q_{11}			★	★		★													★				
Q_{12}			★	★		★													★				
Q_{44}				★		★													★				
SOLUBILITY	★	★		★	★	★	★	★			★	★	★	★	★	★	★	★	★			★	
WEIBULL SHAPE FACTOR						★																	★
HEAT CAPACITY						★							★			★							★
ELASTO-OPTIC COEFF.																							★

TABLE 2 SAMPLE DATA SHEET CaF_2

PROPERTY	VALUE	PROPERTY	VALUE	PROPERTY	VALUE
REFRACTIVE INDEX 3.8μ	[5] 1.41119 (3.82μ)	HARDNESS	[4] 172 knoop	POISSON'S RATIO	[5] 0.28
REFRACTIVE INDEX 1.3μ	[5] 1.42689 (3.82μ)	SHEAR MODULUS		BULK MODULUS	[5] 12.00×10^6 psi
TRANSMISSION 3-5μ		YOUNG'S MODULUS	[4] 15.7×10^6 psi	BRITTLE-DUCTILE TRANSITION TEMP	
TRANSMISSION 8-12μ		YIELD STRENGTH	[13] 5,300 psi 8,000(polytran)	dn/dt	[1] $-1.12 \times 10^{-6} K^{-1}$ (3.39μ)
ABSORPTION COEFF 1.3μ	[25] 0.39×10^{-3}/cm	RUPTURE STRENGTH	[5] 5.3×10^3 psi	PIEZO-OPTIC COEFF.	
ABSORPTION COEFF 3.8μ	[11] $1.48^{-1} \times 10^{-4}$/cm	ULTIMATE STRENGTH		Q_{11}	[1] $-0.52 \pm 0.11 \times 10^{-12}$ Pa^{-1}
ABSORPTION COEFF 2.7μ	[11] $3.64 \times 10^{-4}/cm^{-1}$	THERMAL EXPAN. COEFF.	[1] 18.7×10^{-6}/K	Q_{12}	[1] $1.00 \pm 0.11 \times 10^{-12}$ Pa^{-1} (3.39μ)
ELASTO-OPTIC COEFF.		CRYSTAL STRUCTURE	[7] CUBIC ISOTROPIC	Q_{44}	[1] $0.87 \pm 0.06 \times 10^{-12}$ Pa^{-1} (3.39μ)
BIREFRINGENCE		THERMAL CONDUCTIVITY	[4] 0.080w/cm°K	ELASTO-OPTIC COEFF.	
REFLECTION COEFF.		SPECIFIC HEAT	[15] 0.20400 @ 273°K 0.21200 @ 373°K	HEAT CAPACITY	0.812
IMPACT ENERGY		MASS DENSITY	[4] 3.188/cc	SURFACE ABSORPTION	2×10^{-4}cm (3.8μ)
				[7] SOLUBILITY	1.7×10^{-6}g/g H_2O (26°C)
				[9] WEIBULL SHAPE FACTOR	2.97

TABLE 3 PROPERTIES OF ENGINEERING MATERIALS

PROPERTIES / MATERIAL	CaF_2	KCl	NaCl	ZnS	ZnSe
REFRACTIVE INDEX 3.8μ	[5] 1.41119 (3.8206μ)	[1] 1.47199 (4.00μ)	[4] 1.53	[1] 2.25178 (4.00μ)	[1] 2.43316 (4.00μ)
ABSORPTION 3.8μ	[4] 1.48×10^{-4}/cm	[13] 3.1×10^{-4}/cm	[25] 0.27×10^{-3}/cm	9×10^{-4}/cm	[4] 15.67×10^{-4}/cm (2.8μ)
ABSORPTION 2.7μ	[4] 3.65×10^{-4}/cm	[13] 1.2×10^{-4}/cm	[25] 0.80×10^{-3}/cm	[30] 0.024/cm	[4] 25.06×10^{-4}/cm
YIELD STRENGTH	[13] 5,300 psi 8,000 (polytran)	[10] 3,300 psi	[4] 4,000 psi 1400 psi (polytran)		7,500 psi
YOUNG'S MODULUS	[4] 15.7×10^{6} psi	[5] 4.30×10^{6} psi	[4] 5.80×10^{6} psi	[6] $10.8\times10^{-6}K^{-1}$	[4] 9.75×10^{6} psi
THERMAL EXPANSION COEFF.	[1] $18.7\times10^{-6}K^{-1}$	[1] $37.1\times10^{-6}K^{-1}$	[1] $39.6\times10^{-6}K^{-1}$	[1] $6.8\times10^{-6}K^{-1}$	[6] $7.57\times10^{-6}K^{-1}$
dn/dt	[1] $-1.12\times10^{-5}K^{-1}$ (3.39μ)	[1] $-3.62\times10^{-5}K^{-1}$ (3.39μ)	[1] $-3.63\times10^{-5}K^{-1}$ (3.39μ)	[1] $4.2\times10^{-5}K^{-1}$ (3.39μ)	[1] $6.2\times10^{-6}K^{-1}$ (3.39μ)
COMMENTS					

TABLE 4. BULK ABOSRPTION COEFFICIENTS

	1.3μ	2.7μ	3.8μ
BaF_2	–	[13] 1.8×10^{-3}/cm	[14] 2×10^{-4} /cm
CaF_2	[25] 0.39×10^{-3}/cm	[11] 3.64×10^{-4}/cm	[11] 1.48×10^{-4}/cm
CdF_2	–	–	–
LiF	[25] 0.53×10^{-3} /cm	[26] 1.10×10^{-3} /cm	[25] 1.96×10^{-3} /cm
MgF_2	–	[13] 8.6×10^{-4}/cm	[13] 4.7×10^{-4}/cm
NaF	–	[13] 8.2×10^{-4}/cm	[13] 7×10^{-4} /cm
SrF_2	[25] 1.56×10^{-3}/cm	[14] 5.77×10^{-4} /cm	[11] 1.42×10^{-4}/cm
ThF_4	–	–	–
AgCl	–	–	–
KCl	[25] 0.53×10^{-3} /cm	[13] 1.2×10^{-4} /cm	[13] 3.1×10^{-4} /cm
NaCl	[25] 0.33×10^{-3} /cm	[26] 0.80×10^{-3}/cm	[26] 0.27×10^{-3}/cm
KBr	–	[13] 1.4×10^{-4}/cm	[13] 2.4×10^{-4} /cm
Al_2O_3	[25] 0.75×10^{-3}/cm	[25] 0.75×10^{-3}/cm	[25] 20.2×10^{-3} /cm
BeO	–	–	–
SrO_2	–	–	–
ZnS	–	[30] 24.0×10^{-3} /cm	9×10^{-4}/cm
ZnSe	7.38×10^{-3}/cm	[4] 25.06×10^{-4}/cm	[4] 15.67×10^{-4}/cm
Ge	–	[13] 1.3×10^{-2}/cm	[13] 1.35×10^{-2}/cm
Si	[25] 11.1×10^{-3}/cm	[25] 5.5×10^{-3}/cm	[25] 7.85×10^{-4}/cm
CdTe	–	–	–
GaAs	–	–	–
As_2S_2	–	–	–
GGG	[25] 5.3×10^{-3}/cm	[10] 1.15×10^{-3}/cm	[10] 3.53×10^{-3}/cm

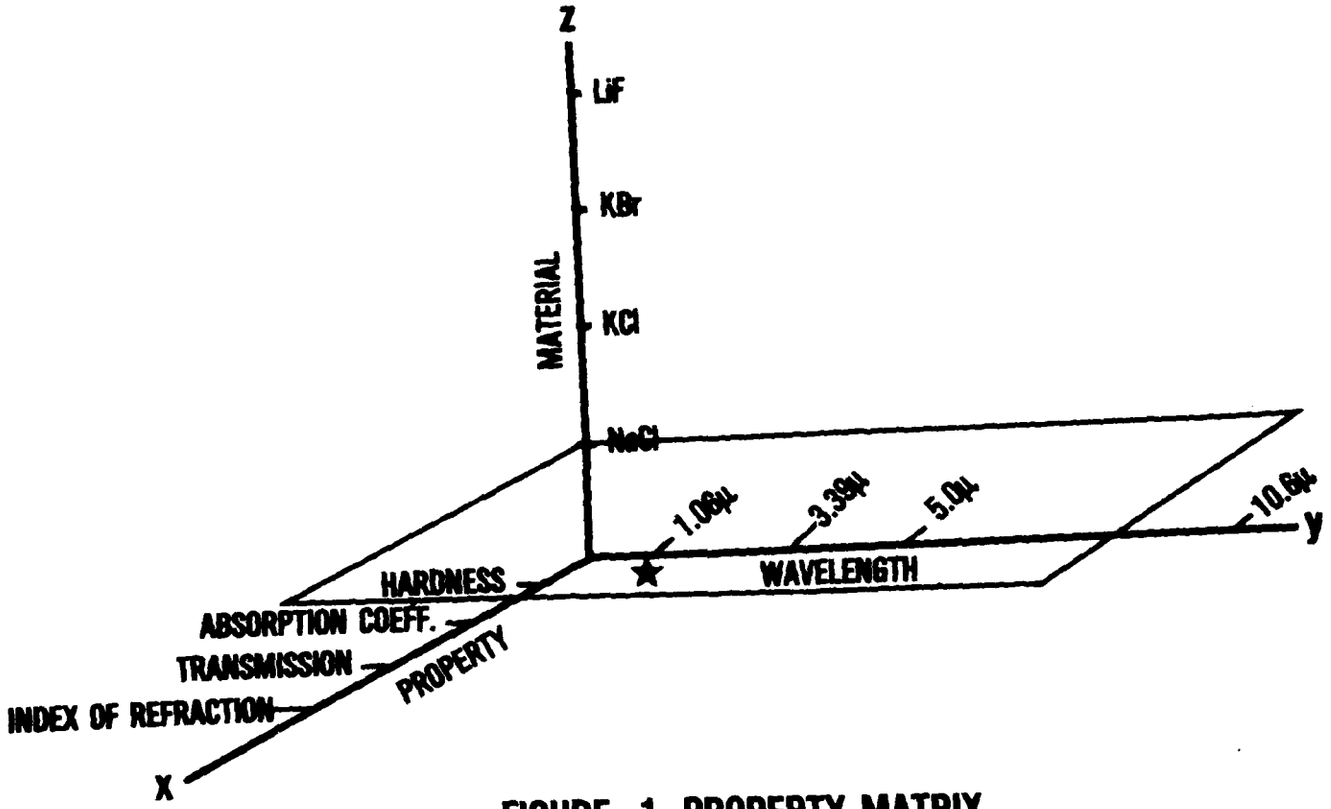

FIGURE 1. PROPERTY MATRIX

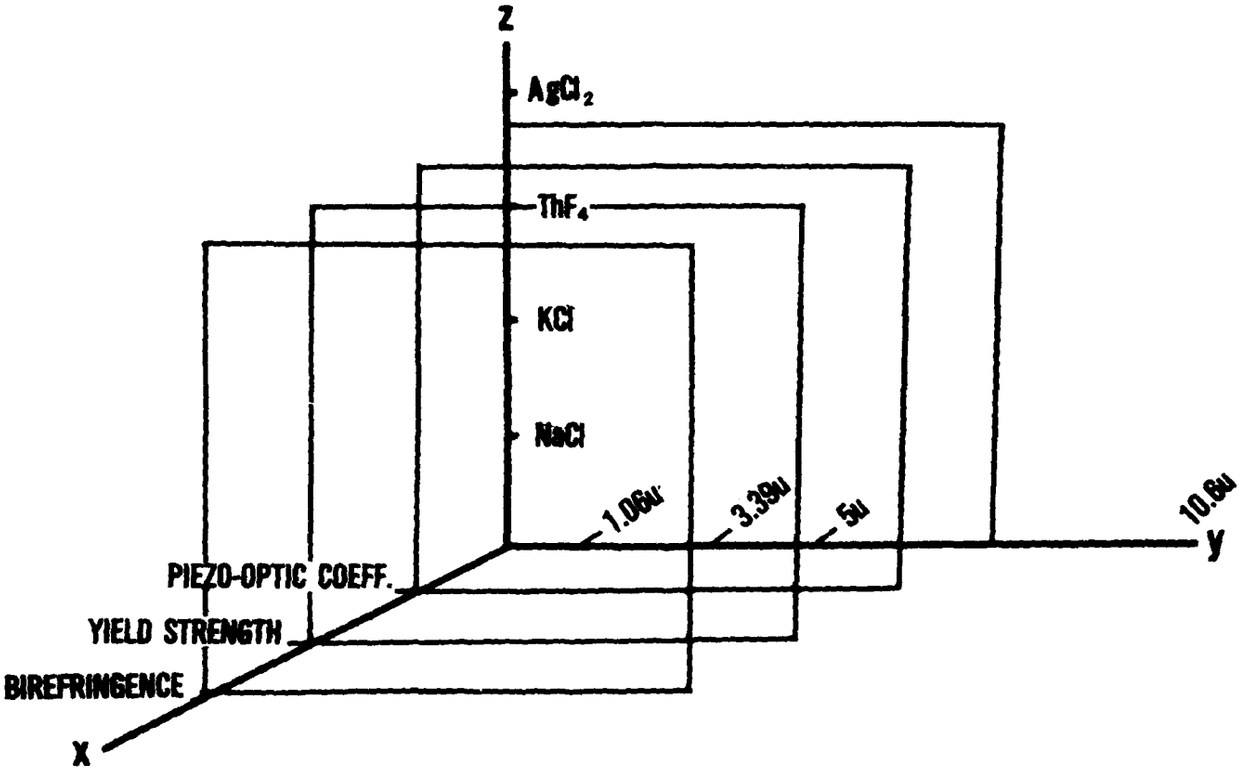

FIGURE 2. MISSING PROPERTIES

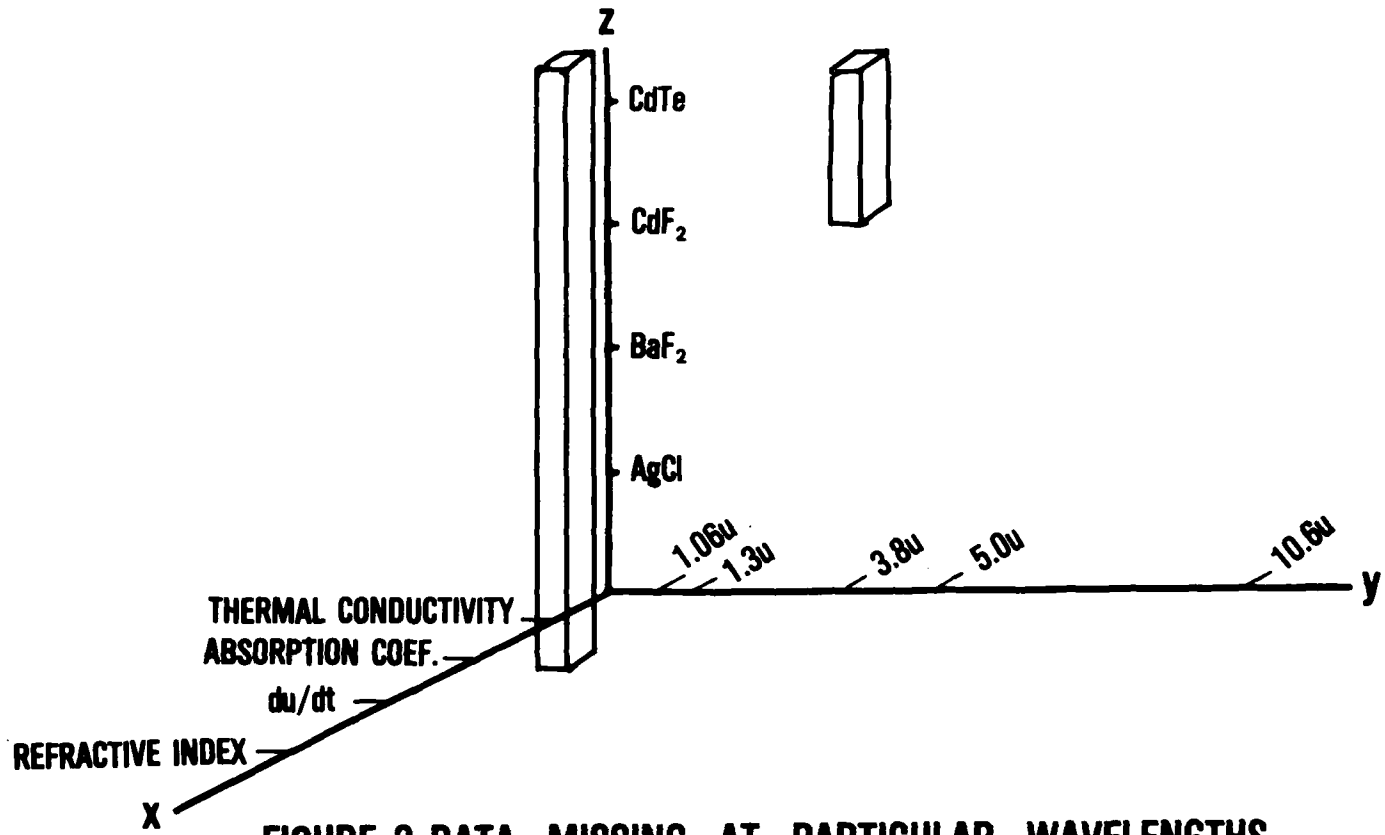

FIGURE 3 DATA MISSING AT PARTICULAR WAVELENGTHS

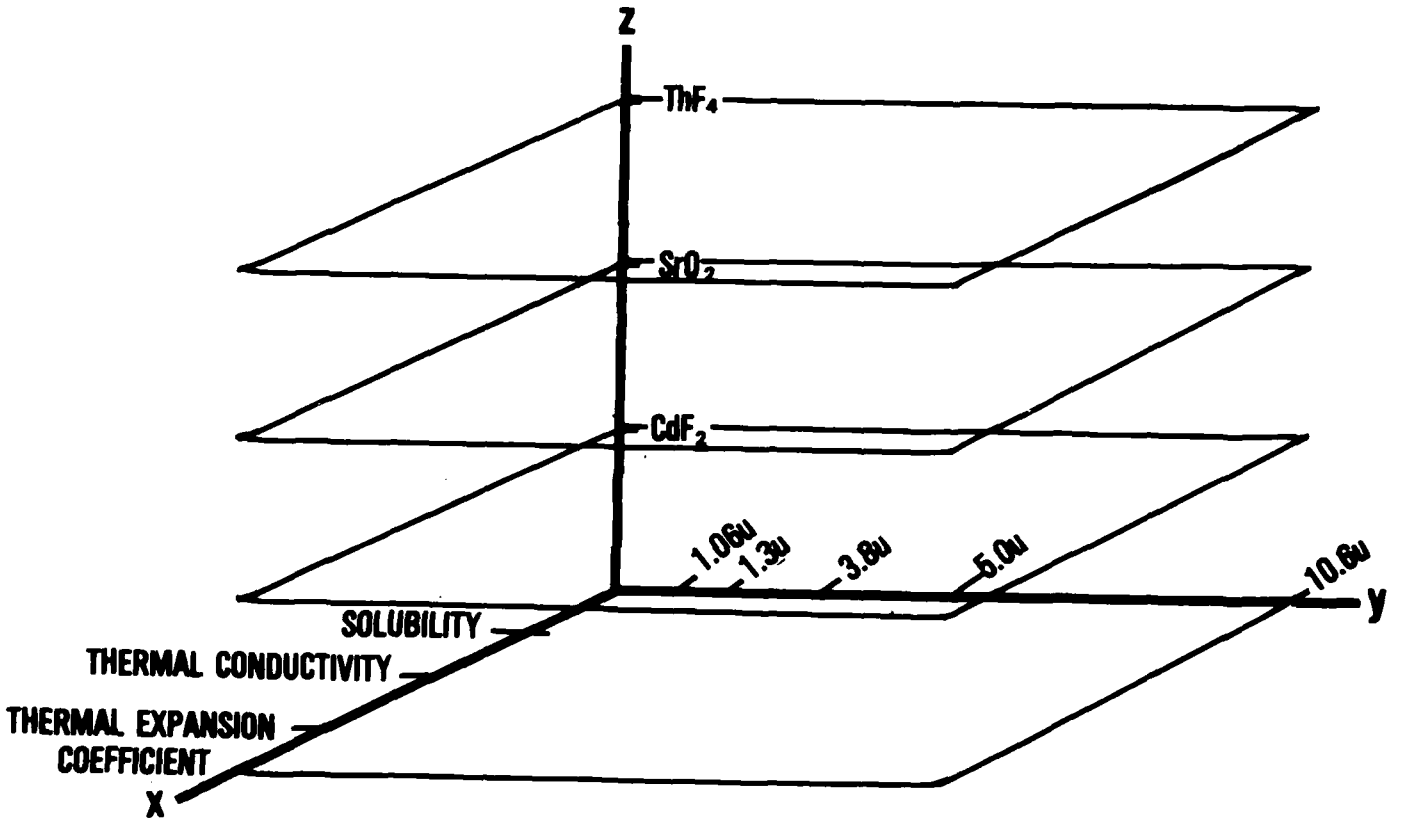

FIGURE 4. MATERIALS NOT WELL CHARACTERIZED

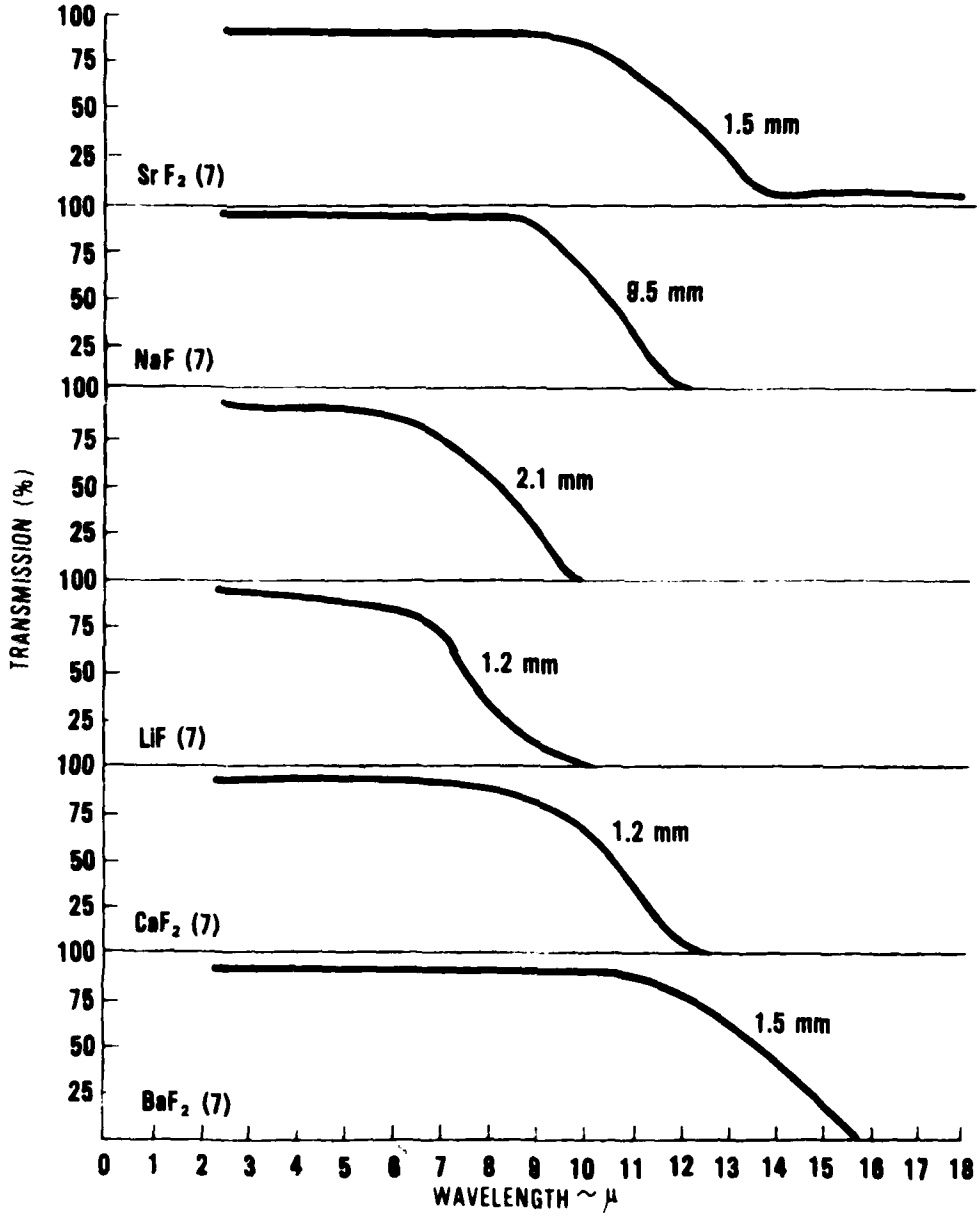

FIGURE 5a INFRARED TRANSMISSION

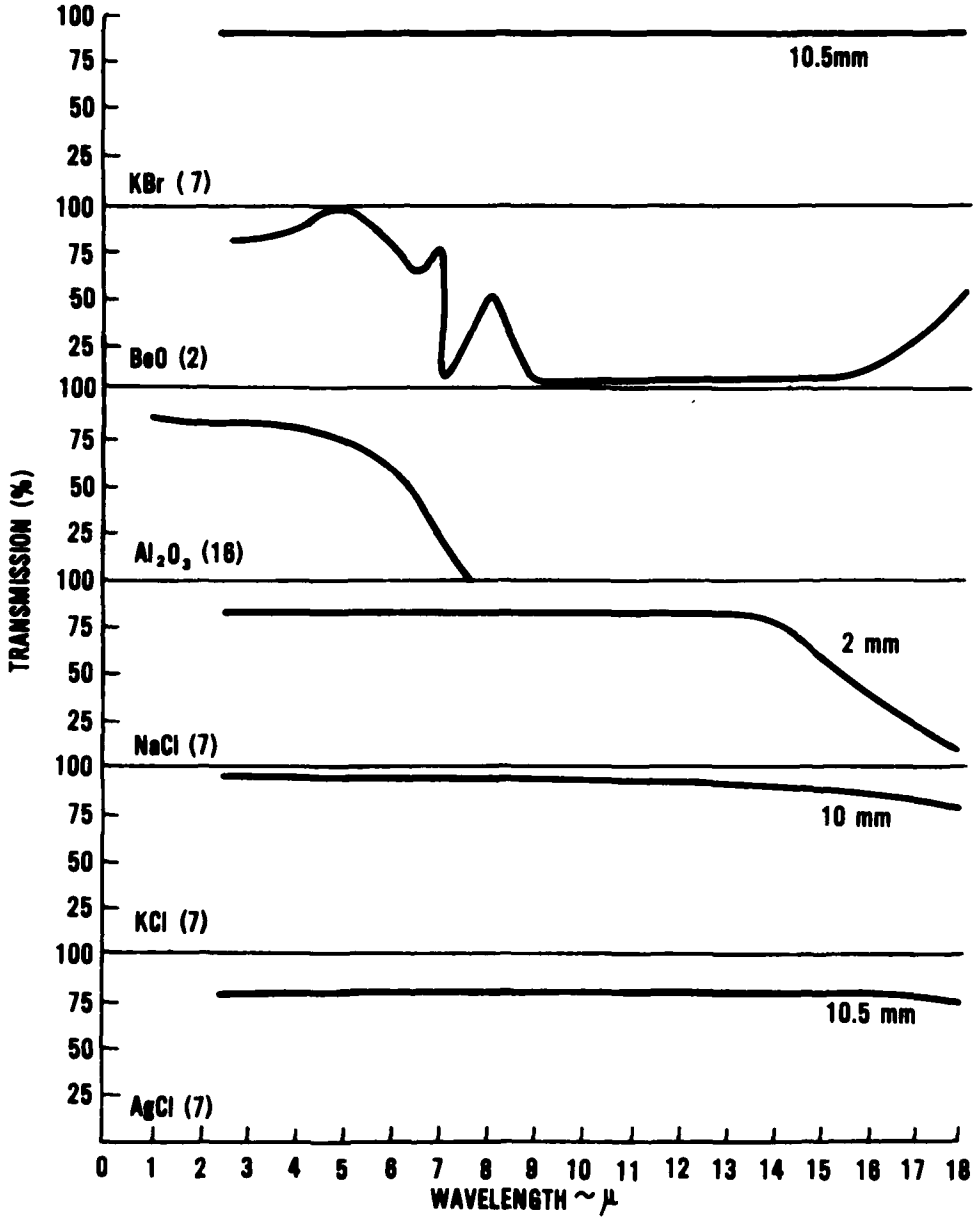

5b INFRARED TRANSMISSION

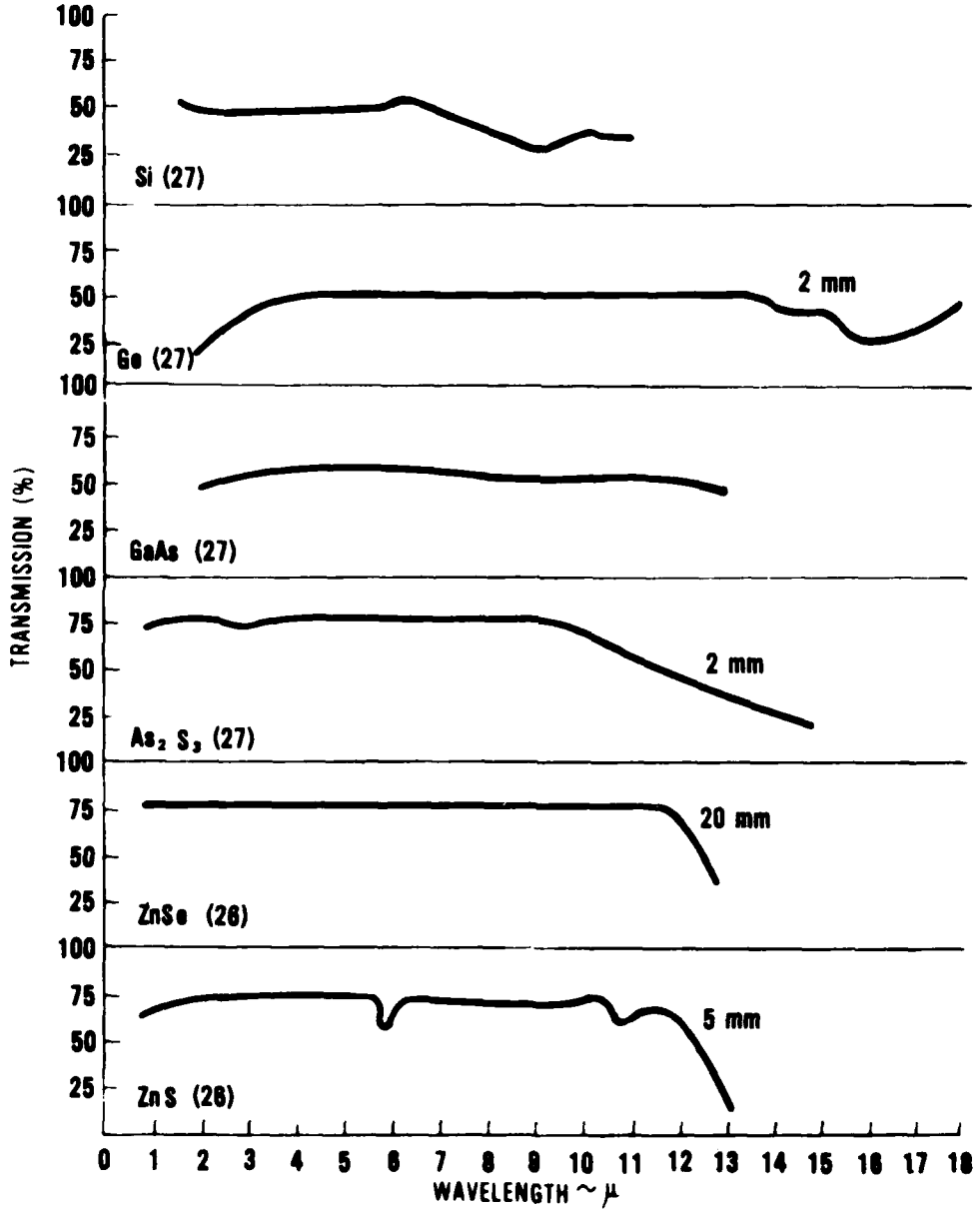

FIGURE 5c INFRARED TRANSMISSION

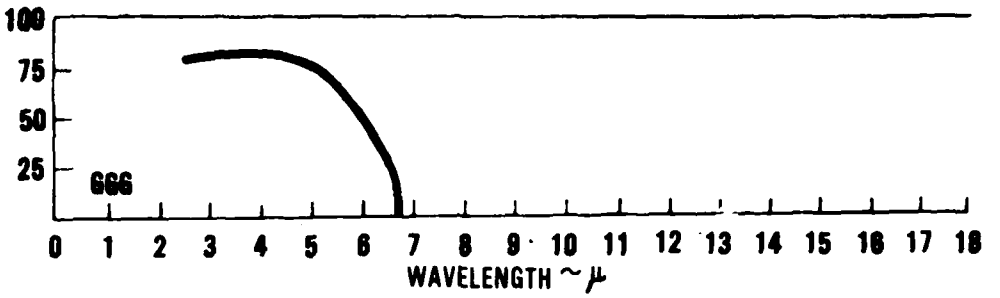

FIGURE 5d INFRARED TRANSMISSION

A NEW PHOTOGRAPHIC TECHNIQUE FOR OBSERVING BULK LASER DAMAGE*

Norman Thomas, John Sonderman, Stan Stokowski, Perry Wallerstein, and Dan Walmer
Lawrence Livermore National Laboratory
University of California
Livermore, California 94550

A damage site camera was developed to record the onset of bulk laser damage in materials. The camera images and magnifies the damage track using forward-scattered laser light. Employing this camera we can detect the presence of very small (<10 μm) damage sites with densities as low as 10/cc. The camera is used at oblique incidence.

We have observed discrete damage sites generated within the bulk of some materials, such as silicate glass, fluorophosphate glass, and KDP crystals, by 1-ns, 1064-nm laser pulses. The energy fluxes at which bulk damage is initiated are in the range of 2 to 20 J/cm^2, much lower than the fluxes required to cause damage by intrinsic processes. Small foreign inclusions (<1 μm diameter) are the cause of these low bulk damage thresholds. The inclusion density varies from 10^7/cc to less than 10/cc. At threshold the damaged volumes are small (1-5 μm in diameter) and thus, can be observed most easily by their forward-scattered light.

Several photographs are shown to illustrate the onset of bulk laser damage in fluorophosphate glass and KDP crystals.

1. Introduction

Bulk damage sites in fluorophosphate glass and KDP crystals are thought to arise respectively from: (1) Metallic particles from the glass melting process. (2) Misoriented crystals which probably have nucleated on impurities. Discrete damage sites result when energy fluxes in the range from2 to 20 J/cm^2 (1 ns at 1064 nm) strike these inclusions. When an intense visible beam from a 5 mw helium neon (632.8 nm) is transmitted along the same light path, the forward-scattered light from these discrete damage sites makes the sites visible to a trained unaided eye and especially to an optically-aided eye. If the light that is forward-scattered from these sites is imaged in an appropriate manner, then the ensemble of damage sites can be viewed or recorded on film.

The most convenient way to observe bulk damage tracks is to view them perpendicularly through an edge of the sample. However, some samples, such as edge-clad laser disks and large KDP crystals which are mounted in an array, make this technique nearly impossible to use. In addition, for small damage sites the forward-scattering cross section is orders of magnitude higher than that for 90° scattering. The only practical choice then is to view the damage sites through the clear aperture of the optic under test.

2. Scheimpflug Condition

The optical axis of the optical system used to image and record bulk damage sites is tilted away (30°) from the axis of the illuminating HeNe laser beam in order to exclude the laser beam from entering the entrance aperture of the system and to enable one to view the entire extent of a bulk damage track through the optic under test. The column of damage sites, which is more or less normal to the flat faces of the optic, must be imaged onto the film plane such that all damage sites are in good focus at one time.

This is done by an imaging according to the Scheimpflug condition [1-3],[1] in which the image plane intersects the line formed by the object plane and lens principal plane. Meeting this condition produces sharp focus between the column of damage sites and the film plane in the damage site camera.

Sharp imagery is attained by application of the lens law giving the relationship between conjugate distances:

$$\frac{1}{A} + \frac{1}{B} = \frac{1}{F} \qquad (1)$$

where

F = focal length of lens
A = distance from object to incident node
B = distance from emergent node to image.

Figure 1 is the principal plane section of the rectifier arrangement. Point O is the lens having focal point at D and D' in object and image spaces, respectively. The object and lens plane traces intersect at S to include the angle.

[1] Figures in brackets indicate the literature references at the end of this paper.

*Work Performed under the auspices of the U.S. Department of Energy by the Lawrence Livermore National Laboratory under contract number W-7405-ENG-48

The object plane vanishing point V is at focal length F from the lens plane to image at infinity. Furthermore, the image at infinity lies in a plane parallel to OV. The lens axis pierces the object plane at point e whose conjugate axial point E is at the image distance determined from the lens law (1). Ultra-focal distances X and X' in figure satisfy Newton's form of the lens law,

$$XX' = F^2. \qquad (2)$$

Assume the image plane trace through E and parallel to OV intersects the lens plane trace at S'. From similar triangles in the object space,

$$\overline{SO} = \frac{\overline{VO}}{X} \quad (X + F) \qquad (3)$$

In the image space S'OE is similar to VDO by construction. Therefore,

$$\overline{S'O} = \frac{\overline{VO}}{F} \quad (X' + F) \qquad (4)$$

Substituting from (2) and reducing

$$\overline{S'O} = \frac{\overline{VO}}{X} \quad (X + F) = \overline{SO} \qquad (5)$$

Therefore, points S and S' coincide, making object, lens, and image plane traces concurrent at S. This concurrence, or the collinearity of object, lens , and image planes in a line through S is called the Scheimpflug condition.

3. Damage Site Camera

In figure 2 the optical layout of the damage site camera is shown. It being used to record bulk damage sites in a 46-mm thick amplifier disk. The HeNe laser is placed on one side of the amplifier disk and co-aligned with the Nd: YAG damage laser beam, which travels in the same direction as the HeNe laser beam. On the opposite side of the optics and facing the two laser sources is the damage site camera. The camera consists of a prism, 632.8 nm bandpass filter (used only if room lights are a problem), camera lens, and film holder. These parts are housed in a light-tight camera housing. The 30^0-60^0-90^0 prism is adjacent to the test optic with a small airspace to prevent surface damage to the optic and prism. This prism is removed during the firing of the 1064 nm pulsed laser.

The camera lens contains a shutter and variable iris. The camera lens has either a 3-inch or 4-inch focal length and is stopped down to f/15. The choice of focal length is determined by the thickness of the optic under test; the 3-inch lens is used for thin optics and the 4-inch lens is used for thick optics. The magnification of the camera varies over the field of view of the optical systems because of the Scheimpflug condition.

The optical axis of the camera is perpendicular to the hypotenuse of the prism and tilted 30^0 from the normal to the optic. The column of damage sites is collinear with the HeNe laser beam and appears to be tilted slightly due to optical path differences as seen by the camera. When an object is viewed through a thickness of glass, the object appears to be closer than if it is viewed through air. The tilted column of damage sites represents the object plane shown in figure 1.

The film holder contains a ground glass screen to permit focusing and tilt adjustment. The image on the ground glass screen is observed in a direction parallel to the optic axis, not perpendicular to the ground glass screen as is usually the case. The image appears brightest in this direction.

When the column of damage sites is viewed at oblique incidence, it appears to be "keystoned" as shown in figure 3. The Scheimpflug condition rectifies the image so that it appears as a column of constant diameter along its longitudinal axis. The linearly variable magnification along the longitudinal axis causes the site density to appear to change from one end of the column to the other. This can be corrected by duplicating the Scheimpflug condition with the enlarger lens, easel, and negative film. An alternative method is to take account of the area magnification when measuring site density on a photograph.

4. Results

We use the damage site camera to observe bulk damage tracks in fluorophosphate laser glass and KDP crystals. Figure 4 is a picture of a severe damage track in fluorophosphate glass generated by 15 J/cm^2 of 1064-nm, 1-ns laser light. The large bright spots at the ends of the track are due to surface scattering of the HeNe beam. The damaging laser beam is ~1 mm in size. We illustrate in figure 5 that with multiple shots the scattering cross section of the damage sites increases, indicating a growth in the damaged volumes. Some of the sites in the final frame in figure 5 are 0.5 to 1 mm in diameter. We illustrate in figure 6 the appearance of fine tracks due to self-focusing when the laser flux is above 30 J/cm^2. We have observed damage sites in fluorophosphate glass with thresholds in the range of 2 - 20 J/cm^2 and densities from 10^2 to

more than 10^7 per cm^3. We believe that the damage-causing inclusions are small (0.5 m) platinum particles introduced during the melting process.

Figure 7 shows a track in a KDP sample. The poor quality of the surfaces and the occurrence of some surface damage obscures the bulk damage somewhat. Better surface polish should eliminate this problem. Bulk damage in KDP occurs at thresholds of 5 to 15 J/cm^2 with densities in the range of 10^4 - 10^6 per cm^3. We are currently investigating the cause or causes of the KDP damage sites.

Figure 8 shows the damage site camera being used to photograph damage sites in a large fluorophosphate disk in the damage lab at Lawrence Livermore National Laboratory.

References

[1] Thompson, Morris M., Manual of Photogrammetry, 2, 812, 1966A.

[2] Moffitt, Francis H., Photogrammetry, International Textbook Company, p. 270, 1967.

[3] Theodore Scheimpflug was an officer in the Austrian Army, who around 1900, pioneered the use of aerial cameras in reconnaissance balloons.

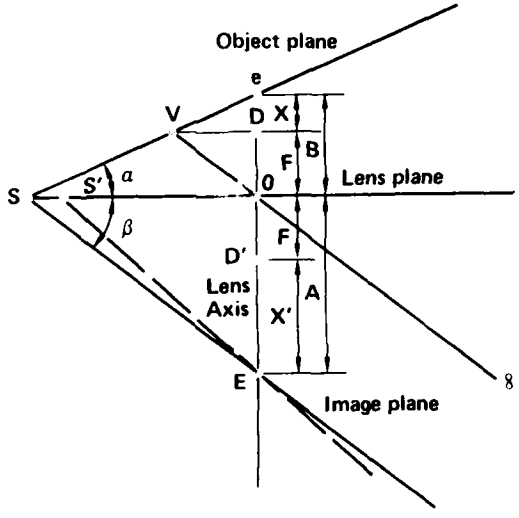

Figure 1. Schematic showing the Scheimpflug condition for imaging at an oblique angle.

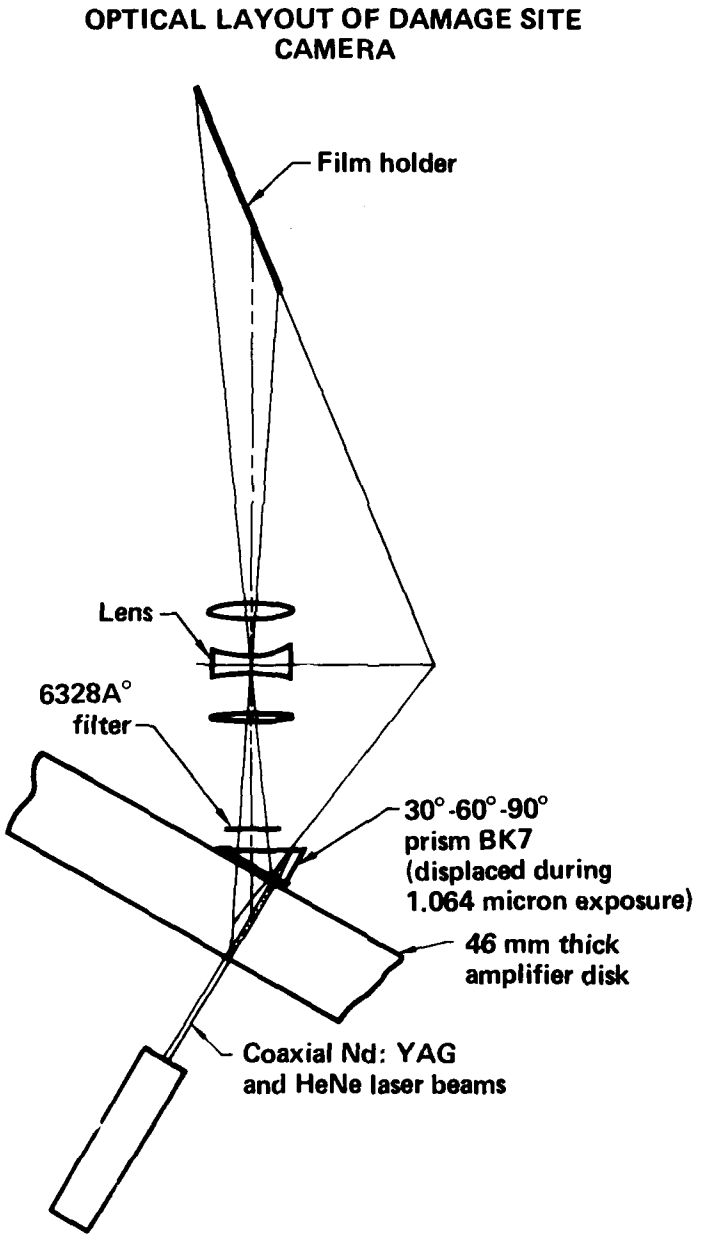

Figure 2. Optical layout of damage site camera.

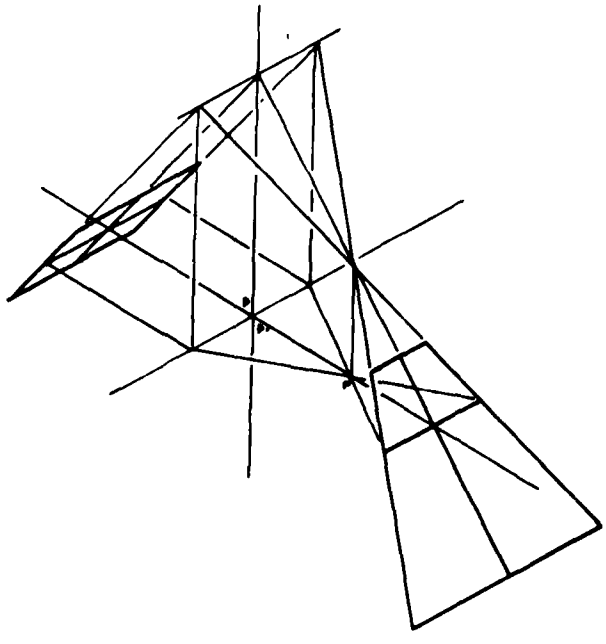

Figure 3. Keystoning from Scheimpflug condition.

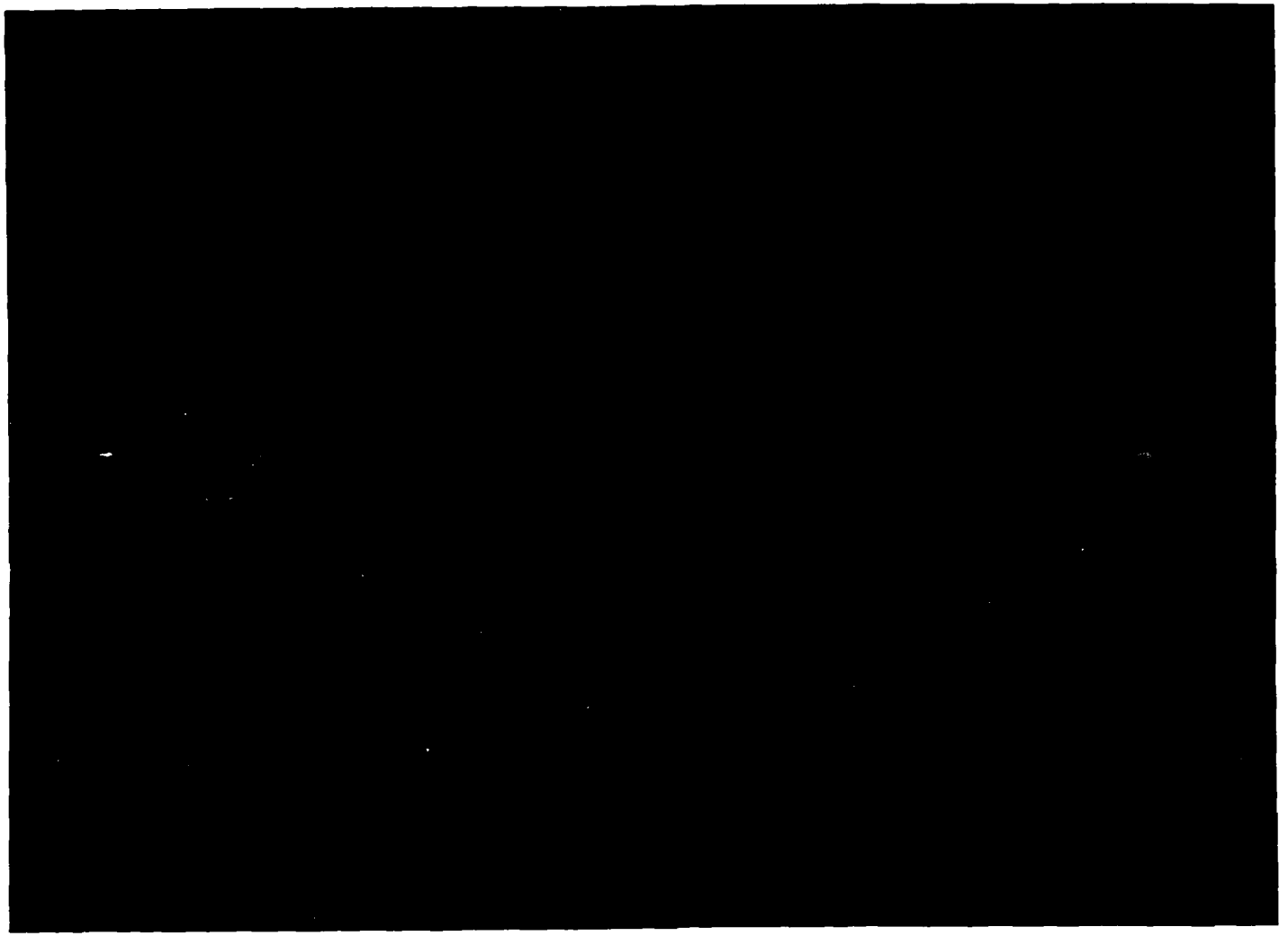

Figure 4. Damage track through a 5-cm piece of fluorophosphate glass produced by 15 J/cm^2 of a 1064-nm, 1-ns laser pulse.

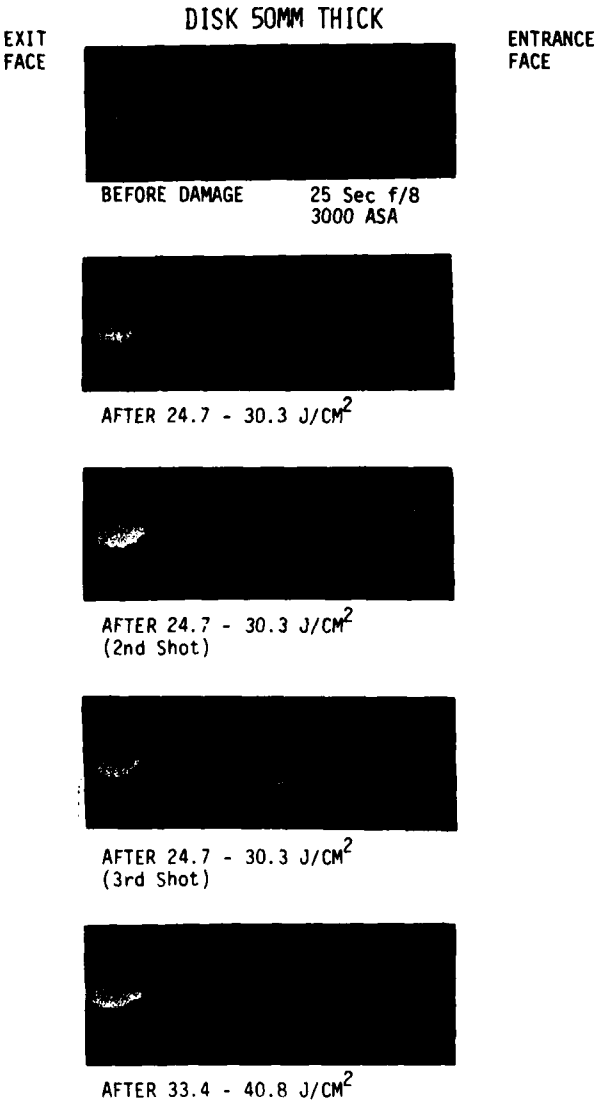

Figure 5. Damage track in fluorophosphate glass showing increasing size of damaged volumes with multiple shots.

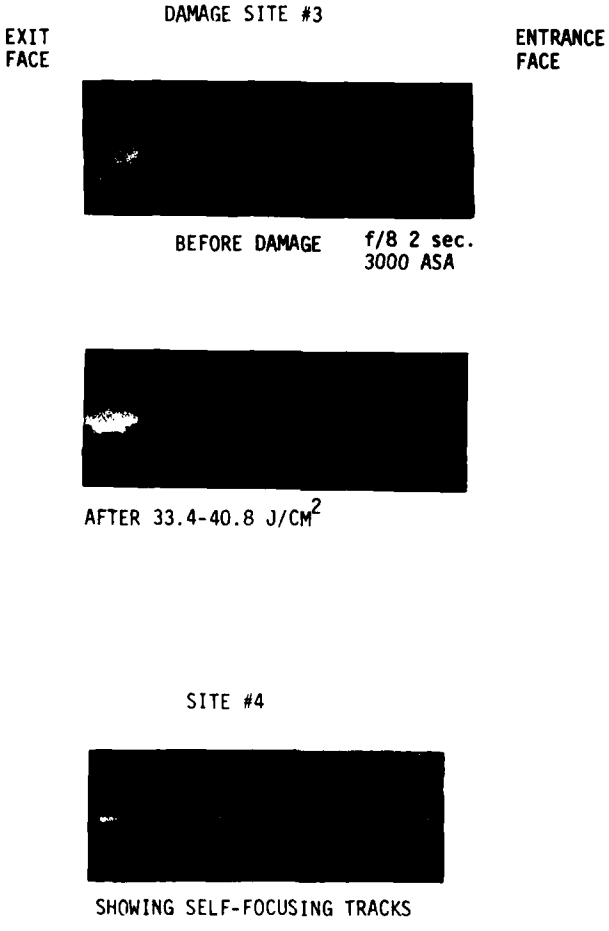

Figure 6. Damage tracks in fluorophosphate glass, one frame showing self-focussing tracks.

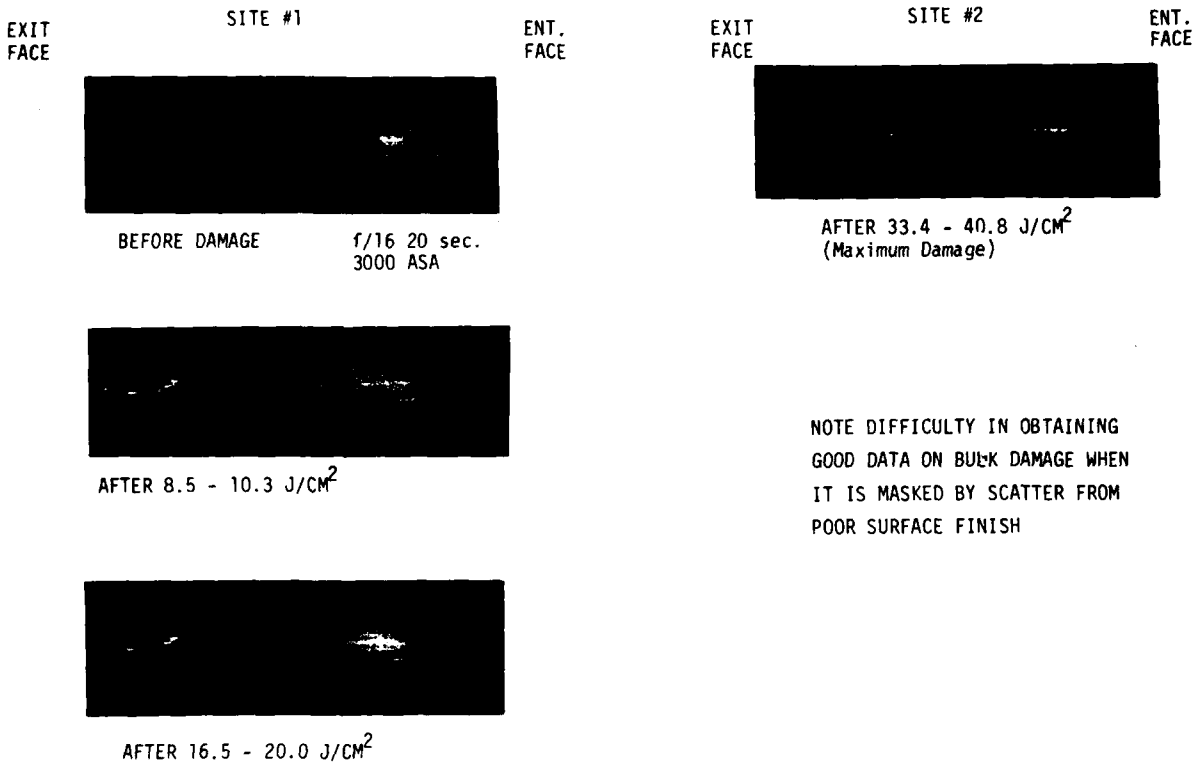

Figure 7. Bulk damage produced in a KDP crystal.

Figure 8. Damage site camera being used in the damage facility.

ULTRAFINE FINISHING OF CERAMICS AND METALS BY FLOAT POLISHING

Y. Namba and H. Tsuwa
Department of Precision Engineering, Osaka University
Suita, Osaka 565, Japan

This paper deals with a method of finishing ceramics and metals to obtain a high degree of smoothness, and also deals with geometrical, crystallographic, magnetic, optical and chemical properties of finished surfaces. Float polishing is developed to polish many electronic and optical materials ultrafinely without deformed layers. Samples were mechanically polished on a tin lap having fine grooves of concentric circles while in a polishing fluid mixed with the pure water and fine powder. The samples were suspended in the polishing fluid by hydrodynamic phenomena due to the specially shaped tin lap. Very good flatness, excellent retention of edge geometry and extremely small surface roughness of 10ÅRz were obtained on the finished surfaces of amorphous materials and single crystals. The surface roughness of 20ÅRz were obtained on polycrystalline materials by float polishing using special techniques in order to reduce crystallographic anisotropy.

Key words: Crystallographic anisotropy; crystallographic perfection; initial permeability; metal mirror; polycrystalline material; polishing; residual stress; sapphire; specular reflectance; surface analysis; surface integrity; surface roughness

1. Introduction

With increasing demand of crystalline devices in the field of electronics and opto-electronics, new finishing techniques have been required, which can not only improve the machining accuracy but also keep the functions of crystals. Most of the functions are structure sensitive, so it is necessary to avoid both the introduction and multiplication of dislocations into the crystals during machining. Generally speaking, the mechanical machining has both high production performance and high quality dimensional and geometrical accuracy, but produces plastically deformed layers. On the contrary, by the chemical and electro-chemical machining it is easy to make fine surface finishes with no deformed layer, but it does not improve geometrical accuracy. Therefore the mechanical machining accompanying with no crystal defects or few crystal defects will be extremely desirable in the leading industries.

Whitton [1][1] polished mechanically W, Ta, Si, Zr, Au, UO_2, Ta_2O_5 and ZrO_2 by the vibratory polisher with 0.05μm Al_2O_3 in water. The results showed that all the materials except gold had surfaces smooth to within 50Å, that W and Ti single crystals had disturbed or deformed layers of less than 250Å and that single crystal Si was not deformed at all. Namba and Tsuwa [2,3] polished sapphire and ferrite single crystals with various fine powders in water on a tin lap, and super smooth surface finishes better than 10ÅRz with crystallographical perfection were obtained. Mechanical machining without plastic deformations seems to be possible from these reports.

There is strong indication that mirror damage and surface roughness are inversely related [4]. Bennett and Porteus [5] have shown that reflectance from a metallic surface at normal incidence is the function of surface topography. Donovan et al. [6] have shown that the optical reflectance of variously polished germanium surfaces is related to the residual surface damage after polishing. Zanzucchi and Duffy [7] also studied the effect of surface damage on the optical reflectance of silicon surfaces. From these researches, the factors influencing the optical reflectance from a surface are considered to be the material of a sample, its crystallographic perfection, wavelength of incident light, surface roughness and slope of surface profile. Therefore, it seems to be necessary to establish a finishing technique which guarantees high shape accuracy, smoothness and good surface integrity on the finished surface in manufacturing mirrors and surfaces for high power lasers.

In this paper, a new finishing method called "Float Polishing" which will be applicable for machining optical materials for high power lasers is described, and geometrical, crystallographic, chemical, magnetic and optical properties of finished surfaces are also described.

2. Method of Float Polishing

Lapping on a lap with abrasives which are harder than a work material has been used for obtaining a flat surface, though it needs skill to maintain the flatness of the lap which affects the shape of finished samples. In polishing, fine abrasives supported in a resilient backing or pitch backing remove very tiny chips from the surface to be polished, and we can obtain a mirror-like surface. Nevertheless, its edge geometry often deteriorates. Moreover, conventional lapping and polishing are always accompanied with damaged layers on the finished surface due to machining.

It is the purpose of this new polishing method called "float polishing," to smooth samples without causing damaged layers on the finished surfaces and to reduce the necessity of skill in polishing. Figure 1 shows the principle structure of a float polishing machine installed in a clean room to prevent relatively hard and large contaminations from damaging samples. Samples put on a discoidal holder of stainless steel and a tin lap having fine grooves of concentric circles are rotated, so that the sample makes a planetary motion. The polishing fluid is a mixture of pure water with a certain fine powder, of which the concentration is usually less than 5wt%. During the polishing operation, the sample is floating in a stable state, or is suspended in the polishing fluid by the hydrodynamic

[1] Figures in brackets indicate the literature references at the end of this paper.

behaviour of fluid, because the samples are flatted sufficiently by diamond-lapping prior to polishing and the tin lap has grooves of 2mm in pitch and fine grooves on their land part due to turning. Polishing pressure is applied on the sample by only the weight of the samples and sample holder so as to maintain the stable movement of samples. It is very easy to control the lap flatness which does not affect the flatness of finished sample directly, because turning the lap surface is only required for flatting, and the wear of the lap during polishing is negligibly small.

The stock removal mechanism [2,3] of the float polishing method may be explained briefly as follows. Atoms on the surface are bonded more weakly than the atoms in the bulk material because the coordination number of the latter is larger than that of the former. Also, the bonding energy of the topmost atoms on the surface has a certain distribution, because the lattice defects can be considered not to be uniformly distributed on the surface layer. Therefore, there is some probability that the topmost atoms of weakest bonding on the sample are removed by the bombardment of particles in the fluid flow without forcing any damage to the bulk material. Hard particles of relatively large size are apt to make scratches on the surface, so it is very important in performing float polishing to select the proper powder as an abrasive.

3. Finishing of Polycrystalline Materials

The greater part of metals and ceramics used in industries is polycrystalline and is cheaper in comparison with single crystals. There are lots of materials which can not be manufactured in the state of single crystal of commercial size. The polycrystalline material is composed of numerous crystal grains having different crystal orientations.

In conventional lapping and polishing, the polished surface is generated by the accumulation of scratches accompanied with plastic deformation. Finer abrasive grains can produce a finer finish and the polished surface becomes bright in proportion to the decrease of surface roughness. In this case, the polished surface has a plastically deformed layer and geometrical irregularity or surface roughness as shown in fig. 2(a). The effect of crystallographic anisotropy does not appear on the polished surface.

Figure 2(b) shows a typical surface of a polycrystalline material polished by a damage-free method such as chemical, electro-chemical or float polishing [3]. Crystalline materials show anisotropy in these polishing processes and the stock removal rate in a certain crystal face differs from that in other crystal faces. Thus steps appear on the surface at the interfaces of grains due to the anisotropy and give a great influence on the geometrical form of the finished surface.

Figure 2(c) shows an ideally polished surface which has both good surface geometry and integrity. It is generally difficult to get this kind of surface finish, however, we developed new polishing method [7] called chemo-mechanical ultrafine finishing or chemo-mechanical float polishing in order to solve this problem in polishing Mn-Zn and Ni-Zn ferrites. It is the most important fact that the trend of the anisotropy of stock removal rate due to crystal surface depends upon finishing methods and the trends of both the float polishing and chemical one with hydrochloric acid are inverse each other. Therefore, the anisotropy due to the crystal surface can be eliminated or decreased by an adequate combination of two different finishing methods and the steps at the grain boundaries may disappear by controlling the hydrogen-ion or polishing powder concentration.

We have not yet obtained such a skillful method as shown in fig 2(c) for polishing metals. So, we propose the surface structure as shown in fig. 2(d) as polished metal surfaces in order to obtain a supersmooth surface with a thin damaged layer. This method is a combination of fig. 1(a) and (b), and intends to terminate the float polishing within the damaged layer which has been generated by the previous machining. It is an important key to teminate the polishing just before the appearance of grain boundaries.

4. Results and Discussion

4.1 Surface Topography

Figure 3 shows the geometrical form of sapphire single crystal finished by float polishing with 70Å SiO_2 powder, measured with Talysurf 10. The finished surface is convex a little, but has a good flatness about 300Å in the length 7mm, though the corners are slightly rounded. The edge can be finished 100Å in radius by float polishing.

Sapphire samples were lapped with SiC and diamond powders, and finished by float polishing with various fine powders such as SiO_2, CeO_2, Fe_2O_3, MgO, ZnO, Cr_2O_3 and LiF. The microscopic topography of the finished surfaces are shown in fig. 4. The lapped surface shown in fig. 4(a) is an aventurine surface which is generated by micro fracture containing cleavage. The diamond-lapped surface seems to be a mirror-like surface, but the microscopic photograph shows the surface is generated by accumulation of scratches accompanying the plastic deformation. Etching the specimen with H_3PO_4 at 320°C reveals a series of etch-pits under the scratches. The surface finished with SiO_2 powder shows the mirror-like surface from the microscopic view with no scratch and no defect as shown in fig. 4(c). Two-step plastic-carbon replica with chromium shadowing on the surface could not show any defect in the transmission electron microscope. The smooth surface like this could be obtained in all cases using various kinds of powders.

Stylus techniques can show the topographic structure of the finished surfaces as shown in fig. 5. The surface roughness Rz corresponding to the tenpoint height in ISO is 0.3μmRz on the lapped surface with SiC. The diamond-lapped surface is 350ÅRz. Molecular smoothness less than 10ÅRz was obtained by float polishing as shown in fig. 5(c). A variety of particles used as abrasives are softer than sapphire, so that those particles are not considered to make scratches onto the sapphire surface. Moreover, the fracture unit or removal unit of sapphire during float polishing may be guessed to be less than 10Å order from the existence of molecular smoothness.

We can finish amorphous materials and single crystals supersmooth less than 10ÅRz in surface roughness by float polishing. On the other hand, the supersmooth surfaces about 20ÅRz [7,8] can be

obtained on polycrystalline Mn-Zn and Ni-Zn ferrites and some metals by using polishing methods shown in fig. 2(c) and (d). The method shown in fig. 2(d) requires a pre-machined surface having both uniform surface topography and a damaged layer. An extremely deep scratch often spoils this method, because grain boundaries apnear on the polished surface while the scratch is being removed.

4.2 Crystallographic Properties

A high energy electron beam (100KeV) impinges on the sample surface at a low angle of incidence and reflection electron diffraction patterns show the informations sensitive to the first few atom layers. Reflection electron diffraction patterns of the finished surfaces prepared by lapping with 8μm SiC and 3μm diamond, chemical polishing, and ultra-fine finishing with SiO_2 and CeO_2 are presented in fig. 6(a) to (e), respectively.

Figure 6(a) and (b) show the Debye rings, characteristic of a rough polycrystalline structure. The mechanism of the lapping of sapphire with diamond involves a combination of the surface flow of asperities by plastic deformation and micro-cutting by diamond. Examination of single-crystal sapphire showed high densities of dislocations are produced within the nearsurface regions by mechanical polishing with a fine diamond compound.

The sample which was chemically polished in a 1:1 H_2SO_4:H_3PO_4 mixture has excellent crystallographic quality as shown in fig. 6(c). The patterns of the surfaces finished with SiO_2 and CeO_2 are similar to the pattern of the chemically polished surface, and give single-crystal patterns. Many Kikuchi lines are visible on the ultrafinely finished and chemically polished surface patterns, indicating a high degree of crystal perfection. It can be seen that the ring pattern characteristic of polycrystalline layer is absent. The lapping damage on the sapphire sample is completely removed without the introduction of further damage, so that the mechanism of this float polishing must be the microfracture accompanying no dislocation or may accompany with a slight surface damage which could not be detected by this electron diffraction analysis.

From Nomarski micrographs after etching the polished sapphire and silicon single crystals, the float polishing may be considered not to introduce any dislocation into the polished surfaces.

4.3 Chemical Properties

A potentially very powerful tool for surface characterization is the ion microprobe mass analyzer (IMMA) which has a high detection limit and high depth resolution. Ion microprobe analysis shows the existence of iron atom or ion on the sapphire surface which was finished by float polishing with Fe_2O_3 powder as shown in fig. 7, where ions of carbon and hydrogen are contaminations. Figure 8 is the observational result of depth profile of $^{56}Fe^+$. The curve does not show the exact chemical composition due to the characteristics of this analysis, but shows iron exists in the first few monolayers on the finished sapphire surface.

Lithium fluoride adhering to the sapphire sample during finishing may be dissolved in boiling water, because LiF is soluble in water. Then the sapphire sample finished with LiF was boiled in water again and again, so that physical adsorption of LiF may be supposed to disappear from the sapphire sample. But the existence of lithium was still detected by IMMA. The depth profile of lithium was the same as above-mentioned iron shown in fig. 8. On the first few atomic layers less than 10Å on the surface finished by float polishing, we could detect some elements which constituted the powder used as abrasives.

Auger electron spectroscopy (AES) is one of the most suitable methods of analyzing the composition at the very topmost surface because it is a non-destructive analysis. Above-mentioned results were also proved by AES [2].

As a result of chemical analysis, the first few atom layers of finished surfaces may be estimated to have a very small amount of atoms due to the powder used in place of abrasives. The surface finished by float polishing is highly clean in comparison with that finished by conventional lapping or polishing, because there is no abrasives embedded onto the sample. Moreover, we can perform float polishing with various kind of powders, for example, SiO_2, CeO_2, γ-Al_2O_3, Cr_2O_3, Fe_2O_3, ZrO_2, ZnO, MgO, $CaCO_3$, LiF and C (graphite) for polishing sapphire, so that we can select the proper powder material and control the elements diffused at the topmost surface of polished sample in order to prevent the effect of diffused impurity atoms. Therefore, good thin films of ZnO single crystal were obtained on the (1012) sapphire substrate finished by float polishing with ZnO powder by mean of chemical vapor deposition method without any pretreatment [9]. Such method seems to be effective in manufacturing mirrors and surfaces for high power lasers.

4.4 Magnetic Properties

Being structure-sensitive, the magnetic properties of the ferrite are often worsened by the deformed surface layer due to machining. Initial permeability is an important factor for Mn-Zn ferrites.

Figure 9 shows the initial permeability spectra for polycrystalline Mn-Zn ferrites finished by diamond-lapping, Cr_2O_3-polishing, float polishing with MgO powder and etching after float polishing. The chemically etched ferrite shows the original permeability spectra. The permeability is structurally sensitive and it is affected not only by the degree of crystallographic perfection but also by elastic stress, therefore rendering low permeability in the specimen having deformed layers due to machining. On the contrary, the sample finished by float polishing shows almost the same magnetic properties as the chemically etched one.

By means of measuring the recovery of the initial permeability due to removal of plastically deformed layers by etching, it was found that the deformed surface layers of the Mn-Zn ferrites lapped with 3μm diamond and polished with Cr_2O_3 powder are 1.5μm and 0.5μm in thickness, respectively.

Figure 10 shows the permeability-temperature relationship of polycrystalline Mn-Zn ferrite finished by various methods at a frequency of 100kHz. Each curve has two maxima. The maximum peak

around room temperature, which is called second peak corresponds to the passage through zero of the first crystal anisotropy constant [10], and this peak is reduced and shifted to the low temperature side in the case of conventional machining. On the contrary, the core finished by float polishing shows almost the same magnetic property as the original material because the polished surface is not plastically deformed or covered by amorphous layers.

Figure 11 shows the permeability-temperature relationship of the etched specimens with uniaxial compressive and tensile stresses. By increasing the compressive stress on a rectangular specimen having a rectangular hole, the second peaks are shifted to the higher temperature and lower permeability side. On the contrary, by increasing the tensile stress on the strain-free sample, the second peaks are shifted to the lower temperature and lower permeability side [11]. The latter shows a similar tendency to machined sample as shown in fig. 10.

It is well known that grinding and lapping will put the surface of Mn-Zn ferrite under compression, and the permeability in this surface layer is greatly reduced. Since the surface layer is subjected to a compressive stress, the interior or bulk is consenquently under tensile stress. From these figures, it can be considered that the float polishing does not give the residual stress on the polished surface. This fact may be available for making mirrors and surfaces for high power lasers.

4.5 Optical Properties

Figure 12 shows specular spectral reflectances of 304 stainless steel at near normal incidence of visible light as a function of surface roughness. The specular reflectance clearly rises with the increase in wavelength and decrease in surface roughness. The surface roughness of 0.07μmRz, 0.16μmRz, 0.35μmRz and 4.6μmRz were obtained by polishing with a 1200-grit, 600-grit, 120-grit and 40-grit SiC coated abrasives, respectively. Supersmooth surface of 0.002μmRz was obtained by the above-mentioned polishing method using MgO powder. The surface roughness of 0.01μmRz, 0.02μmRz and 0.04μmRz were also obtained by polishing with 70ÅSiO_2 and Fe_2O_3 powders and buffing with Cr_2O_3 powder, respectively. The last one was generated by unidirectional shallow scratches, and the others showed grain boundaries under microscopic examination. The reflectance spectra of these three specimens were situated just between two curves of 0.002μmRz and 0.07μmRz in order of surface roughness.

A sample, polished ultrafinely up to 0.002μmRz, was annealed by rapid cooling with N_2 gas after keeping the sample at 1073K for 1 hour and at 1323K for 2 hours in a vacuum chamber in order to remove the effect of the plastically deformed layer on reflectance. The dotted line in fig. 12 shows the reflectance spectrum of the annealed specimen, of which surface roughness became 0.8μmRz due to grain growth during heat treatment. This annealing was not effective in increasing reflectance in the range of visible light. Improvement of surface roughness seems to be more effective than that of surface integrity.

Pure metals of chromium, iron and nickel which constitute 304 stainless steel were also polished supersmoothly with pure water containing 70ÅSiO_2 powder of 2wt%. Reflectance of supersmoothly polished stainless steel is lower than that of nickel, is almost equal to that of chromium, and is higher than that of iron. The last relation seems to be derived from a thicker Fe-rich oxide layer on the pure iron surface than on that of stainless steel. In this range of wavelength, surface roughness affects reflectance more than either the material or damaged layer of the bulk.

Figure 13 shows specular spectral reflectances of 304 stainless steel at near normal incidence of infrared lights as a function of surface roughness. Samples used are the same as shown in fig. 12. The specular reflectance of polished specimen rises with increase in wavelength and decrease in surface roughness. The effect of surface roughness on reflectance becomes smaller in fine surface roughness with increasing wavelength. The dotted line in fig. 13 shows that the reflectance depends upon not only surface roughness but also surface integrity in the range of infrared wavelength, because the dotted curve of the annealed rough surface, 0.8μmRz in roughness, intersects the curve of the finer surface, 0.35μmRz in roughness. The former curve rises more than the latter at the longer wavelength side in spite of rougher surface because of the lack of a damaged layer. Ultrafinely polished pure metals of nickel, iron and chromium have higher reflectance than ultrafinely polished 304 stainless steel at the incidence of infrared lights which have a deeper skin depth than visible light. Therefore, the oxide layer on a pure iron surface seems not to affect the reflectance at all. The specular reflectance is shown to be highly dependent on surface topography, atomoc arrangement and atomic composition on the surface layer.

Figure 14 shows the relationship between specular reflectance and surface roughness as a parameter of material, and makes clear the effect of surface roughness on the specular reflectance at the wavelength of 10.6μm. Pure metals have higher reflectance than stainless steel in the range of finer surface roughness. From above-mentioned results, it may be considered that the supersmooth surface without deformed layer is required for mirrors in the range of infrared light.

5. Conclusions

From this paper the following conclusions may be drawn:

1) Very good flatness, excellent retention of edge geometry and extremely small roughness of 10ÅRz are obtained by float polishing of amorphous materials and single crystals.

2) The finished surface by float polishing is crystallographically perfect, shows the magnetic properties approximately up to the bulk and is free from the residual stress.

3) The first few atomic layers less than 10Å on the finished surface contains the impurity atoms constituting the used powder. The effect of this impurity atom can be removed by proper selection of powder material.

4) In the float polishing of polycrystalline materials, the stock removal rate depends upon their crystallographic orientations of the grains to be finished, so that steps appear on the finished surface at the interface of grains. The chemo-mechanical float polishing is proposed which utilizes an

adequate combination of float polishing and chemical polishing in order to eliminate the anisotropy of stock removal rate on each crystal surface. Extremely small surface roughness of 20ÅRz is obtained by this polishing method of Mn-Zn ferrite and Ni-Zn ferrite.

5) The supersmooth metal surface of 20ÅRz in roughness can be obtained by terminating the float polishing of damaged surface layer to a point prior to the appearance of the grain boundary due to crystallographic anisotropy.

6) Specular reflectances at near normal incidence of visible and infrared lights depend upon material, surface roughness, wavelength and surface integrity.

6. Acknowledgments

The authors would like to express their sincere thanks to Dr. A. H. Guenther of Air Force Weapons Laboratory for encouraging us to present this paper at the Twelfth Annual Symposium on Optical Materials for High Power Lasers. The authors especially wish to thank Miss A. Okumura and Mr. J. Uchikoshi for their help with preparing the manuscript.

This work was supported in part by Grant-in-Aid for Developmental Scientific Research of the Japanese Ministry of Education and the Kurata Foundation under Grant No. 12-9.

7. References

[1] J. L. Whitton, J. Appl. Phys., 36, 3917 (1965).

[2] Y. Namba and H. Tsuwa, Annals of the CIRP, 26/1, 325 (1977).

[3] Y. Namba and H. Tsuwa, Annals of the CIRP, 27/1, 511 (1978).

[4] A. H. Guenther, Private communication.

[5] H. E. Bennett and J. O. Porteus, J. Opt. Soc. Am., 51, 123 (1961).

[6] T. M. Donovan, E. J. Ashley and H. E. Bennett, J. Opt. Soc. Am., 53, 1403 (1963).

[7] Y. Namba and H. Tsuwa, Annals of the CIRP, 28/1, 425 (1979).

[8] Y. Namba and H. Tsuwa, Annals of the CIRP, 29/1, 409 (1980).

[9] Y. Namba and H. Tsuwa (unpublished observations)

[10] K. Ohta, J. Phys. Soc. Japan, 18, 685 (1963).

[11] Y. Namba, H. Tsuwa and K. Kodera, Proc. Japan Soc. Precision Engg., 281 (Mar. 1979). (in Japanese)

AD-A106 548 NATIONAL BUREAU OF STANDARDS WASHINGTON DC F/G 20/5
LASER INDUCED DAMAGE IN OPTICAL MATERIALS: 1980,(U)
OCT 81 H E BENNETT, A J GLASS, A H GUENTHER
UNCLASSIFIED NBS-SP-620 NL

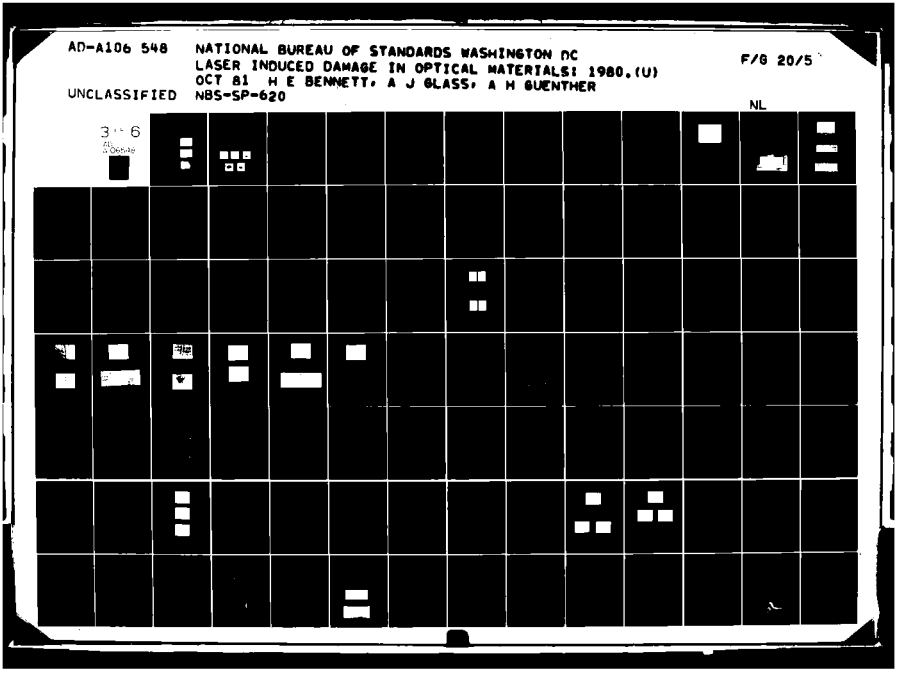

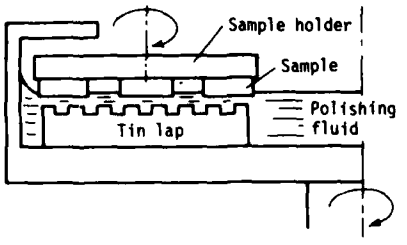

Figure 1. Principle structure of a float polishing machine.

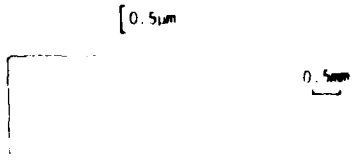

Figure 3. Surface profile of polished sapphire single crystal, which shows the flatness and edge geometry.

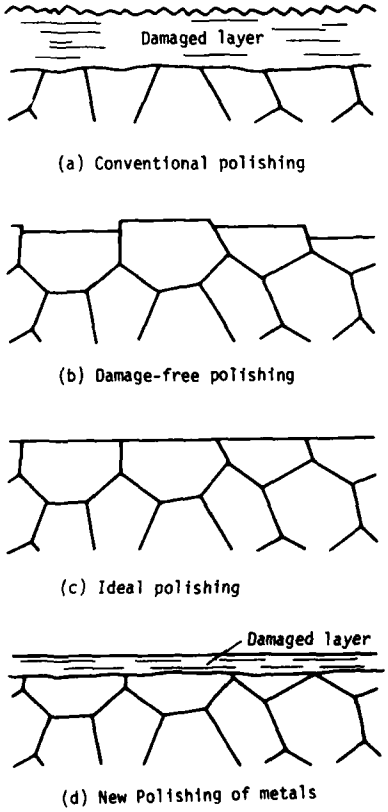

Figure 2. Sectional models of polished surfaces.

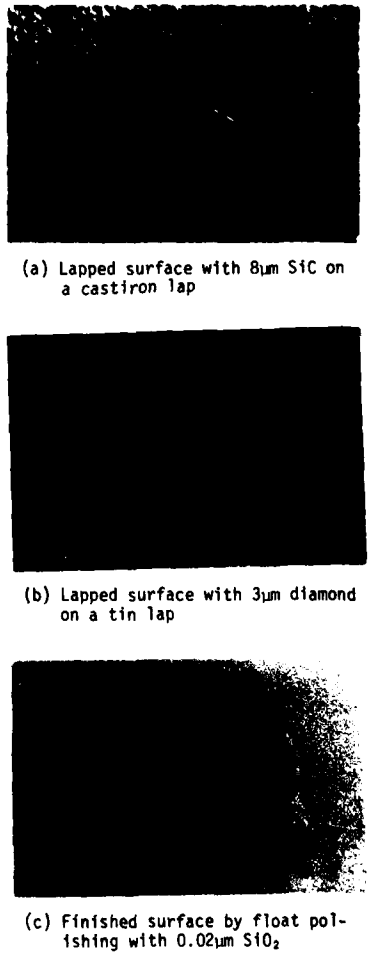

(a) Lapped surface with 8μm SiC on a castiron lap

(b) Lapped surface with 3μm diamond on a tin lap

(c) Finished surface by float polishing with 0.02μm SiO_2

Figure 4. Nomarski micrographs of finished sapphire single crystals.

(a) Lapped surface with 8μm SiC on a castiron lap

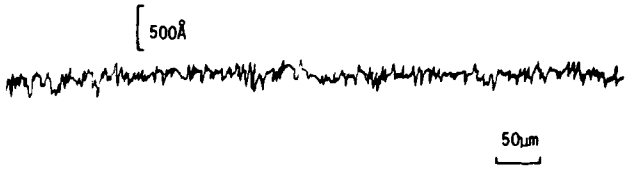

(b) Lapped surface with 3μm diamond on a tin lap

(c) Finished surface by float polishing with 0.02μm SiO_2

Figure 5. Surface profiles of finished sapphire single crystals, measured by Talysurf and Talystep.

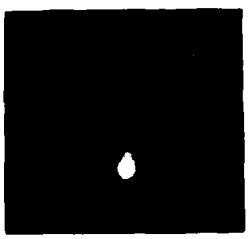

(a) Lapped surface with 8μm SiC on a cast-iron lap

(b) Lapped surface with 3μm diamond on a tin lap

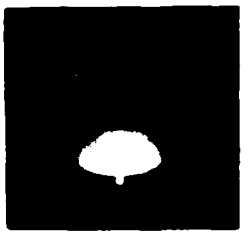

(c) Chemically polished surface with a 1:1 H_2SO_4 : H_3PO_4 mixture

(d) Finished surface by float polishing with 0.02μm SiO_2

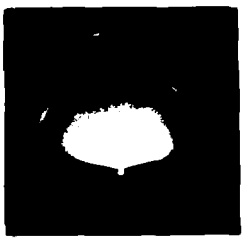

(e) Finished surface by float polishing with CeO_2

Figure 6. Reflection electron diffraction patterns of finished sapphire single crystals.

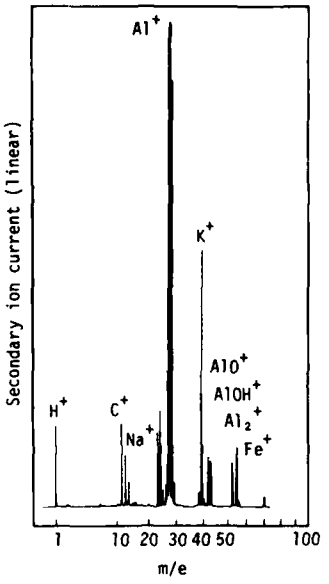

Figure 7. Ion microprobe mass analysis of sapphire single crystal surface finished by float polishing with Fe_2O_3.

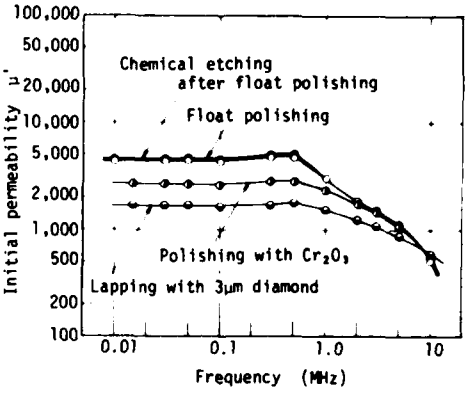

Figure 9. Initial permeability spectra for polycrystalline Mn-Zn ferrites finished by various methods.

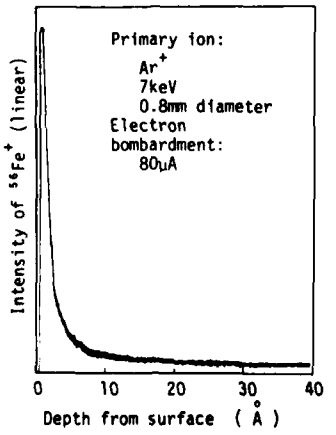

Figure 8. Depth profile of $^{56}Fe^+$ on sapphire single crystal surface finished by float polishing with Fe_2O_3, obtained by ion microprobe mass analysis.

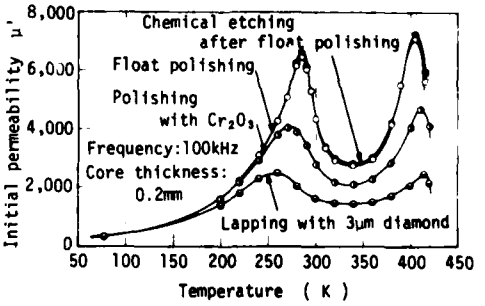

Figure 10. The permeability-temperature relationship of polycrystalline Mn-Zn ferrite cores finished by various methods at a frequency of 100KHz.

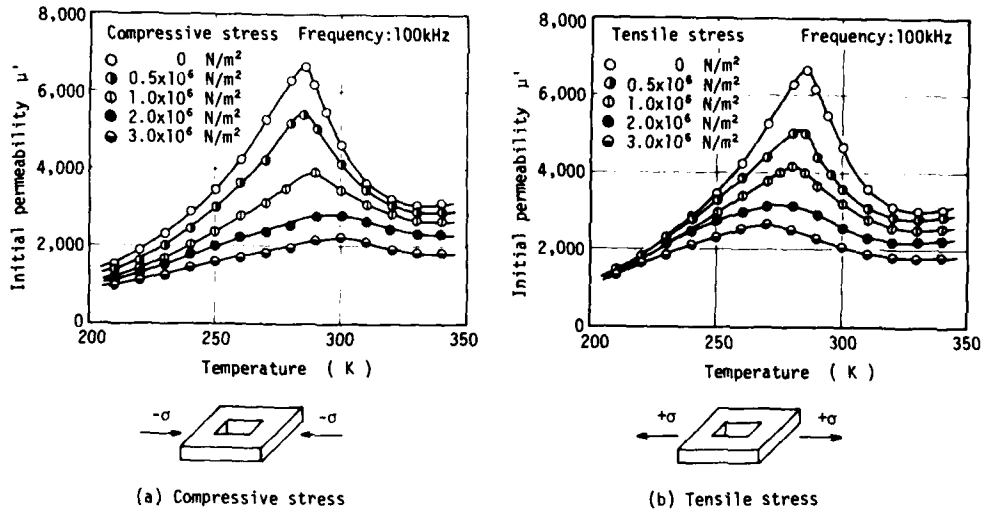

(a) Compressive stress

(b) Tensile stress

Figure 11. The permeability-temperature relationship of etched polycrystalline Mn-Zn ferrite cores as a parameter of uniaxial compressive and tensile stresses.

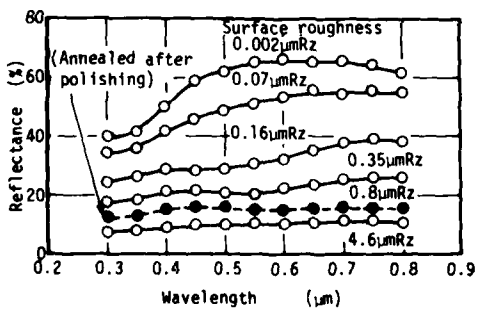

Figure 12. Specular reflectance spectra of AISI304 stainless steel steel finished by various methods at near normal incidence of visible light as a function of surface roughness.

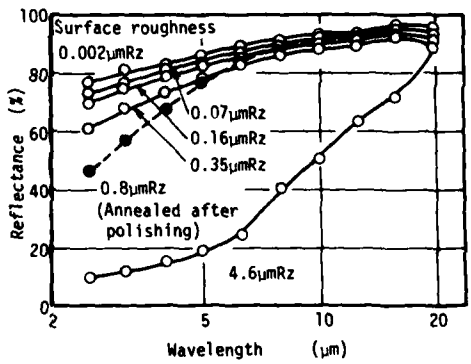

Figure 13. Specular reflectance spectra of AISI304 stainless steel finished by various methods at near normal incidence of infrared light as a function of surface roughness.

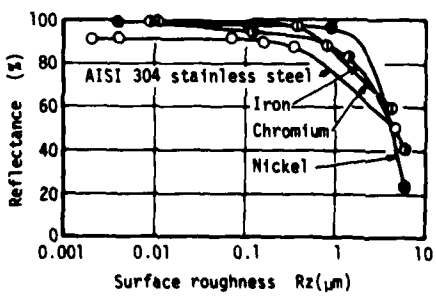

Figure 14. The relationship between specular reflectance and surface roughness as a parameter of material at the wavelength of 10.6μm.

1.06 μm LASER-INDUCED BREAKDOWN OF CO_2-LASER-POLISHED FUSED SiO_2*

P. A. Temple and M. J. Soileau†
Michelson Laboratory, Physics Division
Naval Weapons Center, China Lake, California 93555

Fused silica surfaces have been treated with continuous wave CO_2-laser radiation in an improved raster technique. Laser damage data for 1.06-μm, 9-nsec, small-spot irradiation are presented. It is shown that a reasonably sharp transition from laser damage prone to laser damage resistant surfaces takes place over a small CO_2-laser power range. The transition to high damage resistance takes place at a silica surface temperature where material flow begins to take place, as evidenced by the onset of residual strain in the CO_2-processed part. These data are taken as evidence that microcrack healing is an important mechanism in increased damage resistance in CO_2-polished parts. Also presented are data which show that CO_2-treated surfaces have a small-spot damage threshold at least as high as the bulk damage threshold of SiO_2. In addition, these treated parts show no obvious change in surface appearance, as seen in total internal reflection microscopy. They also show little change in transmissive figure. It is suggested that uniform preheating be used to eliminate the strain presently seen in CO_2-treated parts.

Key words: CO_2-laser glazing; CO_2-laser polishing; fused silica surface; laser damage; laser polishing; surface laser damage; 1.06-μm.

Introduction

Last year [1][1] we reported 1.06-μm, 1-nsec damage data for CO_2-laser-polished fused silica. Those data were for large spot sizes and were taken at Lawrence Livermore Laboratory (LLL). At that time, we reported that the bare surface damage threshold of fused silica was raised by as much as a factor of two by laser "glazing" the surface of Suprasil II substrates. These substrates had previously been mechanically "superpolished" by Zygo, Inc. It was noted, however, that parts treated in this way showed both high strain and a loss of surface figure due to the intense CO_2-laser heating inherent in the glazing process.

This paper reports on recent work employing a new multipass CO_2-laser-polishing technique which results in improved 1.06-μm laser damage threshold but which causes much less disruption to the optical figure of the part. Parts processed by this new multipass system also show a reduction in stress over those produced by the previous technique. Laser damage results gathered at the Naval Weapons Center, which employed a 1.06-μm, 9-nsec, small-spot YAG laser, will be given. These data do not give a damage threshold as such. Rather, they show the response of CO_2-polished fused silica surfaces to 100 shots at I_S, the nominal mechanically polished surface threshold, and to 100 shots at 1.8 I_S, a level where a mechanically polished surface will fail on virtually every shot. The results indicate that it is possible to prepare surfaces in this manner which have an improved damage performance without seriously disrupting the optical figure. Finally, a second set of data will be presented which demonstrates that the surface damage threshold for small spots is apparently similar to the bulk damage threshold.

Processing Technique

Figure 1 is a schematic representation of the CO_2-laser processing apparatus. In this apparatus, a stepping-motor-driven mirror directs the unfocussed CO_2 continuous wave (cw) laser beam at the fused silica part at near-normal incidence. The part is supported in air by two refractory rods. The laser used was an unpolarized 500-watt Photon Sources cw device. At the sample position, the laser beam was approximately Gaussian with a $1/e^2$ radius of 5.2 mm.

Figure 2 is a photograph of the stepping-motor-driven mirror and of the microprocessor-based motor controller. The mirror is flat, uncoated copper and was located ~ 30 in. from the fused silica sample. The raster pattern generated by the mirror is shown in figure 3. Also shown in figure 3 are the scan rate parameters used in the preparation of all the samples.

In the work reported last year, the CO_2-polishing treatment consisted of one set of single, slow passes over the surface in a close-spaced pattern. In the work reported here, the part was exposed to a rapidly scanned beam for several minutes. This resulted in several hundred successive exposures of the entire surface rather than just one exposure, as in the previous work.

In table 1 is shown the time of exposure vs laser power for the CO_2-laser-polished parts discussed in this paper. The lower power, shorter time exposures are used to uniformly warm the part. The highest power was sustained for 10 min. (150 complete raster scans) in all three cases. The part was then cooled by lowering the laser power 10 watts/min. The raster mirror was kept in motion, as described in figure 3, during the entire treatment.

*Work supported by Lawrence Livermore Laboratory and Navy Independent Research Funds.
†Present address: Physics Dept., North Texas State University, Denton, TX 76203.
[1]Figures in brackets indicate the literature references at the end of this paper.

Table 1. CO_2-laser-polishing treatment schedules.

#1		#2		#3	
Power (watts)	Exposure (min.)	Power (watts)	Exposure (min.)	Power (watts)	Exposure (min.)
100	2.5	100	2.5	100	2.5
125	2.5	125	2.5	125	2.5
150	2.5	150	2.5	150	2.5
175	10.0	175	2.5	175	2.5
		200	10.0	200	2.5
				225	10.0

Cool down: Reduce 10 watts each 1.0 min. to 150 watts, then off.

In the processing work reported last year, the passage of the CO_2 beam was clearly visible as a bright-red-to-white spot slowly moving over the surface. In this scheme, as described in figure 3 and table 1, the part was not luminous in treatment #1 and only slightly luminous as a dull red spot rapidly moving over the part in treatments #2 and #3, as viewed in a darkened room.

Sample Handling

In all cases, the parts were 1.52-in.-diameter, 0.25-in.-thick Suprasil II discs mechanically polished by Zygo Corp. to a "superpolish." Prior to CO_2 polishing, these parts were viewed in a Zygo interferometer and then washed in a warm 2% detergent solution in 18 megohm-cm filtered water. The parts were scrubbed with a soft brush and periodically checked for a "water break" by rinsing briefly under pure running water. When the parts showed water uniformly wetting the surface, the part was given a final quick brushing in the detergent solution and rinsed again under running pure water. It typically took 10 min. of soaking to pass the water-break test. The parts were then put into a container of hot pure water for ~ 10 min. to assist in the removal of detergent from the part. To retard evaporation, the parts were cooled by another rinsing under cool pure water. The parts were then blow dried with a jet of pure, filtered nitrogen gas. The water was primarily removed as droplets rather than by evaporation. The entire process described above was performed in a class-100 clean area. In addition, the containers used to store the parts were cleaned and blown out with pure, filtered nitrogen just prior to use.

The parts were then transported to the CO_2-laser exposure area. Unfortunately, while the raster mirror and sample were contained in a 1-m^3 plexiglas box, the air was not filtered; in some cases, it was possible to see particulate contamination on the surface of the part become luminous as the beam passed over it, even at very low laser intensities. For CO_2-laser treatment, the part was supported in a holder consisting of two 2-in.-long, 1/8-in.-diameter horizontal refractory rods placed ~ 1-in. apart. The surface of the part was nearly normal to the beam, with the reflected beam being incident on a carbon block. Finally, the part was allowed to cool ~ 15 min. and then placed in its container.

After CO_2-laser treatment, the parts were viewed (1) in a Zygo interferometer to determine the change in surface figure, (2) in a polariscope to qualitatively observe the change in strain, and (3) through a Nomarski and total internal reflection microscope to observe qualitative surface changes. The parts were handled carefully and, therefore, were not cleaned prior to damage testing. The time period between CO_2-laser treatment and damage testing varied from 1 to 5 days. Some parts have been tested up to one year after treatment with the expected results, and it is felt that the CO_2-laser-polished surface is quite stable. Therefore, except for possible contamination, the surfaces were all considered to be fresh.

Damage Testing

The damage tests reported in this paper were all performed with a Holobeam Series 500QT YAG laser. All data were gathered with a full-width, half-maximum pulse length of 9.0 nsec. The TEM_{00} Gaussian beam was first passed through a pair of rotatable prism attenuators and then focussed by a 162-mm focal length diffraction-limited lens. The calculated spot size was selected by choosing the appropriate laser-to-lens distance. Two spot sizes were used, 26 and 16.5 μm. (The spot size used here is the distance from the beam center to the point where the intensity has fallen to $1/e^2$ of its beam center intensity.)

Damage was assumed to have occurred when a flash was seen. This was verified on several samples; in all cases, a pit was present where a flash was observed, and no pit was present when no flash was seen.

Two types of data are shown in this paper, referred to here as scheme A and scheme B. In scheme A, a spot size of 26 μm was used throughout. Initially, the entrance surface damage threshold of washed, Zygo-superpolished Suprasil II was determined. This number varied significantly over several parts, but a value of I_s = 34.3 GW/cm^2 peak on-axis intensity was chosen as a reference intensity for the remainder of the testing. While this value was later determined to be on the high side of the median damage threshold of Zygo-polished Suprasil II, it was chosen to be representative of bare, mechanically polished fused silica.

The damage resistance of the entrance surface of various parts was then tested by first exposing the entrance surface to 100 shots at I_s and then to 100 shots at 1.8 I_s. These tests were one-on-one exposures on a 0.5-mm grid. This technique was chosen because with CO_2-polished parts it appeared as though the density of sights where damage ultimately occurred was sufficiently small that a 26-μm spot did not sample similar sites on every shot. The intensity of 1.8 I_s was chosen because this was the maximum intensity available at a 26-μm spot size.

In scheme B, the spot size was decreased to 16.5 μm. The beam energy required to damage the part 50% of the time was determined for various depths, starting well behind the entrance surface and

extending forward through the entrance surface and into the air. This was done using a 162-mm focal length lens. With this lens, the beam on-axis intensity dropped to 50% of the maximum beam waist intensity at ±0.8 mm along the beam axis. The sample was moved 0.25 mm farther from the lens for each successive threshold determination. In the normal case of a mechanically polished part, the surface damage threshold is well below the bulk threshold, and the beam energy required to cause damage decreased as the beam waist neared the entrance surface. The beam energy was a minimum with the beam waist at the surface. As the beam waist moved out into the air in front of the part, the required beam energy increased since the beam intensity on the sample surface was less because of the defocussed beam condition. In the case of a part with a surface threshold the same as the bulk threshold, required beam energy would not change as the waist moved toward the surface and would remain essentially constant until the waist moved out of the material, at which point the required beam energy would increase.

Experimental Results

Figure 4 shows the results of damage measurements, using scheme A, on a Zygo mechanically polished part, on an argon ion-milled part, and on three CO_2-laser-polished parts. The results are presented as number of sites which did not damage out of 100 exposures to either I_S or 1.8 I_S.

The mechanically polished part is shown as a nominal 50% damage rate. The value of I_S was chosen by damage testing a part in the usual manner. Five additional parts were tested by exposing 33 sites to I_S and another 33 sites to 1.8 I_S. A 0.5-mm^2 grid was used. The results are shown in table 2.

Table 2. Number of sites which damaged out of 33 exposures.

Part No.	I_S	1.8 I_S
Z1-46	22	33
Z1-47	9	29
Z1-48	24	33
Z1-49	20	33
Z1-50	18	33

Only one part, Z1-47, failed fewer than half the time at I_S, and all the 1.8 I_S exposures caused damage except, again, for part number Z1-47, which failed 29 out of 33 exposures. Table 2 indicates, first, that I_S is a bit on the high intensity side. The second point of interest is that, at 1.8 I_S, most mechanically polished parts failed on every exposure.

The second part, shown in figure 4, was argon ion-milled in an ultrahigh vacuum system using a 2-kV dc gun of the type used for cleaning parts for subsequent low energy electron diffraction studies. The amount of material removed varied from 0.3 to 0.75 μm across the region tested. The removal was greatest in the center of the part and less toward the edges. There was no tendency, however, of the part to damage less in the central region where removal was greatest. The point to be noted is that the surface damaged on only 9 of the 100 sites irradiated at I_S and on slightly more than half of the sites irradiated at 1.8 I_S.

The next three samples are CO_2-laser-polished parts. They were polished according to the schedules shown in table 1. In figure 4, the samples are labeled with the highest CO_2-laser power used to process the part. In table 1, these are called #1, #2, and #3. As can be seen in figure 4, the lowest power treatment shows some improvement over the mechanically polished part. The greatest improvement is in the last two samples, with the 225-watt sample showing no damage at either I_S or 1.8 I_S. Thus, the treatments of 175 watts and 225 watts bracket the range over which a CO_2-polished surface shows a dramatic improvement in damage resistance. A second part similar to the 200-watt sample was made ~ 10 days after the set shown in figure 4 was made. It showed 91 sites surviving at I_S and 68 surviving at 1.8 I_S.

In previous work, we showed that the surface of CO_2-polished fused silica underwent a change, as seen in total internal reflection microscopy (TIRM), from a highly decorated surface, in the unpolished case, to a featureless surface present after CO_2 polishing. Figure 5 shows this effect. In figure 6, we show a similar pair of TIRM photographs of exactly the same area on a 200-watt sample, which shows that it is not necessary to CO_2 polish the part to the point where surface features disappear. The surface has retained essentially all of the mechanical polishing marks which were visible prior to CO_2-laser polishing. While figure 6 consists of a pair of TIRM photographs for a 200-watt sample, a similar lack of change in TIRM appearance is present in the 225-watt sample.

CO_2-laser polishing can result in residual strain in the substrate. Figure 7 shows three photographs of the three laser-polished parts discussed in this paper. These are the sample appearances as seen through a polariscope. It is clear that the 175-watt sample shows little residual strain, while the 225-watt sample shows the most strain. The CO_2-polished surface has gone into tension, as will be discussed in a later section. In spite of the residual strain present after polishing, the optical path length through various regions of the sample has not been seriously disturbed. This can be seen in figure 8, where the interference pattern exists between the two surfaces of the part. In the 225-watt sample, the part is somewhat disturbed; in the 175- and 200-watt cases, it is essentially unchanged.

The results from scheme B damage testing are shown in figure 9, where the beam energy required to damage the sample 50% of the time is shown as a function of sample position. The 0.0 position corresponds to the sample entrance surface being positioned at the beam waist, while the negative position has the beam waist in front of the sample, and the positive position has the beam waist in the bulk of the sample. Data from two samples are shown in figure 9, a mechanically polished sample and a CO_2-laser polished sample (a 225-watt sample). As stated earlier, the calculated spot size was 16.5 μm.

The data from the mechanically polished sample show that when the beam waist is in the bulk of the sample, the beam energy is constant with position, since the bulk is being damaged. As the beam waist is brought close to the sample surface, the energy required to damage the sample is lower. When the beam waist is at the sample surface, the beam energy is a minimum. As the beam waist is moved outside the sample, the beam energy goes up since the beam intensity at the sample surface is less.

The data from the CO_2-polished sample are also shown in figure 9. Here the same bulk behavior is seen as for the mechanically polished part, with 4.5 mJ required to cause bulk damage. However, as the beam waist is positioned nearer the entrance surface, no decrease in required beam energy is seen. When the waist is outside the sample, the required beam energy increases. These data are consistent with the CO_2-polished surface being at least as damage resistant as the bulk. This is in contrast to the mechanically polished part, where a large dip is seen in the data near the surface of the sample due to a weaker polished surface.

Discussion

Figure 4 clearly indicates that proper CO_2-laser polishing does improve the damage resistance of fused silica surfaces at 1.06 μm. In particular, the 225-watt sample showed no damage in 100 exposures at I_S and 100 exposures at 1.8 I_S, while the mechanically polished parts, shown in table 2 and figure 4, damaged on over one-half the exposures at I_S and on nearly every exposure at 1.8 I_S. Large-spot damage tests reported last year on single-pass processed parts showed similar results; that is, a higher damage resistance than the mechanically polished parts. The small-spot tests reported here are consistent with those results.

Figure 8 shows the uniformity of optical path length for the three CO_2-laser polished parts. Only in the case of the 225-watt part is there noticeable disruption in uniformity, while the 200-watt part, which also showed substantial improvement in performance, shows very little change in uniformity. These results are encouraging in that it appears as though the figure need not be destroyed to obtain improved damage resistance. Unfortunately, the front surface figure is not as uniform as might be indicated by figure 8. This is due to bowing of the substrate caused by strain.

The presence of strain is indicated not only by the surface figure but also by figure 7. The source of this strain is shown in figure 10. Figure 10(a) shows a part under CO_2-laser exposure conditions. The part is hottest on the exposed face since it is being heated in a part of the infrared spectrum where the 1/e penetration depth is only a few micrometers and where it is being cooled on all sides both by radiation and by convection. Under these conditions, there will be a nonuniform temperature distribution. The region near the treated face will be hottest, will have expanded more, and will, in effect, be attempting to bow the part. Figure 10(b) shows what can happen if the front surface of the part is hot enough to flow. In this case, the hot face will expand outward, sliding over the cooler substrate. This results in some reduction of the bowing stress being applied to the part. The treated surface is now in quasi-equilibrium with the substrate.

When the CO_2-laser beam is removed, the sample will cool and the entire part will contract. However, the treated surface, which was the hottest, will contract the most. Since this surface was in quasi-equilibrium with the substrate at a high temperature, the cooled treated surface will now be in tension. This is shown in figure 10(c), where the part bowed in a manner which is seen after CO_2 treatment. While this bowing is a problem in the present treatment technique, a treatment technique suggested at the end of this section may avoid the problem.

The question of why CO_2-laser-treated parts are damage resistant remains. The present study and the earlier work reported last year indicate that sublimation is taking place. In all three parts shown in figure 4, on the order of 0.25 to 0.5 μm of material has been removed by sublimation. This will remove some of the damage due to mechanical polishing, along with impurities imbedded in the polished surface. This may account for some of the improvement, particularly in the 175-watt sample. However, it is felt that this is not the primary mechanism. Figure 4 also shows data taken on a very carefully ion-milled part which has had at least as much surface material removed. It is clearly superior to mechanically polished parts, but it is not as good as the 200- or 225-watt samples. In addition, earlier large-spot tests on this part, performed at LLL, revealed that the part damaged at a lower incident flux and that the damage occurred at decorations present because of earlier mechanical damage.

The polariscope photographs, figure 7, show that the residual strain is nearly zero in the 175-watt sample, but that the 200- and 225-watt samples have more strain. The presence of strain is indicative of material flow. Regardless of the bowing under laser heating, no residual strain will be present in the cooled part if no material flow has occurred. The 175-watt sample evidently did not reach a temperature high enough to cause significant flow under the stress present. The other two samples did experience surface flow, with the resulting strain (fig. 7). The word "flow" must be understood in the context of fused silica. Even at very high temperatures, silica is very viscous, and, at the temperatures reached in this work, flow is not liquid-like but rather a non-Hooke's-law behavior! The lack of liquid-like flow is seen in figure 6, where the surface quality is unchanged. Previous work in TIRM microscopy [2] indicates that TIRM is sensitive to strictly surface-air interface structure and not microcrack structure in the substrate.

The much improved damage performance of the 200- and 225-watt samples and the presence of flow in these two samples strongly suggest that microcrack healing is the cause of an improved damage threshold in these samples. Such a conclusion is not inconsistent with figure 6, which shows surface structure only. Fused silica is sufficiently viscous that even at very high temperatures surface features are retained.

The sample surface temperature has not been determined. The temperature at which fused silica will permanently deform under stress is stated to be ~ 1025°C. This surface temperature is evidently bracketed by the 175- and 200-watt samples. In the future, these results suggest that one should uniformly heat the sample to near this temperature before beginning laser processing. In this way, one should be able to eliminate the stress problem since the bowing shown in figure 10(a) would not

be present, and the tendency for outward flow of the laser-treated surface would be minimized. Silica is sufficiently viscous that one would hope to retain the original physical shape of the treated part by this process.

Conclusion

We have demonstrated that proper CO_2-laser polishing of fused silica surfaces can increase the damage resistance of these surfaces to small-spot, 9-nsec, 1.06-μm radiation. The laser damage data shown in this paper demonstrate that, in fact, the CO_2-polishing surface is at least as damage resistant as the bulk material.

The dramatic improvement in damage threshold with the onset of SiO_2 material flow is taken as evidence that microcrack closure is the mechanism responsible for the improved threshold. There is also evidence in the data presented in this paper that removal of surface material by sublimation improves the damage threshold but not to the extent seen in the "softened" samples where material flow occurred. The onset of flow is detected by the presence of residual strain in the treated sample.

Data were also shown which indicated that the surface figure may not be disrupted by proper treatment. Finally, it was suggested that uniform preheating of the sample should be used to reduce the occurrence of strain.

References

[1] Temple, P. A., Milam, D., and Lowdermilk, W. H., CO_2-laser polishing of fused silica surfaces for increased laser damage resistance at 1.06 μm, NBS Special Publ. 568, 229 (1979).

[2] Temple, P. A., An improved dark-field-like surface inspection technique using total internal reflection, SPIE Los alamos Conference on Optics '79, 190, 44 (1979).

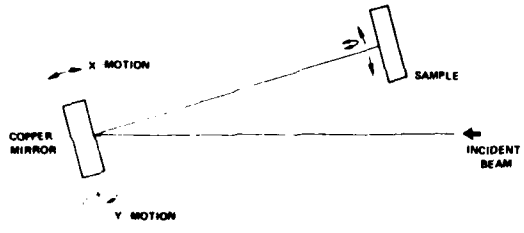

Figure 1. Schematic diagram of the CO_2-laser polishing apparatus. The incident unfocussed laser beam is reflected by a gimballed copper mirror onto the fused silica sample at near-normal incidence. The sample is supported in air.

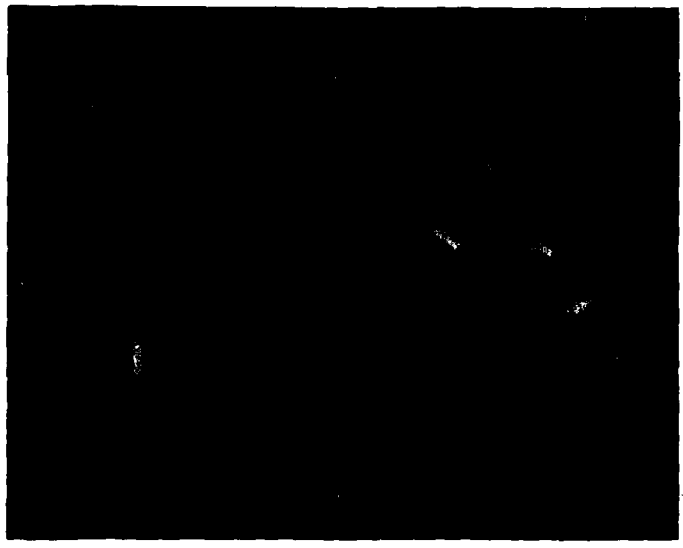

Figure 2. A photograph of the gimballed mirror shown schematically in figure 1 and of the microprocessor-based motor controller.

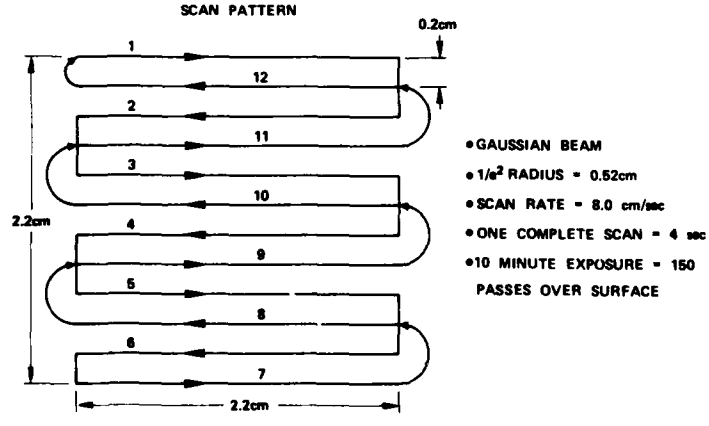

Figure 3. The raster scan pattern used to treat the 1.5-in.-diameter fused silica samples. Also shown are the beam parameters used in CO_2-laser treatment.

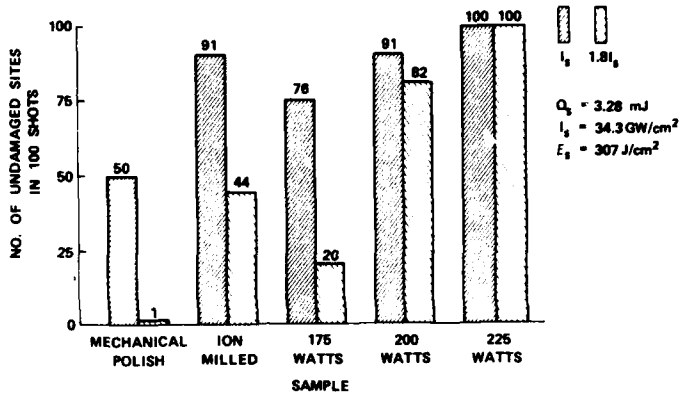

Figure 4. Bar graph showing the number of sites which survived 100 shots at each of two intensities on five samples. The shots were illuminated on a 0.5-mm^2 grid. The lower intensity, I_S, is the nominal damage threshold for mechanically polished silica surfaces, and the higher intensity is 1.8 I_S. The spot size was 26 μm. The mechanically polished part is shown to have survived 50 shots at I_S and one shot at 1.8 I_S (see table 2 for more detail). The ion-milled part had ~ 0.5 μm removed by argon-ion removal using an ultrahigh vacuum, 5-kV dc gun. The three remaining samples were CO_2-polished parts which were treated as per table 1. The 225-watt sample (#3, table 1) survived all 200 exposures at the two test intensities.

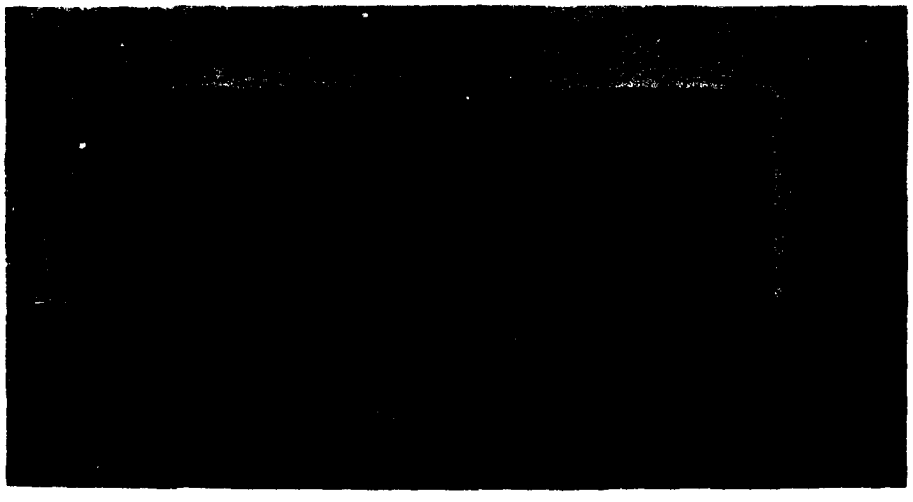

Figure 5. Two TIRM photographs showing the glazing effect observed on a CO_2-polished surface in previous work. TIRM is sensitive to sharp surface features such as nicks.

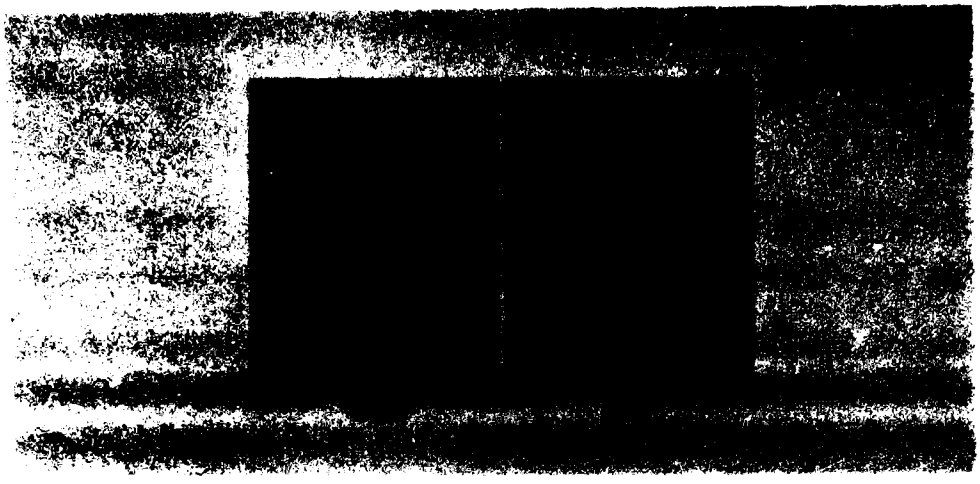

Figure 6. Two TIRM photographs showing the lack of glazing in parts processed by the present technique. The part shown is a 200-watt sample, but the 225-watt sample showed a similar lack of glazing after treatment. As noted in the text, TIRM is responding to surface and not subsurface microcracks.

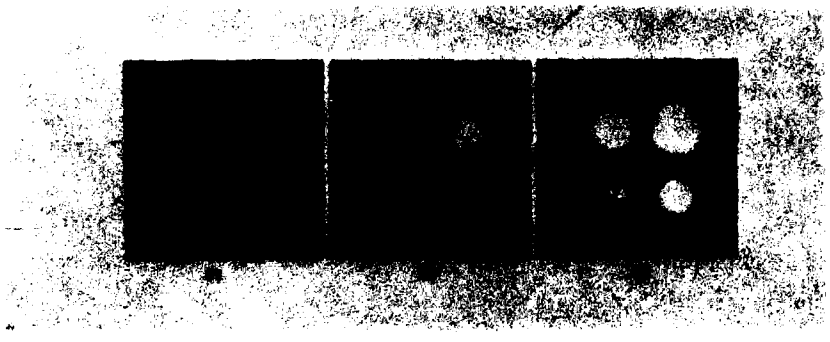

Figure 7. The residual strain present in three parts processed as per table 1. These photographs are the appearance as seen through a polariscope. The presence of strain is taken as evidence of material flow during CO_2 processing.

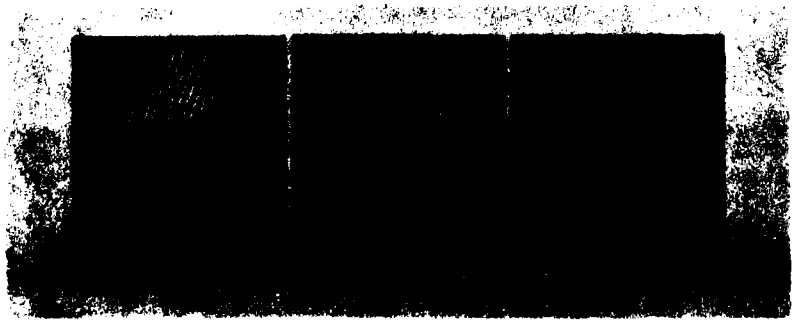

Figure 8. The transmissive figure or bulk figure generated by interference between the front and rear surfaces of three parts produced as per table 1. The 225-watt (#3) sample shows some disruption.

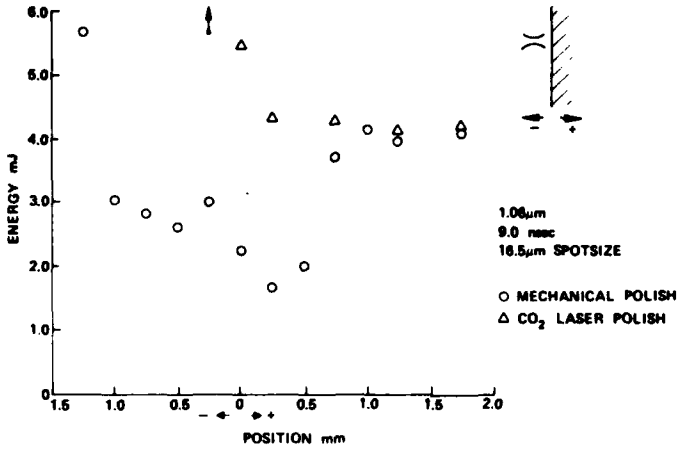

Figure 9. The beam energy required to damage two silica parts as a function of beam waist position. The mechanically polished part shows a dip in the vicinity of the surface which is due to the damage prone, mechanically polished surface. The CO_2-polished part (a 225-watt sample, #2, table 1) shows no such dip, indicating that the surface is at least as damage resistant as the bulk.

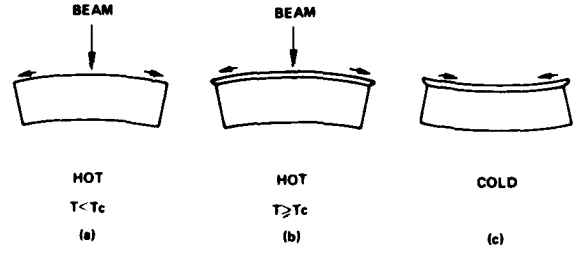

Figure 10. A schematic representation of the mechanism for producing strain in a CO_2-laser processed sample. In (a) is shown the part being irradiated from above. The result is a nonuniform temperature distribution causing the hot upper surface to bow due to greater expansion. In (b) a critical flow temperature, T_C, has been exceeded causing the irradiated surface to flow outward. When the part is cooled (c), the irradiated surface will go into tension. Such residual strain will not be present if no flow has occurred.

The author pointed out that the laser irradiated material is so viscous that Talystep tracing of rough areas are unchanged by irradiation. One questioner reported that on the basis of mass loss measurements material loss appears to be entirely by sublimation. Also for large spot experiments the threshold improvement was about 25%, significant but less than the factor of two obtained in small spot experiments at NWC. Another questioner suggested that microcrack healing may be the mechanism for the improved thresholds observed. It was pointed out by a third questioner, however, that isostatic hot pressing of glass does not increase the damage threshold. Finally a fourth questioner suggested that a low expansion coefficient was important in the process, e.g., BK7 glass breaks when the process is used, but not fused silica.

WAVELENGTH AND TEMPERATURE DEPENDENCE OF THE ABSOLUTE REFLECTANCE OF METALS AT VISIBLE AND INFRARED WAVELENGTHS*

D. L. Decker and V. A. Hodgkin
Michelson Laboratory, Physics Division
Naval Weapons Center, China Lake, California 93555

This paper presents the wavelength dependence of Ag, Cu, and Al from 4000 Å to 10 μm wavelength. An intercomparison of data is made for surfaces prepared with a variety of techniques, including vacuum evaporation and diamond single-point machining. Briefly described, also, are experimental techniques and apparatus developed at the Naval Weapons Center for measuring temperature-dependent changes in the near-normal incidence reflectance of a sample to a precision of a few parts in 10^5. Reflectance results obtained from this instrument are presented for films and bulk material over the same wavelength range as above at temperatures from 270 to 450 K. The sample and reference surfaces were protected in ultrahigh vacuum for these measurements.

A theoretical interpretation of results is presented, including both inter- and intraband electron transition effects, as well as extrinsic surface roughness effects. Of much practical interest for laser mirror applications, especially for pulsed mode operation, is the behavior of many metals upon temperature cycling, including hysteresis and time-dependent "annealing" behavior. Similar effects are also observed in both transport and thermal properties and are generally described under the name "premelting effects."

The data presented in this paper are of immediate engineering value in computing the performance of optical systems whose components necessarily operate at temperatures other than room temperature. It is also hoped that it will stimulate theoretical interest in examining some of the subtle and poorly understood dispersion effects such as those seen in the near-infrared in silver.

Key words: Aluminum; copper; Drude theory; infrared; reflectance; silver; surface roughness; temperature dependence.

Introduction

In an increasing number of applications, optical components are used at temperatures other than at room temperature. It is essential that characterization be made at the actual operating temperature since in many cases a relatively strong temperature dependence of the optical properties is present. The temperature dependence of the optical properties is also of fundamental interest and provides additional information concerning the dispersive mechanisms in the material.

This paper presents measured absolute reflectance as a function of temperature for diamond-machined surfaces of OFHC copper and high-purity electroplated silver as well as an ultrahigh vacuum (UHV), high-purity aluminum film evaporated onto supersmooth polished fused quartz. Data are presented at seven wavelengths from 0.6 to 9.0 μm over the temperature range from -26°C to +160°C. The experiment consists of the measurement of the reflectance R(T) of a sample at temperature T relative to that of a reference mirror R_0 held at room temperature. The absolute reflectance of the reference is inferred to be identical to that of a standard 1.52"-diameter sample which can be measured in the Naval Weapons Center absolute reflectometer [1][1]. The relative reflectance standard and the 1.52"-diameter sample are as nearly alike as possible: identical substrate material, polished in the same manner, and coated in the same vacuum deposition and substrate holder. The absolute reflectance of the sample is then calculated:

$$R(T) = [R(T)/R_0]R_0$$

The absolute reflectance of the 1.52"-diameter standard is known to an accuracy of ±0.001, and it is assumed that the standard used in the relative reflectance measurement is likewise limited. The accuracy of the relative reflectance measurement itself is ±0.0001 [2]. During the relative reflectance measurement, both the sample and reference are protected by UHV, $P < 10^{-8}$ Torr in the present measurement series, except at the highest temperatures. Figure 1 schematically illustrates the essentials of the relative reflectometer. The mirror images the exit slit of the monochromator SL on the sample/reference S. The specularly reflected beam is picked off by M_2 and sent either to a thermocouple detector D_1 or to a photomultiplier D_2, depending on the wavelength of operation. The autocollimator AC is used to align the sample and reference surfaces which are alternately moved into position behind a window in the vacuum wall of the sample/reference container.

Theory

The infrared optical dispersion in metals is a direct consequence of the interaction of the incident electromagnetic fields with the "free" electrons of the metal. Near and above the Debye temperature, damping occurs primarily from electron-phonon collisions, and the primary temperature dependence of the optical absorption arises from the temperature dependence of the phonon population [3]. The real ε_1 and imaginary ε_2 parts of the complex dielectric constant of a free electron metal can be written:

*Work sponsored by the Defense Advanced Research Projects Agency, Office of Naval Research, and Air Force Weapons Laboratory.
[1]Figures in brackets indicate the literature references at the end of this paper.

$$\varepsilon_1 = 1 - \omega_p^2/(\omega^2 + 1/\tau^2) + \varepsilon_s$$

$$\varepsilon_2 = \omega_p^2/(\omega^2 + 1/\tau^2)\omega\tau \quad , \tag{1}$$

where ω_p is the plasma frequency and τ is a phenomenological damping parameter. ε_s is the contribution from higher energy electron excitations. The normal incidence reflectance can be simply computed from Fresnel's law:

$$R = |(\tilde{\varepsilon}^{\frac{1}{2}} - 1)/(\tilde{\varepsilon}^{\frac{1}{2}} + 1)|^2 \quad . \tag{2}$$

For the specific metals and for the range of wavelengths reported in this paper, $(\omega_p\tau)^2 >> (\omega\tau)^2 >> 1$. Approximate expressions for ε_1 and ε_2 can then be derived from eqs. (1,2) and the wavelength-independent reflectance value computed:

$$R = 1 - \frac{2}{\omega_p\tau} \quad . \tag{3}$$

From the elementary free electron model, the plasma frequency can be computed (cgs units):

$$\omega_p^2 = \frac{4\pi ne^2}{m^*} \quad , \tag{4}$$

where n is the electron concentration, e is the electron charge, and m^* is an effective mass. A relationship between the dc electrical conductivity σ and the relaxation time is given by the Lorentz-Sommerfeld expression:

$$\tau = \frac{m^*\sigma}{ne^2} \quad . \tag{5}$$

Over a wide range in temperature above the Debye temperature for most metals, $\sigma \sim 1/T$, and hence τ is proportional to 1/T [4]. From eq. (3), the derivative dR/dT is obtained:

$$\frac{dR}{dT} = -\frac{1}{\omega_p\tau} \cdot \frac{2}{T} \quad . \tag{6}$$

Note that this expression gives a wavelength- and temperature-independent value of dR/dT, since τ implicitly contains an inverse temperature dependence. Table 1 gives room temperature values of ω_p, τ, R, and dR/dT and Debye temperature θ_D for the metals Ag, Cu, and Al.

Table 1. Values of Debye temperature θ_D, relaxation time t, plasma frequency ω_p, reflectance R, and derivative of reflectance with temperature dR/dT for silver, copper, and aluminum. Values of τ and ω_p are for room temperature.

Metal	θ_D (°K)	τ (sec)	ω_p (sec^{-1})	R	dR/dT (/°C)
Ag	220	3.65×10^{-14}	1.30×10^{16}	0.9958	-1.4×10^{-5}
Cu	315	2.73×10^{-14}	1.63×10^{16}	0.9955	-1.5×10^{-5}
Al	396	0.80×10^{-14}	2.23×10^{16}	0.9888	-3.7×10^{-5}

The values of τ are obtained from nonoptical measurements reported in the literature, and values of R and dR/dT are computed from eqs. (5,6), respectively. Additional damping occurs from collisions with crystalline lattice defects, impurity atoms, or with microtopographical structures on the free surface of the metal. The extrinsic effects just listed tend to provide nonreproducible time- and temperature-dependent dispersion. Such effects are observed in the data presented here. Similar effects are also observed in other transport or heat capacity measurements and are poorly understood [4].

Experiment

Figure 2 is a plot of experimental absolute reflectance data at 300 K for high-purity copper surfaces prepared in three different ways over the wavelength range from 0.5 to 20 μm. In the far infrared, the agreement in reflectance values is well within experimental uncertainty. In the near infrared and visible, the reflectance of the diamond-turned surfaces is as much as 0.5% lower than the corresponding data for either the UHV-evaporated or sputtered films. This is believed to be a surface roughness effect. This extrinsic absorption has been previously discussed [5] and is much more noticeable in the silver data later in this paper. The sharp drop in reflectance below 1 μm is a non-Drude effect and is due primarily to the tail of an interband transition $L_3 \rightarrow F.S.$ [6]. Also contributing to the visible/near infrared reflectance drop is an absorption due to lattice disorder which can be modeled by a second carrier. This is also discussed in greater detail in the silver reflectance section.

In figure 3 the absolute reflectance of a diamond-turned OFHC copper surface at 300 K is compared with predictions of the Drude model and with data taken on the same sample at 460 K and after returning to 300 K. The irreversible changes in reflectance are largest in the near infrared and visible, presumably as a consequence of changes in bulk or surface structure and concomitant changes in the extrinsic absorption which is related to that structure. Such "annealing" effects would be expected to be largest in this precise region. The time- and temperature-dependent reflectance behavior at 0.6, 1.4, and 9.0 μm is shown in figure 4, where again the largest irreversible effects are seen at 0.6 and 1.4 μm. The reversible effects in the near and far infrared are well explained by the Drude

model, as shown in figure 5. The experimental values of dR/dT are obtained from reflectance data taken over a 20°C increment at 300 K. For the far infrared, the measured values of dR/dT are considerably larger than the Drude predicted values, but, after "annealing" to 460 K, the data are in excellent agreement with theory. For the near infrared, values of dR/dT are obtained which are smaller than the Drude model prediction and at 1 μm, in fact dR/dT ≈ 0. In the visible, the temperature dependence of the interband transition $L_3 \rightarrow$ F.S. yields values of dR/dT at 0.6 μm, an order of magnitude larger than the Drude values.

The absolute reflectance of silver has a wavelength dependence much like that of copper, although the interband transition $L_3 \rightarrow$ F.S. is at higher energy, and hence the reflectance in the visible is higher [6]. As illustrated in figure 6, the absolute reflectance of both evaporated and sputtered thin films can be essentially equivalent over most of the spectral range from 0.4 to 20 μm [5]. Diamond-turned electroplated silver tends to have a significantly lower reflectance, especially in the visible where the discrepancy can be as large as 1.5%. This variation is thought to be primarily a surface roughness effect. The drop in reflectance in the visible in both silver and copper is only qualitatively understood. The transition $L_3 \rightarrow$ F.S. is at higher energy, and the free electron dispersion is weak in this region. It is possible, however, to fit the reflectance drop with a two-carrier model, in which one carrier has relaxation time and concentration very nearly identical to that indicated in table 1, and a second carrier has a relaxation time five times smaller and a concentration twenty times smaller. The results of this model are shown in figure 7, together with published data for UHV-evaporated silver [7]. Both single- and two-carrier Drude results are also plotted. The second carrier in this model could be interpreted as corresponding to a carrier characteristic of the relatively disordered grain boundary regions of the film. The sign of dR/dT for Drude reflectance is necessarily negative, and the magnitude for the two-carrier model not significantly different from the single-carrier version.

Figure 8 indicates the effect of temperature cycling on a sample of diamond-turned electroplated silver. In the far infrared, all room temperature reflectance values are similar, the 150°C values lower by the expected amount as a result of Drude temperature dependence. However, in the near infrared, very large irreversible changes in reflectance have occurred as a consequence of the cycle in temperature to 150°C. Subsequent examination by Nomarski and two-stage replication transmission electron microscopy indicate that the sample has recrystallized. The surface roughness measured by total integrated scatter increased from an initial value of 28 to 118 Å rms. If the near infrared extrinsic absorption were due to damping of electrons from collisions at grain boundary imperfections, it would be expected that this absorption would decrease after sample recrystallization which resulted in an increase in crystallite size. Just the opposite, in fact, did occur, and hence one concludes that the absorption is related to the surface roughness of the sample. Such a correlation, of course, has long been recognized in silver in the ultraviolet, in association with surface plasmon excitation [8]. An absorption of much smaller magnitude has been observed experimentally in the near infrared as well [9].

It has been long proposed that the anomalous skin effect modification of the Drude theory can account for at least some of the infrared absorption observed on rough metal surfaces [9]. Since the free electron model is strictly valid only from ~ 1 μm to longer wavelength, the anomalous skin effect modification likewise can only apply to this region. Using nonoptical parameters ω_p and τ, the anomalous skin effect for silver predicts a nearly wavelength-independent reflectance from 1 to 10 μm with a slight drop near 10 μm for specularly reflected electrons and a slight increase for diffusely reflected electrons. For diffusely reflected electrons, an additional absorption of approximately 0.0035 above the simple Drude model is predicted. In the present case, it is observed that at 3.8 μm and longer wavelengths, a drastic roughening of the surface has no measurable effect, but at shorter wavelengths, a very large effect. At 1 μm, the change in absorption is ~ 0.02, almost an order of magnitude larger than the maximum predicted from the anomalous skin effect theory.

Another theory has been previously suggested to account for this very large absorption [5]. In its present form, the theory is crude but does provide a basis for at least qualitative comparison. The absorption from this theory arises from the free electron dispersion in the metal, enhanced from the usual situation by a "polarization resonance" which greatly increases the local field. The resonant effect occurs in the rough structure of the surface. The effect is not size but rather shape dependent, assuming that the spatial extent of a given polarizable element is much smaller than the wavelength of the exciting radiation. The fractional change in reflectance ΔR/R is given by the expression:

$$\frac{\Delta R}{R} = -\frac{32kap}{3}\,\frac{\epsilon_2(L-1)}{[L(\epsilon_1-1)+1]^2+L^2\epsilon_2^2} \quad , \tag{7}$$

where k is the wave vector magnitude of the incident light, a is a size parameter, p is a fractional coverage factor, and L is the depolarization factor for a given polarizable surface element. For a oblate spheroid, $L \cong \pi a/4b$, where a and b are the semiminor and semimajor axes, respectively. This expression is valid in the limit $a/b \ll 1$. The ratio a/b is crudely the "average" slope of a spheroid surface. On any real surface, a distribution in slope will be found D(L), and hence the mean fractional change in reflectance is

$$\langle \Delta R/R \rangle = \int_0^\infty D(L)(\Delta R/R)\,dL \quad . \tag{8}$$

The temperature dependence is simply computed:

$$\frac{dR}{dT} = \frac{dR_{DRUDE}}{dT} - \frac{d\langle \Delta R \rangle}{dT} \quad . \tag{9}$$

Using eqs. (7,8) and an empirical slope distribution (fig. 9), the previously plotted UHV silver data (fig. 6) can be very accurately modeled (fig. 10). The empirical slope distribution contains slopes considerably steeper than observed by surface profilometer measurement [10]. However, only a very small fraction of the surface (~ 0.001) need be covered by such structure, so no real inconsistency

exists. Interestingly, depending upon the slope distribution and wavelength, both positive and negative values of dR/dT can be obtained from the resonant absorption model.

From the reflectance data plotted in figure 8 together with much additional data from other temperatures, the dR/dT data plotted in figure 11 are obtained. This data is accurate to at least $\pm 0.5 \times 10^{-5}$/°C, depending upon wavelength. At wavelengths longer than 2.7 μm, the measured values both before temperature cycling and after are essentially in agreement with the Drude model prediction of -1.4×10^{-5}/°C. At shorter wavelengths, the discrepancies lie far outside of experimental uncertainty and are not simply described. For example, the effect of temperature cycling at 1.4 μm is to increase dR/dT; whereas, at 1.0 μm, it results in a very substantial decrease, almost to the Drude value. At 0.8 μm, a positive initial value becomes very large and negative after cycling. These kinds of effects are at least qualitatively within the range of behavior observed with different slope distribution functions and the resonant absorption model.

As a final result, the temperature dependence of the UHV-evaporated aluminum reference mirror was measured. Figure 12 is a plot of previously published UHV absolute reflectance data [11], together with Drude reflectance values. The agreement between the experimental data and the Drude reflectance computed from nonoptical data is in excellent agreement in the far infrared. However, at shorter wavelength, significant discrepancy occurs substantially as a consequence of the interband transitions at 0.8 μm. This reflectance dip was identified in work by Ehrenreich and Philipp [12] from Segall's [13] earlier electron energy band calculation as due to transitions around ω and Σ near k in the Brillouin zone. As shown in figure 12, the experimental values of dR/dT show a double-peaked behavior, from which it is tempting to surmise that there is correspondence with these peaks and the pair of transitions obtained from the energy band calculations. In any case, the observed structure is very non-Drude, with a peak positive value somewhat larger than the Drude magnitude, and at the negative minimum, a value 2.5 times larger than the Drude prediction.

Summary

This paper has provided experimental absolute reflectance and its temperature dependence near room temperature from the visible into the far infrared for diamond-machined silver and copper and UHV-evaporated aluminum films. The near infrared behavior in aluminum includes electron interband effects which yield non-Drude values of reflectance and dR/dT. Interestingly, the aluminum film examined is much more stable on temperature cycling than either the diamond-machined silver or copper. The near infrared behavior in silver and copper includes extrinsic surface and perhaps volume absorption effects that are both temperature and time dependent. The far infrared behavior of diamond-turned silver and copper as well as evaporated aluminum is very well predicted by the Drude theory.

References

[1] Bennett, H. E., and Koehler, W. F., J. Opt. Soc. Am. 50, 1 (1960).

[2] Decker, D. L., in High Energy Laser Windows and Mirrors, DARPA Semiannual Report #2, Project Order #2175, Sept. 1972-Mar. 1973, pp. 34-49.

[3] Sham, L. J., and Ziman, J. M., in Advances in Solid State Physics, Vol. 15, edited by F. Seitz and D. Turnbull (Academic Press, 1963), pp. 221-298.

[4] Borelius, G., in Advances in Solid State Physics, Vol. 15, edited by F. Seitz and D. Turnbull (Academic Press, 1963), pp. 2-48

[5] Decker, D. L., Bennett, J. M., Soileau, M. J., Porteus, J. O., and Bennett, H. E., Opt. Eng. 17, 2 (1978).

[6] Ehrenreich, H., and Philipp, H. R., Phys. Rev. 128, 1622 (1962).

[7] Decker, D. L., and Stanford, J. L., J. Opt. Soc. Am. 61, 679A (1971).

[8] McAlister, J., and Stern, E. A., Phys. Rev. 132, 1599 (1963).

[9] Bennett, H. E., Bennett, J. M., Ashley, E. J., and Motyka, R. J., Phys. Rev. 165, 755 (1968).

[10] Bennett, J. M., and Dancy, J. H., Surface profiling instrument for measuring statistical properties of smooth optical surfaces, *submitted to Applied Optics*.

[11] Bennett, H. E., Silver, M., and Ashley, E. J., J. Opt. Soc. Am. 53, 1089 (1963).

[12] Ehrenreich, H., and Philipp, H. R., Phys. Rev. 132, 1918 (1963).

[13] Segall, B., Phys. Rev. 124, 1797 (1961).

Figures

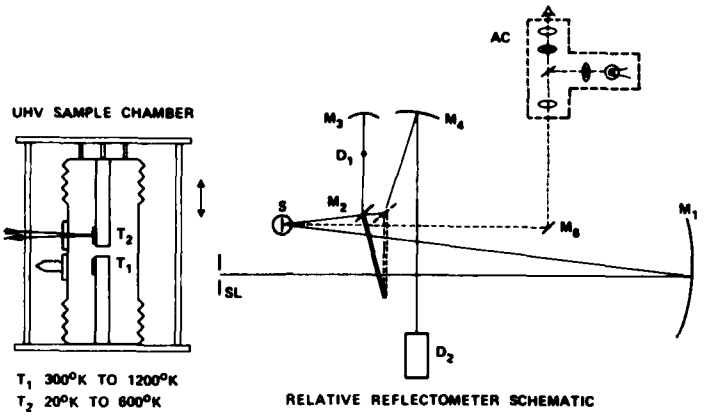

Figure 1. Optical schematic of the relative reflectometer for making temperature dependence measurements. Light from the monochromator exit slit SL is focussed by mirror M_1 onto the sample/reference S. Mirror M_2 picks off the specularly reflected beam and sends it to either M_3 or M_4 for focussing on the thermocouple detector D_1 or photomultiplier D_2, respectively. The autocollimator AC is composed of those parts inside of the dashed lines and is used to align the sample/reference surfaces.

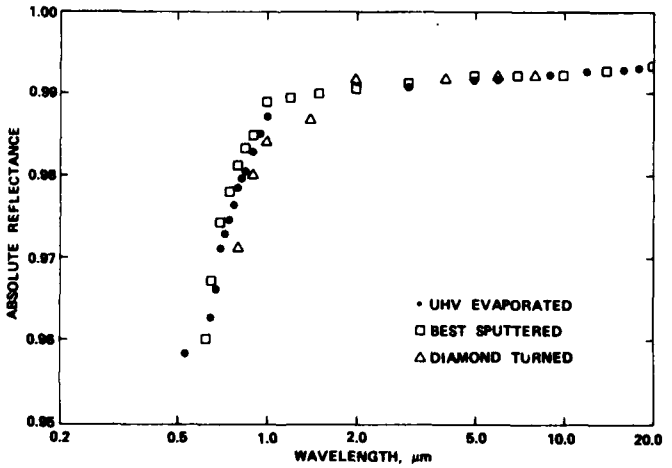

Figure 2. Spectral dependence of the absolute reflectance of copper surfaces prepared by ultrahigh vacuum thermal evaporation, ultraclean sputtering, and diamond turning.

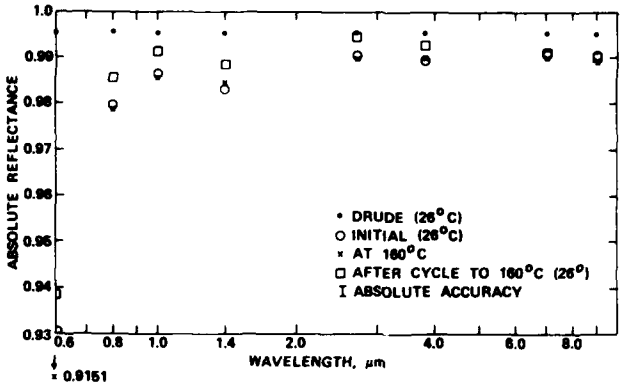

Figure 3. Spectral dependence of the absolute reflectance of a diamond-turned copper surface showing the effects of temperature cycling. Also shown are Drude reflectance values computed from nonoptical parameters (•).

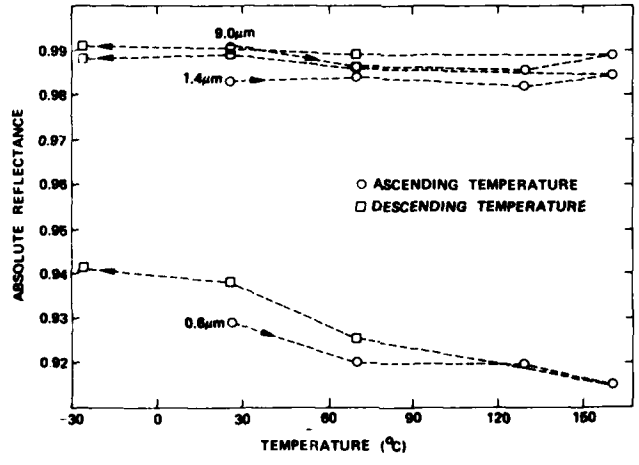

Figure 4. Absolute reflectance of a diamond-turned copper surface plotted as a function of temperature at 0.6, 1.4, and 9.0 μm wavelengths. Data with both ascending and descending temperatures are shown.

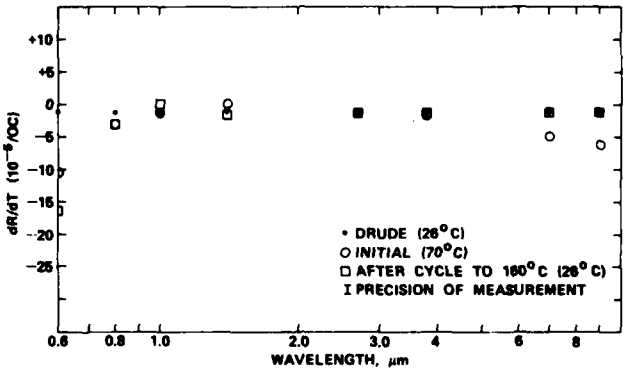

Figure 5. Spectral dependence of the derivative of the absolute reflectance with temperature for diamond-turned copper.

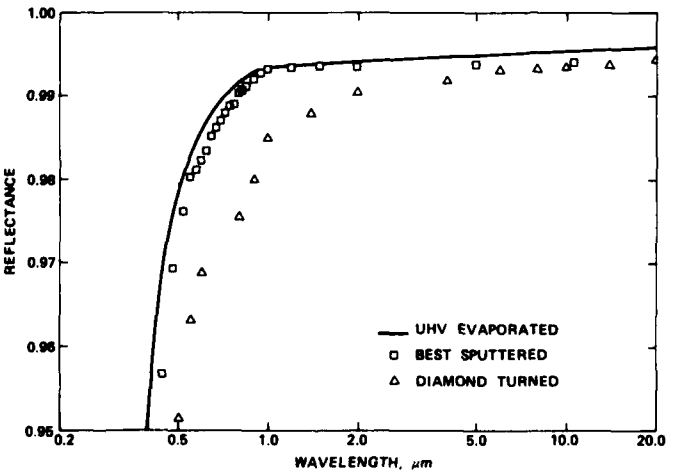

Figure 6. Spectral dependence of the absolute reflectance of silver surfaces prepared by ultrahigh vacuum evaporation, ultraclean sputtering, and diamond turning of electroplated silver.

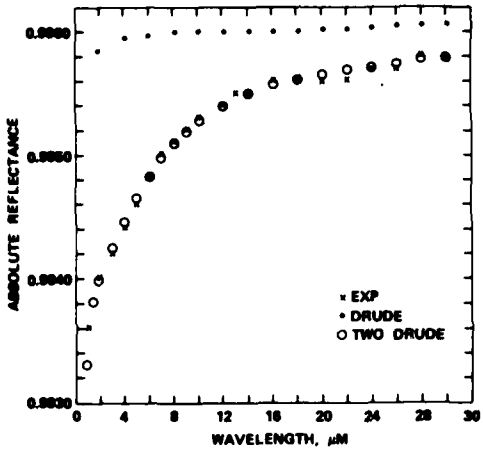

Figure 7. Spectral dependence of the absolute reflectance of ultrahigh vacuum evaporated silver compared to single-carrier and two-carrier Drude models.

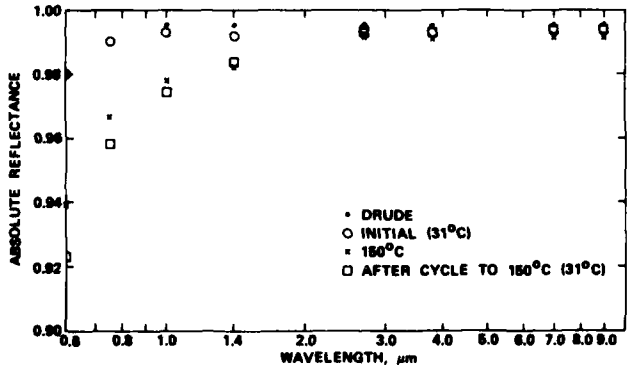

Figure 8. Spectral dependence of the absolute reflectance of diamond-turned electroplated silver showing the effects of temperature cycling.

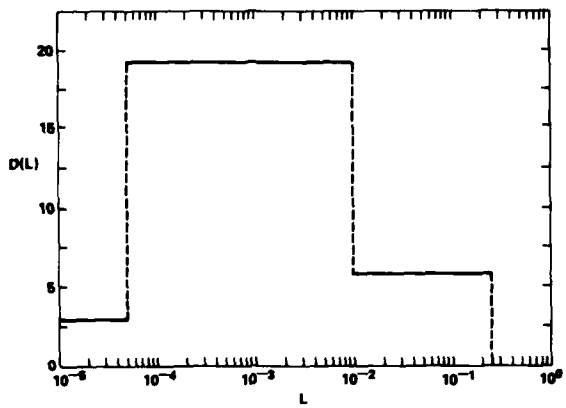

Figure 9. An empirical slope distribution for purposes of modeling the absolute reflectance of an ultrahigh vacuum evaporated silver film using the resonant absorption theory discussed in the text.

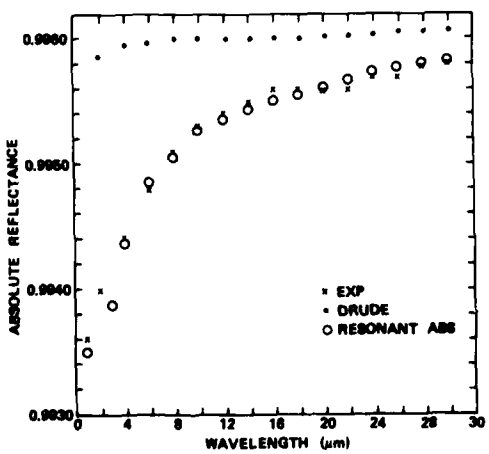

Figure 10. Spectral dependence of the absolute reflectance of an ultrahigh vacuum evaporated silver film compared with the single-carrier Drude model and with the results of the resonant absorption model.

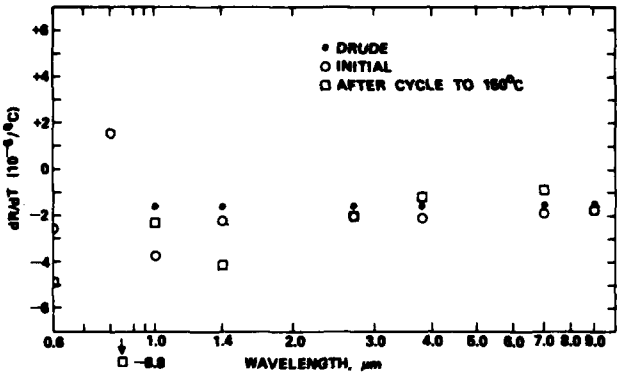

Figure 11. Spectral dependence of the derivative of the absolute reflectance with temperature for a diamond-turned electroplated silver surface compared to the Drude prediction and showing the effects of temperature cycling.

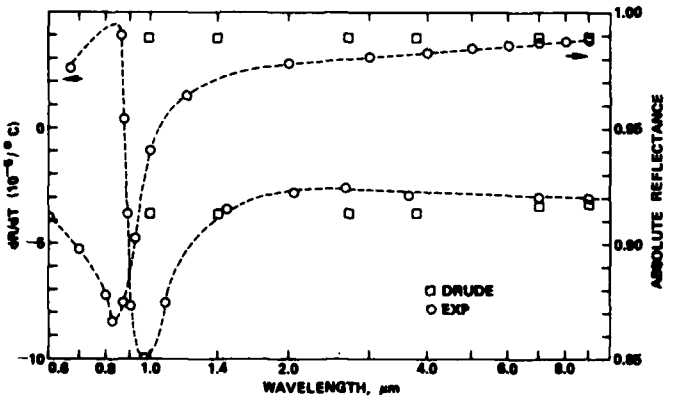

Figure 12. Spectral dependence of the absolute reflectance and its temperature derivative for ultrahigh vacuum evaporated aluminum. Shown for comparison are Drude model results.

The question was raised as to whether the anomalous skin effect could cause the observed effects. The speaker pointed out that the anomalous skin effect cannot cause a positive dR/dt and that something more sophisticated than the Drude theory was needed in the near infrared and in the vicinity of interband transitions. The Drude theory as modified by the anomalous skin effects works well at longer infrared wavelengths.

DEPENDENCE OF METAL MIRROR DAMAGE THRESHOLDS ON WAVELENGTH, MATERIAL, PULSE LENGTH, AND PREPARATION METHOD*

J. O. Porteus, D. L. Decker, S. C. Seitel, and M. J. Soileau†
Michelson Laboratory, Physics Division
Naval Weapons Center, China Lake, California 93555

Multithreshold pulsed laser-damage characteristics of precision diamond-machined Cu, Ag, and Au mirrors have been determined at 10.6, 3.8, 2.7, and 1.06 μm. The effect of pulse length has been examined at 10.6 μm by comparing previously reported results obtained using a 100-nsec TEA laser pulse with new results using a 2-μsec pulse from a hybrid TEA laser. The pulse lengths at 3.8 and 2.7 μm are nominally 100 nsec, while that at 1.06 μm is 9 nsec. Spatial intensity distributions are very nearly Gaussian at all wavelengths with e^{-2} focal spot diameters ranging approximately from 200 μm at 10.6 μm wavelength to 50 μm at the shorter wavelengths. Melt thresholds were calculated from one-dimensional heat flow considerations with a correction for finite focal spot size. Laser waveforms are accurately modeled, and temperature-dependent absorption based on Drude theory is used. Calculated values for Ag are in excellent agreement with experiment, except at 1.06 μm, while calculated values for Cu and Au are in good agreement at 10.6 μm only. An unusually large discrepancy at 3.8 μm suggests a non-Drude-like absorption mechanism that is enhanced by the multi-peaked nature of the waveform at this wavelength. Defect-related damage at submelting fluences has also been studied at the longer 10.6-μm pulse length on Cu mirrors representing a variety of preparation methods. Comparative evaluation of damage characteristics has resulted in identification of two new approaches to improving resistance to defect damage.

Key words: Cold work; crystalline disorder; defect damage; diamond-machined mirrors; Drude absorption; electron-beam melting; laser waveform; melt threshold; metal deposition; pulsed laser damage; slip threshold; thermal diffusion length; thermal stress.

Introduction

Last year we reported a theoretically determined 10.6-μm melt threshold in excellent agreement with a value previously measured on specially prepared, intrinsic Cu [1,2][1]. We also reported thresholds for melting and slip on diamond-turned (DT) Cu that are remarkably close to intrinsic levels. This year we have extended the study of DT metals [1,3], including Cu, Ag, and Au, to shorter wavelengths and a longer pulse length at 10.6 μm.

An important exception to intrinsic damage behavior on figured metal surfaces is the occasional selective, or isolated-spot, damage that causes mirrors to fail catastrophically well below intrinsic threshold levels. As part of a continuing effort to solve this important problem [1,2], we have made an auxiliary study of damage frequencies and thresholds on mirrors prepared by a variety of methods.

The scope of the present work is outlined in Table 1, where the various experimental conditions are summarized, along with the type of data obtained. Pulse lengths given are nominal. Focal-spot diameters are taken at maximum/e^2 of the nearly Gaussian spatial profiles. In the first five rows, the emphasis is on accurate measurement of melt thresholds for comparison with theory, but damage profiles, i.e., thresholds for a variety of features, including slip, pitting, craters, and light emission (flash), were also measured. Samples used for this study are restricted to one sample each of DT Cu, Ag, and Au. A much wider variety of samples representing different preparation methods is included in the auxiliary study represented by the last row of Table 1. Here, only the 10.6-μm, 2-μsec pulse was used. Although damage profiles were measured, the emphasis is on damage frequencies [1] obtained by shooting each sample at a large number of sites with a constant low fluence. All testing, for both profiles and frequencies, is 1-on-1, i.e., one pulse at each site. All test results reported here were obtained in vacuum except for the 1.06-μm tests, which were performed in air.

Table 1. Scope of study.

λ (μm)	Pulse (μsec)	Spot (μm)	Materials	Prep.	Data
1.06+	9×10^{-3}	52.4	Cu,Ag,Au	DT	Damage profile*
2.7	0.1	53.4	Cu,Ag,Au	DT	Damage profile*
3.8	0.1	63.2	Cu,Ag,Au	DT	Damage profile*
10.6	0.1	242	Cu,Ag,Au	DT	Damage profile*
10.6	2	238	Cu,Ag,Au	DT	Damage profile
10.6	2	238	Cu	Various	Damage profile, damage freq.

+Experiment done in air (this wavelength only).
*Melt thresholds computed for comparison.

* Work supported by the Air Force Weapons Laboratory and by the Office of Naval Research.
† Permanent address: Physics Dept., North Texas State University, Denton, Texas 76203.
[1] Figures in brackets indicate the literature references at the end of this paper.

Experimental Apparatus and Measurements

The damage test facilities are the same in principle as those used in other damage studies reported from the Naval Weapons Center (NWC) [1,3,4,5]. To accommodate an increasing workload, the ultrahigh-vacuum test chamber previously used has been replaced by a forepump-evacuated chamber for 2.7-, 3.8-, and 10.6-μm tests. This has resulted in a loss of sensitivity for ion emission due to poorer vacuum (0.4 Torr), and ion emission thresholds are not reported in this work. The lasers are all, in effect, single-mode, multiline sources with excellent reproducibility. The Holobeam Nd-YAG laser that provides 1.06-μm radiation has a very nearly Gaussian temporal waveform with a pulse length of 9 nsec measured at maximum/e^2. The 2.7- and 3.8-μm radiation is produced by a Lumonics HF/DF TE laser, whose 2.7-μm waveform is shown in Fig. 1. At 3.8 μm, the more complex, multipeaked waveform shown in Fig. 2 is produced by sequential lasing on lines of slightly different wavelength. Figure 3 compares the waveform of the CO_2 TEA laser used in previous work [1,2,3] with the much longer pulse recently achieved by hybridizing the TEA laser with a CW section. The hybrid pulse shows no evidence of the mode beating apparent in the TEA laser pulse but contains the vestige of a gain-switched spike in the leading portion.

Samples for the melt threshold study are of oxygen-free, high-conductivity bulk Cu and of Ag and Au electrodeposited by Union Carbide Corp. on Cu substrates. Surfaces were finished in the NWC diamond-turning facility [6] under optimum conditions [1]. Damage profiles were measured by the same multithreshold techniques described in previous work [1,3,7]. Flash and pit formation are observed on-line, while other damage features are subsequently identified using a Nomarski microscope. The rationale and technique for damage frequency testing have been previously discussed [1] and are further described below.

Melt Threshold Computations

The method of computing theoretical melt thresholds is the same as reported earlier [1,2] except for a spot-size correction, which is significant in some of the situations considered here. The steps required to compute the infinite-spot thresholds are as follows: (1) Obtain the room temperature absorptance from measured reflectance data; (2) obtain absorptance vs temperature from electrical conductivity data via the Drude model [8,9]; (3) obtain data on temperature-dependent thermal properties from tables [10]; (4) simulate the laser waveform directly with digital data, or with analytic functions for the 1.06- and 10.6-μm TEA pulses; and (5) compute melt thresholds by a finite difference method (SINDA [11]) applied to a one-dimensional heat flow model. Correct waveform modeling is essential to obtain results accurate to better than about 30% [1]. The accuracy goal here is ±5% of the melt thresholds calculated for infinite spot size.

The spot-size correction is based on the approximation of Dobrovol'skii and Uglov [12] which assumes a rectangular waveform, Gaussian spatial profile, linear variation of absorptance with temperature, and temperature-independent thermal properties. The ratio of the finite-spot threshold θ_r to the infinite-spot threshold θ_∞ is given approximately by

$$\frac{\theta_r}{\theta_\infty} \simeq \frac{\chi}{\arctan \chi} \quad , \tag{1}$$

where

$$\chi = \sqrt{\frac{32}{\pi}} \frac{d}{r} \quad . \tag{2}$$

Here, r is the maximum/e^2 radius of the spatial profile, and d is the thermal diffusion depth, defined by

$$d = \sqrt{\frac{\pi}{4} \alpha t} \quad , \tag{3}$$

where α is the thermal diffusivity, and t is the duration of the rectangular pulse. In order to apply eqs. (1,2) to the present problem, eq. (3) must be replaced by a more general definition of d applicable to nonrectangular waveforms. A physically appropriate approach is to express d in terms of the computed temperature profile in the metal when surface melting first occurs. Temperature profiles are made available in the process of computing the infinite-spot melt threshold. To relate the generalized d to the rectangular waveform, we calculate the temperature profile produced by a rectangular 100-nsec pulse, having just sufficient energy to melt the Cu surface. At depth d, as defined by eq. (3), one finds

$$\Delta T(d) = 0.345 \Delta T(0); \qquad T(0) = T_{melt} \tag{4}$$

Here $\Delta T(d)$ is the temperature rise at depth d, and $\Delta T(0)$ is the rise at the surface; the absolute surface temperature is represented by T(0). Using eq. (4) as the general definition of d in temperature profiles produced by nonrectangular waveforms produces the spot-size correction factors given in Table 2. Spot-size corrections are clearly quite important for the 2.7- and 3.8-μm situations, are less important for the 2-μsec, 10.6-μm pulse, and are insignificant for the short-pulse, 10.6- and 1.06-μm situations. Since the spot-size corrections are approximate, they introduce an additional uncertainty dependent on the magnitude of the correction [12].

Table 2. Spot size correction factors.

λ (μm)	Pulse (μsec)	θ_r/θ_∞ Cu	Ag	Au
1.06	9×10^{-3}	1.00	1.01	1.01
2.7	0.1	1.35	1.51	1.38
3.8	0.1	1.26	1.39	1.36
10.6	0.1	1.00	1.00	1.00
10.6	2	1.08	1.12	1.09

Comparison of Thresholds

Measured and computed finite-spot melt thresholds are compared in the last two columns of Table 3. The short-pulsed 10.6-μm data on Cu are from a preceding study [1] where the present sample was used, while the corresponding Ag and Au data are from an earlier study [3] on different samples. At 10.6 μm, where one expects a ±10% experimental uncertainty and a ±5% or more uncertainty in the computed values, the agreement is quite acceptable in all cases. However, at 3.8 and 2.7 μm, only Ag shows good agreement in support of Drude-like absorption. There are particularly large discrepancies at 3.8 μm for both Cu and Au, suggesting an additional absorption mechanism peculiar to the multiply peaked pulse. If such a mechanism exists, it may have important implications for repetitively pulsed damage thresholds for these two metals. The exceptional case of Ag is evidently associated with the superior machinability of this metal and the resulting smoother surface. At 1.06 μm, the agreement is relatively poor for all three metals and especially poor for Cu. This is not particularly surprising, since absorption is known to be less Drude-like in the near infrared due to extrinsic surface roughness effects.

Table 3. Melt thresholds for DT metals.

λ (μm)	Pulse (μsec)	Spot (μm)	Metal	θ_r (J/cm²) Comp.*	Meas.
1.06†	9×10^{-3}	52.4	Cu	14.7	9.0
			Ag	13.9	10.5
			Au	7.5	5.6
2.7	0.1	53.4	Cu	234	194
			Ag	222	201
			Au	138	123
3.8	0.1	63.2	Cu	245	178
			Ag	224	237
			Au	161	120
10.6	0.1	242	Cu	73.7	69.8** ***
			Ag	59.2	58.8***
			Au	44.9	43.1
10.6	2	238	Cu	415	476
			Ag	349	373
			Au	256	275

†Measurements made in air.
*Values corrected for finite-spot size.
**From reference 1.
***From reference 3 after correction for systematic errors [1].

Figures 4(a) and (b) compare 10.6-μm damage profiles from the Cu sample at nominal pulse lengths of 0.1 and 2 μsec, respectively. The thresholds, except for cratering, all scale approximately in the ratio of 1/6.8 between the two pulse lengths. This nearly equals 1/6.1, the ratio of the generalized thermal diffusion depths for the two cases, obtained by applying eq. (4) to the computed temperature profiles. Since d is proportional to $\sqrt{t}$ for equivalent rectangular waveforms [eq. (3)], this result may be interpreted as supporting a $\sqrt{t}$-scaling law. The scaling of the crater threshold shows a weaker dependence on d, resulting from an inverse dependence on the volume of metal that has been heated. An extreme example of relative increase in crater threshold with reduced pulse length was observed with the even shorter 1.06-μm pulse, where the crater threshold on the Cu surface is roughly 10 times the melt threshold. Shielding by air breakdown may also have been an additional important factor in this case.

Selective-Damage Study

We turn now to a comparative evaluation of Cu mirrors produced or treated by various methods designed to minimize selective (isolated-spot) damage. Substrates are of either Cu or Mo. Fabrication, processing, and finishing techniques are listed in Table 4, together with identifying codes. The deposition methods include some that have shown considerable promise in previous studies, such as chemical vapor deposition (CVD) [1,2] and sputter deposition with dispersion hardening (HSD) [13]. The CVD Cu was applied in a 2-μm layer to a DT Cu substrate without subsequent finishing. The HSD Cu was applied to a polished Mo substrate and subsequently polished. In the electron-beam melting (EM) process, a rastered electron beam is used to melt the bulk Cu substrate or brazed-on sheet Cu before diamond turning. Two unconventional "hard-finishing" methods were included in the study. In both of these, a large amount of cold work is deliberately introduced, either by high-pressure polishing bulk Cu on a hard lap (HP), or by diamond turning the bulk Cu with the unusually large negative top rake angle of -10° (HDT). Cold working has been shown to raise slip thresholds and may thus help raise breakdown thresholds by suppressing exoelectron emission [14].

A special cleaning procedure was used on some samples to determine its effectiveness in reducing selective damage. The procedure consists of a series of ultrasonic rinses in clean acetone which was subsequently removed by blowing with clean N_2. Just before testing, the surfaces were wet with acetone and dried by drawing a lens tissue over them. Since the risk of scratching or otherwise degrading performance is considerable, special cleaning was used only on NWC-prepared samples or where at least two samples of a given type were available for testing. Where special cleaning was not used, samples were simply blown off with clean N_2.

Results of the damage frequency evaluation are given in Table 5. The data are based on up to 300 tested sites per sample, with fewer sites on the poorer samples. Peak energy density was held constant at 225 J/cm², about half the melt threshold of intrinsic Cu under present conditions. However, since the weak points where damage occurs seldom lie on the beam axis, the effective energy density that

Table 4. Cu mirrors: fabrication and processing.

Deposit	Code
None (bulk Cu)	--
Cu sheet, brazed-on	B
Chemical vapor deposit	CVD
Sputter deposit	SD
Dispersion-hardened sputter deposit	HSD
Process	**Code**
None	--
Electron-beam melt	EM
Finish	**Code**
As-deposited (on finished substrate)	--
Conventional polish	P
"Hard" polish	HP
Conventional diamond turned	DT
"Hard" diamond turned (-10° rake)	HDT

Table 5. Cu mirrors: damage frequency.

Sub/Dep,Proc/Finish*	Special clean	% Tested sites**		
		Defect†	Flash	Pit
Cu/EM/DT	yes	1.0	2.7	1.0
Cu//HDT	yes	0.7	1.0	1.4
DTCu/CVD/	yes	1.9	1.9	1.5
Cu//HP	yes	4.1	3.1	2.8
PMo/HSD/P	no	3.1	4.5	4.8
DTCu/CVD/	no	4.6	8.4	10.5
Cu//HP	no	10.2	15.6	10.9
Cu/SD/DT	no	6.1	12.3	14.0
Mo/B,EM/DT	yes	0	46	42.5
Cu//P	yes	5.3	92.1	65.8

*For example, Cu/EM/DT denotes bulk Cu which was electron-beam melted and subsequently diamond turned.

**225 ± 25 J/cm² peak fluence, each site (10.6-μm, 2-μsec, 238-μm spot).

†Visible defect associated with flash or pit.

produces damage is often considerably less than the peak value. The percentage of sites where pitting occurred is shown in the last column, and samples are ranked accordingly. A pit is defined here as any highly localized, laser-induced change in sample appearance observed on-line with a 20-power microscope. The percentage of sites exhibiting one or more visible flashes is shown in the preceding column. Some sites showed obvious visible defects before they were shot, and these defects were often clearly associated with a laser-induced pit and/or flash. Percentages for this occurrence are given in the third column from the right.

Performance of Cu Mirrors

The three top-ranked samples in Table 5 performed nearly equally, with pit frequencies of less than 2%. All three were DT in the NWC facility at some stage of fabrication. The hard-polished sample Cu//HP also performed well, followed closely by the dispersion-hardened sample PMo/HSD/P. The next three samples exhibited pit frequencies of slightly greater than 10%. Since samples nominally identical to two of these three performed much better with special cleaning, there is evidence that the cleaning procedure is beneficial. Possibly PMo/HSD/P would have ranked higher had it been specially cleaned. One of the electron-melted samples and a conventionally polished sample ranked poorly in spite of special cleaning. The former, Mo/B,EM/DT, was degraded by diffusion of braze alloy through the Cu sheet during electron-beam melting. Damage frequencies and thresholds vary markedly over the surface of this sample and are strongly correlated with surface discoloration. The conventionally polished sample Cu//P, which has a flash threshold well below 225 J/cm², clearly demonstrates the need for improved technology in this area.

The thresholds for slip, melting, and flash on these samples are intercompared in Table 6. Samples are listed in order of decreasing melt threshold. The five top-ranking samples on this basis, all of which have melt thresholds exceeding 400 J/cm², include the top-ranking four samples in the damage frequency evaluation (cf., Table 5). Among these, two samples, Cu/EM/DT and DTCu/CVD/, are outstanding for high slip thresholds. In the former case, this suggests that thermal stress and resulting crystalline disorder are important factors in electron-beam melting. With regard to special cleaning, the threshold data support the above evidence that such cleaning is beneficial.

Figures 5 and 6 show Nomarski micrographs of a selective damage site from each of the four top-ranking samples of Table 5. On the Cu/EM/DT site, shown on the left side of Fig. 5, there is a scratch in the upper left. Pits and flashes occurring along this scratch account for all the pitting and a large fraction of the flashes observed on this sample. It is quite conceivable that the scratch was introduced in special cleaning, illustrating a possible negative aspect of the procedure. The right side of Fig. 5 shows visible defects where flashes were observed on the CVD sample. These appear as small light spots occurring below and on the visible grain boundary. Such defects do not necessarily originate in the CVD film, which is only 2-μm thick. The thermal diffusion depth determined for Cu is 19 μm under present conditions. Figure 6 shows selectively damaged sites on the hard-finished samples.

Table 6. Cu mirrors: damage thresholds.

Sub/Dep,Proc/Finish	Special clean	θ (J/cm²)*		
		Slip	Melt	Flash
Cu/EM/DT	yes	259	442	472
Cu/HDT	yes	196	439	484
Cu/SD/DT	no	175	426	464
Cu//HP	yes	200	424	486
DTCu/CVD/	yes	297	411	419
Cu//HP	no	118	397	473
Cu//P	yes	111	394	159
PMo/HSD/P	no	231	367	455
DTCu/CVD/	no	206	355	457
Mo/B,EM/DT	yes	57	173	207

*10.6-μm, 2-μsec pulse.

On Cu//HDT, the damage consists of a ring of pits, apparently associated with dimple-like depressions visible in Nomarski outside the damaged area. These may have acted as traps for contaminants or may have produced increased absorption as a result of their geometry. The right-hand side of Fig. 6 shows a large visible defect where a flash was observed on the polished Cu//HP surface. The nature of the defect is not clear in this case. These micrographs serve to illustrate the important role of surface defects in selective damage. In some cases, the defects are identifiable, e.g., scratches, depressions. Electron microscopy and high-resolution surface analysis of damage sites may provide further useful information.

Conclusions

Previous damage threshold measurements on DT Cu, Ag, and Au at 10.6 μm, using a 100-nsec pulse, have been extended to shorter wavelengths and to a longer pulse length at 10.6 μm. Melt thresholds were calculated from theory for comparison. Accurate waveform inputs, temperature-dependent optical and thermal properties, and a correction for finite-spot size are included in the calculation. The assumed temperature dependence of absorption is based on the Drude model. Agreement between theory and experiment is good (±15%) for all three metals at 10.6 μm, but only Ag produces good agreement at 3.8 and 2.7 μm. Low measured thresholds for Au and especially for Cu at 3.8 μm suggest a roughness-enhanced absorption mechanism peculiar to the multipeaked 3.8-μm pulse. This may have significant implications for repetitively pulsed situations involving either of these metals. Relatively poor agreement between theory and experiment for all three metals at 1.06 μm implies failure of the Drude model at this wavelength. Damage thresholds, except for crater formation, scale nearly as the square root of the pulse length at 10.6 μm when the data are interpreted in terms of equivalent rectangular waveforms.

Cu mirrors prepared by a variety of fabrication methods were evaluated at 10.6 μm for resistance to selective or isolated-spot damage. Both damage frequencies and damage thresholds were measured. Electron-beam processing of bulk Cu substrates before DT is a newly investigated technique that shows considerable promise. "Hard" diamond turning, using a large negative rake angle, is another new approach that produces excellent results. A special cleaning procedure involving ultrasonic cleaning and wet wiping improves results where A-B comparisons are made but increases the risk of scratching. Scratches and other visible surface blemishes are often observed in conjunction with selective damage. Further studies using electron and surface-analytical microscopy, in conjunction with low-level, small-spot damage experiments, are needed for more positive identification of the more subtle surface anomalies associated with selective damage.

References

[1] Porteus, J. O., Decker, D. L., Grandjean, D. J., Seitel, S. C., and Faith, W. N., NBS Special Publ. 568, 175 (1980).

[2] Porteus, J. O., Choyke, W. J., and Hoffman, Appl. Opt. 14, 451, 1980.

[3] Porteus, J. O., Decker, D. L., Jernigan, J. L., Faith, W. N., and Bass, M., IEEE J. Quantum Electron. QE-14, 776 (1978).

[4] Porteus, J. O., Soileau, M. J., Bennett, H. E., and Bass, M., NBS Special Publ. 435, 207 (1976).

[5] Soileau, M. J., Franck, J. B., and Veatch, T. C., On self-focusing and spot-size dependence of laser-induced breakdown, this conference.

[6] Decker, D. L., and Grandjean, D. J., NBS Special Publ. 541, 122 (1978).

[7] Porteus, J. O., Jernigan, J. L, and Faith, W. N., NBS Special Publ. 509, 507 (1977).

[8] Sparks, M., and Loh, E., Jr., J. Opt. Soc. Am. 69, 847 (1979).

[9] Bennett, H. E., Factors limiting the energy transmitted by an optical train, in Laser Induced Damage in Optical Materials, A. J. Glass and A. H. Guenther, eds. (Academic Press, New York, 1981).

[10] Edwards, A. L., A compilation of thermal property data for computer heat-conduction calculations, Report UCRL-50589, Livermore, Calif. (24 Feb. 1969).

[11] Gaski, J. D., Fink, L. C., and Ishimoto, T., Systems numerical differencing analyzer, TRW Systems Report 11027-6003-RO-00 (Sept. 1970).

[12] Dobrovol'skii, I. P., and Uglov, A. A., Soviet J. Quantum Electron. 4, 788 (1974).

[13] Soileau, M. J., and Wang, V., Appl. Opt. 13, 1286 (1974).

[14] Musal, H. M., Jr., Pulsed laser initiation of surface plasma on metal mirrors, this conference.

Figures

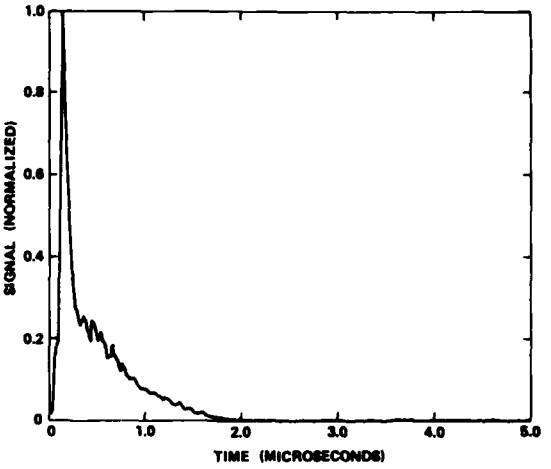

Figure 1. Waveform of 2.7-μm (HF) laser pulse.

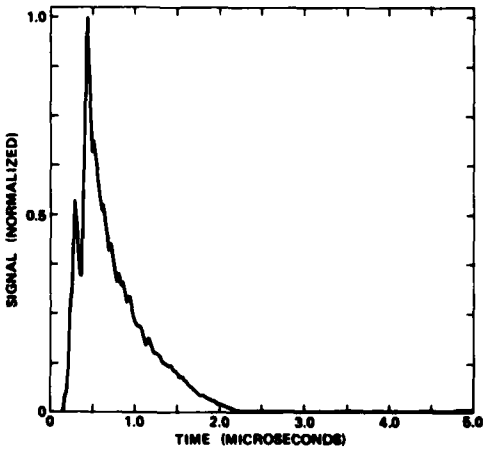

Figure 2. Waveform of 3.8-μm (DF) laser pulse.

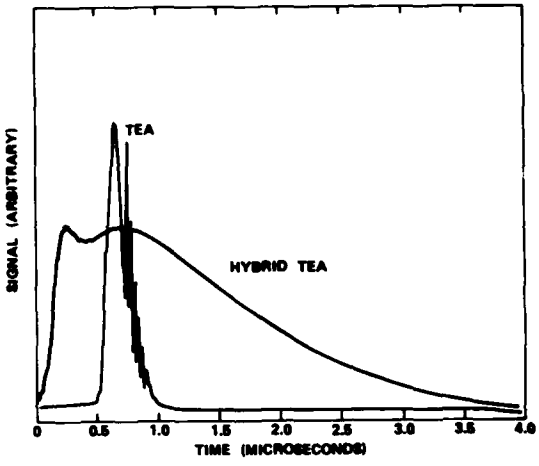

Figure 3. Waveforms of 10.6-μm (CO_2) laser pulses.

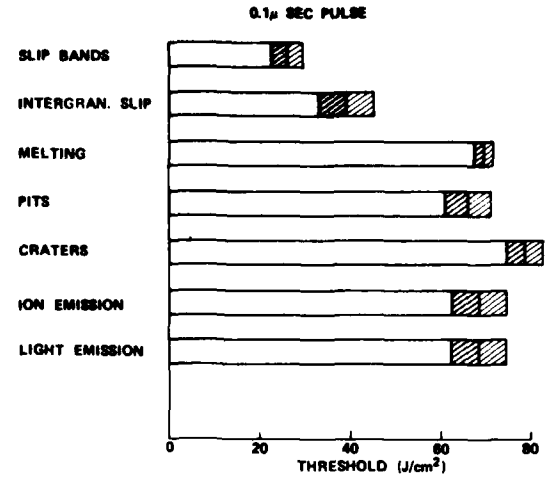

(a)

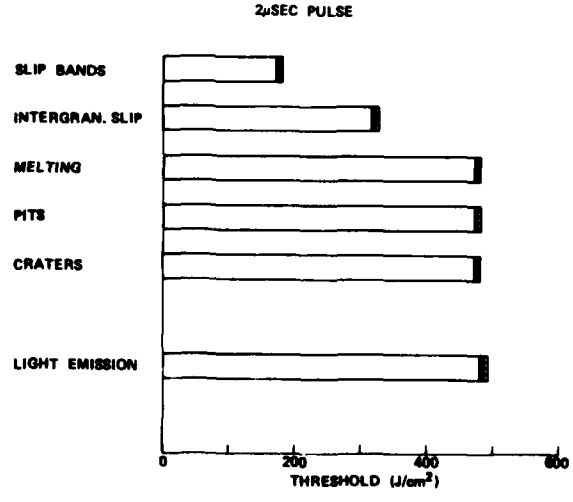

(b)

Figure 4. (a) Damage profile of DT bulk Cu at 10.6 μm with 0.1-μsec TEA pulse. Data from study described in reference [1]. (b) Damage profile of same DT bulk Cu sample at 10.6 μm, but with 2-μsec hybrid pulse.

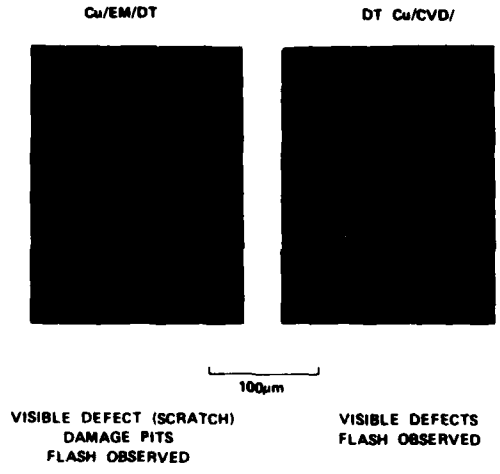

Figure 5. Nomarski micrographs of EM bulk Cu (left) and CVD Cu (right) at selective damage sites. Both samples were diamond turned, but only before deposition in the latter example.

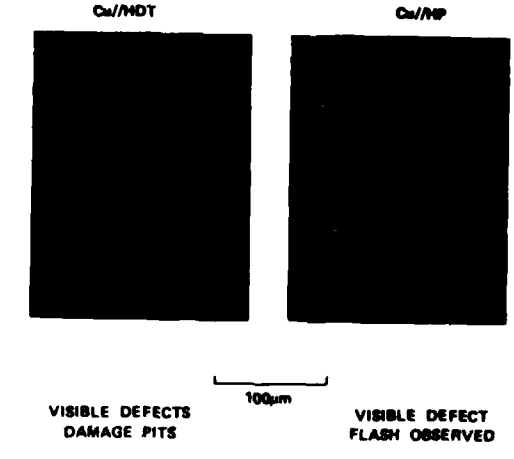

Figure 6. Nomarski micrographs of HDT (left) and HP bulk Cu (right) at selective damage sites.

Discussion not recorded.

REGROWTH IN LASER IRRADIATED ELEMENTAL METALS AND ALLOYS: SURFACE NONUNIFORMITIES AND COUPLING PHENOMENA

Clifton W. Draper
Laser Studies Group
Western Electric Engineering Research Center
P. O. Box 900, Princeton, New Jersey 08540

The last half dozen years have seen a rapid growth in research on the effects of laser surface melting (LSM) and rapid self quenching on metallic systems. Modification of surface sensitive behavior has been demonstrated in a number of alloys systems. Even more recently there has been a renewed interest in laser surface alloying (LSA)--the melting/rapid quenching of predeposited film plus metal substrate.

The coupling process between metallic surface and focussed beam is sensitive to preirradiation surface quality. The resulting LSM or LSA area may be uniform as a result of controlled processing, or very nonuniform due to local variations in the coupling phenomena. Four categories are identified as the major causes for nonuniformities: topographical inhomogeneities, structural/chemical inhomogeneities, impurity effects and interference effects. If LSM or LSA processing is to move out of the laboratory and into the real world the significance of these differences will have to be addressed.

Key words: Laser irradiation, liquid phase regrowth, metal surfaces, nonuniformities

1. Introduction

The last dozen years have seen increasing growth in research on the effects of laser surface melting (LSM) and associated rapid self-quenching on metallic systems. Metastable phases [1,2], unusual microstructures [3,4] and the modification of surface sensitive behavior [5,6,7] have been found in a number of alloy systems following surface irradiation. Even more recently there has been a renewed interest in laser surface alloying (LSA) - the melting/rapid self-quenching of predeposited film plus a controlled portion of metal substrate. Most of the work has been centered around the use of pulsed solid state [8,9] or scanning continuous CO_2 lasers [10,11]. In both cases typical irradiation times, pulse or dwell, are on the order of 1 to 10 msec. Typical melt depths of >100μm are convenient for metallurgical examination.

Very recently [12,13,14] there has been expanding interest in the use of Q-switched lasers for both LSM and LSA processing. The short pulse times, 20 - 200 nsec, result in shallow melt depths, typically less than 10,000Å. This is attractive for making highly concentrated, near-surface alloys from predeposited thin films. The shallow melting has also been used to characterize the redistribution of ion implanted species in metallic hosts [15]. The time in the liquid phase is on the order of the pulse length and quench rates of 10^9 K-sec^{-1} can be achieved. These quench rates approach those predicted as necessary for the metal to glass transition in monatomic metals [16].

This report examines nonuniformities in the coupling process between metallic surface and focussed Q-switched irradiation. It has been found that in both LSM and LSA processing the resulting uniformity of the melt area is very sensitive to preirradiation surface conditions. Such sensitivity has not been noted in the case of continuous CO_2 or pulsed laser processing primarily because the long melt times and deep melt depths wash out effects on the scale to be examined below.

The examples presented should be of general interest to the laser-material processing community. There should be particular interest by those working in the characterization of damage thresholds in high power laser metallic mirrors. Many of the same mirror defects which result in damage sites, should be expected to show up as nonuniformities in the LSM and LSA processing. There has been interest [17,18] in using laser induced vaporization for studying the behavior of nuclear reactor

application materials under transient heating conditions and as a source for chemical reaction species. The contribution to the atomic/molecular fluence that local "hot spots" make relative to the total irradiated area has not been addressed. Zehner et. al. [19] have recently reported the use of Q-switched ruby laser irradiation to produce atomically clean single crystal silicon surfaces, and Papagno et. al. [20] have reported similar results for Q-switched Nd-YAG irradiation of 304 stainless steel. Numerous reports of "frozen in" interference effects have appeared in the recent flurry of literature in laser processing of semiconductor surfaces. Such effects are common in Q-switched irradiation of conventionally prepared metal surfaces. The stringent geometric and topographical requirements within semiconductor technology are only approached for metals in the laser mirror area. There is a general lack of appreciation by these "semiconductor people" as to how ideal a surface these wafers are. Examples are given below which demonstrate just how sensitive laser processing of single crystal metal surfaces are to contamination and surface defects.

2. Experimental

Two Q-switched laser processing systems were employed in order to achieve area coverage surface melting or alloying. In the acousto-optically Q-switched Nd-YAG system, laser pulses are raster scanned with electronically controlled galvanometer mirrors over the stationary samples. A multielement telecentric lens provides flat focussing over the sample field. The lithium iodate frequency doubled, Q-switched Nd-YAG system accomplishes raster scanning through the use of a high precision linear induction table. In both Q-switched systems, spot to spot and line to line overlap are optimized for uniform area coverage of sample surfaces. Typical focussed spot sizes are 20 to 40 μm, and incremental steps are 10 μm spot to spot and 10 - 18 μm line to line. It should be noted that in both cases the Q-switched pulse lengths, 140 nsec (t_p at half power points), and repetition rates (11 KHz at 1.06 μm and 5 KHz at 0.53 μm) are such that melting/resolidification of each irradiated spot occurs 2-3 orders of magnitude faster than the arrival of the next pulse.

Laser irradiated samples are examined under bright field and Nomarski optical microscopy. Scanning electron microscopy has also been utilized to some extent. Unless otherwise noted, all micrographs presented in the figures were made using Normarski differential interference contrast. In addition, Rutherford backscattering and channeling have added invaluable insight to our understanding of the effects of Q-switched irradiation upon the near surface regions of metals and alloy specie therein.

3.1 Observations

For convenience, four causal categories are used to group the examples. These are topographical inhomogeneities, structural/compositional inhomogeneities, contamination effects and interference effects. We make no pretense that these categories are all encompassing, but our experience with literally thousands of samples of various preirradiation surface quality has led us to believe that most postirradiation inhomogeneities in Q-switched LSM and LSA processing can be fit into one of these four categories.

3.2 Topographical Inhomogeneities

Controllable surface melting free of nonuniformities can be obtained on carefully prepared metal surfaces. Figure 1 is a micrograph of a Ni <110> sample which has been implanted with 10^{17} Ag cm^{-2} at an energy of 150 KeV. High dose ion implantated surfaces typically possess a grainy textured surface as a result of sputtering. This is seen in the unirradiated region. The surface was irradiated with the Nd-YAG (1.06 μm) system described above at an incident power density of 114 MW cm^{-2}. The irradiated region shows that the laser pulses produce a pattern of smooth nearly circular annealed regions. The individual melt spots are bounded by features with the appearance of a frozen meniscus. Oron, et. al. [21] demonstrated at last year's 11th Damage Symposium that ion implantation of Al into electropolished polycrystalline Cu followed by controlled oxidation produced a copper mirror with improved environmental stability. As demonstrated above in figure 1, finely focussed Q-switched pulses scanned across an implanted region can produce a smooth annealed region. We recently published [12] work on the motion of implanted Ag, Au and Ta in nickel single crystals during Q-switched irradiation. Metallic liquid - state diffusivities of about 10^{-4} cm^2 sec^{-1} and melt times of hundreds of nanoseconds are consistent with the implanted specie motion of hundreds of angstroms measured using

Rutherford backscattering. It is significant that Q-switched laser annealing of implanted metals can improve the surface topography without drastically reducing the alloying specie concentration. Laser annealing coupled with ion implantation also circumvents somewhat the dose limitations imposed by sputtering. Recycling between implantation and laser annealing (redistribution) allows higher total concentrations to be introduced, while at the same time maintaining a superior surface quality.

Figure 2 contrasts the homogeneous processing described above. Here Mo <111> has been irradiated at 276 MW cm^{-2} with the same laser system. Both preirradiation surfaces were polished metallurgically and cleaned ultrasonically in distilled water. The Ni single crystal, however, was electropolished to remove remnant polishing asperities like those seen on the unirradiated Mo crystal, which was not electropolished. Unusual "frozen in" ripple patterns result from Q-switched pulse melting of some of these asperities as evidenced in the irradiated region of figure 2. Surfaces with gross topographical preirradiation features can be surface melted over large surface areas. Of course, the very shallow melting and short melt times prohibit extensive topographical reconstruction and the irradiated region will retain much of the preirradiation condition. This is seen in figure 3 where frequency doubled Nd-YAG irradiation (0.53 μm) at 37 MW cm^{-2} has been used to produce widely spaced lines of overlapped melted spots in cold rolled polycrystalline Ni. The cold rolled topography is still evident in the annealed lines. Also note that the individual melt spots are less defined, and the repair of the scratch marks in the lower central portion of the micrograph. A similar result is seen in the 1.06 μm irradiation of cold rolled tin-modified copper-nickel (UNS designation C 72500). Figure 4 contains two micrographs of this copper alloy surface irradiated at 114 MW cm^{-2} with a scanning direction parallel (a) and perpendicular (b) to the rolling direction. Note that the processing defects, which initiate at strong coupling centers, propagate in the rolling direction irregardless of scanning direction. Studies on this and other copper alloys of the postirradiation surface density of these defects at 1.06 μm lead us to speculate that the coupling centers are topographical, rather than impurities or laser output fluctuations.

3.3 Structural/Compositional Inhomogeneities

Structural effects may be differentiated from topographical effects in that no amount of surface polishing (mechanical or electrochemical) may remove them. For example, consider an alloy with a duplex structure. The two phases may couple, either because of optical or thermal parameters, differently to the focussed radiation. This behavior has been observed in cross sections of LSM CO_2 processed duplex (ferrite-pearlite) 1040 steel [7]. We have observed coupling problems (nonuniform surface melting) with Q-switched irradiation on duplex-copper alloy systems which correlates with the size and surface density of individual phases.

Compositional effects may be the result of particular elements uniformly distributed in homogeneous single phase alloys. For example, Cu-Zn alloys (brasses) are very difficult to controllably surface melt due to the high vapor pressure of Zn. A different example is a spatial compositional variation which leads to postirradiation nonuniformities. This is seen in figure 5 for low dose (10^{16} cm^{-2}) Hf implanted Ni <110> irradiated at 98 MW cm^{-2} with the Q-switched Nd-YAG system. The left hand side was unimplanted virgin Ni <110> while the right side was implanted prior to laser processing. No mask was present during Q-switched irradiation. The sharp demarcation defines the implanted region edge. The coupling behavior is signficantly different. The differences are due to changes in the optical or thermal properties of the near surface region introduced by the implanted species. Although the implantation process itself may change the surface texture when sputter limited implantation is approached, no significant changes in topography are seen in this sample when comparing virgin and implanted regions which have not been irradiated. Conclusive differentiation between the effects of implanted species or implantation process can be derived from self-implantation. The isolated hillocks within the implanted and irradiated (right hand side) are due to contamination and will be discussed further below.

3.4 Contamination

The reflectance at 1.06 and 0.53 of most metals is >50% and in many cases >90%. Contamination on clean metal surfaces invariably lowers the local reflectance leading to strong coupling and local nonuniformities, in many cases isolated vaporization pits. The resulting features may be isolated as in

figure 5 (right hand side) above or extended in appearance like those due to propagation, as seen in figure 4. That is, an isolated pit formed due to irradiation of local contamination may result in an extended feature, since overlapped Q-switched pulses will in part see the irregularity formed. The coupling of subsequent pulses is altered by the inhomogeneities caused by previous pulses. Clearly the causal mode may change - as isolated contamination may cause a topographical inhomogeneity upon irradiation, which itself may cause a progagated inhomogeneity upon further irradiation.

As mentioned above, the isolated hillocks on the implanted/irradiated region of figure 5 resulted from contamination. In figure 6 is seen the preirradiation boundary between virgin and Hf implanted Ni <110>. Note the isolated dark spots (they are brown in color) on the surface of the implanted portion. They are the cause of the isolated hillocks. Contamination during implanation came about because the vacuum system cold trap was not utilized during this implantation. The virgin surface was masked for the purpose of implantation and, therefore, no contamination is evident. The contamination is probably a high molecular weight silicon or carbon based condensed vapor species. No surface analysis was attempted in order to specifically identify it. The elements, however, must have a lower atomic number than Ni (#28), otherwise the elements would have been detected in the Rutherford backscattering, which has a sensitivity on the scale of a fraction of a monolayer.

Figure 7 demonstrates two problems associated with contamination (unknown origin or nature) in the 1.06 μm irradiation of low dose (10^{16} cm^{-2}) Au implanted (150 KeV) Ni <110>. In figure 7a the "feathery" appearance of the contamination is visible in the unirradiated region. The irradiated region was processed at 114 MW cm^{-2} which is above melting threshold. Note the irregularity of the irradiated region. For example, compare 7a with figure 1. In figure 7b the identical region is shown again. The surface has now been irradiated again, this time at $\sim$ 55 MW cm^{-2} which is below melt threshold. Note however, that the contamination has caused local melting through increased optical absorption.

3.5 Interference

Several types of interference phenomena leading to processing inhomogeneities have been reported in the laser processing of semiconductors. Leamy, et. al. [22] first noted spatially periodic (corresponding to laser wavelength) regrowth in annealing of implanted silicon due to interference phenomena between incoming plane waves and waves originating from surface scattering centers. Affolter et. al. [23] have reported on the formation of "frozen in" circular fringe patterns in Pd surface alloying on Si <111> resulting from the interference of incoming plane waves and spherical waves formed on scattering centers (dust) above the sample surface. In this case the period is irregular and decreases with radial distance.

Many surface nonuniformities that are "frozen in" following Q-switched laser irradiation in metals show features that are evidence of interference phenomena. Figures 8-10 are typical examples. In figure 8 a set of fringes parallel to a preirradiation surface scratch are formed on Ni <100> irradiation at $\sim$ 70 MW cm^{-2}. The spacing between the individual lines is 1 μm corresponding with the Nd-YAG wavelength. Figure 9 compares Ni <100> irradiated at 114 MW cm^{-2} both with (a) and without (b) smoke particles between the sample surface and last system optical components. Note the high density of small features within each larger melt puddle for the sample processed in the presence of the smoke particles.

Finally, in figure 10, an interesting set of three moon shaped and associated ripples are seen on Mo <100> irradiated at 244 MW cm^{-2}. The fringe spacings are irregular and wider than the 1.06 μm laser wavelength. Features like these may be aesthetically appealing to many and certainly present an interesting exercise in optics to those interested in explaining their formation.

Their significance from a point of view of processing uniformity is undoubtedly greater in semiconductor technology than metals processing. This is primarily because semiconductor device features are spatially constructed on a scale so small that these nonuniformities must be addressed.

4.0 Conclusions

As noted in the introduction, the major thrust for laser surface melting and surface alloying

has been the efforts to modify surface sensitive behavior. Quenched in irregularities like those described above may represent processing features that significantly detract from the usefulness of the treatment. For example, they may act as points for local attack in corrosive environments or accelerated wear points in tribological applications. At this point in time, studies have clearly shown that surface melting and surface alloying by laser irradiation can signficantly improve metallic surface behavior in selected aggressive environments. The significance of processing non-uniformities, however, has not to date been addressed.

Acknoweldgements

None of the observations described above would have been possible if the author were not involved in cooperative experimentation with numerous colleagues at Bell Labs. These include J. M. Poate, C. M. Preece, E. N. Kaufmann, L. Buene and D. C. Jacobson. The technical assistance of P. P. Solan, A. Holliday and L. S. Meyer is greatfully appreciated.

References

[1] Elliott, W. A., Gagliano, F. P. and Krauss, G., Metastable phases produced by laser melt quenching, Met. Trans. 4, 2031 (1973).

[2] Laridjani, M., Ramachandrarao, P. and Cahn, R. W., Metastable phase formation in a laser-irradiated silver-germanium alloy, J. Mater. Sci. 7, 627 (1972).

[3] Breinan, E. M., Kear, B. H., and Banas, C. M., Processing materials with lasers, Phys. Today 29 (11), 44 (1976).

[4] Kim, Y-W, Strutt, P. R., and Nawotny, H., Laser melting and heat treating of M2 tool steel: a microstructural characterization, Met. Trans. 10A, 881 (1979).

[5] Anthony, T. R., and Cline, H. E., Surface normalization of sensitized stainless steel by laser surface melting, J. Appl. Phys. 49, 1248 (1978).

[6] Draper, C. W., Woods, R. E., and Meyer, L. S., Enhanced corrosion resistance of laser surface melted aluminum bronze D (CDA-614), Corrosion, NACE 36, 405 (1980).

[7] Preece, C. M. and Draper, C. W., The effect of laser quenching the surfaces of steels on their cavitation erosion resistance, Wear, in press.

[8] Kovalenko, V. S., Volgin, V. I., and Mikhailov, V. V., Electrophysical and electrochemical methods of treating parts-improved technology for laser alloying of the surfaces of structural materials, Tekhnologiya I Organizatsiya Proizvodstva 3, 50 (1977).

[9] Kovalenko, V. S., and Volgin, V. I., Characteristics of laser alloying of an iron surface with vanadium, Fiz. I Khim. Obrab. Mater. 3, 28 (1978).

[10] Seaman, F. D., and Gnanamuthu, D. S., Using the industrial laser to surface harden and alloy, Metal Prog. 108 (3), 67 (1975).

[11] Moore, P. G., and Weinman, L. S., Surface alloying using high-power continuous lasers, SPIE 198, 120 (1980).

[12] Draper, C. W., Preece, C. M., Buene, L., Jacobson, D. C., and Poate, J. M., Laser alloying metal films on nickel, in Laser and Electron Beam Processing of Materials (1979 Proc. Materials Research Society), White, C. W., and Peercy, P. S., eds. (Academic Press, New York, 1980). pp. 721-727.

[13] Jain, A. K., Kulkarni, V. N., Sood, P. K., Sundararaman, M., and Yadav, R. D. S., Laser induced surface alloy formation and diffusion of antimony in aluminum, Nucl. Instrum. Methods 168, 275 (1980).

[14] Mazzoldi, P., Della Mea, G., Battaglin, G., Miotello, A., Servidori, M., Bacci, D., and Jannitti, E., Formation of a noncrystalline phase in aluminum irradiated with a pulsed ruby laser, Phys. Rev. Lett. 44, 88 (1980).

[15] Buene, L., Poate, J. M., Jacobson, D. C., Draper, C. W., and Hirvonen, J. K., Laser irradiation of nickel single crystals, Appl. Phys. Lett. 37, 385 (1980).

[16] Chen, H. S., glassy metals, Rep. Prog. Phys. 43, 23 (1980).

[17] Olstad, R. A., and Olander, D. R., Evaporation of solids by laser pulses. II. zirconium hydride, J. Appl. Phys. 46, 1509 (1975).

[18] Meyer, R. T., Lynch, A. W., and Freese, J. M., Chemical reactions of carbon atoms and molecules from laser-induced vaporization of graphite and tantalum carbide, J. Phys. Chem. 77,

[18] Con't - 1085 (1973).

[19] Zehner, D. M., White, C. W., and Ownby, G. W., Preparation of atomically clean silicon surfaces by pulsed laser irradiation, Appl. Phys. Lett. 36, 56 (1980).

[20] Papagno, L., Scarmozzino, R., and Simoni, F., High power laser etching and Auger electron spectroscopy profiles, Thin Solid Films, 67, 157 (1980).

[21] Summarized by Bennett, H. E., Glass, A. J., Guenther, A. H., and Newman, B., Laser induced damage in optical materials: eleventh ASTM symposium, Appl. Opt. 19, 2375 (1980).

[22] Leamy, H. J., Rozgonyi, G. A., Sheng, T. T., and Celler, G. K., Periodic regrowth phenomena produced by Laser annealing of ion-implanted silicon, Appl. Phys. Lett. 32, 535 (1978).

[23] Affolter, K., Luthy, W., Wittmer, M., Interference effects on the surface of Nd:YAG - laser - reacted Pd-silicide, Appl. Phys. Lett. 36, 559 (1980).

Figure 1. Ni single crystal irradiated with a pattern of Q-switched Nd-YAG laser pulses. The textured preirradiation surface topography is due to high dose Ag implantation. The height of the micrograph is 90 μm.

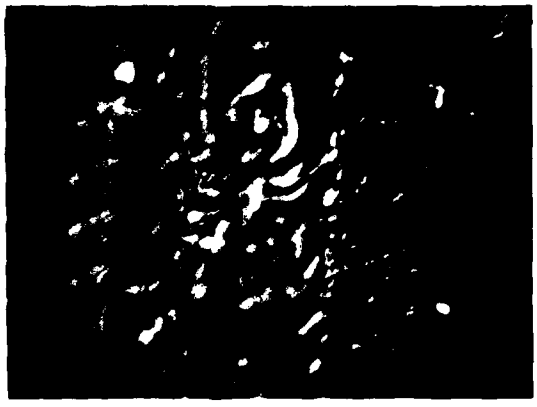

Figure 2. Molybdenum single crystal irradiated with Q-switched Nd-YAG laser pulses. The pre-irradiation surface was mechanically, but not electrochemically polished. The height of the micrograph is 90 μm. Melt spot diameters are 25 μm.

Figure 6 illustrates the air breakdown threshold as defined above. For very short duration and

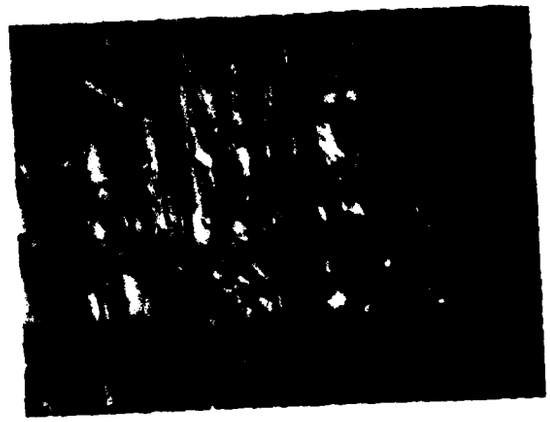

Figure 3. Cold rolled polycrystalline Ni irradiated with widely spaced rows of frequency doubled, Q-switched Nd-YAG laser pulses. Note repair of scratch marks on the lower central and right hand portions of the micrograph. Micrograph height 90 μm.

a b

Figure 4. Cold rolled polycrystalline Sn modified Cu-Ni irradiated with Q-switched Nd-YAG laser pulses. Both parallel (a) and perpendicular (b) scanning relative to the rolling direction. Strong coupling features always propagate in the rolling direction. Micrograph height 90 μm.

Figure 5. Single crystal Ni implanted on right hand side with 10^{16} cm^{-2} Hf and irradiated with Q-switched Nd-YAG laser pulses. Edge of implanted region is sharply demarcated. Coupling in implanted side is not as strong as virgin Ni. Also note hillocks on implanted and irradiated side due to contamination (see Figure 6). Micrograph height 90 μm.

Figure 6. Surface of implanted Ni of Figure 5 prior to irradiation. Contamination on implanted region (right hand side) is condensed carbon or silicon based vacuum pump oil. Strong coupling on these sites leads to hillocks seen above. Micrograph height 90 μm.

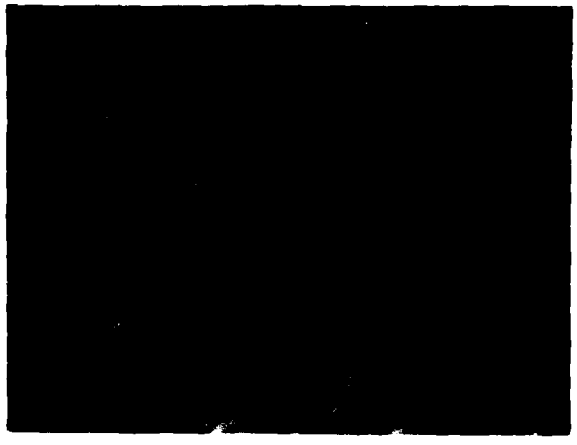

(a)

(b)

Figure 7. Low dose Au implanted single crystal Ni. Contamination of unknown origin with feathery appearance. In (a) lower region has been laser scanned above melt threshold. Compare resulting topography with Figures 1 or 2. In (b) sample has been irradiated again - this time below melt threshold. Note how coupling has been enhanced in contaminated regions. Micrograph height 90 μm.

Figure 8. Set of "frozen in" topographical interference fringes spaced 1 μm apart and parallel to preirradiation scratches. Q-switched Nd-YAG irradiation of Ni single crystal surface. Micrograph height 90 μm.

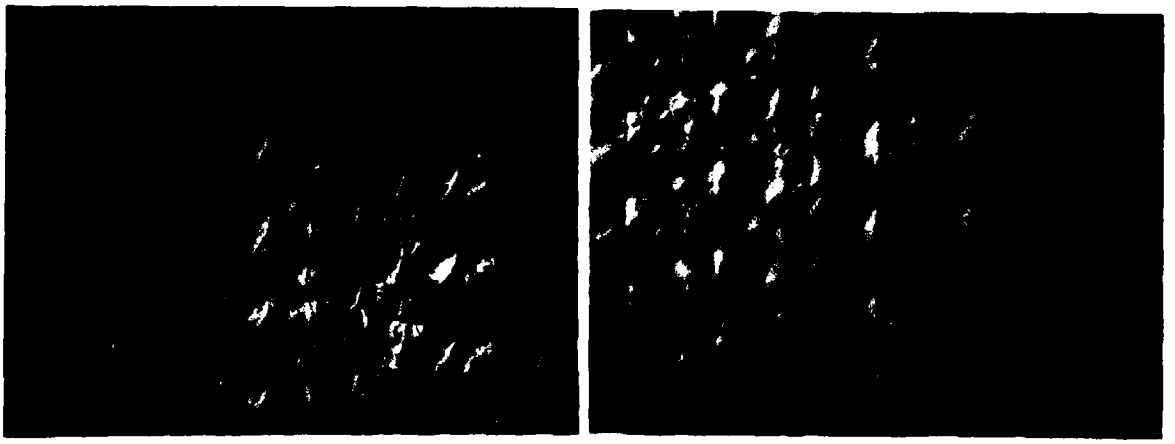

(a) (b)

Figure 9. Single crystal Ni irradiated with (a) and without (b) smoke particles in optical path. Micrograph height 90 μm.

Figure 10. Single crystal Mo irradiated with Q-switched Nd-YAG. A Fresnel type pattern, set up by the interference between a plane wave and a scattering particle spherical wave, has "frozen in" the moon shaped features and associated ripples. Micrograph height 54 μm.

EPITAXIAL REGROWTH AND DEFECTS IN LASER IRRADIATED SINGLE CRYSTAL Ni

Clifton W. Draper
Western Electric Engineering Research Center
Princeton, New Jersey 08540

and

L. Buene, D. C. Jacobson, J. M. Poate and S. Nakahara
Bell Laboratories
Murray Hill, New Jersey 07974

We have used Q-switched Nd:YAG irradiation to melt surface layers of metallic single crystal nickel. The quality of the epitaxially regrown layers has been determined by Rutherford backscattering and channeling as well as by TEM. TEM shows a high density of extended defects (dislocation tangles and walls). We have also observed significant differences between irradiated <100> and <111> crystals cut from the same Ni boule. One explanation for the orientation dependence is that slip occurs more easily in <111> planes of fcc structures and consequently there is a higher density of defect nucleation centers for <111> liquid phase regrowth.

Key words: Defects; epitaxial regrowth; laser irradiation; liquid phase; single crystal

We are using Q-switched laser irradiation to produce surface alloys in the liquid phase [1,2]. The advantages of surface liquid phase alloying using Q-switched lasers is that surfaces can be melted to depths of < 10,000 Å, and alloying takes place in the liquid phase where most species are miscible. To achieve such shallow surface alloying implies fast liquid phase regrowth volocities, ∿5 m/sec., and concurrently, high quenching rates.

In this work we present studies of the defect structures produced by such rapid processing of virgin single crystal Ni samples. Details of the laser systems used appear in another paper presented at this symposium [3]. Samples were examined by Rutherford backscattering (RBS) and channeling, TEM, SEM and Nonarski DIC.

In order to clearly delineate the difference between defects associated with heating below melting threshold and those with liquid phase epitaxial regrowth, we have employed evaporated surface markers of 10 Å of Ag. The liquid phase diffusivity is many orders of magnitude higher then solid phase diffusion and this property is a useful indication of melting. Figures 1 and 2 show RBS and channeling data for 10 Å of Ag evaporated on Ni <110> for various Q-switched frequency-doubled laser irradiations. At and above 35 MW cm^{-2}, Ag is seen to diffuse into the Ni which clearly must be liquid phase diffusion. Moreover, the channeling spectra shows that the density of defects in this regime is much higher than when the sample does not melt.

To investigate the defects remaining after the surface has melted, we have examined Ni crystals with <100>, <110> and <111> orientation cut from the same boule. Figure 3 shows Ni channeling spectra for <100> and <111> orientations. The density of defects is greater for <111> than <100>. It is difficult from channeling analysis to identify the defects except that they are extended with a depth of 3000 Å and densities > $10^{11} cm^{-2}$. TEM analysis for the <111> orientation shows a very dense tangle (10^{12} cm^{-2}) of dislocations within 2000 Å of the surface, whereas for the <100> orientation the dislocations are present in a fairly regular cell array with dimensions of a few thousand angstroms. One explanation for this orientation dependence is that slip occurs more readily in <111> planes and consequently that there is a higher density of defect nucleation centers for <111> liquid phase regrowth.

A more detailed presentation of this subject will be made at the 1980 Materials Research Society meeting (Boston, Massachusetts) in November. The proceedings of that conference will be published.

References

[1] Draper, C. W., Preece, C. M. Buene, L., Jacobson, D. C., and Poate, J. M., Laser alloying metal films on nickel, in Laser and Electron Beam Processing of Materials (1979 Proc. Materials Research Society), White, C. W., and Peercy, P. S., eds. (Academic Press, New York, 1980). pp. 721-727.

[2] Buene, L., Poate, J. M., Jacobson, D. C., Draper, C. W., and Hirvonen, J. K., Laser irradiation of nickel single crystals, Appl. Phys. Lett. 37, 385 (1980).

[3] Draper, C. W., Regrowth in laser irradiated elemental metals and alloys: surface non-uniformities and coupling phenomena, this proceedings.

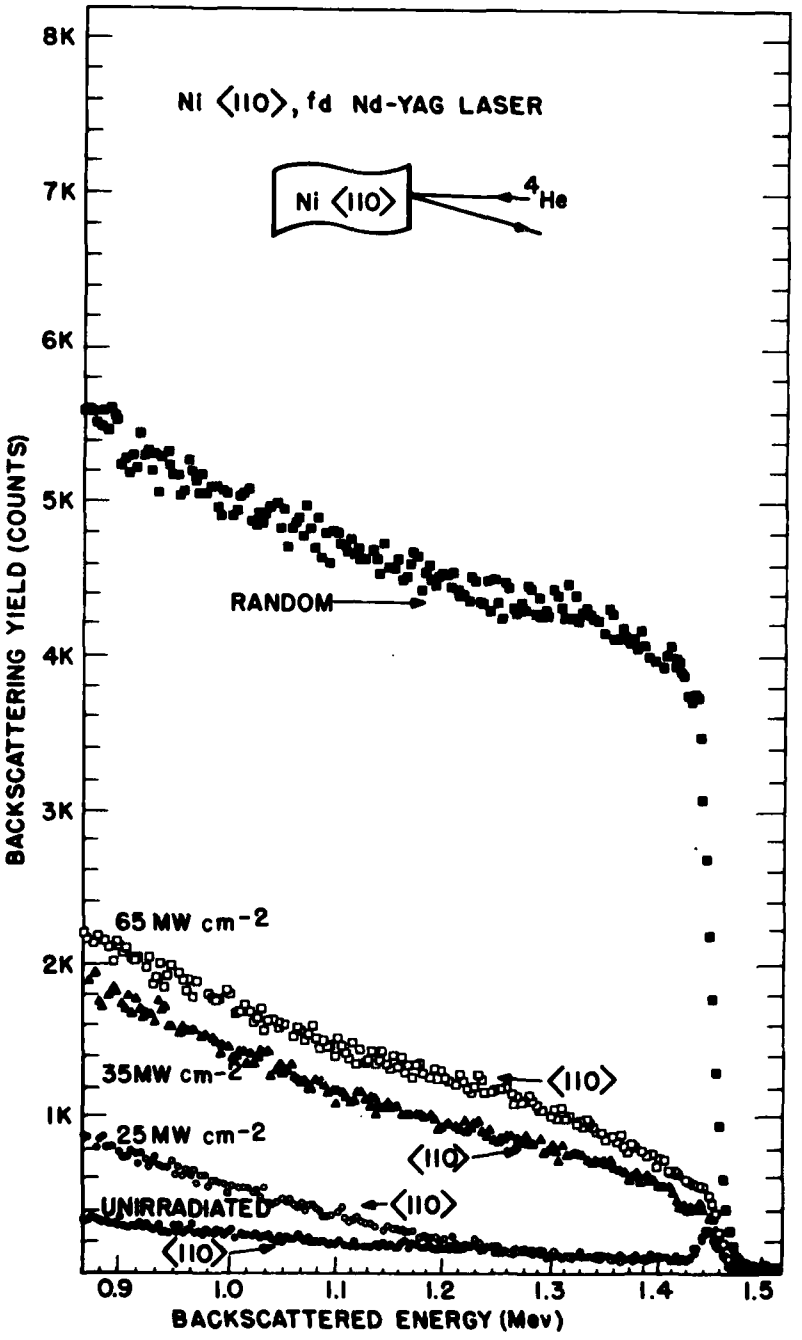

Figure 1. Rutherford backscattering and channeling spectra for Ni <110> with 10 Å Ag vacuum deposited. Sample has been irradiated with frequency doubled, Q-switched Nd-YAG laser. The increases in backscattering yield as a function of incident power density indicate an increasing density of defects. At 25 MW cm^{-2} the sample has not melted. See Figure 2.

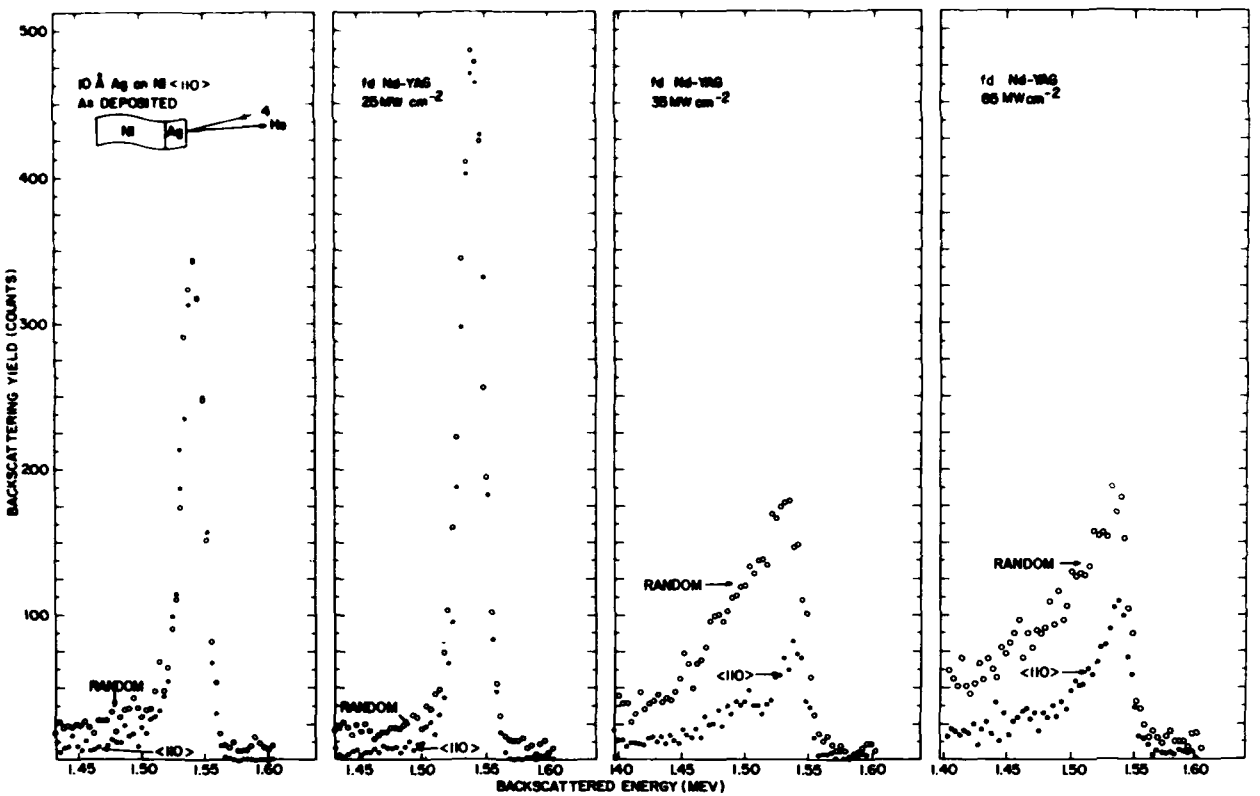

Figure 2. Channeling spectra for 10 Å Ag on Ni <110> as a function of laser incident power density. The as deposited film has no channeling. There is no diffusion of Ag at 25 MW cm^{-2}. At 35 MW cm^{-2} the Ag has diffused and channeling indicates substitutionality. Diffusion over these distances can only be associated with melting.

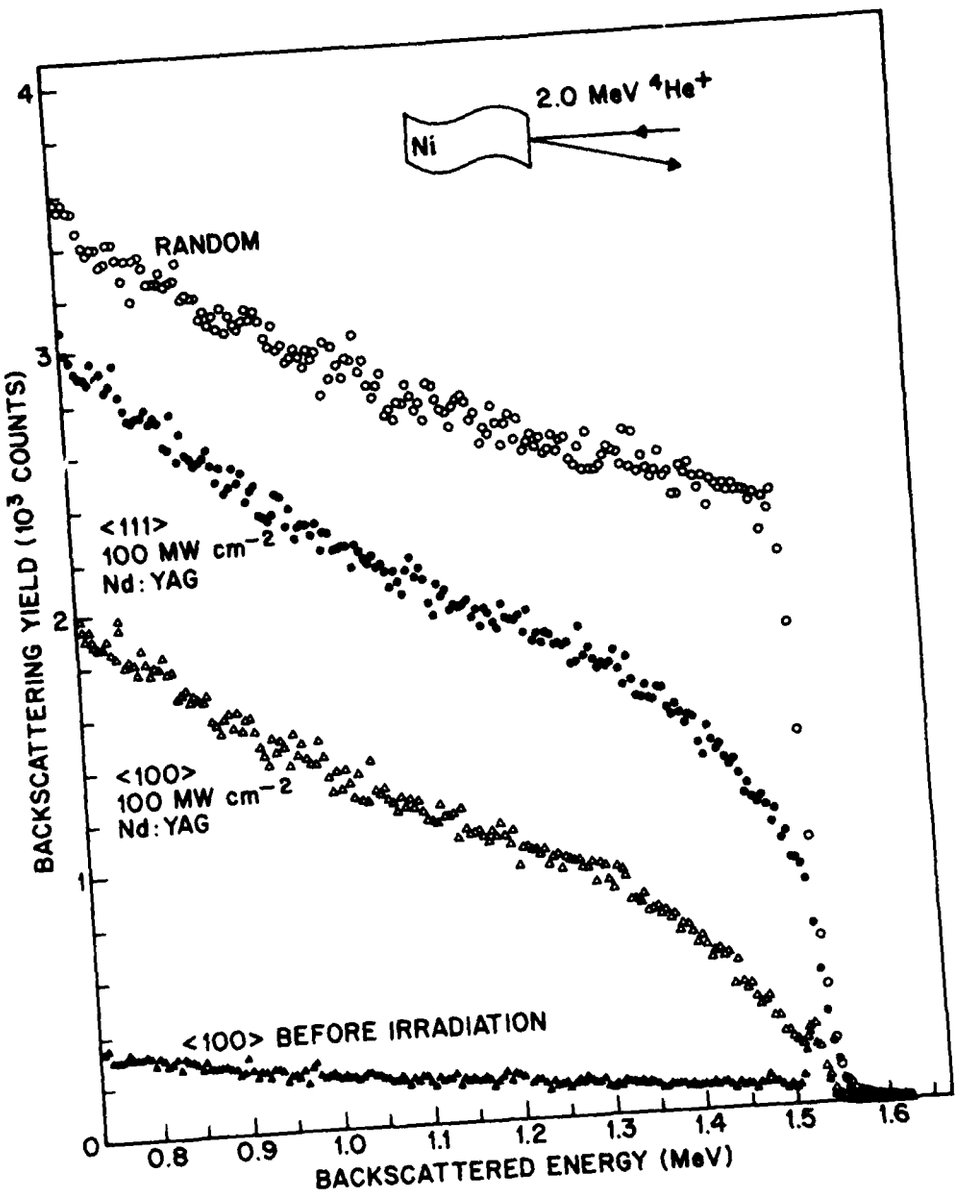

Figure 3. RBS and channeling spectra for Ni <100> and Ni <111> crystal faces irradiated at 100 MW cm^{-2} with a Q-switched Nd-YAG laser. A higher density of defects is indicated for the <111> orientation.

PULSED LASER INITIATION OF SURFACE PLASMA ON METAL MIRRORS*

Henry M. Musal, Jr.
Lockheed Palo Alto Research Laboratories
Palo Alto, California 94304

Plasma formation at the surface of a metal mirror under intense pulsed laser irradiation in an ambient atmosphere usually leads to enhanced thermal and mechanical coupling with consequently increased surface damage.

Exo-electron emission associated with plastic micro-yielding of the metal surface under thermomechanical stress induced by a surface temperature rise (ΔT) is proposed here as a plasma initiation mechanism. Emission starts when ΔT exceeds a relatively small critical value. Rapid buildup of the plasma proceeds via nonequilibrium ionization cascade in the ambient atmosphere when the incident laser flux exceeds a threshold value. Formation of a highly absorbing plasma layer requires delivery of a minimum fluence while the incident flux is higher than the above-mentioned flux threshold. At high values of incident flux, the required fluence decreases to an asymptotic minimum.

The critical temperature rise, threshold flux, and asymptotic minimum fluence required for surface plasma formation are defined here in terms of the pertinent radiation, material, and atmosphere parameters.

Key words: Cu mirrors; surface plasma; air breakdown; laser-induced electron emission; absorption waves; mirror surface damage.

1. Introduction

The formation of a plasma at the surface of a metal mirror under intense pulsed laser irradiation in an ambient atmosphere can lead to enhanced thermal and mechanical coupling of the pulse energy into the mirror. This may cause surface damage to the mirror and/or serious degradation of the reflected beam quality. The physical mechanisms and threshold conditions for surface plasma initiation at metal mirrors under intense pulsed laser irradiation are considered here.

Surface plasma initiation can be considered as a two-step process. First, an initial source of free electrons must be provided. Second, this relatively low electron concentration must increase, by absorption of laser radiation, to a highly absorbing plasma layer. The subsequent energy coupling to the surface and transition to a laser-supported absorption wave (either a radiation-driven subsonic LSC wave or a shock-driven supersonic LSD wave) is beyond the scope of this discussion; however, some results of previous absorption wave studies will be related to the plasma initiation results presented here.

2. Initial electron production

The initial electrons required to start surface plasma formation may be either ejected from the metal surface into the ambient atmosphere by a number of physical processes, or contained within a micro-plasma of vaporized material from the surface. Both of these sources of initial electron production will be considered here.

It can be shown easily that uniform bulk vaporization of the metal surface requires much more laser pulse energy than is present in most instances of surface plasma formation. Furthermore, it is often observed experimentally that plasma initiation occurs at localized sites on the surface. This gives rise to the concept of localized defect site vaporization as a source of initial micro-plasmas. The vaporized material may come from foreign particles on, or embedded in, the surface, or may consist of metal from flakes or bridges over subsurface voids that are in poor thermal contact with the bulk metal and hence can readily vaporize. A substantial concentration of free electrons is present in the vapors of most metals and other materials with high vaporization temperatures. Thus, this mechanism of initial electron production is viable, but it is extremely difficult to characterize because of the vast variability of the parameters that are involved.

Electrons can be ejected from the surface directly into the ambient atmosphere by a number of well-known emission mechanisms, such as multi-photon photoelectric emission, high-field emission, and thermionic emission. The first two of the above-mentioned mechanisms can produce free electrons without the need for a surface temperature rise, although they are enhanced by it. The radiation flux required to produce a substantial electron emission current via these mechanisms is, however, much

* Work supported by Lockheed Palo Alto Research Laboratories Independent Research funds.

higher than is usually present during experimentally observed surface plasma formation. Thermionic electron emission, like vaporization, is a viable mechanism only if the concept of defect sites is invoked to allow the local surface temperature to rise far higher than the average surface temperature.

The most viable of the above-mentioned mechanisms for production of the initial electrons necessary for surface plasma formation both require the presence of surface defect sites. There is no doubt that such sites exist on real mirror surfaces as presently fabricated. It may be possible to effectively eliminate surface defect sites through improved fabrication technology and/or optical radiation conditioning of the mirror surface, so that the thresholds for initial electron production via thermionic emission (from the metal) and/or vaporization (of foreign inclusions) are increased at least to the bulk melt threshold. It is suggested here, however, that exo-electron emission associated with plastic micro-yielding of the metal surface under thermomechanical stress induced by a relatively small surface temperature rise can provide initial electrons for surface plasma formation well below the bulk melt threshold.

Plastic yield of metal mirror surfaces under pulsed laser irradiation conditions well below the melt threshold has been seen experimentally [1, 2] and has been analytically modeled [3]. It has also been observed that electrons are emitted from metal surfaces undergoing plastic deformation induced by mechanically applied stress [4, 5, 6]. This electron emission occurs in the dark (without photo-stimulation), and only during the plastic deformation process [7]. Figure 1 illustrates the suggested electron emission mechanism under pulsed laser irradiation. The surface temperature rise due to absorbed laser radiation induces thermomechanical stress in the near-surface region of the metal. When the yield stress of the metal is exceeded, plastic deformation (yield) occurs, and electrons are ejected from the metal surface at the deformation sites. This electron emission occurs only during the period of plastic deformation, and a thin layer of electrons accumulates in the ambient atmosphere over each site during this time. It is postulated that the number of ejected electrons is proportional to the total plastic strain.

An analytic model [3] of metal surface plastic deformation under pulsed laser irradiation shows that the plastic yield threshold can be defined in terms of a critical surface temperature rise ΔT_y, given by

$$\Delta T_y = \frac{(1 - \nu)\, Y}{\alpha\, E} \tag{1}$$

where Y is the yield stress, ν is Poisson's ratio, α is the coefficient of thermal expansion, and E is Young's modulus of the metal. The laser pulse fluence (F_y) required to produce this surface temperature rise is

$$F_y = \frac{(\pi\, k\, \rho\, C\, T_p)^{1/2}}{2A}\, \Delta T_y \tag{2}$$

where k, ρ, and C are the thermal conductivity, density, and specific heat of the metal; T_p is the pulse duration (rectangular pulse shape assumed); and A is the optical absorptance of the surface at the laser radiation wavelength. This relationship is valid only for small temperature excursions where k, ρ, C, and A can be considered to be approximately constant. If the peak surface temperature rise (ΔT_p) during a laser pulse exceeds ΔT_y on the first pulse, or $2\Delta T_y$ on successive pulses, plastic strain will occur. The increment of plastic strain $(\Delta\varepsilon)$ accumulated on the first pulse is

$$\Delta\varepsilon = \alpha\, (\Delta T_p - \Delta T_y)\ ;\ (\Delta T_p > \Delta T_y) \tag{3}$$

and on successive pulses is

$$\Delta\varepsilon = \alpha\, (\Delta T_p - 2\Delta T_y)\ ;\ (\Delta T_p > 2\Delta T_y) \tag{4}$$

Figure 2 shows the plastic yield threshold (F_y versus T_p) and conditions for first-pulse plastic strain of 0.2 percent calculated via this analytic model, and the surface melt threshold [8], in comparison to experimental data [1, 2, 9] for a copper surface under CO_2 laser pulse irradiation. The plastic yield threshold temperature rise (ΔT_y) for copper with a yield stress of 9×10^3 psi, as calculated from Eq. (1), is seen to be only 20 K. The locus of conditions for first-pulse plastic strain equal to 0.2 percent is shown because this is the minimum amount of plastic strain usually needed for a clear indication of plastic deformation. The correlation between theoretical predictions and experimental data is seen to be reasonably good.

Electron emission from metal surfaces under pulsed laser irradiation has been measured in numerous experiments. It has not yet been clearly established that plastic yielding is the source of these electrons in any of these experiments. Figure 3 shows results of measurements made by Walters et al. [10], for an aluminum surface under CO_2 laser pulse irradiation in an air atmosphere.

Also shown is the theoretical prediction of the time during the laser pulse at which the yield threshold would be reached (surface temperature rise of 100 K). This correlates reasonably well with the onset of electron emission. Bremsstrahlung radiation from ionized air is seen to begin later, indicating the formation of an air plasma (no vapor). It should be pointed out that Walters ascribes the electron emission to thermionic emission from flake- or void-type defect sites, and his calculation (based on a defect site model) of the time at which electron emission would begin also correlates very well with the experimental results. Figure 4 shows results of measurements made by Sharp [11] for metal surface irradiation in vacuum. The theoretical predictions of the conditions at which the yield thresholds would be reached are also shown. Electron emission is seen to begin slightly above these thresholds as would be expected from the plastic strain model. Both Walters' and Sharp's experimental results are consistent with the predictions of the plastic strain electron emission model, but neither confirms that this mechanism was responsible for the electron emission. More definitive experiments are necessary to do this.

3. Ionization buildup

In considering ionization buildup to a highly absorbing surface plasma layer, it is necessary to distinguish between the situation where the initial electrons are ejected into an ambient atmosphere and the situation where a micro-plasma of vaporized material contains the initial free electrons. The significant difference between these two situations involves the energy transfer mechanisms that influence the production of additional free electrons. In both situations the initial free electrons gain kinetic energy from the laser radiation field via inverse Bremsstrahlung during collisions with other particles (molecules, atoms, and ions). The electrons lose energy by exciting the various degrees of freedom (rotation, translation, vibration, electronic excitation, and ionization) of the other particles. If this energy transfer proceeds with near-equality of the electron and heavy-particle temperatures, quasi-equilibrium heating of the gas occurs and the increase in free electron concentration is consonant with the gas temperature. On the other hand, if the electron temperature greatly exceeds the heavy-particle temperature, then the more highly energetic excitation processes (such as ionization) are favored, and a rapid nonequilibrium ionization cascade (breakdown) can occur. This produces a highly absorbing plasma very quickly.

The energy transfer rates in nitrogen (which dominate the kinetics in air) are shown in Fig. 5. These energy transfer rates are normalized with respect to both the electron and nitrogen molecule number densities. This figure can be used to illustrate the initial phase of the above-described breakdown mechanism for polyatomic gases; however, a full description of the evolution requires a detailed radiation-gasdynamic treatment [12].

The electron heating (energy gain) rates for various 10.6-μm radiation fluxes are shown at the left side of the figure. Initially the electron temperature may be very low, but under the influence of the applied laser flux it will very quickly increase until the energy loss rate equals the heating rate. This temperature is determined by the intersection of the total loss rate curve (solid line) with the heating rate curve appropriate to the applied laser flux. For example, for an applied flux of 10^7 W/cm^2 the intersection occurs at an electron temperature of 0.2 eV, and most of the transferred energy goes into vibrational excitation of nitrogen molecules. This is subsequently redistributed among other degrees of freedom of the molecules by molecule-molecule collisions, and the gas heats in quasi-equilibrium. The situation is not much different for fluxes up to 10^9 W/cm^2. However, at a flux of approximately 3×10^9 W/cm^2 the peak of the vibrational excitation curve is exceeded, the electron temperature increases to 1.6 eV, and most of the transferred energy goes into electronic excitation and ionization. This is the flux threshold for breakdown. At flux values high above this threshold almost all of the absorbed and transferred energy goes directly into ionization. It can be shown [10] that in this circumstance an initial electron density of 10^{12} cm^{-3} will cascade to 10^{18} cm^{-3} during passage of a minimum fluence of approximately 2 J/cm^2 in one atmosphere of nitrogen. Because the initial electron concentration is near the mirror surface, it effectively is subjected to both the incident and reflected radiation beams. Thus, in terms of the incident beam, the breakdown threshold flux and asymptotic minimum fluence are approximately one-half of the above-cited values.

Since inverse Bremsstrahlung absorption rates are inversely proportional to the square of the radiation wavelength, and the absolute rate of energy absorption is proportional to the number density of heavy particles, the threshold flux for nonequilibrium electron cascade (breakdown) in air f_{BDA} can be expressed as

$$f_{BDA} = 1.5 \times 10^3 \times (10.6/\lambda)^2 \quad [\mathrm{MW/cm^2}] \tag{5}$$

where λ is the radiation wavelength in microns, and the asymptotic air breakdown fluence requirement ΔF_{BDA} can be expressed as

$$\Delta F_{BDA} = 1 \times (10.6/\lambda)^2 \times (1/p) \quad [\mathrm{J/cm^2}] \tag{6}$$

where p is the ambient air pressure in atmospheres. This fluence requirement is expressed as an increment because it must be provided after the initial electrons are produced, and therefore does not represent the total fluence needed.

Figure 6 illustrates the air breakdown threshold as defined above. For very short duration and high flux pulses, the breakdown is fluence-controlled. At longer pulse durations, the controlling parameter is the threshold flux requirement. The transition between these two regimes is shown as a dashed line because the exact shape of the curve has not been determined. The parameter regime above the breakdown threshold is where breakdown is predicted to occur, while below the curve either the flux or fluence (or both) criteria are not met.

The significant difference between air (or polyatomic gas) breakdown and metal vapor (or monatomic gas) breakdown lies in the electron energy loss mechanisms. Figure 5 shows that if rotational and vibrational energy sinks were not present then, at low laser fluxes, the electron temperature would be determined by losses to the translation and electronic excitation modes of the heavy particles. This allows much higher electron temperatures to be reached at much lower incident laser fluxes, and consequently the threshold flux for nonequilibrium electron cascade is much lower. A study of nonequilibrium processes in metal vapors [12] shows that the threshold incident flux for nonequilibrium electron cascade (breakdown) in metal vapor near a reflecting surface f_{BDV} is

$$f_{BDV} = 1 \times (10.6/\lambda)^2 \quad [MW/cm^2] \tag{7}$$

and the asymptotic breakdown fluence requirement ΔF_{BDV} can be repressed as

$$\Delta F_{BDV} = 1 \times (10.6/\lambda)^2 \times (1/p) \times (\phi_{iV}/\phi_{iA}) \quad [J/cm^2] \tag{8}$$

where ϕ_{iV} and ϕ_{iA} are the ionization potentials of the metal vapor and air, respectively. The ratio ϕ_{iV}/ϕ_{iA} is approximately one-half. The composite metal vapor breakdown threshold is shown in Fig. 6. The comments made previously about the air breakdown threshold curve also apply here.

4. Absorption waves

Although detailed consideration of laser-supported absorption waves is beyond the scope of this discussion, it is useful to summarize some results of previous work [12] for comparison to the breakdown thresholds that have been defined here. Two distinctly different types of laser-supported absorption waves have been identified. Both can be initiated from surface plasmas. One is the so-called laser-supported combustion (LSC) wave, which propagates subsonically up the laser beam (toward the laser). The dominant energy transport mechanism responsible for wave propagation is ultraviolet radiation from the plasma at the wavefront which preionizes the air ahead of the wave. Thermal conduction plays a secondary role in the energy transport. This type of absorption wave can exist at relatively low incident laser fluxes. The second type of absorption wave is the so-called laser-supported detonation [LSD] wave, which propagates supersonically up the laser beam. The strong shock at the front of this wave preionizes the air and is the dominant propagation mechanism. This type of wave can exist only in relatively high incident laser fluxes. Both types of waves effectively absorb most of the incident laser beam. The absorbed energy is converted preferentially into short wavelength broadband radiation in the LSC wave and into gas kinetic energy in the LSD wave. An LSC wave started at a surface will irradiate the surface with ultraviolet radiation for a relatively long time before it propagates away. On the other hand, an LSD wave will propagate away from the surface very quickly, thus "shielding" it from the incident laser radiation.

Detailed numerical solutions of the internal structure of an LSD wave in air over a wide range of laser flux, wavelength, and ambient density have been correlated in terms of a scaling relationship [12], from which an approximate threshold condition for LSD wave existence has been derived. The LSD wave threshold flux (f_{LSD}) is given by

$$f_{LSD} = 10 \times (10/d)^{1/4} \times (10.6/\lambda)^{1/2} \times p^{1/2} \quad [MW/cm^2] \tag{9}$$

where d is the diameter (in centimeters) of either the initial surface plasma or the laser beam, whichever is smaller. This LSD wave threshold is shown in Fig. 6 for 10 μm and 10-cm diameter initiation sites.

Two comparisons between experimental results [10, 13] and theoretical predictions are shown in Fig. 6. The measurements can be interpreted as representing the fluence required to produce a surface plasma within the time period that is indicated. Both experimental results lie significantly below the air breakdown threshold, and well above the metal vapor breakdown threshold, which strongly suggests that the initial electrons were provided by defect site vaporization. The experimental results also represent the observed LSD wave thresholds, and their proximity to predicted LSD wave thresholds for small site initiation is consistent.

5. Discussion

Conditions required for surface plasma formation at metal mirrors under pulsed laser irradiation have been identified, and critical thresholds have been quantified in terms of pertinent radiation, material, and atmospheric parameters. Figure 7 summarizes the threshold relationships for copper under CO_2 laser pulse irradiation in air. The threshold for initial electron production at the

surface via exo-electron emission as a result of plastic strain is determined by the yield threshold. Defect site thermionic emission and/or vaporization as the source of initial electrons is not represented because of its vast variability. The surface melt threshold is shown for reference. Breakdown thresholds for air and metal vapor, and LSD wave thresholds for small and large initiation sites, are also included. Several general observations can be made based on the relative relationships between these various thresholds.

For pulse durations near 1 ns, the air breakdown threshold is below the melt threshold. In this regime, initial electron production via plastic strain exo-electron emission at a surface temperature well below melting could lead to air breakdown and rapid evolution of the surface plasma into an LSD wave which would effectively shield the metal surface from any further significant temperature rise. The anomalously high damage thresholds reported for some copper mirrors under short-pulse CO_2 laser irradiation in an ambient air atmosphere (greater than 20 J/cm^2 in a 1.2-ns pulse) [14] are explainable on this basis.

At pulse durations greater than one 1 μs, large pulse fluences can be delivered at fluxes below the LSD wave threshold. Surface plasmas initiated at mirrors under these conditions will not decouple rapidly, and consequently enhanced energy coupling into the mirrors will occur. Since this regime is very far below the threshold for air breakdown, any such surface plasmas must be vapor initiated at localized defect sites. Therefore, either these sites must be eliminated, or else operation must be kept below the vapor breakdown threshold.

Two modes of mirror surface conditioning, or defect site cleanup, are suggested by Fig. 7. In the first mode, the mirror would be irradiated by laser pulses that are below the vapor breakdown threshold, so that highly absorbing defects could be vaporized without building up a highly absorbing ultraviolet-radiating surface plasma that could damage the surrounding metal surface. Repetitive pulsing might be needed to raise the localized defect site temperature high enough. In the second mode of conditioning, very high flux pulses (above the LSD wave threshold) would be used, so that any plasmas formed by defect vaporization would be quickly decoupled from the mirror surface. This puts operation closer to the melt threshold, so there is less margin for increased energy input into the surrounding mirror surface. Pulse durations in the range from 2 to 10 ns appear to maximize this margin.

Additional theoretical and experimental work is still required to validate the thresholds that have been defined here. However, these results offer a preliminary frame of reference in which new developments and data can be placed, or at least a point of departure for new concepts.

6. References

[1] Porteus, J. O., Decker, D. L., Jernigan, J. L., Faith, W. N., and Bass, M., Evaluation of metal mirrors for high power applications by multi-threshold damage analysis, IEEE J. Quant. Electronics, QE-14, pp. 776-780 (1978).

[2] Porteus, J. O., Decker, D. L., Seitel, S. C., and Soileau, M. J., Dependence of metal mirror damage thresholds on wavelength, material, pulse length, and preparation method, These Proceedings (1980).

[3] Musal, Jr., H. M., Thermomechanical stress degradation of metal mirror surfaces under pulsed laser irradiation, Laser Induced Damage in Optical Materials: 1979, NBS Special Publication 568, pp. 159-173 (1980).

[4] Guroszynski, A., and Sujak, B., Exoelectron emission in vacuum in the absence of light during plastic deformation of aluminum thickly coated with oxide, Acta Phys. Polon., 28, pp. 311-327 (1965).

[5] Arnott, D. R., and Ramsey, J. A., Electron emission from anodically oxidized aluminum due to tensile deformation, Surf. Sci., 28, pp. 1-18, (1971).

[6] Rosenblum, B., Braunlich, P., and Himmel, L., Spontaneous emission of charged particles and photons during tensile deformation of oxide-covered metals under ultra-high vacuum conditions, J. Appl. Phys., 48, pp. 5262-5273, (1977).

[7] Rosenblum, B., Carrico, J. P., Braunlich, P., and Himmel, L., Measurements of tribo-emmision from oxide-covered metals, J. Phys. E, 10, pp. 1056-1062 (1977)

[8] Musal, Jr., H. M., Influence of laser pulse shape on metal mirror damage, Proc. Inter. Conf. on Lasers 78, pp. 267-273 (1978)

[9] Smith, M. J., and Itzkan, I., Repetitive pulse, large area testing of copper mirrors with 10.6 μm radiation, High Power Laser Optical Components Topical Meeting, NBS, Boulder, Colorado, (2-3 Oct 1980).

[10] Walters, C.T., Barnes, R. H., and Beverely, III, R. E., Initiation of laser-supported-detonation (LSD) waves, J. Appl. Phys., 49, pp. 2937-2949 (1978).

above. Micrograph height 90 μm.

[11] Sharp, T.E., Experimental study of the initiation mechanism of laser supported absorption waves, LMSC-D566093, Lockheed Palo Alto Research Laboratories, (Nov 1977).

[12] Boni, A. A., Su, F. Y., Thomas, P. D., and Musal, Jr., H. M., Theoretical Study of Laser-Target Interactions, SAI77-567LJ, Science Applications, Inc., (May 1977).

[13] Maher, W. E., Hall, R. B., and Johnson, R. R., Experimental study of ignition and propagation of laser-supported detonation waves, J. Appl. Phys., 45, pp. 2138-2145 (1974)

[14] Newnam, B. E., and Gill, D. H., Damage resistance of CO_2 fusion laser optics, Opt. Eng., 18, pp. 579-585 (1979).

7. Figures

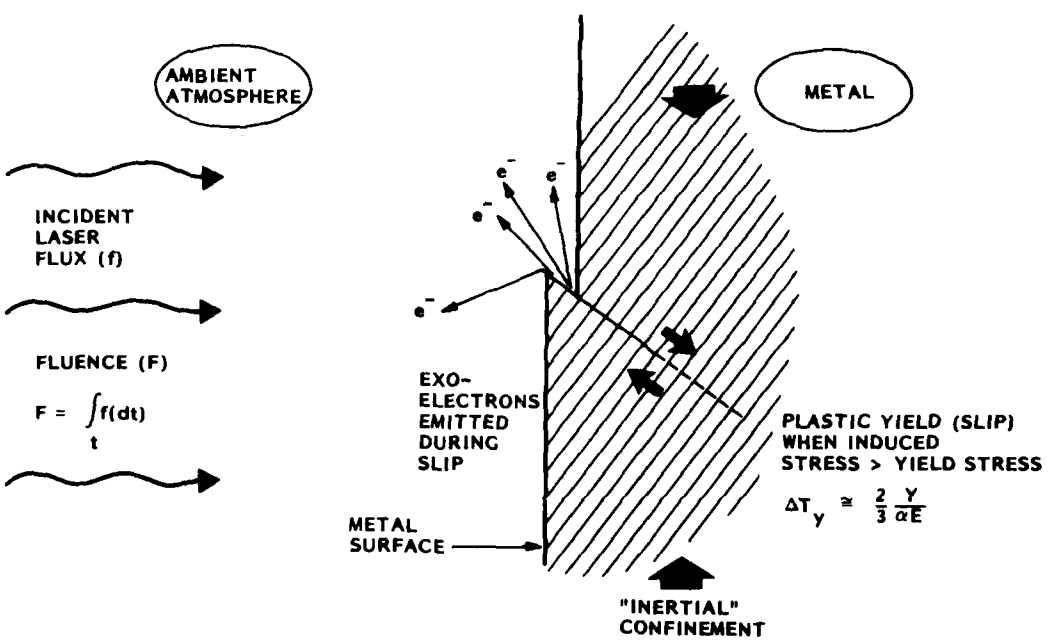

Figure 1. Electron emission from metal surface during plastic deformation under pulsed laser irradiation.

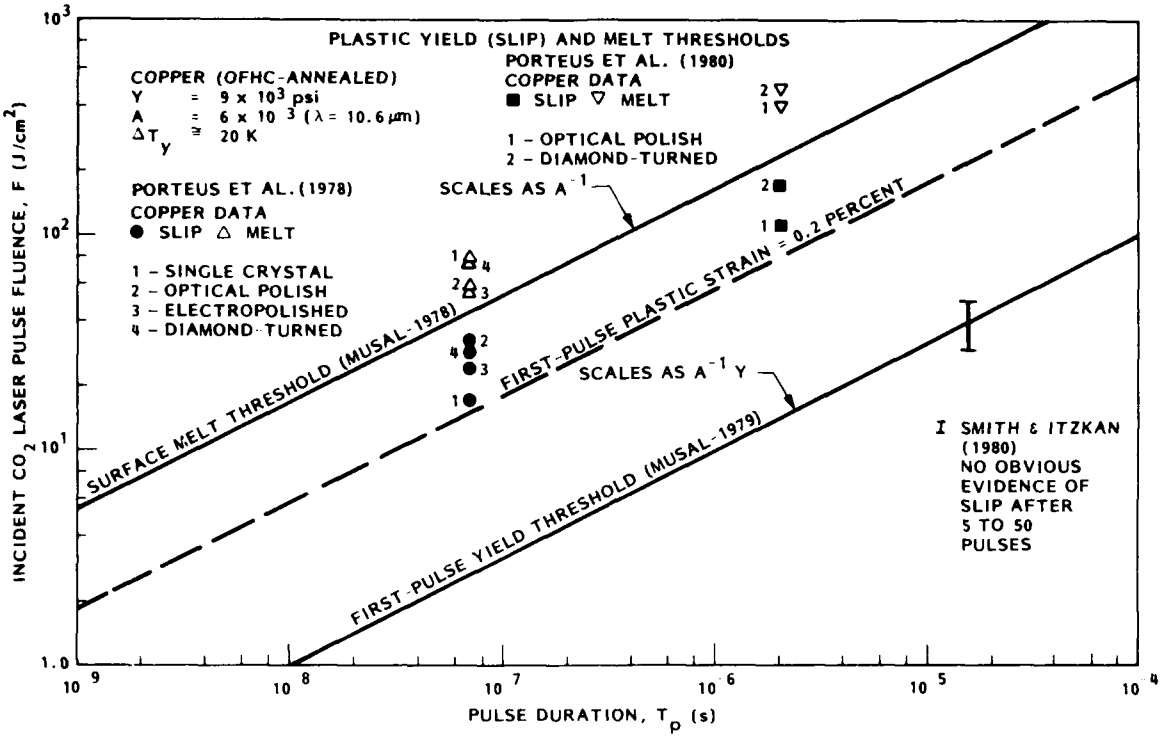

Figure 2. Plastic yield and melt thresholds for copper surface under pulsed CO_2 laser irradiation.

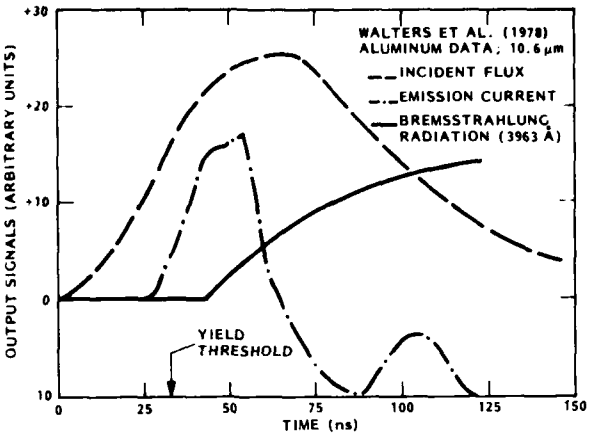

Figure 3. Electron emission current versus time during CO_2 laser pulse irradiation of aluminum surface in air atmosphere.

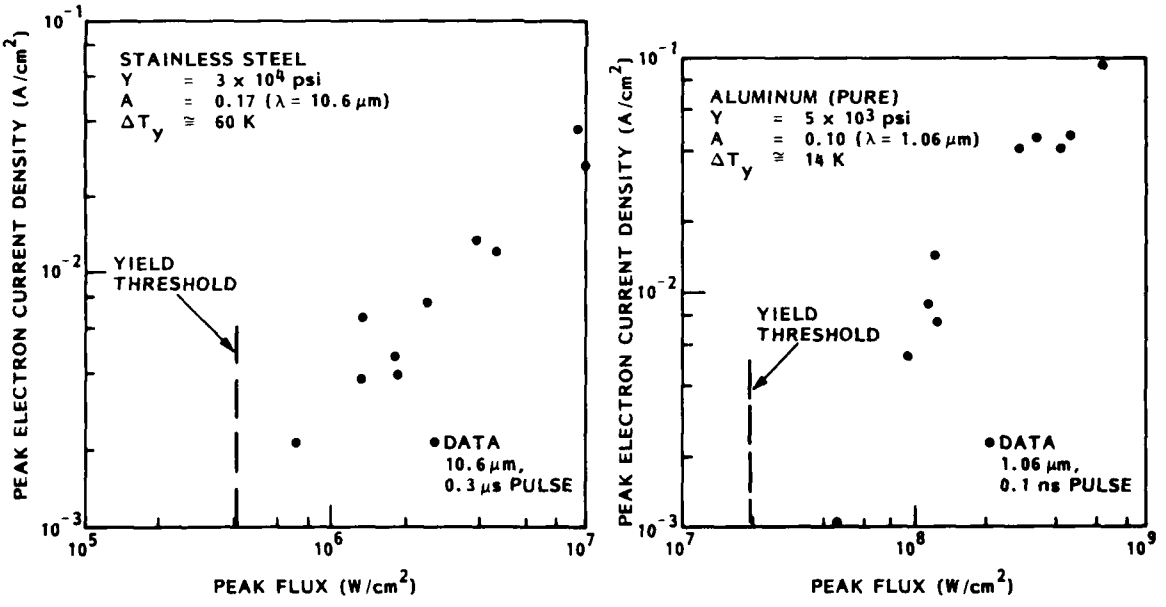

Figure 4. Peak electron emission current density versus laser pulse peak flux for metal surface irradiation in vacuum.

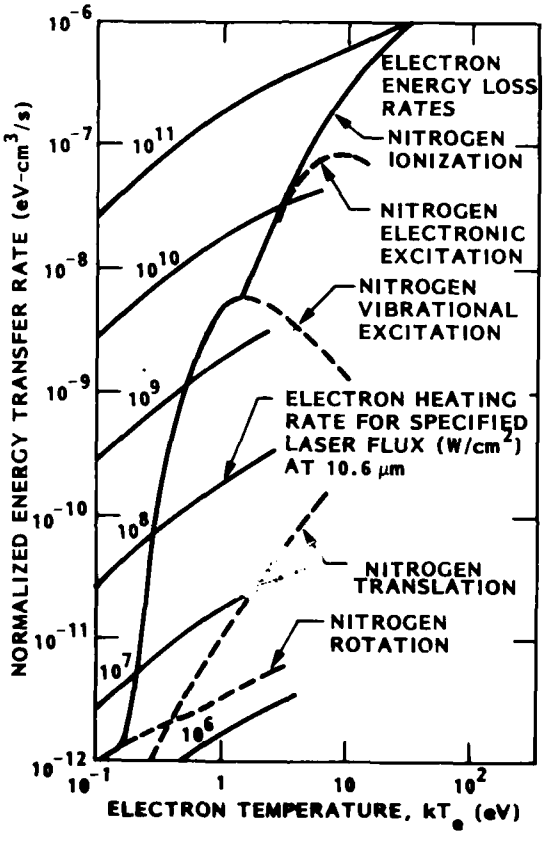

Figure 5. Energy transfer rates in nitrogen.

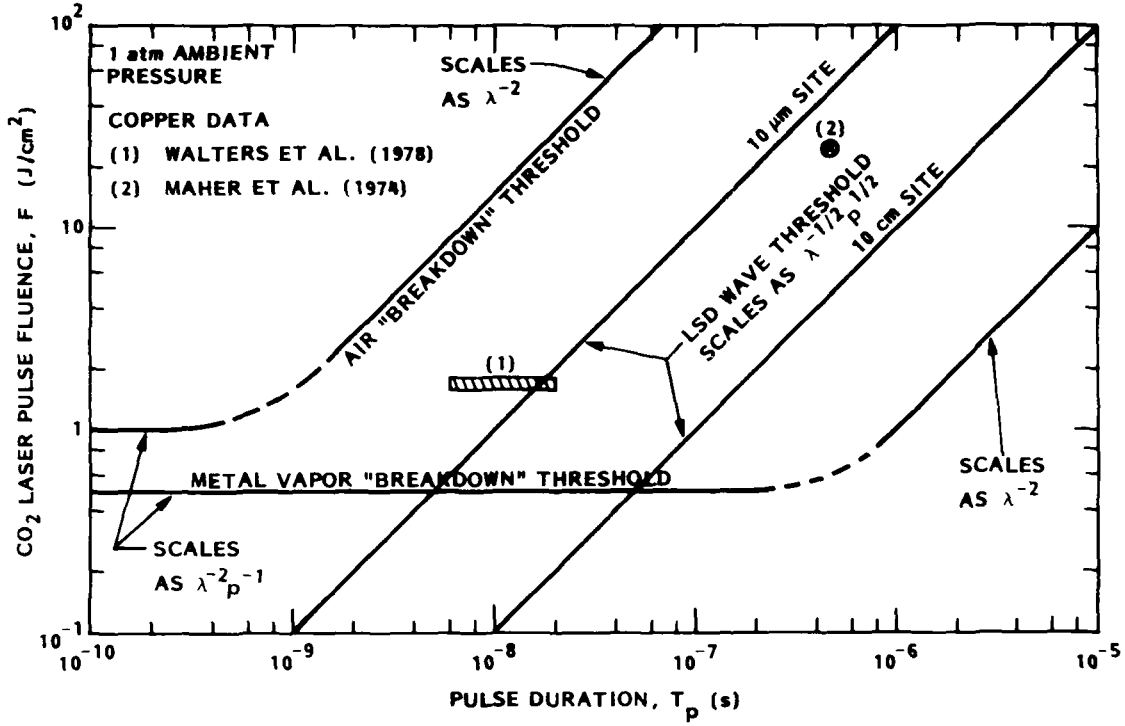

Figure 6. LSD wave thresholds, and breakdown thresholds in air and metal vapor at a metal surface, for CO_2 laser pulse irradiation.

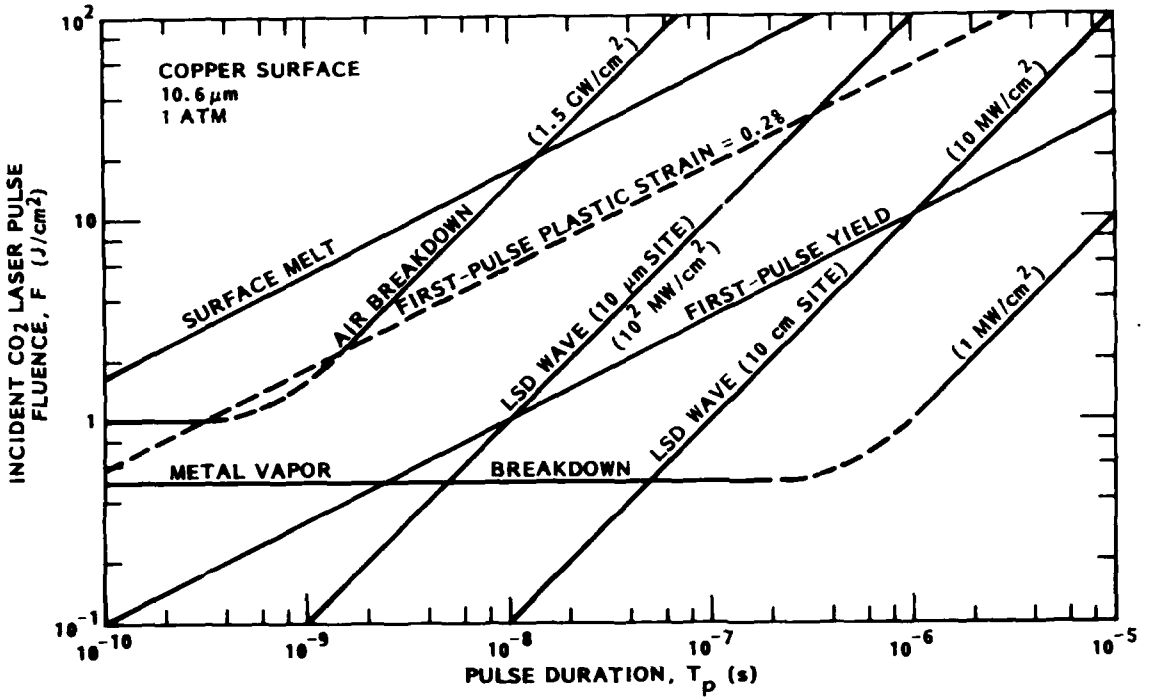

Figure 7. Comparison between melt, plastic strain, breakdown, and LSD wave thresholds for CO_2 laser pulse irradiation of a copper surface in air.

OPTICAL DAMAGE LIMITATIONS FOR COPPER MIRRORS USED IN CO_2-ICF LASER SYSTEMS*

S. J. Thomas, C. R. Phipps, Jr., and R. F. Harrison
Los Alamos Scientific Laboratory
Los Alamos, NM 87545

Because copper optics for CO_2-ICF system applications will be highly stressed, the single-shot damage thresholds which have been reported [1,2], provide only part of the information needed for accurate performance predictions. We report here a performance comparison for copper mirrors finished by different techniques, including single-point diamond turning (SPDT), showing for the first time the relative decrease in 10-μm damage thresholds corresponding to multiple shots, and the loss of reflected beam brightness arising at high fluence levels. We also report the intensity and energy loss due to plasma formation when Cu mirrors are used in air.

Key words: Copper mirrors; CO_2 laser; multishot damage; nanosecond pulse; peak energy density; pulse distortion; single-shot damage threshold; vacuum chamber.

1. Introduction

Copper mirrors are used extensively in the CO_2-ICF laser systems at Los Alamos Scientific Laboratory. These mirrors must withstand repeated short-pulse, high-fluence exposure in both air and vacuum environments. Since single shot damage thresholds give no hint of the fluence levels a mirror can survive in a multishot system, we have measured mirror lifetime as evidenced by the focusability of the reflected beam for up to 100 shots per site at selected fluence levels in a vacuum environment.

The measurement of damage thresholds in air is complicated by the formation of a plasma at the mirror surface; indeed, some mirrors cannct be damaged in air (table 1). We have measured the loss of energy and intensity caused by the air spark absorbing the tail of the pulse. Mirrors that could not be damaged in air had many polishing scratches or machining marks, causing early formation of plasma which protected the mirror surface. However, these mirrors did not perform well in multi-shot lifetime test in a vacuum (see fig. 3.)

2. Description of Test Mirrors

Mirror substrates were 4-inch-diameter copper-plated aluminum-bronze, similar to those used in the Antares Laser System. The copper plating was .040 inch thick. Several vendors used standard optical fabrication techniques in making the test mirrors, while some were finished by single-point diamond-turning (SPDT) techniques at the DOE Y-12 facility. These mirrors are not offered by the vendors and may not represent their products.

3. Experimental Setup and Procedure

Laser damage studies were conducted on the LASL L-9 Gigawatt Test Facility, which produces a gaussian, 1.7-ns pulse tuned to 10.59 μm (P(20)). A schematic of the test setup is shown in figure 1. The samples were placed 10 cm inside the focal point of a 1-m-focal length lens where the $1/e^2$ spot radius was 1 mm. The peak fluence (J/cm^2) at the sample plane was measured on each shot by use of a 200-μm-diameter pinhole located in the reference beam at the same distance from an identical lens. A Laser Precision Corp. ratiometer was employed to record the peak energy density of each laser shot, which was regulated with calibrated CaF_2 attenuators. Prior to each test series, a calibration was performed with an identical pinhole centered at the sample plane, and the B probe of the ratiometer used to measure peak fluence. By this technique, damage plane fluence was determined to ± 2%.

For the studies in vacuum, a vacuum chamber with NaCl windows provided a 100 mtorr test environment. A liquid nitrogen cold trap prevented oil vapors from reaching the samples.

Damage was defined as any change in the mirror surface observable with the aid of a 60X microscope and a white-light source. Damage spots in air were characterized by a diffraction pattern, while in vacuum the spot was always a smooth crater which grew from a single point. We believe the air spark is responsible for the diffraction in the former case.

4. Single-Shot Damage Thresholds

Single-shot damage thresholds were measured by irradiating the sample at 25 different sites, "one-on-one," at or near threshold, and taking the average of the measured threshold fluences. Thresholds for air and vacuum are tabulated in table 1. Vacuum thresholds were nearly the same level indicating we may have reached the melt point of copper.

*Work performed under the auspices of the U. S. Dept. of Energy.

Table 1

Mirror No.	Technique*	Damage Threshold in J/cm²** Air	Vacuum
56SN056	"C"	>25	13.0 ± 1.2
39SN039	"C"	>25	9.6 ± 1.1
7-9-79-1	"C"	>25	13.8 ± 0.4
7-9-79-3	"C"	19.00 ± 1.7	13.1 ± 0.5
3-7-79-53	"C"	16.4 ± 1.4	9.9 ± 1.2
12-11-78-26	"C"	15.7 ± 1.3	13.0 ± 0.8
12-11-78-24	"C"	15.0 ± 0.6	13.7 ± 0.2
3-27-79-45	"C"	16.1 ± 1.47	14.5 ± 0.5
4-23-79-01	"C"	13.9 ± 0.7	9.6 ± 0.2
12-11-78-22	"C"	13.5 ± 0.6	12.0 ± 0.2
4-23-79-2	"C"	12.1 ± 0.5	9.6 ± 0.8
4-17-79-04	"C"	12.2 ± 0.4	12.0 ± 0.4
1-18-79-43	"C"	12.1 ± 0.6	11.5 ± 0.4
1-18-79-42	"C"	11.0 ± 0.4	10.4 ± 0.6
4-17-79-01	"C"	12.5 ± 1.2	11.7 ± 0.4
12-19-78-22	"C"	8.5 ± 0.7	7.9 ± 0.1
12-19-78-23	"C"	11.7 ± 0.6	11.1 ± 0.3
3-23-79-23	"S"	12.9 ± 0.3	12.6 ± 0.3
3-23-79-26	"S"	13.3 ± 0.5	12.3 ± 0.1
3-23-79-25	"S"	21.6 ± 4.6	12.2 ± 0.3
3-23-79-22	"S"	12.3 ± 0.9	12.8 ± 0.2
3-23-79-24	"S"	23.8 ± 1.0	12.2 ± 0.1
Stock Copper	"S"	> 25	10.4 ± 1.2
Stock Alum.	"S"	0.41 ± 0.2	Not tested

*"C" = conventionally polished
"S" = single point diamond turned
**To convert J/cm² to Gigawatt/cm², multiply by 0.602.

5. Multishot Studies In Vacuum

The focusability of the reflected pulse for multiple shots on the same site was measured. A schematic of the experimental layout and diagnostics is shown in figure 2. This setup is similar to the one reported by Gill and Newnam for AR coatings on NaCl windows [3]. The reflected beam from the sample mirror was recollimated and focused through a 350 μm pinhole, and the B probe of the Laser Precision ratiometer was employed to measure transmission. Any change in transmission or focusability was revealed by a change in the ratio B/A. This was normalized to unity for each energy level and plotted versus number of shots. The data for four representative mirrors are shown in figures 3 - 6. Our goal was to find the highest fluence level (per shot) that would allow 100 shots with less than 10% cumulative reduction in the B/A ratio.

We have summarized this data in table 2, where this fluence is compared to the single-shot damage threshold fluence. On the average mirror 8.5 ± 1.0 J/cm² is a safe level, corresponding to 71 ± 12% of the single-shot threshold.[5]

Table 2

Mirror No.	Technique	Per-shot Vacuum Fluence Giving less than 10% Focusability Loss in 100 Shots (J/cm²)	Percent of Single-Shot Damage Fluence
3-23-79-26	"S"	9.5 ± 1.0	77
3-23-79-23	"S"	8.2 ± 0.2	65
3-23-79-22	"S"	8.3 ± 0.1	65
12-19-78-23	"C"	7.5 ± 0.3	70
12-19-78-24	"C"	8.0 ± 0.1	74
12-19-78-23	"C"	10.5 ± 0.1	94*
12-11-78-26	"C"	8.5 ± 0.4	65
56-SN056	"C"	6.6 ± 0.8	51
1-18-79-43	"C"	8.9 ± 0.2	78

Average fluence for 100 shots was 8.5 ± 1.0 J/cm² or 71 ± 12% of the single-shot damage fluence.
"S" = single-point diamond turned
"C" = conventionally polished
* Different spot

6. Pulse Transmission in Air and Vacuum

However, when a mirror is used in air, a spark forms at the mirror surface at approximately 5 J/cm² with a 1.7 ns pulse. To measure the effect of this plasma on the reflected pulse, we employed two fast pyroelectric detectors and a 5 GHz oscilloscope to compare the input pulse to the reflected pulse. The mirror was placed at the focal point of the 1-m focal length lens, and the reflected beam relayed to the second detector by a 33-cm focal length lens. Both pulses were displayed on the same sweep with the reference input pulse first. A typical set of photographs are shown in figure 7. As the fluence increases, an air spark forms at the peak of the pulse and begins to shorten the pulse by absorbing the tail.

A minicomputer analysis was performed to compare the reflected pulse with the input pulse. Results for two mirrors in air are plotted in figure 8 showing transmission of energy and peak intensity versus input fluence. A difference was seen between the diamond turned mirror and the polished mirror in that 11 J/cm^2 caused only slight pulse change with the diamond turned mirror, indicating possibly a lower density spark. The diamond turned mirror is suitable for use in air up to its 100-shot vacuum fluence level.

7. Summary

Single shot damage thresholds can be misleading when measured in air because of the air spark formed at the mirror surface. Single shot damage thresholds for a mirror in vacuum give no hint of its multiple-shot operating fluence level. For multishot use in vacuum, we find both polished and diamond turned mirrors suitable up to approximately 8.5 ± J/cm^2. When used in air, the diamond-turned mirror proved more suitable in that no appreciable pulse distortion was seen up to the 8.5 J/cm^2 level, while polished mirrors were seen to produce distortion at fluences as small as 53% of the multishot level in vacuum. More variations were seen in the polished mirrors than with the diamond-turned mirrors.

8. Acknowledgements

The authors acknowledge the following coworkers for their assistance: J. F. Figueira, A. V. Nowak, L. Sonntag, T. Kaffenberger, and R. Shaw, Data Analyst.

References

[1] B. E. Newnam and D. H. Gill, Opt. Eng., 18, 579, 1979.
[2] Hayden, J. J. and Liberman, I., "Measurements of 10.6 μm damage thresholds in Ge, Cu, NaCl, and other optical materials at levels up to 10^{10} W/cm^2," in Laser Induced Damage in Optical Materials, A. J. Glass and H. Guenther, eds., National Bureau of Standards Special Publication #462, p. 173.
[3] D. H. Gill and B. E. Newman, Digest of Post Deadline Papers, ICF Conference, San Diego, Feb. 7-9, 1978.

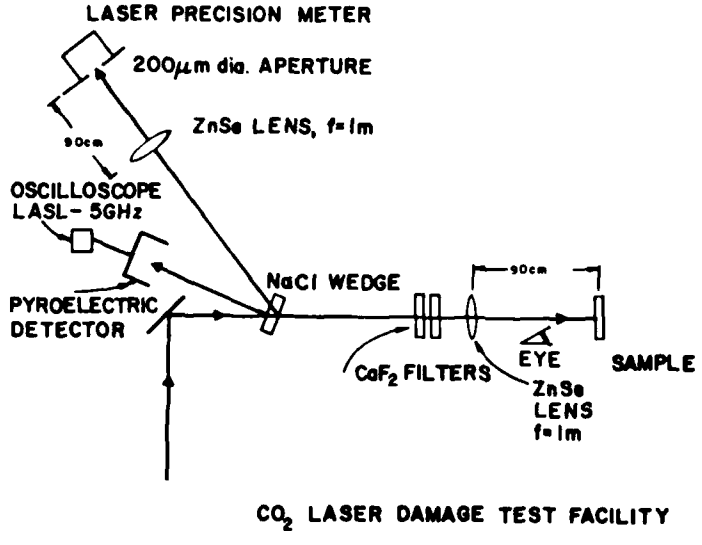

Figure 1. Schematic of experimental setup for measurements in air.

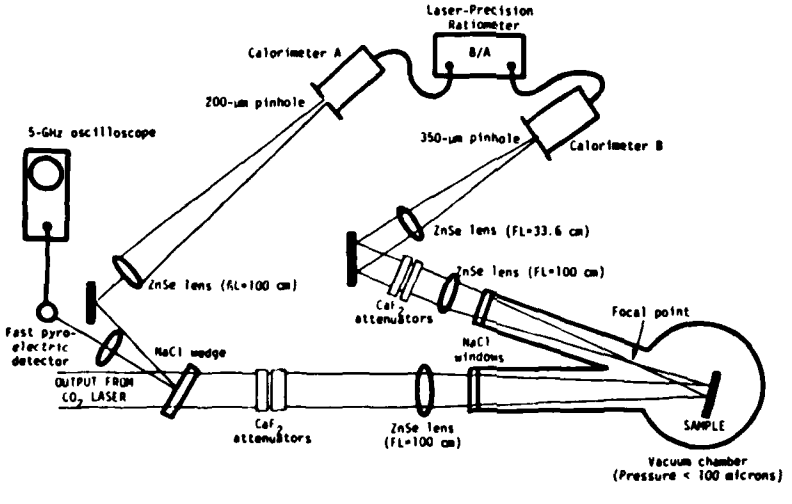

Figure 2. Schematic of experimental setup for vacuum and focusability measurements.

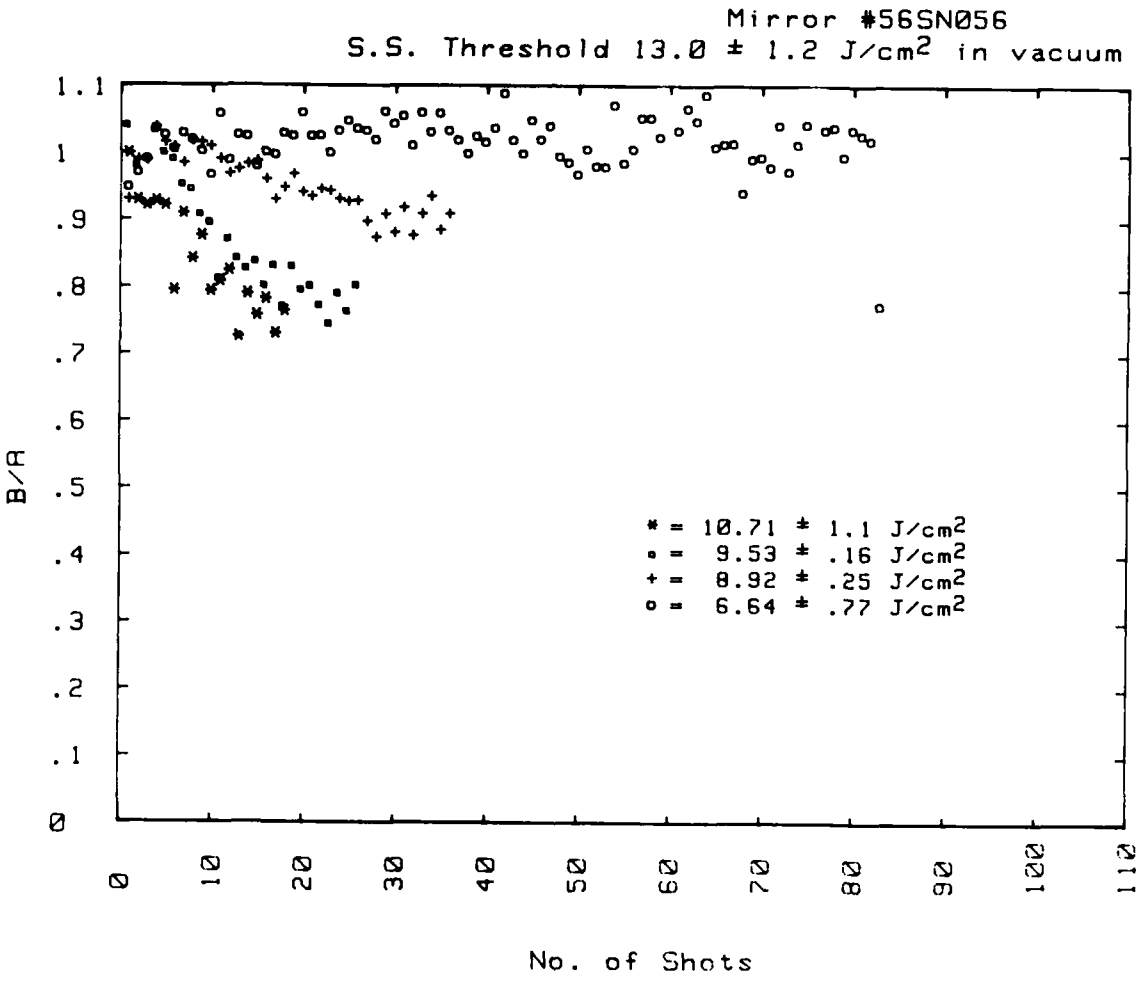

Figure 3. Plot of normalized focusability (B/A) versus number of shots for different fluence levels for a conventionally polished mirror.

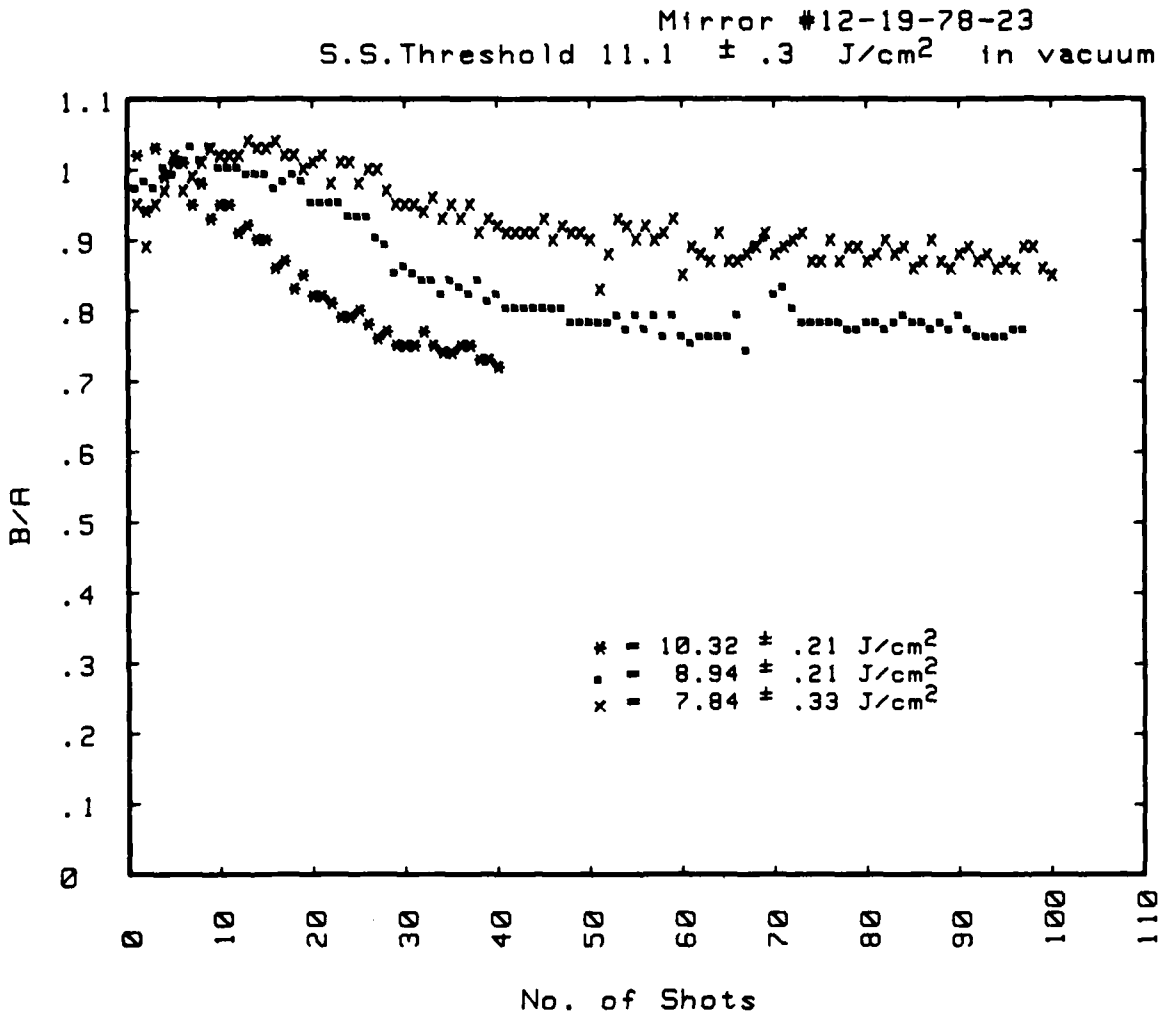

Figure 4. Plot of normalized focusability (B/A) versus number of shots for different fluence levels for a conventionally polished mirror.

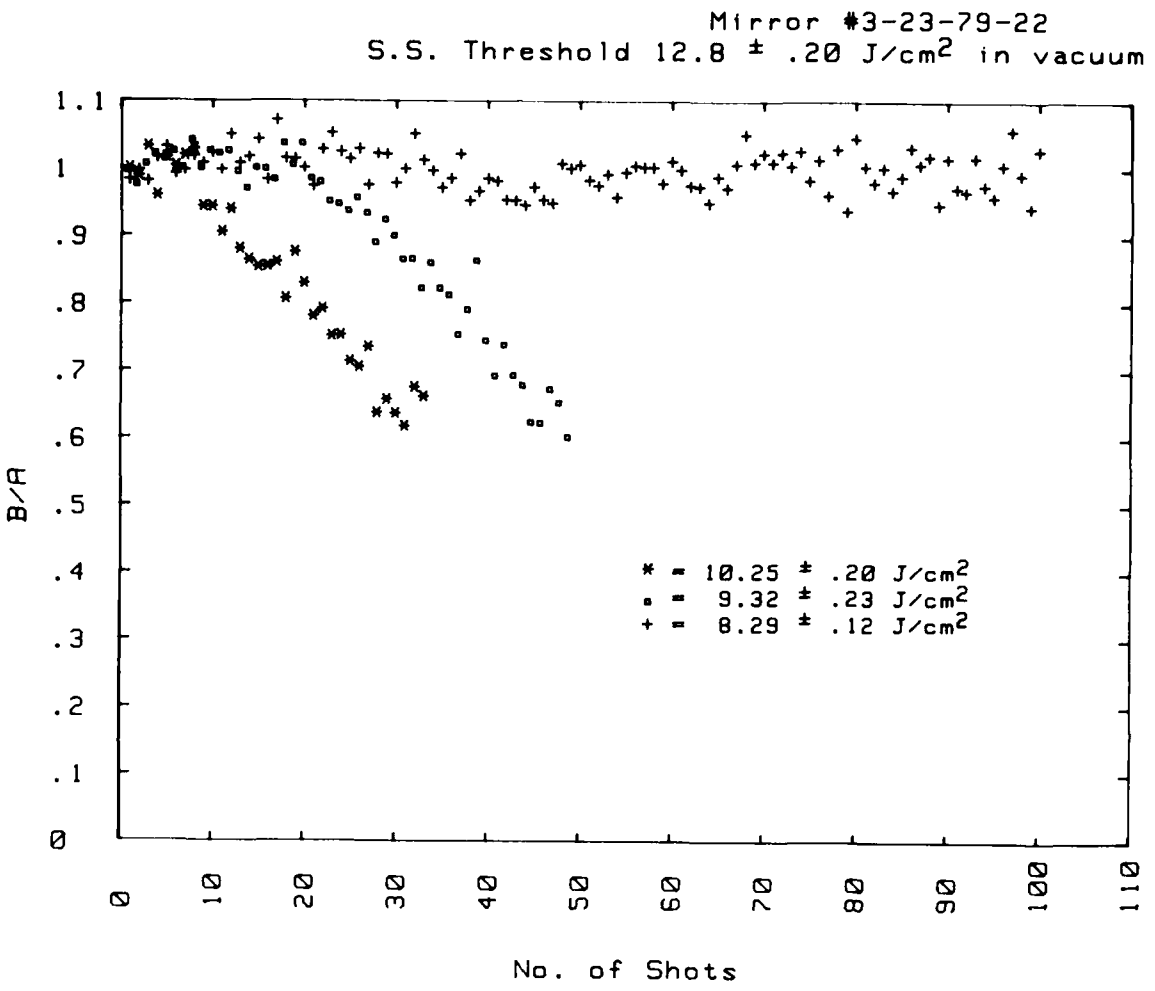

Figure 5. Plot of normalized focusability (B/A) versus number of shots for different fluence levels for a diamond-turned mirror.

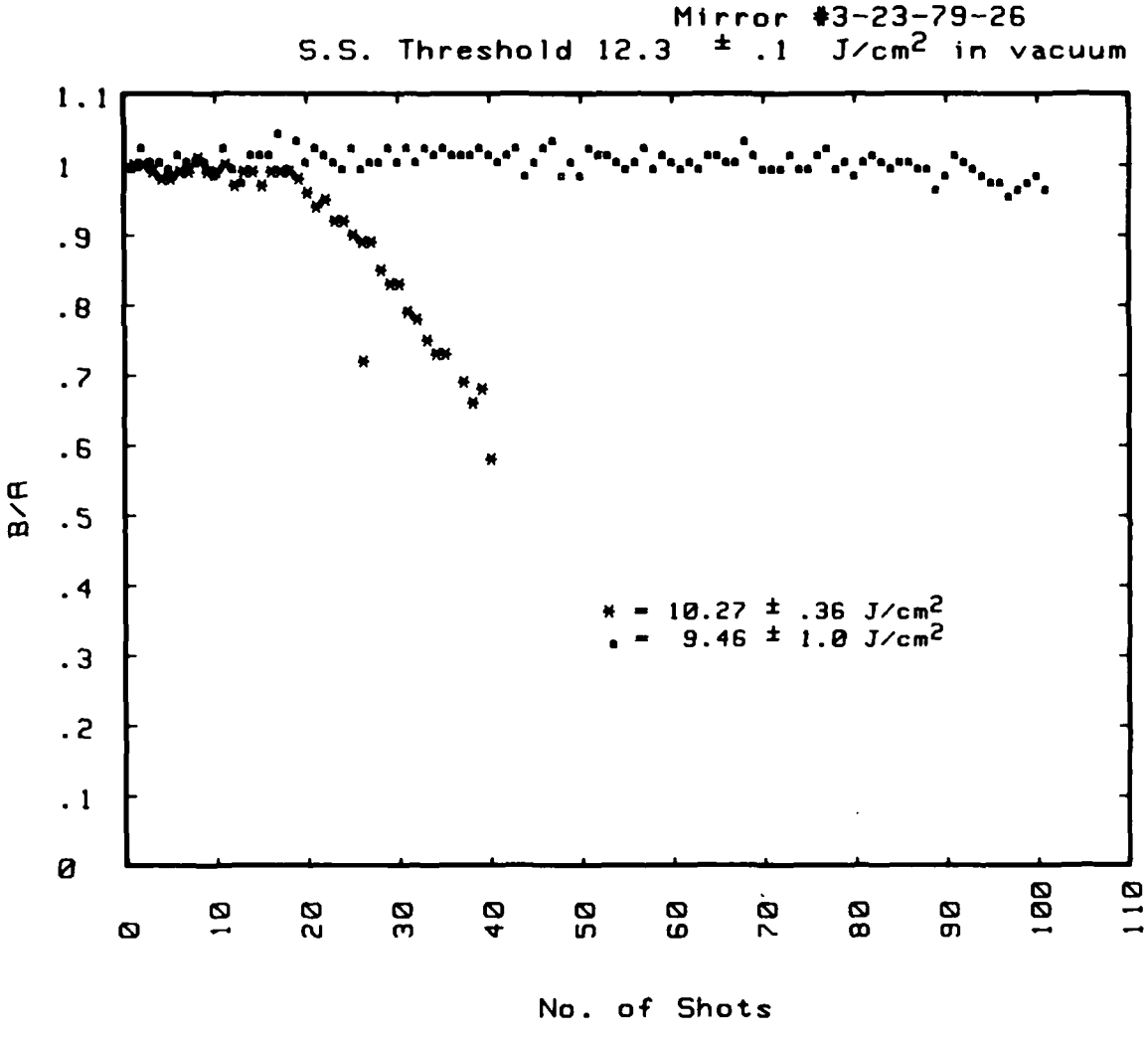

Figure 6. Plot of normalized focusability (B/A) versus number of shots for different fluence levels for a diamond-turned mirror.

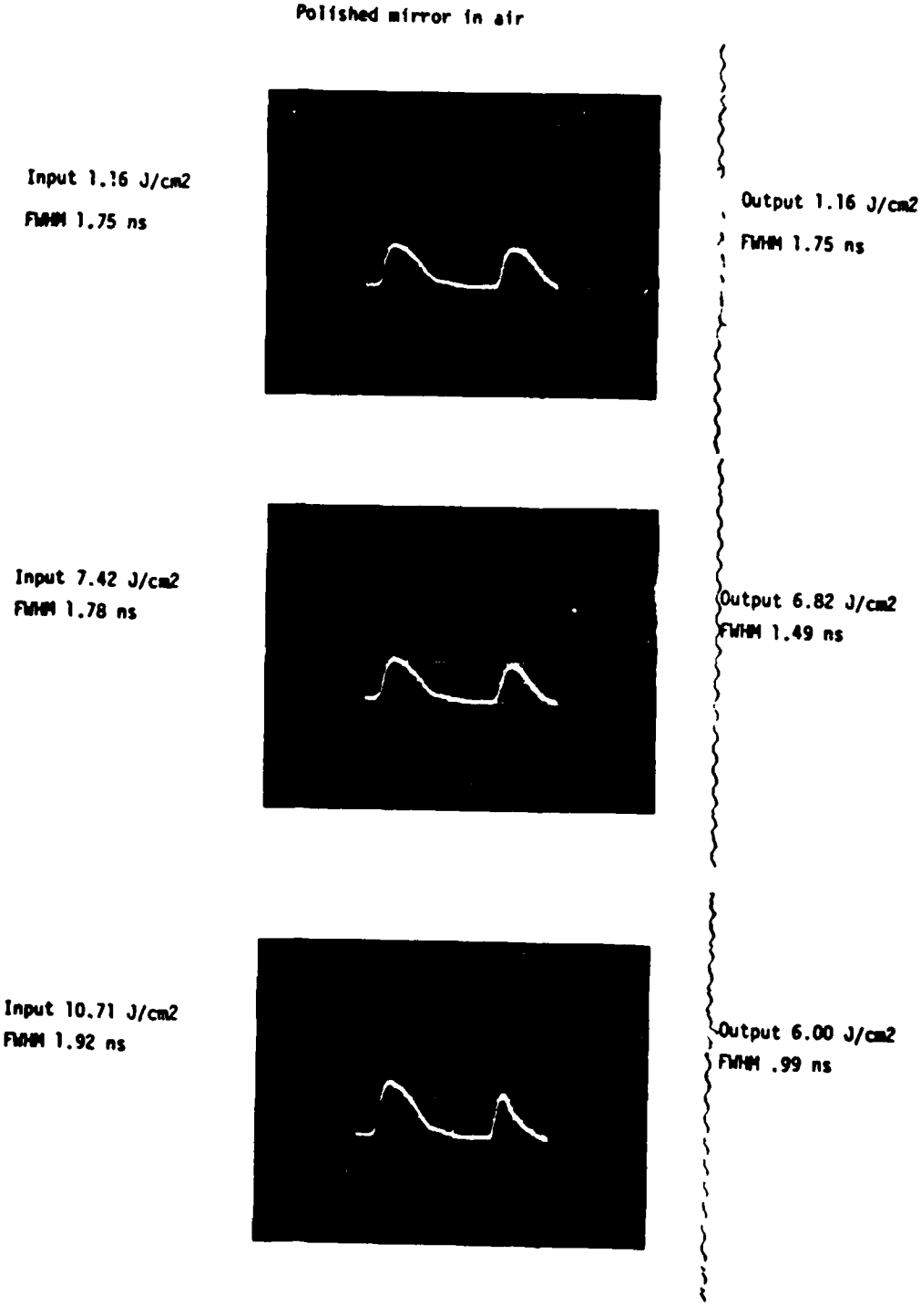

Figure 7. Oscillograms of CO_2 laser pulseforms, input and reflected pulse.

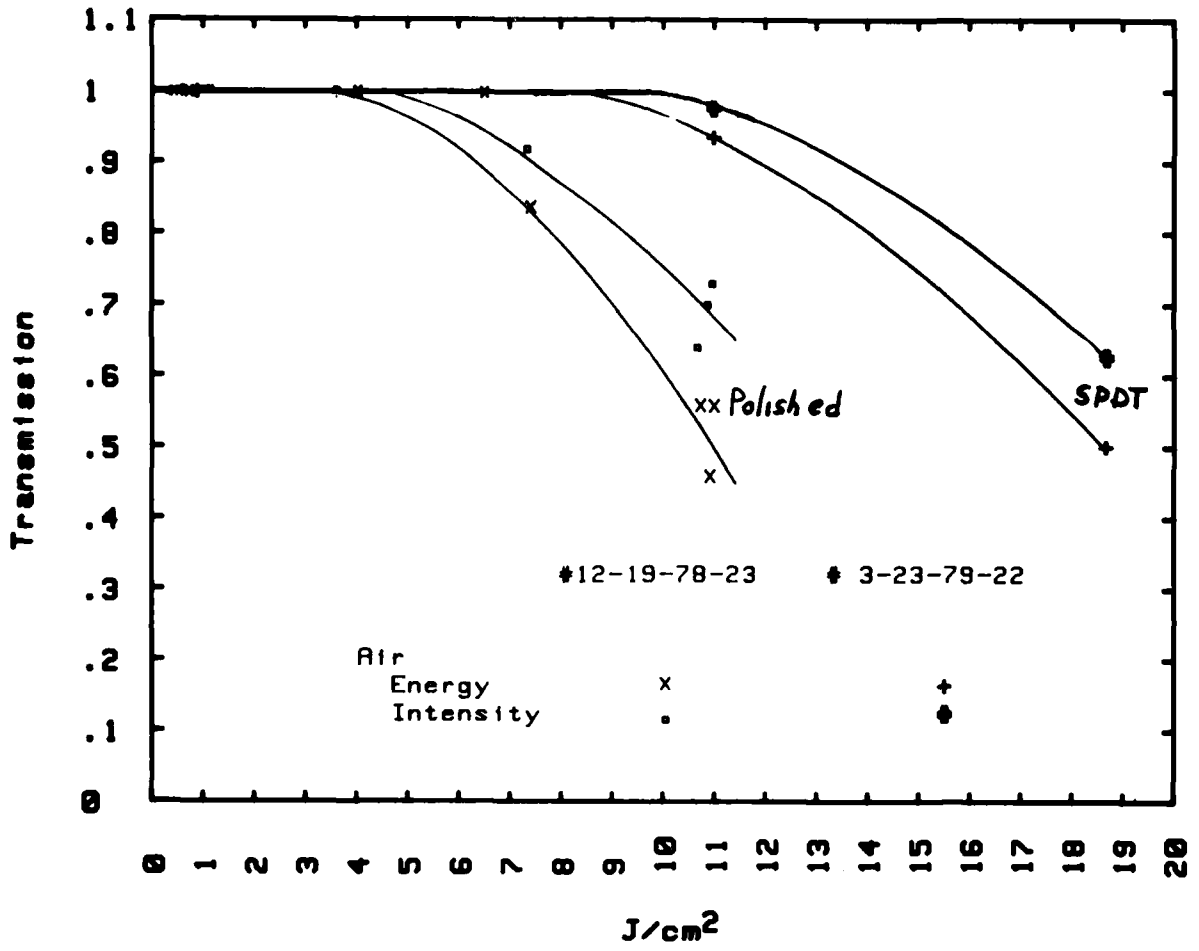

Figure 8. Transmission versus fluence level for a conventionally polished and for a diamond-turned mirror in air showing effects of air spark.

In response to a question, the speaker stated that although the damage levels investigated are higher than required in present systems, Anteres will push mirrors to the levels tested. He also stressed that the damage sites produced in air had a different character than those produced in vacuum. In air the craters were spotty and "diffraction patterns" appeared whereas in vacuum the craters were very smooth, simply enlarging with additional irradiation.

ABSORPTION CALORIMETRY AND LASER INDUCED DAMAGE THRESHOLD MEASUREMENTS ON GERMANIUM AND ZINC SELENIDE

J. Foley, S. K. Sharma, and R. M. Wood
GEC Hirst Research Centre
Wembley Middlesex
England

It has been shown that the absorptance of coated and uncoated germanium samples varies with surface state and ambient atmosphere. Absorption measurements made in air are up to 50% higher than identical measurements made under vacuum. The removable surface absorption on germanium has been shown to be due to both hydrocarbon and water layers, depending on the previous cleaning and ambient conditions. The residual surface absorption depends on the surface polishing procedure. Bulk absorption levels as low as 0.007 cm^{-1} have been measured for freshly cleaned samples. Correlation between the surface condition and the laser induced damage thresholds at 10.6 μm indicates that the damage threshold should be significantly higher in vacuum.

Absorption and laser induced damage threshold measurements have been made on a range of CVD grown ZnSe substrates. Correlation has been shown between the grain size and the direction of measurement and the bulk absorption coefficient.

Key words:
Absorptance:
Infra-red laser windows:
Pulsed CO_2 laser damage:
10 micrometre optical components:

During 1976 an exchange of IR components was made between the USA and the UK; some of the results were reported to this Conference [1]. The components comprised copper mirrors and zinc selenide and germanium windows. Measurements of absorption, reflectance and transmittance were made at GEC and University of Daytona Research Institute and spot measurements of absorptance were also made in UK at STC and AWRE. All the series of measurements made on copper mirrors gave similar results but there was relatively poor agreement between the measurements of absorption made on the coated germanium windows, the UDRI values always lying under the GEC values. Careful analysis of the experimental techniques showed that the only significant difference was that the UDRI measurement was a cw technique performed in a vacuum calorimeter while the GEC measurement was a pulsed measurement made using an air calorimeter. The hypothesis was made that germanium exhibited a surface absorption under normal ambient atmosphere that could be removed under vacuum.

This paper reports the investigation which has been undergone, firstly on germanium in order to investigate this variation of absorption with ambient atmosphere, to investigate the variation of absorption and laser induced damage threshold (LIDT) with surface finish and to document the variation of bulk absorptance with resistivity. Secondly the variation of absorptance and laser induced damage threshold with direction of measurement and surface finish for zinc selenide has also been investigated.

During the last few years the HRC calorimeter has been refined. This differential calorimeter system is now capable of being used to make measurements of absorptions of the order of 0.2% with a 5% repeatability. An addition to this system is the provision of a vacuum cell in which the sample holder (and sample reference) can be inserted, (see figure 1). Use of this system allows measurements to be made under laboratory ambient conditions, under vacuum and under controlled atmospheric conditions. The laser source can be tuned through 80 lines, from 9.2 to 10.9 μm.

Germanium

Use of this calorimeter system to measure the absorption characteristics of a series of uncoated germanium windows has shown that the absorptance varies with surface state and ambient atmosphere. There is also a spatial variation across a surface (of the order of 5%) which can be detected using a small (1 mm diameter) laser probe beam. The measurements made in this paper were made using a relatively large area beam (5 mm diameter) and are consequently averages.

Absorption measurements made in air have been shown to be up to 50% higher than corresponding measurements made under vacuum (see figure 2). The removable surface absorption on these germanium samples is presumed to be due to both hydrocarbon and water layers, depending on the previous cleaning procedure and the ambient conditions. Previously, measurements by attenuated total reflection (ATR) [2] have shown effects with water and hydrocarbon on the surface of infra-red materials.

The amount of water absorbed on germanium surface has been investigated using analytical techniques. A 1" diameter, 4 mm thick sample, W163, was shown to have 16.9 μ cm^3 of water removable from its surface. This corresponds to a layer of water 1.3×10^{-6} cm thick over the geometrical surface area yielding absorption contribution of 0.13% per surface based on the known absorption coefficient of water at 10.6 μm.

The results are shown in figures 3 and 4. Figure 3 shows the measured total absorptance after cleaning versus resistivity for doped germanium samples together with the results obtained by Capron and Brill [3]. This latter curve was made as an average of a series of measurements made on 1 cm thick samples with no allowance made for surface absorption. For further comparison both sets of results were reduced to those equivalent to bulk samples of 1 cm thickness by taking surface contributions to the total absorption into account.

This was arrived at by first comparing the absorptance of a 9 mm thick sample with that of 4 mm thick samples of similar resistivity; from this a bulk absorption coefficient was derived, and then the surface absorptance of the thin samples by subtraction. Since all our samples were polished under the same conditions it was then assumed that all the surfaces had this same surface absorption. In view of the good match between the two sets of results, it appeared reasonable to apply the same connection for surface absorption to the results of Capron and Brill. This yields the lower curve in figure 3; the previous [4] and the correspondingly reduced phonon absorption limits (i.e. after allowance for free carrier absorption) is also shown.

Figure 4 shows the same average curves together with the two sets of measurements made in the absorption calorimeter, the first in air and the second under vacuum. These figures show that there was an appreciable but non-constant removable absorption for all the samples tested. It will be noticed in figure 4 that even in vacuum the measured values do not match up with the calculated averages. This is because polishing with alumina powder, even though giving a good optical finish, leaves a polycrystalline sub-surface (see figure 5, which is an X-ray topograph penetrating ~1 μm). Considerable improvement can be gained in the absorption and LIDT figures by finishing with a technique capable of leaving an undamaged single crystal surface. Examples of this are given in the X-ray topographs shown in figure 6 (Syton polished), figure 7 (ion-beam etched) and figure 8 (acid etched). Absorption values measured on samples finished using these techniques are shown in table 1 together with the corresponding LIDT.

It will be seen from these curves and plotted points that not only can there be a considerable surface absorption which can be drastically decreased by suitable surface finishing but that there is also a considerable contribution brought in by the ambient atmosphere.

Zinc selenide

Absorption and laser induced damage threshold measurements have been made on a range of CVD grown ZnSe substrates. A summary of the results is shown in table 2. This table lists the origin of the sample, grain size, the direction of measurement and the bulk absorption coefficient. Most of these samples are flat, cut parallel to the plane of growth. One sample, however, a block from Raytheon shows some very interesting features. These features are illustrated in figure 9 and a summary in table 3. At first sight the absorption values are anomalous, the measurement values made along the longest direction being considerably lower than those made in the shorter directions in the same plane. The explanation of these results is that the growth is columnar and that the grain size is anisotropic. The block had a defect band parallel to the growth plane. The absorption at 10 μm in this plane is a factor of 3 more than in a parallel plane higher in the block.

Acknowledgement

Part of this work has been carried out with the support of the Procurement Executive, Ministry of Defence, sponsored by DCVD.

References

[1] Gibbs, R and Wood, R.M., Laser induced damage measurements at 10 μm NBS Special Publication 1978

[2] Palik, E.D. et al., Infra-red characterisation of surfaces and coatings by internal reflection spectroscopy, Appl. Optics, 17, No. 11, pp. 1776.

[3] Capron, E.D. and Brill, O.L., Absorption coefficient as a function of resistance for optical germanium at 10.6 μm, Appl. Optics, 12, No. 3, pp. 569

[4] Bishop, P.J and Gibson, A.F., Absorption coefficient of germanium at 10.6 μm, Appl. Optics, 12, No. 11, pp. 2549.

Table 1. Absorption values of germanium samples

Serial No.	Absorption %	Damage threshold MW mm^{-2}
W64	1.6	1.5
W65	1.0	2.0
W51	AR 3.3	2.0-2.5
	AR 3.3	2.5
W52	85% R 0.5	4.8-11.0
	AR 4.0	2.8

Table 2. Measurements made on zinc selenide

Serial No.	Origin	Absorption coefficient (cm^{-1})	Damage threshold (MW mm^{-2})	Grain size (MM)
W8	Raytheon	4.9×10^{-3}	3.2 - 7.5	
W9	"	4.9×10^{-3}	1.5 - 3.8	
W10	"	4.9×10^{-3}	3.2 - 5.5	
W18	AWRE	2.0×10^{-3}	0.8 - 4.5	
W19	"	5.0×10^{-3}	2.2 - 4.7	
W20	"	1.6×10^{-3}	3.6 - 11.2	
W61	"	4.7×10^{-2}	3.1 - 11.0	0.1 - 1
W62	"	1.9×10^{-1}	3.6 - 10.6	0.1 - 1
W63	"	2.1×10^{-1}	3.1 - 3.6	0.1 - 0.5

Table 3. Absorption measurements made on ZnSe block

Position	Thickness cm	Absorption %	Absorption coefficient cm^{-1}	Measurement Direction/ Grain Size*
Centre	2.9	0.97	0.0033	a
Off centre	"	0.97	0.0027	a
Centre	"	1.00	0.0034	a
Centre	2.54	0.98	0.0038	b
Off centre	"	0.98	0.0038	b
Centre	3.88	0.64	0.0017	c

*a = Perpendicular to gas flow in plane of growth 0.02 MM grains.
b = Perpendicular to gas flow perpendicular to plane of growth.
c = Parallel to gas flow in plane of growth 0.1 MM grains.

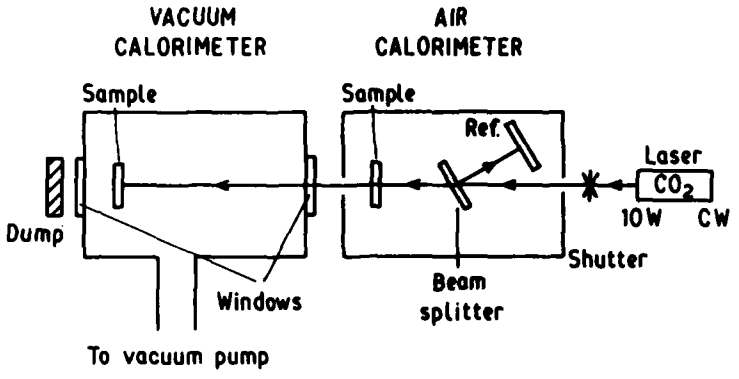

Figure 1. Absorption measurement apparatus.

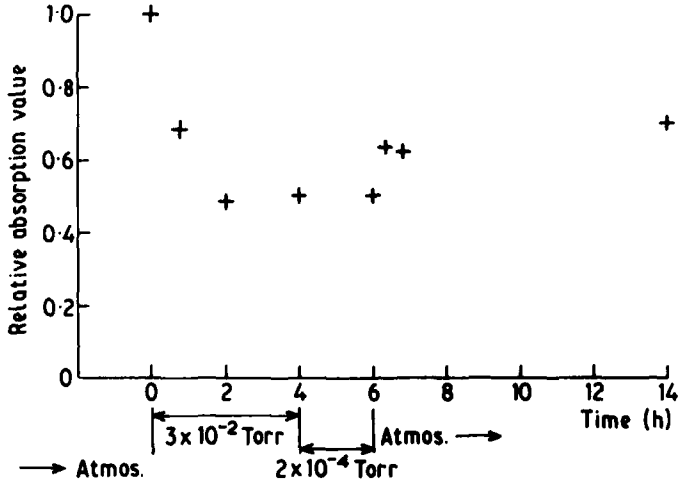

Figure 2. Measured absorption v atmosphere, germanium

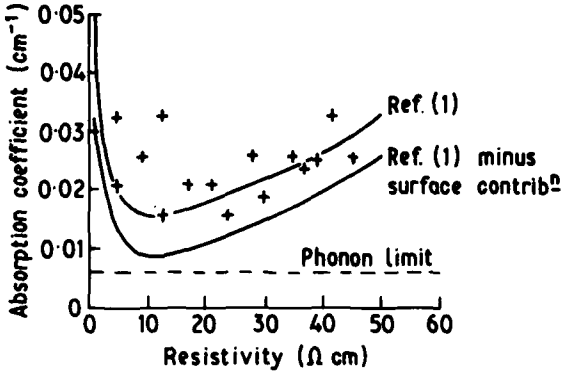

Figure 3. Measured sample absorption v resistivity

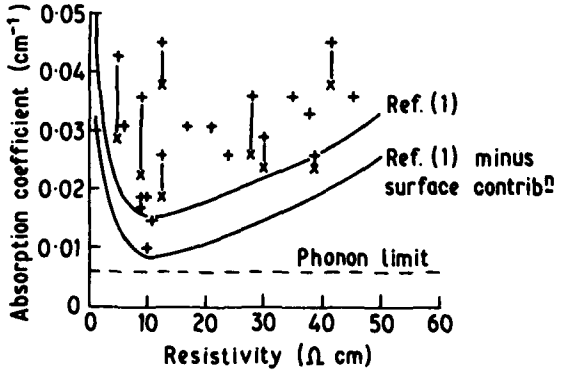

Figure 4. Measured absorption under vacuum resistivity
+ Measurements in air
× Measurements under vacuum

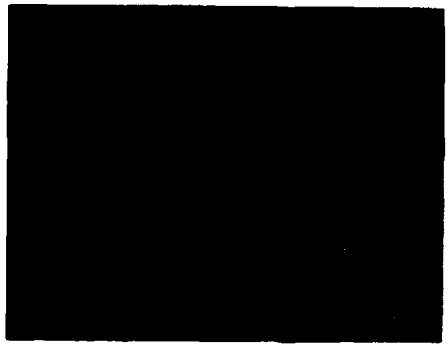

Figure 5. X-ray topograph, germanium polished with alumina

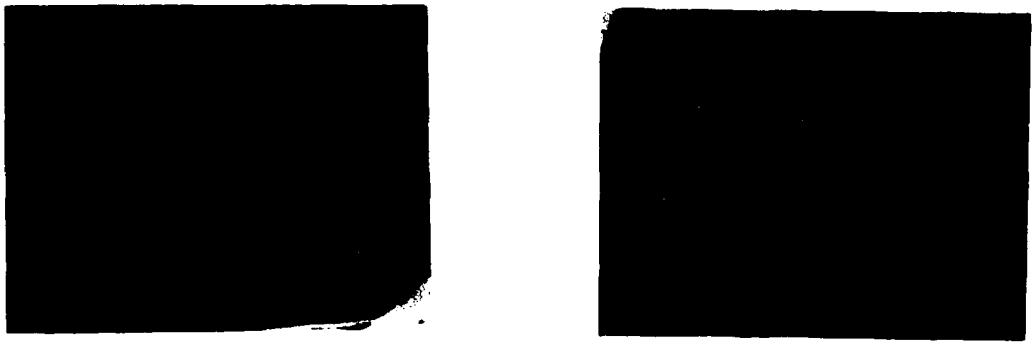

Figure 6. X-ray topograph, germanium polished with Syton

Figure 7. X-ray topograph, germanium, ion-beam etched

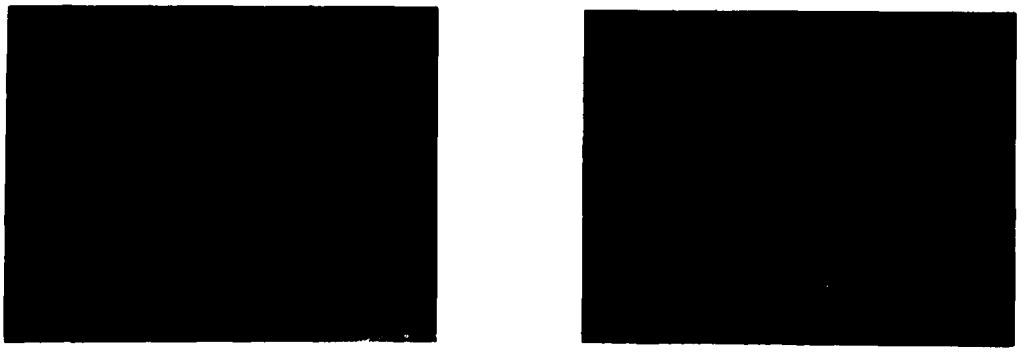

Figure 8. X-ray topograph, germanium acid etched

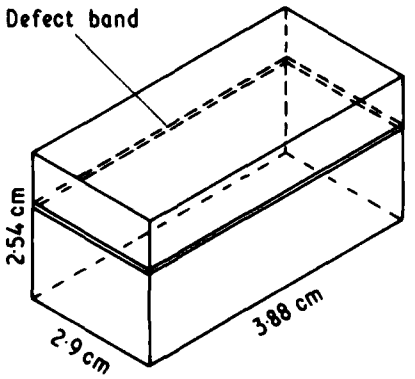

Figure 9. Raytheon ZnSe block

The question was raised as to whether the energy transferred to the gas was properly considered in calorimetry and whether the accomodation coefficient of the gas per surface should be considered. The speaker replied that he believed the inaccuracies resulting from such effects were small since when the input power was varied by 100 times the same results were obtained.

INSENSITIVITY OF THE CATASTROPHIC DAMAGE THRESHOLD OF LASER OPTICS TO DUST AND OTHER SURFACE DEFECTS*

H. E. Bennett
Michelson Laboratory, Physics Division
Naval Weapons Center, China Lake, California 93555

When laser optics are exposed to continuous radiation or to pulse lengths long enough so that the damage level is determined simply by thermal heating, the mechanisms causing catastrophic damage are fairly clear. In particular, the role of surface defects should be predictable from an analysis of the standing wave pattern at the surface, the optical properties and shape of the defects, and simple heat transfer calculations. The conclusion drawn from such an analysis is that although dust and other surface defects may cause small isolated damage sites to occur, these sites will not grow under continued irradiation and produce catastrophic damage unless the defects exceed a critical diameter or are so closely spaced that they significantly affect the average absorption of the surface. Experimental evidence supports this hypothesis. Dust and other small surface defects are thus acceptable in reasonable concentrations on high power continuous wave laser optics provided that they do not exceed the critical size.

Key words: Coating imperfections; cw laser irradiation; digs; dust; laser damage; mirrors; optical components; scratches; surface defects.

Introduction

It is common practice in laser damage experiments carried out in the laboratory to specify the laser damage threshold as that irradiation level at which visible damage first occurs. In many cases, this criterion may be too severe for system applications. There are various references in the literature [1][1] and numerous anecdotal accounts of laser mirrors in actual systems which sustained visible isolated spot damage and then functioned successfully for extended periods of time at the same power levels which initially caused the isolated spot damage. Catastrophic damage to a laser component can occur, however, and a means is needed for predicting at what point a damaged component should be removed from an optical train to prevent catastrophic damage. Knowledge of the importance of scratches, digs, and other substrate or coating defects in untested laser mirrors prior to their exposure would also be helpful. Currently, many laser components are rejected for surface flaws which may not be operationally significant. However, as coating reflectances and hence power levels which the coatings should be able to withstand continue to increase, the identification of critical coating or surface defects which may cause catastrophic damage to the mirror becomes increasingly important. Environmental effects such as dust must also be considered. In most cases, it is not practical to operate lasers in a completely dust-free environment.

This paper deals primarily with damage to components in continuous wave (cw) lasers. It is assumed that coating defects, dust, and other particulates are widely enough spaced so that they may be treated independently. It is also assumed that the reflectance of the laser coating is high enough so that its absorption is much smaller than that of the defect and may be neglected. The heat absorbed by the defect or particulate, then, is determined by the product of the localized power density at the defect site and the defect absorption cross section. The heat lost by the defect or particulate is assumed to occur primarily by diffusion into the surface of the mirror. The balance between heat gain through absorption and heat loss through thermal diffusion then causes the particle to heat up until it either reaches thermal equilibrium or, if heating is continued long enough, produces catastrophic damage.

This paper gives the results of a purely thermal analysis. Its applicability to pulsed laser systems, where damage often is the result of nonthermal processes, is thus unclear. The first topic discussed is a simple thermal diffusion model. The next topic is the local field used in the calculation and the absorption cross section of the defect. Heat transfer calculations are then made for particulates, digs, and scratches on mirror surfaces, and the results are compared with experiment.

Thermal Diffusion Model

A surface defect may either be in poor or in good thermal contact with the surface. If thermal contact is poor, the temperature increase T of a spherical defect upon irradiation with flux $F = nE^2$, where E is the local field and n the index of refraction in the surrounding medium, will be proportional to the ratio of the projected area of the particle to its volume and will be given by

$$T = \frac{3}{2}\frac{nE^2 A\, t}{\rho' c_p' d} \quad , \tag{1}$$

where A is the fractional amount of the incident flux absorbed by the defect per unit area, d the defect diameter, ρ' its density, c_p' its specific heat at constant pressure, and t the time since irradiation began. The temperature rise is proportional to irradiation time and is much more rapid than when the defect is in good thermal contact with the surface. In that case, heat diffuses into the surface both normally and laterally, as illustrated in figure 1. If the absorbing defect is circular, the edges will cool most effectively, and the maximum temperature rise will thus be at the

*Work supported by Naval Sea Systems Command, PMS-405, and Naval Weapons Center Independent Research Funds.

[1]Figures in brackets indicate the literature references at the end of this paper.

center of the defect. If the mirror surface is approximated by a semi-infinite, nonabsorbing plane, the temperature rise at a point on a circular defect whose cylindrical coordinates are r, θ, and z, where z is normal to the plane, r the radius vector in the plane, and θ the angular coordinate in the plane, will be [2]

$$T = \frac{nE^2Ad}{4K}\int_0^\infty J_0(\lambda r)J_1(\lambda d/2)\left\{e^{-\lambda z}\,\mathrm{erfc}\left[\frac{z}{2(\kappa t)^{1/2}} - \lambda(\kappa t)^{1/2}\right] - e^{\lambda z}\,\mathrm{erfc}\left[\frac{z}{2(\kappa t)^{1/2}} + \lambda(\kappa t)^{1/2}\right]\right\}\frac{d\lambda}{\lambda} \qquad (2)$$

where $\kappa = K/\rho c_p$ is the diffusivity of the mirror material having thermal conductivity K, density ρ, and specific heat at constant pressure c_p. The flux is assumed to be absorbed only by the defect of diameter d, and the origin of coordinates is at the point on the mirror plane whose normal passes through the center of the defect. The mirror temperature rise will thus be a maximum on the mirror surface at the origin of coordinates z = r = 0. At that point, eq. (2) reduces to

$$T = \frac{nE^2A\delta}{K}\left[\frac{1}{\sqrt{\pi}} - \mathrm{ierfc}\left(\frac{d}{4\delta}\right)\right] , \qquad (3)$$

where $\delta = (\kappa t)^{1/2}$ is the diffusion depth of the mirror. The function ierfc(x) is defined as

$$\mathrm{ierfc}(x) \equiv \int_x^\infty \left(1 - \frac{2}{\sqrt{\pi}}\int_0^\eta e^{-\xi^2}d\xi\right)d\eta = \int_x^\infty [1 - \mathrm{erf}(\xi)]d\xi \quad . \qquad (4)$$

Table 1 is a tabulation of ierfc(x) for small values of x. For very small values of x, eq. (4) can be expanded [3] to give

$$\mathrm{ierfc}(x) = \frac{1}{\sqrt{\pi}} - x + \frac{x^2}{\sqrt{\pi}} - \frac{x^4}{6\sqrt{\pi}} + \ldots \quad , \qquad (5)$$

so that

$$T \cong \frac{FA}{2K}\left(d - \frac{d^2}{4\pi\delta}\right) \quad . \qquad (6)$$

Equation (6) holds to four decimal places for $d/4\delta < 0.1$. As δ (and hence time) increases, a steady state is reached where heat flow out of the defect equals heat flow in, and the defect temperature no longer increases with time. This behavior is in contrast to that in which the defect is in poor thermal contact with the surface, in which case its temperature increases without limit [eq. (1)]. The surprising result that a limiting temperature exists for continuously irradiated small defects in intimate contact with the surface is a consequence of lateral diffusion and depends on the assumption that the defects are spaced widely enough apart so that they do not affect each other. If the defect density becomes too great (as occurred in one experiment where dirt was scattered heavily on the mirror surface [4]), this condition is violated, and the surface temperature may rise without limit. For moderate defect densities, however, a limiting temperature T_{max} will be reached. Catastrophic failure will thus not occur unless that limiting temperature is high enough so that the defect size begins to grow as a result of film delamination or decomposition.

Table 1. $\mathrm{ierfc}(x) \equiv \int_x^\infty [1 - \mathrm{erf}(\xi)]d\xi$.

x	ierfc(x)	x	ierfc(x)
0.00	0.5642	0.90	0.0682
0.05	0.5156	0.95	0.0587
0.10	0.4698	1.00	0.0503
0.15	0.4269	1.1	0.0365
0.20	0.3866	1.2	0.0261
0.25	0.3491	1.3	0.0183
0.30	0.3142	1.4	0.0127
0.35	0.2820	1.5	0.0086
0.40	0.2522	1.6	0.0058
0.45	0.2248	1.7	0.0038
0.50	0.1997	1.8	0.0025
0.55	0.1768	1.9	0.0016
0.60	0.1560	2.0	0.0010
0.65	0.1371	2.1	0.0006
0.70	0.1201	2.2	0.0004
0.75	0.1049	2.3	0.0002
0.80	0.0912	2.4	0.0001
0.85	0.0790	2.5	0.0001
		2.6	0.0000

If $x \leq 0.10$, $\mathrm{ierfc}(x) = \frac{1}{\sqrt{\pi}} - x + \frac{x^2}{\sqrt{\pi}} \cong \frac{1}{\sqrt{\pi}} - x$.

From eq. (6), the limiting temperature for disc-like particles is

$$T_{max} = nE^2Ad/2K \quad . \qquad (7)$$

A similar relation holds for scratches. In this case, significant lateral diffusion only occurs normal to the scratch direction. The limiting temperature rise reached by an absorbing line (i.e., a scratch) of length ℓ and width d is [5]

$$T_{max} = \frac{2nE^2A}{K\pi}\left(\frac{d}{2}\sinh^{-1}\frac{2\ell}{d} + \ell\sinh^{-1}\frac{d}{2\ell}\right) \quad . \tag{8}$$

In this case, T_{max} is larger for a given value of d than it is for a circular defect. It occurs at the center of the scratch.

Local Field

In order to calculate the temperature rise for a surface defect under irradiation, the local field E must be known. In most particulate absorption calculations, this is no problem, since the particulates are suspended in a cloud, and the local field is the incident field to a good approximation. However, when the particulates are on an optical surface, the problem is complicated both by image fields induced by the particle itself and by the standing wave fields set up by surfaces or by multilayer films. Consider this last problem first. A typical standing wave pattern for a high reflectance multilayer [6] is shown in figure 2. There is a node at the reflector surface. A similar node typically exists for uncoated metal surfaces. Thin surface contaminants such as adsorbed films, stains, etc. are often less than a quarter of a wavelength in thickness and hence are exposed to a local field which is significantly lower than that of the incident flux. Partly for this reason, stains and chemisorbed surface layers often have very little effect on optical performance of good reflectors. Particulates, however, are another story. Those large enough to be of concern are usually more than a quarter of a wavelength thick, in which case the average local field acting on the particle may be equal to or larger than the incident field. For particles many wavelengths in diameter, the average local field is approximately equal to the incident field of the radiation. As a first approximation, it seems conservative to make that same assumption for smaller particulates, scratches, etc.

A second question is the effect of the local image field created by the particle. Bloembergen [7] in a classic paper pointed out that such image fields could significantly enhance the possibility of laser damage when cracks or grooves existed in the surface. The local field seen by a particulate on the surface exposed to air is actually reduced by this effect, as shown schematically in figure 2. The average field it sees is given by [7]

$$E = E_0/[1 + (n_D^2 - 1)L] \quad , \tag{9}$$

where n_D is the index of refraction of the particle and L is a parameter which equals one-third for a sphere and one-half for a cylinder. If $n_D = 1.5$, a typical value for dielectrics such as dust, then from eq. (9), $E = 0.7E_0$, where E_0 is the field strength of the incident radiation. On the other hand, the local field in a scratch or pit in the surface will be enhanced, since the surrounding medium is now the surface material, not air. The local field in this case is given by [7]

$$E = E_0/\{1 + [(1/n_D)^2 - 1]L\} \quad , \tag{10}$$

and if $n_D = 1.5$, the local field at the bottom of a hemispherical dig would be 1.2 times that in the undamaged film layer. For a hemicylinder, it would be 1.4 times that in the undamaged film. Fortunately, typical scratches have a depth-to-width ratio which is much lower than that of a hemicylinder. Figure 3 shows a profile of standard #20 and #60 scratches on glass [8]. The width-to-depth ratio is approximately a factor of 10, or 5 times that of a hemicylinder. Local field enhancement would thus be much lower than for the hemicylinder and, to a first approximation, may be neglected. It should be remembered, however, that the resulting threshold values developed here for scratches and digs are less conservative than those for dust and other particulates on the surface.

Absorption Cross Section

The next question to ask is what value to use for A, the fraction of the flux which is absorbed. It is composed of two parts: (1) the size and absorptance per unit cross sectional area of the particulate or of the scratch and (2) a geometrical factor giving the ratio of the absorption cross section to the geometrical cross section. In scattering theory, this geometrical factor is called the efficiency factor. As a first approximation, it can be equated to the efficiency factors calculated, for example, by Mie theory. Figure 4 shows the result of one such calculation [9]. The dashed line gives the efficiency factor for absorption by spherical particles, which may be contrasted with the better known efficiency factor for scattering shown by the solid line.

The abscissa is the "size parameter" $x = \pi d/\lambda$ often used in scattering calculations, and a wavelength of 514 nm is assumed. The particulate material is assumed to have an index of refraction $m = 2.2 - j0.00409$ and thus an absorption coefficient of 10^3 cm^{-1}. As the absorption coefficient or size parameter increases, the efficiency factor for absorption Q_a and for scattering Q_s both approach unity. The extinction efficiency factor $Q_e = Q_s + Q_a$, which represents the ratio of the energy abstracted from that incident on the particle, then approaches 2, the so-called extinction paradox. It results from the fact that both diffraction around an absorbing particle and absorption reduce the light coherently (i.e., specularly) reflected or transmitted. If only absorption were important, the extinction efficiency would be unity for large, strongly absorbing particles.

As the particle size decreases and approaches the wavelength in magnitude, resonances occur in both Q_s and Q_a, and Q_a becomes small compared to unity. For small, weakly absorbing spheres, the energy absorbed is linearly proportional both to the absorption coefficient and to the amount of absorbing material present, i.e., to the spherical volume. In this region, when resonances are ignored,

$$Q_a = (4/3)\pi(d/2)^3\alpha/\pi(d/2)^2 = (2/3)(d\alpha) = (2/3)(\lambda/\pi)\alpha x \quad . \tag{11}$$

When $d < \lambda$, Q_a is thus linearly proportional to x, as seen in figure 4. The efficiency factor for absorption thus greatly reduces the absorptance of most small particles compared to that calculated from their geometrical cross section alone. In our calculations, there is then an additional safety factor for dust particles in the infrared arising from the size of Q_a. As the defect size increases

relative to the wavelength, this safety factor disappears, eq. (11) no longer holds, and Q_a for absorbing particulates approaches unity.

Theoretical Predictions

The various factors in eqs. (3,7,8) are now determined, and an approximate prediction of the limiting sizes of surface defects below which catastrophic damage will not occur can be made. If the laser run time is known, eqs. (3 or 6) can be used to predict critical defect sizes. More conservative are the predictions from eqs. (7,8) which give limiting defect sizes for continuous irradiation. Figure 5 gives these limiting defect sizes for both circular defects and scratches. (A very conservative temperature rise, 200°C, was assumed in making these calculations. Measured temperature rises before catastrophic damage of 500-600°C have been reported [10] for films on ultra-low expansion (ULE) quartz. Such a value would increase the allowed flux levels by over a factor of two.) Two substrates are assumed copper and ULE quartz. The ordinate gives the product FA in Kw/cm^2. If the absorptance of the defect is assumed to be unity and the absorption efficiency factor is disregarded, the ordinate is equal to the incident flux. Such an assumption may result in values which are too low by an order of magnitude in typical cases. The defect diameter or scratch width d is plotted on the abscissa. Diagonal lines give the limiting defect sizes for the two types of substrates. The solid lines represent circular defects, and the dashed lines represent scratches. Scratch sizes are indicated using the current MIL 13830, revision L, specification that scratch widths in micrometers are nominally one tenth the scratch number. Dig sizes are given in MIL 13830 as ten times the dig number. Thus, a #10 scratch is 1-μm wide, while a #10 dig is 100 μm in diameter. Dust is also indicated. Most dust particles are in the 1-μm-size range. Particles larger than 10 μm in diameter are more properly characterized as grit or fine sand than as dust. Using this definition, it is clear that even with the unfavorable assumption that A = 1, isolated dust particles are well below the critical size range for catastrophic damage for irradiation levels up to 5 Kw/cm^2 for ULE or to well over 100 Kw/cm^2 for copper. A scratch as large as #80 is marginally adequate at the 1 Kw/cm^2 flux level and a #40 scratch at the 2 Kw/cm^2 level for ULE quartz. Copper mirrors should support flux loadings over 100 Kw/cm^2 with such defects. A #40 dig, however, is a serious matter, and if it absorbs strongly, it is predicted to limit the ULE mirror to power levels as low as 0.1 Kw/cm^2 and the copper mirror to 40 Kw/cm^2. These predictions suggest that the specifications for surface quality in laser mirrors should be revised to be unsymmetric with typical scratch/dig values of 80/5 or 40/2 instead of the more common optical surface quality specifications such as 60/40. Such specifications depend on the quoted relationship between scratch width and number. Since the primary quantity used to determine scratch number is visual appearance rather than width, there is some uncertainty in the quality control techniques in current use.

Comparison with Experiment

There are little carefully taken data available on damage vs defect size or defect size before and after irradiation. One series of tests [11] on coated ULE quartz using a cw laser operating nominally at 3.8 μm produced the result shown in figure 6. Various defects are shown both before and after irradiation at the 1 Kw/cm^2 flux level. The large defect seen in the center before irradiation is replaced by a large fracture of the multilayer film coating after irradiation. Some melting at sites of the three prominent defect sites ringing the large defect is also observed. Damage occurred almost immediately after irradiation began, but the damage site did not grow or change during subsequent extensive irradiation. The size of the fractured defect site after irradiation is about 0.4 mm. It thus corresponds in diameter to a #40 dig and should have caused catastrophic damage if its absorption were near unity. However, although the multilayer film fractured, the silver coating which formed the first evaporated layer on the ULE substrate remained intact, reducing A from unity to less than 0.1. A flux level of 1 Kw/cm^2 is then predicted from figure 5 to be supportable indefinitely by this defect site. Experimentally, laser exposures of 30-40 sec caused no change in the appearance of the defect site.

Why then did the fracture occur on initial irradiation? The answer lies in the poor thermal contact between the initial defect and the surface. If d = 0.1 mm, A ~ 1, ρc_p = 1.97 J/cm^3 (silicon dioxide), and T = 600°C, the temperature rise reported [10] to create catastrophic damage in films on ULE surfaces, the time at an irradiation level of 1 Kw/cm^2 required to bring the defect to a high enough temperature to damage the coating is calculated from eq. (1) to be t = 8 msec. Initial damage then would be predicted to occur almost instantly, in agreement with experiment.

Figure 7 illustrates the damage observed in the same series of experiments on a multilayer-coated ULE substrate which had a heavy scratch through the coating. The scratch was 0.3-0.4 mm in width and was so severe that the underlying silver coating was removed as well as the dielectric multilayer. The scratch absorption at 3.8 μm, the wavelength at which the test was run, was thus large. Under these conditions, catastrophic failure would be predicted from figure 5, and it did indeed occur. In another sample, a similar scratch, although of about the same width, did not penetrate the silver layer. When this sample was irradiated, catastrophic failure did not occur, a result again predicted by figure 5.

Conclusion

An analysis of the temperature reached by defect sites on mirror surfaces shows that a steady-state condition will exist for defects below a critical size in which the heat loss by diffusion into the mirror surface equals the heat gain caused by irradiation. Defects less than that critical size will thus not grow in size under continued irradiation and will not result in catastrophic damage to the mirror. Good thermal contact with the mirror is required, however, for this steady-state condition to exist. If this contact is not initially present, defects may heat rapidly to sufficiently high temperatures to cause fracture or melting of the mirror coating at isolated sites. Good thermal contact will be established by this process, and the damage sites will not grow further under continuous irradiation unless during the initial fracture or melting process they reached the critical size. Small damage sites on a laser mirror are thus not necessarily cause for concern. In particular, dust particles, defined here as particulates having diameters less than 10 μm, do not present a hazard to laser operation unless they form a nearly continuous layer on the mirror surface. Exposed scratches

in the normal size range (#80 or less) also will not cause catastrophic damage in most laser optics applications. Digs, however, are much more serious and even sizes as low as #10 are cause for concern.

The limited amount of cw laser irradiation data available are in agreement with the above theoretical analysis. Pulsed laser irradiation is much more complicated since processes which are nonthermal in origin such as avalanche breakdown, multiphoton excitation, shock wave phenomena, etc. may be involved. The above conclusions should thus not be applied to laser mirrors intended for pulsed applications without further study.

References

[1] Jungling, Lt. Col. K., Air Force Weapons Laboratory (private communication).

[2] Carslaw, H. S., and Jaeger, J. C., Conduction of Heat in Solids (Oxford University Press, Oxford, 1959), p. 264.

[3] Dwight, H. B., Tables of Integrals and Other Mathematical Data (The Macmillan Company, New York, 1947), p. 129.

[4] Saito, T. T., Charlton, G. B., and Loomis, J. S., 10.6 micrometer cw laser damage studies of metal substrate mirrors, NBS Spec. Publ. 414, 103 (1974).

[5] Carslaw, H. S., and Jaeger, J. C., *op. cit.*, p. 265.

[6] Bennett, H. E., and Burge, D. K., Simple expressions for predicting the effect of volume and interface absorption and of scattering in high reflectance or antireflectance multilayer coatings, J. Opt. Soc. Am. 70, 268 (1980).

[7] Bloembergen, N., Role of cracks, pores, and absorbing inclusions on laser induced damage threshold at surfaces of transparent dielectrics, Appl. Opt. 12, 661 (1973).

[8] Bennett, J. M., Burge, D. K., Rahn, J. P., and Bennett, H. E., Standards for optical surface quality using total integrated scattering, in Contemporary Optical Systems and Components Specifications, SPIE, Vol. 181 (1979), pp. 124-132.

[9] Rosasco, G. J., and Bennett, H. S., Internal field resonance structure: Implications for optical absorption and scattering by microscopic particles, J. Opt. Soc. Am. 68, 1242 (1978).

[10] Küster, H., and Ebert, J., Pyroelectric measurement of absorption in oxide layers and correlation to damage threshold, NBS Spec. Publ. 568, 269 (1980).

[11] Kyser, D. S., Bennett, H. E., Stanford, J. L., Kelsal, D., Krosney, M., and Siahatgar, S., Survivability test on multilayer dielectric coatings on ULE substrates, in Naval Weapons Center Technical Publication 6178, Part 1, August 1980, p. 16.

Figures

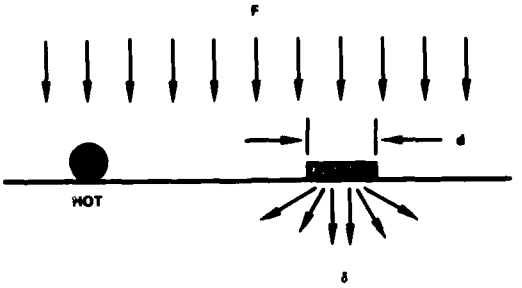

Figure 1. Comparison of irradiation by flux F on an absorbing defect in poor thermal contact with substrate (left side) and in good thermal contact (right side). The arrows below the horizontal line indicate thermal diffusion into the highly reflecting substrate, which has a diffusion depth δ.

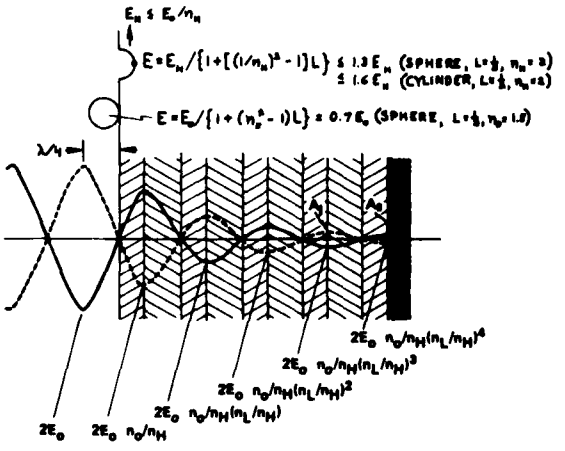

Figure 2. Local fields in a pit or groove on the surface, at a spherical particulate, and at the surface of a highly reflecting multilayer dielectric film.

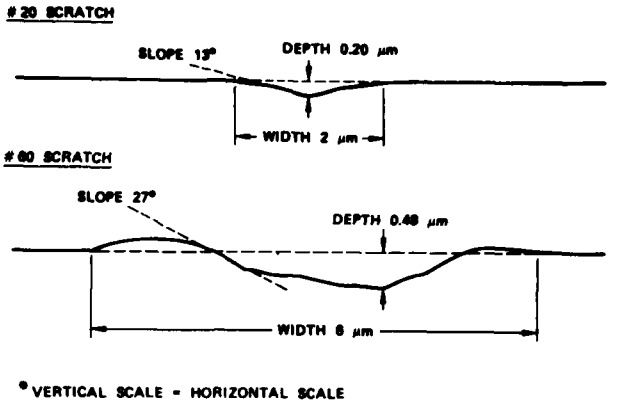

Figure 3. Profiles of #20 and #60 standard scratches on glass. The scratch standards were supplied by Frankford Arsenal and were analyzed using a Talystep stylus profilometer having a lateral resolution of approximately 1 μm (after reference 8).

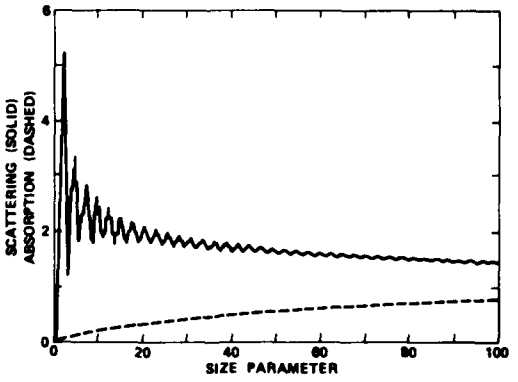

Figure 4. Efficiency factors for scattering and absorption of spherical particles having a complex index of refraction of 2.2 - j0.00409 at λ = 514 nm. The absorption coefficient of the material is then 1000 cm^{-1} (after reference 9).

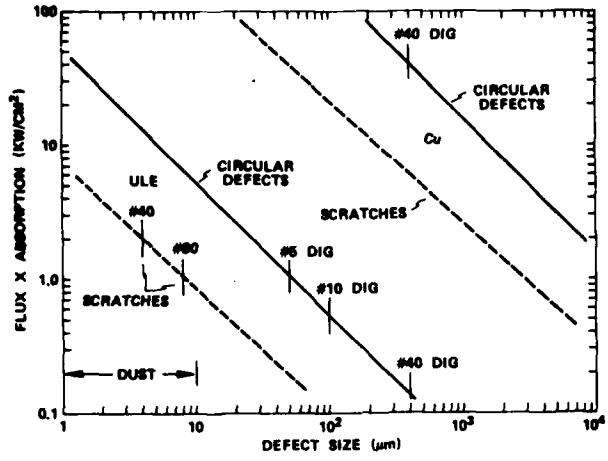

Figure 5. Limiting defect sizes for catastrophic damage under continuous irradiation for ULE quartz substrates (lower left) and copper substrates (upper right) calculated from eqs. (7,8). Scratch and dig values are indicated by the vertical lines.

Figure 6. Defect sites on a ZnS/ThF_4/Ag multilayer film having a reflectance of 0.999 at 3.8 μm before and after irradiation by a 3.8-μm laser. Some of the sites where melting occurred are circled.

Figure 7. Heavy scratch in a ZnS/ThF_4/Ag multilayer film after exposure to a 3.8-μm laser. A magnified image of the area on the right edge of the melted region is shown on the right side.

It was suggested that defects within a multilayer film should have less effect than those on the surface since for internal defects diffusion can take place in all directions. The speaker pointed out that although the effects might be less in some cases, it depended entirely on where and how large the internal defect was, since at some points the internal fields in a multilayer film can be much larger than that at the film surface. It was also suggested that spiking in a CW laser output may alter the results obtained, which are based on a constant irradiation level. The speaker agreed.

MULTIPLE-SHOT LASER DAMAGE THRESHOLDS OF ULTRAVIOLET REFLECTORS AT 248 AND 308 NANOMETERS

Stephen R. Foltyn and Brian E. Newnam
Los Alamos Scientific Laboratory
Los Alamos, New Mexico 87545

Multiple-shot damage thresholds of dielectric reflectors have been measured at 248 and 308 nm. Standard irradiation conditions were a 10-ns pulsewidth, 0.6-mm spot diameter and 35-Hz pulse repetition frequency. The reflectors, from various sources, were composed of oxide and fluoride films.

Although damage was generally initiated at visible film defects, there was no correlation between damage susceptibility and the appearance of these defects. At levels near threshold, damage was most often observed as an increase in white-light scatter of a site with no growth upon continued irradiation; at higher levels, the damage site grew with successive shots.

Test sites were subjected to at least 10^3 shots and some sites received as many as 2.5×10^4 shots; however, with only one exception damage was found to occur within the first few shots or not at all.

Reflectors at 248 nm typically had damage thresholds in the 1.0-1.8 J/cm^2 range with two samples exhibiting unexpectedly high thresholds of 2.8 and 3.0 J/cm^2. In some cases, a subthreshold pre-irradiation treatment resulted in a 20-25% enhancement in damage resistance.

Key words: Excimer lasers; fluoride coatings; laser damage; multiple-shot damage; oxide coatings; pre-irradiation; thin films; ultraviolet reflectors

1. Introduction

An area of interest to Inertial Confinement Fusion and Molecular Laser Isotope Separation programs is the development of damage-resistant optical coatings. In order to address the problem of improving reflectors for wavelengths applicable to these programs, we have recently concluded a series of multiple-shot damage threshold measurements on multilayer coatings designed for 248 and 308 nm. The purpose of this initial effort was to evaluate some candidate materials and to collect useful information for optimizing coatings made from these materials.

2. Experimental details

2.1. Test specimens

As presented in table 1, the coatings - all quarter-wave dielectric stacks - were provided by both commercial vendors and research organizations. Various oxide and fluoride materials were employed. To preclude any possible variations in the coating damage thresholds due to substrate material and roughness, all but a few coatings were deposited on 38 mm × 5 mm Suprasil 2 substrates which had been batch polished by Laser Optics, Inc. to a roughness of ∿ 12 A RMS.

Table 1. Description of test specimens.

Coating suppliers

- Design Optics
- Lambda/Airtron
- National Research Council, Canada
- Northrop
- Optical Coating Laboratories, Inc.

Coating materials

- PbF_2/Na_3AlF_6
- HfO_2/SiO_2
- Al_2O_3/NaF
- Sc_2O_3/MgF
- ThF_4/Na_3AlF_6

2.2. Test facility

Our experiment, shown schematically in figure 1, utilized a pinhole/detector combination to directly measure the peak fluence (J/cm^2) in the incident beam. In order to account for changes in pulse energy or focusability during a test, a ratio technique was used whereby part of the input beam was focused through a pinhole to continuously monitor peak fluence A. During calibration before testing the samples, a similar arrangement at B measured the test fluence. Thus, the ratio B/A was determined. For the threshold tests, pinhole/detector B was replaced by the test sample and the test fluence was computed, while running, by using fluence A, the calibration ratio B/A and the filter transmission. The laser-induced damage to the coatings was observed visually with the aid of a 25 to 100X microscope and bright white-light illumination.

It was fortunate that a commercial laser proved useful for these tests in that the device has provided, thus far, turnkey operation for tens of millions of shots. Table 2 lists details of the laser as well as applicable test conditions. It should be noted that, while the laser is capable of operating at up to 150 Hz, detector limitations dictated an upper limit of 35 Hz. Tests were conducted at this limit in order to accumulate many shots on a test site in a short time.

Table 2. Test conditions

Laser	Lumonics 861 Multigas Excimer System operating on KrF (248 nm) or XeCl (308 nm) at pressure, voltage, and mixture specified by manufacturer
Single-pulse energy	250 mJ (248 nm); 80 mJ (308 nm)
Pulse repetition frequency	35 Hz all tests
Pulse length	10-12 ns
Mean spot diameter	0.62 mm (248 nm); 0.66 mm (308 nm)

2.3. Beam characterization

In reporting any damage threshold measurements, proper characterization of the beam at the sample location is a necessity. Figures 2 and 3 are spatial profiles of the focused beam obtained by pinhole scans in the plane normally occupied by the coating under test. The mean value of the spot diameter (I_0/e^2 level) determined from these profiles was 0.62 mm. We also monitored the temporal pulse, as shown in figure 4, which had a nominal width of 12 ns FWHM.

2.4. Characterization of damage and damage thresholds

At each test fluence 10 sites were irradiated. These sites were distributed over the entire surface of the reflector. At levels near threshold, damage was most often observed as the enlargement of an already present defect. Some sites grew with continued irradiation. At levels appreciably over threshold, a "burn pattern" of the beam profile occurred accompanied by rapid growth and flaking on successive shots. The damage threshold in these tests was defined as the highest fluence at which 10 of 10 sites survived 1000 shots without damage. In addition, we defined an "upper limit" which is the highest fluence at which at least 1 of 10 sites survived 1000 shots without damage. Of special note is that in all cases but one, damage occurred within the first five shots or it did not occur at all. Discussion of this one exception will follow later in this report.

3. Results

Typical data - in this case for a 248-nm reflector composed of the Sc_2O_3/MgF_2 quarter-wave layer combination - are presented in figure 5. According to our definitions, the damage threshold is 1.7 J/cm^2 and the upper limit is 2.6 J/cm^2. Note that this type of threshold distribution provides more information than simply the thresholds themselves. The result that 2 of 10 sites survived at 2.6 J/cm^2 is a measure of the uniformity of the coating's damage resistance and the potential performance of this design. The slope of the fitted line in figure 5 then indicates the degree to which this reflector is approaching its potential.

There was a wide variation in the slopes observed during these tests. Figure 6 is an example of two 248-nm reflectors of Al_2O_3/NaF layers produced in the same coating deposition. Of the six reflectors produced in this series, Run 1, No. 1 (solid line) had the highest threshold. It also had the steepest slope. Our overall observation has been that of every set of comparable reflectors, the highest damage threshold belonged to the reflector with the steepest slope.

Another type of nonuniformity, of macroscopic dimensions, was observed in one case. Figure 7 presents the data obtained for a single 248-nm reflector of ThF_4/Na_3AlF_6 design. The performance was quite good as indicated by the dotted line (a companion reflector had a steeper slope and a damage threshold of 3.0 J/cm^2), but one portion of this reflector, comprising about one-third of the

total surface area, exhibited weaker behavior. The cause is unknown and no other samples exhibited similar properties. However, this example demonstrates the importance of sampling sites over the entire surface.

The results of all tests in this series are compiled in table 4.

Table 4. Results

248 nm Reflectors

Materials	Design	R	Threshold (J/cm²)10/10	Upper Limit (J/cm²)1/10	Comments
PbF_2/Na_3AlF_6	$S(LH)^{10}$	0.740	0.03	-	fogged
HfO_2/SiO_2	$S(HL)^8H$	0.978	0.8	1.0	
HfO_2/SiO_2	$S(HL)^8H$, MgF_2 Overcoat	0.984	1.0	1.4	
Al_2O_3/NaF		0.452	0.3	0.6	peak-shifted, fogged, sub. unk.
Al_2O_3/NaF		0.105	0.4	1.1	badly fogged, sub. unk.
Al_2O_3/NaF	$S(HL)^{20}H$	0.959	1.0	2.1	run 1, Si substrate
Al_2O_3/NaF	$S(HL)^{20}H$	0.961	1.1	2.1	run 1, Si substrate
Al_2O_3/NaF	$S(HL)^{20}H$	0.972	1.2	2.6	run 2
Al_2O_3/NaF	$S(HL)^{20}H$	0.966	1.3	2.3	run 2
Al_2O_3/NaF	$S(HL)^{20}H$	0.966	1.3	2.4	run 1
Al_2O_3/NaF	$S(HL)^{20}H$	0.919	1.7	2.2	run 1, slightly fogged
Sc_2O_3/MgF_2	$S(LH)^{13}$	0.976	1.7	2.6	
$Sc_2O_3/MgF_2(45°)$	$S(LH)^{13}$	0.966	1.8	2.5	tested at 45°
$Sc_2O_3/MgF_2(45°)$	$S(LH)^{13}$	0.836	1.0	1.3	tested at 0°
ThF_4/Na_3AlF_6	$S(HL)^{17}H$	0.961	2.8	3.9	run 1
ThF_4/Na_3AlF_6	$S(HL)^{17}H$	0.949	3.0	3.4	run 2, different dep. cond.
			308 nm Reflectors		
ThF_4/Na_3AlF_6	$S(HL)^{19}H$	0.833	< 0.4	-	peak-shifted, delayed damage
HfO_2/SiO_2	$S(HL)^8H$	0.976	1.6	2.4	run 1
HfO_2/SiO_2	$S(HL)^8H$	0.976	2.2	3.6	run 2, different dep. cond.
HfO_2/SiO_2	$S(HL)^8HL^2$	0.961	2.0	2.8	

4. Discussion of results

Salient points about the reflector designs are:

1. PbF_2/Na_3AlF_6 Very weak, probably no contender.

2. HfO_2/SiO_2 Relatively weak, but possessed high reflectance. Provided the only direct comparison of wavelength scaling in these tests in that fluence threshold was $\propto \lambda^4$, as previously observed by Newnam and Gill [1].

3. Al_2O_3/NaF Design motivated by the high threshold measured by Newnam and Gill in 1978 [1] with 22-ns pulses at 266 nm. Ignoring the fogged specimens of unknown design, the rest are in the 1.0-1.7 J/cm² range (comparable to the previous 266-nm values when scaled per $t^{\frac{1}{2}}$ and λ^4). Two coatings deposited on very smooth (3-4 A rms) Si substrates appeared slightly weaker, possibly due to coating stresses induced by higher thermal expansion of Si as compared to SiO_2.

4. Sc_2O_3/MgF_2 High thresholds. Resistance of 45° reflector tested at 0° was lower by half indicating the effect of large deviations from correct coating thicknesses.

5. ThF_4/Na_3AlF_6 Highest thresholds, even for the weak area of one reflector discussed above. Hygroscopic nature could limit its application unless well protected.

Since the thresholds for this last reflector design were very high at 248 nm, we must address the poor performance of this same design at 308 nm. The comments in table 4 provide a clue. The reflectance peak of this reflector was shifted so that R at 308 nm was only 83% and T nearly 10%. This was caused by a slight error in coating thicknesses during the evaporation procedure. The result is that a significantly larger amount of laser energy at 308 nm penetrated into the inner layers than would have occurred for a properly tuned reflector design. This also would explain the observation illustrated in figure 8 of delayed damage after the start of irradiation. At nearly any fluence level damage did occur, but only after a certain number of shots. The onset of damage was heralded by a color change, the result of interference caused by the probable separation of the

coating layers. Continued irradiation led to catastrophic flaking of the coating. It has been reported by several researchers [2,3,4] that a considerable amount of water exists between layers and at the film - substrate interface of the ThF_4 films. This fact and our observations lead us to speculate that laser heating of this interlayer water caused enough stress to rupture the coatings. In the 248-nm reflectors of these materials the coating thicknesses were correctly tuned as quarter waves resulting in high reflectance. In this case, laser energy density diminishes rapidly with depth into the coating stack, and the water in the outer layer simply outgasses without problematic stress.

5. Pre-irradiation conditioning

One final topic was addressed briefly in these studies: the effect of preconditioning on the damage threshold of a particular test site. By irradiating a site with 1000 shots at threshold before actually ascertaining the damage level, an improvement was observed in most of the reflector designs tested. The results shown in figure 9 for the best Al_2O_3/NaF reflector were typical in that a 20-25% threshold increase was obtained and the slope remained the same. One example of each coating material combination was preconditioned, and the results for these are listed in table 5. All materials except ThF_4/Na_3AlF_6 exhibited improved thresholds. However, the 248-nm HfO_2/SiO_2 reflector showed no effect while the greatest improvement was observed in a 308-nm reflector of the same design.

Table 5. Effect of preconditioning.

	Material	Effect
248 nm reflectors		
	Al_2O_3/NaF	threshold increased 24% ($1.7\ J/cm^2$ to $2.1\ J/cm^2$)
	Sc_2O_3/MgF_2	threshold increased 22% ($1.8\ J/cm^2$ to $2.2\ J/cm^2$)
	$HfO_2/SiO_2, MgF_2$	threshold increased 20% ($1.0\ J/cm^2$ to $1.2\ J/cm^2$)
	HfO_2/SiO_2	no effect
	ThF_4/Na_3AlF_6	no effect
308 nm reflectors		
	HfO_2/SiO_2	threshold increased 27% ($2.2\ J/cm^2$ to $2.8\ J/cm^2$)
	ThF_4/Na_3AlF_6	no effect

We speculate that the preconditioning causes evolution of adsorbed contaminants from the reflector surface thereby reducing the absorption of laser energy. However, we have not yet determined if the resultant improvement in the damage resistance is permanent or temporary. More investigation of this effect is clearly motivated.

6. Conclusions

In our tests of 248-nm and 308-nm dielectric reflectors we have observed damage thresholds of $1.0\text{-}3.0\ J/cm^2$. In addition, we have observed wide variations in site-to-site damage thresholds, supportive evidence for λ^4 scaling and the adverse effect of incorrect layer thicknesses. We have shown that in some materials a subthreshold pre-irradiation treatment results in a 20-25% improvement in damage resistance.

References

[1]. Newnam, B. E., and Gill, D. H., Ultraviolet damage resistance of laser coatings, NBS Spec. Pub. 541, 190 (1978).

[2]. Donovan, T.M., and Temple, P. A., The relative importance of interface and volume absorption by water in evaporated films, NBS Spec. Pub. 568, 237 (1979).

[3]. Humpherys, T. W.; Lusk, R. L.; and Jungling, K. C., Surface microanalysis techniques for characterization of thin films, NBS Spec. Pub. 568, 257 (1979).

[4]. Anderson, W. J., Manson, W. N., Characterization of small absorptions in optical coatings, poster presentation at Twelfth Annual Symposium on Optical Materials for High Power Lasers, Boulder, Colorado (Sept. 30-Oct. 1, 1980).

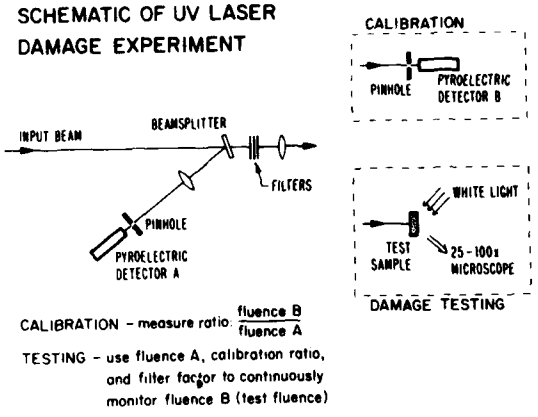

Figure 1. Schematic of ultraviolet laser damage experiment.

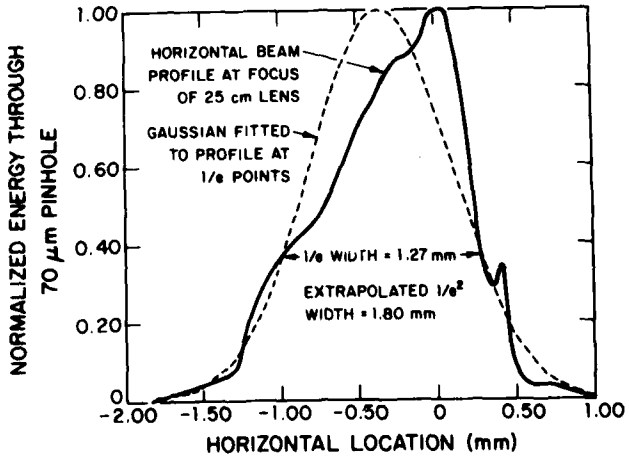

Figure 2. Spatial profile of focused 248-nm laser beam (horizontal).

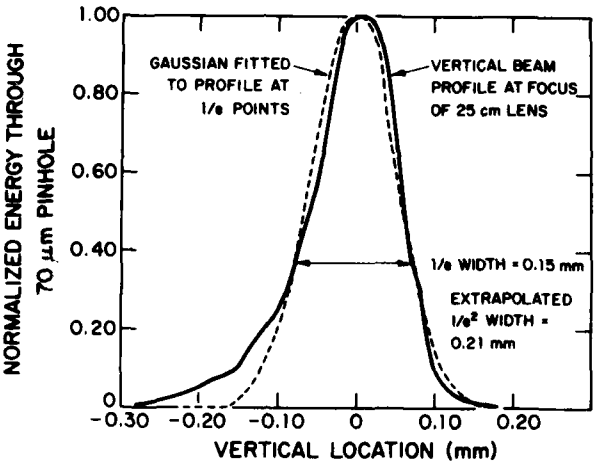

Figure 3. Spatial profile of focused 248-nm laser beam (vertical).

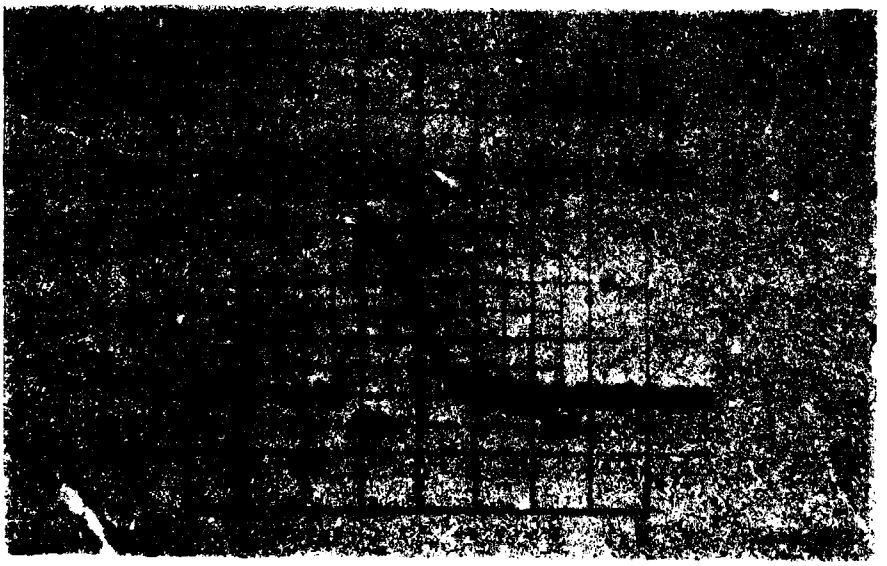

Figure 4. Laser temporal pulsewidth at 248 nm. FWHM is 12 ns.

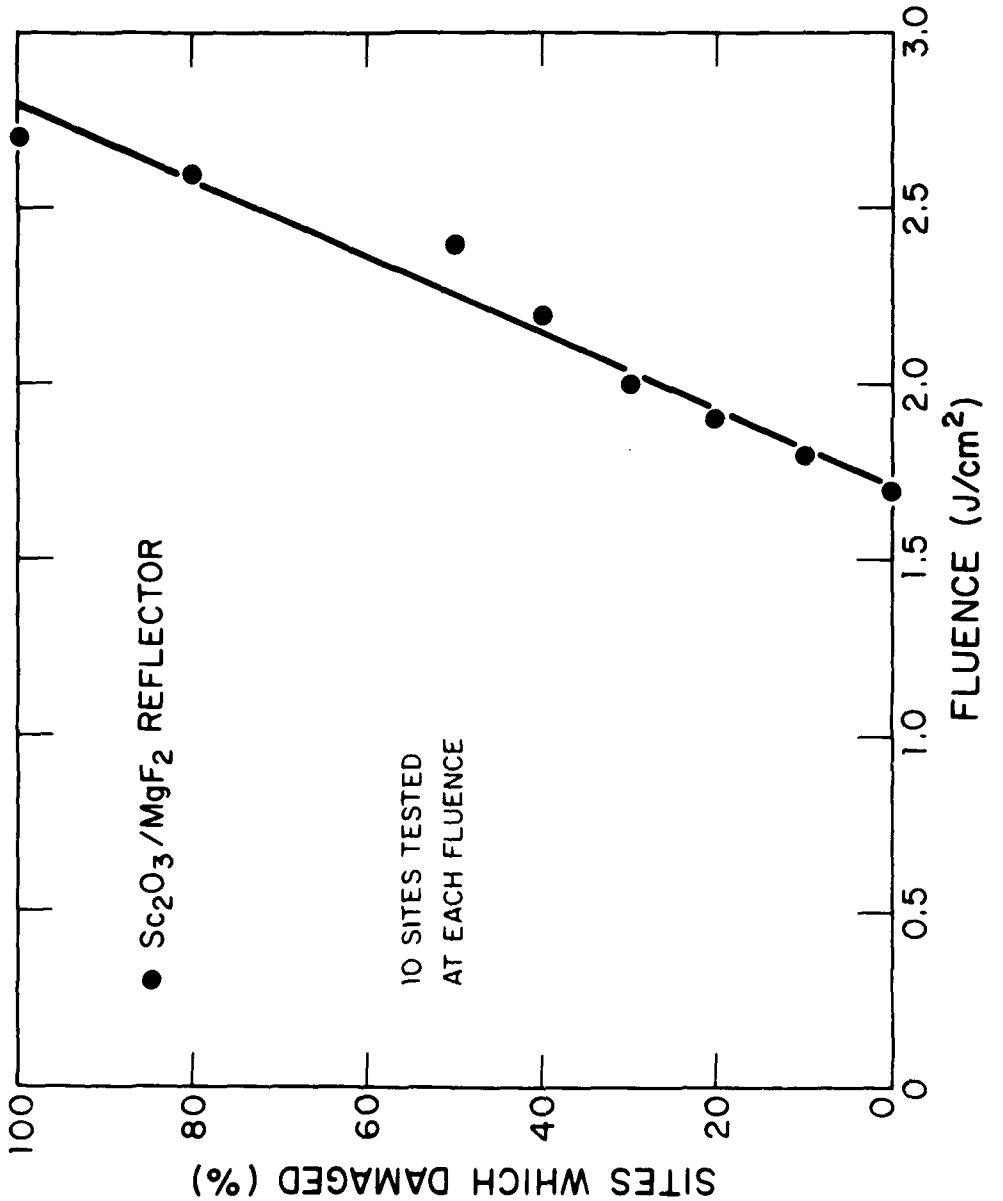

Figure 5. Damage versus laser fluence at 248 nm.

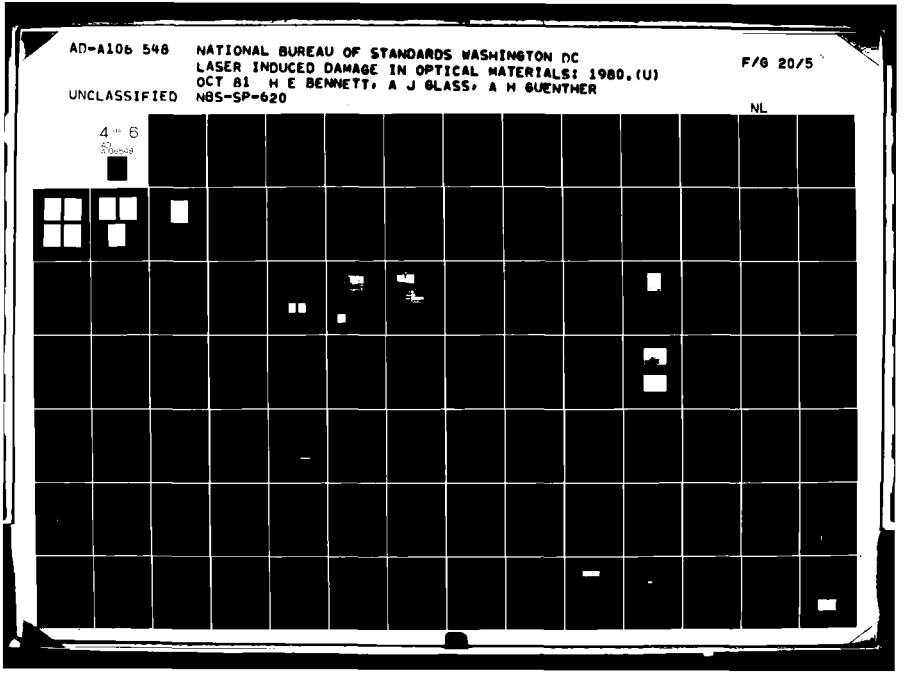
AD-A106 548
NATIONAL BUREAU OF STANDARDS WASHINGTON DC
LASER INDUCED DAMAGE IN OPTICAL MATERIALS: 1980,(U)
OCT 81 H E BENNETT, A J GLASS, A H GUENTHER
F/G 20/5
UNCLASSIFIED
NBS-SP-620
NL
4 OF 6

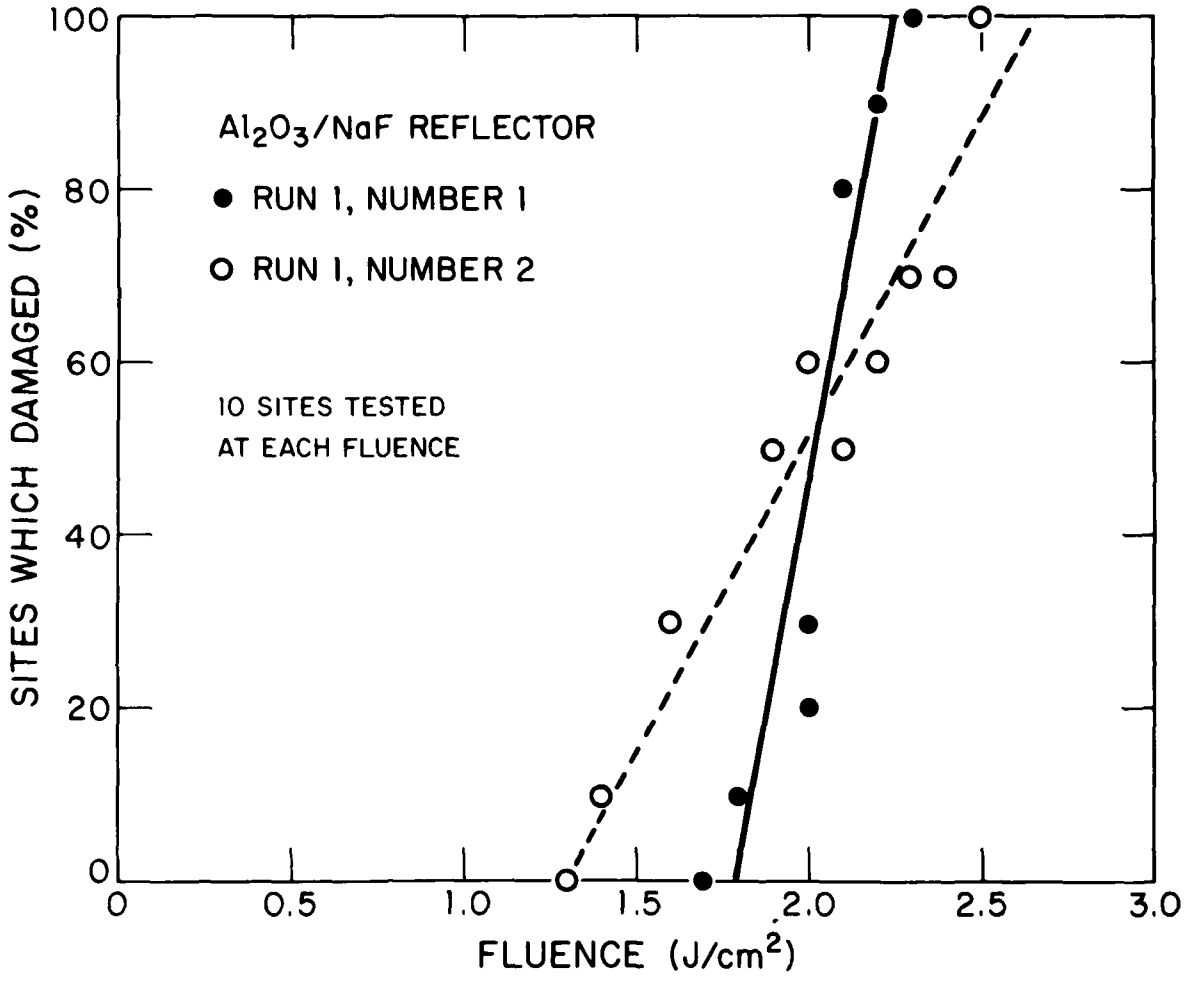

Figure 6. Damage versus laser fluence at 248 nm.

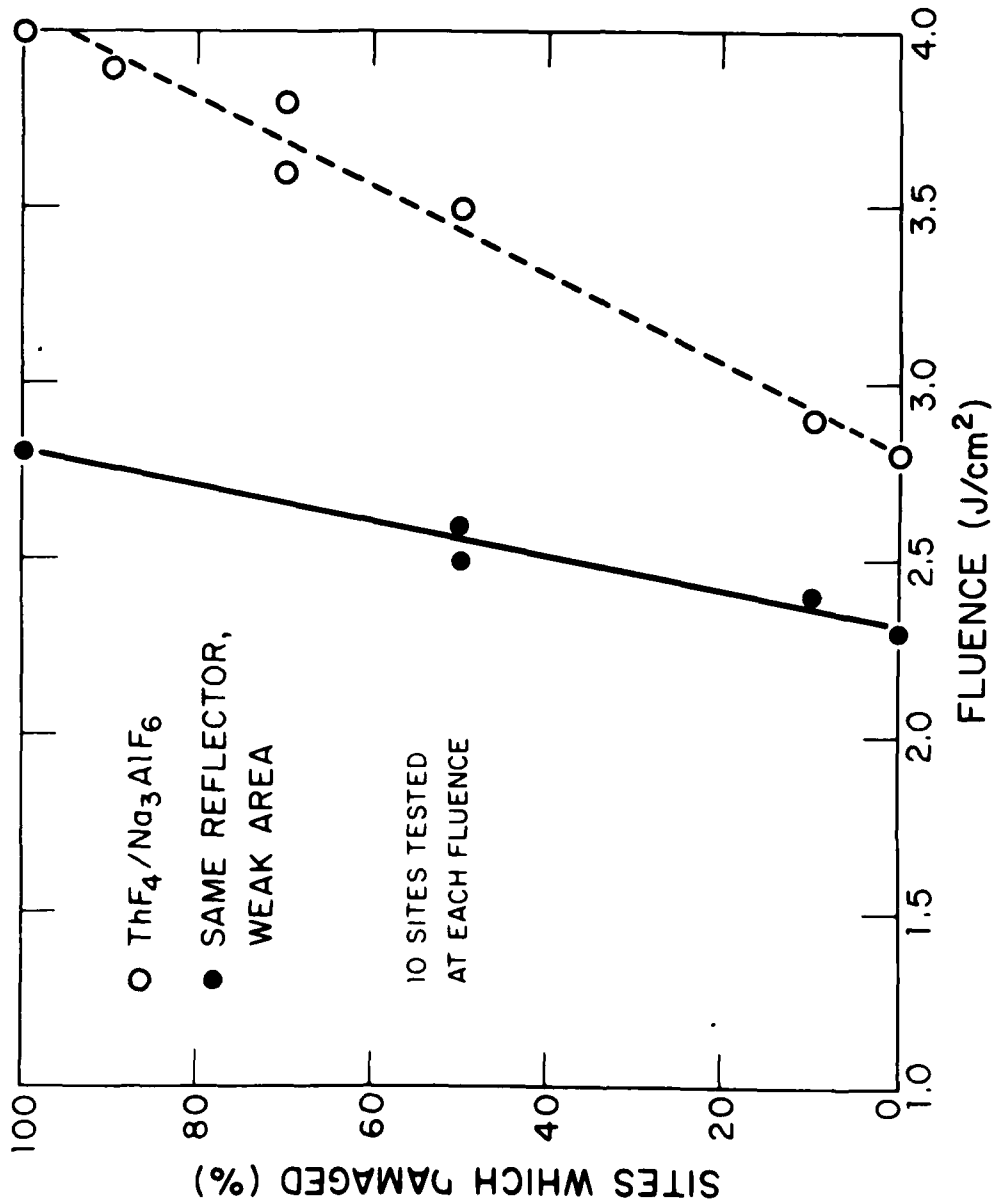

Figure 7. Damage versus laser fluence at 248 nm.

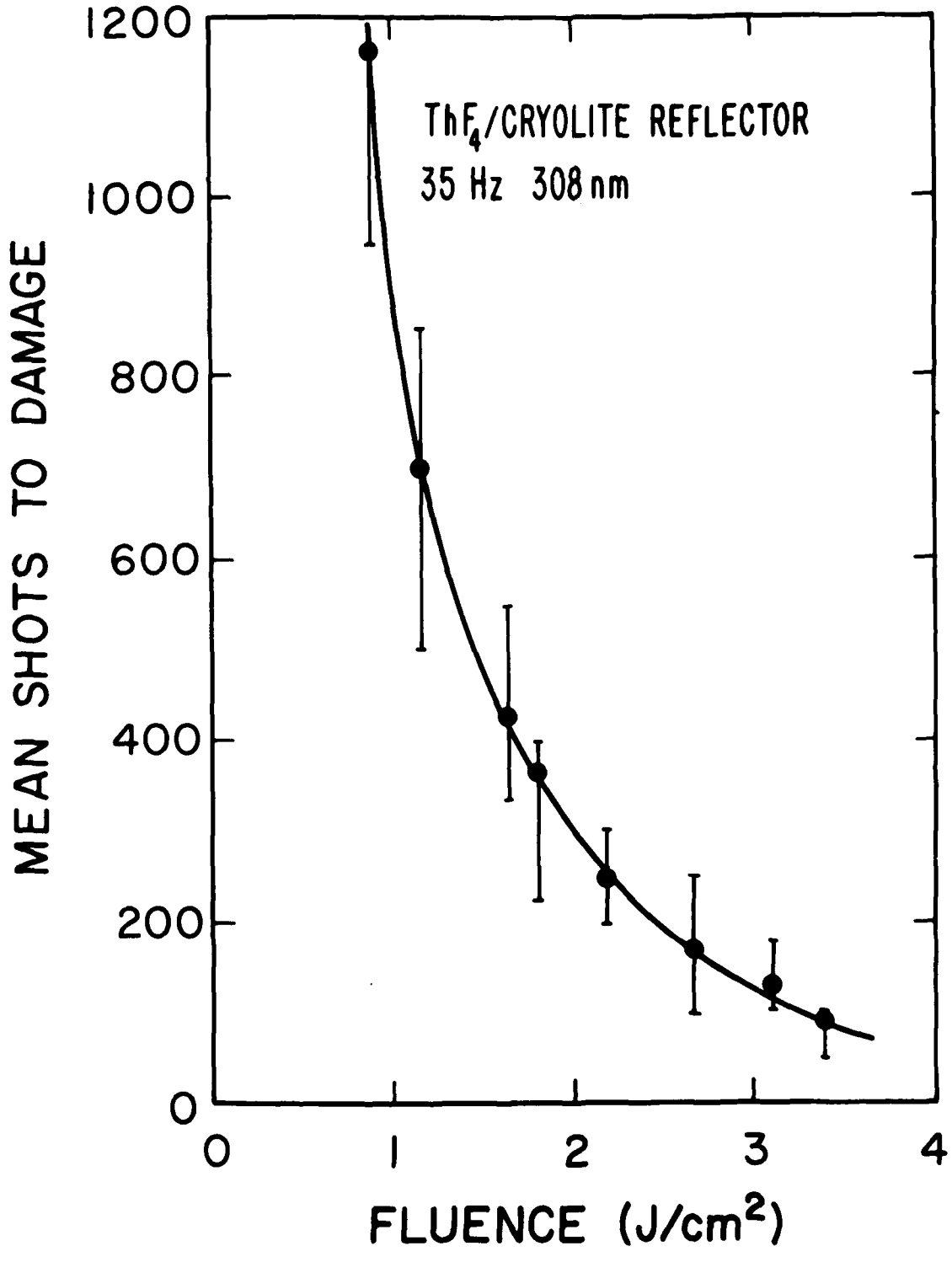

Figure 8. Number of laser shots to obtain damage versus fluence at 308 nm.

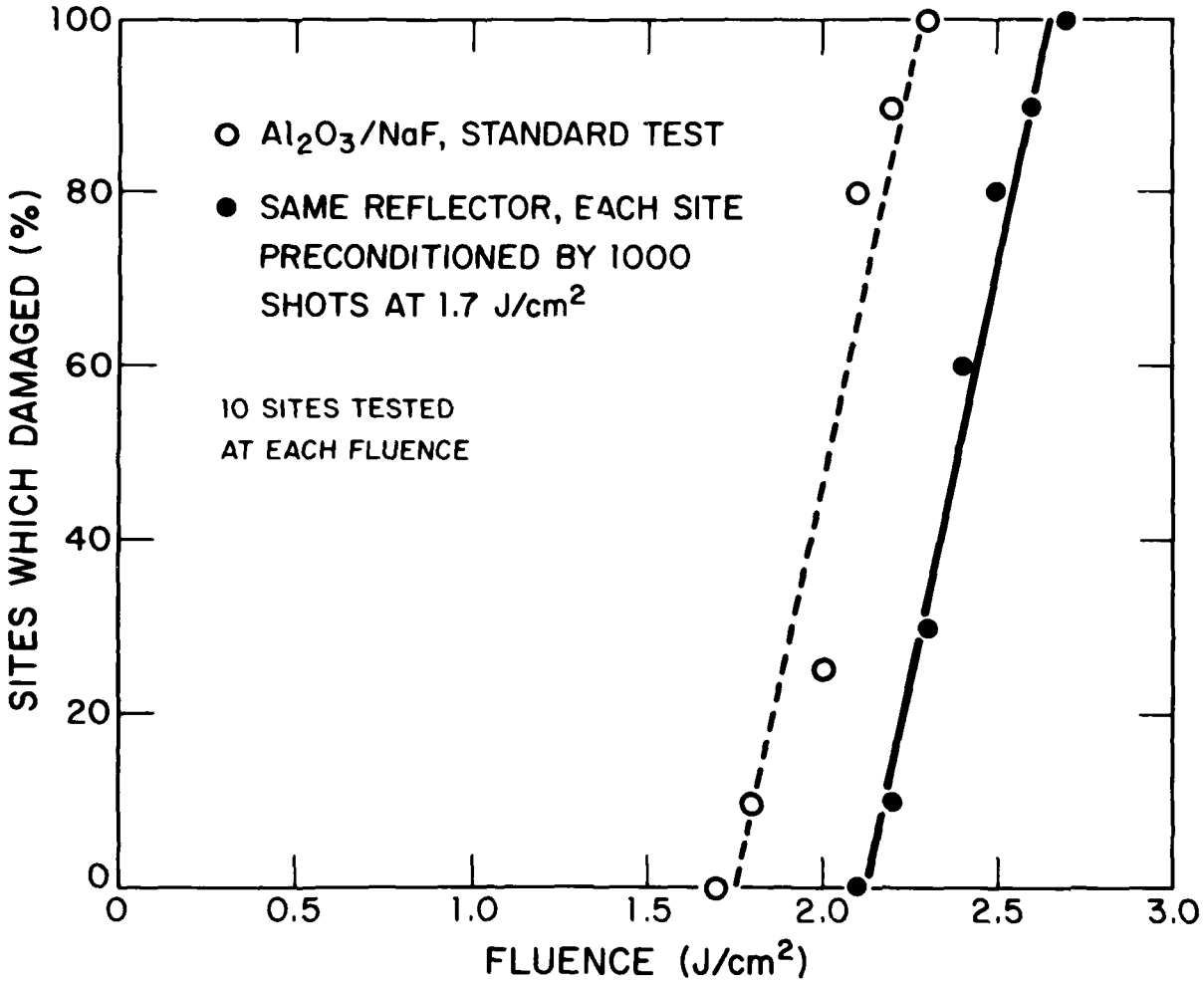

Figure 9. Influence of laser preconditioning at 248 nm on the damage threshold behavior.

In response to a question the author stated that they intended to do similar experiments on bulk material. To a question on surface cleanliness, the author responded that all surfaces were cleaned before testing except one. No significant change in damage threshold between the cleaned and uncleaned samples was observed.

A NOVEL TECHNIQUE FOR INVESTIGATING IMPURITY INITIATED SHORT PULSE LASER DAMAGE IN THIN FILMS

T. A. Wiggins*, T. W. Walker and A. H. Guenther
Air Force Weapons Laboratory
Kirtland Air Force Base, New Mexico 87117

A preliminary study has been conducted to investigate the effects of spot size on the laser induced damage threshold in thin films. Damage was produced by the interference fringes of two beams from a frequency-doubled Nd-YAG laser with a nearly Gaussian spatial profile. Fringes of spacing from 5 to 125μm were used on ZnS, ZrO_2 and ThF_4/ZnS films. The damage threshold and morphology were observed and are reported.

Microscopic examination indicated that the appearance within a damaged region, which is as narrow as 1μm, is not different from that produced by a single beam whose half-intensity diameter is a hundred times larger. Interesting results concerning the relative importance of scratches and other defects were revealed by Nomarski microscopic observation of the damage morphology.

It has been reported that laser damage to thin films is initiated primarily by small-size dielectric impurities and the dependence of the damage threshold on pulse length, film thickness, wavelength, and material investigated. In the present study it was observed that the damage threshold increased with decreasing film thickness in agreement with previous observations. However, there was no significant increase or decrease in threshold for the two-beam case over that for a single beam when the increased energy density due to interference effects is considered. In concert with previous observations it is concluded from the damage morphology and the absence of a spot size dependence that the source of damage initiation is impurities smaller than 1μm for these 5 ns pulse lengths.

Key words: Laser damage; impurity-induced damage; thin films; damage threshold; ZrO_2; ZnS; ThF_4.

1. Introduction

The role of coating defects and impurities in determining the laser damage threshold of thin films was discussed at the 1979 Symposium on Laser Induced Damage in Optical Materials [1][1]. An impurity model was presented which accounts for the observed changes in the damage threshold as a function of laser pulse length, wavelength, thin film material and film thickness. The implications of such a model to damage threshold changes with laser spot size is now under investigation.

DeShazer, et al. [2] and Wang, et al. [3] have measured a spot size dependence of laser damage in thin films and related the results to a simple model [2] which was based on the probability of finding a defect within the laser spot. In contrast to the above work we have performed a spot size

*Permanent address: Physics Department, The Pennsylvania State University.

1. Figures in brackets indicate literature references at the end of this paper.

dependence experiment on ZrO_2, ZnS and ThF_4/ZnS films and have found no spot size dependence down to sizes less than 5 μm.

2. Role of Impurities in the Spot-Size-Dependent Damage Threshold

The impurity model [1] predicts that for short (5 to 15 ns) laser pulses the most easily damaged impurities are in the submicron size range. The temperature change of an absorbing impurity is determined by the Mie absorption cross-section, the incident intensity and pulse duration, the radius of the impurity, the thermal conductivity and diffusivity of the defect and the thermal conductivity of the film containing the defect. The samller the impurity size, the larger are the thermal losses and the less likely that the particle will be damaged. However, if the particle is too large, more energy is required to heat the larger mass and the particle is also less likely to be damaged. Therefore, there is an optimum particle size for a given laser pulse length which balances size and mass and is thus the easiest to damage. If the laser pulse length is increased, it can be shown [1] that the easiest-to-damage particle size increases and vice versa for shorter pulse lengths. In the nanosecond pulse regime, calculations [1] show that the easiest-to-damage impurities are in the submicron (~ 0.5 μm) diameter range.

To connect these results to a laser spot size dependence, it is important to note that within thin films the impurities are distributed in both number and size. Artem'ev, et al. [4,5] have found that as the size of the impurity decreases the number density increases. This trend cannot continue indefinitely, but Leonov [6] has shown that in many bulk materials the number density of impurities with a radius between 0.3 μm and 0.5 μm, is about $10^{12}/cm^3$.

An observed spot size dependence can have at least two causes. First, the spot size can be small enough and the easiest-to-damage particles far enough apart so that there is a low probability of hitting one of these particles with the laser beam. In this case, a higher energy is required to damage the next-easier-to-damage particle which is in the laser spot. Another phenomenon which can occur is that the laser spot is small enough so that the easiest-to-damage particle is larger than the laser beam and thus only partially illuminated. In this case more energy must be added and a laser spot size dependent damage threshold is observed. By thermal calculations this would not occur until the spot size was less than 0.5 μm.

We can make an estimate of the laser spot size at which impurities of the easiest-to-damage size begin to be missed by the laser beam. From previous calculations [1], 5 ns laser pulses at a 1.06 μm laser wavelength should damage particles in the 0.3 μm to 0.5 μm diameter range. Using the results of Leonov and noting that thin films have far more impurities than their bulk form, we can make a conservative assumption that there are at least 10^{12} impurities per cm^3 in the 0.3 to 0.5 μm diameter range. For a 0.5 μm thin film this would correspond to 5×10^7 impurities per cm^2. In a 2 μm diameter beam there would be about one impurity.

This simple and conservative analysis indicates that the laser spot size would have to be near 1 μm before the damage threshold would increase.

3. Experimental Arrangement

The samples were illuminated by two beams from a frequency-doubled Nd-YAG laser system consisting of an oscillator and two amplifiers. The measured pulse time was 5 ns with a variation of less than 0.5 ns. The experimental arrangement is shown in figure 1. A dielectric beam splitter directed about half of the energy to a 99 percent mirror which was set at the proper position and angle to make the beams cross at a suitable angle on a sample. The maximum difference in the path lengths between the two beams corresponded to 0.5 ns. A lens was placed in the beam before the beam

splitter produced a focus for both beams at the sample site. Lenses from 2-4 m focal length were used, depending upon the angle required.

The angles used were such that the spacing between the interference maxima ranged from 5 to 125 μm, the angle being given by $\theta = \lambda/d$, where λ is the laser wavelength and d is the fringe spacing. This spacing was calculated from the geometry of the experiment and confirmed by observation of damage produced using a calibrated microscope.

An energy monitor was operated from a beam splitter situated just before the focusing lens. A second detector near the sample site was used to measure the relative intensity of the two beams. The measured ratio was 1.3 for a typical experiment indicating that the maximum intensity on the sample was 3.5 times that of the stronger beam while the minimum intensity was 0.02 that of this beam.

The energy variation on the sample was observed with an optical multichannel analyzer (OMA) placed at a position equivalent to that of the sample. Using a magnifying lens to project an image onto the analyzer, the energy variation could be recorded for fringe spacings larger than 20 microns. An example of the recorded intensity as a function of position on a sample is shown in figure 2. This analyzer was also used as an aid in aligning the beams on the sample.

The sample could be translated or rotated in its plane so that areas separated by a few mm could be irradiated with successive pulses. A series of pulses having decreasing intensities, as determined by the adjustment of the first amplifier, were used. The energy of each pulse was recorded.

Visual observation of a plasma formed at the surface and observation of enhanced scattering using auxiliary illumination were used as rough guides in determining the occurrence of damage. At suitable intervals, the sample was removed and examined in a Nomarski microscope to determine the threshold for damage. These observations were made both for the case of two beams on the sample and for the single, stronger beam.

4. Results

Two types of observations were made. One was the relative energy required for the two beams, compared with that for one beam, needed to produce minimum damage to a particular sample as judged by microscopic observations. ZnS and ZrO_2 films of thicknesses from 0.1 to 1 μm on fused silica, and ThF_4 and ZnS quarterwave coatings for 10.6 μm on a silicon substrate and on an Ag-coated substrate were tested.

It was observed that the energy threshold decreased for increasing film thickness as has been reported previously [1]. For all samples used the energy threshold for two beams compared with that for a single beam was lower by a factor of 2-3. Considering that the peak energy due to interference was on the order of 3.5 times that for a single beam, assuming perfect spatial and temporal overlapping of the beams, it is concluded that no spot-size dependence of threshold was observed in this experiment, the decreased threshold being accounted for by the enhanced energy density due to interference. It would appear that the initiation of damage is due to a source smaller than that probed in this experiment. That is, reducing the width of the area irradiated from several hundred microns to less than 5 μm produced no change in the damage threshold. This result is quite different from that observed in bulk damage wherein there is an increase in threshold for a reduced area of illumination.

The other type of observation used was Nomarski microscopic examination of damage morphology. The consistent result of these observations for all samples was that the appearance of the surface was not different in the illuminated areas for the two-beam case from that over all the area for the single beam case. For near threshold conditions it appeared that in both cases the damage consisted of discrete areas of size 1 μm or less, in

agreement with theoretical estimates. Some examples of the damage produced are shown in figures 3 and 4. All photographs in these figures are shown with the same magnification. Figure 3 shows the damage produced in a 0.5 μm thick ZrO_2 film on silica. A shows the result when a single beam is used. B, C, and D show the resulting damage for fringe spacings of 25, 10, and 5 μm, respectively. Figure 4 shows the damage produced in quarter-wave layers of ThF_4 and ZnS for 10.6 μm on a Ag-coated metal substrate. A shows the damage due to a single beam, B and C for 25 and 10 μm spaced fringes, respectively, due to two beams.

The effect of scratches on the surface generally was to increase the likelihood of damage. For the single-beam case long tracks of increased density of damage were observed along directions where scratches could be seen extending beyond the damaged area. The occurrence of damage here extended farther from the center along these directions than for neighboring areas suggesting that a smaller energy density is required when a scratch is present. These tracks are intermittent for the two-beam case appearing only when the interference produced a large energy density. For some cases, and in particular a 1 μm thick film of ZrO_2, it appeared that damage was was avoided along a particular direction having the appearance of a scratch. This behavior can be seen in figure 3C and in figure 5 which shows the damage in a 1 μm thick ZrO_2 coating on silica by two beams which produced 10 μm fringe spacings. This peculiar result will be investigated further.

5. Conclusion

It is concluded from these preliminary experiments that a reasonable source for initiation of laser damage to thin films is some type of defect that has a size less than 1 μm, the density of which depends upon the nature and thickness of the film.

Continuation of this work is planned, with improved methods of energy measurements and beam alignment, for other materials, pulse lengths, wavelengths, and fringe spacings.

6. Acknowledgments

One of us (TAW) acknowledges the support of his work under the Intergovernmental Personnel Act program of the Air Force Weapons Laboratory. The authors thank G. Fiorenzo and E. Miesak for their technical assistance.

7. References

[1] Walker, T. W., Guenther, A. H., Fry, C. G., Nielson, P., and Vaidyanathan, A., NBS Spec. Pub. #568, 405-416 and 479-496 (1979).

[2] DeShazer, L. G., Newnam, B. E., and Leung, K. M., NBS Spec. Pub. #387, 114-123 (1973).

[3] Wang, V., Guiliano, C. R., and Garcia, B., NBS Spec. Pub. #435 216-229 (1975).

[4] Artem'ev, V. V., Bonch-Bruevich, A. M., Morichev, I. E., Ivanova, N. L. and Vinogradskii, A. G., Sov. Phys. Tech. Phys. 22, 106 (1977).

[5] Artem'ev, V. V., Bonch-Bruevich, A. M., and Svechnikov, M. G., Sov. Phys. Tech. Phys. 23, 1467, (1978).

[6] Leonov, R. K., Zakharov, S. I., Dmitrieva, I. A., and Gandel'man G. M., Sov. J. Quant. Elec. 8, 729 (1978).

8. Figures

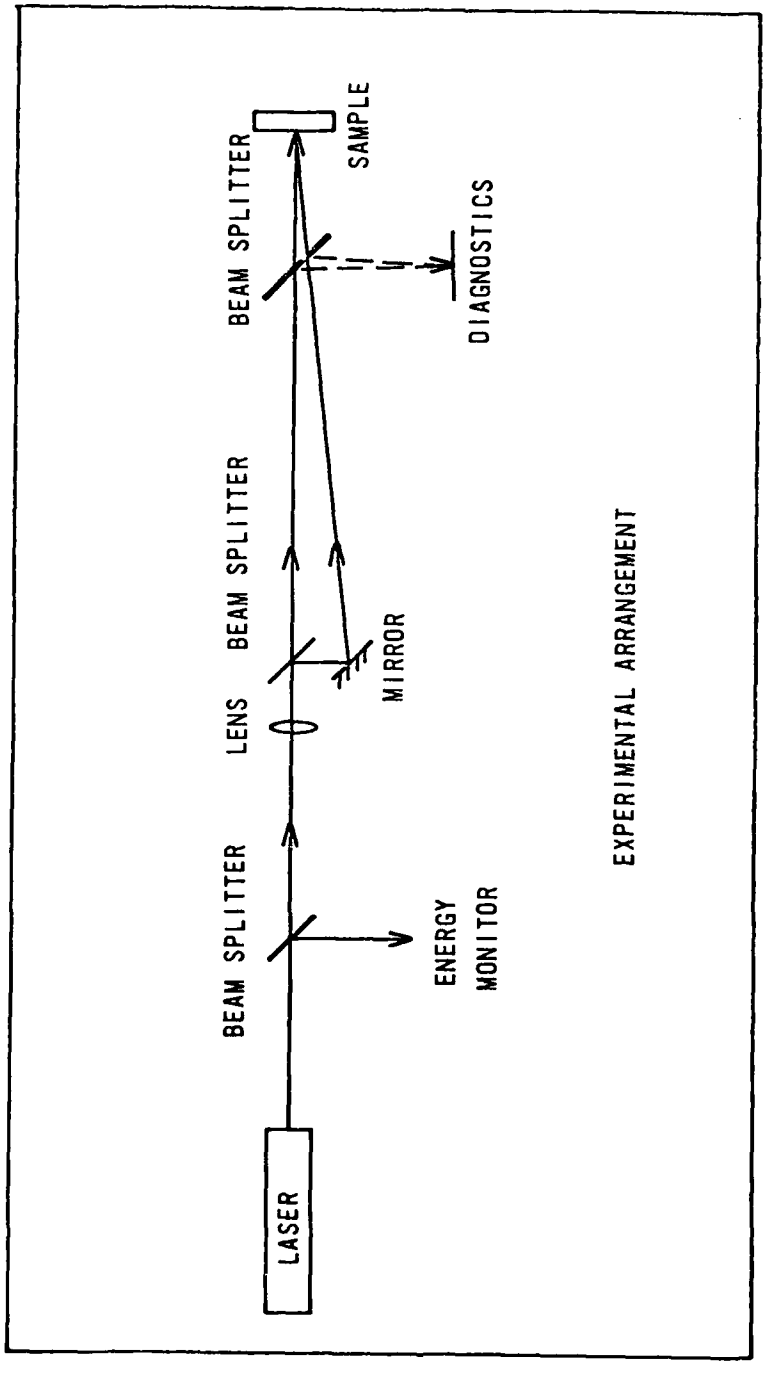

Fig. 1. Experimental arrangement used.

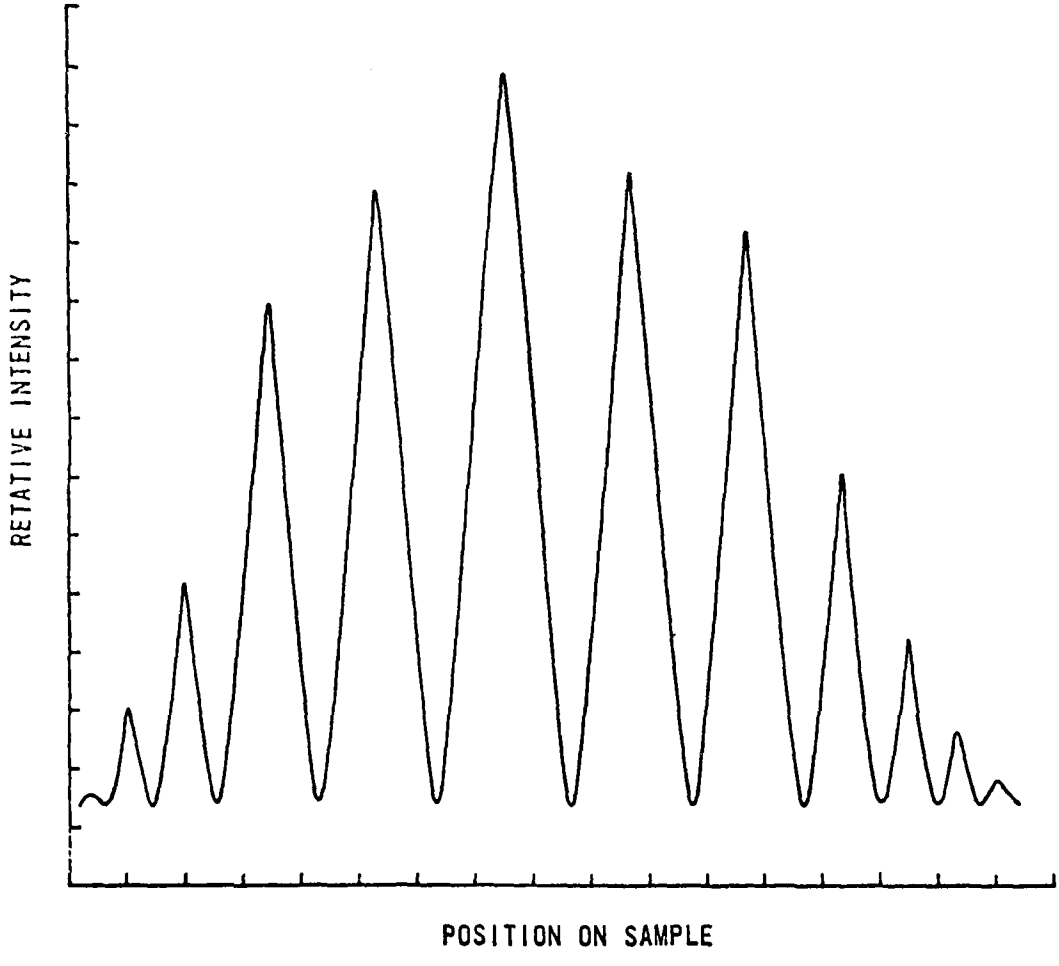

Fig. 2. Relative intensity across a portion of a sample on which 25 μm fringes were produced.

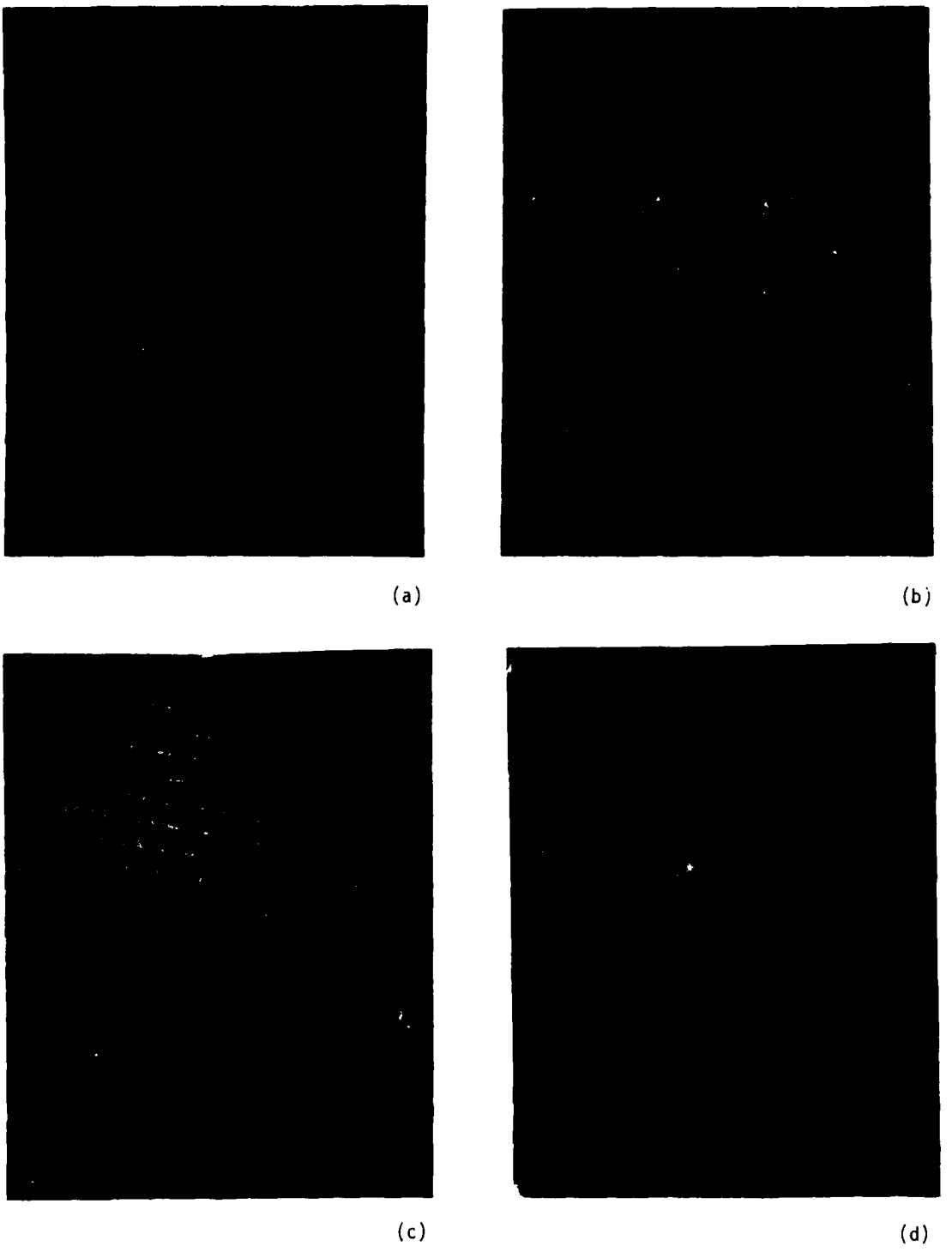

Fig. 3. Nomarski photographs of damage produced on 0.5 μm thick ZrO_2 film by (A), a single beam, and by two beams with fringe spacing of (B) 25, (C) 10, and (D) 5 μm.

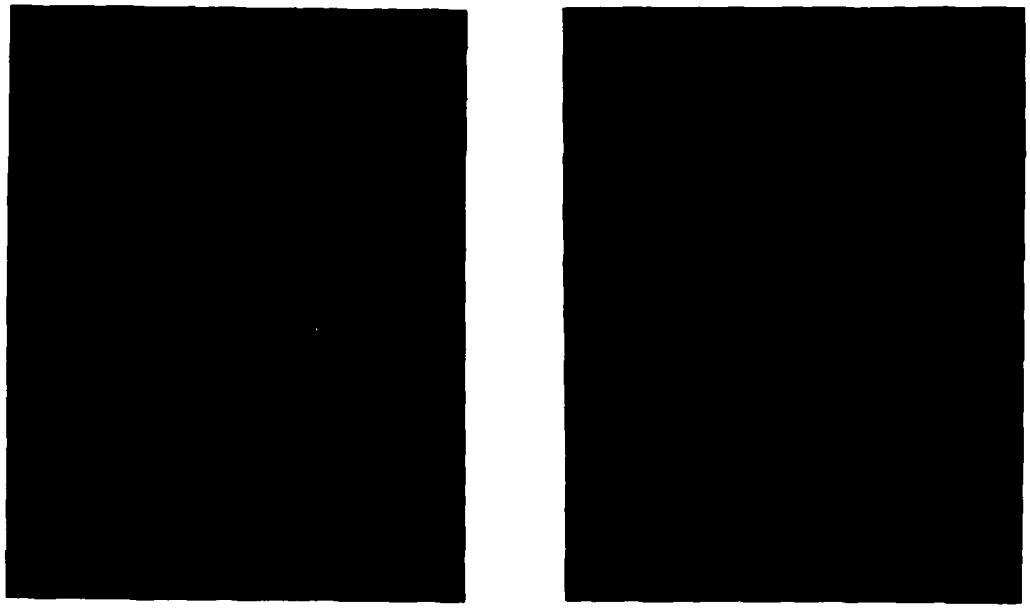

(a) (b)

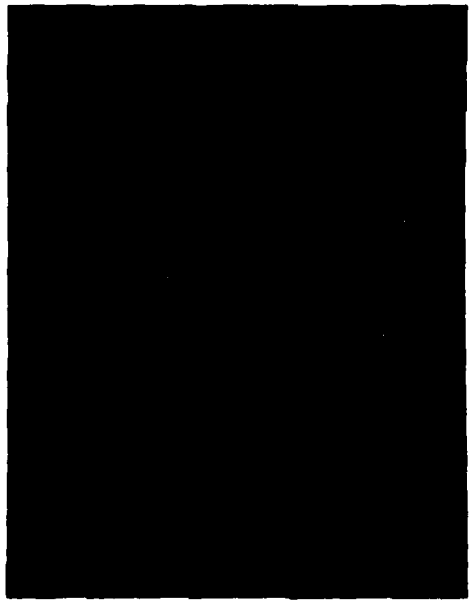

(c)

Fig. 4. Nomarski photographs of damage produced on quarter-wave coatings for 10.6 μm of ThF_4 and ZnS on a Ag-coated metal substrate by (A) a single beam and by (B) 25 and (C) 10 μm fringes.

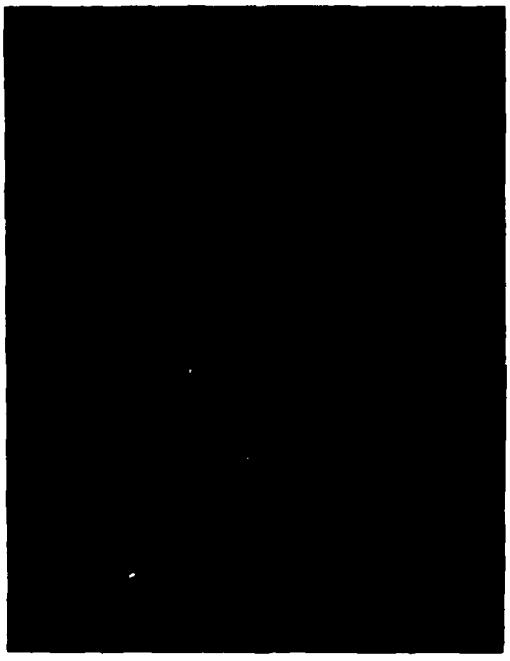

Fig. 5 Nomarski photograph of damage produced on a 1 μm thick ZrO_2 film by two beams which produced a fringe spacing of 10 μm.

EVALUATION OF BICHROMATIC COATINGS DESIGNED FOR PULSED LASER FUSION APPLICATIONS AT 0.53 AND 1.06 MICROMETERS

G. RICHARD WIRTENSON AND JAMES B. WILLIS
LAWRENCE LIVERMORE NATIONAL LABORATORY
UNIVERSITY OF CALIFORNIA
AND
E.A. ENEMARK
OPTICAL COATING LABORATORY, INC.

Various bichromatic coatings designed to operate at both 0.53 and 1.06 micrometers have been evaluated for spectral performance and laser damage threshold to determine the suitability of these coatings for 1 nanosecond pulse laser fusion experiments and to establish baseline data. Anti-reflection, partially transmitting high reflection, and maximum reflection coatings, consisting of titania and silica layers, were deposited onto BK-7 substrates. For each type of coating, two different designs were examined. Spectral measurements indicate the coatings met performance goals. Laser damage threshold values at 1.06 micrometers were similar to those of previous monochromatic production coatings, while damage levels at 0.53 micrometers were about one-half these 1.06 micrometer values.

Key words: Anti-reflection coatings, bichromatic, damage, high energy laser, laser damage, pulsed laser, reflectors, thin film.

1. Introduction

Laser fusion experiments have demonstrated more efficient ignition of the target as the wavelength of the incident laser radiation decreases. Additional experiments are planned which will study laser fusion reactions utilizing both 0.53 and 1.06 micrometer laser beams. The shorter wavelength will be obtained by inserting frequency doubling crystals into the 1.06 micrometer beams. The optical components following the frequency doubling stage will be used for both wavelengths. Consequently, the coatings on these optics must function at both wavelengths. In order to evaluate existing capability with regard to coatings proposed for these optics, the experiment reported here was undertaken.

2. Approach

For this initial experiment, the approach taken was in response to the hypothetical question -- what coatings might be supplied in response to an immediate need? Consequently, commonly used coating materials and existing coating processes were used. The coating designs were regarded as practical approaches consistent with the given spectral requirements.

Conventionally polished BK-7 substrates were coated with multi-layer designs consisting of titania and silica. Two different designs for each of three different types of coatings were deposited. The coating types were anti-reflectors, partially transmitting high reflectors, and maximum reflectors. The coated parts were evaluated for spectral performance, physical and environmental durability, and laser damage threshold at both 0.53 and 1.06 micrometers.

3. Coating Designs

The spectral requirements for the anti-reflection coatings were for reflectances less than 0.25% at both wavelengths with a goal of less than 0.1%. A major consideration was manufacturability. Because the eventual application is the coating of large area optics and because the coating thickness might vary by a few percent over the optical surface, the coating must provide for low reflectance for such a coating thickness variation.

Finally, laser damage considerations were important. For laser fusion systems in general, the weakest link in the optical train has been anti-reflection coatings. Increasing the damage threshold will allow for greater energy throughput and, thus, improved system performance.

Both theoretical designs for the anti-reflection coatings met the spectral specifications. The anticipated advantage for the simple (narrow band) design was that fewer layers might improve the coating's energy handling capabilities. Fewer layers meant less coating material and, thus, less absorption. For the complex (broad band) design, more layers resulted in broader regions of low reflectance. This thicker coating, however, might exhibit lower damage thresholds because of potentially greater absorption. The theoretical spectral performance curves for these anti-reflection coatings are shown in Figures 1 and 2.

Both reflector designs, the partial transmitter and the maximum reflector, compared a two-to-one stack to a two-stack design. "Stack" is merely a term for a set of coating layers consisting of alternating materials of high and low indices of refraction. The two designs are shown in Figure 3. The two-to-one design provides high reflectance at the two wavelengths of interest in one stack. The ensemble is a combination of one reflecting stack for one wavelength deposited over a reflecting stack at the other wavelength.

The two-to-one stack used fewer layers. However, the regions of maximum reflectance are not as broad as those for the ensemble design. For the ensemble, a choice had to be made as to which stack was to be deposited first. In either case, radiation reflected by the first deposited reflector would of necessity pass through the second deposited reflector. Since the 0.53 micrometer reflector was half the thickness of the 1.06 micrometer reflector and, thus, probably less absorbing, the choice was to deposit the 1.06 micrometer reflector first and then the 0.53 micrometer reflector. See Figure 3.

Theoretical performance curves for these designs are shown in Figures 4, 5, 6, and 7. The two-stack design provides greater manufacturing tolerances because of broader regions of high reflectance. The partial transmitters were to pass approximately 3% of the incident radiation.

4. Results

All coating designs were successfully deposited. The measured spectral curves are shown in Figures 1 and 2, and 4 through 7 for comparison to theory. The coatings passed the adhesion, hardness, and humidity tests of MIL-M-13508.

Damage threshold data are presented in Table I. Both the 0.53 and 1.06 micrometer data were obtained using comparative damage test techniques[1]. All damage testing was performed at UC/LLNL.

5. Discussions

The coatings met the spectral and environmental requirements. However, the damage test results were lower than desired, especially at 0.53 micrometers for the anti-reflection coatings. Previous samples of the broad band design had been found to damage at higher energy levels. See Table II.

There is no clear explanation for the variation in damage results for the reflector coatings. Again, the 0.53 micrometer data was not as high as hoped. In addition, one design concept for the reflectors did not clearly excel with regard to energy survivability. In some cases, the two-to-one design was more damage resistant while the two-stack design was better in others.

The possibility does exist that the titania is damaging more readily at the shorter wavelength because of increased absorption. The absorption edge occurs at about 0.35 micrometers. It could be that the absorption decreases very slowly with increasing wavelength and that we are seeing a manifestation of this at 0.53 micrometers. This must remain as conjecture, however, until additional experiments are performed.

6. References

[1] Milam D., Willis, J. B., Rainer, F., and Wirtenson, G. R., Determination of Laser Damage Thresholds by Comparison with an Absolute Laser Damage Standard, UCRL-84830 preprint, (Accepted for Publication), Applied Physics Letters.

TABLE I

Coating Type	Damage Threshold, Range (mean), J/cm^2 0.53 μm	1.06 μm
Anti-reflection		
Narrow band	2.4 - 3.5 (2.5)	4.0 - 6.5 (5.5)
Broad band	2.4 - 3.5 (2.5)	4.0 - 6.5 (5.5)
Partially transmitting high reflection		
2:1	2.5 - 5.0 (3.5)	6.5 - 9.0 (7.5)
Ensemble	~ 2.5 (2.5)	7.0 - 11.0 (8.5)
Maximum reflection		
2:1	2.0 - 5.0 (3.0)	7.0 -13.0 (11.0)
Ensemble	3.5 - 7.0 (5.0)	6.5 - 9.0 (7.0)

Table 1. Damage Threshold of coatings at 1 nanosecond, 1.06 mm.

Table II

Previous measurements on broad band AR design samples

6.2 ± 0.7
3.0 ± 0.5
5.4 ± 0.6
4.8 ± 1.0

Table 2. Previously measured damage threshold data on anti-reflection coating.

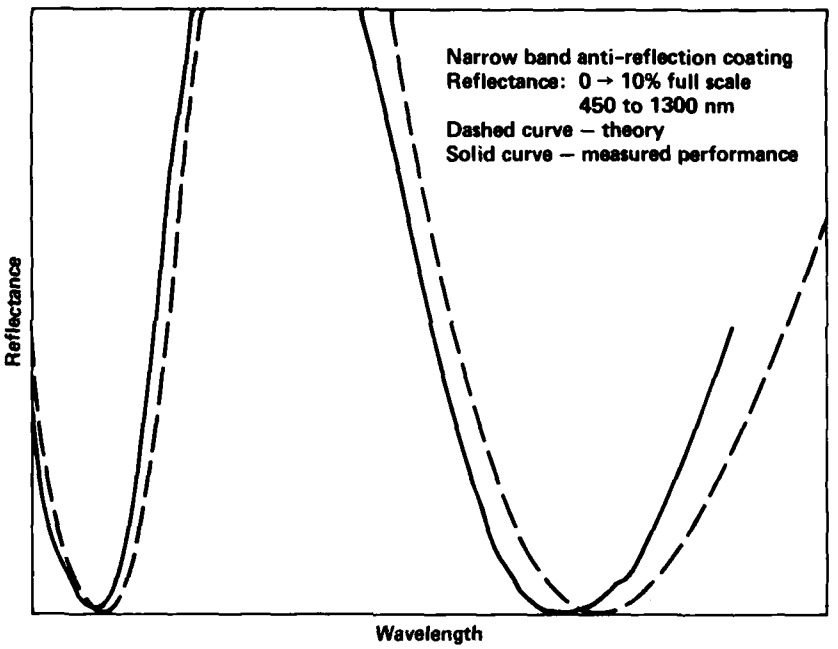

Figure 1

Figure 1. Reflectance of a narrow band anti-reflection coating.

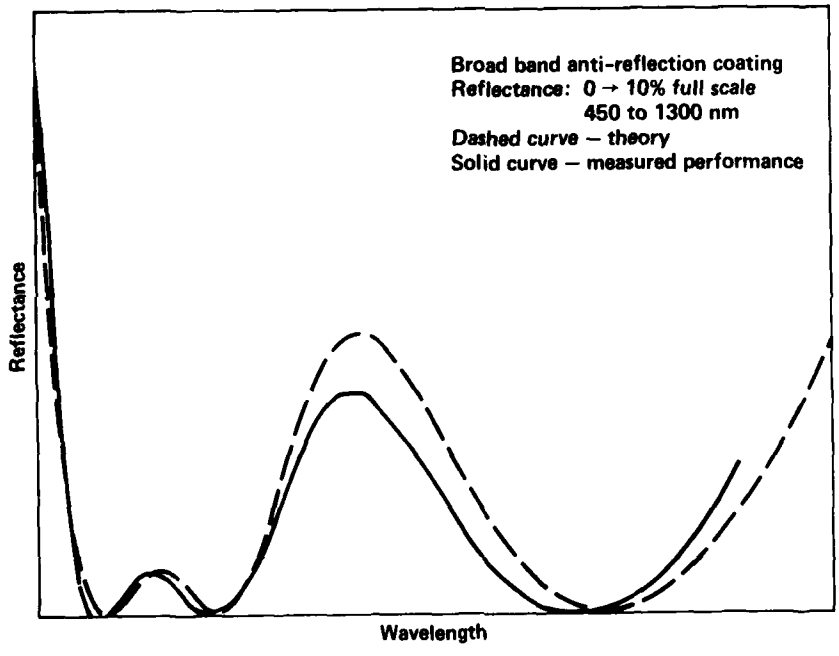

Figure 2

Figure 2. Reflectance of a broad band anti-reflection coating.

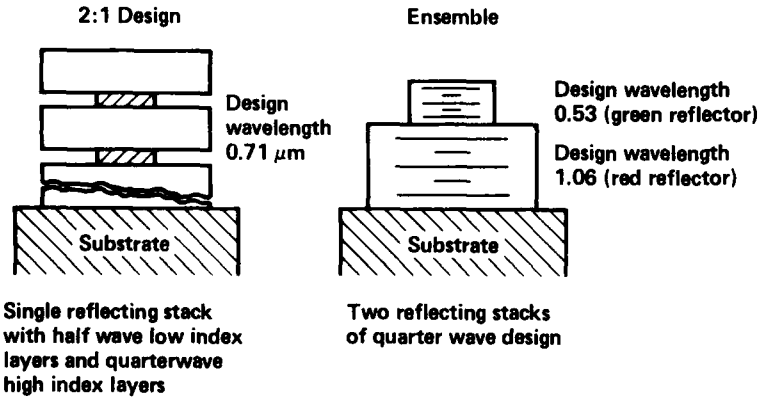

Figure 3. Schematic of evaluate reflector designs.

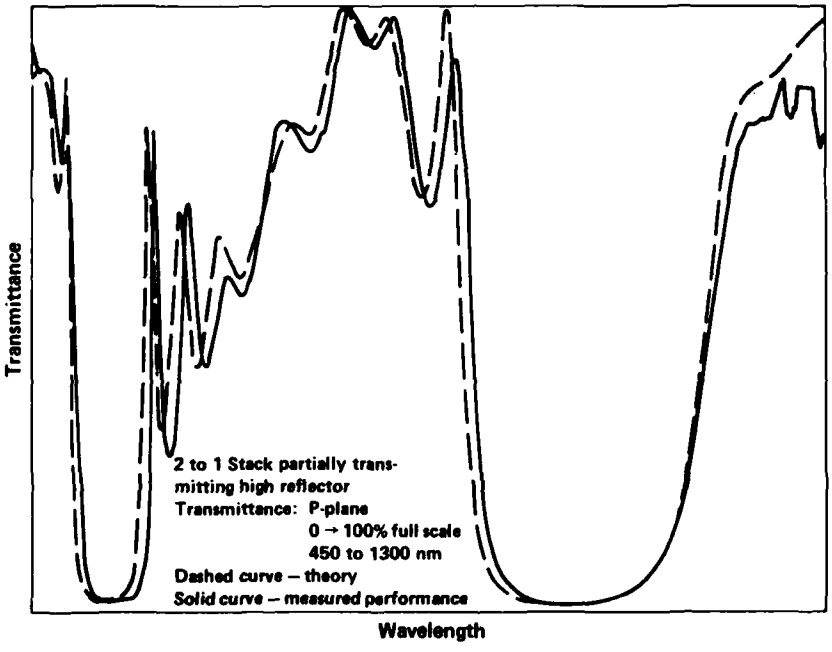

Figure 4

Figure 4. Transmittance of a 2 to 1 stack partially transmitting high reflector.

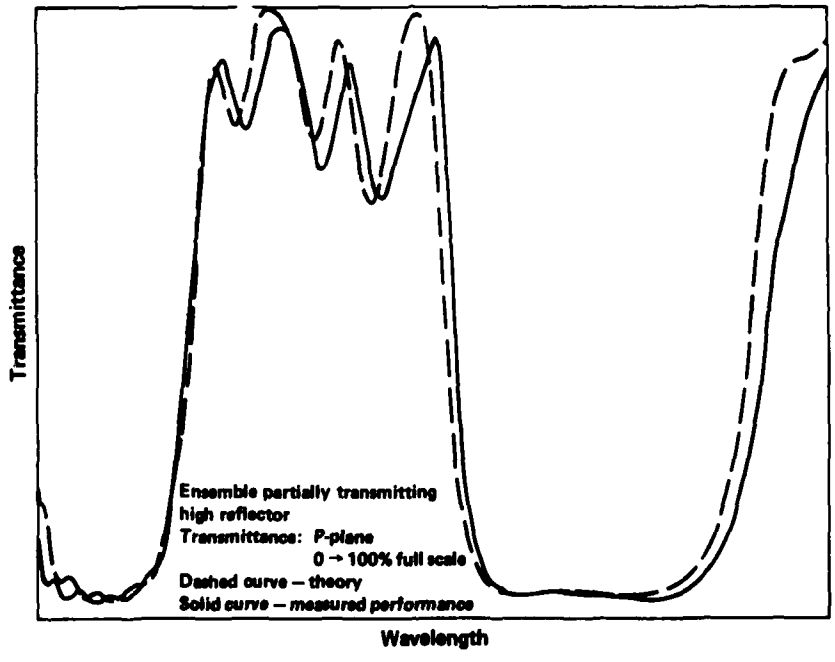

Figure 5

Figure 5. Transmittance of an ensemble partially transmitting high reflector.

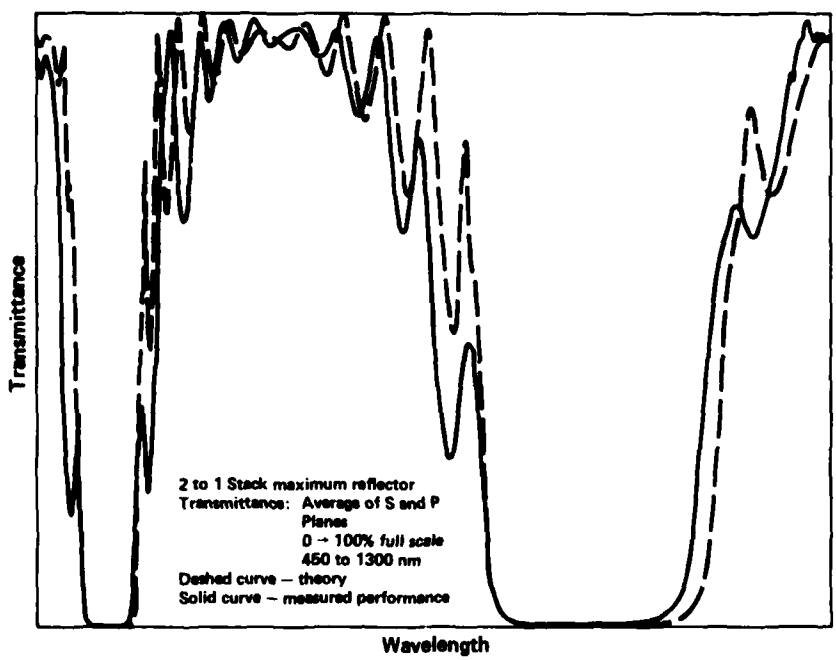

Figure 6

Figure 6. Transmittance of a 2 to 1 stack maximum reflector.

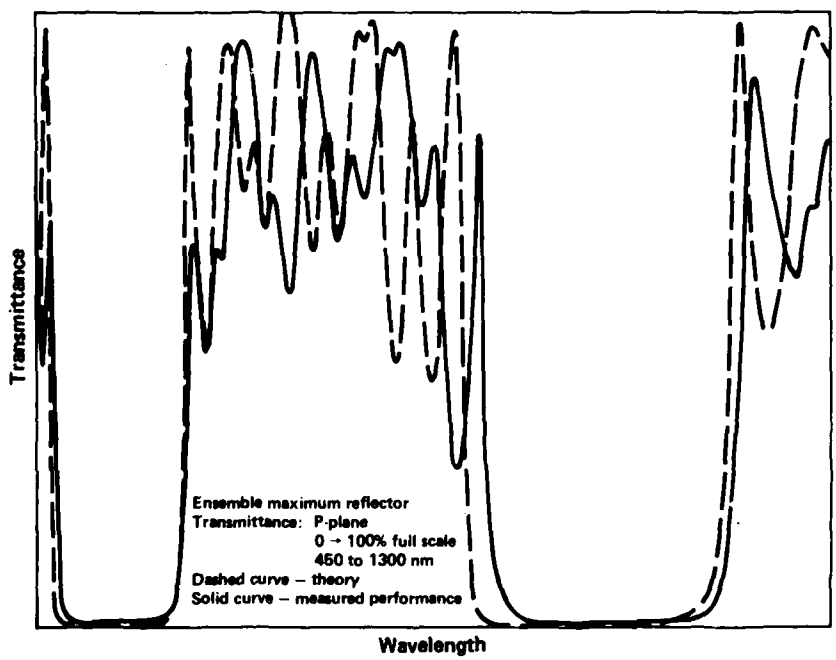

Figure 7

Figure 7. Transmittance of a ensemble maximum reflector.

SURVEY OF DAMAGE THRESHOLDS AT 532 NM FOR PRODUCTION-RUN OPTICAL COMPONENTS*

T. F. Deaton, F. Rainer, D. Milam, and W. L. Smith
University of California
Lawrence Livermore National Laboratory
P. O. Box 808
Livermore, California 94550

We report the results of a survey of 532-nm, 0.7-ns damage thresholds for a variety of optical components. The optics were all samples from current production runs, which included high-reflector and anti-reflector films, beam dumps, leached AR surfaces, and multiwavelength AR and HR films.

The experiment was similar to the usual 1064-nm damage measurement. The green light pulses were produced by frequency-doubling 1-ns pulses from a Nd:glass laser. The 532-nm beam was then focused to a spot size of about 2 mm diameter at the sample. Beam profiles were recorded on a vidicon and on 1-Z photographic plates.

Thresholds for the AR and HR films were typically 2-5 J/cm^2, somehwat lower than might have been expected. Some of the beam dumps damaged at 2 J/cm^2. Bare and graded-index surface thresholds were found to be comparable to 1-ns, 1064-nm thresholds.

Key words: Laser-induced damage, pulsed lasers

1. Introduction

We have measured 532-nm, 0.7-nm damage thresholds for a variety of production-run optical components important in the operation of Nd-glass laser fusion drivers at the second-harmonic wavelength. This initial survey had two principal objectives: A survey of the damage resistance of currently available materials and coatings; and a test at 532-nm of the beam diagnostics techniques used for 1064-nm damage measurements at this Laboratory. The sample set included bare surfaces, anti-reflecting and highly-reflecting films, and other more exotic designs such as multi-wavelength anti-reflecting films and beam dumps.

2. Experimental

The experiment was similar to the 1064-nm damage measurements done at this laboratory over the past several years [1].[1] The Nd:glass laser used for this experiment produced 1064-nm pulses of length 1.0 ns with very high reproducibility. The pulses were frequency-doubled in a potassium dihydrogen phosphate (KDP) crystal (Type I). The second harmonic conversion efficiency was typically less than 0.25, so that the second harmonic beam had a pulse length of approximately 0.7 ns. After the doubler the second harmonic and fundamental beams were spatially separated by a prism, and the fundamental beam interrupted by a beam block. The layout of the green damage experiment is shown in figure 1.

The green light was focused with a BK-7 lens of focal length 3.0 m. The sample was placed approximately 2.2 m behind the lens, so that the spot size at the sample was 2 mm diameter. We recorded the beam profiles by multiple exposure on 1-Z film and on a vidicon. Energy was measured with an LLNL-designed absorbing glass calorimeter. The samples were irradiated once per site at nearly normal incidence, except for those coatings designed for use at 45° incidence.

Damage was detected by laser-induced light emission and by post-examination for increased white light scattering. Except for some of the 6-inch diameter samples, all the samples were also examined by Nomarski microscopy after the experiment.

The peak fluence for each shot was computed from the beam profile and calorimetric data using standard techniques developed for the 1064-nm damage measurements of LLNL. Our experience indicates that the combination of 1-Z film multiple exposure and absorbing glass calorimeter yields peak fluence values accurate to within about ±10 percent. A correlation plot between peak fluences computed from profiles recorded by the vidicon and on film is shown in figure 2. For most shots the computed fluences agreed to within ±10 percent which is completely acceptable given that the second harmonic beam had considerable modulation apparently as a result of interference effects from the KDP doubler.

*Work performed under the auspices of the U. S. Dept. of Energy Office of Basic Energy Sciences and Lawrence Livermore National Laboratory under contract No. W-7405-Eng-48.

[1]Figures in brackets indicate the literature references at the end of this paper.

3. Results and Discussion

Thresholds are shown in table 1. For reference, we note that the long-term average 1064-nm, 150-ps thresholds are 3.9 J/cm^2 for anti-reflecting (AR) films and about 5 J/cm^2 for highly reflecting (HR) films [2]. By comparison, some 532-nm thresholds are lower than we would expect for 0.7-ns pulses. In particular, we find agreement with the results of tests on the Argus laser at LLNL; some beam dumps damaged at about 2 J/cm^2.

Bare surface and graded index thresholds at 532-nm are comparable to 1-ns, 1064-nm thresholds. This result agrees with the small but existing data base [3,4]. The low thresholds of the beam dumps could possibly be attributed to the presence of large internal standing-wave fields [5], but we do not always find correlation between internal fields and thresholds, and that explanation would not account for the low thresholds observed in some other AR and HR films.

4. References

[1] Milam, D., Measurement and Identification of Laser-Damage Thresholds in Thin Films, S.P.I.E. Technical Symposium East, Washington, D. C. (March 28-30, 1978).

[2] Milam, D., Laser-Induced Damage at 1064-nm, 125 psec, Applied Optics 16: 1204 (1977).

[3] Newnam, B.E., and Gill, D. H., Spectral Dependence of Damage Resistance of Refractory Oxide Optical Coatings, NBS Spec. Pub. 292, p. 462 (1976).

[4] Smith, W. L., Bechtel, J. H., and Bloembergen, N., Picosecond Laser-Breakdown at 5321 and 3547 Å: Observation of Frequency-Dependent Behavior, Phys. Rev. B 15:4039 (1977).

[5] Thomas, N., private communication.

Table 1. 532-nm 0.7-ns Damage Data

SAMPLE	DAMAGE THRESHOLD J/cm^2
High-Reflector Films, .532-nm	
CVI	4.9 ± 0.5
CVI (45°)	2.1 ± 0.5
Design Optics	5.4 ± 0.6
Multiwavelength High-Reflector Films (1.06 and .532-nm)	
Spectra-Physics	2.5 ± 0.6
Spectra-Physics (45°)	4.6 ± 0.5
Beam Dumps -	
CVI-BSR 5300-1 (45°) (Ref >99% 532, R <15% 1.06)	7.7 ± 0.8
Spectra-Physics (10°) (Reflect 1.06, transmit .532)	2.2 ± 0.3
Anti-Reflector Films	
LLNL-Window	3.2 ± 0.8
Cryolite (debris shield)	3.3 ± 0.7
Design Optics	1.3 ± 0.4
OCLI AR (both sides)	
Front (1007-179)	6.2 ± 0.7
Rear (1007-177)	3.0 ± 0.5
OCLI AR (1007-179) (rear)	5.4 ± 0.6
OCLI AR (1007-177) (rear)	4.6 ± 1.0
Partially-Reflecting Films	
Spectra-Physics (50%R@ .532 and 1.06)	3.4 ± 0.8
LLNL-Design (50%R@ .532 μm)	3.0 ± 0.6
Bare Polished Glass Surfaces	
Silica (Zygo #403)	17.5 ± 2.0
Silica (Zygo #343)	17.5 ± 3.0
BK-7 (#2039)	23.5 ± 3.5
Leached AR Surfaces	
#1250 O.I.-289 glass	11.8 ± 1.2
#9237 O.I.-289 glass	13.1 ± 1.7

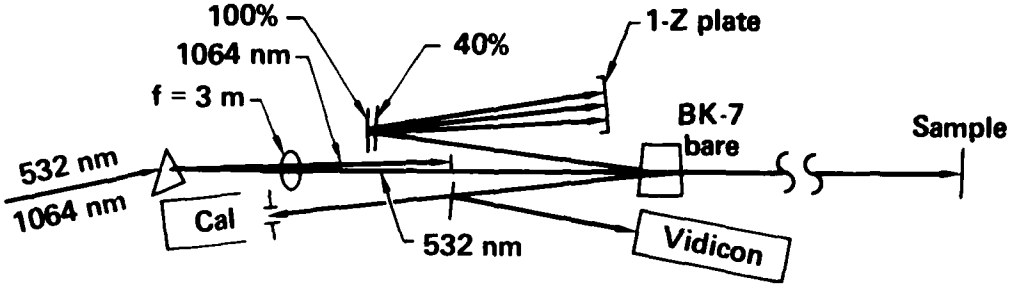

Figure 1. Optical layout for second harmonic damage experiment.

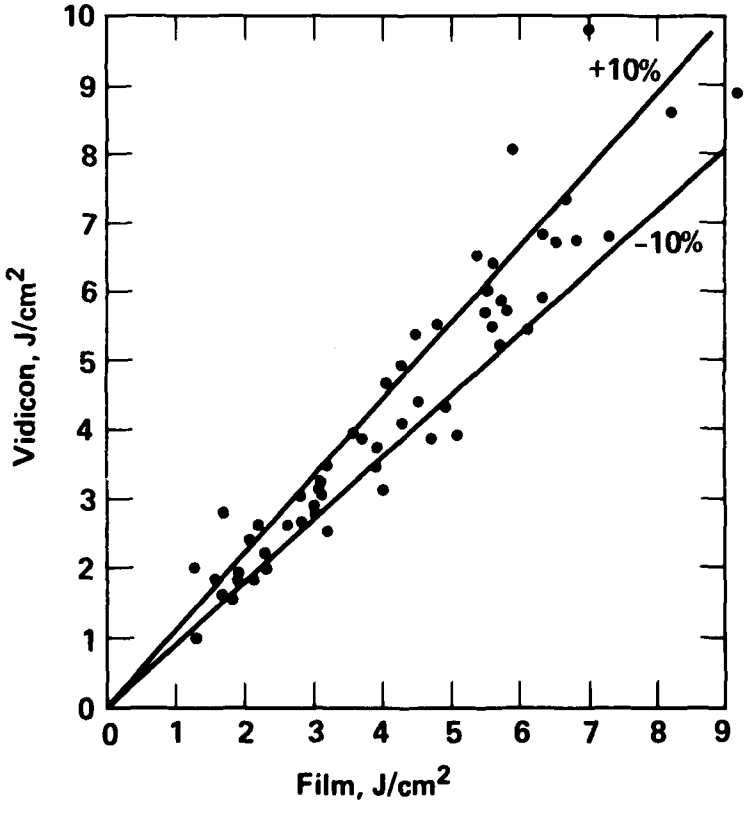

Figure 2. Comparison of peak fluence values from Vidicon and 1-2 film.

LASER-INDUCED DAMAGE IN ANTIREFLECTION COATINGS FOR $LiNbO_3$ CRYSTALS*

M. J. Soileau†
Michelson Laboratory, Physics Division
Naval Weapons Center, China Lake, California 93555

Substrate preparation before coating and coating cleanliness are the dominant factors affecting laser-induced damage to antireflection-coated $LiNbO_3$. Careful control of these factors resulted in an order-of-magnitude improvement in the laser-induced damage threshold.

Key words: Antireflection coatings; coating damage; laser damage; $LiNbO_3$ coatings; surface damage; Q-switch.

Introduction

Antireflection (AR) coatings for $LiNbO_3$ crystals for use with lasers operating at 1.06 μm are among the simplest to design and manufacture. A variety of hard oxide coating materials are available which have refractive indices nearly equal to the square root of the index of $LiNbO_3$. Thus, a single quarter-wave-thick coating can be deposited which will have minimum reflection loss and will meet military specifications for hardness, adhesion, and environmental stability. Despite the advantages of simplicity of design and wide choice of good coating materials, laser-induced damage to AR coatings on $LiNbO_3$ Q-switches limits the useful output power of many laser systems operating at 1.06 μm [1][1]. In this work, the mechanisms for laser-induced damage to AR-coated $LiNbO_3$ at 1.06 μm were studied. The experimental resu'ts indicate that the laser-induced failure limits for these coatings were determined by (a) substrate cleanliness, (b) linear absorption in the coating, and (c) cleanliness of the outer surface of the coating.

Experimental

The experimental setup for the laser-damage testing is shown in figure 1. The laser sources used in this work were an electro-optic Q-switched Nd:YAG laser with a 9-ns pulsewidth (FWHM) and a dye Q-switched Nd:glass laser with pulsewidth variable from 25 to 50 ns (FWHM) [2]. Both lasers were constrained to operate in the TEM_{00} spatial mode. The laser energy was focussed on the entrance surface of the AR-coated crystals. The energy of each pulse was measured with a pyroelectric detector which, in turn, was calibrated with a thermopile calorimeter. The intensity at the specimen was controlled by varying the angle between a pair of Glan polarizers which had been arranged in a polarizer/analyzer configuration. The analyzer remained fixed to ensure that the beam polarization at the specimen was constant for all intensities. The temporal pulse shape was monitored with high-speed photodiodes. The beam was sampled going into the specimen and after transmission through the specimen. A coaxial HeNe laser was used for alignment of the optical system, centering of the focussing lens, and monitoring particulates and other scattering centers in the specimen. Each site was irradiated only once, and the laser-induced damage threshold was taken to be that intensity which produced (with 50% probability) a perceptible change in the coating when viewed with an optical microscope. The focal spot radius was varied by varying the distance of the focussing lens to the laser cavity waist [2]. Unless otherwise stated, all data presented in this paper were taken with a focal spot radius of 41 μm ($1/e^2$ point in the intensity).

The laser-induced damage results were provided to the coating vendor [3], who then varied the coating process parameters in an effort to produce coatings of higher thresholds. The coating material and coating process parameters were considered proprietary by the vendor and were not supplied to the author.

Experimental Results

The laser-induced damage shown in figure 2 is characteristic of the type of damage observed at the beginning of this research effort. The failure threshold for the coating shown in figure 2 was approximately 2 GW/cm^2 (pulsewidth 30 ns, focal spot radius 41 μm). Note that there are many defects under the coating; these defects are absorbing sites and points of coating delamination. The area of coating delamination in the micrograph to the right is much larger than the area of the focussed laser beam. The large area of coating delamination was interpreted as evidence that the coating was highly stressed.

The above results were supplied to the coating vendor [3], and, based on these results, the coating process parameters were modified. The next batch of coatings showed marked improvements. The improved coatings had laser-induced damage thresholds on the order of 4 to 5 GW/cm^2. The damage sites showed some evidence of defects, but no coating delamination was observed. The morphology of the damage sites indicated that the failure mechanism was melting caused by linear absorption in the film.

The linear absorption failure mechanism was also supported by analysis of the temporal shape of the pulse transmitted through the specimen and the pulsewidth dependence of the laser-induced damage threshold (fig. 3). Failure near threshold due to linear absorption should occur at the end of the pulse and thus should not alter the pulse shape of the transmitted beam. As can be seen in figure 3, the pulse shape of the transmitted beam was not perceptibly altered for damage near threshold for the coating labeled "T-coat." Also, figure 3 shows the pulsewidth dependence of the damage threshold of

*Work supported by the Office of Naval Research and Navy Independent Research Funds.
†Present address: Physics Dept., North Texas State University, Denton, TX 76203
[1]Figures in brackets indicate the literature references at the end of this paper.

this coating as compared to the dependence predicted by a thermal failure mode. [4]. Possible reasons for the high linear absorption in this coating are the lack of proper stoichiometry in the coating and/or residual impurities. However, this is highly speculative since the coating vendor did not reveal the coating material or coating process parameters.

Further improvements in the coatings were made as is shown in figure 4. Note that the coating is nearly featureless in the region away from the damage site. The lack of uniformity in the damage crater in this micrograph indicates that damage was still associated with coating defects. However, analysis of the transmitted waveforms shown in figure 5 suggests that the coating failure mechanism in this case is not linear absorption. The laser-induced failure threshold of this specimen varied from 5 to 20 GW/cm^2 as different positions on the specimen were probed. The photo on the left in figure 5 corresponded to a damage event at 5 GW/cm^2. Real time observation of the scattered 0.6328-μm radiation from the coaxial HeNe laser showed that damage occurred at a scattering center initially present in the coating. The sharp peak in the transmitted pulse (shown inverted in the photo in the left of fig. 5) suggested that damage was due to vaporization of a surface particulate. This result, the large variation in threshold with position, and microscopic examination of the scattered HeNe light indicated that particulates on the outer surface were causing the laser-induced failure.

Based on the above results, attempts were made to clean the coating exterior surface. The first attempt at cleaning was to drag a lens tissue (saturated with ethanol or pure acetone) across the surface. This technique had no effect on the laser-induced damage threshold or the visual appearance of the coating. Next, the coating was cleaned by vigorous rubbing with a tissue saturated with ethanol or pure acetone. This technique resulted in a marked decrease in the visible scattering from the surface, and the damage threshold was found to be 15 to 20 GW/cm^2 over the entire surface for the I-coated specimen. The photo on the right in figure 5 corresponds to failure near threshold of the cleaned coating. Failure near threshold in this case occurs at the peak of the pulse, and the transmitted beam is abruptly truncated. This is characteristic of the avalanche breakdown mechanism [5]. Similar attempts were made to clean the T-coat, but no improvement in damage threshold was observed. (This is as expected since there is strong evidence that the T-coat failure mechanism was linear absorption in the coating.)

The coated $LiNbO_3$ surfaces accumulated laboratory dust within a few hours after cleaning and had to be recleaned before each test. A strippable coating [6] was applied to the surface of the I-coated sample after cleaning in an effort to minimize this problem. This coating did protect the cleaned surface from contamination. The protective coating was stripped off after one month, and the specimen was remeasured. The strippable coating had no detectable effect on the laser-damage threshold.

Summary

Figure 6 summarizes the results of these measurements. Initial laser-induced measurements at 1.06 μm indicated that damage to AR-coated $LiNbO_3$ was initiated by defects on the $LiNbO_3$ surface under the thin film. Microscopic examination of the damaged coatings indicated that these surface defects were sources of localized absorption. Surface defects were also found to be points of delamination of coatings with high internal stress. These coatings failed at approximately 2 GW/cm^2. Monitoring of the transmitted waveform showed that damage occurred near the end of the laser pulse. From this we concluded that the mechanism of failure was thermal rather than dielectric breakdown.

Based on the results of the initial damage testing, the coating vendor modified the substrate preparation and coating deposition procedures [3]. These changes produced coatings which failed by linear absorption with an average threshold of approximately 5 GW/cm^2. Further improvements resulted in coatings with damage thresholds of 5 to 20 GW/cm^2. Microscopic inspection showed that damage to the improved coatings was associated with defects on the outer surface of the coating. Attempts to clean the surface by dragging a lens tissue saturated with acetone across the surface failed. We found that vigorous rubbing with saturated tissue did remove the surface particles and increased the damage threshold to 15 to 20 GW/cm^2. Analysis of the waveform of the pulse transmitted through the improved coatings indicated that the failure mechanism was avalanche breakdown.

References

[1] Teppo, E. A., unpublished.

[2] Soileau, M. J., Bass, M., and Klein, P. H., NBS Special Publ. 568, 497 (1979).

[3] Crystal Technology, Inc., 1051 E. Meadow Circle, Palo Alto, Calif. 94303.

[4] Sparks, M., and Loh, Jr., E., J. Opt. Soc. Am. 69, 847 (1979).

[5] Fradin, D. W., Yablonovitch, E., and Bass, M., Appl. Opt. 12, 700 (1973).

[6] The strippable coating used was a liquid polymer called "Carbo-film," purchased by American Drug and Chemical, 9015 Poinsettia, Culver City, Calif. 09230. This material hardens when exposed to air and is easily removed with tape after hardening.

Figures

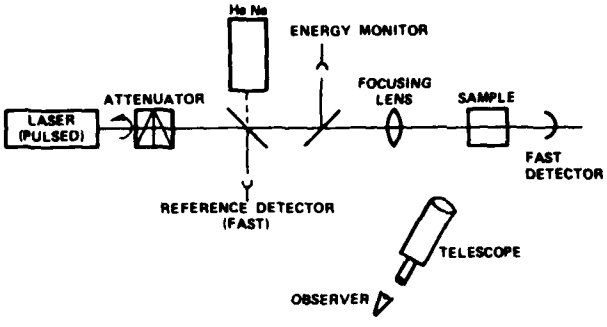

Figure 1. Schematic of laser damage facility. The laser sources were pulse lasers (9 to 50 ns) operating at 1.06 μm. The focussing lens was an aberration-corrected doublet with a 162-mm focal length. The various detectors used to characterize the laser pulse are discussed in the text.

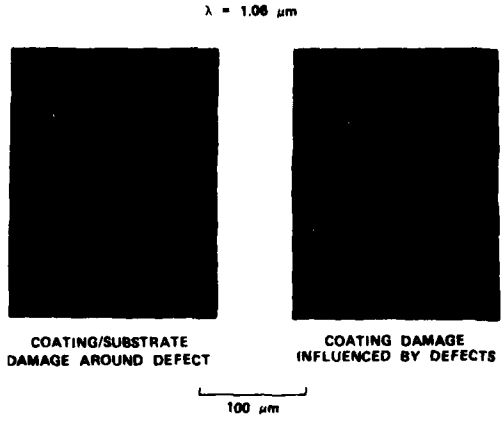

Figure 2. Defect-related coating damage. Note the high density of defects. These defects are sources of local melting (left micrograph) and coating delamination. The total area of coating delamination is much larger than the area irradiated by the laser. The focal spot radius for the two damage sites shown above was 41 μm ($1/e^2$ point of the intensity).

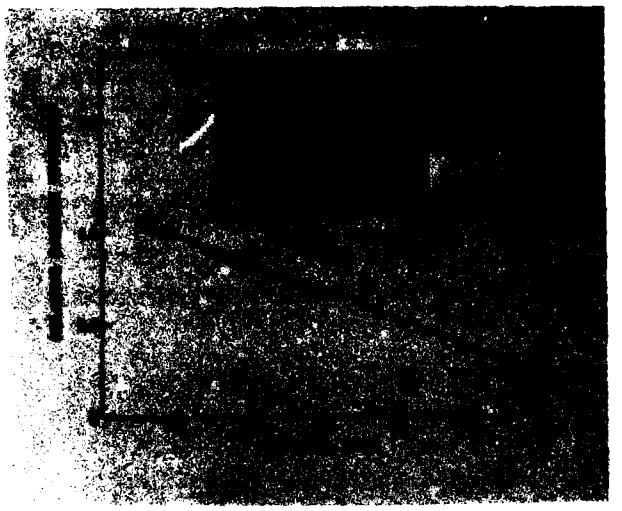

Figure 3. Thermal failure in T-coated $LiNbO_3$. The photo insert is an oscilloscope trace of the input (top trace) and the transmitted pulse through the specimen (bottom trace). No distortion of the transmitted pulse is seen for failure near the laser-damage threshold. The slight difference in pulse shape is due to preamplifier distortion of the reference pulse (top trace). The solid line shown in the above graph is the pulsewidth dependence predicted for laser-induced damage caused by linear absorption.

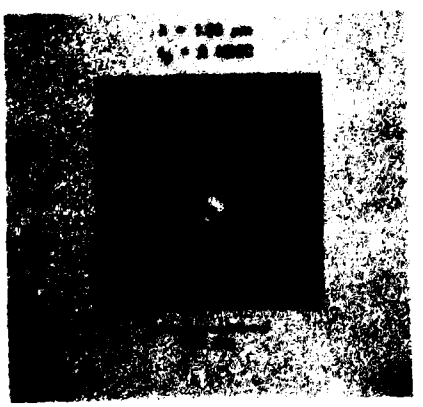

Figure 4. Improved antireflection coating. This micrograph is a damage site on an improved coating (I-coat) on $LiNbO_3$. The damage site shown was produced with a 1.06-μm laser with a 9-ns pulsewidth (FWHM) and a focal spot radius of 26 μm ($1/e^2$ point of the intensity). Note that while the surface is relatively free of scattering centers, evidence of defects is seen at the crater center and along the crater rim.

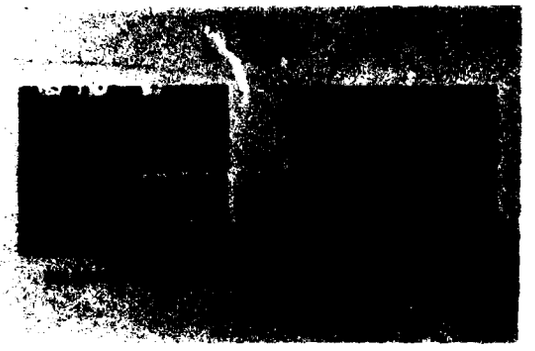

Figure 5. Transmitted waveform distortion for I-coated $LiNbO_3$. The trace on the left (inverted) corresponds to failure at 5 GW/cm^2 and was observed to occur at a scattering center initially present on the coating surface. The sharp spike in the inverted trace to the left is due to the visible flash which resulted from the vaporization of the surface defect. The photo to the right is characteristic of failure near the laser-damage threshold after the coating had been cleaned. This type of failure is characteristic of avalanche breakdown.

Figure 6. Summary of laser-induced damage to antireflection-coated $LiNbO_3$ surfaces. Threshold values given are peak power densities for which damage occurred with 50 percent probability. The top bar is typical laser damage caused by defects on the $LiNbO_3$ surface. The middle bar is characteristic of improved coatings which failed by linear absorption. The bottom bar is representative of the best coating measured. The high value of 20 GW/cm^2 was measured after vigorous cleaning of the coating with lens tissue saturated with either pure acetone or ethanol. The above thresholds were for laser wavelength equal to 1.06 μm and pulsewidths of approximately 30 ns. The focal spot radius was 41 μm for the top two bars and 26 μm for the bottom. The maximum intensity available for the 41-μm focal radius was 10 GW/cm^2 and would not damage the improved coatings when properly cleaned. The focal spot radius was reduced to 26 μm, and the damage threshold was determined to be 15 to 20 GW/cm^2 for the I-coated specimens.

MULTITHRESHOLD HF/DF PULSED LASER DAMAGE MEASUREMENTS ON EVAPORATED AND SPUTTERED SILICON FILMS*

T. M. Donovan, J. O. Porteus, and S. C. Seitel
Michelson Laboratory, Physics Division
Naval Weapons Center, China Lake, California 93555

and

Paul Kraatz
Northrop Research and Technology Center
Palos Verdes Peninsula, California 90274

Previously, we reported a comparison of damage resistance of various coating materials deposited by vacuum evaporation and measured at 2.7 and 3.8 μm. It was found that Si films fail by a thermal process and, in agreement with other studies, that high-index materials, such as Si, tend to have lower thresholds than low-index dielectric materials, such as NaF, Al_2O_3, and SiO_x, which by comparison are relatively outstanding performers. In this paper, we report results of tests which show that the thresholds of magnetron-deposited sputtered Si films are enhanced over those deposited by vacuum evaporation. The sputtering process leads to lower hydrogen impurity content (100 ppm vs 200 ppm), lower absorption (20 cm^{-1} vs 40 cm^{-1}), and a factor of two or more enhancement in damage threshold over vacuum-evaporated Si films. Further improvement may be possible by optimization of the sputter-deposition parameters.

Key words: Absorption; evaporation; hydrogen and oxygen impurity; magnetron sputtering; pulsed HF/DF laser damage thresholds; silicon films.

Introduction

Silicon is an important coating material for chemical laser applications. Its high index of refraction is a design advantage whereby broadband-enhanced reflectance mirrors can be fabricated with a minimal number of high/low index optical pairs, and its chemical stability and hardness are advantages when the application involves adverse or hostile environments, including the chemical environment of the HF/DF laser cavity.

Evaporated Si films are generally amorphous and known to contain defects (dangling bonds) which occur either at points or on the surfaces of voids [1][1]. The resulting porosity allows H_2O to penetrate the matrix, and this contamination, along with the defects, can account for anomalously high absorption [2] and low HF laser damage thresholds [3] reported for evaporated films.

Sputtering and reactive sputtering are practical low-temperature techniques for depositing Si films, but the methods have not been investigated for purely optical applications, partly because of problems with thickness uniformity. Because of other advantages such as the convenient formation of multilayer structures by the periodic addition of oxygen to the sputter gas to form, e.g., $(Si/SiO_x)^n$, and the possibilities of in situ cleaning and annealing by ion beams, we have initiated a study of the properties of sputtered Si films.

Preliminary results show that for comparable conditions of source material, base pressure, and substrate temperature, sputtered films have lower H_2O contamination levels, lower HF (2.8 μm) absorption, and higher pulsed HF/DF damage thresholds than films deposited by vacuum evaporation. The improvement possibly relates to the lower source temperature (less outgassing) and the more energetic source atoms which are characteristic of the sputtering process. Further reductions in absorption and increases in damage threshold may be possible by optimization of the sputter parameters.

Experimental

The films described here were deposited by either e-beam evaporation in a baked, cryo-pumped, ultrahigh vacuum (UHV) system or by dc sputtering using a magnetron source (Varian s-gun) in a baked turbomolecular pumped UHV system. The deposition conditions are compared in table 1. As can be seen in this comparison, the base pressure, deposition rates, substrate temperatures, and Si source material were similar for the two techniques. Film morphology was determined by high resolution transmission electron microscopy (TEM) on thin (300 Å) witness samples deposited on NaCl substrates. The amorphous film structure was verified by transmission electron diffraction (TED). Scanning electron microscopy (SEM) was used to examine cross sections of 2-μm-thick films deposited on fused quartz.

The H concentration and spatial distribution in the films were measured by resonant nuclear reaction analysis (RNRA) [5], used previously to determine parts-per-million quantities of H in optical coatings [6]. The H and O concentration relative to the concentration of these elements in the 6N Si starting material was determined by secondary ion mass spectroscopy (SIMS)[2].

Finally, the absorption at HF (and DF) wavelengths was determined by laser calorimetry, and the HF/DF pulsed damage thresholds were determined by multithreshold analysis [3].

*Work supported by the Defense Advanced Research Projects Agency and Navy Independent Research Funds.
[1]Figures in brackets indicate the literature references at the end of this paper.
[2]SIMS measurements were made by Charles Evans and Associates, San Mateo, Calif.

Table 1. Deposition parameters of evaporated and sputtered Si films.

Deposition method	Source material	Deposition rate	Base pressure	Deposition pressure	Substrate temperature	Power
e-Beam evaporation	6N Si Specialty Metals	1-5 Å/sec	$1x10^{-9}$ torr	$3x10^{-7}$ torr	200°C	------
dc Magnetron sputtering	6N Si Specialty Metals	5 Å/sec	$2x10^{-9}$ torr	$3x10^{-3}$ torr Ar sputter gas	220°C	0.7 KW

Results

A transmission electron micrograph from a 300 Å witness sample deposited by magnetron sputtering in a reactive gas mixture (Ar + 10% H_2) is shown in figure 1. Shown as an inset to figure 1 is a TED pattern. The TED pattern reveals the amorphous structure of the film. The TEM pattern clearly shows inhomogeneities in the form of a network of low density regions surrounding islands of higher density material. This type of structure with variations of island size and relative width of low density regions is also observed with evaporated films and is believed to result from the nucleation and growth of individual islands which fail to coalesce completely when the growing islands impinge during growth of the film. SEM patterns on 2-μm-thick samples that have been fractured and viewed on-end reveal a columnar structure which probably has its origin in the island morphology for thin films (300 (300 Å) shown in figure 1.

With evaporated Ge, more homogeneous morphologies have been obtained by high substrate temperatures [7]. Preliminary work with these sputtered films suggests that the application of a negative bias to the substrate during deposition (causing bombardment of the growing film with Ar ions) is effective in producing a more homogeneous structure than seen in figure 1.

Hydrogen and Oxygen Concentration and Spatial Distribution

Hydrogen concentration and spatial distribution in both sputtered and evaporated Si were measured using RNRA [5]. Hydrogen and oxygen profiles relative to the Si starting material were determined by SIMS analysis. Resonant nuclear reaction analysis of a magnetron Si film deposited on a Mo substrate is shown in figure 2. ^{19}F ions interact at a resonant energy of 16.4 MeV with H nuclei to form ^{16}O and ^{4}He ($^{1}H(^{19}F,\alpha\gamma)^{16}O$), emitting a gamma ray which is detected as a measure of H concentration. By incrementally increasing the ^{19}F energy and allowing the resonant energy to occur deeper in the film because of energy losses, a profile of the H concentration with depth is obtained. The incident ^{19}F energy is plotted in figure 2 along the upper horizontal axis, and the derived depth into the film is plotted on the lower axis. It is of interest to note that the derived thickness inferred from the stopping power of crystal Si is within experimental error (±10%) of the measured film thickness, indicating the film is within 10% of the bulk Si density.

While the average H content is below 100 ppm, there are buildups of H on the surface (0.009 H/Si) and particularly at the film-substrate interface (0.018). The SIMS-derived profile of the film is shown in figure 3. The H profiles for the two techniques are qualitatively similar including the large film-interface component. The SIMS oxygen profiles are similar except for excess O at the surface of the film which probably relates to surface oxidation. The otherwise similar distribution of O and H suggests H_2O contamination in the film with a large concentration at the film-substrate interface.

Shown in figure 4 is a RNRA profile of an evaporated Si film deposited on a quartz substrate. The surface and interface regions show large contamination levels (0.01 and 0.016, respectively) similar to the magnetron-deposited film; however, the film-substrate interface region is broader, and the average H content is higher (200 ppm). The H and O profile as determined by SIMS analysis is shown in figure 5. The data at the substrate-film interface, in this case, were badly distorted by "charging" when the sputter-etch beam penetrated to the quartz substrate material. It is clear, however, that there is about twice the H and somewhat higher O levels as is found in the magnetron-deposited films, and the interface regions are broader.

If we assume the H concentration is a measure of the OH^- content of the films, then the absorption of the HF laser wavelength (2.7 - 2.9 μm) would be twice as high in the evaporated films due to increased OH^- absorption. This was observed by measurement of the 2.8-μm absorption by HF laser calorimetry which is summarized in table 2. The spectral absorption derived from transmission measurements of both evaporated and sputtered films is shown in figure 6. The trend of these measurements also suggests a lower 2.8-μm absorption in the sputtered films. The absorption at the DF wavelengths (3.8 μm) was 10 cm^{-1} or less for sputtered films, verifying the downward trend of the spectral data.

Multithreshold Pulsed HF/DF Laser Damage

Multithreshold damage measurements were made on both evaporated and sputtered films. The details of the measurement and analysis and results for several coating materials, including evaporated Si, are given elsewhere [3]; only a brief description is given here. The samples were irradiated in a regular array of 50 spots with a distribution of damaging and nondamaging pulse energies. Light emission is noted by direct observation with a low-power microscope. A diagnosis of failure processes is then made by microscopic examination using a Nomarski microscope. Failures in these coatings generally occurred by thermal processes (melting, flow, erosion, or perforation) rather than by thermomechanical processes such as delamination or cracking.

Table 2. Absorption of evaporated and sputtered silicon films.

Deposition method	HF $\beta(cm^{-1})$	DF $\beta(cm^{-1})$
Evaporated	50[a]	----
Evaporated	39.8±4	----
Magnetron sputtered	18±2.8	7.4±2.5
rf Diode[b] sputtered	17.5	----

[a] From reference [2].

[b] This film was deposited during the course of this investigation in a commercial (Randex) rf diode sputtering system.

The results at HF and DF wavelengths for a typical evaporated film are shown in figures 7(a) and (b), respectively. As mentioned above, the film failed by melting with the melt (or flow) threshold at DF about twice the HF melt threshold, which probably relates to lower absorption at DF. The magnitude of both thresholds is in agreement with earlier measurements [3].

The results for a typical magnetron-sputtered film are shown in figures 8(a) and (b). The primary damage process is also thermal, as observed for evaporated films, with the melt or flow threshold occurring at about twice the evaporated film threshold at HF. The DF threshold shows even further improvement, emphasizing what we interpret as the adverse effect of H_2O contamination and absorption at 2.8 μm.

Conclusion

Both evaporated and sputtered Si films fail or are damaged by thermal processes (melt, flow, erosion, and perforation) when irradiated with sufficient pulsed HF/DF laser energy. The thresholds for damage are higher in the sputtered films than in evaporated films. Further, the thresholds for both deposition methods are higher at DF than HF wavelengths. The higher HF threshold in the sputtered films we interpret as due to lower OH^- absorption in these films. The higher DF thresholds follow because the DF absorption is half the HF absorption. The OH^- contamination levels with both methods of deposition we attribute to the porous character of the films which, in both cases, is accentuated at the film-substrate interface.

Further improvement in film properties will require higher density, more homogeneous films. In situ substrate cleaning by ion milling, higher substrate temperatures during film deposition, and/or ion annealing to increase the thermal energy and surface mobility of the growing Si atoms are possible methods for achieving the desired improvements in film structure.

References

[1] Brodsky, M. H., et al., Phys. Rev. B16, 3556 (1977).

[2] Holmes, S. J., Multilayer Enhanced Reflectors for the HF Laser Wavelength Region, Final Technical Report on Contracts N60530-79-C-0261 (1980) and N00123-78-C-0629 (1979) China Lake, Calif.

[3] Porteus, J. O., Donovan, T. M., Jernigan, J. L., and Faith, W. N., Multithreshold evaluation of 100-nsec pulsed laser damage to coating materials at 2.7 and 3.8 μm wavelengths, NBS Special Publ. 541, 202 (1978).

[4] Moustakas, T. D., et al., Solid State Commun. 23, 155 (1977).

[5] Leich, D. A., and Tombrello, T. A., A technique for measuring hydrogen concentration versus depth in solid samples, Nucl. Instrum. Methods 108, 67 (1973).

[6] Donovan, T. M., Temple, P. A., Wu, Shiu-Chin, and Tombrello, T. A., The relative importance of interface and volume absorption by water in evaporated films, NBS Special Publ. 568, 237 (1979).

[7] Donovan, T. M., and Heinemann, K., Phys. Rev. Lett. 27, 1794 (1971).

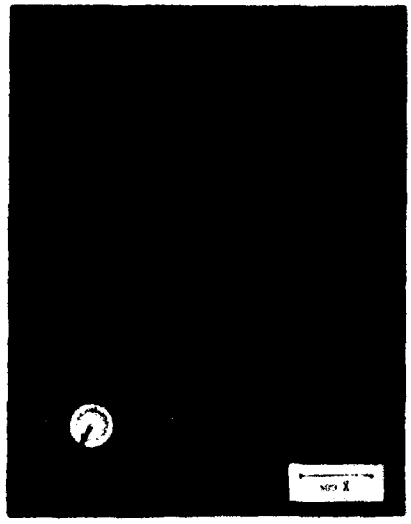

Figure 1. Transmission electron micrograph and transmission electron diffraction pattern of an amorphous Si film deposited by dc magnetron sputtering in an Ar + 10% H_2 reactive gas mixture.

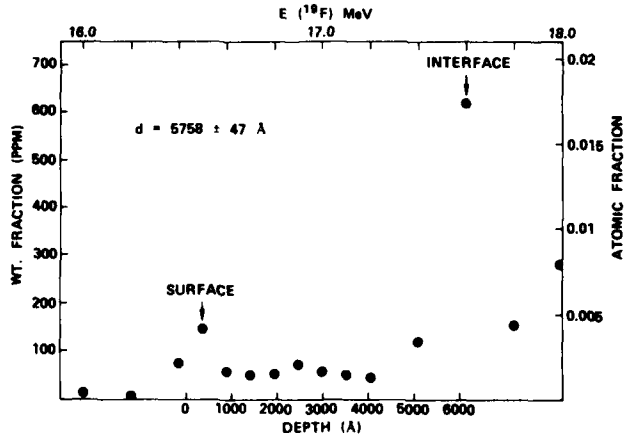

Figure 2. Resonant nuclear reaction analysis profile of H in an amorphous Si film deposited by dc magnetron sputtering in Ar (analysis performed by Wu and Tombrello, CalTech).

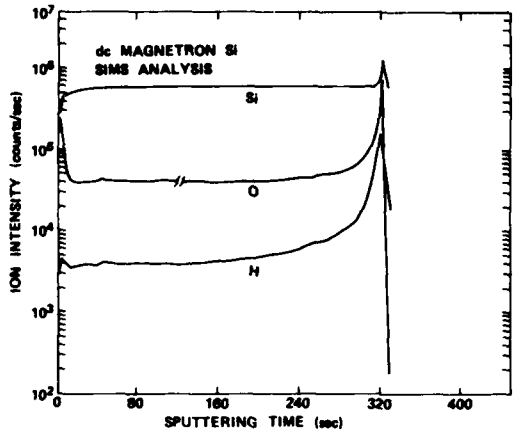

Figure 3. Secondary ion mass spectroscopy analysis of H and O in magnetron-deposited amorphous SiH (analysis performed by Charles Evans and Assoc.).

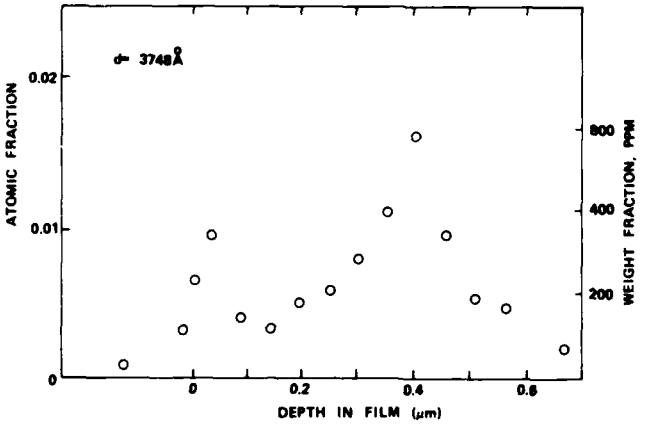

Figure 4. Resonant nuclear reaction analysis profile of H in an amorphous Si film deposited by e-beam evaporation (Wu and Tombrello).

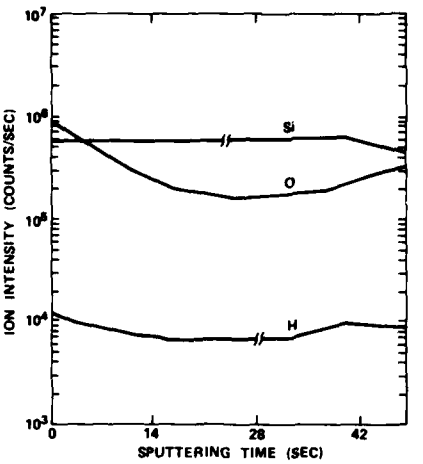

Figure 5. Secondary ion mass spectroscopy profile of H and O in an amorphous Si film deposited by e-beam evaporation (Charles Evans and Assoc.).

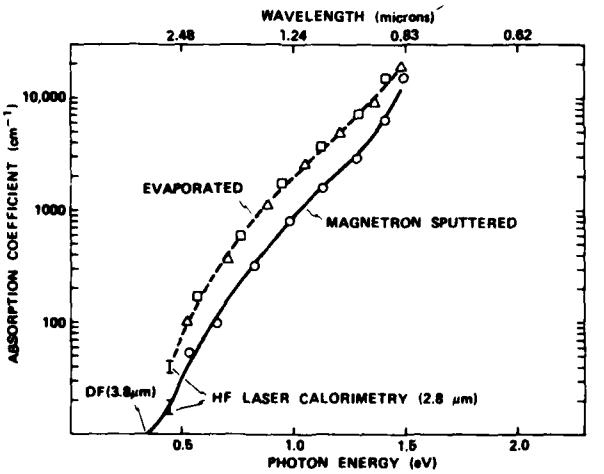

Figure 6. Absorption coefficients determined from transmission measurements on evaporated and sputtered films. Points at 0.44 eV (2.8 μm) and 0.33 eV (3.8 μm) were made by laser calorimetry.

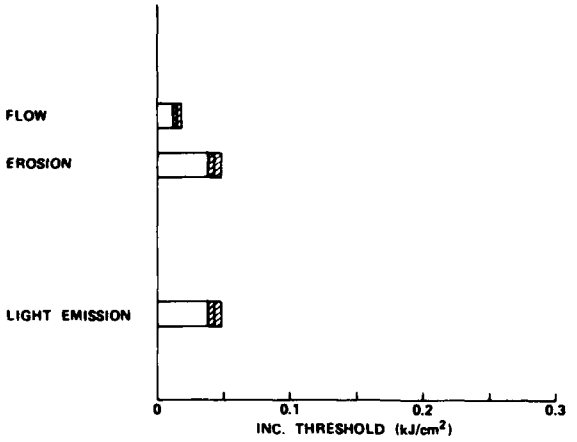

(a)

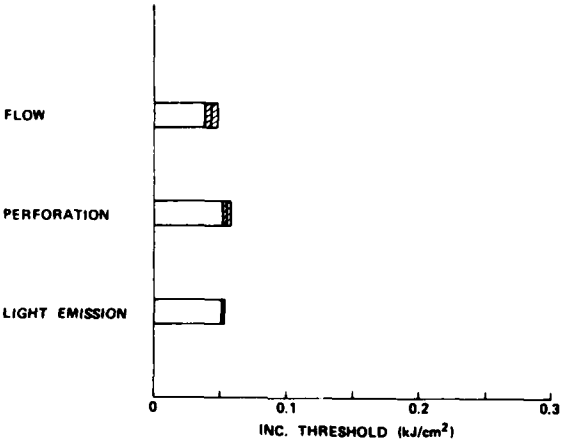

(b)

Figure 7. (a) HF and (b) DF pulsed laser damage profiles of an amorphous Si film deposited by e-beam evaporation.

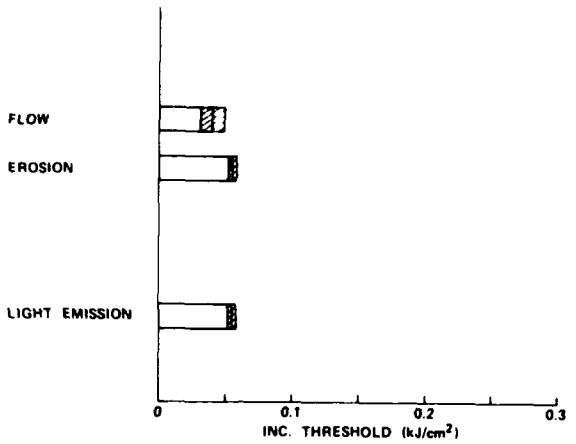

(a)

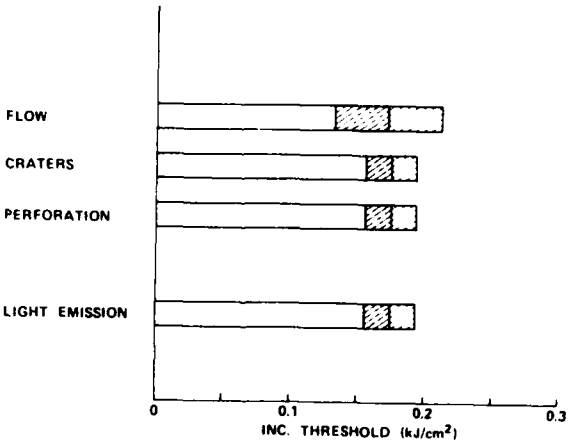

(b)

Figure 8. (a) HF and (b) DF pulsed laser damage profiles of an amorphous Si film deposited by dc magnetron sputtering.

THE USE OF ION-BEAM DEPOSITED DIAMOND-LIKE CARBON FOR IMPROVED OPTICAL ELEMENTS FOR HIGH POWERED LASERS

S. Aisenberg and M. Stein
Applied Science Laboratories
335 Bear Hill Road
Waltham, Massachusetts 02154

The use of thin films of ion-beam deposited diamond-like carbon (DLC) appears to provide a number of properties that could result in improved optical elements (windows, mirrors) for high powered lasers. Many of these properties have already been described.

Of particular importance for high powered lasers is the ultra-smooth nature of the ion-beam deposited DLC plus its transparency, chemical inertness, and barrier properties. Several mechanisms predict and explain why DLC films are observed to be smoother than the substrate, and can result in improved transmission and reflection coefficients. The problem of high power surface breakdown associated with microscopic irregularities in the substrate can be reduced as a result of the ion-beam deposition energy and the smoothing effects of a film of ion-beam diamond-like carbon. The relationship of DLC to high power breakdown at surface defects, as well as plasma breakdown will be discussed to show how the ion-beam diamond-like carbon coating can improve performance.

Key Words: Diamond-like carbon, thin films, ion beam deposition, surface smoothness, barrier properties.

1. Introduction

We have developed and have been studying for some time a novel ion beam deposition process that can be used to deposit films of material in unusual forms. Of particular interest are the diamond-like carbon films which are deposited by this ion beam deposition process. It appears that many of the resulting properties may help meet the objectives of increasing high power capability of laser mirrors and windows. This paper will describe the basic ion beam deposition process, the physics of this unique process, and some of the resulting properties that have been observed while looking at other applications of this material. Of particular importance will be the optical properties, the adhesion, and the surface smoothness. Other properties will relate to the electrical, dielectric, and barrier properties. We also suggest that the physics of the deposition process may result in unusually smooth films. The physics related to the smoothness will be discussed in a later section.

2. Ion Beam Deposition Process

The ion beam deposition process basically consists of ionizing carbon atoms and then accelerating these carbon atoms to a substrate operated at an appropriate bias potential. As a result of the charge on the carbon ions and of the substrate bias, the carbon atoms are deposited on the surface with a kinetic energy far in excess of the energy normally obtained by thermal evaporation, or by sputter deposition or by liquid phase growth.

As a result of the unusually high energy it is expected that materials with unusual physical properties can result.

The basic experimental set-up used for the deposition of carbon ions is shown in Figure 1. The system consists of a carbon ion source chamber operated as a glow or Penning type discharge where carbon is introduced by sputtering from the carbon electrodes. A gas such as Argon is introduced into the discharge chamber which is operated at a pressure of about 20 microns. An axial magnetic field is used to extend the path length of the electrons. As a result of this magnetic field the collision of the electrons with the electrodes is delayed and the probability of ionization is increased so that the discharge can operate at a lower gas pressure. Argon ions bombard the carbon cathode and sputter carbon atoms into the plasma where some of them are subsequently ionized. The carbon ions, along with Argon ions are extracted through a differentially pumped aperture along the axial magnetic field and are directed towards a substrate, placed in a lower pressure chamber on the other side of the differential pumping aperture.

In order to minimize contamination from other materials, the anode, cathode and extractor aperture are all machined from very high purity carbon.

In another mode of operation where faster deposition is desired, a few percent of hydrocarbon gas is added to the Argon gas to provide another source of carbon atoms in addition to the carbon sputtered from the carbon electrodes. This process gives rise to the inclusion of hydrogen ions in the plasma extracted into the ion deposition chamber.

The deposition chamber is operated at a pressure of about 10^{-4} to 10^{-5} torr as a result of a high speed oil diffusion pump. This oil diffusion pump is backed by a mechanical fore pump. A low temperature freon trap is used to help reduce deposition chamber contamination and pressure.

For the diamond-like carbon films, a substrate potential of about -40 to -100 electron volts is found to be of particular interest. The substrate is operated at a negative potential of about 300 electron volts in the early stages of deposition in order to produce ion beam cleaning of the substrate. The ion beam cleaning is permitted long enough so that about 10 monolayers or so of substrate material is sputtered off. This gives rise to a substrate whose surface cleanliness is greater than normally obtained in a vacuum in this range. If the substrate, however, has significant contamination, then this sputter cleaning will not be sufficient to remove the contamination. The preliminary sputter cleaning is primarily designed to remove monolayers of contamination and monolayers of background gas.

When the substrate potential is dropped to about -40 to -100 electron volts, then it is found that there is a net deposition of the carbon. Apparently, the removal of carbon from the surface by sputtering at these potentials is less than the rate of arrival of carbon atoms on the surface so that there is a net build-up of carbon. The measured deposition rates are about 3 to 10 angstroms per second, which are sufficiently fast for most applications.

As a result of the sputtering of the surface simultaneously with the deposition of the diamond-like carbon, the effect of background gases in the deposition chamber is reduced since it is expected that the surface concentration of impurity gas atoms will be less than would be expected for the case of equilibrium.

A number of techniques have been devised for applying potentials to the substrate even though the substrate is of an insulating material. These techniques are also used for conducting metallic substrates since the build up of diamond-like carbon on the surface will result in an insulating layer which would normally make it difficult to apply a surface potential. Additional details on the ion-beam deposition technique and extensions of the technique have already been published in a number of publications and patents.[1-4]

3. Physics of Unique Deposition Process

The physical processes involved in the deposition of ion beam deposited carbon are responsible for some of the unique properties that have been observed. The energy and momentum delivered to the surface by the ions result in an increased mobility of the surface atoms which permits them to move around and nucleate into crystallographic orientations which are not normally encountered by other deposition techniques.

In general, the ions are incident on the surface with an energy of about 40 to 100 electron volts and by a series of collisions share the energy among the other carbon atoms on the surface. The energy and momentum transmitted to gas atoms on the surface probably result in a significant removal of gas monolayers since these are not tightly bound. Carbon atoms which are not in a tight lattice position will also have a tendency to be sputtered or removed from the surface. Thus, there is a preferential "distillation" resulting in a refinement of the properties of carbon atoms remaining on the surface.

Not only does the incident ion striking the surface remain relatively mobile, even after it is neutralized and becomes an energetic atom, but the scattering atoms on the surface that absorb some of this momentum and energy in turn become mobile. In other words the daughter products of the collision cascade in turn become mobile so that each incident ion can result in as many as 100 energetic secondary atoms on the surface. In general, a surface atom with an energy of 1 eV has an equivalent kinetic energy of about 11606° Kelvin. This equivalent temperature should result in a significant increase in surface mobility even though it may last for a relatively short time. The mean free path of a "hot" surface atom may be larger than first anticipated. In addition, we suspect that the surface charge brought to the surface gives rise to additional effects which help to significantly enhance the smoothness of the resulting film. This effect is so important that we will discuss it in more detail in a later section.

4. Optical Properties

As a result of the high atom energy associated with the ion beam deposition process we anticipated that materials with unique properties would be produced. In particular, the high energy of the surface carbon atoms, and their resulting mobility is an analog to the mobility associated with carbon crystallizing into a diamond form. For this reason a prediction was made that carbon in an insulating transparent form would be produced by this process and this was observed and documented in our earlier work.[1] Our observations of film properties were confirmed through subsequent work of other researchers a number of years later[5], who utilized our basic technique and performed independent measurements of the properties.

Of particular importance here, are the optical properties. diamond-like carbon is essentially an insulator or semiconductor and the absence of free electrons results in a transparent film as well as a film of high electrical resistivity. Both of these results were observed in films produced by us and by others. The film is transparent enough so that one can see pronounced interference fringes. When the film is thick enough this indicates an absence of significant loss in the film.

Even more important, we were able to make optical transmission measurements in the infrared range for films deposited on silicon substrates. The results are shown in Figure 2, where the transmission is shown for the range from 2.5 microns to 50 microns, for diamond-like carbon on silicon substrates about 4 millimeters thick. The curve shows the transmission on the blank silicon substrate and the transmission on a substrate coated with diamond-like carbon. Note that the additional loss in the range from 7 to 50 microns is essentially very small. Note also that the transmission for the coated silicon is different from the silicon blank in the shorter wave length range. The data, however, show that the transmission is higher for silicon blanks coated with the diamond-like carbon. We attribute this to the fact that the index of refraction of the diamond-like carbon is intermediate between that of silicon and air and therefore performs matching functions and reduces the transmission lost due to interface reflection. In any event, the absorption of the film appears to be relatively small. This property should be studied in more detail.

5. Adhesion

One critical property associated with thin films is the demonstration of useful adhesion to the substrate. We have found that the diamond-like carbon film has a very strong adhesion to many substrates. In particular, the adhesion to silicon is very good because of the silicon carbide bond. The adhesion to aluminum substrates is also quite impressive.

We have deposited this diamond-like carbon on a wide range of substrate materials including paper, plastics, rock salt, silicon, germanium, as well as various metals. The substrate temperature rise is quite low and is in the order of 10°C depending on the deposition rate. We have been able to deposit film on all substrates considered. The only limitation so far is that the substrate should be compatible with operation in a vacuum chamber.

The adhesion is measured by a perpendicular pull post technique, illustrated in Figure 3. A load cell is placed between an air piston and the pull post connected by a chain to the load cell yoke. The chain is utilized to help insure a perpendicular pull. The pressure in the air piston is linearly increased and a recorder shows the increase in the output from the load cell as a function of pressure. The breaking point is readily determined. We have measured adhesive forces of 5000/psi on silicon substrates. The measurement is largely determined by the strength of the adhesive used to attach the pull post to the film. In about half of the cases, the film is observed to come off the substrate and adhere to the adhesive, while in the remaining cases the film is observed to separate from the adhesive and remain on the substrate. The adhesive strength for material with lower bulk strength, of course, is found to be lower.

6. Additional Observed Properties

The properties that have been observed by us[1] and reported by others[5] can be summarized in the following:

1. Optically transparent - Water clear or pale yellow. Low IR absorption in thin film form (0.3 to 10μ).
2. Insulating - 10^{11} to 10^{12} ohm-cm AC and DC resistivities. May be less insulating at faster deposition rates.
3. Good adhesion to substrate - Pull test measurements on metal substrates showed up to 5,000/psi adhesion.
4. Can be deposited on various substrates.
5. Chemically inert to all known solvents - These include HF, HNO_3, HCOOCH, bases acetone, trichloroethane, chloroform, and ethyl acetate.
6. Film is unusually smooth - Scanning electron microscope shows film is smoother than substrate.
7. Apparent reduction in surface optical losses - Reports indicate that the film increases both transmission and reflection at the substrate surface.
8. Film is free of pinholes.
9. Film is diamond-like - Amorphous and/or polycrystalline, with crystallites in the 50 to 100 angstrom range according to X-ray diffraction line broadening. Definite lines assignable to diamond have been reported. Films show a cubic lattice with lattice constant close to those for cubic diamond.
10. Hard - Films are very hard as shown by scratch tests.
11. Density - 2.36 g/cm^3
12. Low porosity
13. Moisture and gas barrier - Hydrophobic
14. High index of refraction - About 2 in visible range, from ellipsometric measurements.
15. High dielectric constant - About 16, from capacitance measurements.
16. Erosion resistant - Reported to be good from rain erosion tests.
17. Low surface potential - About 0.1 volt negative, as determined by Kelvin vibrating electrode method.
18. High dielectric breakdown voltage - 10^6 volts/cm from measurements.
19. Film thickness is normally about 800 angstroms, but has been made up to 10μ. For thicker films, the films may separate from substrate, probably due to difference of thermal expansion coefficient.
20. Free standing films obtained by dissolving substrate are flexible.
21. There is no curl in free standing film, showing an absence of built-in stress.

Many of the above properties are relevant to helping meet the objectives of higher power ratings for laser windows and mirrors. Some of the more important ones would be chemical inertness, barrier properties to moisture, optical transparency, adhesion, sufficient low optical absorption, and probably very important, the unusually high degree of surface smoothness.

7. Expected Effect on Surface Breakdown Processes

Depending on the major cause of high power breakdown on the surface of mirrors and lasers it is anticipated that many of the properties of the diamond-like carbon film could be beneficial in reducing the surface breakdown processes. This is due in part to the sputtering associated with the deposition associated with the ion beam deposited diamond like carbon. This can result in removal of surface impurities and possibly surface intrusions.

In addition, if the diamond-like carbons form a coating over slight irregularities in the surface then the local electrical field of the metal projections can be reduced because of the higher dielectric constant of the diamond-like carbon. In addition, the diamond-like

carbon can probably be specially modified to reduce many of the electron emission processes involved with surface breakdown. Included in the surface breakdown processes are:

a. Photoemission

b. Schottky emission

c. Field emission

d. Thermonic emission

e. Electron emission by ion metastable bombardment

In addition, the properties of the coating are expected to reduce problems due to surface dust on the film, and surface water. These factors deserve additional research, but based on our knowledge of the physical properties of our diamond-like carbon and a consideration of the various surface breakdown processes we feel that this is one important beneficial aspect of the diamond-like carbon.

8. Enhanced Surface Smoothing Due to the Additional Free Surface Energy

One of the most interesting factors that we have encountered in conjunction with our study of the ion beam deposited diamond-like carbon is related to the observations that the films are frequently observed to be much smoother than that of the substrate. At first we ascribed this to the increased surface mobility, but it became apparent that there is another mechanism associated with driving the ion beam deposited film towards a state corresponding to an even smoother surface. We propose this as something that should be considered and studied for confirmation by other investigators.

Briefly, we postulate that deposition films containing relatively mobile atoms will tend to proceed to a state of minimum energy and because of the free surface energy associated, this surface will tend therefore, to go to a situation of minimum area. This minimum area, of course, corresponds to a surface with a minimum number of irregularities. The higher the free surface energy is per unit area, the stronger the driving force towards a smooth surface. Another requirement, of course, is that the surface be mobile so that the atoms can then move to a situation corresponding to a minimum surface energy. An example, of course, is liquid metal vs. a non-liquid metal. Until the metal is made liquid, the surface tension of the liquid metal cannot operate in order to give a very smooth metallic surface. An example is the surface of liquid mercury.

The reported free surface energy of liquid metals is in the range of 10^3 dynes/cm or equivalently 10^3 ergs/cm^2. This is sufficient in the case of liquid mercury for example, to give rise to quite a smooth surface.

We have done some calculations and have found that the free surface energy due to electrical surface charge is orders of magnitude greater than that reported for liquid metals. Assuming simple geometry, the energy stored in the surface electric charge is equal to:

$$E = \tfrac{1}{2} \frac{Q^2}{C} \qquad (1)$$

where E is the energy on the surface, Q is the charge on the surface, and C is the capacity of the surface. Another equivalent representation is:

$$E = \tfrac{1}{2} \, CV^2 \qquad (2)$$

where V is the potential difference of the surface. If we assume the geometry of a plain parallel capacitor then the energy per unit area E/A is given by:

$$E/A = \tfrac{1}{2} \, \varepsilon V^2/d \qquad (3)$$

where ε equals permitivity of the material adjacent to the surface, V is the potential difference between the surface and a reference surface, and d is the spacing to the reference surface.

If we view the plasma sheath adjacent to the substrate for ion beam deposition as the reference surface and conservatively assume a potential difference on the surface of about 1 volt, and a sheath thickness of about 1 mm and ε=1, then the energy per unit area on the surface associated with the charge on the surface is computed to be 5×10^5 erg/cm^2 which is about 500 times greater than that for liquid metal alone. A more refined calculation would, of course, depend on a more specific definition of the surface potential and the geometry associated with the surface charge on the substrate.

It is therefore seen that by adding a surface charge to a surface that has relatively mobile atoms, one would expect this extra driving force to result in a significant increase in the smoothness of the surface.

Figure 4 shows some scanning electron micrograph studies for the film deposited on polycarbonate substrates. The upper photograph illustrates the representative area of the scratched polycarbonate surface while the lower photograph shows a representative area after being coated with diamond-like carbon. It is apparent that the scratches are less pronounced and that in general the surface appears to be much smoother and the scratches seem to be less pronounced. A more detailed study of the surface roughness utilizing techniques such as electron scanning microscopes should be performed and more specific numerical values for the smoothness should be obtained. In general, the data reported for scanning electron microscope studies of our diamond-like carbon surfaces have indeed reported smoother surfaces although there is an absence of numerical analysis and numerical characterization.

Even in the absence of surface charge. one would expect that the higher atom energy on the surface would result in an increased tendency for smoother surfaces. This is due to the greater average energy for the surface atoms. For example, if one assumes that the ions are incident on the surface with about 100 electron volts energy, then the average surface energy of carbon atoms would be intermediate between thermal energy and 100 electron volts. If one assumes an average value of 50 electron volts for the mobile atoms while they are on the surface this corresponds to a free surface energy which is about 75 times that reported for liquid metals. Thus the higher kinetic energy of surface atoms can be expected to result in a significant increase in surface smoothness.

Additional studies can help verify the physics and properties associated with smooth diamond-like carbon films, and the ion beam deposition process.

References

(1) S. Aisenberg, R. Chabot, "Ion Beam Deposition of Thin Films of Diamond-Like Carbon", J. Appl. Phys. 42,2953,(1971)

(2) S. Aisenberg, R. Chabot, "Physics of Ion Plating and Ion Beam Deposition", J. Vac. Sci. Tech. 10,104,(1973)

(3) U.S. Patent No. 3,904,505, September 9, 1975. Apparatus for Film Deposition, By S. Aisenberg

(4) U. S. Patent No. 3,961,103, June 1, 1976. Film Deposition, By S. Aisenberg

(5) E.G. Spencer, P.H. Schmidt, P.C. Joy, and F. J. Sansalone, "Ion Beam Deposited Polycrystalline Diamond-Like Films", Appl. Phys. Letters, 29,118,(1976)

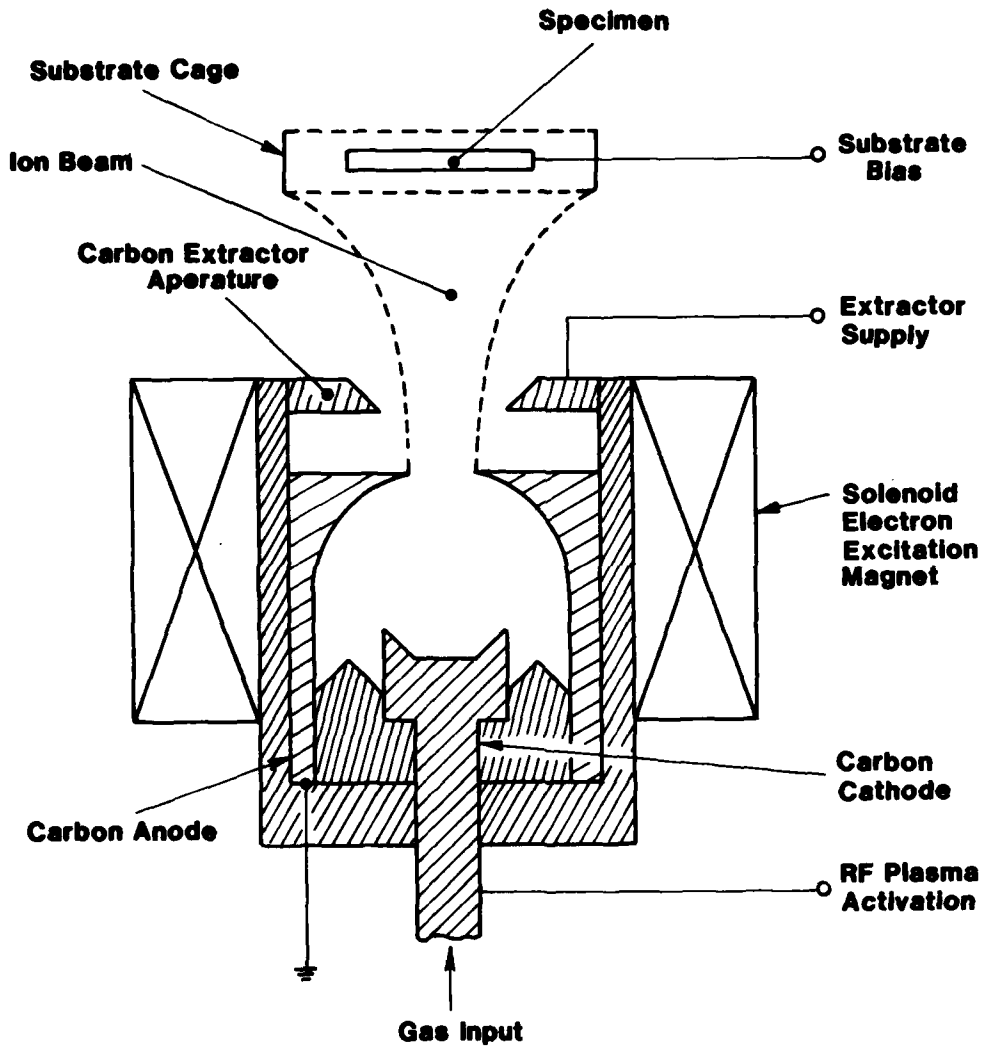

Figure 1. Cross Sectional View of Cylindrical Carbon Ion Deposition Source.

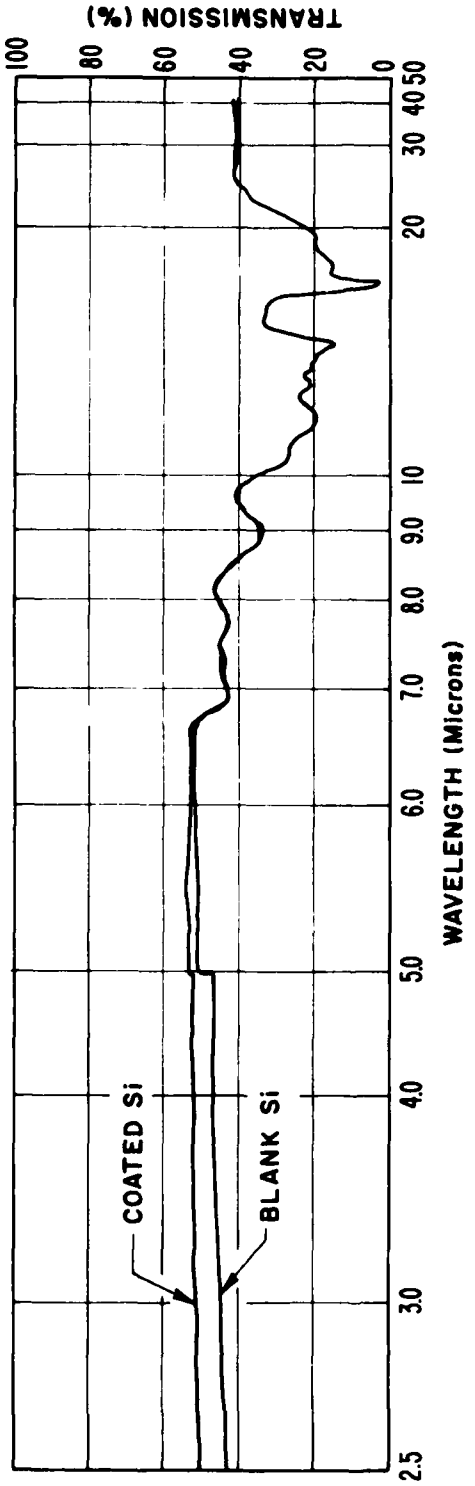

Figure 2. Measured optical transmission data showing low loss in the infra-red range (2.5 micron to 50 micron) for diamond-like carbon on silicon substrate--note enhanced transmission effect.

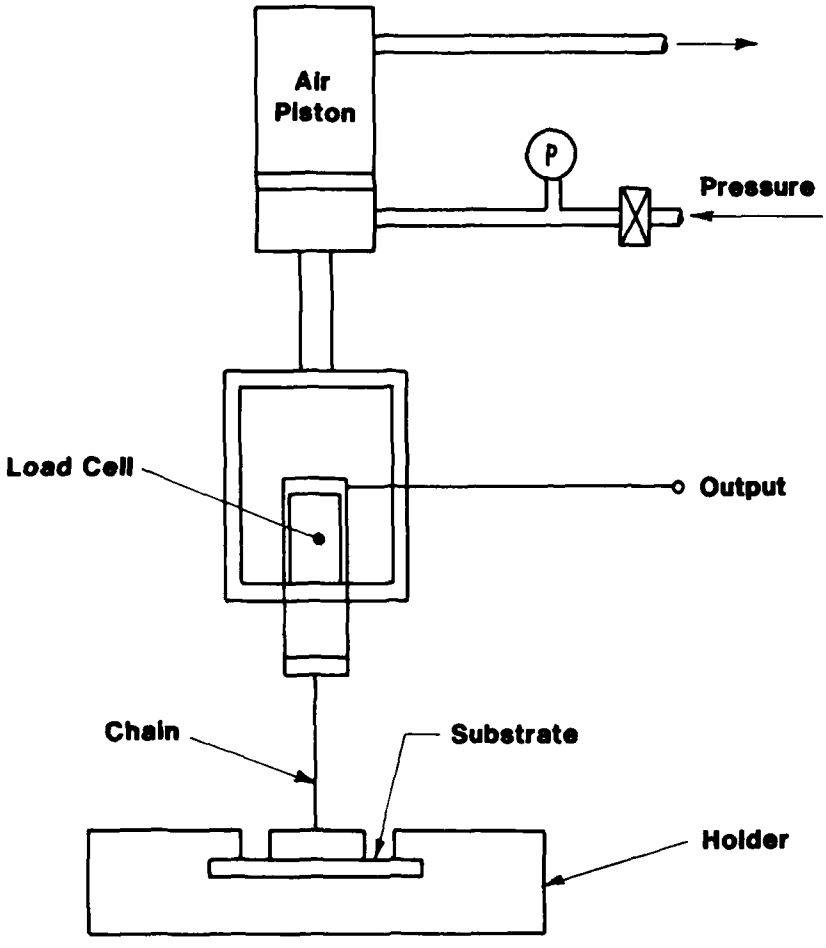

Figure 3. Illustration of Adhesion Tester Using Load Cell and Pneumatic Piston.

Figure 4a. S.E.M. photograph of uncoated press polished polycarbonate.

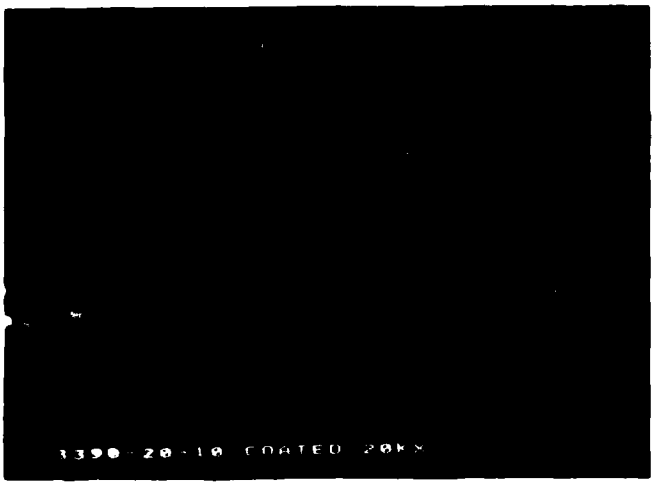

Figure 4b. S.E.M. photograph of diamond-like carbon coated press polished polycarbonate.

There was lively discussion of this paper. The first question was "what's the catch?" The questioner suggested that diamond-like films should replace most others if they are as good as were represented. The author replied that there were many possible problems which had not been addressed as yet. For example, the question of impurities has not been investigated and hydrocarbon and water content must be reduced. The problem of coating large areas had only been addressed conceptually. He reported that in their 18-inch diameter vacuum system they not coat up to 3-inch diameter substrates at the rate of 3-10 A/sec. By running continuously they can obtain thicknesses of 0.1 inch per mouth. The author reported that ancedotal accounts have it that an 800Å thick coating provides rain erosion protection at a rainfall rate of 2-3 inches per hour and velocity of 400 knots. The coefficient of friction was also said to be reduced and the wear resistance of stainless steel blades increased by such coating thicknesses. The author was not able to cite any documented laboratory results supporting such claims and it was suggested that more work should be done in that area before any further presentations.

ION-BEAM DEPOSITED Ge-As-Se GLASS FOR APPLICATIONS IN THE 1μ TO 16μ WAVELENGTH REGION

W. C. Herrmann, Jr.
Optic-Electronic Corporation
Dallas, Texas
and
J. R. McNeil
Physical Science Laboratory
Department of Electrical and Computer Engineering
New Mexico State University
Las Cruces, New Mexico 88003

We have investigated application of Ge-As-Se glass as an optical coating material for use in the 1μ to 16μ wavelength region. Thin films of the material have demonstrated the following desirable characteristics: low absorption over the wavelength region of 1μ to 16μ; low inherent stress; amorphous, homogeneous structure. Laser damage tests have been performed at 1.06μ and 10.6μ. Interpretation and results of the damage tests are discussed. The films are robust and resistant to attack by HF.

The deposition technique employed ion beams to pre-clean the substrate and to deposit the Ge-As-Se material. Deposition was a hybrid process, with coating material initially being sputtered by the ion beam and subsequently being generated thermally due to target heating by the ion beam. Thus the advantages of sputter deposition are realized during initial stages of film growth, and faster deposition rates can then be achieved using thermal generation. Films of Ge-As-Se in excess of 100μ thick have been easily deposited, and a variety of materials has been used as substrates. This same sputter-thermal technique has been applied to other thin film materials.

Key words: Ion beam; sputtering; chalcogenide glass; coating.

1. Introduction

Sputtering techniques have been used for many years to produce thin films of outstanding quality [1,][1]. This is presumably due to the high arrival energy of particles at the substrate (~10 eV) compared to that found in thermal deposition (~0.1 eV). Although several different arrangements can be employed for sputtering, the use of ion beams for deposition has distinct advantages over other sputter techniques. First, there is greater flexibility in adjusting ion beam parameters than with other arrangements; beam current density and ion energy are, to a great extent, independently adjustable. The geometric arrangement of the ion source, sputter target, and optical substrate allows more flexibility than in other sputter arrangements. Third, the sputter target and the optical substrate can be situated in a high vacuum environment ($\leq 10^{-4}$ Torr), which is not always the case for other sputtering arrangements. The substrate does not require biasing. The target can be dielectric material, since the ion beam can be neutralized.

One drawback of sputter deposition is the low deposition rate that is achieved for most thin film materials. This is a particularly serious problem in the case of large optics that are to be coated.

We have used ion beam techniques to deposit films of several materials to incorporate the advantages mentioned above. In addition, we have demonstrated a technique using ion beams to achieve high deposition rates and thus overcome the disadvantage mentioned. One of the materials investigated was a chalcogenide glass composed of $Ge_{33}\ As_{12}\ Se_{55}$. This appears to be a very attractive material for use in high energy laser applications. The deposition technique is first discussed below, and the characteristics of the Ge-As-Se films examined are then given.

2. Experimental Arrangement

The experimental arrangement included two Kaufman-type ion beam sources. One source was used to direct ions to the optical substrate for cleaning prior to coating. The other source produced a beam incident on the target used for coating. The two ion sources had a range of total beam current controllable from 0.01 mA to 80 mA and beam voltage of 50 V to 2000 V. Figure 1 illustrates the arrangement. The substrate is rotated and can be heated. The average target to substrate distance is six inches. The sputter target is thermally isolated. Also included in the arrangement are a crystal deposition rate monitor and a quadrapole residual gas analyzer used to monitor conditions in the deposition chamber.

[1] Figures in brackets indicate the literature references at the end of this paper.

Note that this same arrangement can be used to simultaneously sputter the target material and ion bombard (peen) the substrate as it is being coated. This technique has been employed in the past to reduce stress in films of Cr [2] and to change the physical characteristics of C films [3].

3. Sputter-Thermal Deposition

The deposition process first included pre-cleaning by ion beam bombardment of the substrate. Next, the second source was used to sputter the target material onto the optical substrate. During this stage of deposition, the total ion beam current directed onto the target was low (<10 mA). The sputter deposition rate increased linearly with ion beam current and was relatively low for a current less than approximately 10 mA. See figures 2-5. For the particular geometry we employed, the Ge-As-Se deposition rate was approximately 8 Å/sec for 10 mA beam current. In this case the beam acceleration voltage was 1500 V, corresponding to a power input to the target of 15 W.

Increasing the beam current past 12 mA in the case of the Ge-As-Se target caused the deposition rate to increase drastically. The deposition rate at 20 mA beam current was approximately 70 Å/sec.; at 30 mA the deposition rate was greater than 300 Å/sec. See figure 2. We attribute this increase in deposition rate to thermal effects resulting from target heating by the ion beam. If this is the case, then the majority of particles arriving at the substrate have thermal kinetic energy, and a small percentage have an energy of several eV.

This same behavior was observed for targets of ZnS and MgF_2. However, a target of Ge did not show this increase in deposition rate for ion beam currents up to 50 mA.

Note that at a beam current of approximately 8 mA directed onto the Ge-As-Se target, the surface of target began to melt. Thus the increase in deposition rate for beam currents greater than 10 mA might be due at least in part to a change in sputter coefficient of the Ge-As-Se material. However, the Ge target also melted at the surface but did not display the abrupt change in deposition rate. Also, ZnS was not observed to melt, and it did display the abrupt change in deposition rate. From this it appears there is no direct connection between a change in state of the sputter target and the abrupt increase in deposition rate.

A number of substrate materials were used in the deposition of the Ge-As-Se material. These included BK-7, Ge, ZnSe, Cu, Ag, Al, and the film characteristics on those materials are discussed below.

4. Properties of Ge-As-Se Films

The Ge-As-Se glass[2] displayed several attractive features when deposited as a thin film. Very thick films of the material could be easily deposited using the techniques described, indicating the material has low intrinsic stress. Films in excess of 125μ were separated from substrates and observed to be freestanding. During deposition of the thick films no difficulty was experienced in ion source operation. This is not always the case; some thin film materials such as Cd backstream into the ion source and interfere with the source operation. Also, during deposition of thick films the quartz oscillator thickness monitor operated satisfactorily. This is also indicative of film quality, because with many materials, film flaking, etc., causes poor oscillator performance.

Figures 6 and 7 illustrate the optical transmission characteristics of the material in bulk (1.4 mm thick) and thick film form, respectively. The bulk film indicates very little structure in the transmission from less than 1μ to nearly 16μ. The index of refraction of the bulk material of approximately 2.5 causes surface reflections which account for the low transmission seen in figure 6. The structure seen in figure 7 is most likely due to interference effects between reflections off the front and back surfaces off the film.

Figure 8 illustrates the transmission characteristics of a λ/2 film of Ge-As-Se deposited on a NaCl substrate, where λ = 11μ. First note the high optical transmission at multiple half-wavelengths of optical thickness, indicating low absorption over this spectral region. Optical reflection measurements of halfwave thick films at 16μ indicated the film had less than 0.2% absorption. Second, the behavior shown in figure 8 indicates the film structure is very homogeneous. Because of the uniform behavior of transmission at odd multiple quarter-wavelengths, it can be seen that

$$\frac{dn(t)}{dt} \approx 0,$$

where t is the optical thickness of the film. From the behavior described above, it can be seen that the index of refraction of the film is approximately 2.7, slightly greater than that of the bulk material.

X-ray fluorescence analysis of the bulk and thick film (>50μ) material indicated the films are deficient by approximately 15% in As content. This most likely accounts for the higher refractive index of the film, resulting from excess $GeSe_2$ concentration [4].

[2] Tradename AMTIR, available from Amorphous Materials, Inc., Garland, Texas.

Films deposited on various substrates were exposed to laser radiation at 1.06μ and 10.6μ for damage testing. Figures 9 and 10 summarizes the results of these measurements. Damage threshold was considered to occur at the first visible signs of film deterioration.

The adherence of the films and various substrates was examined using a Sebastian I coating test arrangement, in which a small stud was epoxied to the film surface. The force required to pull the stud free from surface was measured. For the results to be meaningful, it naturally must be assumed that the presence of the epoxy does not change the film characteristics. Most tests were performed on thick films of Ge-As-Se glass. A typical value for the adhesion of thick films (50μ) to BK-7 was 5-8 kpsi; to Ge, 4-6 kpsi; to NcCl, 3-5 kpsi. Some thin films deposited on NaCl did not adhere well but demonstrated good long term stability at ambient temperature and at 60% relative humidity. For comparison, the same test was performed on other coating/substrate combinations. Results indicated an adhesion of 8-10 kpsi for MgF_2 on BK-7; kpsi 6-8 for Ag on BK-7; and 0.5-1.1 kpsi for bulk AMTIR.

Thick (50μ) Ge-As-Se films displayed high resistance to attack by HF. Concentrated HF was left on films for over ten hours with little visual damage evident. Note that one reason the thick films are so protective could be due to closure of pinholes. The films are attractive for application involving corrosive environments of HF or DF.

Because of the protective nature of the films, we have considered the possiblity of using Ge-As-Se films as "sealer" layers. For instance, a multi-layer ZnS/NaF film structure can be deposited on a hygroscopic substrate and be protected by Ge-As-Se overcoat. This, in turn, could be antireflection (AR) coated, so that the glass effectively becomes the incidence medium for the less durable multi-layer structure.

5. Conclusions

In conclusion, we have applied a hybrid deposition technique involving ion beams to several coating materials. The technique employs the advantages of sputter deposition during the initial stages of film growth, and faster deposition rates can be subsequently achieved using thermal generation. Films of Ge-As-Se have been deposited using this technique. The films are easily applied, have low absorption over the wavelength region of 1μ to 16μ, have low inherent stress, have an amorphous, homogeneous structure, and are robust and resistant to attack by HF. One possible application of the material is for use as lamination in construction of a lightweight, low cost window material when used with NaCl.

References

[1] L.I. Maissel and R. Glang, eds. Handbook of Thin Film Technology, McGraw-Hill, New York (1970).

[2] D.W. Hoffman and M.R. Gaerttner, J. Vac. Sci. Technol, 17, 425 (1980).

[3] C. Weissmantel, Proc. 7th Intern. Vac. Congr. and 3rd Intern, Conf. Solid Surfaces (Vienna 1977).

[4] Personal correspondence, Ray Hilton, Amorphons Materials, Inc., Garland, Texas.

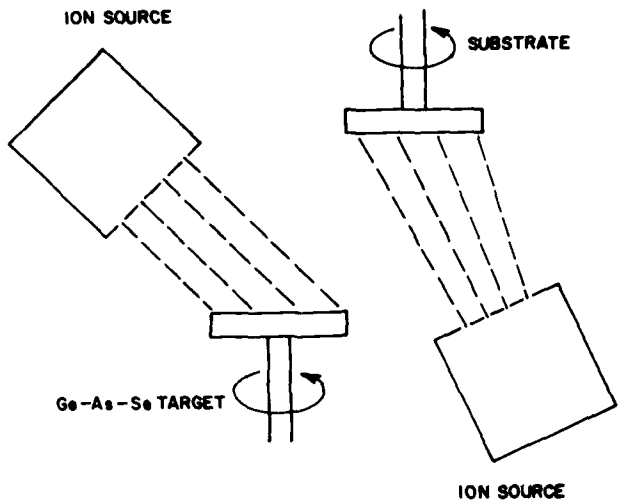

Fig. 1. Experimental arrangement used for ion beam deposition.

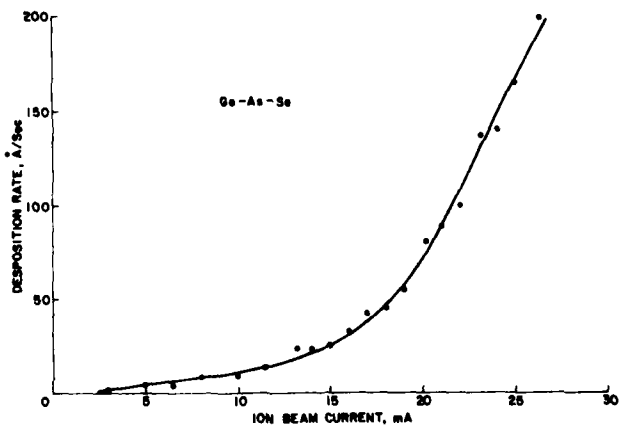

Fig. 2. Deposition rate of Ge-As-Se vs total ion beam current.

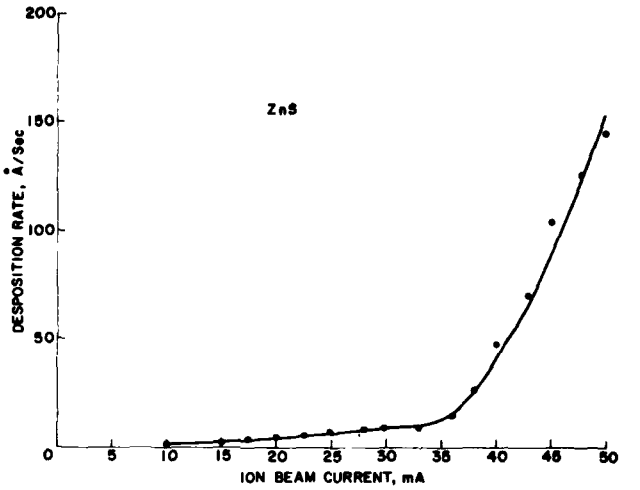

Fig. 3. Deposition rate of ZnS vs total ion beam current.

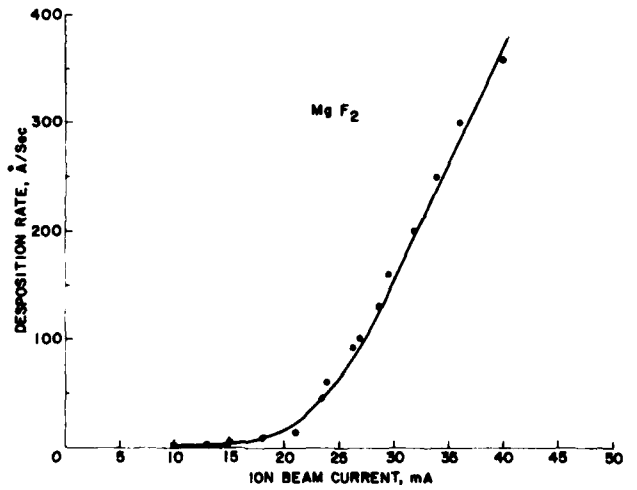

Fig. 4. Deposition rate of Mg F_2 vs total ion beam current.

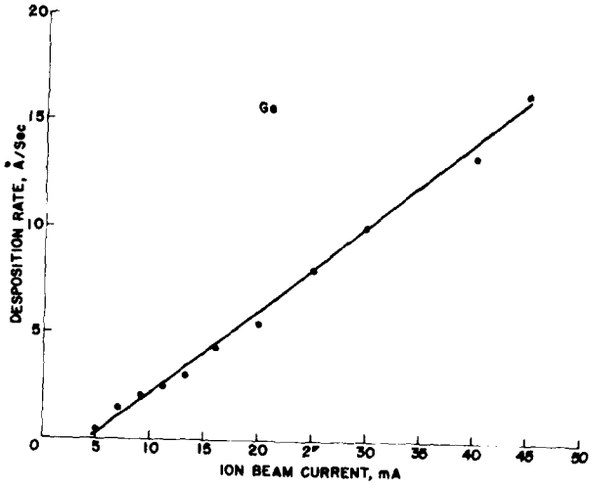

Fig.5. Deposition rate of Ge vs total ion beam current.

Fig. 6. Optical transmission of bulk (1.4mm) Ge-As-Se glass for 2.5μ - 50μ (upper) and 0.5μ - 2.5μ (lower).

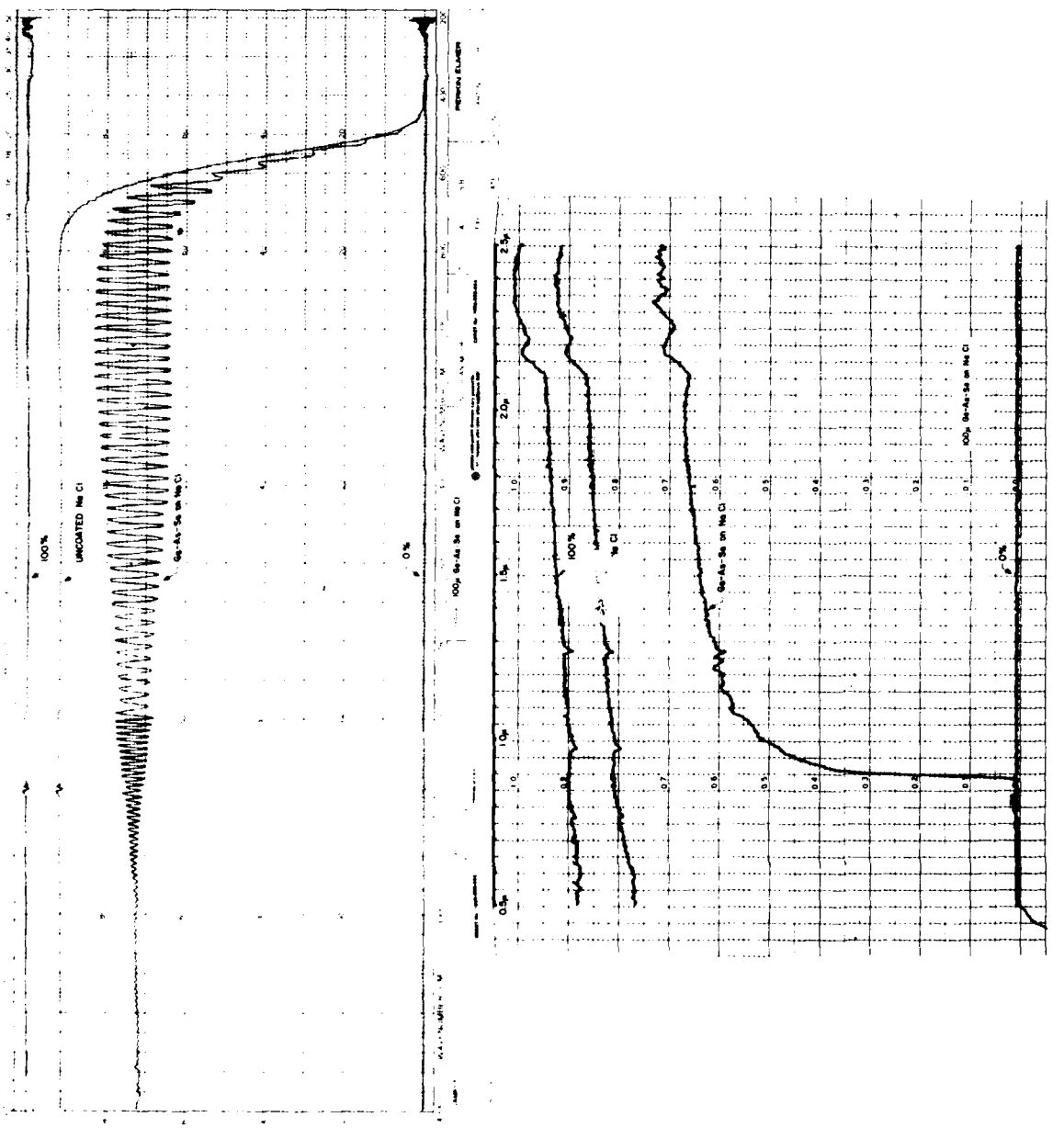

Fig.7. Optical transmission of thick film (125μ) Ge-As-Se glass for 2.5μ - 50μ (upper) and 0.5μ - 2.5μ (lower).

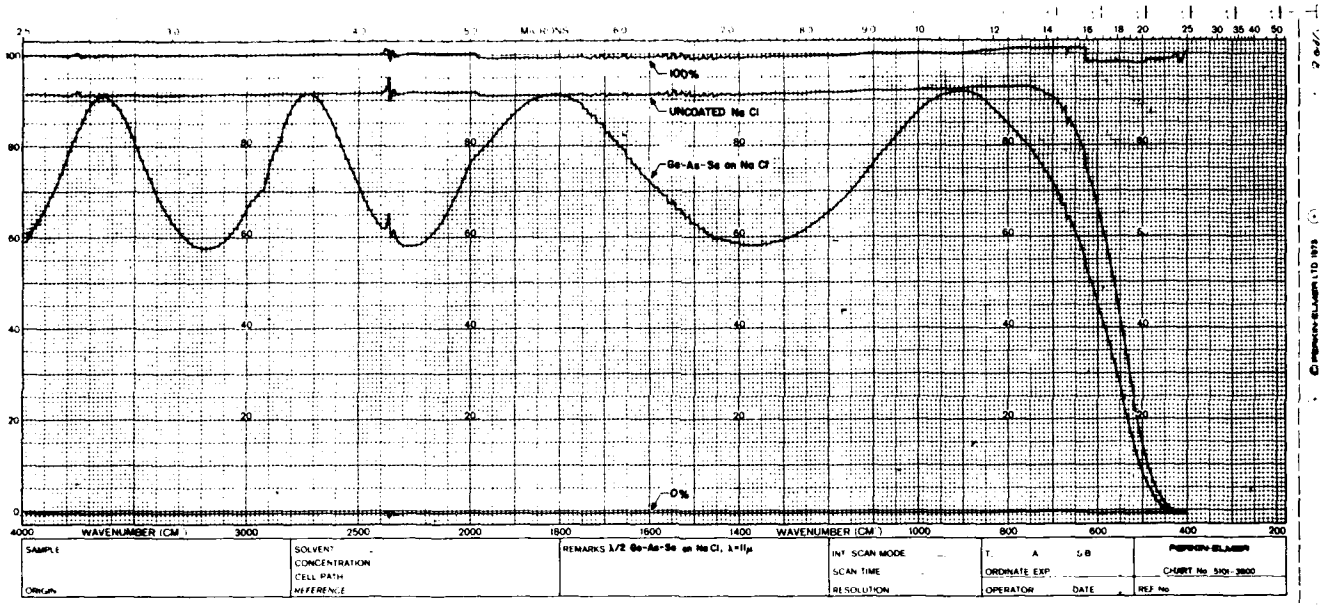

Fig. 8. Optical transmission of λ/2 film of Ge-As-Se glass, where λ=11μ.

LASER DAMAGE AT 1.06μ

τ = 20 nsec

Material	Intensity, MW/cm²
Bulk Ge-As-Se	>70
100 Ge-As-Se on BK-7	>70
100 Ge-As-Se on NaCl	>70
λ/2 Ge-As-Se on BK-7	>40
λ/4 Ge-As-Se on BK-7	>110
Bare Cu	>450
Bare Diamond-Turned Al	>50

Fig. 9. Results of laser damage testing Ge-As-Se at 1.06μ.

LASER DAMAGE AT 10.6μ

τ = 1.2 nsec

Material	Intensity, GW/cm²
100μ Ge-As-Se on NaCl[1]	2.3

τ = 5 sec

Material	Intensity, MW/cm²
Bulk Ge-As-Se	>0.18
100μ Ge-As-Se on NaCl	>0.20
λ/2 Ge-As-Se on NaCl	>0.17
Bare ZnSe	>0.35
Bare Mo[2]	>0.20
($ZnSe/ThF_4$) on Ag/Cr/Mo[2]	>0.23
$(ZnSe/ThF_4)^3$/Mo[3]	>0.15

(1) Thomas, S., LASL, private communication, 1980.

(2) Saito, T. T., Charlton, G. B., and Loomis, J. S., Natl. Bur. Stand. Spec. Publ. 414, 103 (1974).

(3) Huguley, C. A. and Loomis, J. S., Natl. Bur. Stand. Spec. Publ. 435, 189 (1975).

Fig. 10. Results of laser damage testing Ge-As-Se at 10.6μ.

In response to a question concerning film composition the author stated that the silicon deficiency causes the film index to be 2.75 instead of the 2.5 value typical of bulk material. The composition was not found to change with deposition rate using a sputter-thermal process. Calorimetric measurements of film absorption coefficient have not yet been done, although CW damage measurements suggest that it is similar to the bulk material, 0.05 cm^{-1}.

CHARACTERIZATION OF SMALL ABSORPTIONS IN OPTICAL COATINGS

Wayne J. Anderson
Physics Department
United States Air Force Academy, Colorado 80840

and

Wilford N. Hansen
Physics Department
Utah State University
Logan, Utah 84322

Probably the main causes of laser damage in thin films used as optical coatings are impurities and non-stoichiometry, especially at interfaces. This paper considers the problems of identifying absorbing species, locating them in the optical structure and measuring the amount of absorbing species present. The ability to have large electromagnetic fields of the desired distribution in a multilayer system is used to optimize multiple reflection spectroscopy for the characterization of thin layers. The absorption coefficient caused by impurities in several Th F_4 films are calculated as a function of angle of incidence and polarization. The position of these impurities is predicted by comparing the absorption coefficients measured with several techniques. The method is general and can be applied to give accurate results on systems of multiple phases and varying substrate. While the method is valid for general stratified media, its accuracy depends upon the information content of the particular reflection spectrum.

Key words: Absorption; coatings; internal reflection spectroscopy; silicon monoxide; thorium fluoride; zinc selenide; zinc sulfide.

1. Introduction

Impurities are a main cause of laser damage in thin films because of their absorption bands at working frequencies. It is therefore important to identify these impurities, find their location, and determine the amounts present. In a previous work we showed how reflection measurements could detect water, hydrocarbon, and SiO impurities in multilayer coatings [1]. In this work we use the reflection spectra to calculate the complex index of refraction for the impurity bands of multilayer film stacks. The complex refractive index is calculated as a function of polarization, angle of incidence and film thickness, and the results are compared to determine the amount and position of the impurity in the multilayer stack.

2. Technique

In this study emphasis is on characterizing small absorptions. Various techniques were used to enhance the sensitivity of the absorption methods used. Multiple reflections using both internal and external spectroscopy were used to multiply the observed absorbance. The angular settings and polarizations were chosen to maximize the $\langle E^2 \rangle$ field in the region of interest. The experimental procedures are described in reference [1]. The procedures and method of analysis of the reflection spectra can be found in reference [2].

The technique is to use experimental data to tabulate Re $G(\omega) = \frac{1}{2} \ln (R_s/R_b)$ where R_s is the sample reflectance and R_b is the same sample reflectance assumed to be electromagnetically bleached in the frequency region of interest. The method uses the causality of the special reflection function $G(\omega) = \ln [r_s(\omega)/r_b(\omega)] = \frac{1}{2} \ln (R_s/R_b) + i(\phi_s - \phi_b)$ and the application to this function of the transformation given by Peterson and Knight [3] hereafter referred to as the PK transform. Here the r refers to the Fresnel reflection coefficient $r = \sqrt{R}\, e^{i\phi}$ where ϕ is the phase angle. Application of the PK transform to the Re $G(\omega)$ found from the reflection spectrum yields Im $G(\omega) = (\phi_s - \phi_b)$. The phase angle for the bleached sample, ϕ_b, is found using the literature optical constants away from the absorption peaks and using a linear extrapolation to obtain ϕ_b through the region being analyzed [4]. The complex index of refraction, $n = n + ik$, is found from r_s using an iteration technique [5]. The technique will be illustrated with a ZnS film deposited on a germanium substrate.

3. Results and Discussion

3.1 ZnS Film

The reflection spectrum of a ZnS film deposited on a germanium substrate is shown in figure 1. The dashed line is the assumed bleached reflectance used to calculate the complex index for the impurities in the film. The imaginary part of the index is shown in figure 2. The structures at 1600, 2400, and 3400 cm^{-1} are caused by water. More than the usual detail is seen in the structure of the water bands. The amount of water can be found by using the optical constants of bulk water [6] and assuming that the measured extinction coefficient scales linearly with the water concentration. The magnitude of the peaks indicates an impurity concentration of approximately 1%. Since the angle of incidence is beyond the critical angle, the electric field only penetrates the film ≈1500Å thus the impurity peaks are caused by the equivalent of about 10-15Å or one or two monolayers of water. This monolayer of water was probably on the substrate surface at the time of deposition in spite of careful cleaning procedures. The hydrocarbon structure at 2900 cm^{-1} is again caused by a monolayer structure at the film substrate interface. The absorption at wave numbers less than 800 cm^{-1} is due to the Ge substrate and is of no interest.

3.2 ThF_4 Films

ThF_4 films deposited by the AFWL, Kirtland AFB, NM, were investigated by internal and external reflection spectroscopy. The films were deposited on silver and ZnSe substrates. The reflectance curves for these films were previously published in reference 1.

Figure 3 is the impurity extinction coefficient for a 2.23μ ThF_4 film deposited on silver plus 100Å of SiO at the Silver/ThF_4 interface. The main peaks are caused by water as shown by the bulk water extinction coefficient in the same figure. The SiO peak at 1100 cm^{-1} appears in the parallel polarized spectrum but not in the perpendicular as would be expected because the $\vec{E}$-field goes to zero at the metal surface for perpendicular polarization but not for parallel polarization. This same effect could explain why the extinction coefficient of the water impurity is greater for the parallel than the perpendicular polarization spectra. A large water concentration near the silver/ThF_4 interface causes the parallel polarized absorption spectra to be greater than the perpendicular. The magnitude of the peaks would indicate approximately a 5% water concentration in the film with the concentration being greatest near the substrate.

The internal reflection spectra were taken on 0.5μ ThF_4 films deposited on ZnSe substrates. The angle of incidence was varied from 30-70° with both polarizations being used. Figure 4 is the impurity extinction coefficients measured at 30° angle of incidence with both polarizations. This sample had a 100A film of SiO at the film/substrate interface. The structures at 1100 cm^{-1} are caused by the SiO. The double peak structure with parallel polarization indicates an anisotropic SiO film. The spectrometer was not sensitive to the reflectance near 3200 cm^{-1} because of the low sample throughput, thus the values obtained near this frequency are not reliable. Both parallel and perpendicular polarizations have large $\vec{E}$-fields near the interface. These results confirm those of figure 3 that the water is found at the interface. The large values of the extinction coefficient compared to figure 3 would indicate an order of magnitude larger impurity concentration but if the water is primarily at the interface then the results are in agreement with those of figure 3.

Increasing the angle of incidence decreases the penetration of the $\vec{E}$-field into the ThF_4 film using internal reflection. Figure 5 is the impurity extinction coefficient for the same sample used in figure 4 but at a 71.8° angle of incidence. The same double peak structure is observed at 1100 cm^{-1} for the SiO peak using parallel polarization. The penetration of the $\vec{E}$-field into the ThF_4 film decreases by approximately a factor of 2 going from 30° to 70° angle of incidence. The magnitude of the water impurity peaks has increased by roughly this same ratio over those of figure 4.

Figures 6-7 are the extinction coefficients for a 0.5μ ThF_4 film on ZnSe measured with perpendicular polarization and angles of incidence from 30-70°. Again the measured impurity extinction coefficient increases with increasing angle of incidence because of the varying penetration depth of the $\vec{E}$-fields. The values of the extinction coefficient at 45° incidence and 3400 cm^{-1} in figure 6 are uncertain because of the low throughput of the sample.

4. Conclusions and Recommendations

All of the films studied in this report were found to contain significant absorbing species as contaminants. These species were identified, located, and the amount estimated using the bulk absorption coefficients. The P-K Transform allows quantitative information to be obtained from the reflection spectra.

Thorium fluriode films all contained large amounts of water. The water impurity in the ThF_4 films is greatest at the film-substrate interface and is approximately 5-10% of the mass of the film. From our results, it is apparent that avoidance of water in ThF_4 films will require elaborate procedures but having information on the location will aid in designing deposition techniques to minimize the contamination. Sputter etching the sample substrate and presputtering the ThF_4 source may help reduce the water contaminate at the interface.

Silicon monoxide films were characterized by taking polarized spectra and were shown to be anisotropic near the absorption band at 1100 cm^{-1}.

The ZnS film was contaminated with water and hydrocarbon impurities amounting to one or two monolayers each. The impurities are located at the film-substrate interface and probably can be eliminated with feedback from spectroscopic data. The water impurity peaks have structure not observed before in bulk water spectra.

It is suggested that the spectroscopic measurements procedure discussed above be used routinely in optical deposition laboratories to evaluate the deposition process. A further study of ThF_4 deposition techniques is recommended to minimize the water contaminate. Time studies would yield valuable information on the diffusion rate of water in ThF_4.

5. Acknowledgements

The support of this work by the Air Force Weapons Lab. Kirtland AFB, New Mexico, under contract F29601-79-R-0081 is gratefully acknowledged. Part of the work was done at the Naval Weapons Center, China Lake, CA, with help from NWC personnel. Special thanks go to Drs. Hal and Jean Bennett for their valuable discussions and assistance. The computer time for this project was furnished by the Frank J. Seiler Laboratory, USAF Academy, CO.

6. *References*

[1] Hansen, Wilford N., Pearson, Lee, Hansen, Galen, and Anderson, Wayne J. "Laser Induced Damage in Optical Material," 1979, P. 247, NBS Special Publication 568.

[2] Hansen, W. N., Reflection Spectroscopy of Optical Coatings J. Opt. Soc. Am., 69, 264 (1979).

[3] Peterson, C. W., and Knight, B. W., J. Opt. Soc. Am. 63, (1973) 238.

[4] Hansen, W. N., Abdou, W. A., "Analysis of Solid-Liquid Interphase Spectra via Causal Transformation," J. Phys. (Paris) 38, C5-207, (1977)

[5] Anderson, W. J. and Hansen, W. N., J. Opt Soc. Am. 67, (1977) 1051.

[6] Rusk, Alvin N., Williams, Dudley, and Querry, Marvin R., J. Opt Soc. Am. 61, 91971) 895.

7. Figures

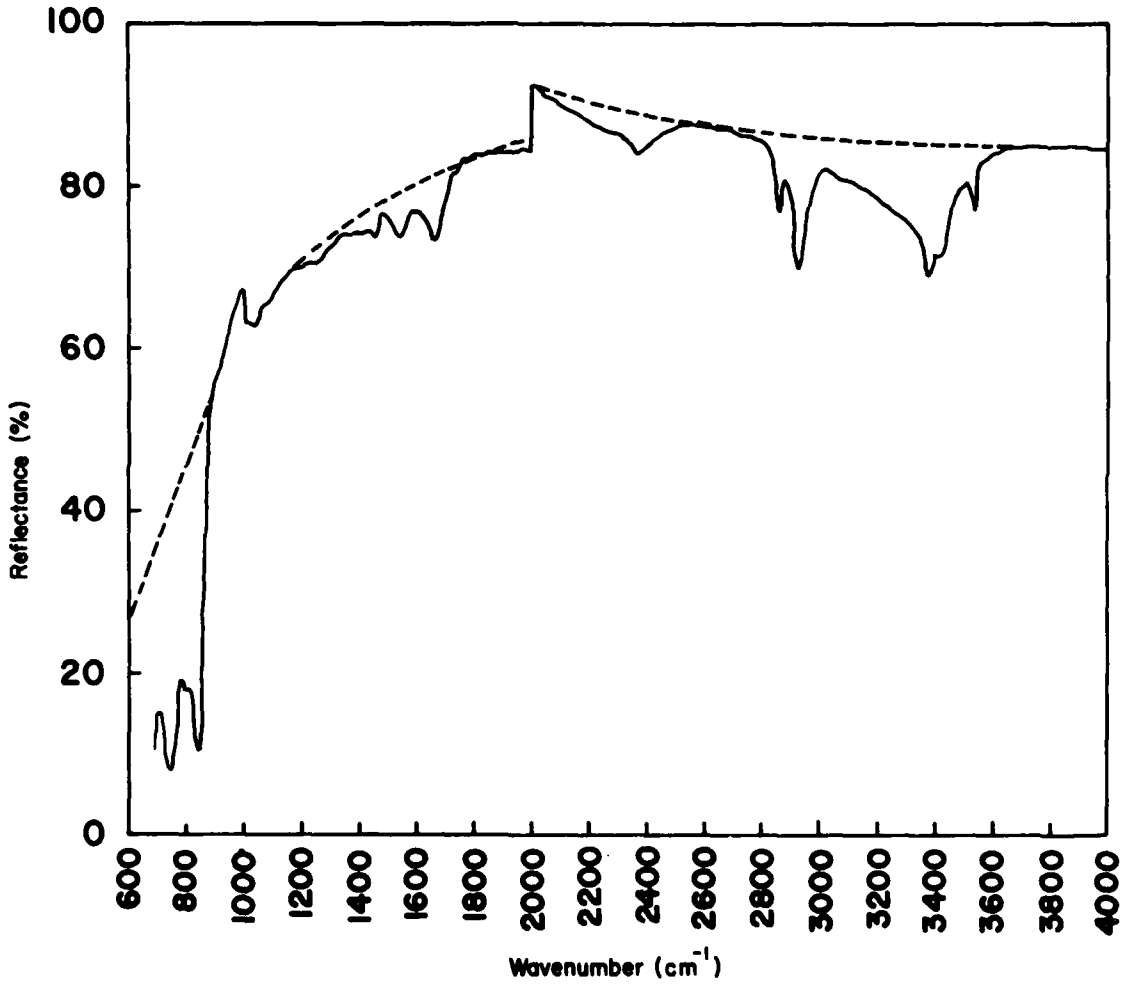

Figure 1. Internal reflection spectra of 0.5μ ZnS film on a Ge plate at an angle of incidence of 33.7% with 36 reflections. The continuous line is R_s while the dashed line is the assumed R_b.

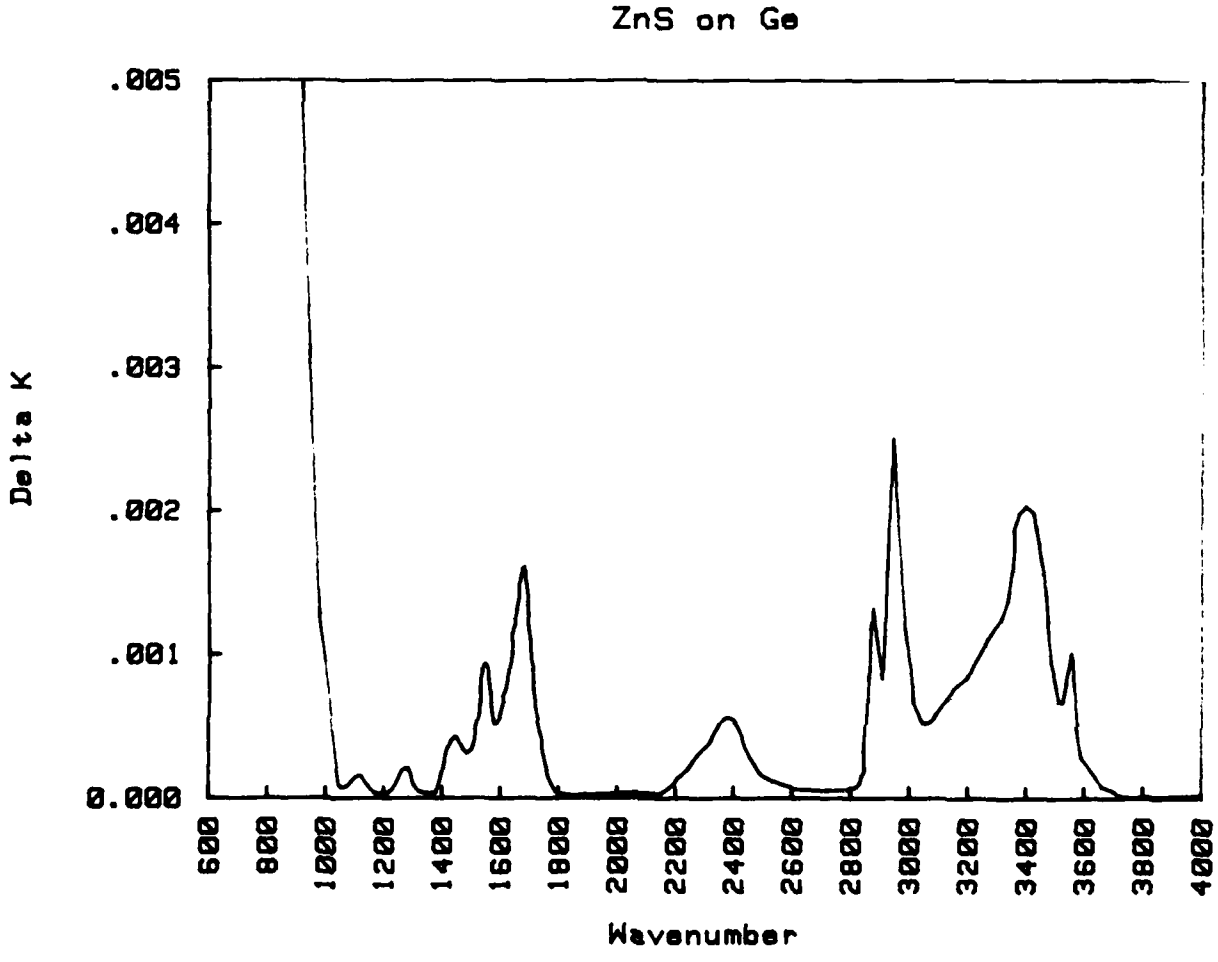

Figure 2. The impurity extinction coefficient for the film of figure 1.

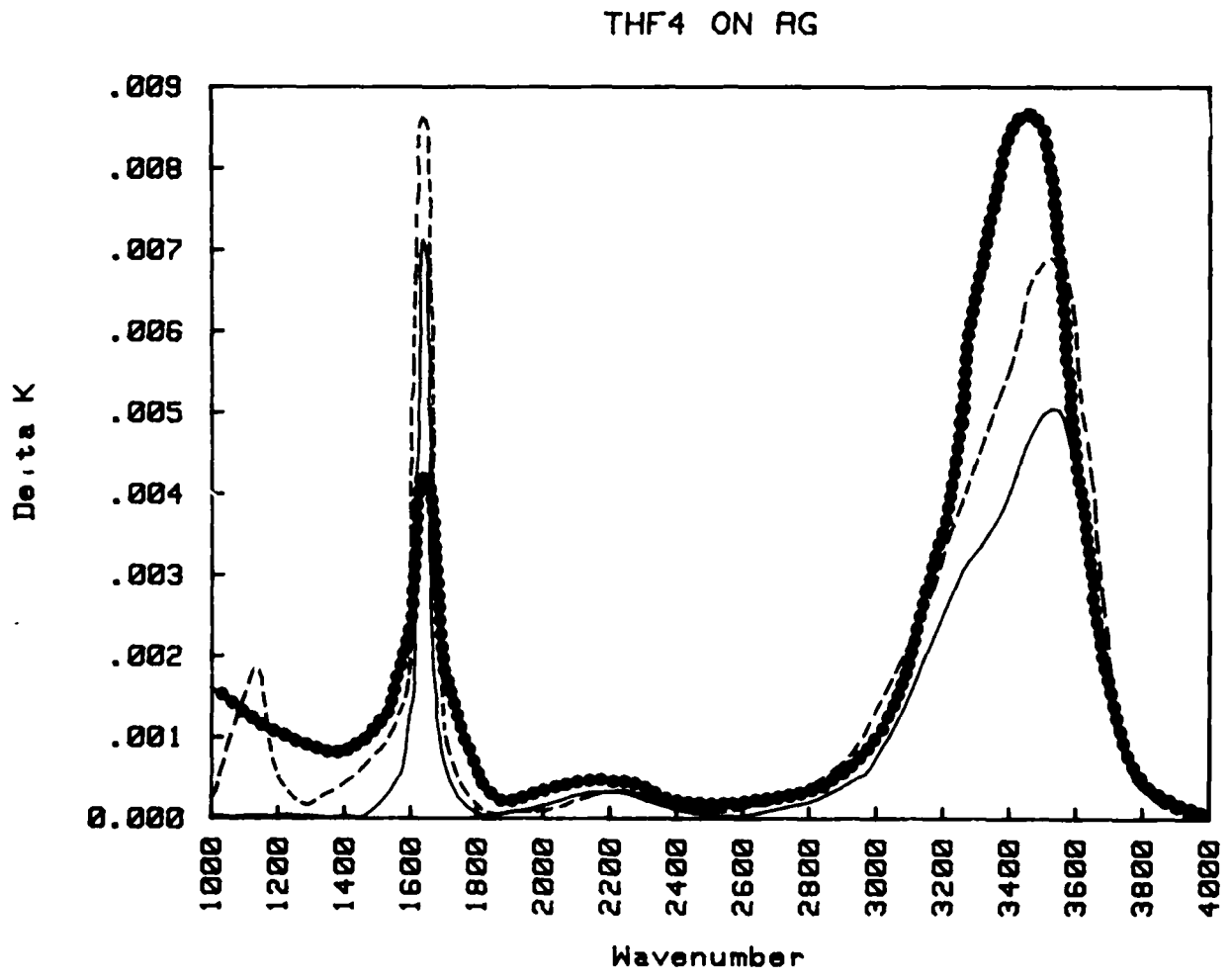

Figure 3. The impurity extinction coefficient for a 2.23μ ThF_4 film on silver plus 100Å SiO at the Silver/ThF_4 interface. The angle of incidence was 45° with perpendicular (solid line) and parallel (dashed line) polarization. The dotted line is the extinction coefficient for bulk water from Ref 6 plotted on a relative scale.

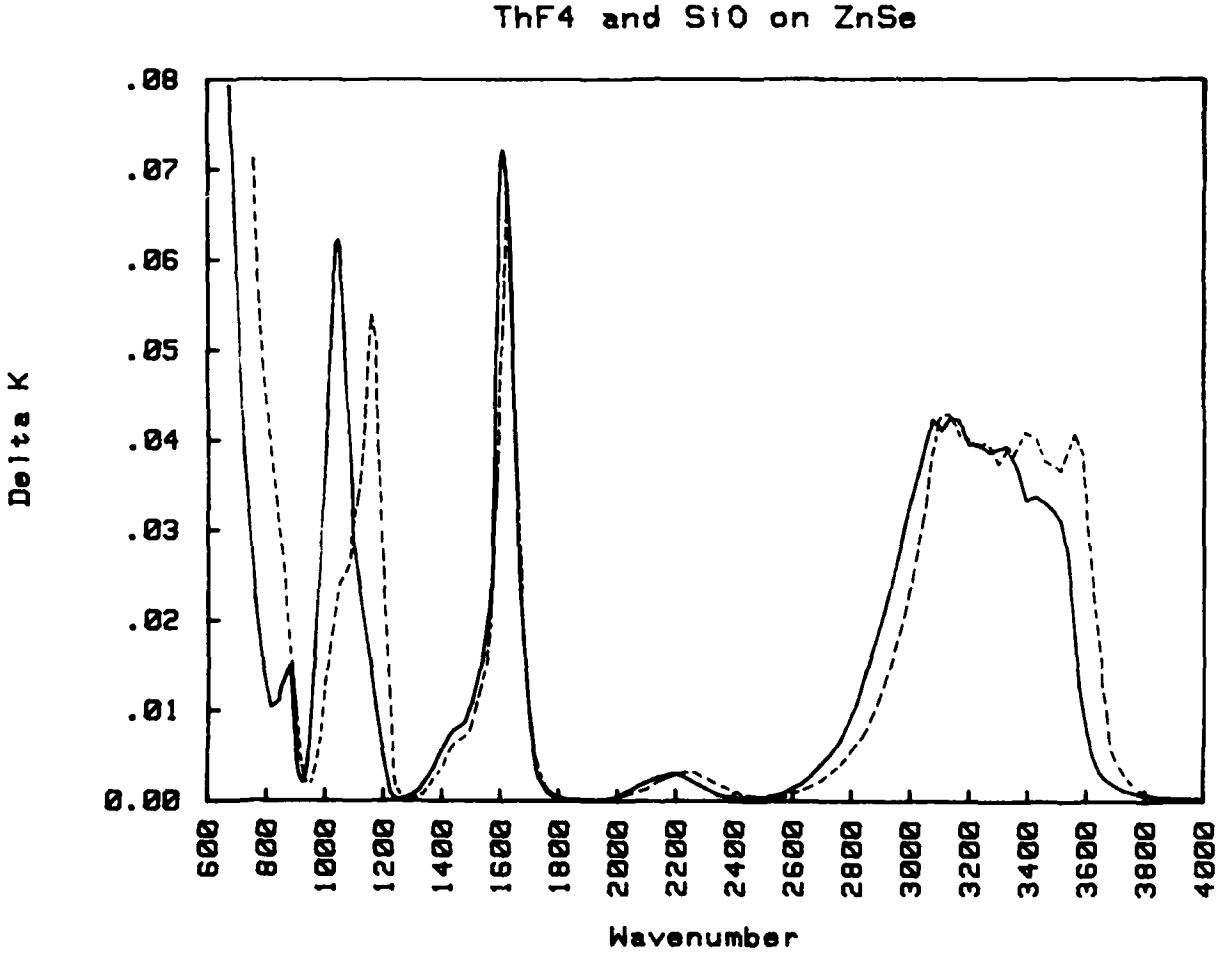

Figure 4. The impurity extinction coefficient for a 0.5μ ThF_4 film on a ZnSe substrate with 100Å SiO at the ZnSe/ThF_4 interface. The angle of incidence was 30° with perpendicular (solid line) and parallel (dashed line) polarization.

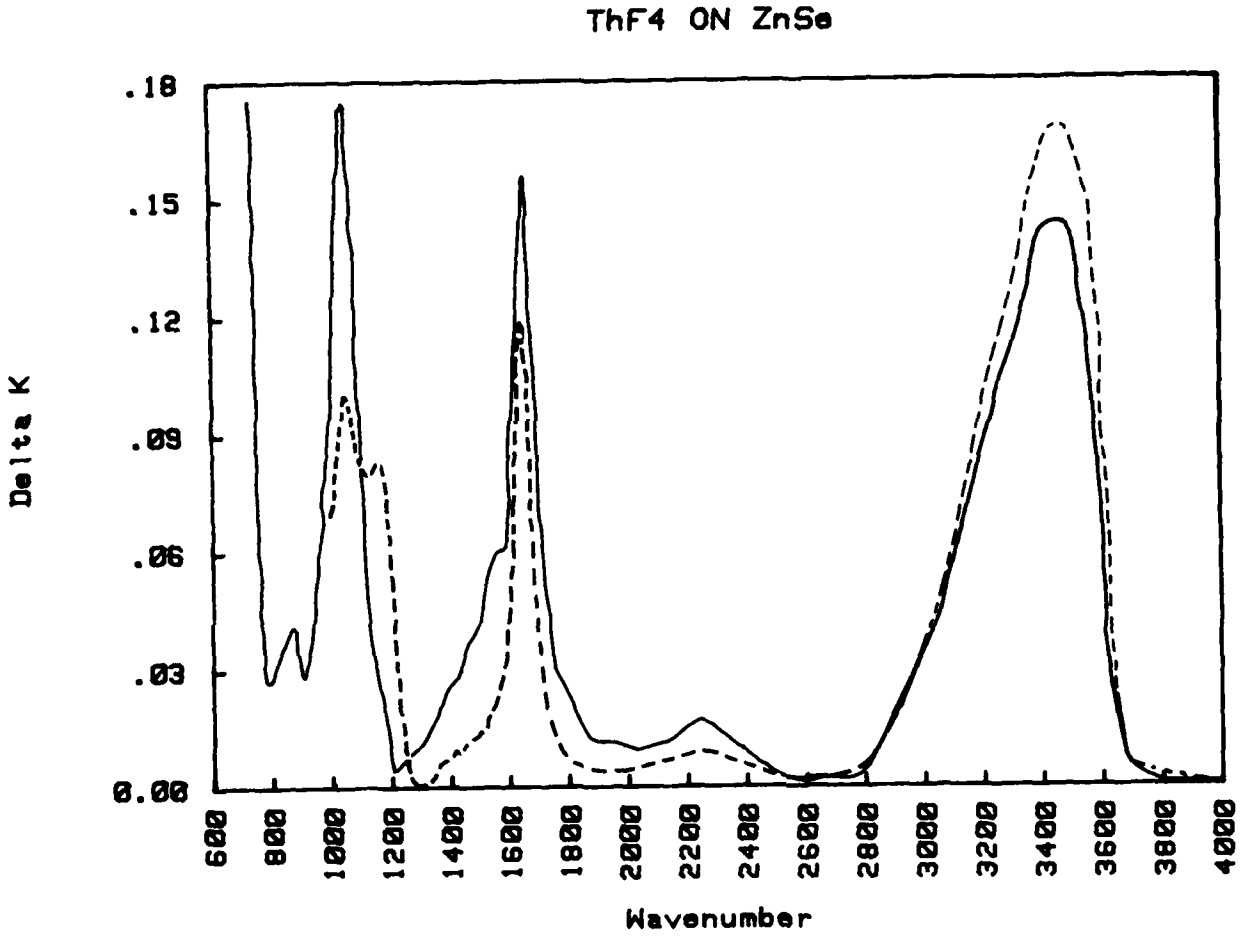

Figure 5. The same film used in figure 4 but with 71.8° angle of incidence.

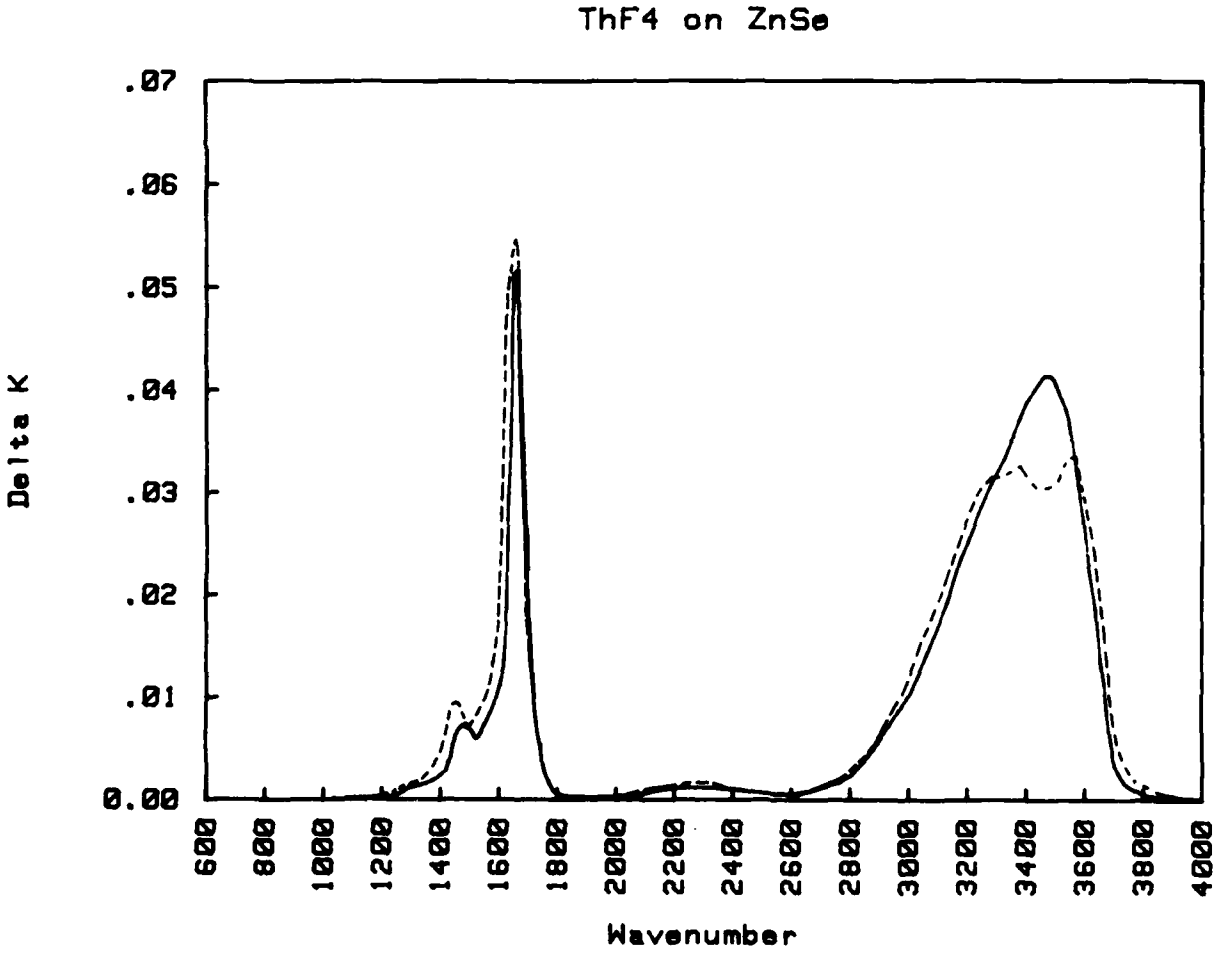

Figure 6. The impurity extinction coefficient for a 0.5μ ThF_4 film on a ZnSe substrate measured with perpendicular polarization at 30° (solid line) and 45° (dashed line) angle of incidence.

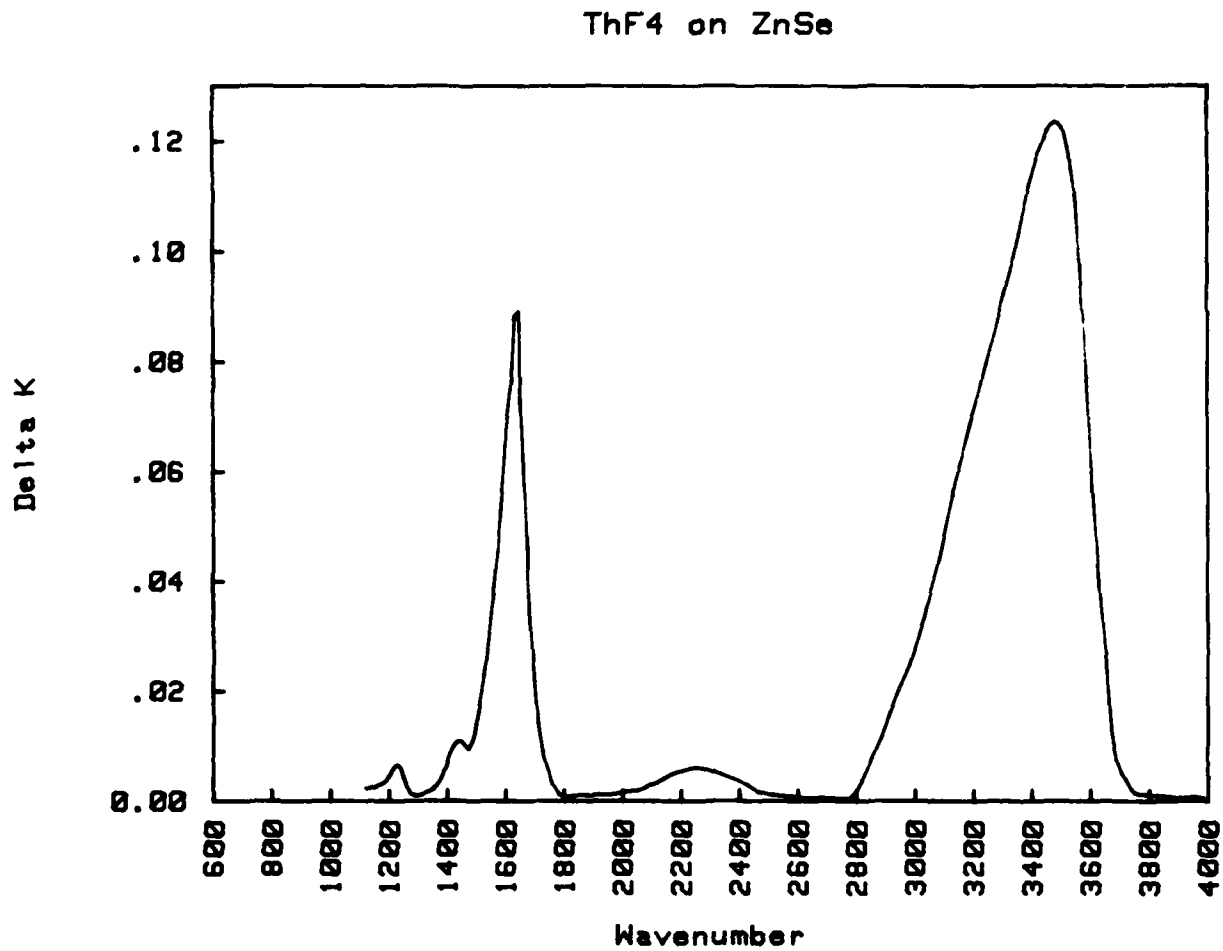

Figure 7. The impurity extinction coefficient for the film of figure 6 measured at 71.8° angle of incidence with perpendicular polarization.

DESIGN AND CONSTRUCTION OF THREE INFRARED ELLIPSOMETERS FOR THIN-FILM RESEARCH

Thomas A. Leonard, John Loomis, Kevin G. Harding, and Marion Scott
University of Dayton Research Institute, KL 102
Dayton, Ohio 45469

The University of Dayton Research Institute (UDRI) has designed and is building three infrared ellipsometers in support of the Air Force high-energy laser program. One of these instruments is a conventional null type ellipsometer for operation in the 3.39 to 4.00 μm wavelength range. Ellipsometric parameters are determined with a precision of 0.01° at any angle of incidence from 20° to 85°. Repeatability and absolute accuracy also approach 0.01° which yields optical constants accurate to 0.1 percent in some cases. All components are mounted on removable carriers for easy interchange, although operation is normally in the PCSA (Polarizer, Compensator, Sample, Analyzer) configuration.

The system software has special provisions for the second instrument which is also a null type ellipsometer dedicated to monitoring vacuum deposited coatings in real time at 3.39 μm. The software can model non-ideal components in the optical path using Jones or Mueller matrices and provide completely corrected data with a single zone measurement after the instrument is characterized. The third instrument is a rotating polarizer, automated ellipsometer tunable from 1 to 12 μm. A dedicated computer operates the instrument and reduces data.

Key words: Diode laser; ellipsometer; infrared; polarizer; thin films

1. Design Considerations

The three infrared ellipsometers designed and being built at UDRI are summarized in table 1. Each of these instruments has special design and component considerations. The OCEL ellipsometer is named after the Optical Components Evaluation Laboratory at Kirtland Air Force Base where it is being used. It was originally intended for measurement of differential phase retardation on thin film coatings although it is versatile enough in design to be changed to any desired configuration. All components are mounted on precision carriers which in turn mount on a granite rail. This feature is essential to maintain 0.01° angular repeatability which is necessary if the design goal of 0.01° accuracy for ellipsometric parameters is to be met. The distinction between precision and accuracy is a pertinent subject when discussing ellipsometry. Precision refers to confidence in small variations of a parameter with respect to the perhaps not too accurately known value of that parameter, whereas accuracy refers to confidence in the absolute value of a parameter with respect to the real world.

Table 1. Ellipsometers designed and being built at the University of Dayton Research Institute

	OCEL	DOF	ARPE
type	four zone manual null	single zone in situ monitoring	Automated Rotating Polarizer
wavelength coverage	3.39 - 4.00	3.39	1 - 12 μm
source	tunable diode laser and HeNe laser	HeNe laser	Nernst glower and monochromator
angle of incidence	20 - 85° plus transmission	fixed	20 - 85° plus transmission
design accuracy	0.01° for Δ and Ψ	0.01° for Δ and Ψ	0.5% for n and k

The DOF ellipsometer which is installed at The Developmental Optics Facility at Kirtland Air Force Base contains many of the same design features of the OCEL ellipsometer but it is intended to be permanently mounted under a large vacuum chamber for in situ monitoring of thin film coatings during deposition. There is not time to make four zone measurements which cancel certain unavoidable instrument errors so special software was developed to model the instrument and provide high final accuracy once the instrument is characterized.

The Automated Rotating Polarizer Ellipsometer (ARPE) will be completed in late 1981. It is a state-of-the-art instrument which is intended to provide much of the baseline ellipsometric data for

infrared materials in the coming decade. It uses a dedicated computer for control and data reduction so that the operator only inserts the sample and sets the angle of incidence. As shown in table 1 the wavelength coverage and accuracy desired are very optimistic and may require compromises in some regimes. The principle of operation is patterned after other rotating polarizer ellipsometers designed for high precision[1,2].

The user of an ellipsometer usually wants to know the accuracy of an instrument in terms of something he is familiar with, such as the complex index of refraction, N, of materials to be measured.

$$N = n + i\,k \qquad (1)$$

n = index

k = extinction coefficient

The ellipsometer, on the other hand, measures the ellipsometric parameters, ψ and Δ, which are the differential amplitude and phase change of the p and s reflected light at some angle of incidence, ϕ_o.

$$\tan \psi = \left| \frac{r_p}{r_s} \right| = \text{reflectance ratio}$$

$$\Delta = \delta_p - \delta_s = \text{differential phase shift}$$

The complex ratio of p and s reflectivities combines the information from these two measured parameters.

$$\rho = \frac{r_p}{r_s} = \tan \psi\, e^{i\Delta} \qquad (2)$$

Fortunately it is straightforward to specify the expected precision and accuracy available for the ellipsometric parameters, since they can be directly related to polarizer (P) and analyzer (A) angular settings with respect to the plane of incidence which are needed to obtain a null. Most component limitations and errors have calculable effects on the null positions and once the components are characterized these perturbations can be removed from the data. An alternative and more practical approach is to make null measurements in complementary zones to obtain an average null position. This is standard practice in classical null ellipsometry where a set of four zone measurements (four pairs of P and A angular settings) can in fact eliminate nearly all pertinent instrument errors[3]. This procedure cannot, of course, correct for inaccuracies in angular position although offsets with respect to the plane of incidence for the polarizer, analyzer, and compensator are cancelled. Also the effects of birefringence, in for example, a vacuum chamber window are not eliminated in differential phase shift. This problem will be discussed in conjunction with the software written for the DOF ellipsometer.

Now, unfortunately, when an attempt is made to calculate optical constants such as N, from the ellipsometric parameters the question of accuracy becomes much more complicated. The ellipsometric parameters are very general in nature since they change with angle of incidence and can result from extremely complex interactions at the surface. The complex index of refraction is a fixed, intrinsic property of individual materials. If the reflecting sample in an ellipsometer is a single interface of a homogeneous optically thick material, then its index is given by:

$$N = N_o \tan \phi_o \left[1 - \frac{4\rho}{(1+\rho)^2} \sin^2 \phi_o \right]^2 \qquad (3)$$

N_o = complex index of ambient material (usually 1)

It can be seen that errors in n and k resulting from variations in ψ and Δ are related to n, k and ϕ_o. This means that if the user wants to know the expected error in n and k resulting from errors in , and Δ due to instrument limitations, the values of n and k must be specified. That is, an instrument with given angular errors will provide more accurate results for some materials than for others. The angle of incidence must also be specified, however, for the single interface example ϕ_o can be independently selected so that its errors make a minimum contribution to N. This ϕ_o turns out to be between 40° to 60° over a wide range of indices and a choice of ϕ_o = 50° is usually appropriate to minimize error propagation from ϕ_o.

If the reflecting surface is in fact made up of multilayers, the question of index accuracies due to instrument limitations becomes even more complex. The index and thickness (t) of each layer and of the substrate will affect the accuracy obtainable for every material in the coating. It is

always possible to calculate the ellipsometric parameters that will be measured at any angle of incidence for a multilayer coating, no matter how complex, as long as the thickness and index of each layer are accurately known. The opposite problem, of finding N and t for various layers from measured ellipsometric parameters, is not always tractable. The single interface case can be solved analytically as given by eq. 3, but adding more than one additional layer compounds the problem tremendously. Measurements at different angles of incidence plus the aid of a computer will allow convergence towards a consistent set of N's and t's given assumptions about the model.

ARPE provides a good example of the expected accuracy for N given known instrument limitations. The major components of ARPE are shown in figure 1. In operation the computer has the option of setting the two fixed polarizers at their optimum azimuth for the sample being studied. These two polarizers bracket both the sample and a third polarizer rotating at 3000 rpm. This rotating polarizer causes the signal reaching the detector to be amplitude modulated at the second (100 hz) and fourth (200 hz) harmonic of the rotation rate. The relative amplitudes and phases of these two harmonics are dependent on the settings of the stationary polarizers and also the properties of the sample. The instrument settings monitored by the computer are shown in table 2. Through an A/D converter and Fourier processing, the phases of the two harmonics are measured with respect to the rotating polarizer position. Assuming we can measure these phases to an accuracy of 0.01° the final uncertainty in N can be calculated over a matrix of n and k values for the case of a single interface. This result is shown in table 3 where the uncertainty is expressed as a percent of the value being measured. The design goal of 0.5% uncertainty in n and k for this instrument is met within the heavy line region. Clearly the instrument is not suitable for measuring very low k values but this is a basic limitation of reflection ellipsometry.

Table 2. Instrument parameters which are read and analyzed by the ARPE computer.

- ϕ_0 - angle of incidence
- ϕ_1 - azimuth of first polarizer
- ϕ_2 - azimuth of second polarizer
- $\gamma_{2\omega}$ - phase of 100 hz signal
- $\gamma_{4\omega}$ - phase of 200 hz signal
- λ - wavelength

Many iterations and optimization procedures can be incorporated into the control software for this instrument. As mentioned, there are optimum settings for the stationary polarizers depending on the n and k being measured. Table 3 in fact has optimized these polarizer settings for individual determinations of n and k. When completed the instrument will automatically converge to the optimum machine settings or average over a series of settings in a procedure similar to four zone averaging in a null type ellipsometer. A table similar to table 3 can be constructed for the case of a single layer on an optically thick substrate. The index, N, of the substrate must be specified and also the optical thickness of the layer has an influence on final uncertainty. The results are generally about the same as given in table 3 with some regions better and some worse. The primary result, however, is that uncertainty in optical thickness is the limiting factor in determining n and k of layers and not instrument limitations.

Table 3. The minimum percent error in n and k for a single interface reflection with polarizer settings optimized for n and k separately. The uncertainty in the five measured instrument settings was assumed to be 0.01° and the angle of incidence was fixed at $\phi_0 = 50°$.

$\Delta n/\Delta k\%$

	$k = 10^{-4}$	10^{-3}	0.01	0.1	1.0	5.0	10	25	75
n=1.0	.04	.03	.03	.03	.06	.51	2.0	16	152
	73	5.3	.57	.10	.07	.15	.23	.47	1.5
1.5	.05	.05	.05	.05	.06	.34	1.3	9.9	101
	218	16	1.4	.18	.10	.11	.25	.46	1.4
2.5	.08	.08	.07	.07	.08	.36	.77	5.5	61
	25200	238	9.0	.93	.14	.14	.28	.44	1.4
4.0	.14	.14	.12	.12	.13	.24	.47	3.2	38
	92100	707	29	2.7	.25	.22	.22	.42	1.4
				10	.32	.22	.39	1.2	14
					1.8	.42	.47	.46	1.3
					30	.79	.63	.88	4.1
						4.4	1.5	1.5	1.6

2. Component Selection

All components for these instruments were purchased through commercial vendors except for miscellaneous mounting hardware and detector electronics. It was not immediately apparent what mechanical, electrical, and optical components were best suited to each particular instrument. Information on polarizers for example, is not easily available and extensive testing was done at UDRI to identify the best choices for each instrument.

The OCEL ellipsometer is the most appropriate instrument on which to base the discussion of component selection. Figure 2 shows the major components for this instrument. As mentioned previously, the mounting base for optical components is a precision granite rail. This was deemed essential to maintain the required 0.01° repeatability so that mechanical limitations would not affect measurement results. The polarizers are mounted in stepper motor driven stages with 0.01° readout. Stages from three separate vendors were tested against a machine shop rotary stage calibrated to 0.0006°. Two vendors were found to be accurate to within one step (±0.01°) over the full 360° range and they exhibited no backlash in agreement with their performance specifications. The third vendor did not meet their own specifications and the stages were not suitable without improvements. In general, when accuracies of this order are needed, vendors specifications should be checked.

A great deal of time was spent selecting the proper polarizer for each instrument and wavelength range. Some of the parameters which must be considered are extinction ratio, beam deviation, and wavelength coverage. In addition, it was deemed essential that the optics be transparent in the visible for ease of alignment. Table 4 itemizes the polarizers that were considered for the three instruments.

Table 4. Some polarizer options which cover the 3.39-4.00 μm Range and are transparent in the visible. All of these polarizers were purchased and tested at UDRI except for the Glan prism.

Type	Extinction Ratio at 3.39-4.00 μm	Beam Deviation (mr, half angle)	Angular [1] Acceptance (degrees)	Transparent [2] Range (μm)
Cd Te reflection	10,000	2	0.5	visible -23
ZnSe Stacked Plates (six)	800	0.3	2	0.6-17
Rutile Glan Prism (TiO_2)	10,000	0.2 [4]	2	0.5-5.0
Grid on $BaF1_2$ Substrate	43	< 0.1	15	0.2-12
Ion Beam Etched Grid on ZnSe	5000	< 0.1	10	0.6-17
Dichroic Calcite	6000 [3]	< 0.1	15	visible -16

1 This is the angular offset from the optical axis in the critical plane which lowers the extinction ratio by approximately half.

2 Although the material is transparent over this range the polarizing properties may be minimal off the design wavelength for some types.

3 Only near 3.39 μm (also excellent at 4.00 μm).

4 Deviation can only be reduced to this value with a compensating wedge which is attached to the prism.

The cadmium telluride reflection polarizer was examined because of the high extinction coefficient it offers. This is overshadowed, however, by its large beam deviation, difficulty of alignment, and large size. The beam deviation can, of course, be reduced to an acceptable level but this would require an even more cumbersome mount. This type of polarizer is excellent for an application in which beam deviation is of no concern (non-rotating application) and for high-power, fixed wavelength lasers.

The zinc selenide stacked plate polarizers offer the advantage of a moderate extinction coefficient over a very broad wavelength range. They, unfortunately, suffer from beam deviation which is barely tolerable. Beam deviation is an important parameter in the ellipsometer since rotation of the polarizer or analyzer can offset the null position if the beam is deviated off the detector. Stacked plate polarizers were obtained from two separate vendors and in both cases the typical beam deviation was 0.3 milliradians even though efforts were made to select units with low deviation.

These polarizers are still attractive for their broad wavelength coverage and they may be the only alternative for the automated ellipsometer which must operate from 1 to 12 μm.

There are materials suitable for fabrication of Glan prisms in the 3 to 4 μm range. The advantage of this type of polarizer is a very high extinction ratio over a wavelength range of about 1 micron. However, beam deviation is again just marginally acceptable. Two of the three vendors contacted were willing to guarantee 0.2 mr deviation or less but only with the addition of a compensating wedge. This wedge would be rotated with respect to the prism and then fastened in place to cancel any beam deviation from the prism.

Traditional infrared grid polarizers offer very low extinction ratios in the 3 to 4 μm range although their extinction does improve with longer wavelength. The unit tested at 3.39 μm had a line spacing of 0.25 μm yet only provided an extinction ratio of 43. This is in contrast to an ion beam etched grid polarizer (not commercially available) with a line spacing of 0.3 μm and an extinction ratio of 5,000 at 3.39 μm. We have not examined these polarizers in sufficient detail to explain the difference in extinction but we are having several ion beam etched grid polarizers fabricated for possible use on ARPE[4]. This strong distinction in performance should lead to a renaissance in infrared ellipsometry if the ion beam etched grids yield this high extinction over a broad wavelength range.

Dichroic calcite is an excellent polarizer choice for the helium-neon wavelength of 3.39 μm and also for other specific wavelengths[5]. Units with a 2-cm aperture are available at very low cost and they are the type of polarizer used on the single wavelength DOF ellipsometer. We also use them on the OCEL ellipsometer at 3.39 and 4.00 μm because of the high extinction ratio. Table 5 gives the measured extinction ratio for this type of polarizer at selected wavelengths between 3.39 and 4.00 μm.

Table 5. Measured extinction ratio of dichroic calcite polarizers 1mm thick. The bandwidth for these measurements was $\leq$ 0.01 μm.

Wavelength (μm)	Extinction ratio
3.39	6000
3.60	5
3.80	140
4.00	2000

The choice for an adjustable compensator was a much easier task than polarizer selection. Table 6 shows the two materials available in the form of Babinet-Soleil compensators. Magnesium fluoride is the most appropriate material because of its lower cost and lower index. Cadmium sulphide is needed for operation beyond 6.5 μm. However, there are 3 components and thus 6 surfaces in a Babinet-Soleil compensator which leads to an unacceptably low transmission of only 35% for cadmium sulphide. The use of a broadband AR coating on all surfaces is necessary to raise transmission to about 90% over a selected wavelength range.

Table 6. Babinet-Soleil compensator choices for the 3.39-4.00 μm wavelength region which are also transparent in the visible. Compensators made with both materials were purchased and tested at UDRI.

Material	Wavelength coverage	Ordinary index at 3.39 μm
magnesium fluoride (MgF_2)	0.12-6.5 μm	1.4
cadmium sulphide (CdS)	0.6-14	2.3

The choice of a source-detector combination for the OCEL ellipsometer was limited by bandwidth and signal level considerations. A Nernst glower source with a monochromator for wavelength selection required a high detectivity detector such as LN_2 cooled indium antimonide because of low signal levels for bandwidths less than 0.1 μm. In addition the depth of null obtainable (and thus the null position accuracy) was limited by ambient noise. A diode laser was selected to provide adequate power (1/2 mw) in a narrow bandwidth (0.01 μm) tunable over the 3.6 to 4.0 μm range[6]. An uncooled lead selenide detector provides sufficient sensitivity so that null position accuracy is limited by polarizer mount accuracy rather than depth of the null. A 3.39 μm helium neon laser covers this standard wavelength on the OCEL ellipsometer and facilitates comparisons with measurements made on the DOF ellipsometer. The choice of a source for ARPE is defined by the 1 to 12 μm wavelength coverage. A Nernst glower in conjunction with a monochromator is the only means of covering this wavelength range. A dual element (InSb and HgCdTe) LN_2 cooled detector will permit bandwidths of 1% without compromising system accuracy.

3. Software

The computer software developed for these null ellipsometers is intended for use in an interactive mode with the ellipsometer operator. There are four basic functions the software can perform: 1. find initial zone settings; 2. calculate optical constants from data; 3. model non-ideal instruments; 4. develop a correction matrix for a non-ideal instrument. In addition, specialized software is being developed for ARPE.

The use of four zone measurements is usually essential with a null type ellipsometer to cancel certain unavoidable component errors. The NULLSYS program calculates the polarizer and analyzer settings for each of the four zones when the operator enters a guess at the complex index of the sample and the angle of incidence. These zone settings assume an ideal instrument and a single interface at the sample surface. Measurements are usually based on the procedure of setting the compensator for quarter-wave retardation at an azimuth of $\pm$ 45° to simplify calculation of the ellipsometric parameters, although the NULLSYS programs are not limited by this constraint.

The operator can quickly find the correct zone settings assuming the initial guess was good. These four pairs of polarizer-analyzer settings are then averaged to yield the ellipsometric parameters. NULLSYS can then be used to calculate the correct index of the material. If the sample is not a single interface but is made up of multiple layers, NULLSYS in conjunction with FILM[7] can calculate the ellipsometric parameters expected at a given angle of incidence. This calculation can be made regardless of the complexity of the multiple layers as long as the index and thickness of each layer are accurately specified. However, to measure indices of materials in multilayer samples is not necessarily possible unless the model is defined beforehand. Measurements at different angles of incidence along with an explicit model can yield indices and thicknesses through iterative techniques if approximate solutions are known. The case of a single layer on a substrate can in fact be solved analytically so that a measurement at a single angle of incidence will give the index or thickness of the layer if the substrate is known. Measurements at more than one angle of incidence are needed if neither index nor thickness of the layer is known, as is the case for the examples in the next section.

NULLSYS can also model optical flow through non-ideal components of a null ellipsometer and determine the correct null settings. Each component is specified using either Jones or Mueller calculus so that imperfections or limitations such as finite extinction ratios, depolarization, and extraneous components (such as vacuum chamber windows) can be correctly modeled. This procedure also allows a quick check on the effect of nonperfect components on final accuracy.

Special software was developed for the DOF ellipsometer to deal with equipment and data taking constraints. Figure 3 shows the optical layout of the DOF ellipsometer. All components are mounted on a single granite bench located under a large vacuum deposition chamber. The optical beam path is turned upward into the deposition chamber where it reflects from the sample and is returned to the rail. There are two vacuum chamber windows plus up to four mirrors in the chamber which affect the beam in addition to the sample. Mirrors are required in the chamber because of complex reflecting surfaces on the sample. The turning mirrors on the rail are configured in two orthogonal pairs to cancel effects of any differential phase or reflection coefficients. The intent is to monitor ellipsometric parameters while a sample is being coated. The polarizer and analyzer will be preset to provide a null when the sample reaches the desired differential phase and reflection coefficients. This will clearly require a calibration technique for the instrument which accounts for: 1. lack of time to do four zone measurements; 2. birefringence in the vacuum chamber windows; 3. effects of turning mirrors. The NULLSYS program will do this by deriving a correction matrix for the instrument from measurements on known samples. Three samples will be characterized in the OCEL ellipsometer and then measured in the DOF ellipsometer at the same angle of incidence. The DOF data, which contains the effects of the extraneous components, will be used by NULLSYS to develop a correction matrix for the ellipsometer in that particular configuration. This correction matrix will be universal in the sense that it should correct for all instrument limitations from a single zone measurement.

The ARPE ellipsometer will require specialized data reduction software distinct from the null ellipsometer programs. The real time nature of the ARPE data, however, lends itself to error correction techniques similar to four zone averaging. A dedicated computer will handle all data reduction tasks plus operate the instrument and interface with the operator. Once the sample is inserted and the angle of incidence is chosen the computer will optimize instrument settings for maximum accuracy and also scan in wavelength.

4. Null Instrument Measurements

Initial measurements with the OCEL ellipsometer confirmed the 0.01° precision and repeatability that were desired. Components can be removed from the rail and the sample can be removed and replaced in its kinematic holder without altering the 0.01° repeatability on a particular sample. The instrument can be entirely disassembled and when it is assembled and recalibrated with respect to the new plane of incidence, measurements on a given sample repeat to 0.01°.

The question of absolute accuracy is not as easy to test with an ellipsometer. Sample uncertainties and the possibility of impurity monolayers on the surface can strongly affect measured parameters. Measurements at different angles of incidence on the same sample provide data which can be fitted to a model of the sample interface. This tests the accuracy of the model in describing the interface and also tests the accuracy of the ellipsometer with respect to angle-of-incidence changes. Table 7 shows an example of this type of measurement. Three separate samples were measured at three angles of incidence with the OCEL ellipsometer. The diode laser source was used at 3.80 μm with zinc selenide stacked plate polarizers. Each sample consisted of a layer of

material on a silver substrate. The complex index of the silver substrate was known and the index and thickness of the three layers was determined. These two parameters are not independent in reflection ellipsometry so an iterative technique was used with the software to find a consistent index and thickness at each angle of incidence. The data clearly shows very good repeatability for all three angles of incidence. The extinction coefficient of these layers is not accurately determined with this type of measurement because of its low value (about 0.001) and the thinness of the layers.

Table 7. Thickness and index determinations for three different layers on a silver substrate. The ellipsometric parameters were measured with four zone averaging.

Angle	ψ	Δ	T(A)	n
		Silicon (Si)		
70°	44.47	173.04	5270	3.643
55	44.72	175.68	5290	3.638
45	44.93	176.78	5294	3.643
		Silicon Oxide (Si O)		
70	44.77	-134.03	10,150	1.850
55	44.71	-165.27	10,140	1.850
45	45.12	-173.82	10,140	1.843
		Aluminum Oxide (Al_2O_3)		
70	44.66	-118.03	11,970	1.590
55	45.22	-159.49	11,950	1.588
45	44.80	-172.45	11,960	1.591

Wavelength, 3.80 μm
Assumed Index of Substrate, (1.4, 23)

Acknowledgment

A portion of this work is supported by the Air Force Weapons Laboratory, Kirtland AFB, NM 87117 under contract F29601-79-C-0027.

References

[1] Stobie, R. W., Rao, B., Dignam, M. J., Automatic ellipsometer with high sensitivity and special advantages for infrared spectroscopy of adsorbed species, Appl. Optics 14 999 (April 1975).

[2] Aspnes, D. E., Studna, A. A., High precision scanning ellipsometer, Appl. Optics 14 220 (January 1975).

[3] Azzam, R. M. A., and Bashara, N. M., Ellipsometry and Polarized Light, North Holland, New York, 1977.

[4] Garvin, H. L., Garmire, E., Somekh, S., Stall, H., and Yariv, A., Ion beam micromachining of integrated optics components, Appl. Optics 12 455 (March 1973).

[5] Bridges, T. J., and Kluver, J. W., Dichroic calcite polarizers for the infrared, Appl. Optics 4, 1121 (Sept. 1965).

[6] Laser Analytics, Inc., 25 Wiggins Ave., Bedford, MA 01730, Model LSA.

[7] Loomis, J. S., FILM - A program for design and evaluation of multi-layer thin-film optical coatings, (June 1977) available from UDRI, KL-102, Dayton, Ohio 45469.

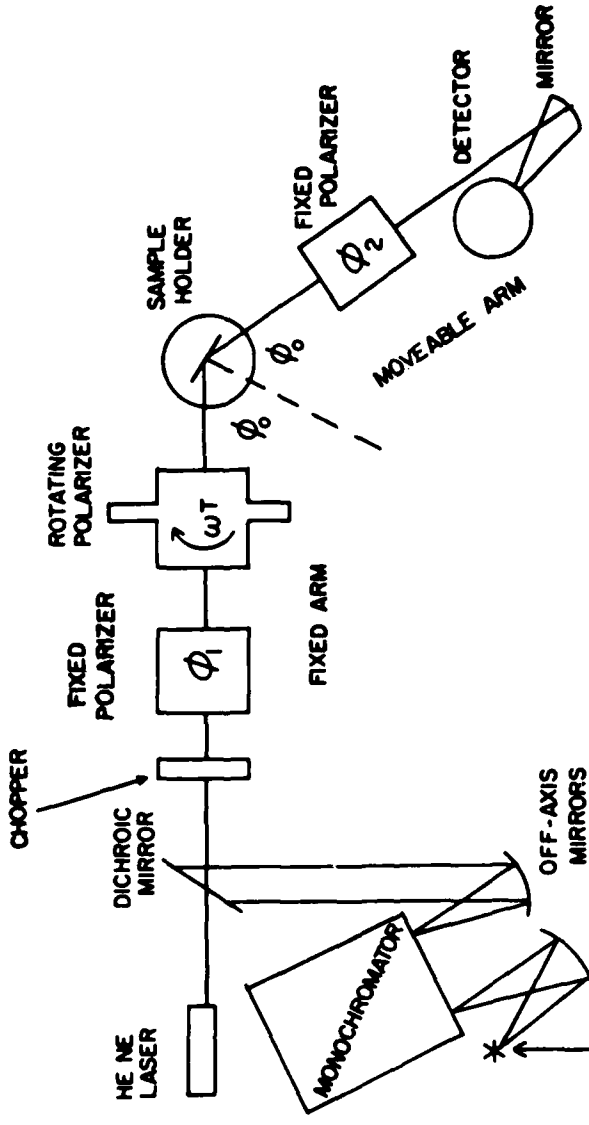

Fig. 1. Major components of the automated rotating polarizer ellipsometer (ARPE).

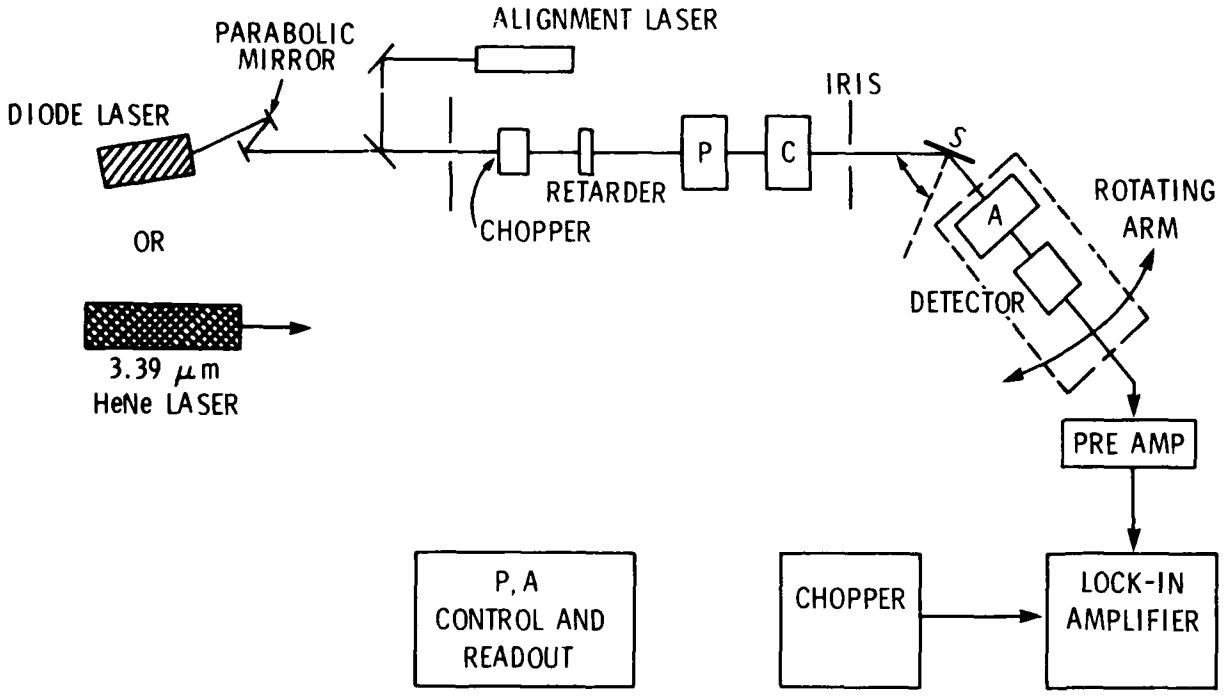

Fig. 2. The major optical and electronic components of the OCEL ellipsometer shown in the polarizer compensator sample analyzer (PCSA) configuration.

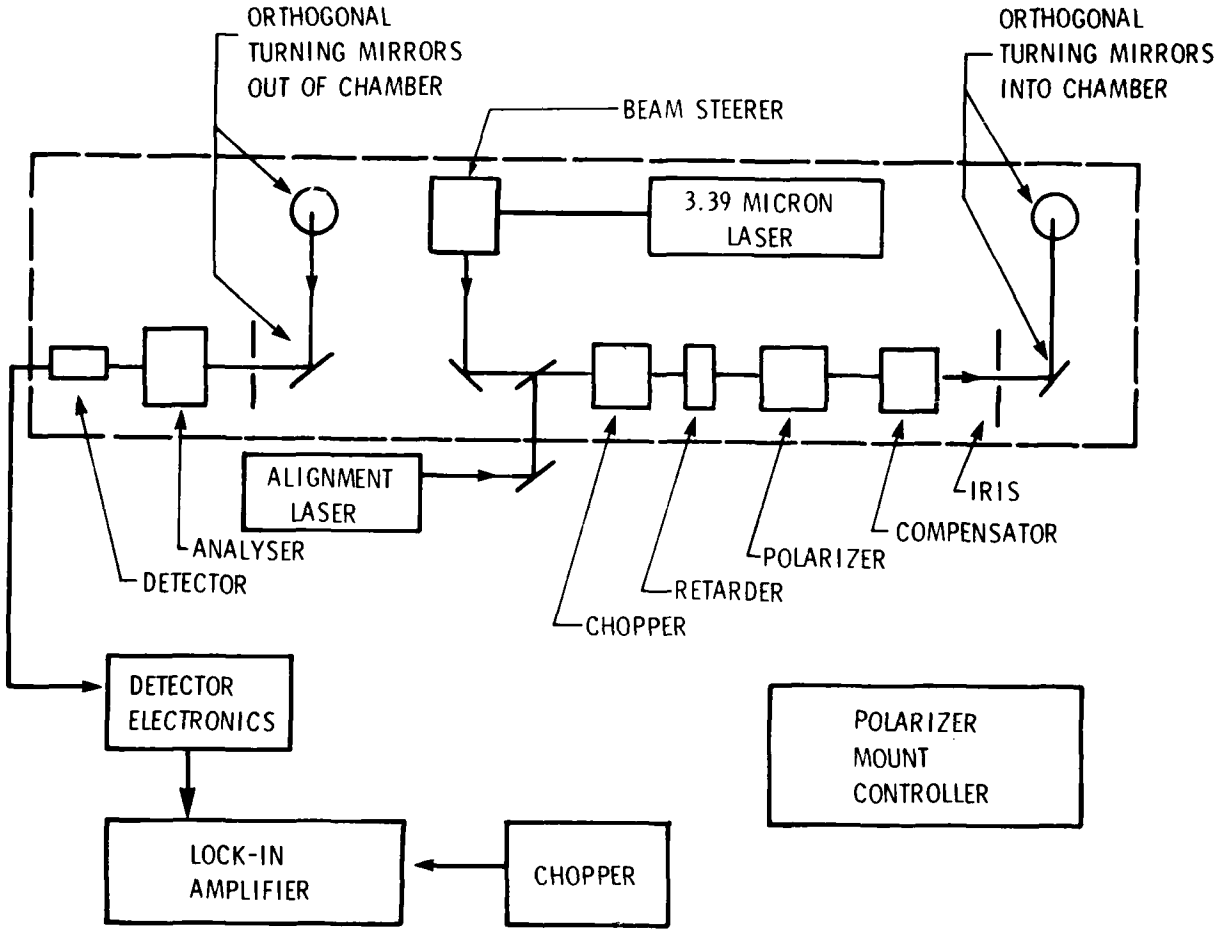

Fig. 3. Optical layout of the DOF ellipsometer shown in one of several possible arrangements which will mate to the vacuum chamber windows.

The question of using germanium polarizers was raised. The author replied that they used cadmium telluride instead because they wanted the instrument to be able to be aligned visually. They also used ion beam etched zinc selenide; the resulting polarizer was surprisingly good.

MULTILAYER THICKNESS UNIFORMITIES REQUIRED TO MEET WAVE FRONT ERROR TOLERANCES IN LASER MIRRORS*

H. E. Bennett and D. K. Burge
Michelson Laboratory, Physics Division
Naval Weapons Center, China Lake, California 93555

The wave front error tolerance per mirror in typical laser optical trains is quite severe. Expressed in terms of an equivalent figure error in the visible region, values of an eighth wave are not uncommon for mirrors in infrared systems, and values of one hundredth of a wave have been suggested for mirrors in some ultraviolet laser optical trains. The effect of figure error, i.e., error in the geometrical shape of the mirror, is well known and for a metal-coated mirror is the only one of significance. However, if the mirror has a multilayer dielectric coating, an additional apparent figure error may be introduced by the physical thickness and phase change differences produced by coating thickness nonuniformities. This source of wave front error has been largely unrecognized but can be significant. For example, a 2% variation in thickness uniformity for a typical infrared multilayer coating may create a wave front error at the operating wavelength equal to that produced by a mirror whose optical figure is in error by an eighth wave in the visible. The entire wave front error tolerance for the mirror may thus be used up by a slightly nonuniform coating. Such wave front errors usually cannot be determined unambiguously by interferometric measurements made in the visible region. If multilayer dielectric mirrors are used, the wave front error should thus ideally be measured at the operating wavelength, often a difficult task. A discussion is given of thickness uniformity requirements for dielectric multilayer films and possible ways to achieve this uniformity.

Key words: Film thickness nonuniformity; high power laser mirrors; multilayer dielectric films; optical figure measurement; vacuum deposition techniques; wave front distortion.

Introduction

The objective in many laser applications is to deposit the laser energy efficiently in a small area. If the output wave front is aberrated, the peak of the focussed intensity falls approximately exponentially as the root-mean-square (rms) wave front distortion increases [1,2][1]. A diffraction-limited system is one in which this wave front distortion reduces the peak intensity to not less than 80% of its maximum height [3]. The maximum rms wave front distortion in this case is approximately $\lambda/14$, the well-known Maréchal criterion. A twice-diffraction-limited system has an rms wave front distortion of $\lambda/7$, and so on. The peak intensity does not decrease by as much as a factor of two for a two-times diffraction-limited system, and the integrated intensity over the focal spot does not decrease as rapidly as the peak intensity; so failing to meet the Maréchal criterion does not mean the system is unacceptable. However, it is a convenient design goal around which to plan an optical train.

In order to achieve a given rms wave front distortion in the output beam, an error tolerance for each of the individual components in the optical train must be established. In an actual design, this error budget would take into consideration the flux falling on the mirror, the mirror size, and various other factors. As a first approximation, however, one can assign equal error budgets to all components. The peak-allowed figure error for mirrors is then τ_{fm}, where [4]

$$\tau_{fm} = \sqrt{\frac{\lambda^2}{10\pi^2 N} - \frac{2}{N}\sigma_T^2} \quad . \tag{1}$$

Here σ_T^2 is the thermally induced figure error for the optical train, and N is the number of components in the train. In figure 1 a plot of mirror figure requirements for an optical system containing ten components and operating at the nominal deuterium fluoride (DF) wavelength (3.8 μm) is compared to those for a similar system operating at 10.6 μm, the nominal CO_2 wavelength. The thermal distortion requirements are quite severe even at CO_2 wavelengths, particularly if distortions in the various mirrors are correlated, indicated by the subscript cor, rather than uncorrelated, indicated by unc. The better the initial optical figure, the more tolerance is allowed for thermal distortion. However even if no thermal distortion is allowed, the optical figure tolerances at DF wavelengths are approximately an eighth wave in the visible wavelength region, indicated by $\lambda_V/8$. (Since opticians check optical figure in the visible region, the infrared figure error is given here as its equivalent in visible wavelengths. At the operating wavelength, 3.8 μm, the actual figure error corresponding to $\lambda_V/8$ would be approximately $\lambda/50$.)

The figure error at the operating wavelength is the result of two contributing processes: (1) optical polishing and (2) coating. Unfortunately, the latter contribution has been virtually unrecognized. It is again composed of two parts: (1) the contribution from the physical thickness variations of the thin film coatings across the mirror and (2) the contribution from differences in phase change on reflection. For metal coatings, these effects are both negligible since the coatings are thin, typically 1000-1500 Å, so the physical thickness variations are very small even for a large percentage film nonuniformity, and differences in phase change result only from variations in the

*Work supported by the Defense Advanced Research Projects Agency.
[1]Figures in brackets indicate the literature references at the end of this paper.

complex index of refraction of the metal across the mirror, not from interference effects between layers. Variations in index of a deposited metal film are negligible if good coating procedures are used. For dielectric coatings, it is quite a different story. The films are thick, typically 4000-6000 Å or more for each film of a multilayer dielectric (MLD) coating designed for a wavelength of 3.8 μm, and there are eight to twelve films in most multilayer stacks. A scale drawing of a typical MLD coating for 3.8 μm is shown in figure 2. The four-layer-pair $(ZnS/ThF_4)^4ZnS^xAg$ MLD coating in this case is over 50 times as thick as the metal coating alone. A thickness variation of 1% in each coating layer, if cumulative, will be seen to cause an equivalent figure error (EFE) in this coating of half the allowed $\lambda_V/8$. A thickness variation of 2% in the multilayer coating thickness will allow no tolerance at all for the optical polisher.

This MLD film effect, although not well known, has been verified experimentally. A few of the optical companies have had feedback from customers who have tried to use MLD coatings for critical applications. It has also been reported in the literature, as Professor H. A. Macleod, author of the book Thin-Film Optical Filters, pointed out when one of the authors brought up this problem. A letter in Applied Optics in 1967 by Ramsay and Ciddor of Australia reported [5] the effect in a multilayer film they deposited for the visible region. It consisted of quarter wave pairs having the design $(ZnS/MgF_2)^6ZnS$ on a Homosil (silica) substrate. The thickness nonuniformity of the coating was approximately 2% from center to edge. They found that the apparent optical figure of the part varied from concave to flat to convex, depending on the wavelength at which the measurement was made. A reproduction of the illustration in their paper showing this effect is given in figure 3.

Achieving the necessary coating uniformity for laser applications is not too difficult for small mirrors. However, there is no relaxation in uniformity requirements as the mirror size increases; whereas, the difficulty in achieving uniform coatings increases rapidly as mirror size increases. Achieving sufficiently uniform coatings on large mirrors designed for laser applications will thus pose a challenging problem for the optical coating industry.

Theory

To understand the effect, consider an optical flat. Its optical figure is defined as the variation in optical path length between the surface of the flat and a flat reference surface. This optical path length is given by the interference equation, which if the standard sign conventions are followed [6] and $\bar{n} = n - ik$, where $\bar{n}$ is the complex index of refraction, and n and k are the real index and extinction coefficient, respectively, is written

$$N\lambda = 2d - (\beta_1 + \beta_2)\lambda/2\pi \quad , \tag{2}$$

where N is the order of interference, λ the wavelength, d the physical separation between the flat and the reference surface, and β_1 and β_2 are the phase changes on reflection at the flat and reference surfaces. Since β_1 are β_2 are positive quantities, the optical path length is less than the physical path length. If a film is now deposited on the flat, the interference equation becomes

$$N'\lambda = 2d' - (\beta_1' + \beta_2)\lambda/2\pi \quad , \tag{3}$$

where the phase change at the film-covered surface is β_1' and $d - d' = t$, the film thickness. The change in optical path length $(N-N')\lambda$ is then

$$(N-N')\lambda = 2t - (\beta_1 - \beta_1')\lambda/2\pi \quad . \tag{4}$$

If the change in optical path length across the flat is spatially invariant, the apparent figure of the flat after coating is unchanged. However, if it varies spatially either in thickness or in phase change on reflection, the apparent figure will change after coating. The resultant fringe error ΔN is then obtained by subtracting eq. (4) for one film thickness from itself using a different film thickness and hence another value of β_1'. If we define the film thickness at the design value to be t_o and the phase change to be β_o, then changes in these parameters will give a fringe error given by

$$\Delta N = \frac{2}{\lambda}(t_o - t) + \frac{\beta_o - \beta}{2\pi} \quad , \tag{5}$$

where t and β are now the values for the off-design film. Equation (5) was used in calculations for the coating considered in figure 4. An index of 2.25 was assumed for ZnS and 1.51 for ThF_4. Quarter waves were assumed for all layers except the ZnS next to the Ag-coated substrate. The multilayer was assumed to be tuned to 3.8 μm, so that the quarter wave film thicknesses were 4222.2 Å for ZnS and 6291.4 Å for ThF_4. To correct for the phase change of Ag, the thickness of the final ZnS layer was then 8236.7 Å. The total thickness of the multilayer stack was 5.03 μm. Tolerances on DF laser mirrors of $\lambda_V/8$ suggested in figure 1 correspond to a fringe error of approximately 0.040, or a thickness variation of 2% over the mirror surface. Since some of the tolerance must remain with the optical polisher (they would like to have all of it), the tolerance on coating thickness variations across the mirror should be 1% or better.

If we disregard the contribution of the phase change for the moment, the significance of the sign of ΔN and the EFE caused by film nonuniformity will become clear. Imagine the figure test to be made between a flat to be tested and a slightly inclined flat master. If the flat to be tested is coated with a uniform film, fringes will be formed which are parallel to the axis of the wedge. If locally the film thickness is increased, the air space will decrease, and the fringes will be shifted locally toward the wedge axis. In this case, ΔN will be negative. If we define the EFE as positive when the film thickness is increased, then the EFE is positive when the fringe shift ΔN is negative and equals $-\Delta N/2$, since the change in optical path length equals twice the change in thickness. The EFE is then

$$EFE = (t - t_o)/\lambda + (\beta - \beta_o)/4\pi \quad , \tag{6}$$

where a positive EFE at the edge of a flat relative to its center makes the part concave.

Consider now the effect of phase change on reflection on the EFE. By our sign convention, when the multilayer films are a quarter wavelength in optical thickness, $\beta_0 = 180°$. If the films become thicker than a quarter wave, the phase angle decreases so that the two terms in eq. (6) are of opposite sign. Table 1 gives values of the phase term and the EFE for a typical multilayer infrared reflector design. (In this example, the Ag film is assumed to be of uniform thickness.) More refined designs are used in practice, but the design $(ZnS/ThF_4)^4ZnS^xAg$ illustrates the principle.

Table 1. Equivalent figure errors caused by film nonuniformities for $(ZnS/ThF_4)^4ZnS^xAg$ film designed for 3.8 μm.

$t - t_0$	0%	1%	2%	3%	4%	5%
$\beta_{3.8\ \mu m}$	180.0°	177.6°	175.2°	172.2°	170.2°	167.6°
$EFE_{3.8\ \mu m}$	0.00	0.01	0.02	0.03	0.04	0.05
$\beta_{0.63\ \mu m}$	174.6°	96.9°	-74.6°	-161.9°	-226.5°	-381.4°
$EFE_{0.63\ \mu m}$	0.00	-0.03	-0.19	-0.23	-0.24	-0.37

Commonly, the control of film thickness in multilayer high reflectance coatings is associated with the decrease in reflectance observed if the deposited layers are too thick or too thin so that the "match point" is missed. Some coating facilities have developed computer programs to calculate how much "undershoot" is needed on the next layer to compensate for the "overshoot" if a layer is too thick. This problem is quite different from that discussed here. In our case, coating uniformity across the part, not coating thickness per se, is the important parameter. A coating whose layer thicknesses are badly off will exhibit no EFE if the layer thicknesses are uniform across the part. Conversely, layer thickness nonuniformity will not strongly affect the reflectance of a mirror provided the layer thicknesses are close to the match point. In the example shown in figure 4, a nonuniformity of 5% in layer thickness changes the reflectance by only 6 parts in 10^5. A decrease of this magnitude would be undetectable even with the best measuring instruments. However, the same nonuniformity causes an EFE which exceeds the assigned total figure error budget of $\lambda_V/8$ by 2.5 times.

Figure Measurement

Optical figure measurements are normally made in the visible region, usually at a wavelength of 0.633 μm. Before the advent of the HeNe laser, they normally were made at 0.546 μm, the mercury green wavelength. The wavelength was not very important as long as only the geometrical shape of the mirror was being measured. However, if the mirror is MLD coated, the wavelength becomes very important. If the design wavelength is not in the visible region, an additional serious complication is introduced since the optical figure measured at any visible wavelength is not easily related to that at the wavelength where the part is to be used. Thus, not only is it difficult to achieve sufficient film uniformity, but it is also difficult to check whether or not it has been achieved. Figure 5 illustrates this point. It shows the calculated reflectance of a $(ZnSe/ThF_4)^4$ film on CaF_2 designed for high reflectance at a wavelength of 10 μm. Since this MLD coating is deposited on a dielectric rather than a metal, the maxima and minima are emphasized. Notice the rapid variation of reflectance with wavelength in the visible region. This variation causes the phase change on reflection to also vary rapidly with wavelength in the visible region, as seen in figure 6, making it difficult or impossible to accurately deduce optical figure at the design wavelength from figure measurements made using a HeNe laser.

Figure 7 shows a comparison of the EFE at 0.6328 μm and at 3.8 μm for the coating described in figure 2. No correction for the change in index of refraction with wavelength was made in these calculations, so the quantitative results given indicate concepts, not the actual performance of this MLD system. It happens that the ratio 3.80/0.6328 = 6.005 so that if dispersion of the index is ignored, there is an inflection point in phase change nearly at the HeNe wavelength if the film thicknesses are exactly correct. The phase angle in the visible is strongly affected by the secondary maxima, however, and varies rapidly with thickness error. It also happens in this example to have a slope which is opposite in sign to that in the infrared. Thus, an MLD coating which is too thick in the center of the mirror would make the mirror appear to be slightly convex at 3.8 μm but would make it appear concave at 0.6328 μm. If the variation in thickness were gross, it could be picked up by the visible figure measurements, since the EFE decreases monotonically with increasing thickness error in the visible. The relationship is not linear, however, so exact correlation between the visible and infrared figure errors will be exceedingly difficult. If the percentage thickness errors for the various films were not all the same, the picture would become even more complicated. It is thus not clear that the equivalent figure at 3.8 μm could be derived to the required accuracy from measurements made using a HeNe laser.

If the nominal film design is known, it may be possible in principle to deduce the film-induced figure error in the infrared by measuring the apparent figure error at a variety of wavelengths in the visible region using a dye laser, combining these measurements with those made in the near infrared, and deducing the infrared figure error. Several possible difficulties are apparent. Reliable values for the wavelength dispersion of index of refraction for materials in thin-film form will be required. Also, we have been assuming that the thickness of each film was in error by the same percentage, which will not necessarily be true in an actual situation. Finally, the film design must be known in detail, and variations in thickness observed during the coating run should be available to make visual analysis successful. It will be difficult to obtain this data in most cases.

A more satisfying approach is to measure the optical figure directly at the operating wavelength. In the case of the 3.8-μm film, this approach would require a sensitivity of better than 1/50th wave at 3.8 μm, a difficult task. However, infrared interferometers have been developed with very good fringe sensitivity. Kwon, Wyant, and Hayslett, for example [6], describe an infrared Twyman-Green interferometer which used with a CO_2 laser achieved a sensitivity estimated as $\lambda/10$ at a wavelength of 10.6 μm and was limited by the number of resolution elements in the vidicon. Wyant estimates [7] that using a point diffraction interferometer (a half wave plate with a pinhole in it) and a 32-element linear pyroelectric array detector, it should be possible to obtain figure measurements at 3.8 μm with an accuracy of $\lambda/128$.

Another approach giving information on film-induced apparent figure changes utilizes a scanning reflectometer to measure the reflectance as a function of wavelength over the mirror surface. Figure 8 shows the theoretical reflectance as a function of wavelength for the multilayer design of figure 2, assuming there is no absorption in the films and no interface absorption. Of particular interest are the minima on either side of the quarter wave point. The drop in reflectivity is not large – only about 4% – and both the magnitude and wavelength position of the dip are affected by absorption in the coatings as well as by film thickness errors, so significant uncertainty is present in the test. However, it provides a fairly direct measure of the film behavior near the operating wavelength and is a strong argument for developing a scanning reflectometer with wavelength capability for evaluating large MLD-coated infrared mirrors.

Still another approach is to determine the Optical Transfer Function for the mirror at the operating wavelength directly. By monitoring the image formation capability of the mirror and hence the ratio of the on-axis focussed intensity to the flux imaged by the mirror, the rms wave front distortion can be determined. Although this technique will probably not be as sensitive for a single mirror element as an interferometric figure measurement, it has the advantage of directly measuring the quantity of interest, namely, the achievable focussed intensity.

Coating Chamber Design

The foregoing analysis establishes the requirements which have to be met by the coating system. It must be capable of depositing MLD coatings uniform to 1% or better in thickness. It is important to realize that meeting this requirement represents a significant advance in the state of the art of depositing dielectric coatings. No coatings as uniform as this have ever been deposited on large substrates. Statements by systems houses that coating technology is well established and therefore need not be of concern are a disservice to the technical community and reveal a lack of understanding of the coating process as applied to large optics. A major effort will be required to meet this challenge.

A discussion of techniques for depositing uniform films should begin with a theoretical analysis of the problem. Theoretical treatments of film deposition uniformity are all based on one of two models for the evaporation source. Either it is assumed to be a point source, in which case the material emitted has a distribution

$$dm = (m/4\pi)d\omega \quad , \tag{7}$$

where m is the total mass of material emitted and dm that emitted into solid angle $d\omega$, or it is a Lambertian source, in which case

$$dm = (m/\pi)\cos\phi d\omega \quad . \tag{8}$$

In practice, sources usually tend to be most nearly Lambertian. Using eqs. (7,8), if the material is deposited on a surface element dS of the substrate whose normal is at an angle θ to the line connecting dS and the source, then $d\omega = (dS\cos\theta)/r^2$, where r is the source-to-substrate distance. Letting ρ be the mass of the deposited film of thickness t and letting $dm = \rho t$ so that dS is the unit area, we obtain for a point source

$$t_p = \frac{m}{4\pi\rho}\frac{\cos\theta}{r^2} \quad , \tag{9}$$

and for a Lambertian source,

$$t_\ell = \frac{m}{\pi\rho}\frac{\cos\phi\cos\theta}{r^2} \quad , \tag{10}$$

where t_p and t_ℓ are the film thicknesses deposited from a point source and a Lambertian source, respectively. Equations (9,10) are the basic equations used for estimating the thickness uniformity of films deposited under various deposition geometries. If the substrate is parallel to the source plane so that $\phi = \theta$ and if the distance between the source plane and the substrate plane is h so that $\cos\theta = h/r$, the film thickness from a point source is given by

$$t_p = \frac{m}{4\pi\rho}\frac{\cos^3\theta}{h^2} \quad , \tag{11}$$

and from a Lambertian source by

$$t_\ell = \frac{m}{\pi\rho}\frac{\cos^4\theta}{h^2} \quad . \tag{12}$$

For Lambertian sources, the film thickness obtained for a given mass of material evaporated then decreases as the square of the vertical source-to-substrate distance and as the fourth power of the cosine of the angle. Thus, if the source is positioned directly below the substrate, the diameter of the circular area on the substrate having a thickness uniformity within 1% of that directly above the source is 0.14 h. For a 4-m-diameter mirror, the coating distance required to achieve 1% uniformity would then have to be over 28 m, or about 94 feet. To obtain a 10-μm-thick film of a material such as ZnS having a density of 4 gm/cm^3 at this distance would then require over 35 g of evaporant. Since the mean free path is approximately [9] 5×10^{-3}/(pressure in torr), the vacuum in the chamber should then be $\sim 10^{-7}$ torr.

To obtain a more manageable size chamber, several approaches may be taken. The first is to place a stationary mask over much of the mirror, which then will rotate behind the mask about an axis either passing through or displaced from the source and cut the mask aperture to produce uniform deposition on the mirror. If the source were centered under the mirror, the mask would to a first approximation be a $\cos^4\theta$ function. If a short coating distance were used for a large mirror, effects caused by nonnormal incidence deposition could be minimized by exposing only the mirror radius and not centering the source under the mirror. A second approach is to offset the source from the axis of rotation of the mirror and choose the source-to-substrate distance and source offset to maximize

film uniformity. A mask will still be needed to correct for the residual error remaining. A third approach, one which is frequently followed when very uniform coatings are required, is to use a double-planetary arrangement for the substrate mount so that the substrate performs an epicyclic motion about the source axis. It is also possible to think of moving the source rather than the substrate to produce film uniformity. Such a system has been built, operates effectively, and has been patented [10], but has not gained acceptance in the coating industry because of its additional complexity. It is mathematically equivalent to rotation of the substrate.

The choice of source-to-substrate distance and source offset is important for a rotating substrate scheme and may be optimized. For example, if the substrate to be coated is concave and a source having a point source distribution function were placed at the center of curvature of the substrate, it would produce a uniform coating over the entire substrate surface. Double-planetary systems are often tilted to approximate this situation. If the source is Lambertian, it should be mounted at the surface of the sphere of which the substrate to be coated is a part rather than at its center for maximum uniformity. In the more general case of a planar substrate, the relationships are more complicated. The geometry of this case is shown in figure 9. For a Knudsen (Lambertian) source, the distribution of film thickness is given by [11]

$$t = \frac{m}{\pi\rho} \frac{h^2(h^2 + s^2 + d^2)}{[(h^2 + s^2 + d^2)^2 - 4s^2d^2]^{3/2}} \tag{13}$$

The ratio t/t_o, where t_o is the thickness of the film at the axis of rotation of the substrate, is then

$$\frac{t}{t_o} = \frac{(h^2/d^2 + 1)(h^2/d^2 + s^2/d^2 + 1)}{[(h^2/d^2 + s^2/d^2 + 1)^2 - 4s^2/d^2]^{3/2}} \tag{14}$$

Plots of thickness variation [12] as a function of s/d for various values of h/d are given in figure 10. When $h \sim d$, i.e., the substrate height is approximately the same as the source offset, the coating thickness increases toward the edge of the substrate. As the height increases relative to the offset, the coating thickness becomes greatest at the center and falls off more and more rapidly as the edge is approached. In the region $1.3 < h/d < 1.4$, the best uniformity is achieved consistent with a monotonically decreasing thickness toward the edge. The worst uniformity is found when $h/d \sim 2.0$. It then begins to improve, and by the time $h/d = 10$, it is within 1% at all points on substrates having radii up to 70% of the source offset. For a 4-m-diameter mirror, the source-to-substrate distance required to achieve $h/d = 10$ is 28 m, which agrees with our initial simple calculation of the source-to-substrate height required for 1% uniformity. If the chamber is to be shorter than that, the optimum situation is to go to an h/d value of between 1.3 and 1.4 and accept the fact that masking will be required to remove the residual thickness nonuniformities. A significant improvement in coating uniformity is predicted [13] if the mirror to be coated is strongly concave rather than flat, as assumed above. If the mirror is strongly convex, the coating uniformity is predicted to be significantly worse than that obtained from the above equations.

Figure 10 can also be used to estimate the best thickness uniformity achievable using an unmasked double-planetary system. The results are formally the same as for the single-planetary system. However, in practice, double-planetary rotation gives significantly better uniformity, primarily because many sources tend to be strongly anisotropic. Figure 11 shows the distribution pattern of a typical electron beam source as an example [14]. The double-planetary motion averages out such nonuniformities. However, it doubles the diameter of the coating chamber.

Masking

Masking can significantly improve the uniformity of evaporated coatings and has in some cases been the primary technique for achieving coating uniformity. One of the most successful rotating mask systems [15] is shown in figure 12. The surface to be coated is above the top of the picture and thus is not shown. With this system, eleven- and thirteen-layer coatings of ZnS and cryolite were deposited on interferometer plates 20 cm in diameter with a thickness nonuniformity of less than 0.1% across the plate aperture [16].

Usually the mask shape is arrived at empirically. As systems become larger, this approach becomes very expensive, and analytic mask design becomes increasingly attractive [17]. In addition to the advantage of minimizing the amount of expensive tank time required to prove out a mask design, the analytical approach lends itself to special work geometries, such as highly curved surfaces, to achieving large monitor-to-work ratios to minimize monitoring errors and to the possibility of achieving much more uniform coating distributions than would be possible by cut-and-try methods without a prohibitive amount of time and labor.

Conclusion

Severe optical figure tolerances are required for individual mirrors used in the multielement optical train of a laser even though the laser is operating at infrared frequencies. The error in mirror figure is caused not only by the geometrical shape of the mirror but also by its coating. The coating contribution is negligible when thin metal films are used but can become very important when the coating is composed of MLD films. In order to meet typical mirror figure specifications in infrared laser systems, the thickness uniformity of these MLD films across the mirror surface must be about 1% or better. Such uniformities are difficult to achieve and become increasingly demanding as the diameter of the mirror to be coated increases. An additional complication is that the optical figure of the coated mirror can no longer be checked quantitatively using conventional visual techniques. The coating may even make the mirror appear convex in the visible region, although at the operating infrared wavelength it acts as if it were concave. One solution is to make the interferometric figure measurement at the operating wavelength in the infrared. Another is to measure the change in reflectance as a function of wavelength in the vicinity of the infrared design wavelength for the multilayer film and a third is to measure the Optical Transfer Function of the mirror at the design wavelength directly. Once the measurement problem is solved, there is still the problem of how to deposit such a uniform multilayer film on a large mirror substrate. By careful design of the coating chamber,

it is possible to optimize the coating uniformity. However, it appears that masking between the source and the substrate will still be required to achieve sufficiently uniform coatings for the most critical applications.

References

[1] Hogge, C. B., Butts, R. R., and Burlakoff, M., Characteristics of phase aberrated nondiffraction limited laser beams, in Laser Digest, Report AFWL-TR-73-131, Kirtland Air Force Base, NM (1973), p. 105.

[2] Loomis, J. S., Optical quality of laser windows, in Proceedings of the Fourth Annual Conference on Infrared Laser Window Materials, ed. by C. R. Andrews and C. L. Strecker, DARPA, Arlington, VA (1975), p. 281.

[3] Bennett, H. E., Factors limiting the energy transmitted by an optical train, in Laser Induced Damage in Optical Materials, ed. by A. J. Glass and A. H. Guenther (Academic Press, New York, 1981).

[4] Bennett, H. E., Thermal distortion thresholds for optical trains handling high pulse powers, NBS Special Publ. 462, 11 (1976).

[5] Ramsay, J. V., and Ciddor, P. E., Apparent shape of broad band, multilayer reflecting surfaces, Appl. Opt. 6, 2003 (1967).

[6] Bennett, Jean M., Precise method for measuring the absolute phase change on reflection, J. Opt. Soc. Am. 54, 612 (1964).

[7] Kwon, O., Wyant, J. C., and Hayslett, C. R., Rough surface interferometry at 10.6 μm, Appl. Opt. 19, 1862 (1980).

[8] Wyant, J. C., Optical Sciences Center, University of Arizona, Tucson, private communication, 1980.

[9] Yarwood, J., High Vacuum Technique (John Wiley and Sons, New York, 1956), p. 1.

[10] Thelen, Alfred J., Bergfelt, Nils H., and Eufusia, Eugene A., Vacuum coating apparatus utilizing rotating sources, U.S. Patent 3,382,843 (May 1968).

[11] Behrndt, K. H., Thickness uniformity on rotating substrates, in 1963 Transactions of the Tenth National Vacuum Symposium of the American Vacuum Society (Macmillan, New York, 1963), p. 379.

[12] Ramprasad, B. S., Radha, T. S., and Ramakrishna Rao, M., On uniformity of film thickness on rotating substrates, J. Vac. Sci. Technol. 9, 1227 (1972); On uniformity of film thickness on rotating substrates having a large source-to-substrate height, Thin Solid Films 20, 547 (1974).

[13] Bastien, R. C., Hasan, W., Kurdock, J. R., and Ledger, A. M., Large Optics Coating Chamber Study, Perkin-Elmer Report 14634A (20 June 1980).

[14] Graper, E. B., Distribution and apparent source geometry of electron beam heated evaporation sources, presented at the 1972 National Vacuum Symposium of the American Vacuum Society, Chicago, IL, October 1972.

[15] Netterfield, R. P., CSIRO, Division of Applied Physics, Sydney, Australia, private communication, 1980.

[16] Netterfield, R. P., Schaeffer, R. C., and Sainty, W. G., Coating Fabry-Perot interferometer plates with broadband multilayer dielectric mirrors, Appl. Opt. 19, 3010 (1980).

[17] Bloom, Arnold L., and Fischer, Dennis, Computer design of masks for coating tanks with planets, J. Opt. Soc. Am. 69, 1438 (1979), abstract only.

Figures

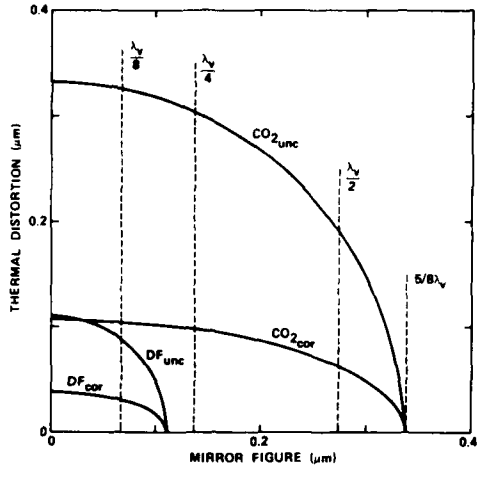

Figure 1. Initial mirror figure and allowed thermal distortion limit required for a ten-component diffraction-limited optical train if each component has an equal error budget. Dashed lines indicate the corresponding figure error in visible wavelengths.

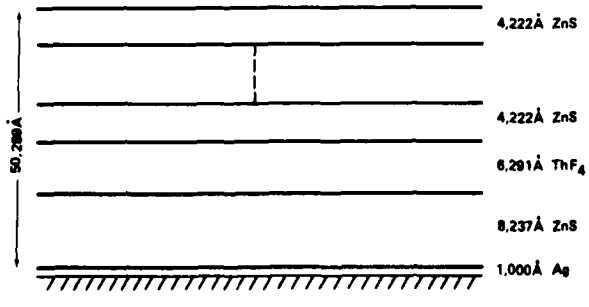

Figure 2. Scale drawing of a $(ZnS/ThF_4)^4ZnS^XAg$ multilayer film designed for a wavelength of 3.8 μm in the infrared region. Note the thickness of the dielectric layers is 50 times that of the metal layer.

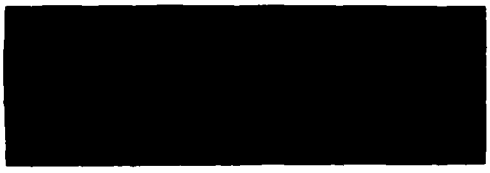

WAVELENGTH (nm)	APPARENT FIGURE
546	λ/60 CONCAVE
578	λ/∞ FLAT
644	λ/10 CONVEX

5 CM SUBSTRATE DIAM
2% FILM THICKNESS VARIATION
13 LAYER ZnS/MgF_2 COATING

Figure 3. Apparent change in optical figure at different wavelengths for a multilayer-coated mirror surface (after reference 5).

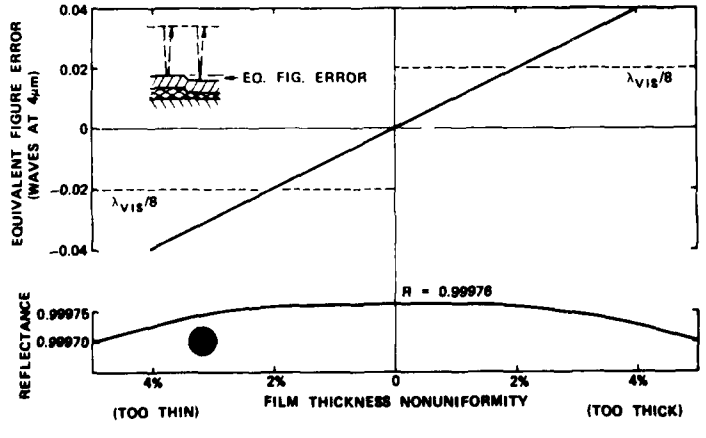

Figure 4. Equivalent figure error in a MLD-coated mirror caused by nonuniform film thickness across the mirror. The multilayer coating design is $(ZnS/ThF_4)^4$-ZnS^XAg, and the design wavelength is 3.8 μm. The dashed lines give the corresponding figure error in visible wavelengths. They would not be the observed figure errors if measurements were made in the visible, however, because of phase shift.

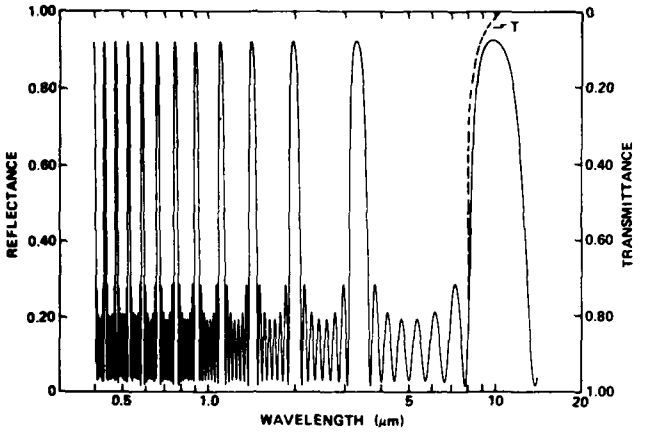

Figure 5. Calculated reflectance and transmittanceof a $(ZnS/ThF_4)^4$ multilayer film on a 25-mm-thick CaF_2 substrate as a function of wavelength.

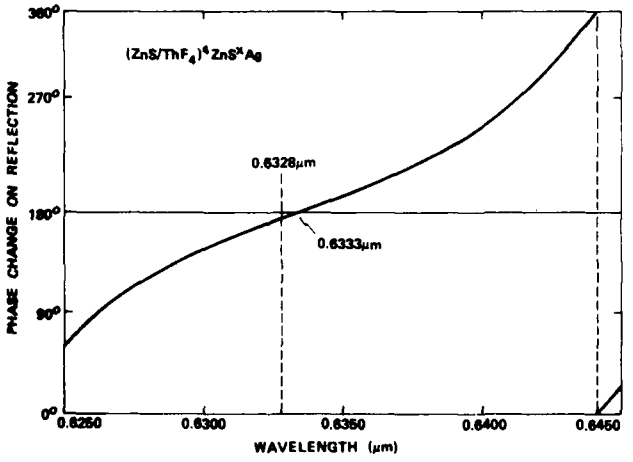

Figure 6. Phase change as a function of wavelength near 0.6328 μm for multilayer film design $(ZnS/ThF_4)^4ZnS^XAg$.

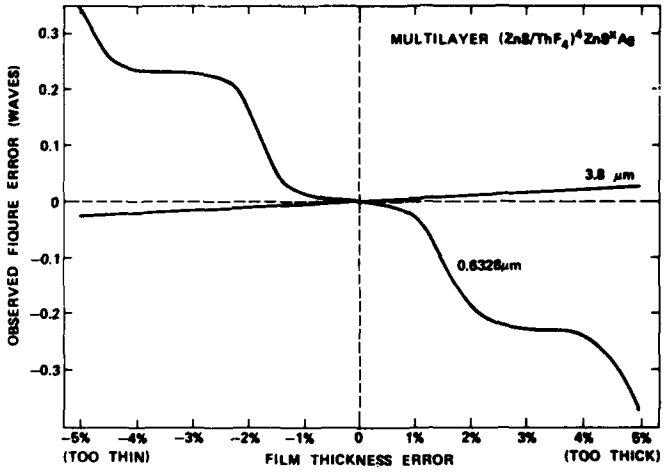

Figure 7. Figure error as a function of thickness for multilayer film design $(ZnS/ThF_4)^4ZnS^XAg$.

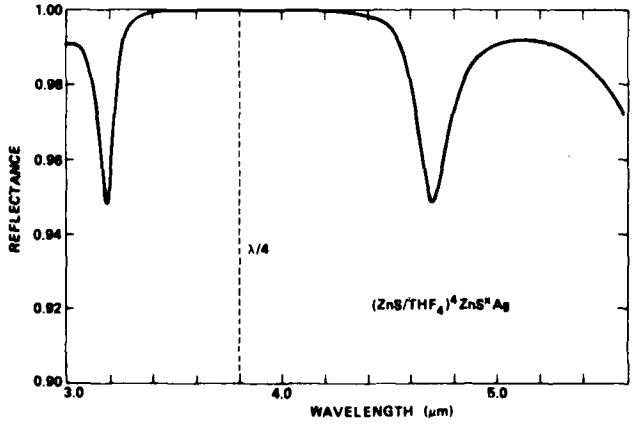

Figure 8. Theoretical reflectance of a $(ZnS/ThF_4)^4ZnS^XAg$ multilayer film with quarter wave thickness at a wavelength of 3.8 μm.

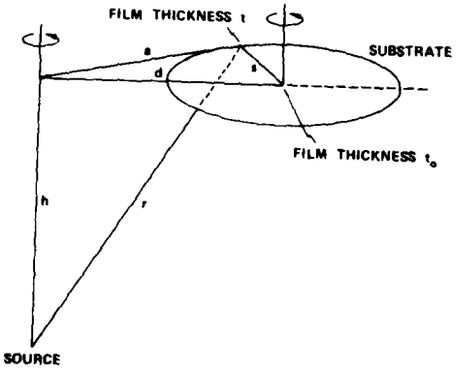

Figure 9. Coating geometry for a planetary system. In a single-planetary system the substrate only rotates about its own axis, whereas in the double-planetary system it also rotates about the h axis.

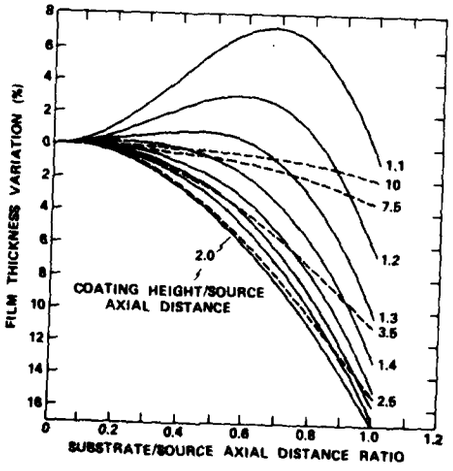

Figure 10. Variation in thickness with the substrate radius/source offset ratio as a function of the coating distance/source offset ratio. The solid lines indicate that the thickness uniformity at the edge of the sample is worsening with increasing coating distance; the dotted lines that it is improving.

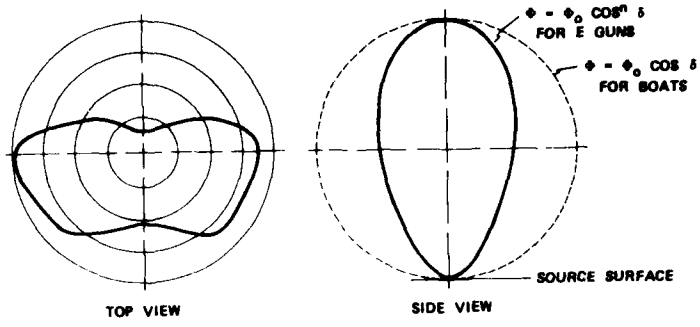

Figure 11. Distribution pattern looking down on a typical electron beam source (after reference 14).

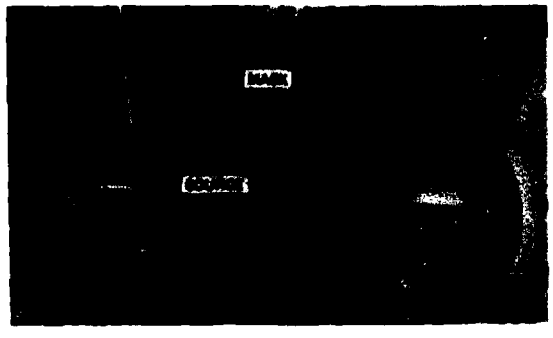

Figure 12. Rotating mask used to achieve multilayer film thickness nonuniformities of 0.1% (after reference 15).

AD-A106 548 NATIONAL BUREAU OF STANDARDS WASHINGTON DC F/G 20/5
LASER INDUCED DAMAGE IN OPTICAL MATERIALS: 1980,(U)
OCT 81 H E BENNETT, A J GLASS, A H GUENTHER
UNCLASSIFIED NBS-SP-620 NL

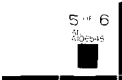

It was suggested that adaptive optics might remove the wavefront errors caused by nonuniform film thickness. The author agreed but expressed the opinion that it was desirable to obtain the best possible surfaces first, then rely on adaptive optics only to correct for the remaining wavefront errors.

THE ROLE OF ABSORBING DEFECTS IN THE LASER DAMAGE OF TRANSPARENT MATERIALS

Yu. K. Danileiko, A. A. Manenkov, and V. S. Nechitailo
Lebedev Physical Institute
Moscow, USSR

Key words: Laser damage; absorbing defects; inclusions.

1. Introduction

In early studies of laser induced damage, it was found that absorbing defects, like platinum metallic inclusions in glasses [1] considerably reduce the damage threshold. This fact has motivated numerous experimental and theoretical investigations of the role of absorbing defects in laser damage of transparent optical materials of different kinds (crystals, glasses, polymer materials). In a short paper it is impossible, of course, to present a review of all the experimental results and theoretical ideas concerning the influence of absorbing defects on laser damage processes. Therefore, in this paper, we restrict ourselves to only a brief review of research carried out in our laboratory at the Lebedev Physics Institute. For more complete and detailed information on this research, the reader should refer to the collection of [2] papers in which a summary of research carried out by other groups is presented as well. Extensive information on the problem under discussion can also be found in the proceedings of the Laser Damage Symposium [3-4].

In part 2 of this paper, we present some experimental results obtained in our laboratory concerning the role of absorbing defects, both in bulk and surface damage, of a number of typical materials (crystals) and glasses) which are used in laser optics. We discuss particularly the effects of thermal treatment of materials on damage thresholds and the cumulative effects on the damage process of multiple laser pulse irradiation. These effects provide a definite indication of the dominant role played by absorbing defects in the laser damage process, and they are of practical significance for understanding damage mechanisms, and for the technology of high power laser materials.

In part 3 we discuss physical processes in which the small absorbing defects produce macroscopic damage in transparent solids. A model is considered which includes thermal explosion of the absorbing defects heated by the laser pulse and the photoionization of the surrounding medium produced by thermal uv-radiation of the hot defects. The damage threshold and its dependence on the size, other parameters of the defects, and on the wavelength and pulse width of laser radiation, are derived from the analysis of this model. Estimates of the damage threshold for typical cases are presented, which show that the processes considered are highly effective and that absorbing defects, even if of a very small size (of the order of 100 A), can be an essential source for laser produced damage in real transparent optical materials.

2. Experimental Results

2.1 Light Scattering Studies for Testing Concentration of Defects and the Damage Process

In attempting to understand the mechanism of laser damage of real optical materials, which always contain, to some extent, impurities or structural defects, we made an attempt to find a correlation between the observed damage threshold and the characteristics of defects as determined by light scattering techniques. The influence of defects of small size (<0.1 μm) on the damage threshold was of particular interest to us because the role of the defects of large size (>0.1 μm), such as Pt inclusions in glasses, is obvious. Usually large size inclusions are not of high concentration, and they can be easily excluded from the interaction area by means of proper focusing of radiation inside the sample. The concentration of small defects, even in perfect optical materials, may be large enough ($\gtrsim 10^7$ cm^{-3}) to prevent their exclusion, even by very tight focusing of the laser beam. It was

found that some correlation between the damage threshold and the Rayleigh scattering intensity exists for a number of materials such as sapphire, ruby, crystalline quartz, and glasses. The light scattering intensity characterizes the size and concentration of defects. Thus, the intensity of the Rayleigh scattering I_R (measured relative to the intensity of the Mandelshtam-Brillouin scattering used as the internal standard) was proposed [5] as the proper criterion of the optical purity and laser damage resistance of transparent materials. It should be noted, however, that the correlation of the damage threshold and the intensity of the light scattering may not be observed in every case, because the nature of defects in solids is different and their characteristics strongly depend on the technological conditions of the material production. Thus, this correlation should be regarded not as a universal law but rather as a tendency.

Under very intense laser radiation close to the damage threshold, a nonlinear relation between the intensities of Rayleigh scattering and incident light was found in a number of materials [6]. A detailed investigation of the characteristics of this nonlinear scattering effect showed, in particular, that in some materials, under conditions of repeated laser pulse irradiation, the intensity of the scattered light increases from one pulse to another. After a number of pulses (which is different for each material, and depends on the ratio of the single shot damage threshold to the incident observation beam intensity) the damage becomes visible and the intensity of the scattering grows abruptly. Figure 1 illustrates the accumulation effect in light scattering which has been observed [7] in the heavy flint glass TF-8. The characteristics of nonlinear scattering are apparently connected with the dynamics of microdefects, which causes microdamage. The accumulation effect in scattering and damage is interpreted as a growth process of the initial defect structure of the investigated material under multi-shot laser radiation, which results in visible macrodamage.

Taking account of the accumulation effect was determined to be important for an understanding of the mechanism of laser damage. Thus, statistical properties of laser damage can be more adequately explained, we believe, by this accumulation effect, rather than by intrinsic electron avalanche process, as was proposed by some authors [8,9].

2.2 The Role of Inclusions and Impurities and the Thermal Treatment Effect

Taking into account the importance of the role played by defects in laser damage of transparent materials, we investigated which particular defects have the most influence on the damage threshold. These investigations showed [10] that inclusions (such as metal and semiconductor particles) and impurity clusters considerably reduce the damage threshold, while atomic impurities isomorphically doping crystals and glasses have no appreciable effect on the damage thresholds. It was found that thermal treatment greatly affects the surface and volume damage thresholds. Thus, these thresholds are definitely connected with the presence of defects, because their state strongly depends on the thermal treatment. Actually, valence transformations of impurity atoms, phase transformations of inclusions, and the processes of formation and decomposition of clusters are typical processes observed in solids which have been subjected to thermal treatment. Investigations of the thermal treatment effect for ruby, sapphire and alkali halide crystals [10,11] have shown that the final results depend on the treatment conditions such as gas atmosphere, temperature and temporal regimes. For example, for sapphire crystals containing impurities of C_o, Ni and Fe, high temperature annealing at $T \approx 1800°C$ in an oxygen atmosphere results in a significant increase of the damage threshold, whereas for samples containing Ti and Mg impurities, thermal treatment at the same conditions considerably reduces the damage thresholds. We conclude that these thermal effects are connected with the formation and decomposition of foreign phase, absorbing inclusions of a metallic or semiconductor nature.

For alkali halide crystals, a considerable increase in the laser damage threshold can be achieved by high temperature treatment in a proper temporal regime, which includes annealing at a temperature close to the melting point, followed by rapid cooling. Table I illustrates some typical results obtained in our laboratory on the thermal strengthening of sapphire and NaCl crystals for laser radiation of 15 ns pulse duration at 0.69 μm and 1.06 μm wavelengths, respectively.

Table I.
Bulk Damage Thresholds (GW/cm^2)
Before and After Thermal Treatment

		Before	After
Sapphire	0.69 μm	10	400
NaCl	1.06 μm	10	100

2.3 Surface Damage

Surface damage was studied in detail particularly for ruby laser elements. It was found [12,13] that the damage threshold essentially depends on the quality of polish. Investigation of the structure of the surface layer by electron microscopy and light scattering showed that this dependence is connected with defects formed in the polishing procedure. Microcracks with inclusions of abrasive particles, and liquid components of polishing materials, effectively absorb laser radiation in the vicinity of these defects. The thickness of the defective surface layer strongly depends on a polishing technique, but usually varies in the vicinity of 1.0 μm.

Theoretical analysis [14] of the process of laser heating of an absorbing surface layer based on a solution of the heat conductivity equation gave good agreement with experimental results. In particular, it explained the dependence of the damage threshold on the thickness of the defective surface layer and on the laser pulse duration. According to this analysis for pulses with duration, τ, which is longer than the characteristic time, τ_c, of heat diffusion from the surface layer, the damage threshold seem to be inversely proportional to the square of the layer thichkness, h, and independent of τ, while for short pulses ($\tau < \tau_c$)I_d varies inversely with pulse width: $I_d \sim \tau^{-1}$.

This prediction has been found in a good agreement with the experimental observation [15] of the pulse width dependence of the surface damage threshold for ruby samples (fig. 2). In particular, the inflection point on the dependence $I_d(\tau)$ corresponds to the condition $\tau \approx \tau_c$, with the τ_c value ($\tau_c = c\rho h^2/K$, where c, ρ and K are thermal capacity, density and thermal conductivity of the material, respectively) estimated from the measured defective layer thickness.

This corroboration of the thermal mechanism of surface laser damage led us to the idea of the thermal evaporation of an absorbing surface layer, formed by abrasive polish. The experiments showed that the annealing of ruby crystals at T = 1600 to 1700°C results in a considerable increase of the surface damage threshold. By the evaporation technique, we were able to achieve rather high surface damage thresholds for ruby samples, typically 5 x 10^{10} W/cm^2 at the 10 ns pulse width, which were close to the bulk damage thresholds. Among such high resistance surfaces, those oriented parallel to the $(11\bar{2}0)$ or $(11\bar{2}1)$ crystallographic planes [16] were especially perfect. After high temperature treatment, such selectively oriented surfaces have extremely small atomic-scale roughness, as is indicated by observation of light scattering.

3. Theoretical Analysis

Several theoretical models of laser damage mechanisms connected with absorbing inclusions have been considered in literature. One of the most effective processes analyzed in detail by Hopper and Uhlman [17] consists of thermoelestic stress directly produced in medium surrounding the hot inclusion. In this analysis, the process of heating was considered to be linear in the laser radiation intensity and the achievement of critical stress was accepted as a criterion of damage. However, for the majority of optical materials (such as inorganic crystals and glasses) at least with short laser pulses, the description is hardly adequate to the real physical situation, because in the damage region very high temperatures are apparently achieved, and the above assumption of linearity may be involved. The dependence of the absorption coefficient of defects and also other parameters of the material such as the heat conductivity coefficient, on the temperature which changes

over a wide range during the laser heating process, should be taken into consideration for the correct description of the damage process.

We have analyzed [18] such a nonlinear process of laser heating, solving the proper heat conductivity equation. The analysis showed that the process of heating of inclusions at laser radiation intensities above some threshold level has the character of a thermal explosion. The threshold of the explosion for small inclusions, with a dimension much smaller than the laser wavelength, has been determined as follows:

$$I_{expl} = \frac{\lambda}{18\pi} \frac{(\varepsilon' + 2)^2 + \varepsilon''}{\varepsilon''} Q(I_L) , \tag{1}$$

where ε' and ε'' are the real and imaginary parts of the electric susceptibility of the inclusion material at the laser wavelength, λ, $Q(I_L)$ is the intensity dependent term of the thermal power accumulated in the absorbing inclusion. The analysis of nonlinear heating of a spherical particle for long and short laser pulses, with rectangular temporal shape of durations $\tau >> \tau_c$ and $\tau << \tau_c$, respectively, gives the following expressions for $Q(I_L)$ assuming single-photon absorption.

$$Q(I_L) = \frac{2d_1 \ell n\xi}{a^2\beta(\xi - 1)}, \quad \tau >> \tau_c \tag{2}$$

$$Q(I_L) = \frac{c_1\rho_1 T_0}{\xi\tau} \{1 - \exp [-\xi (T_c/T_0 - 1)]\}, \quad t << \tau_c \tag{3}$$

Here $\tau_c = c\rho a^2/K$ is the characteristic time of thermal diffusion, ξ is the temperature nonlinearity parameter of the absorption coefficient of the inclusion, $\beta = (1 + 2d_1/d_2)/3$, d_1 and d_2 are parameters relating to the thermal conductivity of the inclusion and the surrounding medium, respectively, at the temperature T ($K_1 = d_1/T$, $D_2 = d_2/T$), and T_0 and T_c are the initial and critical damage temperatures of the absorbing inclusion.

We have carried out calculations for a typical example of metallic inclusions of size 2a = 300 A, with $\xi = 0.1$, $\varepsilon' = 9$, $\varepsilon'' = 17$ at $\lambda = 0.69$ μm, and $\tau = 30$ ns (formulas (1) and (2) should be used in this case). We find a value of $I_{expl} = 2 \times 10^9$ W/cm^2. This value approximately corresponds to the laser damage thresholds typically observed in optical materials, such as crystals and inorganic glasses, containing metallic inclusions of submicron sizes. This indicates that the thermal explosion of absorbing defects is an effective mechanism in initiating laser damage in transparent solids.

To support this conclusion, we have analyzed [19] the process of development of damage from the initial step of microdamage to the final stage of macrodamage of observable size. The two following processes have been considered:

1. Ionization of the surrounding region by uv-radiation of hot exploded inclusions. --Owing to the absorption of laser radiation by free carries, this process must result in heating of the surrounding medium similar to the initial heating of the inclusion, which will have an explosive character and lead to a further spread of the absorption region, and finally, to the formation of macrodamage.

2. Formation of microcracks whose surfaces have considerable charge.--Electrical discharge in these cracks could be accompanied by uv-radiation. Its influence on the surrounding medium is similar to that of the thermal explosion of an absorbing inclusion.

The efficiency of uv-ionization was estimated on the basis of the black body radiation theory [20,21]. The radiation power of heated small particles in the spectral range d is given by

$$dE = 4\pi c\sigma(\omega)e_0(\omega)d\omega \ , \tag{4}$$

where

$$e_0(\omega) = \frac{h\omega^3}{4\pi^3c^3[\exp\ (h\omega/KT) - 1]} \tag{5}$$

is the intensity distribution of the black body radiation, and

$$\sigma(\omega) = \frac{12\pi\omega a^3\varepsilon''}{c[\varepsilon' + 2)^2 + \varepsilon''^2]}$$

is the absorption cross-section of the particle. Using the Kirchhoff law for the emitted and absorbed energy, we have obtained the following expression for the temperature of the inclusion:

$$(KT)^5 = \frac{\pi^2c^2h^4\omega_L I_L}{25} \tag{6}$$

For inclusions of the size 300 A heated by laser light at $\lambda = 0.69$ μm, $I_L = 2 \times 10^9$ W/cm^2 gives a value $T = 5 \times 10^4$ K. The thermal radiation corresponding to such a temperature has its maximum in the spectral distribution at $\lambda_{max} = 700$ A with power $E_{max} = 5.6 \times 10^{-3}$ W. Such intense uv-radiation will lead to ionization of the surrounding medium and formation of free carriers with a high concentration ($n > 10^{19}$ cm^{-3}). The absorption of laser radiation by these carriers will cause strong heating of the lattice in the interaction region and cause irreversible changes. The given estimates seem to be reasonable enough, and indicate the efficiency of the uv-ionization mechanism as an additional source of absorption of laser radiation.

4. Conclusions

The experimental results and theoretical analysis presented in this paper show that absorbing defects, even of a very small size ($a \simeq 10^{-2}$ μm), play a significant, injurious role in laser produced damage in optical materials. This conclusion is also supported by recent experimental and theoretical studies [22], which have shown that intrinsic damage may be realized only in very pure, specially selected samples of optical materials.

This indicates that the problem of purification of materials and eliminating absorbing defects is of great practical importance for the production of damage resistant optical materials. The thermal treatment of optical elements under proper conditions can serve in some cases, as it has been demonstrated for the ruby rods, as an effective technological tool to increase both the surface and bulk damage thresholds by a considerable margin.

References

[1] Avizonis, P. V. and Farrington, T., Appl. Phys. Lett., 7, 205 (1965).

[2] Proc., P. N. Lebedev Physical Institute, USSR Academy of Sciences, Vol. 101, Basov, N. G. and Prokhorov, A. M., eds., "Nauka" Publ. House, Moscow (1978).

[3] Glass, A. J. and Guenther, A. H., Appl. Optics, 12, 637 (1973).

[4] Glass, A. J. and Guenther, A. H., Appl. Optics, 13, 74 (1974).

[5] Glass, A. J. and Guenther, A. H., Appl. Optics, 14, 698 (1975).

[6] Danileiko, Yu. K., Manenkov, A. A., Nechitailo, V. S., Ritus, A. I., Kvantovaya Electronika, 1, 1812 (1974).

[7] Danileiko, Yu. K., Manenkov, A. A., Nechitailo, V. S., Khaimov-Malkov V. Ya, JETP, 59, 1083 (1970).

[8] Danileiko, Yu. K., Manenkov, A. A., Nechitailo, V. S., Kvantovaya Electronika, 3, 438 (1976).

[9] Bass, M. and Barrett, H., Appl. Optics, 12, 690 (1973).

[10] Bloembergen, N., IEEE J. Quant. Electron., QE-10, 375 (1974).

[11] Akulenok, E. M., Danileiko, Yu. K., Nechitailo, V. S., Piskun, A. D. and Khaimov-Malkov, V. Ya., JETP Lett., 16, 366 (1972).

[12] Gorshkov, B. G., Danileiko, Yu. K., Epifanov, A. S., Lobachev, V. A., Manenekov, A. A., and Sidorin, A. V., JETP, 72, 1171 (1977).

[13] Danileiko, Yu. K., Khaimov-Malkov, V. Ya., Manenkov, A. A., Prokhorov, A. M., IEEE J. Quant. Electron., QE-5, 87 (1969).

[14] Danileiko, Yu. K., Manenkov, A. A., Prokhorov, A. M., Khaimov-Malkov, V. Ya., JETP, 58, 31 (1970).

[15] Danileiko, Yu. K., Manenkov, A. A., Prokhorov, A. M., Khaimov-Malkov, V. Ya., see ref. 2, p 9.

[16] Danileiko, Yu. K., Manenkov, A. A., Nechitailo, V. S., Khaimov-Malkov, V. Ya., Fizika Tverdogo Tela, 16, 1725 (1974).

[17] Hopper, R. W. and Uhlman, D. R., J. Appl. Phys., 41, 4023 (1970).

[18] Danileiko, Yu. K., Manenkov, A. A., Prokhorov, A. M., Khaimov-Malkov, V. Ya., JETP, 63, 1032 (1972).

[19] Danileiko, Yu. K., Manenkov, A. A., Nechitailo, V. S., Kvantovaya Electronika, 5, 194 (1978).

[20] Landau, L. D. and Lifshitz, E. M., Statistical Physics, Moscow, "Nauka" (1964).

[21] Landau, L. D. and Lifshitz, E. M., Electrodynamics of Continuous Media, Moscow, (1957).

[22] For a review of these results, see Manenkov, A. A., in Laser Induced Damage in Optical Materials, edited by Glass, A. J. and Guenther, A. H., NBS SP-509, Washington, DC, 455 (1977).

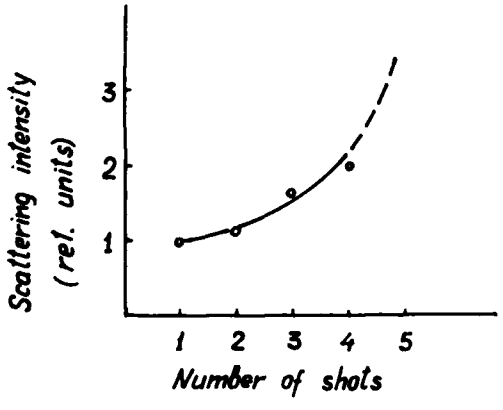

Figure 1. Cumulative effect of repeated exposure on light scattering in TF-8 sample.

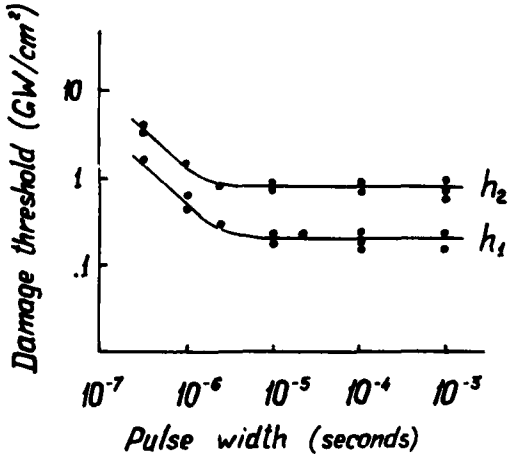

Figure 2. Pulse width dependence of surface damage threshold in ruby. h_1 and h_2 represent two different surface layer thicknesses ($h_1 > h_2$).

PULSE-WIDTH AND FOCAL-VOLUME DEPENDENCE OF LASER-INDUCED BREAKDOWN

E. W. Van Stryland, M. J. Soileau, Arthur L. Smirl,
and William E. Williams
North Texas State University
Denton, Texas 76203

The laser-induced breakdown fields at 1.06 μm of fused SiO_2, single-crystal NaCl, and air were measured as a function of focal volume and laser pulse width while keeping all other parameters, including the specimen, constant. The laser pulse width was varied from 40 psec to 31 nsec, and the focal volume was varied by over two orders of magnitude. The dependence of the breakdown field for NaCl and SiO_2 on the laser pulse width t_p and the focal volume V was empirically determined to be $E_B = AV^{-1}t_p^{-1/4} + C$ and the dependence for air to be $E_B = (AV^{-1} + C)\, t_p^{-1/4}$, where A and C are material-dependent constants. Current theories of laser-induced breakdown are carefully compared with these present measurements and are found to be inconsistent.

Key words: Air breakdown; laser damage; NaCl; picosecond phenomena; self-focusing; SiO_2.

1. Introduction

The laser-induced breakdown thresholds at 1.06 μm for fused SiO_2, single crystal NaCl, and air were determined as a function of laser focal-spot size, for pulse widths ranging from 40 psec to 31 nsec. These experiments represent the first damage data, over a range of three orders of magnitude in pulse width, that clearly separate the temporal and spot size dependences of damage thresholds by keeping all parameters, including the specimen, constant. Recent work has shown that in many cases laser-induced breakdown thresholds vary greatly among specimens of a given material [1-3]. Thus, pulse-width and focal spot-size dependence data are difficult to interpret, unless the same specimen is studied at all pulse widths and all focal spot sizes. The present measurements demonstrate that the dependence on focal volume observed previously for nsec optical pulse widths also applies to the psec regime [1]. It is observed, over the range of pulse widths, t_p, and focal spot sizes used in these experiments, that the electric field, E_B, necessary to induce breakdown for NaCl and SiO_2 varies as

$$E_B = A/(t_p^{+1/4}V) + C \quad , \tag{1}$$

and the breakdown field for air varies as

$$E_B = (A/V + C)/t_p^{1/4} \quad , \tag{2}$$

where A and C are material-dependent constants, and V is the focal volume [4]. The depth of focus for a Gaussian beam focused by an aberration-free lens is proportional to ω_0^2/λ, where ω_0 is the $1/e^2$ radius of the intensity and λ is the laser wavelength. The focal volume is proportional to the depth of focus times the focal area; that is

$$V \propto \omega_0^4/\lambda \quad , \tag{4}$$

The observed dependences of eqs. 1 and 2 may explain many of the apparent discrepancies of pulse width and spot size dependences found in the literature. For example, for large focal volumes the temporal dependence of eq. 1 is masked by the constant term, whereas for small focal volumes, where the first term dominates, the breakdown field would appear to scale as $t_p^{-1/4}$. Identical empirical fits for NaCl and SiO_2 imply that damage mechanism are similar in bulk samples of these two materials. For air, the pulse width dependence is quite different. The observed dependences on focal volume and pulse width, as well as the difference between the solid samples and air, are not explained by current theories of laser-induced breakdown. However, while the quantitative behavior cannot be explained, qualitatively the empirical fits presented above are consistent with the recently proposed multiphoton-initiaed avalanche breakdown model presented in Refs. 1 and 2 as described in Sec. IV.

2. Experiment

The laser source for the psec studies was a passively mode-locked, microprocessor-controlled [5] Nd:YAG laser system operating at 1.06 μm. A single pulse of measured Gaussian spatial and temporal intensity distribution was switched from the mode-locked train and amplified. The temporal pulse width was variable between 30 to 200 psec [full width at half maximum (FWHM)] by selecting various etalons as the output coupler. The width of each pulse was monitored by measuring the ratio, R, of the square of the energy in the fundamental (1.06 μm) to the energy in the second harmonic, produced in a $LiIO_3$ crystal. This ratio is directly proportional to the laser pulse width as long as the spatial profile remains unchanged [6]. The ratio was calibrated by measuring the pulse width using type-I second-harmonic autocorrelation scans. The observed three-to-one signal-to-background ratios indicated clean mode locking [7]. To ensure that the ratio, R, is proportional to the pulse width and provides a valid pulse width monitor, scans were performed for all three output coupler etalons.

The laser half-angle beam divergence was 0.38 mrad. The beam divergence and the position of the beam waist were determined by pinhole scans of the spatial profile at six positions along the propagation direction. Two lenses of focal lengths 5.0 and 8.0 cm were used at various distances from the beam waist to produce the focal-spot radii for these experiments. The lowest f-number condition used in these experiments was f/7.4. Spherical aberrations were determined to be negligible for this worst case situation using the procedure suggested by Ireland et al. [8]. Computation of spherical aberrations caused by a singlet lens indicated that errors in the field were less than 4% for the worst case. The lenses used however, were doublets corrected for spherical aberration. Aberrations caused by focusing through the planar surfaces of the samples was calculated to cause an error in the field of less than 0.1% for the worst case. Diffraction limited performance of the 5.0 cm focal-length lens was verified by knife edge scans of the 6.1 μm radius spot [1]. The calculated 5.0 μm radius was subsequently scanned and verified to be diffraction limited to within the experimental uncertainty of ±0.4 μm. The energy on target was varied by changing the angle between the calibrated pair of Glan polarizers that were arranged to keep the direction of polarization at the sample surface constant. The output energy of the laser and the energy transmitted through the sample were continuously monitored by sensitive photodiode peak-and-hold detectors. These detectors were determined to be linear over their range of use and were absolutely calibrated with respect to a pyroelectric energy monitor. The pyroelectric detector was in turn checked with a thermopile calorimeter.

The nsec data was taken on the same bulk samples using a Q-switched Nd:glass laser operated in the TEM_{00} mode [1]. The same focusing lenses were used, and the same procedures for determining the beam divergence (0.7 mrad) and beam waist were employed as for the psec measurements. Again, a calibrated pair of Glan polarizers were used to vary the energy on target. The laser output was monitored directly by a pyroelectric detector which was calibrated with the same calorimeter used for the psec experiments. The nsec pulse widths were determined directly from oscilloscope traces taken with a fast photodiode (rise time $\leq$500 psec).

The breakdown threshold at a given pulse width was taken to be that intensity which produced damage 50% of the time. Each site was irradiated only once. Damage was defined as the appearance of a visible flash or as the observation of scattered light from a coaxial HeNe laser as viewed through a 20 x, long-working distance microscope in accord with the methods used by previous investigators. The microscope was also used to verify that damage had occured at the beam focus and was not due to inclusions. For psec damage to NaCl, there was a small range of incident energies where damage had occured as determined from the scattered HeNe beam, but no flash was observed.

In addition to the 1-on-1 experiments, where each site was irradiated only once, an n-on-1 experiment was performed at the largest spot size (19.3 μm) for the solid samples. This was done by irradiating the same spot with one or more pulses of insufficient intensity to damage prior to irradiating with a damaging pulse. No measureable change in threshold was observed.

3. Results

The results of these damage experiments are displayed in Fig. 1. All values quoted for electric field are rms fields corresponding to the peak on axis intensity. The error bars are relative errors determined by how well the threshold for damage is defined and the reproducibility of the data. The absolute errors include relative errors as well as errors in the measurement of the energy, focal-spot radius, and pulse width. These errors are estimated to be 20% for the breakdown electric fields.

The breakdown fields for NaCl and SiO_2 are plotted as a function of $t_p^{-1/4}v^{-1}$ in Fig. 2. Figure 3 is a plot of the product $t_p^{-1/4}E_B$ as a function of V^{-1} for air. Table I gives least-squares fits to straight lines for the data displayed in Figs. 2 and 3. From these fits it is seen that the breakdown field for air varies as $t_p^{-1/4}$ independent of the focal volume, whereas the breakdown fields in the solid materials appears nearly independent of pulse width for large focal volumes.

Table 1. Empirical fits for the rms breakdown electric field (MV/cm) for the three materials studied, where t_p is the laser pulse with in psec (FWHM) and ω_0 in μm is the focused beam radius at the $1/e^2$ point in intensity. The NaCl is (Harsaw Chemical Co. 6801 Cochron Road, Salon, Ohio 44139) single-crystal laser grade. The SiO_2 is high-purity, water-free fused quartz obtained from General Electric (General Electric No. 125, high-purity, water-free fused SiO_2 acquired from Mark Optics, 1510 East Street, Gertrude Road, Santa Anna, Calif. 92705).

NaCl	$E_B = \frac{1.3610^4}{\tau_p^{1/4}\omega_0^4} + 2.69$
SiO_2	$E_B = \frac{3.3010^4}{\tau_p^{1/4}\omega_0^4} + 9.52$
Air	$E_B = [\frac{1.1610^5}{\omega_0^4} + 150]\frac{1}{\tau_p^{1/4}}$

In addition we include previously unpublished data taken from the work of Ref. 1 in Table II. There the damage thresholds of a total of 13 different NaCl samples are given for three different focal-spot radii. All the data presented in Table II used 31-nsec (FWHM) pulses. Table III gives the least-squares fits of the data of Table II of eq. 1. Good fits are obtained for all the samples tested.

In the nsec experiments, the transmitted pulse was sharply terminated near the peak by the laser-induced plasma, resulting in approximately 50% transmission. This is in contrast to the greater than 80% transmission observed for the psec pulses. In addition, a slight trend toward higher transmission at the shorter pulse widths was evident. Thus, either breakdown takes place near the end of the pulse, or the breakdown process takes place on a time scale of the order of the pulse width. A third possibility that appears inconsistent with our nsec measurements but consistent with the psec data is that the plasma blocks transmission for a period short compared to the psec pulses used. Anthes and Bass, [9] using psec pulses, have made streak camera recordings of the transmitted damaging pulses in fused quartz at 0.53 μm. They found that the avalanche blocked transmission near the

Table II. The rms breakdown electric field (MV/cm) for NaCl samples using 31 nsec (FWHM) 1.06 μm pulses of focal spot radius ω_o ($1/e^2$ radius in intensity) as indicated. Sample 6 is the sample used for the psec data.

Sample	ω_o(μm) 6.1	10.3	19.1
1	4.17	3.18	2.92
2	4.24	3.45	3.13
3	4.12	3.39	2.68
4	3.05	1.89	1.97
5	1.44	1.18	0.99
6	3.10	2.57	2.14
7	5.46	4.03	3.67
8	6.67	3.85	3.90
9	4.86	4.13	3.03
10	4.81	3.93	3.89
11	5.36	3.58	3.54
12	4.64	4.13	3.78
13	5.20	3.81	3.59

Table III. Empirical fits for the rms breakdown electric field (MV/cm) to eq. 1 of the text for the samples of NaCl of Table II. The laser pulse width is t_p which is in all cases 31000 psec (FWHM) and ω_o in μm is the focused beam radius at $1/e^2$ point in intensity. R^2 is the coefficient of determination which is a measure of how closely the equations fit the experimental data. The closer R^2 is to one, the better the fit.

Sample	$A(10^4)$	C	R^2
1	2.31	2.96	0.996
2	1.98	3.21	0.985
3	2.32	2.93	0.918
4	2.27	1.84	0.988
5	0.751	1.05	0.948
6	1.58	2.28	0.938
7	3.31	3.72	0.997
8	5.62	3.68	0.992
9	2.79	3.45	0.862
10	1.82	3.85	0.998
11	3.63	3.43	0.996
12	1.45	3.89	0.953
13	3.06	3.59	0.999

peak of the pulse in a time shorter than the 6-psec streak camera resolution. However, they also noted that the transmission recovered on a psec time scale. In point of fact, they observed approximately 80% transmission similar to the psec studies reported here.

4. Discussion

The problem of laser-induced breakdown of highly transparent materials has been studied by many workers [10] and has been the subject of at least three review papers [11-13]. Laser-induced breakdown in NaCl was first studied in 1966 by Olness [14] and in 1968 by Yosajima et al. [15] and has been extensively studied since that time. However, direct comparison of the results of this work with prior data is difficult since in many cases exact experimental parameters (such as focal-spot radius) are unknown for much of the published work. In some publications, the data has been reduced using focal radii scaled to correct for self-focusing making direct comparison with these results impossible [16]. In a few cases for which direct comparison can be made, agreement with this work is mixed. For example, Fradin et al. [17] measured the breakdown threshold of NaCl for pulse widths of 10.3 and 4.7 nsec and focal-spot radii of 8.8 to 24 μm. They found a breakdown threshold field of of E_B = 2.1 MV/cm which had little or no dependence on pulse width or spot size, which is in excellent agreement with our results over the same range of focal volume. In a later work, Fradin et al. [18] measured E_B for NaCl over the 15 psec to 10.3 nsec range with focal-spot radii of 8.8 to 15.3 μm. They observed a dependence of the breakdown electric field on pulse width consistent with a $t_p^{-1/4}$ dependence and no focal radius dependence. The weak focal-spot radius dependence we observed over the same range of focal radii is consistent with their results. As shown in Table I, we found a much weaker pulse width dependence for comparable focal radii. However, for small focal-spot radii, we did observe a $t_p^{-1/4}$ dependence for the breakdown fields.

The NaCl specimen used in this work was 1 of 13 NaCl crystals tested at 1.06 μm with 31-nsec pulses [1,2]. (See Tables II and III) The breakdown fields among these 13 specimens varied by a factor of 4.6 for a given focal-spot radius and pulse width. Such sample to sample variations indicate that material defects affect the breakdown measurements and thus make direct comparison with other results questionable. Manenkov [3] reported 1.06 μm measurements for what he claimed was intrinsic NaCl. He reported E_B = 5.4 MV/cm for nsec pulse widths and focal-spot radii equal to either 3.25 or 8.49 μm (both focal radii are called out in the paper but it is not specified which corresponds to the breakdown field given). If the E_B corresponds to the smaller radius, then Table I gives a value 2.8 times larger than the breakdown field reported by Manenkov. If the E_B given corresponds to the larger radius then Table I gives a value 0.6 times smaller than the Manenkov value.

Various physical mechanisms and sources of systematic error have been suggested to explain experimentally observed focal-spot size and pulse-width dependences of laser-induced breakdown. Some workers claim that the observed dependence of E_B on focal radius is due to self-focusing, [19-21] and they scale their results in accordance with the technique suggested by Zverev and Pashkov [19]. Zverev and Pashkov [19] predict that a plot of P_B^{-1} (P_B is the power at which breakdown occurs) vs ω_o^{-2} yields a straight line given by

$$\frac{1}{P_B} = \frac{2}{I_B \pi \omega_o^2} + \frac{1}{P_{cr}} \quad , \tag{4}$$

where P_{cr} is the critical power for self-focusing and I_B is the breakdown intensity. The basic

assumption of this procedure is that I_B is the intrinsic breakdown intensity and is independent of the focal-spot radius.

It is clearly seen from Fig. 4 that this scaling technique cannot be used for our experiments. Figure 4 is a plot of P_B^{-1} vs ω_o^{-2} for SiO_2 for pulse widths of 44 psec. All of the data for the different pulse widths follow a similar pattern. Our data cannot be fit to a straight line for any of the specimens examined. Other workers [21] have reported deviations from the straight-line fit for large spot sizes similar to that shown in Fig. 4. These workers [21] disregarded the large spot size data by arguing that, for large focal radii and powers near P_{cr}, the constant shape solution to the nonlinear wave equation (on which the Zverev and Pashkov [19] procedure is based) is no longer valid. However, this argument cannot explain the small focall radii data shown in Fig. 4.

It has been clearly established that, with the possible exception of a small number of specimens tested by Manenkov, [3] the laser-induced breakdown fields are not intrinsic and vary greatly even for specimens of a given material from the same supplier [1,2,14]. This violation of the basic assumption that the damage is intrinsic casts doubt on previously published data where the Zverev and Pashkov [19] scaling was used to interpret breakdown thresholds.

Another test of the role of self-focusing in laser-damage experiments is the apparent pulse-width dependence due to the transient nature of electrostriction [22]. The extent of the electrostrictive contribution to n_2, the nonlinear index of refraction, decreases as the dinemsionless quantity X increases. The quantity X is given by [23]

$$X = \omega_o / v t_p \quad . \tag{5}$$

where v is the speed of sound in the medium. Kerr [23] has shown that for $X < 1$ electrostriction is the dominant self-focusing mechanism and for $X > 1$ the contribution due to electrostriction is inversely proportional to X. Consider the case where the focal spot radius is 19.3 μm. For this case, P_B is the largest and the effect of self-focusing should be the greatest. For this focal spot size in NaCl and the longest pulse width (31 nsec) used in this work, X is 0.16 and electrostriction dominates. For the 19.3 μm focal spot radius and a 100 psec pulse width, X is 50, and electroscriction is negligible. Therefore, if self-focusing were significantly contributing to these experimental results, there would be a large pulse-width-dependence of E_B for the 19.3 μm focal-spot radius. As can be seen from Table I, the pulse-width-dependent term in the expression for E_B is negligible for a 19.3 um focal-spot radius for both SiO_2 and NaCl.

A possible explanation of this apparent discrepanay with self-focusing theory is given by including the effects of plasma defocusing [24]. Yablonovitch and Bloembergen [25] showed that the negative n_2 caused by free electrons in a preplasma limits the self-focal radius. Experiments in semiconductors demonstrating these self-defocusing effects are discussed in Refs. 26 and 27. In our experiments the focal radius determined from linear optics is smaller than the limiting self-focal radius calculated using the procedure in Ref. 25. In Ref. 1 it was argued that when these conditions are satisfied the effects of self-focusing can be neglected in calculating focal plane peak intensities. One might ask how self-focusing effects can be compensated by plasma defocusing prior to reaching the breakdown or plasma threshold. For input powers of the order of P_{cr} (the critical power for self-focusing) self-focusing affects the beam diameter significantly only near the geometric focus, and the index changes are small. For example, the index change in NaCl for intensities near the breakdown threshold is of the order of 10^{-4}. The index change due to the free-electron plasma is

$$\delta n^- = \omega_p^2 / \omega^2 \quad , \tag{6}$$

where ω_p is the plasma frequency and ω is the laser frequency [28]. Equation 6 implies that negative index changes on the order of 10^{-4} can be achieved for prebreakdown plasma densities 10^{-2} times smaller than the critical density required for the plasma frequency to be resonant with the laser. It is therefore possible for plasma defocusing to negate the effects of self-focusing well before damage occurs. A more definitive explanation of the combined role of self-focusing and plasma defocusing will require careful analysis of the nonlinear wave equation including both effects. We have included all the focal parameters used to compute the breakdown fields so that these data can be corrected for self-action effects if future studies show that corrections are needed. Because of the several reasons given above, the data presented in this paper do not include any self-focusing corrections (even though P_B exceeds many estimates of P_{cr}).

Ireland et al. [8] pointed out that spherical aberrations due to low f-number focusing optics can give an apparent dependence of breakdown intensity on computed focal-spot radii. Analysis of worst-case aberrations and focal plane scans both confirm that the observed dependence of laser-induced breakdown on focal volume was not due to systematic errors in the determination of focal-spot size.

Bettis et al. [29] proposed a model for laser-induced breakdown in solids which incorporated both spot size and pulse-width dependences. Their model, which is based on the dynamics of laser-induced plasma formation, predicts that the bulk breakdown field scale as

$$E_B = t_p^{-1/4} \omega_o^{-1} \quad . \tag{7}$$

The pulse-width dependence predicted is similar to that observed for small focal volumes in this work

but is inconsistent with the observed focal-spot radius dependence and the lack of pulse-width dependence measured for large focal volumes.

Diffusion of energetic electrons out of the region of high electric field is a possible mechanism for the observed focal volume dependence. The model for laser-induced gas breakdown proposed by Kroll and Watson [30] predicts that electron diffusion gives rise to increased breakdown thresholds for small focal volumes. The results of our work for air as shown in Table I and Fig. 3 and prior work [1,31,32] at 1.06, 2.7, 3.8, and 10.6 μm are in reasonable agreement with the predictions of their model if only spot radius dependence is considered. However, diffusion is inconsistent with the observed temporal dependence measured in this work. Diffusion would result in decreased thresholds at short pulse widths since it represents an electron-loss mechanism.

The electron avalanche breakdown model also predicts a pulse-width dependence of laser-induced breakdown [11]. The pulse-width dependence is determined by the ionization rate in the exponential buildup of the free-electron plasma. The observed pulsewidth dependence of the breakdown field in NaCl for a 5 μm focal-spot radius is in reasonable agreement with the predictions of the recent theory due to Sparks et al. [33] which predicts a $t_p^{-1/4}$ dependence for all focal volumes. Again, agreement is good for small focal volumes, however, the breakdown field for NaCl for the 19.3 μm focal radius is nearly independent of pulse width over the 40- to 31000-psec region. From the results of Refs. 1 and 2, we know that selected high-purity specimens have breakdown field thresholds at 1.06 μm high as two to three times greater than the specimen reported in this work. The theory of Sparks et al. [33] is for intrinsic breakdown and does not predict a focal volume dependence and, thus, should not be applied to a defect dominated process.

The focal volume and temporal dependence found in this work is qualitatively consistant with the multiphoton-initiated avalanche breakdown model given in Refs. 1 and 2. That model assumes that for large focal volumes avalanche breakdown is initiated by the conduction-band electrons which are initially present. These starter electrons can be present from thermal ionization of shallow traps, thermionic emission from impurities, etc., therefore the large focal volume damage data will not represent "intrinsic" damage. Table II lists the 1.06 μm, 31-nsec pulse-width damage thresholds for various NaCl specimens at several focal-spot radii. These data are for the same specimens used in Refs. 1 and 2. The least squares fit to eq. 1 for each specimen is also shown in Table III. Note that the constant term C in eq. 1 is sample dependent and varies by nearly a factor of 4 for the several NaCl samples shown.

For small focal volumes (focal volumes smaller than the inverse of the zero field free-electron density) the "starter" electrons for the avalanche must be generated by multiphoton ionization of defect states within the gap. The increased thresholds at small focal volumes are then a direct consequence of having to initiate the avalanche by a higher-order multiphoton process. The rate of increase of the free electron density, N, is then given by

$$\frac{dN}{dt} = \alpha(E,t)N + W_n(E,t)n \quad , \tag{8}$$

where $\alpha(E,t)$ is the ionization rate for the cascade process, n is the density of defects of ionization energy E_D, and n is the integer part of E_D/E_L, where E_L is the laser photon energy, $W_n(E,t)$ is the n-photon ionization rate. The solution to this equation is

$$N(t) = N_o \exp\left\{\int_0^t \alpha(E,t')\,dt'\right\} + \int_0^t nW_n(E,t') \times \exp\left\{-\int_0^{t'} \alpha(E,t'')dt'' + \int_0^t \alpha(E,t'')dt''\right\} dt' \quad . \tag{9}$$

where N_o is the density of free elctrons initially present. For large focal volumes the buildup of the free-electron plasma, which leads to breakdown, is dominated by the simple cascade process described by the first term in the above equation and breakdown occurs when N(t) reaches a critical value. For this case the temporal dependence will be determined by the cascade ionization rate $\alpha(E,t)$. For focal volumes smaller than the inverse of the zero-field free-electron density there will be no free electrons within the focal volume, and breakdown is initiated by the second term. The first term of eq. 8 dominates as soon as starter electrons are available. Braunlich et al. [34] have predicted a time dependence for laser-induced damage caused by multiphoton processes. The time dependence is then given by the rate at which the n-photon processes produce starter electrons for the avalanche. However, more information about the n-photon rate is needed in order to determine if this model gives the small focal volume temporal dependence measured in this work.

We have argued that the prebreakdown plasma results in a negative change in the nonlinear index and counters the effects of self-focusing. The model outlined above assumes that for small focal volumes no free electrons are present until they are generated by multiphoton processes. The question of whether or not self-focusing would contribute to the multiphoton processes which initiate breakdown remains unanswered. At what point in time for a psec pulse multiphoton absorption of defects is great enough to cause a carrier density sufficient to negate the effects of self-focusing is now known. However, the effects of self-focusing on the intensity are clearly not in accord with previous theories. The resolution of this question is the subject of our current theoretical and experimental investigations.

5. Summary

The laser-induced breakdown field, E_B, at 1.06 μm, was measured for various focal volumes and laser pulse widths on the same samples. The results of these measurements for solid materials were fit to a simple linear dependence of E_B on the product $t_p^{-1/4}V^{-1}$, where t_p is the laser pulse width (FWHM) and V is the focal volume. For air the product $t_p^{-1/4}E_B$ was linearly dependent on V^{-1}. The essential difference between the results on air and solid materials was that the temporal dependence

of E_B for air varies as $t_p^{-1/4}$ for all focal volumes whereas for large focal volumes in the bulk materials the $t_p^{-1/4}$ temporal dependence is masked by the constant term as given in eq. 1 or Table I. This constant term in eq. 1 destroys the scaling with $t_p^{-1/4}$ as predicted by avalanche breakdown theory and requires the experimenter to perform damage experiments at several pulse widths, as was done in this work. These results presented here are consistent with a qualitative model for defect dominated laser-induced breakdown which incorporates avalanche breakdown as well as multiphoton ionization of defect levels. Other current models are either inadequate or inconsistent with the results presented here.

Acknowledgments

The authors acknowledge the support of the Naval Weapons Center, the Office of Naval Research, The Robert A. Welch Foundation, The Research Corporation, and the North Texas State University Faculty Research Fund.

References

[1] M. J. Soileau, Ph.D. Thesis, University of Southern California, 1979, unpublished.

[2] M. J. Soileau, M. Bass, and P. H. Klein, in Proceedings of the 11th Annual Symposium on Laser Induced Damage in Optical Materials Natl. Bur. Stand. (U.S.) 1981.

[3] A. A. Manenkov, Natl. Bur. Stand. (U.S.) Spec. Publ. 509, 445 (1977).

[4] In Ref. 1, for nsec pulses, is was found that the intensity I_B necessary for breakdown varied as $I_B = K/V + D$, where K and D were constants. This is not inconsistent with the present data since the first term in the square of the empirical equation for the volume dependence of the field is negligible for nsec pulses (i.e., $E_B^2 = K^2/V^2 + 2KD/V + D^2$, where $K^2/V^2 << 2KD/V + B^2$). The difference is observed when the temporal dependence for psec pulses is included.

[5] Quantel model YG-40, 928 Benecia Avenue, Sunnyvale, Calif 94086

[6] W. H. Glenn and M. J Brienza, Appl. Phys. Lett. 10, 221 (1967).

[7] D. J. Bradley and G. H. C. New, Proc. IEEE, 62, 313 (1974).

[8] C. L. M. Ireland, A. Yi, J. M. Aaron, and C. Grey Morgan, Appl. Phys. Lett. 24, 175 (1974).

[9] P. Anthes and M. Bass, Appl. Phys. Lett. 32, 412 (1977).

[10] Proceedings of the Annual Conference on Laser Damage, edited by A. J. Glass, and A. H. Guenther, (Americal Society for Testing Materials, Philadelphia, 1969), Spec. Publ. 469; Natl. Bur. Stand. (U.S.), Spec. Publ. 341 (1970); 356 (1971); 372 (1972); 387 (1973); 414 (1974); 435 (1975); 462 (1976); 509 (1977); 54 (1978); 568 (1979).

[11] Nicolaas Bloembergen, IEEE J. Quantum Electron. QE-10, 375 (1974).

[12] David W. Fradin, Laser Focus, 41, 45 (1974).

[13] W. Lee Smith, Opt. Eng. 17, 489 (1978).

[14] D. Olness, Appl. Phys. Lett. 8, 283 (1966).

[15] Y. Yosajima, M. Takeda, and Y. Inuishi, Jpn. J. Appl. Phys. 7, 552 (1968).

[16] W. Lee Smith, J. H. Bechtel, and N. Bloembergen, Opt. Commun. 18, 592 (1976).

[17] D. W. Fradin, E. Yablonovitch, and M. Bass, Appl. Opt. 12, 700 (1973).

[18] D. W. Fradin, N. Bloembergen, and J. P. Letelier, Appl. Phys. Lett. 22, 635 (1973).

[19] G. M. Zverev and V. A. Pashkov, Sov. Phys. JETP 30, 616 (1970).

[20] David W. Fradin, IEEE J. Quantum Electron. QE-9, 954 (1973).

[21] W. Lee Smith, J. H. Bechtel, and N. Bloembergen, Phys. Rev. B 12, 706 (1975).

[22] W. Lee Smith, J. H. Bechtel, and N. Bloembergen, Phys. Rev. B 15, 4039 (1977).

[23] Edwin L. Kerr, Phys. Rev. A 4, 1195 (1971).

[24] R. W. Hellwarth, Natl. Bur. Stand. Spc. Publ. 341, 67 (1970).

[25] E. Yablonovitch and N. Bloembergen, Phys. Rev. Lett. 29, 907 (1972).

[26] A. A. Borshch, M. S. Brodin, and N. N. Krupa, Sov. J. Quantum Electron. 7, 1113 (1977).

[27] Yu, K. Danileiko, A. A. Manenkov, and A. Y. Sidorin, Natl. Bur. Stand. Spec. Publ. 541, 305 (1978).

[28] J. Marburger, in Progress in Quantum Electronics (Pergamin, New York, 1975), pp. 35-110.

[29] J. R. Bettis, R. A. House II, and A. H. Guenter, Natl. Bur. Stand. Spec. Publ. 462, 338 (1976).

[30] Normal Kroll and Kenneth M. Watson, Phys. Rev. A 5, 1883 (1972).

[31] D. E. Lencioni, Appl. Phys. Lett. 23, 12 (1973).

[32] M. J. Soileau, Appl. Phys. Lett. 35, 309 (1979).

[33] M. Sparks, T. Holstein, R. Warren, D. L. Mills, A. A. Maradudin, L. J. Sham, E. Loh, Jr., and F. King, Natl. Bur. Stand, in press

[34] P. Braunlich, A. Schmid, and Paul Kelley, Appl. Phys. Lett. 26, 150 (1975).

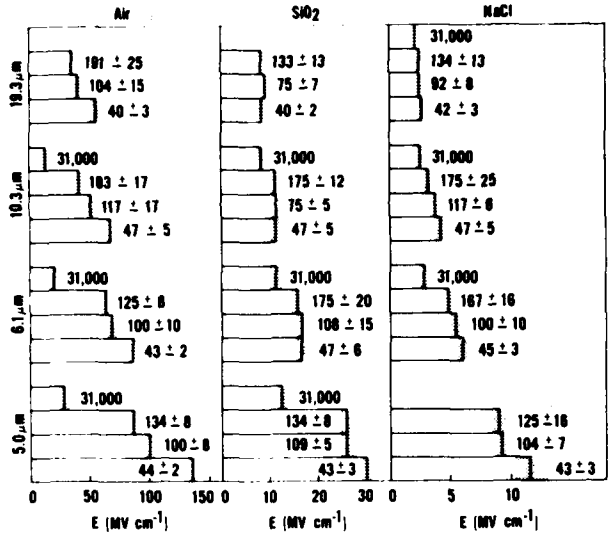

Figure 1. The experimentally determined breakdown electric field, E_B, (RMS), for Air, SiO_2, and NaCl are tabulated for focused spot sizes ($1/e^2$ radius in intensity) of 5.0, 6.1, 10.3, and 19.3 μm and various optical pulsewidths (FWHM) in psec, as indicated within or adjacent to the bars.

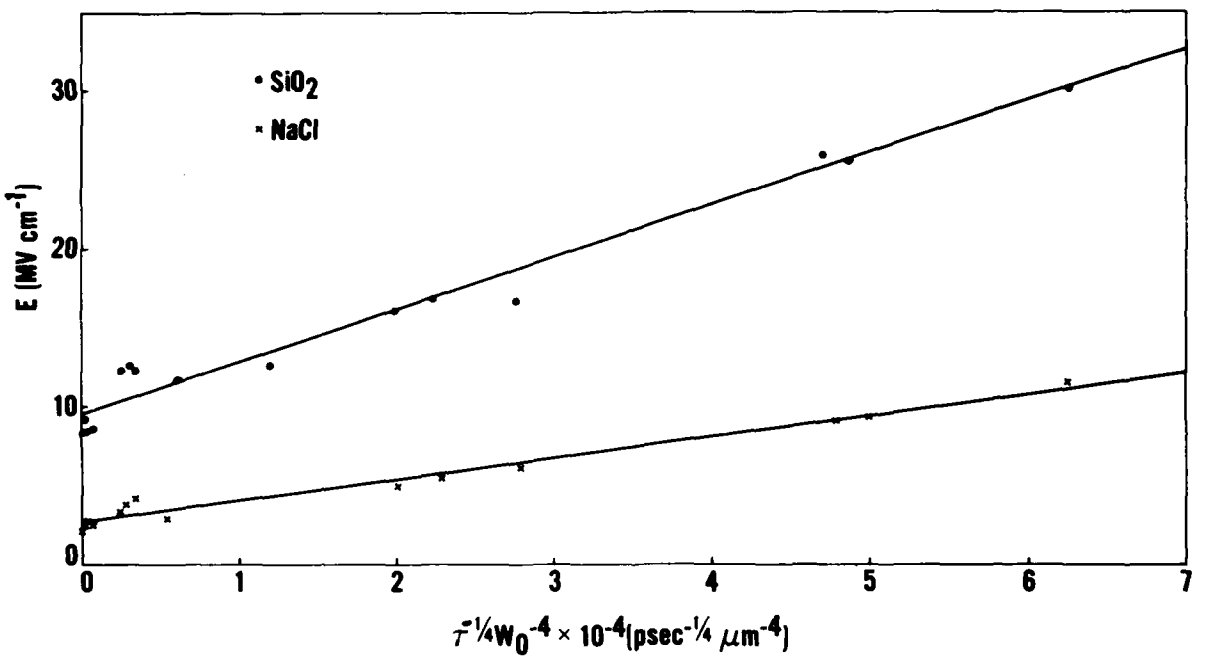

Figure 2. The RMS breakdown electric field data for Harshaw single-crystal laser-grade NaCl and for General Electric high-purity water-free fused quartz is plotted as a function of $t_p^{-1/4}\ \omega_o^{-4}$ where t_p is the laser pulsewidth (FWHM) in psec and ω_o is the focal spot radius at the $1/e^2$ point in intensity in m. The solid lines are least squares fits of the data to straight lines.

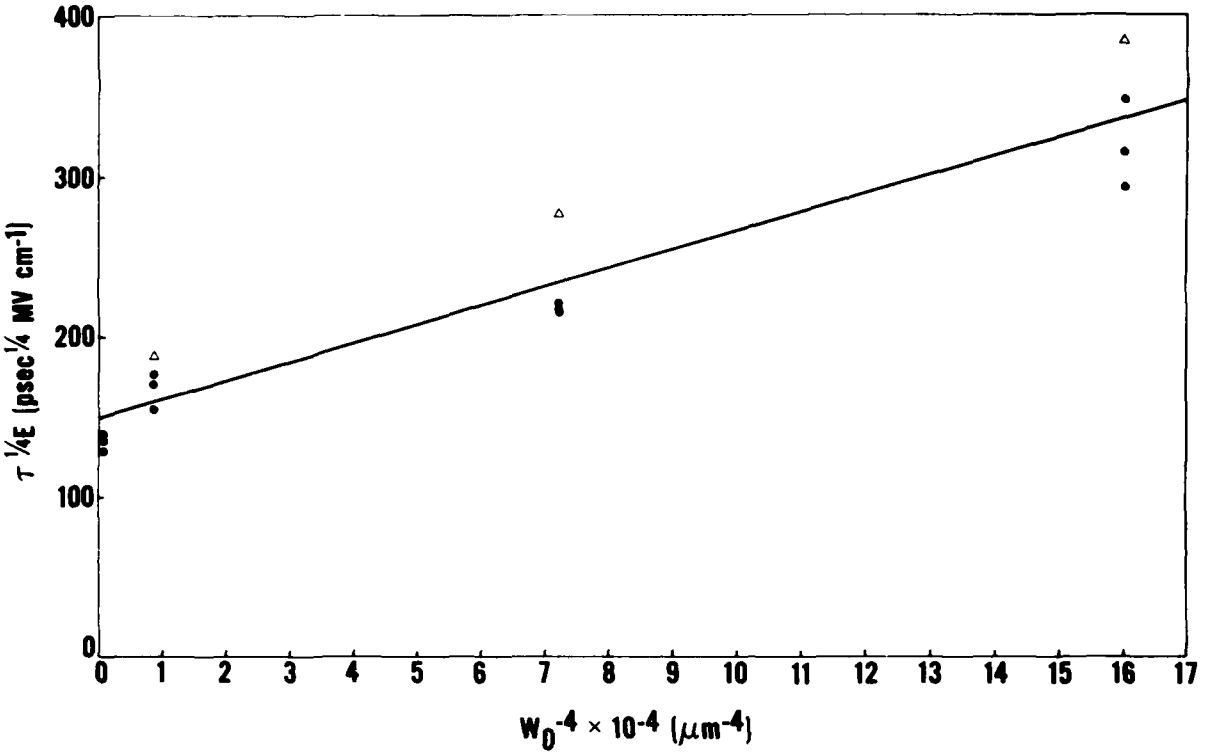

Figure 3. The produce $E_B\ t_p^{1/4}$ for air is plotted as a function of ω_o^{-4}. The RMS breakdown field is E_B in MV/cm. t_p is the laser pulsewidth (FWHM) in psec and ω_o is the focal spot size ($1/e^2$ radius in intensity) in μm. The solid curve is a least squares fit of the data to a straight line. The open triangles correspond to the 31 nsec data. The systematic deviation of the 31 nsec data from the fit is eliminated if the t_p dependence if changed to $t_p^{0.23}$ rather than $t_p^{0.25}$.

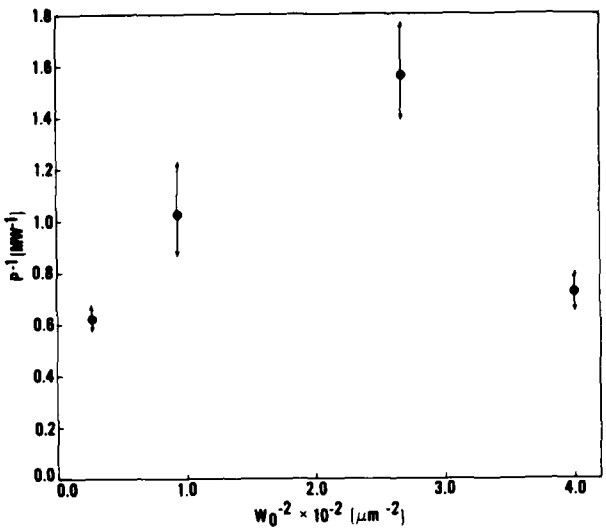

Figure 4. A representative plot of the inverse of the power, P_B, needed to induce breakdown versus ω_o^{-2}, where ω_o is the $1/e^2$ radius in intensity at the laser focus calculated using Linear Gaussian optics. Here data for SiO_2 using 44 psec (FWHM) pulses is presented.

The sodium chloride tested was not heat treated. The suggestion was made that Mannenkov's data indicated that to get the narrow range of damage threshold for NaCl, it should be heat treated. The author replied that he is repeating Mannenkov's measurements.

ON SELF-FOCUSING AND SPOT-SIZE DEPENDENCE OF LASER-INDUCED BREAKDOWN

M. J. Soileau
Department of Physics, North Texas State University
Denton, Texas 76203

and

J. B. Franck and T. C. Veatch
Michelson Laboratory, Physics Division
Naval Weapons Center
China Lake, California 93555

The laser-induced breakdown power (P_B) was measured for various neat liquids and various combinations of miscible liquids. P_B for the neat liquids and the mixtures was found to be proportional to $1/n_2$ (n_2 is the nonlinear index of refraction). From this result, we conclude that self-focusing dominates the breakdown process for these liquids (CS_2, benzene, nitrobenzene, chlorobenzene, bromobenzene, and toulene). The dependence of P_B for the neat liquids and mixtures on the f-number of the focusing optics was then measured and found to be in excellent agreement with the predictions of self-focusing theory for liquids with large n_2's. The liquids were then used as a "model system" to compare the results of similar measurements in single-crystal NaCl. This comparison indicates that the observed focal spot-size dependence in NaCl is not due to self-focusing.

Key words: Kerr liquids; laser induced breakdown; laser damage; NaCl; self-focusing.

1. Introduction

The laser-induced breakdown power (P_B) was measuerd in neat Kerr liquids and mixtures of Kerr liquids for a variety of focal conditions. The miscible Kerr liquids allow one to "nonlinear index match" various materials and separate the self-focusing contribution to the laser-induced breakdown process from other material dependent processes. The experimental results show that laser-induced breakdown in liquids with large optical Kerr constants is dominated by self-focusing and P_B is independent of focal conditions. However, for liquids with relatively low Kerr constants the self-focusing contribution to the breakdown process appears to be a function of the focusing condition. Comparison of the laser-induced breakdown measurements in liquids with similar measurements in NaCl indicate that the observed dependence of P_B on focal conditions in NaCl cannot be explained by simple self-focusing theory.

There was a two-fold motivation for this work. First, there is a growing interest in materials with large nonlinear refractive indices for use in bistable optical devices and phase conjugation. Second, there is a continuing controversy as to the role of self-focusing in laser-induced damage. Of particular interest is the role of self-focusing in the focal radius dependnece of the laser induced breakdown fields in bulk optical materials. For example, Smith et al. [1] used the observed focal radius dependence of laser-induced damage at 1.06 μm with 30 psec pulses to infer the critical power for self-focusing for various materials, e.g., P_{CR} = 166 kW for NaCl. However, in earlier work by Fradin et al. [2] the lack of focal radius dependence for the laser-induced breakdown field in NaCl for 15 psec pulses at 1.06 μm was interpreted to mean that $P_{CR} >> 1.5$ MW. Recent work has shown that the focal radius dependence of breakdown fields is sample dependent and is dependent on the range of focal radii used in the experiment, i.e., there is no single, simple spot size scaling law that can be applied to laser-induced breakdown measurements [3,4,5]

2. Experimental

The experimental setup was identical to that used in laser damage experiments in our laboratory (see Figure 1 in reference 6). The laser source used in this work was an electro-optic Q-switched Nd:YAG system constrained to operate in the TEM_{00} spatial mode. The energy of each pulse was measured with a pyroelectric detector which was calibrated with a thermopile calorimeter. The laser pulsewidth was 9 nsec (FWHM) and was measured with high speed photodiodes read by a 1 GH oscilloscope. The input power was calculated from the measured energy and measured pulsewidth. The power at the specimen was controlled by varying the angle between a pair of Glan polarizers arranged in a polarizer/analyzer configuration. The analyzer remained fixed to ensure that the beam polarization at the specimen was constant for all intensities. A coaxial HeNe laser was used to align the optical system, center the focusing lens, monitor the position of the linear otpics focal point, and to monitor occurance of increased scatter associated with laser induced breakdown in the solid and liquid specimens. Each site in the solid samples was irriated only once, and the laser-induced breakdown threshold was taken to be that power which produced, with 50% probability, a perceptible change in the specimen when viewed with a 20x microscope.

The laser beam was focused into the specimen by either a 162 mm or a 51 mm focal length lens. The 162 mm lens was a corrected doublet and the 51 mm lens was a "best form" singlet designed for minimum spherical aberrations. Table I summarizes the focal conditions used in these experiments. In all cases the focusing lens diameter was much longer than the laser beam diameter ($2\omega_s$) at the lens. The effective f/no. of a lens under these conditions is the lens focal length divided by the beam

Table I. Focal parameters. The effective f/no. was controlled by adjusting the distance (z) between the focusing lens and the cavity waist. Varying z changed the beam radius (ω_2) at the focusing lens. The quantity ω_{02} is the $1/e^2$ radius of the intensity in the lens focal plane calculated using linear optics.

f(cm)	z(cm)	ω_s(cm)	f/No.	ω_{02}(μm)
16.2	195	0.125	65	47
16.2	377	0.221	37	26
5.1	195	0.125	20	14
5.1	377	0.221	12	7.9
5.1	610	0.350	7.3	5.5

diameter ($2\omega_s$) at the lens. The beam diameter at the lens, and thus the effective f/no. was varied by changing the distance from the laser cavity waist to the focusing lens. The effective f/no. used in these experiments was varied over the range f/7.3 to f/65.

The Gaussian parameters of the laser output beam was determined by a series of pinhole and edge scans of ω_s, the radius of the unfocused beam at the $1/e^2$ point in the intensity. The accuracy with which we could define the beam parameters was ±4% and was limited by the accuracy of the measurements of the unfocused beam radius.

The quantity ω_{02} listed in Table I is the $1/e^2$ radius of the intensity in the focal plane of the focusing lens calculated using linear Gaussian optics and the experimentally determined beam parameters (position and size of the cavity waist and beam divergence). Spherical aberrations were calculated for each focal condition and were found to be negligible except for the f/7.3 condition. For this case the ω_{02} radius listed contains a 0.5 μm correction for spherical aberrations.

The quantity ω_{02} is used to label the results in many of the figures in the following sections of this paper. One of the conclusions of this work is that self-focusing dominates much of these results. Thus, one should view ω_{02} as a parameter which labels how tightly the beam was focused into the specimen. The actual focal radius in the presence of self-focusing is undoubtly much different from that calculated using linear optics.

3. Results

Figure 1 summarizes the results of laser-induced breakdown measurements in various neat Kerr liquids. The nonlinear index of refraction, n_2, is plotted as a function of P_B^{-1}, the inverse of the power required for laser-induced breakdown. The n_2 and P_B values have been normalized to the values for neat CS_2 ($n_2 = 3.29 \times 10^{-11}$ e.s.u. and $P_B = 14 \pm 1$ kW). The n_2 values used were calculated using the optical Kerr constants in reference 7. The materials measured are listed to the right of the graph in the order of decreasing n_2. The error bar shown in characteristic of the approximately 10% uncertainity in determining P_B, the power at which laser-induced breakdown occurs with 50% probability. These data were taken with a weakly focused beam, i.e., f/37.

The solid line in Figure 1 is the least squares fit of the data and the equation for this line is shown to the right of the plot. The parameter r^2 is the coefficient of determination and is a measure of how good the equation fits the data (r^2 equals one for a perfect fit). Note the linear relationship between n_2 and P_B^{-1}.

Figure 2 is a plot of n_2 vs P_B^{-1} for various mixtures of CS_2 and ethanol. Since these liquids are miscible, n_2 can be continuously varied by varying the relative concentrations of the two liquids. The data point in the upper right of the graph in Figure 2 corresponds to neat CS_2 and is used as the normalization point for the other data shown. The focal condition for these data was f/65. The focal radius for this arrangement, calculated using linear optics, was 47 μm.

The solid line in Figure 2 is the least squares fit of the data. The equation on the right of the graph is the equation for this line. As was the case with the neat liquids, the laser-induced breakdown <u>power</u> (P_B) is inversely proportional to the nonlinear index of refraction (n_2). This type of dependence is strongly suggestive that self-focusing or some other process which depends on $\chi^{(3)}$ (the third order nonlinear suceptability) was dominating the laser induced breakdown process.

Another test of the influence of self-focusing in laser-induced breakdown is to measure P_B as a function of how tightly the laser beam is focused into the specimen. This can be done with a series of lenses with different focal lengths at the same position relative to the cavity waist or by varying the position of the focusing lens relative to the cavity waist. In this work two lenses were used at various distances from the cavity waist resulting in a variation in f/no. from f/65 to f/7.3 (see Table I).

Figure 3 contains the results of measurements of P_B for various neat liquids over a wide range of focal conditions. The bar graph on the left in Figure 3 is P_B for neat CS_2 for five different focal conditions. Each bar corresponds to a given focal condition and is labeled by the focal spot radius (ω_{02}) calculated using linear Gaussian optics. The reader is reminded that the actual focal radius is quite likely different from that predicted by linear optics. Table I should be consulted for a more complete description of the focal conditions which corresponds to the ω_{02} values listed.

The table on the right in Figure 3 summarizes the results of P_B measurements for CS_2 and five other neat liquids. The P_B values listed are the mean values over the five focal conditions listed in Table I (f/65 to f/7.3) and σ is the deviation. The small standard deviation in P_B over this large range of focal conditions is strong evidence that self-focusing is dominating the laser-induced breakdown process in these high n_2 liquids.

Figure 4 is a summary of the results of measurements of P_B as a function of both n_2 and the focal conditions. Note that P_B for neat nitrobenzene and the 1:1 mixture of CS_2 and ethanol are essentially independent of the focal conditions. The 1:1 mixture of CS_2 and ethanol was chosen to give n_2 which matched the n_2 for neat nitrobenzene. For toluene and the 1:4 CS_2 - ethanol mixture (nonlinear index matched to the n_2 for toluene) there appeared to be a trend to higher value of P_B for more tightly focused beams. The range of values of P_B for toluene was only slightly outside the ±10% uncertainity in the various values of P_B. However, P_B for the 1:4 CS_2 - ethanol mixture showed a significant increase in P_B for tightly focused beams. This trend is most pronounced for the 1:9 CS_2 - ethanol mixture for which case P_B increased by a factor of three as the focusing condition was varied from f/65 to f/7.3. This result is not consistent with simple self-focusing theory.

The dependence of P_B on focal conditions for single crystal NaCl is contrasted with that of neat CS_2 in Figure 5. P_B for NaCl decreases with f/no. for large f/nos. but is nearly independent of f/no. for small f/nos. The laser induced breakdown intensity (I_B) calculated using the measured values of P_B and the focal radii calculated from linear optics is nearly constant for large focal radii and increases for small focal radii. As is shown in the discussion that follows the CS_2 results can be easily explained by simple self-focusing theory. However, the NaCl results shown in Figure 5 and the results shown in Figure 4 for low n_2 liquids are not explained by simple self-focusing theory.

4. Discussion

P_B for various neat Kerr liquids was measured over a variety of focal conditions (Figure 1 and 3). The results of these measurements indicate that for these liquids P_B is inversely proportional to n_2 and nearly independent of focal conditions over the range of f/65 and f/7.3. The results in Figure 4 show that P_B for mixtures of CS_2 and ethanol "nonlinear index matched" to neat nitrobenzene are the same as P_B for the neat liquid to within experimental uncertainity. This is a particularly noteworthy result when one considers that the chemical composition, the electronic structure and vibrational structure of the CS_2 - ethanol mixture are greatly different than those of the neat nitrobenzene. These results are all consistent with a model that assumes that self-focusing causes catastropic beam collapse which in turn results in the observed optical breakdown.

The miscible Kerr liquids allow one to continuously vary n_2 and investigate in detail the relationship between n_2 and P_B. The results shown in Figure 2 are compared with the predictions of self-focusing theory in Table II. The first equation in the left hand column is taken from Marburger's review paper on self-focusing [8]. P_{CR} is the critical power for self-focusing (expressed in c.g.s. units) and P_2 is the least power required for catroscopic self-focusing or a symmetric gaussian beam. The third line in Table II compares the derivative of n_2 with respect of P_2^{-1} with the experimentally determine slope of the n_2 vs P_B^{-1} dependence. The two slopes agree to within 10%. The final line in Table II shows that the calculated values of P_2 for CS_2 (from the Kerr constant in reference 7) and the experimentally determined value of P_B of neat CS_2 agree within 20%. The results of Table II show that the absolute value of P_B and the dependence of P_B and n_2 agrees quite well with that of P_2 predicted from simple self-focusing theory.

Table II. Comparison of Self-Focusing Theory and Experimental Results.

Theory	Experiment
$P_{CR}=\frac{A[8]}{n_2}$ where $A=\frac{c\lambda^2}{32\pi^2}$ $P_2=\frac{3.27\ A}{n_2}$	Measured P_B vs n_2 for various mixtures of CS_2 and ethanol with f/65 focal arrangement.
$\frac{d(n_2)}{d(P_2^{-1})}=3.72\ A$	$\frac{(n_2)}{(P_B^{-1})}=3.4\ A$
$P_2(CS_2)=17.3$ kw [7]	$P_B(CB_2)=14\pm1$ kw

The simple self-focusing model discussed above does not explain the results for the low index liquids presented in Figure 4 or the NaCl results shown in Figure 5. We have no difinitive explanation for this departure from the predictions of self-focusing theory. However, in the discussion that follows we propose a model for these results which we hope will stimulate discussion of this subject.

Our speculation is that for tightly focused beams the negative nonlinear change in the index of refraction due to the free electron plasma associated with optical breakdown cancels or partially cancels the positive index change due to the nonlinear polarizability of the bound electrons. In a paper in these proceedings Bryant

et al. [9] presented detailed theoretical calculations which predict that plasma defocusing will be dominant nonlinear effect in Ge at 2.7 μm. Hellwarth [10] first pointed out in 1970 that the free electron contribution to the nonlinear polarizability of a medium could cause defocusing of high power beams and perhaps pervent catastrophic breakdown. Yablonovitch and Bloembergen [11] used Hellwarth's plasma defocusing model to predict a limiting self-focal radius, i.e., a radius at which plasma defocusing cancels self-focusing. The calculations of this self-focal radius for sapphire agree quite well with the radii of damage tracks which had been attributed to self-focusing. In recent work Soileau [3,4] has suggested that the effects of self-focusing can be neglected for linear optics focal radii (i.e., focal radii calculated assuming linear optics) smaller than the limiting self-focal radius (also see Ref. 5). One of the major problems in testing this model is that one needs to know the breakdown intensity in order to calculate the limiting self-focusing radii; but to accurately determine the breakdown intensity one must better understand the contribution of optical self-action.

5. Summary and Conclusions

Kerr liquids and mixtures of Kerr liquids are good model systems for studying the influence of self-focusing in laser-induced breakdown experiments. Laser-induced breakdown in neat Kerr liquids and mixtures with high value of n_2 is explained by simple self-focusing theory, i.e., a theory that includes only the nonlinear polarizability of the bound electrons. P_B measured with tightly focused beams for NaCl and liquids with low n_2 cannot be explained by the simple self-focusing theory. A possible explanation for the observed discrepancies is the failure of the theory to include nonlinear effects such as plasma defocusing due to the free electron associated with optical breakdown. Until such time as a more complete treatment of self-action is available, workers should avoid adjusting laser-induced breakdown results for the presumed effects of self-focusing, and should include all the experimental parameters with the data presented.

Acknowledgments

The authors acknowledge the support of the Air Force Materials Laboratory and the Office of Naval Research.

References

[1] W. L. Smith, J. H. Becktel, and N. Bloembergen, Physical Review B 12, 706-714 (1975).

[2] D. W. Fradin, N. Bloembergen, and J. P. Letellier, Appl. Phys. Lett. 22, 635-637 (1973).

[3] M. J. Soileau, Ph.D. Thesis, University of Southern California, Aug. 1979.

[4] M. J. Soileau, M. Bass, and P. H. Klein, "Laser-Induced Damage in Optical Materials", 1979, pp. 497-518, NBS Special Publication, 568 (1979).

[5] E. W. Van Stryland, M. J. Soileau, A. L. Smirl, and W. E. Williams, "Pulsewidth and Focal Volume Dependence of Laser-Induced Breakdown," these proceedings.

[6] M. J. Soileau, "Mechanisms of Laser-Induced Breakdown in Antireflection-Coated $LiNbO_3$ Crystals," these proceedings.

[7] Y. R. Shen, Physics Letters, 20, 378-380 (1966).

[8] J. H. Marburger, Progress in Quantum Electronics, (Pergamin Press, 1975), pp. 35-110.

[9] G. W. Bryant, A. Schmid, Peter Braunlick, P. Kelly, and D. Ritchis, "Interactions of Intense 2.7 μm Picosecond Laser Pulses with Germanium," these proceedings.

[10] R. W. Hellwarth, "Laser-Induced Damage in Optical Materials, 1979," NBS Special Publications, 341, p. 67.

[11] E. Yablonovitch and N. Bloembergen, Phys. Rev. Lett. 29, 907 (1972).

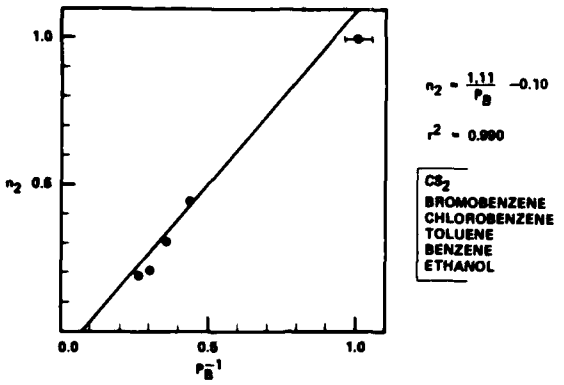

Figure 1. n_2 vs P_B^{-1} for neat liquids (f/37). The data has been normalized to the CS_2 values, i.e., $n_2(CS_2) = 1$ and $P_B(CS_2) = 1$. The n_2 value used were calcualted using the Optical Kerr constants from Reference 7. The materials are listed on the right in the order of decreasing n_2. P_B was determined by measuring the input power which produced optical breakdown with 50% probability. The error bar shown for the CS_2 point is characteristic of the ~±10% uncertainity in determining P_B for all the points shown. In this case the beam was wealy focused into the cell (f/37). The focused spot radius, calculated using linear optics, was 26 μm.

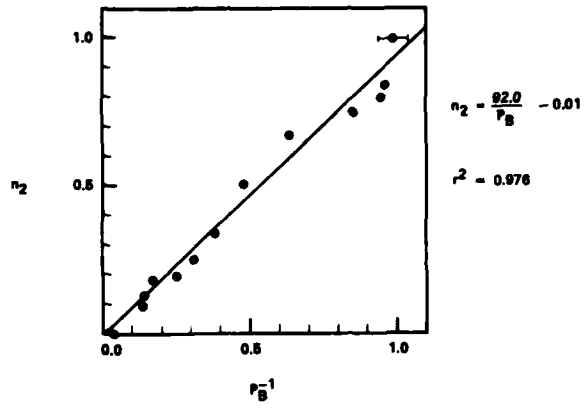

Figure 2. n_2 vs P_B^{-1} for CS_2:Ethanol mixtures. The point in the upper right corresponds to neat CS_2 and the point in the lower left corresponds to neat ethanol. The data above has been normalized to the values for neat CS_2. n_2 was varied by changing the relative concentration of CS_2 and ethanol in the mixture. Since n_2 for CS_2 is approximately 160 times larger than that of ethanol [7] the normalized n_2 values shown above are approximately equal to the volume fraction of CS_2 in the mixture. This data was taken using the f/65 focal condition (see Table I).

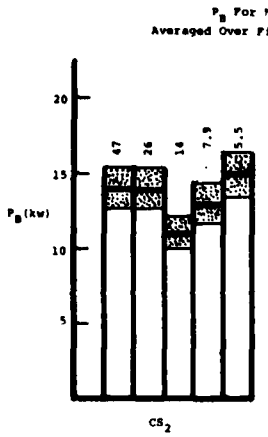

Neat Liquid	Average P_B	σ
CS_2	14 kw	$\pm$ 1 kw
NB	25 kw	$\pm$ 3 kw
CB	35 kw	$\pm$ 4 kw
BB	36 kw	$\pm$ 3 kw
Benzene	51 kw	$\pm$ 5 kw
Toluene	54 kw	$\pm$ 9 kw

Figure 3. P_B for various neat liquids for five focal conditions. The data in the bar graph is for CS_2 for the five focal conditions listed. The numbers on top of each bar label each focal condition. These numbers are the focal radii calculated from linear optics. The reader is refered to Table I for a more complete description of the focal conditions. The table on the right is the average P_B and the standard deviation for the five conditions for various liquids. NB, CB, BB, are abbreviations for nitro, cloro, and bromobenzene.

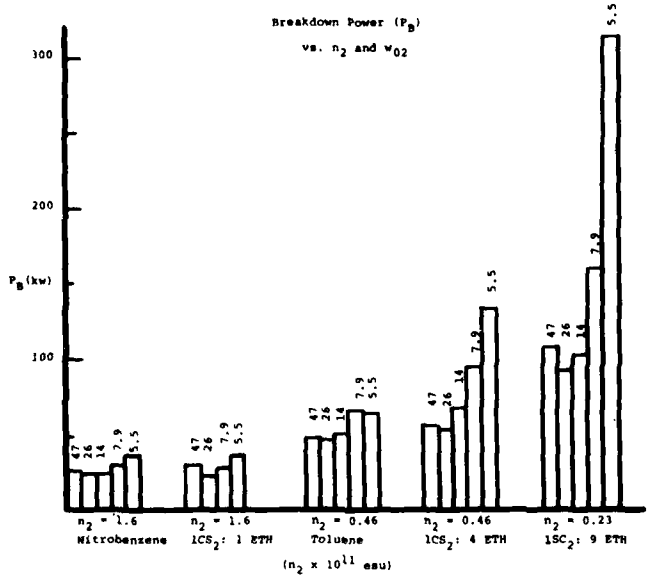

Figure 4. Breakdown Power (P_B) vs n_2 and ω_{02}. The number on top of each bar corresponds to the focal radius calculated from linear optics (ω_{02} in Table I) for a given focal condition. These numbers for ω_{02} should only be taken as an indication of how tightly the beam is focused since self-focusing can greatly alter the beam radius at the lens focus.

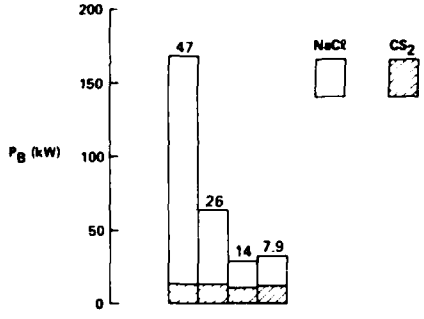

Figure 5. P_B vs Focal Radius. In this plot the variation in P_B for NaCl with the focusing condition is compared to similar measurements in next CS_2. The label on top of each bar corresponds to the focal radius calculated using linear Gaussian optics. The dependence of P_B of NaCl is not consistent with simple self-focusing theory.

The suggestion was made that the spot size in the material be measured. The possibility was suggested that small errors in spot size could account for the observed discrepancy. The author replied that the spot size did not need to be known accurately for comparison measurements. For some liquids good ageement was found with the theory, for others not.

DEFORMATION OF INTENSE LASER BEAMS TIGHTLY FOCUSED INSIDE NaCl: A COMPARISON OF THE MULTIPHOTON-POLARON AND AVALANCHE MODELS OF OPTICAL BREAKDOWN

P. Kelly and D. Ritchie
National Research Council
Ottawa, Canada K1A 0R6

and

P. Braunlich, A. Schmid, and G. W. Bryant
Department of Physics
Washington State University
Pullman, Washington 99164

Computer simulations of the interaction of intense picosecond laser pulses (λ = 532 nm) with NaCl in the focal volume of a 2.54 cm focal length aberration-free lens indicate that severe beam deformation may take place at photon fluxes corresponding to the single-shot damage threshold measured under these experimental conditions. This deformation is the result of a change in the dielectric function which, in turn, is caused by free carriers generated via multiphoton-assisted avalanche ionization and/or multiphoton absorption. Strong self-defocusing prevents local photon fluxes from reaching values required to raise the lattice temperature sufficiently for damage to occur. We conclude that either both the avalanche ionization as well as the multiphoton-polaron absorption mechanisms of laser breakdown are invalid in their present form or that the experimentally determined damage thresholds do not pertain to the intrinsic properties of NaCl.

Key words: Avalanche breakdown; Beam deformation; Beam depletion; Free carrier absorption; Multiphoton absorption; Polaron absorption.

1. Introduction

A build-up of very large free carrier concentrations (10^{18}-10^{20} cm^{-3}) during the interaction of intense laser pulses with wide-gap optical materials is thought to be a prerequisite for damage occurrence according to all models of laser breakdown proposed so far [1,2].[1] Recent reviews of this subject were given by Smith [3] and Brawer [4]. Two basic modes of carrier generation are invoked: avalanche ionization of valence electrons after multiphoton generation of so-called starting electrons [5,6] and multiphoton ionization [1,7].

The changes of the dielectric function

$$\varepsilon(\omega) = \varepsilon_I + i\varepsilon_{II} \tag{1}$$

and the ensuing deformation of Gaussian beams, associated with high carrier densities, have been discussed by Yablonovitch and Bloembergen [5] based on a simple Drude model of conductivity and free carrier absorption, and by Schmid et al. [2] who retain the Drude conductivity term for ε_I and replace the phenomenological free carrier absorption contribution to ε_{II} by free-electron--acoustic-phonon interaction. Detailed calculations of the spatio-temporal flux distribution in the focal volume of an aberration-free lens in NaCl on the basis of the latter mechanism and on the multiphoton ionization-polaron absorption model of laser damage have been presented by Kelly et al. [8]. Severe beam self-defocusing and even beam break-up was shown to take place due to the free-carrier induced reduction in the refractive index. Beam depletion, assumed to be small, was neglected. These calculations were performed in an attempt to explain the damage morphology observed by Smith and coworkers [9] as a possible consequence of the combined effects of self-focusing (via n_2E^2) and self-defocusing. Here n_2 is the nonlinear refractive index and E the rms field strengths of the optical photon field.

The characteristic damage vestiges of about 1 μm diameter and 10 μm spacing along the beam axis, observed at damage threshold and described in reference [9], could not be simulated by these model calculations, quite possibly due to insufficient spatial resolution. (In this connection it is of interest to note that a recent discussion of aberration effects on the flux distribution in the focal volume of short focal length lenses could not account for the damage morphology either [10].) Smith et al. [9] believe that local statistical variations of the density of starting electrons are the reason for the damage microsites. They discount any effects of free carriers on the dielectric function and consider only self-focusing. A calculation by these authors of the spatial temperature distribution, i.e. the crystal volume inside an ellipsoidal isotemperature surface $T = T_M$ (T_M = 1074°K is the melting point of NaCl) and its apparent coincidence with a severely damaged region in the focal volume of the laser beam, is taken as one of several important clues for the validity of the avalanche model of laser breakdown [3]. Nevertheless, in light of earlier discussions of the multiphoton-assisted avalanche model which indicated that the free carrier density may reach 10^{20} cm^{-3} for picosecond pulses at damage threshold [6], a detailed computation of self-defocusing based on the avalanche model was clearly desirable.

We have applied the computer code "PULSE," developed by Kelly et al. [8], to this problem and also recalculated the multiphoton-polaron case, because recent improvements in the code now account fully for beam depletion. Thus, direct comparison of both damage mechanisms is possible. The

[1] Figures in brackets indicate the literature references at the end of this paper.

obtained results are remarkable: neither of the two basic models of laser-induced breakdown predict damage at the experimentally determined threshold because of very pronounced self-defocusing.

2. Models of Optical Breakdown

The details of the avalanche ionization model [3,4,6,9] and the multiphoton-polaron absorption model [2,7] of laser breakdown are available from the literature. Three aspects of the photon interaction with optical materials are considered in these model calculations. They concern the mechanisms of carrier generation and their effects on the dielectric function and on lattice heating.

i) Carrier generation

In NaCl, exposed to 532 nm photons, the density, n_c, of free carriers in the conduction band changes according to

$$\dot{n}_c = \omega_i n_c + \sigma^{(4)} n_v F^4 \tag{2}$$

in the avalanche model. The second term in equation (2) supplies the initial electrons. However, avalanche ionization quickly provides the majority of carriers [9]. Its rate is given by

$$\log \omega_i = 3.58 \log E + 8.62 . \tag{3}$$

Here E is the rms electric field strength in units of MV cm^{-1} and ω_i is the avalanche ionization rate in sec^{-1}. Only multiphoton carrier generation is retained in the multiphoton-polaron model. All symbols and parameters used above and from here on are explained in table 1.

ii) Lattice heating

In the avalanche model, lattice heating is obtained from the Drude-type conductivity. The energy absorbed per unit time and volume is

$$c_0 \rho \dot{T} = n_c e^2 \tau E^2 / m(1 + \tau^2 \omega^2) . \tag{4}$$

The detailed mechanism by which electrons gain energy from the photon field is often referred to as inverse Bremsstrahlung.

According to Pokatilov and Fomin [11], "dressed" electron (or polaron)-phonon scattering with instantaneous relaxation of the excited carriers back to the lower edge of the conduction band is taken as the mechanism by which energy is gained by the lattice in the multiphoton-polaron model [2,7]. It has a cross section σ_p and yields

$$c_0 \rho \dot{T} = \sigma_p F \hbar\omega . \tag{5}$$

Beam depletion is accounted for by subtracting the appropriate number of photons in all processes involving the absorption of photons. While this is straightforward for processes involving $\sigma^{(4)}$ and σ_p, the absorbed number of photons per unit volume of crystal materials in the avalanche ionization process is calculated from the energy gained by the lattice according to equation (4) together with the energy required to produce an increase in n_c during a small time interval which, chosen for computational convenience and the desired numerical accuracy, was $\Delta t = 0.03489$ psec.

iii) The dielectric function

Having independently accounted for absorption as described above, only changes in the refractive index, n, need be considered:

$$n = \sqrt{\frac{1}{2}} \left[\varepsilon_I + \sqrt{\varepsilon_I^2 + \varepsilon_{II}^2} \right]^{1/2} + n_2 E . \tag{6}$$

The real and imaginary parts of the dielectric function (eq. 1) are taken from the Drude model or from more accurate calculations of the polaron conductivity in the presence of collisions with acoustic phonons [2]. The self-focusing term $n_2 E^2$ is added phenomenologically. For lack of more precise information, we have simply chosen the Drude expressions for all calculations based on the avalanche model:

$$\varepsilon_I = n_0^2 [1 - 4\pi e^2 \tau^2 n_c / m n_0^2 (1 + \tau^2 \omega^2)]$$

and

$$\varepsilon_{II} = 4\pi e^2 \tau n_c / m (1 + \omega^2 \tau^2) \omega .$$

The value for the collision time τ is still subject to much debate [4]. We used the most recent one available, stated by Brawer [4] to be $\tau = \frac{1}{7.8} \times 10^{-13}$ sec, because it is also consistent with the choice $\tau^2 \omega^2 > 1$ in ε_{II}, made in earlier calculations of multiphoton-polaron damage [2,7]. An expression by Gurevich et al. is again taken for ε_I. It is stated in reference 2.

3. Beam Deformation

Beam deformation is a consequence of the nonuniform beam profile (e.g. a Gaussian) and photon-induced local changes of the refractive index. The computer code "PULSE" was developed to simulate the complete spatio-temporal behavior of short light pulses traversing optical materials [8]. It was designed to be applicable for any conceivable initial laser beam profile and beam shape (e.g. focused into the material), material distribution (e.g. uniform or layered, materials with refractive index interfaces, clad optical fibers and coatings on substrates). The particular experimental arrangement simulated in the present work is schematically shown in figure 1. It represents the configuration employed by Smith et al. [9,12] in their studies of the damage thresholds in alkali halides at λ = 532 nm. The FWHM pulse length is 21 psec.

In the model of the pulse, the energy is carried by 10^4 macroscopic "photons" of 10^{11} photons each whose trajectories are followed through the medium [13]. A Gaussian, clipped at the $1/e^3$ values of the peak flux profile in radial direction and in time, is attributed to the pulse and both, the pulse and the medium, are considered rotationally symmetric. These "photons" are injected into the solid with an appropriate group velocity to mimic refraction on the solid interface and focusing by the external f = 2.54 cm lens. In the absence of nonlinear photon-material interaction, the focal spot is located 0.2 cm behind the interface air-NaCl. Appropriate equation of motion (Snell's law of refraction and changes in group velocity) of each "photon" are solved to find the changes in direction, group velocity and total photon content (correction for absorption). Simultaneously, the material rate equations (2-5) are solved to determine index n and temperature T. This is achieved by treating all equations as finite differences equations with a time step Δt. For this purpose the interaction volume is divided into cells forming the grid schematically depicted in figure 2. The cell size used in the present calculation is Δr = 0.9 μm in radial direction and Δx = 7 μm in the direction of beam propagation along the axis. The time step chosen is Δt = 0.03489 psec. A total of 30 cells in radial and 100 in x-direction form the grid. Further details of "PULSE" are given in reference 13.

Selected flux distributions obtained from both models are presented in figure 3. They show the passage of a 21 psec pulse through the focal region in NaCl in successive time steps of 200 Δt (see indication on the right side of each picture). The peak rms field strength of this pulse is 12.7 MV/cm which corresponds to the measured damage threshold [9,12]. The numbers on the left side and on the x-axis indicate dimensions in μm. The "expected" location of the focal spot is at (F,r) = (2000 μm, 0). The direction of the beam is from left to right. The color code for the local photon fluxes is given in table 2. Severe beam deformation, particularly past the plane through F perpendicular to the beam axis, is obvious for both models. Yet, the details are distinctly different. This feature is interesting because it points to possibilities of discriminating between the two models of laser damage. For example, the time-integrated spatial flux distribution in a plane past the focal volume could be measured and compared with calculations.

The spatial distribution of the carrier density n_c at t = 1200, Δt = 41.9 psec after arrival of the pulse at (F,r) = (1500 μm, 0) is shown in figures 4 and 5 and the color code is given in table 3. Clearly, the spatial gradient of the refractive index associated with such a distribution is responsible for the observed beam-scattering away from the center of the focal volume.

The spatio-temporal evolution of the lattice temperature T was monitored as well. Remarkably, it did not increase more than 4K above the initial temperature of 300K at any point in the interaction volume for either one of the two models. Thus, damage believed to be the result of rapid temperature pile-up, approaching the melting point T_M = 1074°K, is prevented in the discussed case for which breakdown was observed in the experiment by Smith et al. [9,12]. This may only be explained as follows:

i) Neither one of the two models of laser damage does account for the measured damage data simulated here, and quite possibly, for all other classic experiments in alkali halides which have been used as the basis for the establishment mainly of the avalanche model; or

ii) not the intrinsic damage properties of the material have been observed in the experiment performed by Smith et al. [9,12], but some extrinsic feature caused the material to fail in the intense photon field of the laser pulse.

Two avenues of further research have to be pursued to resolve this issue. The first one concerns the improvements of the present models. For example, primary defect formation was recently shown to drastically influence the kinetics of the processes occurring during the damage event [14]. In particular, the densities of free carriers required for breakdown to be initiated are up to one order of magnitude smaller than those obtained when the photochemical reactions, involving these defects, are disregarded as was the case in the present investigation. The second one is the production of improved wide gap materials and the performance of new experiments in an attempt to experimentally observe true intrinsic breakdown phenomena.

Acknowledgment

This work was supported by AFOSR contract number F49620-28-C-0095 and by the National Research Council, Ottawa, Canada.

References

[1] Bräunlich, P. and Kelly, P. J. Appl. Phys. 46, 5205 (1975).

[2] Schmid, A., Kelly, P., and Bräunlich, P., Phys. Rev. B 16, 4569 (1977).

[3] Smith, W. L., Optical Engineering 17, 489 (1978).

[4] Brawer, S., Phys. Rev. B 20, 3422 (1979).

[5] Yablonovitch, E. and Bloembergen, N., Phys. Rev. Lett. 29, 907 (1972).

[6] Bräunlich, P., Schmid, A., and Kelly, P., Appl. Phys. Lett. 26, 150 (1975).

[7] Kelly, P., Schmid, A., and Bräunlich, P., Phys. Rev. B 20, 815 (1979).

[8] Kelly, P., Ritchie, D., Schmid, A., and Bräunlich, P., Proceedings of the 11th Annual Conference on High Laser Power Optical Materials, A. Glass and A. Guenther (ed.), Boulder, Colorado, 1979 (in press).

[9] Smith, W. L., Bechtel, J. H., and Bloembergen, N., Harvard Technical Report 665 (1976).

[10] Bryant, G. W. and Schmid, A., Proceedings of the 12th Annual Conference on High Laser Power Optical Materials, A. Glass and A. Guenther (ed.), Boulder, Colorado, 1980 (in press).

[11] Pokatilov, E. P. and Fomin, V. M., Phys. Stat. Solidi B 73, 553 (1976).

[12] Smith, W. C., Bechtel, J. H., and Bloembergen, N., Phys. Rev. B 15, 4039 (1977).

[13] Bräunlich, P., Bryant, G., and Kelly, P., Annual Report for Contract AFOSR Number F49620-28-C-0095 (1979).

[14] Bräunlich, P., Brost, G., Schmid, A., and Kelly, P., Proceedings of the 12th Annual Conference on High Laser Power Optical Materials, A. Glass and A. Guenther (ed.), Boulder, Colorado, 1980 (in press).

Table 1. List of symbols.

n_c : free carrier density, concentration of electrons in the conduction band [cm^{-3}].

n_v = 2.24 x 10^{22} [cm^{-3}]: concentration of valence electrons

ω : angular frequency of photons

F : photon flux [number of photons per cm^2 and sec]

λ = 532 [μm]: photon wavelength

E : rms optical field strength [MV/cm]

α_i : avalanche ionization rate [sec^{-1}]

$\sigma^{(4)}$ = 1.45 x 10^{-111} [cm^8 sec^{+7}] four-photon absorption cross section

σ_p = 1.5 x 10^{-17} [cm^2]: polaron absorption cross section

m = 0.75 m_e: mass of free carriers

ρ = 2.165 [g cm^{-3}]: mass density

c_o = 2.0 [cal $g^{-1}K^{-1}$]: specific heat

T : temperature [K]

e : electron charge

τ = (1/7.8)10^{-13}sec: electron phonon collision time

Δt = 0.03489 [psec]: time interval used in code "PULSE"

n_o = 1.54 refractive index in the absence of photon-material interactions

n : refractive index in the presence of photon-material interactions

n_2 = 6.4 x 10^{-13} [esu]: nonlinear refractive index

ϵ = ϵ_I + iϵ_{II}: dielectric function

Table 2. Color code for the photon flux [phot. $cm^{-2}sec^{-1}$].

$<10^{27}$	Black
10^{27}	White
$10^{27.5}$	Blue
10^{28}	Green
$10^{28.5}$	Red
10^{29}	Yellow
$10^{29.5}$	Magenta
10^{30}	Cyan

Table 3. Color code for carrier density [percent of valence electron density].

$<10^{-5}$	Black
10^{-5}	White
$10^{-4.5}$	Blue
10^{-4}	Green
$10^{-3.5}$	Red
10^{-3}	Yellow
$10^{-2.5}$	Magenta
10^{-2}	Cyan
$10^{-1.5}$	Blue
10^{-1}	Green
$10^{-0.5}$	Red

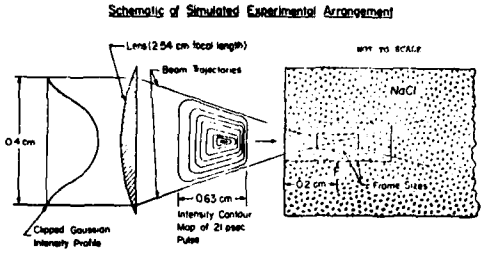

Figure 1. Schematic arrangement of the experiment performed by Smith et al. [9,12].

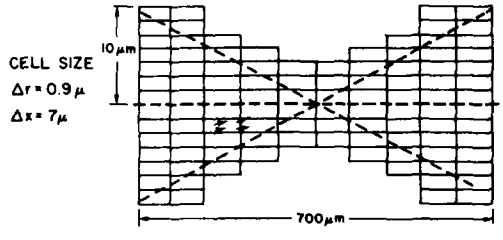

Figure 2. Schematic of the grid geometry used in the computer simulations.

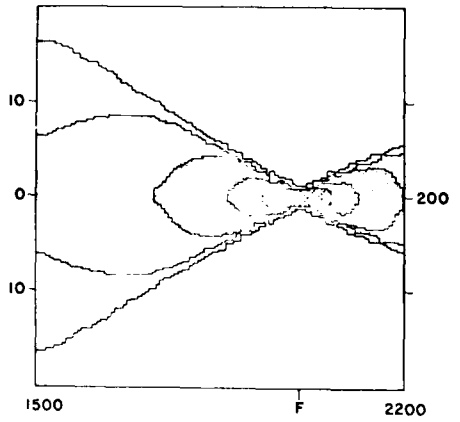
10
0
10
200
1500
F
2200

3a

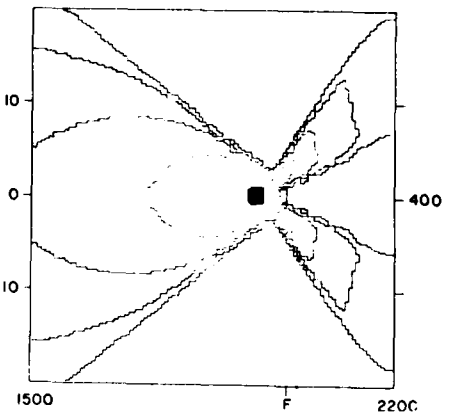
10
0
10
400
1500
F
2200

3b

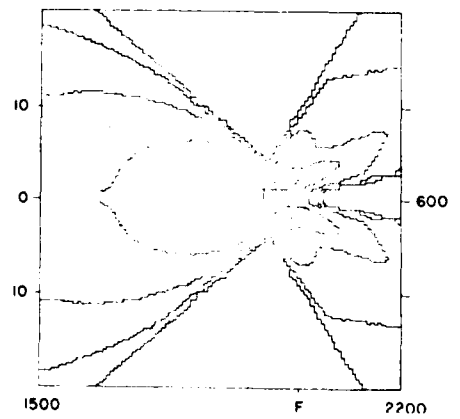
10
0
10
600
1500
F
2200

3c

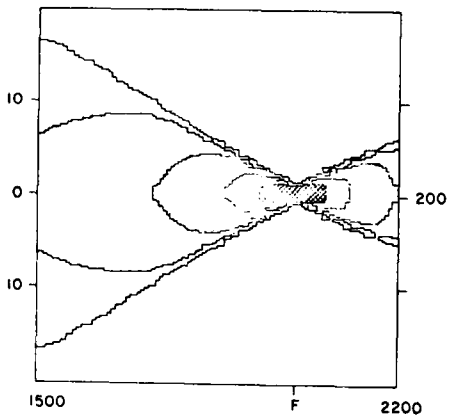
10
0
10
200
1500
F
2200

3d

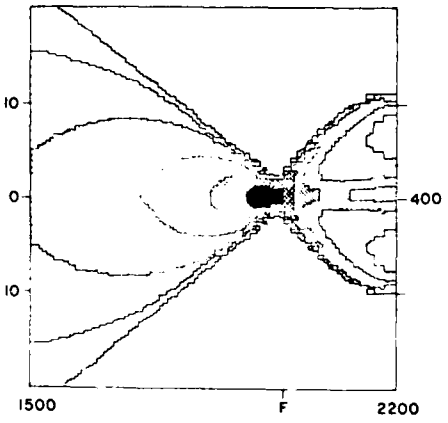
10
0
10
400
1500
F
2200

3e

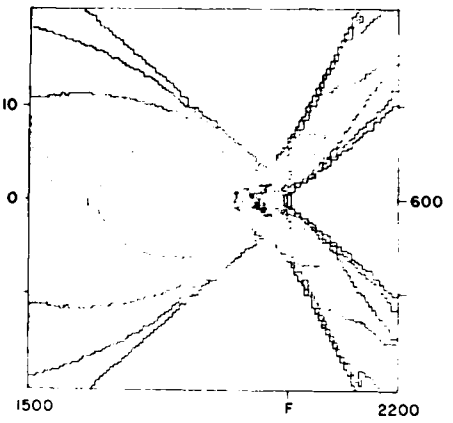
10
0
600
1500
F
2200

3f

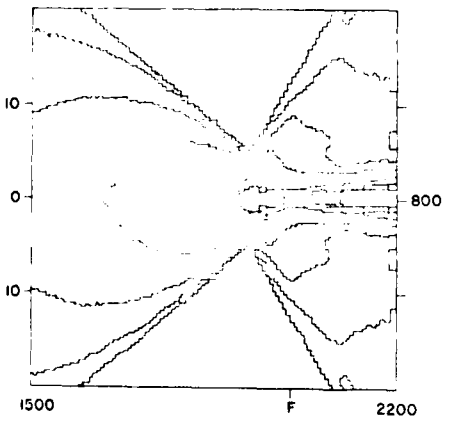
10
0
10
800
1500
F
2200

3g

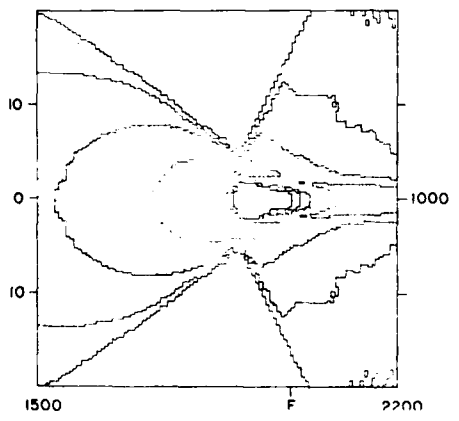
10
0
10
1000
1500
F
2200

3h

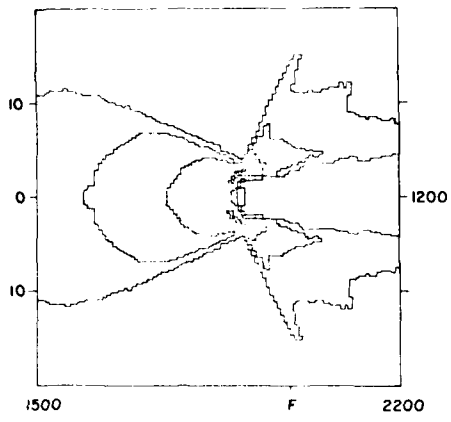

3i

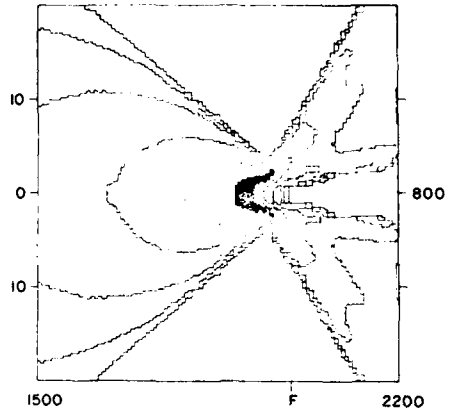

3j

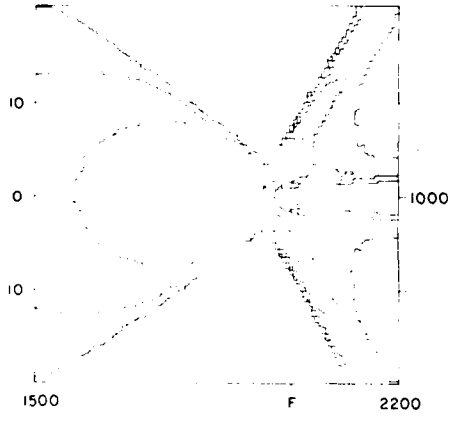

3k

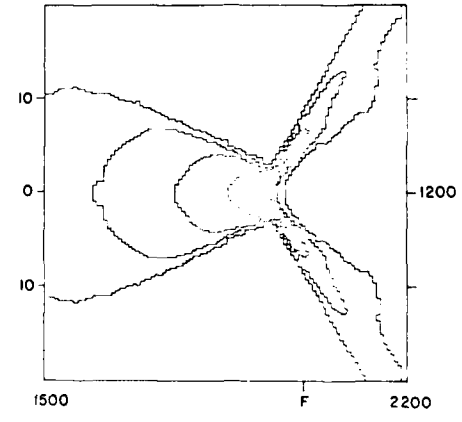

3l

Figure 3. Photon flux distributions at various times (in multiples of Δt as indicated at the right of each frame) in the focal volume. The pictures in the left column were obtained from the avalanche model, those in the right column from the multiphoton-polaron model. The color code is given in table 2.

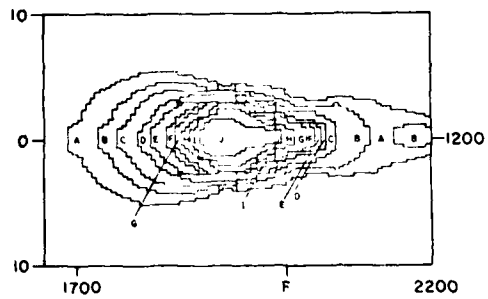

4a

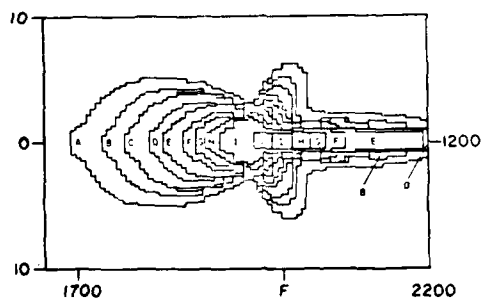

4b

Figure 4. The spatial distribution of the free carrier concentration reached at 41.9 psec = 1200 x Δt by avalanche ionization. The color code is given in table 3.

A CORRELATION OF LASER DAMAGE VESTIGE STRUCTURE AND SPHERICAL ABERRATIONS

P. Braunlich, G. Bryant, and A. Schmid
Department of Physics
Washington State University
Pullman, Washington 99164

Model calculations of spherical aberration effects on Gaussian beam propagation yield spatial intensity variations along the beam propagation direction. These intensity oscillations are compared with experimentally observed damage vestige sequences.

Key words: Damage morphology; Gaussian beam; Laser damage; Spherical aberration.

1. Introduction

Several sophisticated laser damage experiments [1-4][1] have recently shown that at threshold laser damage in wide band-gap materials results in a peculiar breakdown pattern along the beam propagation axis. This morphology was not entirely identical in all experiments yet similar enough qualitatively to be more than fortuitous. In general, damage vestiges of the order of 1 μm in size are found statistically distributed around the focal point with separation distances between them of the order of 5 to 10 times the size of individual vestiges. No clear trend with wavelength or with other experimental parameters has emerged so far. Earlier attempts to explain this intriguing behavior have used the avalanche ionization breakdown model to account for the statistical distribution of damage sites [1-3] or have resorted to qualitative arguments invoking spherical aberrations [4] in the laser pulse focussing system. Such aberrations were supposed to modulate the Gaussian intensity profile near the focal point and to enhance the local intensity sufficiently to trigger breakdown.

Unfortunately, no quantitative analysis was provided to back up the second hypothesis. We present here such an analysis for two different wavelengths, i.e. 1.06 μm and 0.53 μm, and consider different degrees of aberrations (i.e. different quality lenses) and different initial beam cross sections a_o. In the end, we will compare the observed damage morphology with our results.

2. Theory

We use a standard wave equation for the laser field

$$E(\vec{r},t) = \varepsilon(z,\vec{x}_\perp)\exp(i(kz - \omega t))$$

where z is the beam propagation directions and $\vec{x}_\perp$ represents points in the plane perpendicular to z, k is the usual wavevector $k = \omega n/c$. We assume the focussing lens to be located at z_L and the sample entrance surface to be situated at $z_s (z_s > z_L)$. Imposing the paraxial approximation on the field we solve

$$i\frac{\partial \varepsilon}{\partial z} + \frac{1}{2k}\nabla_\perp^2 \varepsilon = 0 \tag{1}$$

and find the field at any point $(z,\vec{x}_\perp)$

$$\varepsilon(z,\vec{x}_\perp) = \frac{k}{2\pi i(z-z_p)}\int d^2x_\perp\, \varepsilon(z_p,\vec{x}'_\perp)\exp\left(ik\frac{|\vec{x}_\perp - \vec{x}'_\perp|^2}{2(z-z_p)}\right) \tag{2}$$

if the field is known in the plane $z = z_p$. We thus find the field inside the sample by projecting it first from the lens to the sample surface, and from there into the sample, properly taking into account the changes in refractive index. The field is then described by

$$\varepsilon(z,\vec{x}_\perp) = \frac{kk_o}{(2\pi i)^2(z-z_s)(z_s-z_L)}\int d^2x'_\perp\, d^2x''_\perp\, \varepsilon(z_L,\vec{x}''_\perp)$$

$$\times \exp\left(ik_o\frac{|\vec{x}'_\perp - \vec{x}''_\perp|^2}{2(z_s-z_L)}\right)\times\exp\left(ik\frac{|\vec{x}_\perp - \vec{x}'_\perp|^2}{2(z-z_s)}\right)$$

$$(k_o = \omega/c)\,. \tag{3}$$

We now introduce spherical aberrations by following Born and Wolf [5] in our choice of $\varepsilon(z_L, \vec{x}_\perp)$:

$$\varepsilon(z_L,\vec{x}_\perp) = E_o\exp\left(-\frac{x_\perp^2}{2a_o^2}\right)\exp\left(-ik_o\left(\frac{x_\perp^2}{2R_o} + Bx^4\right)\right) \tag{4}$$

[1] Figures in brackets indicate the literature references at the end of this paper.

R_0 is the nominal focal length of the lens, a_0 is the Gaussian 1/e cross sectional width of the beam and B is the factor that determines the degree of spherical aberration. In damage experiments, the parameters R_0 and a_0 are usually known. Less so, however, is B. We therefore will test several values for B, i.e. 0.01 cm^{-3}, 0.05 cm^{-3}, and 0.1 cm^{-3}, which were chosen by taking experimental parameters known from damage experiments and by calculating B according to Ireland's [6] method. Using expression (4) in eq. (3) we can map out the intensity distribution along the beam axis.

3. Results

In figures 1-4 we show the results of our calculations for $\lambda = 1.06\mu$ and 0.53μ, $0.01\ cm^{-3} \leq B \leq 0.1\ cm^{-3}$ and $0.1\ cm \leq a_0 \leq 0.3\ cm$. In each case a 1.27 cm focal length R_0 is assumed in accordance with the lens reported in reference 1. The intensities are plotted normalized by E_0^2.

Several general features appear when the spherical abberations are included. First the primary peak in intensity no longer occurs at the geometrical focal spot, but instead occurs prior to it. Moreover, the main peak is smaller when the aberrations are included than it is for the corresponding Gaussian beam indicating the extra transverse spread of the beam when the aberrations are included. This decrease can be as much as two orders of magnitude when the aberrations are large. When the spherical aberration is sufficiently strong and the beam not too narrow, oscillations occur in the on-axis intensity resulting from constructive and destructive interference. We will consider these oscillations in intensity as a possible explanation for the multiple damage sites. The intensity is only shown prior to the focus in the figures. Beyond that point there are no more oscillations in intensity and it approaches that for the diffraction limited Gaussian beam without aberration.

Comparing figures 1-4 shows the effect of the beam radius a_0, wavelength λ and aberration B on the pulse propagation. First, as the beam becomes broader, the spherical aberration (proportional to x^4) becomes more important. For small a_0 the oscillations disappear and the main peak approached in magnitude the intensity of the Gaussian beam at the focus. For large a_0 the main peak is much smaller relative to the Gaussian focal intensity while the secondary peaks are much larger relative to the main peak. The absolute magnitude of intensity increases for increasing a_0 simply because a broader beam is focused.

When λ is varied the aberrations become more important for smaller λ. Decreasing (increasing k_0) is equivalent to simultaneously decreasing R_0, which compresses the oscillations, and increasing B, which enhances the magnitude of the oscillations. Consequently, similar trends occur for decreasing λ that occur for increasing a_0. The main peak decreases relative to the peak of the Gaussian beam while the side peaks become more important. Although the positions of the secondary peaks are insensitive to changes in a_0, they are sensitive to changes in λ. The pattern is compressed for small λ. This also occurs for a Gaussian pulse without aberration. Pulses for smaller λ are much more sharply focused because diffraction is less important.

When B is increased the pattern spreads out and the side peaks become more important. This contrasts with the change that occurs when λ is increased and the pattern spread out but the side peaks become weaker. In all cases, the trends observed for a_0 and B at one wavelength occur at all other wavelength considered between 0.53μ and 10.6μ. However for very long wavelengths ($\lambda \geq 10.6\mu$) the oscillations are only present for large beams ($a_0 \geq 0.3$ cm) or large aberrations ($B \geq 0.1\ cm^{-3}$).

If we now compare our results with published damage morphologies we find that at $\lambda = 1.06$ and $B = 0.01\ cm^{-3}$ [1], the observed vestige spacing is appreciably smaller than the calculated intensity peak separation. At 2.7 μm [4] the spacing becomes more comparable. However, at 2.7 μm spherical aberrations are less important than at shorter wavelengths, and better agreement at larger wavelength is therefore intriguing. We note, that the calculated intensity peaks are situated closer together the farther away from the focus they are, in general agreement with the trend in morphology observed in reference 1. Since our calculations show no intensity modulation peaks past the focal spot we also find agreement with the results of Anthes and Bass [3] who found no damage sites past the focal spot.

Despite the interesting qualitative agreements the lack of better quantitative agreement makes the significance of spherical aberrations seem less compelling. Note, however, that the intensity regime in which damage takes place is poorly explained as long as self-focussing effects are disregarded. We anticipate proper accounting of self-focusing to greatly enhance the peak structure and thus magnify effects due to spherical aberrations. Pertinent investigations are presently underway.

4. Acknowledgment

This work was supported by AFOSR through contract number F49620-78-C-0095.

References

[1] Smith, W. L., Bechtel, J. H., and Bloembergen, N., Opt. Commun. 18, 592 (1976).

[2] Smith, W. L., Bechtel, J. H., and Bloembergen, N., Phys. Rev. B 15, 4039 (1977).

[3] Anthes, J. P. and Bass, M., Appl. Phys. Lett. 31, 412 (1977).

[4] Danileiko, Yu. K., Lebedeva, T. P., Manenkov, A. A., and Sidorin, A. V., Sov. Phys. JETP 47, 401 (1978).

[5] Born, M. and Wolf, E., Principles of Optics, 5th ed. (Pergamon, Oxford, England, 1975).

[6] Ireland, C. L. M., Aaron, J. M., and Grey Morgan, C., Appl. Phys. Lett. 24, 175 (1974).

Figures

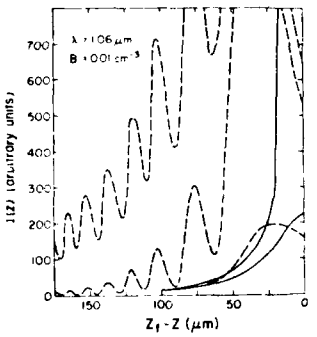

Figure 1. *On-axis intensity distribution prior* to focus z_f at λ = 1.06 μm and B = 0.01 cm^{-3}. Solid lines: A_0 = 0.1 cm lower curve, a_0 = 0.3 cm upper curve, case of no aberrations. Dashed lines: include aberrations a_0 = 0.1 cm, 0.2 cm, 0.3 cm in order of increasing magnitude of curve.

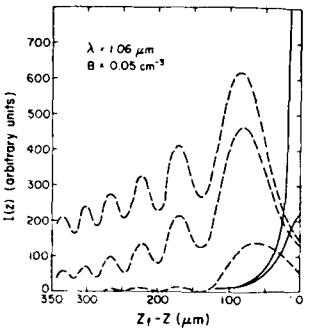

Figure 2. On-axis intensity distribution prior to focus z_f at λ = 1.06 μm and B = 0.05 cm^{-3}. Solid lines: no aberrations a_0 = 0.1 cm lower curve, a_0 = 0.3 cm upper curve. Dashed lines: include aberrations, a_0 = 0.1 cm, 0.2 cm, 0.3 cm in order of increasing magnitude of curve.

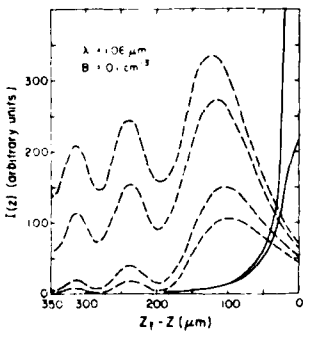

Figure 3. On-axis intensity distribution prior to focus z_f at λ = 1.06 μm and B = 0.1 cm^{-3}. Solid lines: a_0 = 0.1 cm lower curve, a_0 = 0.3 cm upper curve, no abberations. Dashed lines: include aberrations, a_0 = 0.01 cm, 0.2 cm, 0.3 cm in order of increasing magnitude of curve

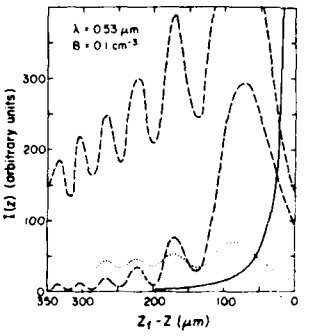

Figure 4. On-axis intensity distribution prior to focus z_f at λ = 0.53 μm and B = 0.1 cm^{-3}. Solid line: no aberrations, a_0 = 0.1 cm. Dashed lines: aberrations included a_0 = 0.1 cm and 0.2 cm for lower and upper curve respectively. Dotted curve: scaled by 10^{-1}, a_0 = 0.3 cm.

THE ROLE OF LASER-INDUCED PRIMARY DEFECT FORMATION IN OPTICAL BREAKDOWN OF NaCl

P. Bräunlich, G. Brost, and A. Schmid
Department of Physics
Washington State University
Pullman, Washington 99164

and

P. Kelly
Division of Physics
National Research Council
Ottawa, Canada K1AOS1

Rapid and efficient formation of primary defects (V_k-, F-, and H-centers, self-trapped excitons) influences the kinetic processes involved in laser-induced optical breakdown in alkali halides. These processes have been studied for the case of NaCl exposed to short (30 psec to 30 nsec) laser pulses at λ = 532 nm wavelength.

Rapid defect formation acts as a drain on the free electrons and holes, produced by multiphoton absorption in the laser photon field. As a consequence, the rate of temperature increase of the lattice by free or "dressed" carrier absorption is reduced and, thus the damage threshold is increased. This effect is compensated by additional channels of energy deposition to the lattice which are provided by formation of and photon absorption by the generated primary defects.

The net effect of the photochemical processes of primary defect formation is a slight reduction in the damage threshold and a marked decrease of the free carrier densities required for damage to occur. Beam deformation, caused by free-carrier induced changes of the dielectric function, should therefore be less pronounced than that predicted by model calculations of laser damage in the absence of primary defect formation.

Key words: Damage threshold; Excitons; NaCl; Optical breakdown; Point defects; Primary defects.

1. Introduction

In a series of classic experiments performed at the Naval Research Laboratories and in Japan in the 1970's, the group of Kabler, Williams, Faust, Bradford [1],[1] and later Suzuki and Hirai [2] have demonstrated that primary defects such as V_k-, F-, H-centers, and self-trapped excitons are produced extremely rapidly and efficiently from multiphoton-(and possibly impact ionization)-generated excitons in alkali halides and alkaline earth halides [3]. The formation of primary defect centers, all of which are strong absorbers of photons in the UV to IR region of the electro-magnetic spectrum, were suspected by Williams and Kabler [4] to seriously affect, if not invalidate, the mechanisms by which according to the basic damage theories, energy from an intense photon beam is deposited to the lattice of these solids:

1. *In addition to polaron (or free carrier) absorption, new channels of energy deposition to the lattice are created by the intense photon field of the laser pulse itself and, thus, theoretical laser damage thresholds may be reduced drastically below the predictions of either the avalanche or multiphoton models.*

2. *The efficient removal of electron-hole pairs by the rapid processes of primary defect formation reduces the multiphoton--or avalanche--generated free carrier concentration and, as a result, affects the free carrier absorption mechanisms of Joule lattice heating in such a way as to increase the theoretically predicted damage threshold.*

The net effect of these two processes is difficult to assess without a detailed study of the complex dynamics involved in the damage process. This analysis is presented in following sections of this paper.

2. Laser-Induced Primary Defect Formation

In 1975 Bradford, Williams, and Faust [1] discovered that, beginning with a virgin KCl crystal, only about 9 psec are required from the onset of its exposure to a 2660 Å pulse of 25 psec duration to create F-centers in their ground state at 12 K. Suzuki and Hirai [2] reported that F-centers are formed in a similar process with a rise time of 11 ± 9 psec in KI at room temperature. In this case, a short pulse of 3470 Å photons was used. Similar results were obtained in NaBr by Williams et al. in 1978 [3]. Very rapid formation of the lowest triplet state ($^3\Sigma_u^+$) of the self-trapped exciton (STE) has also been observed in KI (rise time $\leq$ 210 psec at 5 K) [2] and in NaCl (rise time ~5 psec at 12 K) [3].

Apparently, the reactions

$$e + h \rightarrow F(1s) + H$$
$$e + h \rightarrow STE(^3\Sigma_u^+) \qquad (1)$$

[1] Figures in brackets indicate the literature references at the end of this paper.

are very fast in all the halides that have been investigated to date. In these experiments electrons (e) and holes (h) are created by a multiphoton absorption process during the exposure of the crystal to short laser pulses. While the holes self-trap spontaneously (within $\leq 10^{-13}$sec) to form V_k-centers, the formation of the self-trapped exciton (STE) or of F-H-center pairs can occur on a psec time scale. By simultaneously measuring the free electron concentration and the formation time of the STE ($^3\Sigma_u^+$) states, Williams et al. [3] were able to determine the cross section of the process

$$e + V_k \rightarrow STE(^3\Sigma_u^+) \qquad (2)$$

to be $\sigma \geq 2 \times 10^{-14}cm^2$ in NaCl. Such a large cross section means that electron capture by the self-trapped hole (V_k-center) is an efficient and, most likely, dominant mechanism for the decay or trapping of free electrons under the conditions prevailing in these multiphoton experiments.

The detailed processes involved in STE, F- and H-center formation after e-h pair generation have been the subject of intensive research in recent years. A review of this work was given by Williams in 1978 [5]. We will not repeat any details here. Instead, we will briefly sketch only the main features of those primary defect centers believed to be relevant in the context of this present study.

2.1. The V_k-Center (Self-Trapped Hole)

As mentioned above, e-h pairs are created in a multiphoton absorption process (typically two-photon absorption is utilized). Spontaneous self-trapping of the hole to form a V_k-center is an exothermic reaction. The energy E_{Vk} gained by the system is not precisely known [6]. On the basis of a simple classical model, Gilbert [7] has estimated it to be about 1.5 eV for KCl, a value that is a reasonable approximation for NaCl as well.

The properties of the self-trapped hole have been reviewed by Kabler [8]. Important for our consideration concerning the role of V_k-centers (and other primary defects) in the laser damage mechanism are:

i) The above mentioned spontaneous conversion of a free hole to a V_k-center by self-trapping;

ii) Absorption of photons by and dissociation of the V_k-center;

iii) Thermally stimulated V_k-center reorientation and migration;

iv) Electron capture by V_k-centers to form self-trapped excitons which, as we will show later, will remain either in various excited states during the time of laser exposure or convert rapidly to a close F-H pair. According to Williams [5], the latter can be thought of as an isomer of an STE.

Process i) has been discussed before. The rate at which free holes of concentration p are converted to V_k-centers is $p\tau_{Vk}^{-1}$ with $\tau_{Vk} \leq 10^{-13}$sec in NaCl. While the system gains energy E_{Vk} per generated V_k-center, this energy may not be immediately available as a temperature increase of the phonon system.

There are several indications that point to spontaneous dissociation of the V_k-center after absorption of near infrared and visible photons. Calculated potential barriers of the excited V_k-center have no minimum. Since no luminescence due to the self-trapped hole alone has ever been observed, dissociation must occur extremely rapidly before any radiative transition can take place. It has also been shown that reorientation can be observed down to liquid He temperatures during V_k-center excitation by photon absorption [8]. This can only be explained if the self-trapped hole is released (dissociated) and retrapped at a different site, because the probability for thermally stimulated reorientation is extremely small at these low temperatures.

Thermally stimulated reorientation deserves further consideration because it provides a mechanism for V_k-center diffusion out of the usually small focal volume of the laser beam employed in laser damage experiments. The probability for reorientation and, thus, migration of a V_k-center has been shown to be proportional to $\nu\exp(-E_{reor}/kT)$. The most recent experiments by Larson et al. [9] confirmed earlier measurements [8] of $E_{reor} = 0.29$ eV for NaCl. Assuming a frequency factor $\nu = 10^{12}$ to $10^{13}sec^{-1}$, the probability per V_k-center to reorient at the highest temperature of interest (melting point at 1074 K) becomes about $2.5 \times 10^{-3}sec^{-1}$ to $2.5 \times 10^{-2}sec^{-1}$. Even when we assume that only one single reorientation process is required for the V_k-center to migrate out of the focal volume, we arrive at reorientation times (or survival times due to diffusion) that are considerably longer than the longest laser pulses employed ($\leq$ 100 nsec). Reorientation is insignificant also when it is compared with photon absorption and the associated spontaneous dissociation of V_k-centers. With a cross section $\sigma_{Vk} \approx 10^{-17}cm^2$, this process has a probability $\sigma_{Vk}F$ for V_k-center decomposition. Here F is the photon flux of the laser beam which, at the damage threshold, is larger [10] than $10^{27}cm^{-2}sec^{-1}$. Thus, photon-induced dissociation is by far the dominant mechanism for V_k-center removal and, therefore, we neglect V_k-center reorientation and migration.

Let us now turn to optical absorption by V_k-centers. The absorption spectrum peaks at 3.28 eV and has a width at half maximum of 1.11 eV. Neither the absolute value of the absorption coefficient is known [8] nor is the T-dependence of this absorption band. We neglect the latter and attempt to arrive at an approximate cross section σ_{Vk} by assuming the band to either have a Lorentzian or Gaussian shape. In both cases σ_{Vk} is at least $10^{-17}cm^2$ at λ = 5320 Å, the wavelength of interest for our calculations. This cross section implies an oscillator strength of about 0.2 which seems reasonable in light of similar values obtained for F-centers and other absorption centers.

2.2. The Self-Trapped Exciton

According to Williams et al. [3], capture of a free electron by a V_k-center is nonradiative and populates directly the metastable $^3\Sigma_u^+$-level of the STE. Further relaxation to the ground state proceeds both nonradiatively as well as via phosphorescence emission with decay time

$$1/\tau_{STE} = 1/\tau_R + \nu_s \exp(-E_s/kT) . \qquad (3)$$

For NaCl $\tau_R = 3.4 \times 10^{-4}$sec, $\nu = 4.1 \times 10^{+10}$sec, and $E_s = 0.099$ eV. At temperatures encountered in laser damage experiments (295 K $\leq T \leq$ 1074 K) τ_{STE} is on the order of 1 nsec and, thus, considerably longer than the time required to populate an excited state via absorption of 5230 Å photons. As we will show below, at photon fluxes $F \geq 10^{27}cm^{-2}sec^{-1}$ encountered in damage experiments, excitation of the STE($^3\Sigma_u^+$) state and eventual dissociation of the self-trapped exciton is more probable than decay to the ground state. For this reason we neglect the latter processes in all our considerations of laser damage in NaCl.

The efficiency of electron capture by V_k-centers to form the lowest metastable state of the STE was estimated to be 0.19 per multiphoton-created e-h pair in NaCl at 15 K [5]. While this apparently does not justify the assumption of free carrier decay to be due to electron captur into the $^3\Sigma_u^+$-state alone, we will show below that, for the purpose of our work, one does not go wrong in doing so nevertheless. Other channels for electron capture are available with similarly fast reaction times, leading, e.g. to the formation of close F-H pairs which, in turn, can either recombine rapidly or act as photon absorbers and, thus, contribute to the laser damage process as well. In effect then, it may be equivalent to either assume decay of n_c solely to the $^3\Sigma_u^+$-state or allow for both STE and F-H formation, provided the absorption cross section for photon absorption at 5320 Å is not grossly different for all three species, or recombination of close F-H pairs is a very rapid and efficient process at τ > 300 K as well, leaving only relatively small concentrations of separated (and stable) F-H pairs.

There indeed are indications that close (unstable) F-H pair production could occur with almost unit efficiency at elevated temperatures [3,5]. In this case, a calculation of the energy transfer from the laser photon field to the phonon system via unstable F-H pair formation would have to be based on electron - V_k-center recombination with about the same lifetime as was found for STE formation (namely $\tau = \nu V_k \sigma$) and the assumption of instantaneous F-H pair recombination. The total energy transferred in this process is then simply that required to generate the original e-h pair.

In the previous paragraphs it has become clear that the dynamics of the primary defect creation and recombination in the laser damage process is not only complex, but that the information available to date on lifetimes, efficiencies, cross sections, etc., is not complete. We were, therefore, forced to abandon any attempts of establishing a complete set of rate equations covering all transitions involved in the relevant reaction kinetics. Instead, we calculated a number of plausible scenarios, all of which fall within the boundaries defined by the maximum conceivable additional energy absorption of the lattice (corresponding to the minimum breakdown thresholds within the selected damage model of multiphoton-polaron absorption) and maximum reduction of the free carriers by primary defect formation.

2.3. The F-H Pair

Trapping of a free electron by a V_k-center was shown to produce a self-trapped exciton in the $^3\Sigma_u^+$ state. Another channel for V_k - e recombination leads to the formation of a close (or correlated) pair consisting of an F-center and an H-center. At this point, a few remarks concerning close (unstable) and stable F-H pairs are in order. As mentioned earlier, the $^3\Sigma_u^+$-state of the STE and the ground state of the correlated F-H pair are isomers, that is they are nothing but two minima (that of the F-H complex is slightly higher than the metastable state of the STE [3,5]) in a multidimensional diagram of the potential energy. An F-H pair is formed from an excited STE by rearrangement of two adjacent halogens in the lattice, always commencing with a so-called "very close," unstable pair in which the F-center and the H-center are direct neighbors (F-H pair precursor). In KI and KBr, these pairs are apparently formed with unit efficiency, however, many of them recombine back to a STE within less than 10 psec below 15 K. In our calculation it may, therefore, not be necessary to even consider these pairs because of their rapid transformation back to STEs. However, laser damage calculations make little sense if one were to demand restriction of the lattice temperature to below 15 K. Therefore, the rather efficient production of so-called close or correlated (that is just separated) F-H pairs must be discussed and considered carefully. On the other hand, stable (separated and uncorrelated) F- and H-centers are produced with very low efficiencies (for example $\leq$ 0.015 in KCl), and we are justified in assuming that their role in laser damage is relatively

unimportant. The definition of separated (yet close and still correlated) F-H pairs depends to some degree, on the experimental technique with which they are studied. For example, Williams et al. [3] find it convenient to measure F-center absorption 46 psec after e-h formation. In KCl the number of F-centers of this type produced per e-h pair increases from 0.18 at 15 K to 0.4 at 300 K and 0.8 at 880 K. Measurements of this kind are unavailable for NaCl; however, at 15 K the lowest triplet state of the STE is formed with similar efficiency (0.19). It is conceivable that in the NaCl experiment part of the absorption ascribed to the metastable STE was in fact caused by close F-H pairs whose spectrum is shifted to smaller wavelengths as compared to the spectrum of an F-center. It thus, overlaps the 5320 Å wavelength of the probe beam (see fig. 1) [3]. This brings us again back to the possible equivalence of two different model calculations, namely one that is entirely based on the STE as the sole primary defect to be generated, being a surrogate for all or absorbing species and, on the other side, one that assumes close F-H pairs are formed as well.

3. Models of Dielectric Breakdown at Optical Frequencies

The work reported here did not aim at finding criteria to discriminate between the avalanche ionization [11] or multiphoton absorption picture of damage [10,12]. The sole purpose was to study whether the incorporation of primary defect formation changes theoretically predicted breakdown thresholds. Both damage models rely on the build-up of large free carrier concentrations. Consequently, free carrier depletion and additional energy deposition to the lattice, brought about by primary defect formation, is expected to affect predicted damage thresholds in a manner that must be quite similar in both model description. Therefore, either one of these damage models might serve as a basis for these studies. We have opted for the multiphoton model for two reasons: a) most of the classic experiments on fast primary defect formation were performed using multiphoton free carrier generation and b) our previous investigation concentrated on the multiphoton mechanism of laser damage. It is described in detail in references 10 and 12. Here we sketch only its principal features. Specifics, given in table 1, related to NaCl exposed to intense pulses ranging from 30 psec to 30 nsec FWHM duration at 5320 Å (frequency-doubled Nd-YAG).

The multiphoton mechanism of carrier generation produces electrons at a rate $dn_c/dt = F^4 n_v \sigma^{(4)}$. Here n_c is the free electron density, F the photon flux, and $\sigma^{(4)}$ the generalized four photon cross section, its value (see table 1) being a reasonable estimate. Occasionally, this process of carrier generation has been criticized as being not observable in a transparent solid above order 2 because avalanche breakdown supposedly sets in before any measurable multiphoton absorption occurs. For example, Liu et al. [13] could not measure 3-photon absorption in NaCl at λ = 3550 Å. We believe that the experimental technique used in reference 13 may have to be responsible for the failure to observe the effect. Recently developed new methods [14] yielded 3-photon cross sections in CdS and PbI_2 of $\sigma^{(3)} = 3 \times 10^{-80} cm^6 s^2$. Even though direct measurements of $\sigma^{(4)}$ are not available at this time we are, in light of these new experimental results, strengthened in our conviction that the value listed in table 1 is correct within about one order of magnitude.

Disregarding for the moment carrier recombination during the duration of the pulse and discounting any contribution of free holes in the damage process, the free carrier density is

$$n_c(t) = n_v(o) \left[1 - \exp(-\sigma^{(4)} \int_o^t F^4(t')dt'\right]. \quad (4)$$

F(t) is the local photon flux, and n_v the density of valence electrons. To approximate the temporal pulse profile of the laser, we assume a clipped Gaussian

$$F(t) = F_p \exp[-\alpha(\frac{t}{t_p} - \beta)^2] \quad (5)$$

with α = ln 16 and $\beta = \frac{3}{\sqrt{\alpha}}$, t_p being the pulse length. The temperature increase of the lattice is computed from

$$c_o \rho \, dT/dt = F(t) n_c \sigma_p \hbar\omega . \quad (6)$$

The symbols in eq. (6) are explained in table 1, and σ_p is the cross section for photon absorption by polarons (free carriers) as calculated from the theory by Pokatilov and Fomin [15]. For acoustical-phonon scattering in NaCl at 5320 Å, $\sigma_p = 1.5 \times 10^{-17} cm^2$. As soon as T has reached 1074 K (melting point of NaCl), damage is assumed to occur. Damage thresholds E_B given as rms optical field strength for damage occurrence at the center of the pulse ($t = t_p/2$), calculated with this theory, are given in table 2 (case I) together with the densities n_c of free carriers reached at the onset of damage. These data form the basis for comparison with the results obtained from the new model calculations that consider the generation of primary defects in the lattice and their effects on lattice heating during the laser pulse.

4. Calculation of the Maximum Reduction in the Damage Threshold Due to Primary Defects

The lower limit of the breakdown threshold E_B corresponds to the case that considers only the additional absorption of photon from the laser field due to the creation of primary defects. The drain on the free carrier (polaron) concentration is neglected. The rate equations reflect this situation in the following manner: rapid defect formation is incorporated on the basis of the cross sections and lifetimes discussed in section 2. The energy of defect formation is assumed to be instantaneously deposited to the lattice. The defects formed are the V_k-center and the STE in its

lowest metastable state $^3\Sigma_u^+$. The latter is assumed to spontaneously dissociate back to a V_k-center and a thermalized free electron, thus its formation rate does not appear in the rate equations:

$$\frac{dn_c}{dt} = \sigma^{(4)}F^4 n_v$$

$$\frac{dp}{dt} = \sigma^{(4)}F^4 n_v - p\tau_{vk}^{-1} + F\sigma_{vk}V_k$$

$$V_k = n_c - p$$

$$n_v = N_v - p \,. \qquad (7)$$

Only the rate of temperature increase is affected in this case

$$c_o\omega \frac{dT}{dt} = F\sigma_p n_c \hbar\omega + FV_k\sigma_{vk}\hbar\omega + 2\hbar\omega V_k v\sigma \,. \qquad (8)$$

Here c_o and ω are the specific heat and the mass density of the crystal, respectively. The last term in eq. (8) corresponds to simplified expression for the energy gained by the lattice in a cycle consisting STE($^3\Sigma_u^+$) formation and subsequent release of the electron from the STE back to the conduction band by a two-step photon absorption process (see sec. 5), leaving a V_k-center behind. These rate processes are schematically shown in figure 2. The damage thresholds and the concentration of n_c, p, and V_k at the moment of damage onset (T = 1074 K) computed within this simplistic model are listed in table 2, case II. Compared to case I, we note a reduction in both the free carrier concentration as well as the damage thresholds. The former is readily explained by the fact that in the dynamic process the build-up of n_c does not need to reach values as high as before in order to cause damage because the additional channels of energy deposition to the lattice have the effect that now the polaron absorption rate $F\sigma_p\hbar\omega n_c$ is not required by itself to push the lattice temperature up to the melting point.

Of interest is the relative modest reduction in E_B caused by primary defect formation despite the extremely rapid formation of V_k-centers ($\leq 10^{-13}$sec) and STEs ($\leq 10^{-13}$sec at V_k-center concentrations $\geq 5 \times 10^{19}$cm^{-3}).

5. A Realistic Model

After calculating the maximum reduction of the laser damage threshold E_B that can be expected due to the formation of primary defects in NaCl, we now attempt to discuss the influence of these defects on laser damage in more detail. The previous considerations were based on a somewhat oversimplified model that did not take into acount the details of STE absorption and decomposition as well as the energy released to the lattice in the process of STE formation and photon-induced decomposition. In addition, the role of F-H pairs were neglected. This was necessary because instantaneous decomposition of the STE was assumed in order to assess the lower limits of E_B.

The subsequent treatment of the detailed model is still somewhat limited in that not all microscopic processes occurring during the interaction of intense photon fields with NaCl are considered. There are several reasons for this. The most important one is derived from the results obtained in section 4. The maximum changes in E_B that can be expected turned out to be far less severe than originally anticipated. After discussing a number of plausible models for the photochemical reaction kinetics involved, it became apparent that, up to a point, any improvement in model sophistication did not yield significant changes in E_B. We therefore limit our discussion to the case presented below. It represents a realistic model for assessing the Kabler-Williams problem in laser damage. It goes without saying that this model was not developed to calculate details of primary defect formation per se. In particular, separated F-H pairs are neglected and very closely associated F-H pairs are taken as isomers of the self-trapped exciton with identical absorption and decomposition properties. As a consequence, no details of the F-H formation are incorporated and the kinetics of their generation, migration, decomposition and conversion to secondary centers such as F' etc. cannot be studied with this model.

A schematic of all electron and hole transitions considered in the realistic model is shown in figure 3. Electrons of density n_c and holes, p, are again created by four-photon absorption. Free carrier or polaron absorption of photons occurs with cross section σ_p and is followed by instantaneous relaxation of the so produced hot carriers back to the lower edge of the conduction band CB. Formation of V_k-centers occurs with a rate $p\tau_{vk}^{-1}$. The rate of trapping free electrons, n_c, by V_k-centers to form STEs in the metastable $^3\Sigma_u^+$-state is $\sigma n_c V_k v$, where σ is the trapping cross section, v the average thermal velocity of free carriers and V_k the V_k-center density.

The STE($^3\Sigma_u^+$) states of density S absorb 5320 Å photons with an estimated oscillator strength of about 0.2. This yields again a cross section $\sigma_s = 10^{-17}$cm^2. In the process, excited states of

density S* of the STEs are populated (see fig. 1). In the intense photon field of a laser pulse having a peak power close or equal to the damage threshold, we feel justified to neglect decay of this excited state back to lower STE-levels. Therefore, we consider further excitation in a second photon absorption process up to a state at the end of the high energy tail of the STE($^3\Sigma_u^+$) absorption spectrum to be the dominant or only possible transition. Again, σ_{S*} is about $10^{-17}cm^2$. We further assume that this step removes the electron sufficiently from the self-trapped hole to cause decomposition of the STE. In the process the V_k-center is assumed to be recreated and a hot electron is left in the conduction band. Its relaxation contributes to lattice heating.

Formation and photon-induced decomposition of V_k-centers is described as before (sec. 4). The rate equations are now obtained as a straightforward extension of the previous model:

$$\begin{aligned}
\dot{n}_c &= \sigma^{(4)}F^4 n_v - \sigma n_c v V_k + \sigma_{S*} S^* F \\
\dot{p} &= \sigma^{(4)}F^4 n_v - p\tau_{vk}^{-1} + \sigma_{vk} V_k F \\
\dot{V}_k &= p\tau_{vk}^{-1} - \sigma_{vk} V_k F - \sigma n_c v V_k + \sigma_{S*} S^* F \\
\dot{S} &= \sigma n_c v V_k - \sigma_S S F \\
\dot{S}^* &= \sigma_S S F - \sigma_{S*} S^* F \; .
\end{aligned} \tag{9}$$

Within this model the increase in lattice temperature T is treated in the following manner: in addition to the polaron or free carrier absorption and relaxation cycle which contributes to the growth rate of the lattice energy an amount $\sigma_p n_c F\hbar\omega$ and the rate of energy gain $\sigma_{vk} V_k F\hbar\omega$ due to photon-induced V_k-center dissociation, the formation of STEs and their decomposition into a free electron and a V_k-center are now major contributors to the lattice energy.

Trapping a free electron by a V_k-center to form the $^3\Sigma_u^+$-state is again not exactly equivalent to energy deposition to the lattice in the form of a temperature increase because most of the 2.7 eV energy difference between this state and the lower edge of the conduction band must be considered the binding energy. Just as discussed in section 3, we again have to ask whether this energy is dumped into the phonon system only after STE-decomposition. The question then is, should the energy absorbed in the two-photon cascade transition in the process $S \rightarrow S^* \rightarrow e$ or the energy of formation of the $^3\Sigma_u^+$-state be considered gained by the lattice. In the first case the energy gain is $[\sigma_S SF(2\hbar\omega)]$ and in the second $\sigma n_c v V_k \times 2.7$ eV + $\sigma_S SF(2\hbar\omega - 2.7$ eV). We have discussed both and found very little difference in the effect on E_B. We present here only the latter. The increase in lattice energy is taken to be:

$$\begin{aligned}
c_o\dot{T} &= \sigma^{(4)}F^4 n_v(4\hbar\omega - E_g) + (\sigma_p n_c + \sigma_{vk} V_k)F\hbar\omega \\
&\quad + \sigma n_c v V_k(2.7 \text{ eV}) + \sigma_{S*} S^* F(2\hbar\omega - 2.7 \text{ eV}) \; .
\end{aligned} \tag{10}$$

Note that the energy of V_k-center formation is again assumed to be available as an increase in the temperature of the lattice phonon system only after dissociative photon absorption as in the discussion presented in section 4. Thus in the case of the V_k-center we adopted the opposite point of view as compared to the formation of the STE. We repeat that the effect of these choices concerning the exact microscopic mechanism of lattice heat increase have little effect on the damage thresholds calculated within these models. The time evolution of the carrier and defect densities as well as the lattice temperature during a 30 psec pulse according to eqs. (9) and (10) is shown in figure 4. The temporal pulse shape is a Gaussian clipped at the $1/e^3$-points. Its total pulse length is 62.4 psec and its width is t_p = 30 psec (eq. 5). The peak photon flux is chosen such that the time of damage onset (that is the temperature T has reached the melting point T_M) coincides with the temporal pulse center. All carrier concentrations plotted in figure 4 are given in percent of the valence electron density $N_v = 2.24 \times 10^{22}cm^{-3}$. Due to the nonlinear generation processes for free carriers all densities start to increase only just prior to damage. Of interest is the high concentrations of the primary defect centers reached during the pulse despite their effective decomposition in the intense photon field. These results are consistent with the fact that self-trapped excitons in the $^3\Sigma_u^+$-state are detected practically without measurable delay after the generating pulse in the experiment performed by Williams et al. [3].

A compilation of the damage thresholds vs. the reciprocal FWHM laser pulse length t_p^{-1}, calculated from the two models described in sections 4 and 5 is shown in figure 5. For comparison, an experimentally determined threshold at t_p = 21 psec [11,16] is indicated. Since there is a lack of additional data at λ = 532 nm, we have plotted an empirical curve for λ = 1.06 m as reported by Van Stryland et al. [17] in order to indicate the general trend of experimental $E_B(t_p^{-1})$ relations. Clearly, the effect on E_B of free carrier removal by primary defect formation is completely overcome

by the efficient new channels for energy deposition to the lattice that are created by the photochemical processes of defect generation. Yet, the overall reduction in E_B is relatively small. This last observation may account for the fact that, up to this point in time, no evidence of laser-induced chemical effects in alkali halides on the bulk damage threshold was ever observed, even though the directional emission of halogen atoms from crystals exposed to intense photon fields, measured by Schmid et al. [18], was taken as an early warning for the efficiency and intensity of damage precursor formation on the surface. In the bulk, the observation of stable color centers after exposure of a laser pulse up to damaging fluxes had actually never been reported. Severely damaged LiF crystals, however, are known to emit thermoluminescence [19].

At this point we come back to the question of how to handle close F-H pairs within the context of our problem. The exact kinetics of their recombination back to any STE-state or, via nonradiative transitions, back to the relaxed lattice is unknown. The absorption properties of ionized F-center separated F-H pairs are well documented as are the cross sections for electron capture by an ionized F-center (Cl vacancy). Such absorption and capture process will influence the damage threshold to some extent. Considering the fact that any F-H pair formed removes an STE and produces just another absorbing series, we anticipate little change in E_B computed in the case described in section 5 by including in detail the process of excitation and recombination of F-H pairs in the presence of the laser photon field. It seems obvious that, by lumping all formed primary defects together with their first state, the STE, and associating with it a representative absorption cross section ($10^{-17}cm^2$), the effect of primary defect formation on laser damage thresholds is fairly well represented indeed by the model of section 5.

In conclusion we find the efficient and rapid formation of primary defects in NaCl exposed to intense photon fluxes at λ = 532 nm severely effects the kinetics of free carrier generation and deposition of energy from the photon field to the lattice. Yet, the overall effect of these photochemical processes on the laser damage threshold remains relatively small because of the partially offsetting contributions provided by free carrier removal and photon absorption caused by formation and decomposition of these defects. The reduction in free carrier concentrations at damage onset over those calculated when no primary defects are assumed to be formed, however, is considerable. It is expected to have a significant effect on free-carrier induced beam deformation [20].

References

[1] Bradford, J. N., Williams, R. T., Faust, W. L., Phys. Rev. Lett. 35, 300 (1975).

[2] Suzuki, Y. and Hirai, J. Phys. Soc. Japan 43, 1679 (1977).

[3] Williams, R. T., Bradford, J. N., Faust, W. L., Phys. Rev. B 18, 7038 (1978).

[4] Williams, R. T. and Kabler, M. (private communication).

[5] Williams, R. T., "Photochemistry of F-Center Formation in Halide Crystals," Semiconductors and Insulators 3, 251 (1978).

[6] Sonder, E. and Sibley, W. in Point Defects in Solids, edited by J. H. Crawford and L. M. Slifkin (Plenum Press, NY, 1972), Vol. 1.

[7] Gilbert, T. L., cited in Reference 8.

[8] Kabler, M. N., "Hole Centers in Halide Lattices," in Point Defects in Solids, edited by J. H. Crawford, Jr. and L. M. Slifkin (Plenum Press, NY, 1972), Vol. 1, pp. 327-380.

[9] Larson, L. A., Oda, T., Braunlich, P., and Dickinson, J. T., Solid State Comm. 32, 347 (1979).

[10] Schmid, A., Kelly, P., and Braunlich, P., Phys. Rev. B 16, 4569 (1977).

[11] Smith, W. L., Optical Engineering 17, 489 (1978).

[12] Kelly, P., Schmid, A., and Braunlich, P., Phys. Rev. B 20, 815 (1979).

[13] Liu, P., Yen, R., and Bloembergen, N., IEEE, QE-14, 5741 (1978).

[14] Catalano, I. M., Cingolani, A., Ferrara, M , and Lugara, M., Optica Acta 27, 625 (1980).

[15] Pokatilov, E. P. and Fomin, V. M., Phys. Stat. Solidi B 73, 553 (1976).

[16] Smith, W. L., Bechtel, J. H., and Bloembergen, N., Phys. Rev. B 12, 706 (1975).

[17] Van Stryland, E. W., Soileau, M. J., Smirl, A. L., and Williams, W. E., Phys. Rev. B (1980), submitted for publication, private communication, and 1980 Boulder Conference on High Laser Power Optical Materials.

[18] Schmid, A., Braunlich, P., and Rol, P., Phys. Rev. Lett. 20, 1382 (1975).

[19] Frechette, V. D. and Cline, C., Appl. Phys. Lett. 10, 39 (1967).

[20] Kelly, P., Ritchie, D., Braunlich, P., Schmid, A., and Bryant, G. W., "Deformation of Intense Laser Beams Tightly Focused Inside NaCl: A Comparison of the Multi-photon-Polaron and Avalanche Models of Optical Breakdown" (1980 Boulder Conference on High Laser Power Optical Materials).

Acknowledgments

This work has been supported by the U.S. Department of Energy, Laser Fusion Program, under contract No. DE-AS08-79DP40105 and by the National Research Council of Canada, Ottawa.

Table 1. List of Symbols

n_c	=	free carrier density, concentration of electrons in the conduction band [cm^{-3}].
N_v	=	2.24×10^{22} [cm^{-3}]: concentration of valence electrons at t = 0, $N_v = n_v(0)$.
n_v	:	concentration of valence electrons [cm^{-3}].
p	:	concentration of free holes [cm^{-3}].
V_k	:	concentration of self-trapped holes (V_k-centers) [cm^{-3}].
S	:	concentration of self-trapped excitons (STE) in the $^3\Sigma_u^+$ metastable state [cm^{-3}].
S*	:	concentration of STEs in an excited state 2.38 eV above the S -state [cm^{-3}].
ω	:	angular frequency of photons.
F	:	photon flux [number of photons per cm^2 and sec].
F_p	:	peak flux of laser pulse.
λ	=	532 [nm]: photon wavelength.
E	:	rms optical field strength [MV/cm].
$\sigma^{(4)}$	=	1.45×10^{-111} [cm^8 sec^{+7}] four-photon absorption cross section.
σ_p	=	1.5×10^{-17} [cm^{-2}]: polaron absorption cross section.
σ	=	2×10^{-14} [cm^2]; cross section for electron capture by a V_k-center into the $^3\Sigma_u^+$-state of the STE.
σ_{vk}	=	10^{-17} [cm^2]; cross section for photon absorption by and dissociation of a V_k-center.
σ_S	=	10^{-17} [cm^2]; absorption cross section of a STE in the $^3\Sigma_u^+$ metastable state.
σ_{S^*}	=	10^{-17} [cm^2]; absorption cross section of the excited S*-state of the STE leading to STE dissociation.
τ_{vk}	=	10^{-13} [sec]; lifetime of a free hole.
m	=	0.75 m_e; mass of free carriers.
ρ	=	2.165 [g cm^{-3}]: mass density.
c_o	=	2.0 [cal $g^{-1}K^{-1}$]: specific heat.
T	:	temperature [K].
e	:	electron charge.
E_g	=	8.6 [eV]; band gap of NaCl.
T	:	temperature.
T_m	=	1074 [K] melting point.
t	:	time [sec].
t_p	:	FWHM of laser pulse length.
v	=	10^7 [cm sec^{-1}]; average thermal velocity of free electrons.

Table 2. Comparison of carrier and defect concentrations reached at onset of damage and of laser damage thresholds for various FWHM laser pulse lengths at λ = 532 nm in NaCl.

Model	t_p [psec]	E_B [MV/cm]	$n_c \times 10^{-20}$ [cm^{-3}]	$p \times 10^{-20}$ [cm^{-3}]	$V_k \times 10^{-20}$ [cm^{-3}]	$S \times 10^{-20}$ [cm^{-3}]	$S^* \times 10^{-20}$ [cm^{-3}]
CASE I:							
Fourphoton-polaron absorption without primary defects (see section 3)	30	14.5	30	----	----	----	----
	300	8.5	8.4	----	----	----	----
	3,000	5.28	2.2	----	----	----	----
	30,000	3.31	0.55	----	----	----	----
CASE II:							
Fourphoton-polaron absorption; maximum reduction of E_B by primary defects (see section 4)	30	9.36	2.24	1.12	1.12	----	----
	300	5.92	0.45	0.16	0.43	----	----
	3,000	3.80	0.16	0.022	0.14	----	----
CASE III:							
Fourphoton-polaron absorption; full effect of primary defects (see section 5)	30	10.9	2.01	1.16	0.85	2.7	2.7
	300	6.78	0.482	0.17	0.56	0.604	0.603
	3,000	4.25	0.128	0.021	0.107	0.138	0.138
	10,000	3.43	0.071	0.008	0.063	0.068	0.068

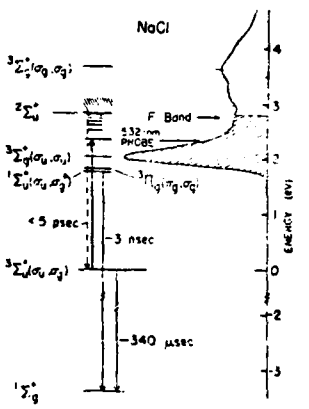

Figure 1. Energy levels of the self-trapped exciton in NaCl are shown along with the transient absorption spectrum as measured a few microseconds after electron pulse excitation at 10 K. The transient absorption spectrum also includes the F band shown by the dashed curve. The heavy arrow originating by $^3\Sigma_u^+$ corresponds to absorption of a 532 nm probe photon in the present experiment. The dashed arrow is a schematic representation of the population of $^3\Sigma_u^+$ from free-carrier states, observed in this experiment to occur in less than 5 psec. The 3 nsec fluorescence and 340 μsec phosphorescence transitions are also indicated. (From R. T. Williams et al., Phys. Rev. B 18, 7038 (1978))

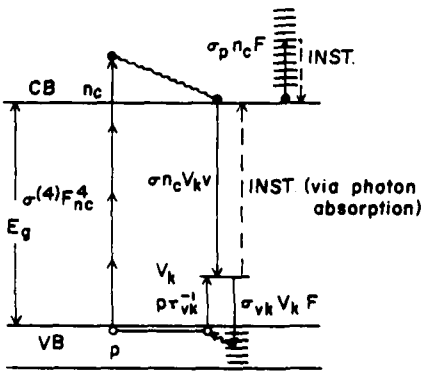

Figure 2. Schematic representation of the energy levels and transitions involved in the laser damage process and in laser induced primary defect formation. Note that trapping of a free electron by a V_k-center creates a self-trapped exciton, the energy levels of which are omitted. This model accounts for instantaneous replenishment of carriers that are used in the formation of primary defects. It is, therefore, a case that provides the largest reduction in the damage threshold by ignoring the drain on the carriers and fully incorporating the transfer of energy to the lattice due to primary defect formation. The symbols are listed in table 1.

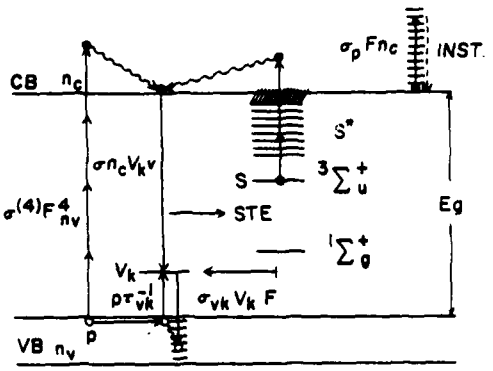

Figure 3. Schematic representation of a realistic model of the processes involved in laser damage in the presence of primary defect formation. The STE is taken as a surrogate for all absorbing defects formed by trapping a free electron in a V_k-center. All symbols are explained in table 1.

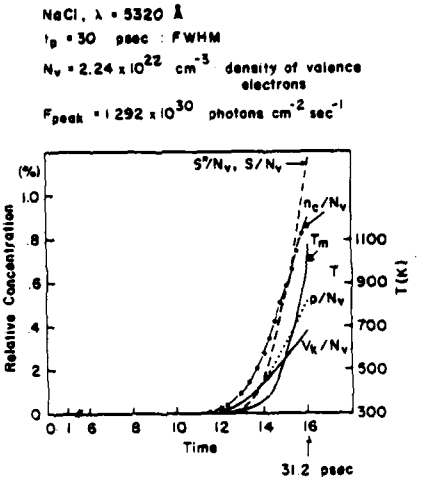

Figure 4. The time evolution of the free carrier concentration n_c, the hole concentration p, the V_k-center concentration V_k, the concentration S of self-trapped excitons in the metastable $^3\Sigma_u^+$-state and in an excited state, S*, and the lattice temperature T during a laser photon pulse of λ = 532 nm FWHM 30 psec pulse traversing NaCl. All densities are normalized to N_v, the valence electron density at time t = 0.

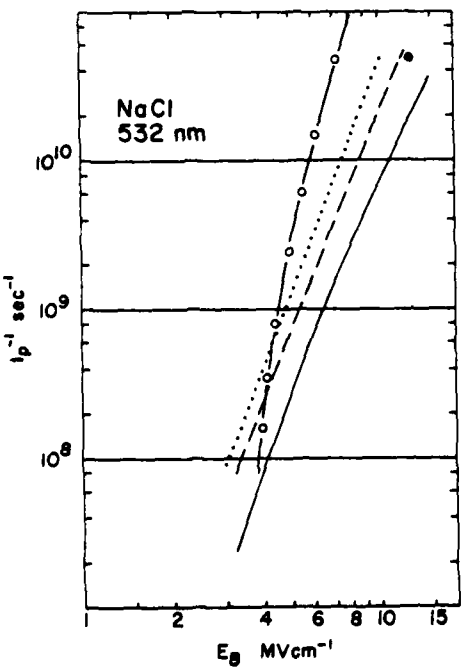

Figure 5. Laser rms breakdown field-strength as a function of the reciprocal FWHM width t_p of the laser pulse for NaCl at λ = 532 nm. Solid line: in the absence of primary defects. Dotted line: maximum reduction in E_B caused by primary defects assuming zero drain on (or instant replenishment of) the free carrier concentrations n_c and p (Fig. 2). Dashed line: E_B in the presence of primary defects according to the realistic model of section 5 (Fig. 3).

● : experimental data point (Ref. 16)

—○— : curve fitted to experimental data obtained at 1.06 μm (Ref. 4). The radius of the focal volume in this experiment was 6.1 μm.

No discussion of this paper.

THE HIGH FREQUENCY ELECTRON SCATTERING RATE AND DRUDE ZENER THEORY IN COMPOUND SEMICONDUCTORS

B. Jensen
Department of Physics
Boston University
Boston, Massachusetts 02215

Recent advances in laser and semiconductor device technology have generated a growing concern over the validity of the standard transport theory in the limit of small length scales, high frequencies, and high field intensities. This has necessitated a reexamination of the foundations of transport theory and the necessary quantum extension in these limits. In this paper, the response of free carriers in a polar semiconductor to a high frequency electric field is examined. A frequency dependent relaxation time has been derived for free carriers in polar semiconducting compounds with the band structure of the Kane theory from a quantum extension of the Boltzmann transport equation. The expression obtained reduces to the usual quasiclassical Boltzmann result in the limit of low frequencies, elastic scattering mechanisms, and parabolic bands, and gives the quantum result at high frequencies when used in the Drude Zener formula for the optical conductivity. A high frequency extension of the Drude theory is thus obtained which gives the observed λ^3 dependence of the absorption coefficient characteristic of polar scattering in III-V and II-VI compounds in the near infrared, and reduces to the usual λ^2 dependence at sufficiently low frequencies. At high intensities, the scattering rate becomes a function of field intensity.

Numerical results for the electron scattering rate are calculated as functions of frequency and carrier concentration and compared with available experimental data for a number of III-V compounds.

Key words: Laser damage; optical constants; optical materials; semiconductors; stimulated bremsstrahlung absorption; wavelength dependence.

The validity of the classical Drude Zener theory at high frequencies and high field intensities can be examined by observing the optical absorption of free electrons in semiconducting compounds. High intensity free carrier absorption (stimulated bremsstrahlung absorption) is of interest in connection with the problems of plasma heating and electronic cumulative ionization in gases and crystalline dielectrics under the influence of high power laser radiation. Of relevance for both these problems is the derivation of a formula for the mean rate of change of the energy of an electron under the action of a field. These topics have been treated by various authors [1]-[15].*

The classical Drude theory gives the rate of change of an electron in a high frequency field as

$$dW/dt = (e^2E^2/2m\omega^2)1/\tau \tag{1}$$

where E is the electric field intensity, ω the angular frequency, m the electron mass, e the electron charge, and $1/\tau$ the electron scattering rate.

The quantum formula can be expressed in the form [16]

$$\langle dW/dt \rangle = \langle \vec{J}.\vec{E} \rangle / n_e = \sigma \langle E^2 \rangle / n_e \tag{2}$$

with the identification

$$\langle E^2 \rangle = E^2/2 \tag{3}$$

where $\langle\ \rangle$ denotes the ensemble average and

$$\sigma = n_e e^2/m_n \omega^2 \langle 1/\tau \rangle, \qquad \omega\tau >> 1 \tag{4}$$

is the optical conductivity obtained from a quantum mechanical calculation [16]-[17]. The latter is proportional to the real part of the refractive index times the absorption coefficient. The carrier concentration is denoted by n_e.

The electron scattering rate is defined as

$$1/\tau = \langle 1/\tau \rangle \tag{5}$$

and it can be shown that this reduces to the usual expression in the limit of low frequencies, and elastic scattering mechanisms [16], and becomes frequency dependent in the near infrared [16]-[18]. Using eqs. (3-5) in eq. (2) one obtains for the quantum expression

$$\langle dW/dt \rangle = (e^2E^2/2m_n\omega^2)1/\tau \tag{6}$$

which is identical in form to the classical Drude expression in eq. (1). In eq. (6), m_n is the effective mass at the band edge and the correction for the dependence of effective mass on the Fermi energy in degenerate materials is incorporated into the definition of $1/\tau$.

It is found experimentally [19]-[21] that the classical Drude theory holds at low intensities in the far infrared and the experimental relaxation time if identified with

$$\tau = 1/\langle 1/\tau \rangle \tag{7}$$

* Figures in brackets indicate the literature references at the end of this paper.

gives the *dc* mobility as

$$\mu = e\tau/m^* \tag{8}$$

where m^* is the effective mass at the Fermi surface. This is found from the Kane theory [22] to be

$$m^* = m_n(1 + 2E_f/G) \tag{9}$$

where E_f is the Fermi energy measured relative to the conduction band edge and G is the band gap energy.

The Drude result breaks down in the near infrared at low intensities in the sense that $1/\tau$ becomes frequency dependent rather than a constant [23]-[26] and breaks down at low frequencies and high intensities in the sense that $1/\tau$ becomes a function of E [7], [14].

The frequency dependence of $1/\tau$ in the near infrared can be accounted for by a quantum mechanical calculation which gives the experimentally observed wavelength dependence of the absorption coefficient at high frequencies as follows [16]-[18]

$$n\alpha = (\omega_p^2/\omega^2 c)1/\tau \propto \begin{cases} \lambda^3, & \text{polar scattering} \\ \sim\lambda^4, & \text{impurity scattering} \end{cases} \tag{10}$$

while at low frequencies such that $\omega\tau >> 1$ one recovers the classical result

$$n\alpha = (\omega_p^2/\omega^2 c)1/\tau \propto \lambda^2 \tag{11}$$

$$\omega_p^2 = 4\pi n_e e^2/m_n$$

$$1/\tau \longrightarrow \text{constant} \tag{12}$$

The frequency dependence of $1/\tau$ is shown in figure 1 for various samples of InP, GaAs, and InAs. Uncompensated materials such that $n_e = N_i$, where N_i is the impurity concentration, are considered. For each material, sample A includes the contribution of polar optical mode scattering only. Samples C, D, and I include the contribution of polar and impurity scattering. The samples are identified, and numerical values of the low frequency limit of $1/\tau$ and the corresponding *dc* mobility are given in table 1. The scattering rates are calculated as discussed in [18]. Polar optical mode scattering dominates at high frequencies and is approximately independent of carrier concentration for light to moderately doped materials while impurity scattering strongly affects the low frequency ($\hbar\omega \sim k_0T$) limit. The dashed line shows the high frequency limit of the wavelength dependence for polar optical mode scattering.

Figure 2 gives a comparison of values of the mobility calculated here for InP (solid line) with theoretical values (dashed line) and the maximum experimental values (■, ○, ▲, □, X, ●) from [27]. In figure 2, the dashed line is the mobility calculated in [27], figure 14 for a compensation ratio of 1. Figure 3 gives a comparison of the mobility calculated here for uncompensated InAs (solid line) with theoretical values (dashed line) and the highest experimental values for a given concentration (X, △, ▲) for [27]. The polar mobility, which becomes increasingly unimportant at these concentrations, is also shown. The method of calculation is discussed in [18]. Figure 4 gives the theoretical results for mobility versus carrier concentration calculated here (solid line) and compares these with theoretical (dashed line) and experimental (●, ○, ■) results given in [28], figure 2. The solid circles are experimental results for bulk GaAs and the open circles are the electron mobilities in GaAs layers of modulation doped GaAs-AlGaAs superlattices in which the effect of impurity scattering is thought to be greatly reduced. These values lie close to the theoretical curve for $n_e \leq 5 \times 10^{17}$ where polar scattering dominates. The dashed line is a theoretical result (Brooks-Herring) from [28].

Figure 5 gives theoretical results for $e\tau/m_n$, $m_n = .071m$, for GaAs. The effective mass correction is omitted to illustrate the concentration dependence of τ while figure 4 gives the mobility with the effective mass correction included as calculated from (8). Figure 5 shows the maximum reported experimental mobilities for a given carrier concentration (●, ■, ▼) indicated by the solid symbols and compares these with the result for $e\tau/m_n$ calculated here (solid line) and with alternate theoretical calculations for the mobility (dashed line and + + + +). The experimental and alternate theoretical calculations are obtained from various sources discussed in detail in [18]. The alternate theoretical curves are both flatter than that obtained here and both give a higher mobility at high carrier concentrations. This is also true of the theoretical curve calculated here (solid line) and alternate theoretical curves (dashed line) shown for InP in figure 2. The difference is thought to be due to the treatment of screening in the alternate theoretical calculations and is discussed elsewhere [29].

In the limit $k_0T/E_f << 1$, one can approximate the impurity scattering rate $1/\tau^I$ by

$$1/\tau^I = 1/\tau_0^I \frac{(\ln 4E_f/k_0T + \frac{1}{2})}{12n_e V_c} \left[1 - \frac{\delta_c}{2\ln(4E_f/k_0T) + 1}\right] \tag{13}$$

where

$$\delta_c = 2(1 - [1 - a/\gamma(a)]^2) \tag{14}$$

$$a = E_f/G, \quad \gamma(a) = 1 + 2a$$

and

$$1/\tau_0^I = a^I/\pi\hbar^2 c_0 \tag{15}$$

$$q^I = 8N_i V_c (e^2/e_0)^2/\lambda_c^4, \quad c_0 = (G/2m_n)^{1/2} \tag{16}$$

$$1/V_c = 2/\pi^2 \lambda_c^3, \quad \lambda_c = \hbar/m_n c_0 \tag{17}$$

In (16), e_0 is the lattice dielectric constant and $N_i = n_e$ for uncompensated samples. Numerical values of the above constants in terms of experimental parameters are given for InP, GaAs, and InAs in table 2. The factor $12 n_e V_c$ in (13) is given as a function of the Fermi energy as

$$6 n_e V_c = \beta^3(a)\gamma^3(a) = 8[a(1+a)]^{3/2} \tag{18}$$

where

$$\gamma^2(a) = 1/[1 - \beta^2(a)] = (1+2a)^2 \tag{19}$$

$$\beta(a) = 2[a(1+a)]^{1/2}/(1+2a)$$

and $\beta(a)$ is proportional to the electron velocity at the Fermi surface using the hyperbolic band structure of the Kane theory. In the limit of parabolic bands $n_e V_c$ becomes proportional to the electron velocity as

$$12 n_e V_c = 2\beta^3(a) = 2(V_f/c_0)^3 \tag{20}$$

$$\beta(a) << 1, \quad \gamma(a) = 1, \quad a << 1$$

and one recovers the usual v^{-3} dependence of the impurity scattering rate. The values of V_c and λ_c for a given compound are functions only of G and m_n, or equivalently, of m_n and c_0. Equations (13-17) thus involve only experimentally available quantities.

Equation (13) is the lowest order term in a series expansion in powers of $k_0 T/E_f$. The exact result must be evaluated using methods of numerical integration.

GaAs in the material which gives the most satisfactory agreement with the calculated theoretical results. As shown in figures 4 and 5, the alternative theoretical calculations (dashed lines) differ from that calculated here (solid lines) in a manner similar to that observed for InP in figure 2. A maximum experimental mobility of 8500-8600 cm^2/v sec has been reported [30]-[32] as compared with a mobility of 8300 cm^2/v sec calculated here for polar scattering in the purest sample. The scattering rate for polar scattering is discussed in [18]. Agreement is obtained at low concentrations in figures 4 and 5 between the two theoretical calculations (dashed and solid lines) for GaAs as it is for InP in figure 2. The difference at high concentrations is apparently due to the treatment of the impurity scattering screening parameter. This is discussed in more detail elsewhere [29], but the form of eq. (13) can be obtained by assuming that effective electrons involved in the screening are those in the thermal layer of the Fermi surface for $\hbar\omega < k_0 T$. It has been recognized that deviations between computational methods at high carrier concentrations are due to the way in which the ionized impurity scattering rate is corrected for degeneracy [33].

Poth et al. [34] have discussed the mobility in GaAs at 77°K and have noted that the experimental mobilities at high concentrations were below theoretically predicted values and were independent of a wide variety of conditions of material preparation. This cast doubt on the assumption that all such highly degenerate materials were electrically compensated, although it was noted that compensation might play a role at low concentrations where an increased scatter in mobility values is observed. In figure 6, the experimental data of Poth et al. is plotted along with the impurity scattering mobility as calculated from the analytical expression in (8) using (13). As is shown, the analytical expression gives good agreement with the experimental data in the region where $k_0 T/E_f << 1$ and the approximation is valid, and also exhibits a fall below 10^3 cm^2/v sec at slightly higher concentrations. Since only uncompensated materials are considered here, and no adjustable parameters are involved in (13), differences between experiment and previous theoretical calculations might also have arisen as a result of the treatment of screening. The impurity scattering mobility is also plotted at 300°K and at 4°K in figure 6 to show the temperature dependence obtained from (8) and (13). For comparison, the total numerically integrated mobility including the contributions of polar plus impurity scattering is also shown at 300°K.

In tables III, IV and V, the results for the exact numerically integrated scattering rate and the approximate analytical expression are compared for InP, GaAs and InAs. It is seen that the polar impurity scattering rate decreases at high carrier concentrations and the mobility is mainly determined by impurity scattering which can be readily estimated with eqs. (8) and (13).

In table VI, the frequency dependent scattering rate is given as a function of wave number and carrier concentration n_e for InP, GaAs and InAs using the experimental parameters listed in table 2.

In summary, the polar optical mode and impurity scattering rates which give the quasiclassical Drude limit of the quantum theory have been derived and calculated for a variety of compounds. When used in the Drude Zener formula at high frequencies, these give the necessary quantum mechanical extension.

This research was supported by the Department of Energy under contract # DE-AC02-79ER10444.A000

References

[1] A. V. Vinogradov, Sov. Phys. JETP 43, 521 (1976)

[2] A. V. Vinogradov, Sov. Phys. JETP 41, 540 (1975)

[3] F. B. Bunkin, A. E. Kazakov, M. V. Fedorov, Sov. Phys. Uspekhi 15, 416 (1973)

[4] F. B. Bunkin, M. V. Fedorov, Sov. Phys. JETP 22, 844 (1966)

[5] S. Z. Belozerov, G. M. Zverev, V. S. Naumov, V. A. Pashkov, Sov. Phys. JETP 35, 158 (1972)

[6] I. B. Bernstein, C. E. Max, J. J. Thomson, Phys. Fluids 21, 905 (1977)

[7] G. H. Glover, J. Appl. Phys. 44, 1295 (1973)

[8] A. S. Epifanov, A. A. Manenkov, A. M. Prokhorov, Sov. Phys. JETP 20, 223 (1975)

[9] L. V. Keldysh, Sov. Phys. JETP 6, 763 (1958); 20, 1307 (1965); 34, 788 (1958)

[10] B. V. Paranjabe, Phys. Rev. 122, 1372 (1960)

[11] V. P. Silin, Sov. Phys. JETP 20, 1510 (1965); 11, 1277 (1960); 14, 617 (1962)

[12] A. Vaidyanathan, T. S. Walker, A. H. Guenther, IEEE J. Quantum Electron, 16, 89 (1980)

[13] Ya. B. Zel'dovich, Yu. P. Raizer, Sov. Phys. JETP 20, 772 (1965)

[14] E. M. Conwell, High Field Transport in Semiconductors, Academic Press, New York (1967)

[15] P. J. Price, IBM Journal, 193 (April 1959)

[16] B. Jensen, Ann. Phys. 95, 229 (1975)

[17] B. Jensen, Ann. Phys. 80, 284 (1973)

[18] B. Jensen, Phys. Status Solidi 86, 291 (1978); J. Appl. Phys. 50, 5800 (1979)

[19] R. N. Zitter, K. As'Saadi, J. Phys. Chem. Solids 35, 1593 (1974)

[20] S. Perkowitz, J. Phys. Chem. Solids 32, 2267 (1971)

[21] R. T. Holm, J. W. Gibson, E. D. Palik, J. Appl. Phys. 48, 212 (1977)

[22] E. O. Kane, J. Phys. Chem. Solids 1, 249 (1957)

[23] J. K. Kung, W. G. Spitzer, J. Electrochem. Soc. 121, 1482 (1974)

[24] B. V. Dutt, M. Al-Delami, W. G. Spitzer, J. Appl. Phys. 47, 565 (1976); 48, 2110 (1977)

[25] A. Kahan, AFCRL, Physical Sciences Research Papers, No. 537, AFCRL-TR-73-0122 (1973)

[26] E. D. Palik, R. T. Holm, "Nondestructive Evaluation of Semiconductor Materials and Devices," chap. 7, J. N. Zemel, Ed. Plenum (1979)

[27] D. L. Rode, Phys. Rev. B, 10, 3287 (1971)

[28] R. Dingle, H. L. Stormer, A. C. Gossard, W. Wiegmann, "Gallium Arsenide and Related Compounds 1978," (Inst. Phys. Conf. Ser. No. 45) p. 520

[29] B. Jensen, to be published

[30] J. I. Pankove, "Optical Processes in Semiconductors," (Prentice Hall, Englewood Cliffs, N. J. (1971)

[31] O. Madelung, "Physics of the III-V Compounds," Wiley, New York (1964)

[32] D. Long, "Energy Bands in Semiconductors," Wiley, New York (1968)

[33] M. A. Littlejohn, R. A. Sadler, T. H. Glisson, J. R. Hauser, "Gallium Arsenide and Related Compounds 1978," (Inst. Phys. Conf. Ser. No. 45) p. 242

[34] H. Poth, H. Bruch, M. Heyen, P. Balk, J. Appl. Phys. 49, 285 (1978)

Table 1

(T = 300°K)

InP	m^*/m_n	$n_e(cm^{-3})$	$1/\tau(sec^{-1})$	$e\tau/m^*(cm^2/Vs)$
A	1	4.69×10^{15}	5.38×10^{12}(polar)	4.53×10^{3}(polar)
B	1	2.25×10^{16}	5.51×10^{12}	4.41×10^{3}
C	1	6.27×10^{16}	5.75×10^{12}	4.23×10^{3}
D	1	4.13×10^{17}	7.57×10^{12}	3.22×10^{3}
F	1.02	6.17×10^{17}	8.42×10^{12}	2.83×10^{3}
G	1.06	1.23×10^{18}	1.03×10^{13}	2.22×10^{3}
H	1.10	2.13×10^{18}	1.20×10^{13}	1.85×10^{3}
GaAs				
A	1	3.40×10^{15}	3.00×10^{12}(polar)	8.30×10^{3}(polar)
B	1	2.80×10^{16}	3.30×10^{12}	7.10×10^{3}
C	1	6.30×10^{16}	3.60×10^{12}	6.70×10^{3}
D	1	1.40×10^{17}	4.00×10^{12}	6.20×10^{3}
E	1	3.40×10^{17}	5.10×10^{12}	4.90×10^{3}
H	1.10	2.20×10^{18}	1.00×10^{13}	2.20×10^{3}
I	1.14	3.40×10^{18}	1.20×10^{13}	1.90×10^{3}
K	1.26	8.70×10^{18}	1.30×10^{13}	1.50×10^{3}
L	1.48	2.50×10^{19}	1.50×10^{13}	1.20×10^{3}
InAs				
A	1	6.19×10^{15}	1.43×10^{12}(polar)	5.13×10^{4}
B	1	1.60×10^{16}	1.56×10^{12}	4.69×10^{4}
C	1	3.96×10^{16}	1.73×10^{12}	4.22×10^{4}
D	1	5.07×10^{16}	1.81×10^{12}	4.05×10^{4}
E	1	8.08×10^{16}	1.99×10^{12}	3.68×10^{4}
F	1.02	9.02×10^{16}	2.04×10^{12}	3.52×10^{4}
G	1.06	1.12×10^{17}	2.15×10^{12}	3.22×10^{4}
H	1.10	1.37×10^{17}	2.26×10^{12}	2.95×10^{4}
I	1.20	2.16×10^{17}	2.52×10^{12}	2.42×10^{4}
J	1.30	3.16×10^{17}	2.73×10^{12}	2.06×10^{4}

Table 2 [30]-[32]

T = 300°K	InP	GaAs	InAs
G(eV)	1.35	1.43	.36
m_n/m	0.073	0.071	.024
e_o	15.0	13.1	14.3
$(G/2m_nc^2)^{\frac{1}{2}}$	1/234	1/224	1/266
λ_c(cm)	1.23×10^{-7}	1.21×10^{-7}	4.26×10^{-7}
g^I(eV^{2}cm)	$5.42\times10^{-29}N_i$	$6.95\times10^{-29}N_i$	$7.16\times10^{-28}N_i$
$1/\tau_o^I$(sec^{-1})	$2.97\times10^{-7}N_i$	$3.81\times10^{-7}N_i$	$4.66\times10^{-6}N_i$
$1/V_c$(cm^{-3})	1.09×10^{20}	1.14×10^{20}	2.62×10^{18}

T = 77°K	InP	GaAs	InAs
G(eV)	1.41	1.51	.41
$(G/2m_nc^2)^{\frac{1}{2}}$	1/234	1/224	1/266
$1/V_c$(cm^{-3})	1.27×10^{20}	1.05×10^{20}	4.16×10^{18}
g^I(eV^{2}cm)	$4.87\times10^{-29}N_i$	$7.15\times10^{-29}N_i$	$5.26\times10^{-28}N_i$
$1/\tau_o^I$(sec^{-1})	$2.67\times10^{-7}N_i$	$3.92\times10^{-7}N_i$	$3.42\times10^{-6}N_i$

Table 3

InP. T = 300°K. A comparison of results for the impurity scattering rate for degenerate InP obtained by numerical integration with those calculated using the approximate analytical formula. Unstarred quantities are obtained by numerical integration. Crossed quantities (+) are calculated using the approximate analytical formulas. The values of $1/\tau^I$ and $1/\tau^{I+}$ are the numerically integrated and analytical values of the impurity scattering rates, respectively. The polar scattering rate, calculated as discussed in [18], is denoted by $1/\tau_p$ and the total scattering rate is $1/\tau_T$ where $1/\tau_T = 1/\tau^I + 1/\tau_p$. The total mobility, including the contributions of polar plus impurity scattering, is given by $\mu_T = e\tau_T/m^*$.

Sample

$a = E_f/G$	n_e(cm^{-3})	$1/\tau_T$(sec^{-1})	$1/\tau_p$(sec^{-1})	$1/\tau^I$(sec^{-1})	$1/\tau^{I+}$sec^{-1})	μ_T(cm^{2}V.)
.01	6.17×10^{17}	8.42×10^{12}	4.98×10^{12}	3.45×10^{12}	$3.30\times10^{12+}$	2.83×10^{3}
.03	1.23×10^{18}	1.03×10^{13}	4.64×10^{12}	5.69×10^{12}	$6.18\times10^{12+}$	2.22×10^{3}
.05	2.13×10^{18}	1.20×10^{13}	4.24×10^{12}	7.74×10^{12}	$7.46\times10^{12+}$	1.85×10^{3}
.09	$4.47\times10^{18+}$	$1.29\times10^{13+}$	$4.00\times10^{12+}$		$8.89\times10^{12+}$	$1.60\times10^{3+}$
.13	$8.18\times10^{18+}$	$1.38\times10^{13+}$	$4.00\times10^{12+}$		$9.75\times10^{12+}$	$1.40\times10^{3+}$
.24	$2.36\times10^{19+}$	$1.51\times10^{13+}$	$4.00\times10^{12+}$		$1.11\times10^{13+}$	$1.09\times10^{3+}$
.45	$7.66\times10^{19+}$	$1.55\times10^{13+}$	$3.00\times10^{12+}$		$1.25\times10^{13+}$	$.826\times10^{3+}$
.50	$9.45\times10^{19+}$	$1.57\times10^{13+}$	$3.00\times10^{12+}$		$1.27\times10^{13+}$	$.773\times10^{3+}$

Table 4

Degenerate InAs. T = 300°K. A comparison of results for the impurity scattering rate for degenerate InAs obtained by numerical integration with those calculated using the approximate analytical formula. Quantities which are crossed (+) are obtained by use of the approximate analytical expression. Agreement between the two methods of calculation is expected to improve with decreasing temperatures and increasing carrier concentrations. Mobilities are calculated using $m^* = (1 + 2a)m_n$, the effective mass at the Fermi surface, and uncompensated samples with $N_I = n_e$ are considered. The impurity scattering mobility is $\mu^I = e\tau^I/m^*$ and the total mobility is $\mu_T = e\tau_T/m^*$ where $1/\tau_T = 1/\tau_p + 1/\tau^I$.

Sample	$a = E_f/G$	$1/\tau^I (sec^{-1})$	$1/\tau^{I+} (sec^{-1})$	$n_e (cm^{-3})$
k	.25	2.50×10^{12}	2.39×10^{12}	$.7254 \times 10^{18}$
L	.30	2.70×10^{12}	3.04×10^{12}	$.9605 \times 10^{18}$
M	.40	2.90×10^{12}	3.27×10^{12}	1.5350×10^{18}
N	.45	2.90×10^{12}	3.37×10^{12}	1.8600×10^{18}
O	.50	3.25×10^{12}	3.46×10^{12}	2.3560×10^{18}
P	.60	3.43×10^{12}	3.60×10^{12}	3.4000×10^{18}

Sample	$1/\tau_p (sec^{-1})$	$1/\tau_T (sec^{-1})$	$\mu_T (cm^2/.s)$	$I^+ (cm^2/V.s)$
k	$.862 \times 10^{12}$	3.37×10^{12}	1.45×10^4	1.69×10^4
L	$.776 \times 10^{12}$	3.47×10^{12}	1.32×10^4	1.51×10^4
M	$.626 \times 10^{12}$	3.53×10^{12}	1.15×10^4	1.24×10^4
N	$.551 \times 10^{12}$	3.45×10^{12}	1.12×10^4	1.15×10^4
O	$.536 \times 10^{12}$	3.79×10^{12}	0.965×10^4	1.06×10^4
P	$.471 \times 10^{12}$	3.90×10^{12}	0.855×10^4	0.925×10^4

Table 5

GaAs. Temperature dependence of the mobility in highly doped but uncompensated GaAs. All mobilities are in $cm^2/V.sec$. All quantities superscripted I are impurity scattering rates and mobilities calculated using the approximate analytical expression for the impurity scattering rate given in eqs. (8) and (13). The total mobility, which includes polar and impurity scattering, and is calculated using numerical integration, is given at T = 300°K for comparison. The analytical expression is a better approximation at lower temperatures, as it requires $k_0T/E_f << 1$. All mobilities are calculated using the effective mass at the Fermi level as given by the Kane theory, and it is assumed that $n_e v_c$ = constant.

Sample	(at 77°K)	(sec^{-1})	(sec^{-1})	(sec^{-1})
$a = E_f/G$	$n_e \times 10^{-18} cm^{-3}$	$1/\tau^I (300°K)$	$1/\tau^I (77°K)$	$1/\tau^I (4°K)$
.01	.536		9.19×10^{12}	1.93×10^{13}
.05	1.98	1.02×10^{13}	1.44×10^{13}	2.45×10^{13}
.07	3.10	1.14×10^{13}	1.56×10^{13}	2.56×10^{13}
.09	4.45	1.21×10^{13}	1.63×10^{13}	2.64×10^{13}
.13	8.01	1.32×10^{13}	1.73×10^{13}	2.74×10^{13}
.24	2.25×10	1.51×10^{13}	1.91×10^{13}	2.92×10^{13}
.45	7.25×10	1.69×10^{13}	2.08×10^{13}	3.09×10^{13}
.50	8.92×10	1.72×10^{13}	2.11×10^{13}	3.12×10^{13}

$a = E_f/G$	$\mu_T (300°K)$	$\mu^I (300°K)$	$\mu^I (77°K)$	$\mu^I (4°K)$
.01	3900		2680	1290
.05	2200	2210	1580	932
.07	1900	1910	1410	859
.09	1800	1740	1310	809
.13	1500	1480	1150	728
.24	1200	1110	890	582
.50	780	719	595	403

Table 6

300 K. Values of $(1/\tau) \times 10^{-12} sec^{-1}$ for samples characterized in Table 1. Sample A includes the contribution of polar optical mode scattering only. All other samples are uncompensated materials with $N_i = n_e$ and include the contributions of polar plus impurity scattering.

InP							
$1/\lambda(cm^{-1})$	A	B	C	D	F	G	H
218	5.38	5.51	5.75	7.57	8.42	10.3	12.0
438	5.79	5.84	5.93	6.62	7.01	8.03	9.18
654	5.08	5.12	5.18	5.67	5.94	6.65	7.52
871	4.38	4.40	4.45	4.83	5.04	5.60	6.31
1090	3.82	3.83	3.87	4.15	4.31	4.76	5.34
2180	2.28	2.28	2.29	2.38	2.43	2.57	2.76

GaAs							
$1/\lambda(cm^{-1})$	A	B	C	D	F	G	H
230	3.00	3.30	3.60	4.00	5.50	6.30	10.0
461	2.80	2.90	3.00	3.30	4.10	4.40	7.30
692	2.40	2.40	2.50	2.60	3.10	3.30	5.40
1040	1.80	1.90	1.90	2.00	2.30	2.40	3.80
2310	1.00	1.00	1.00	1.00	1.10	1.10	1.50

InAs							
$1/\lambda(cm^{-1})$	A	B	C	D	F	G	H
203	1.43	1.56	1.73	1.81	2.04	2.15	2.26
232	1.43	1.54	1.68	1.74	1.94	2.03	2.13
290	1.40	1.48	1.58	1.63	1.78	1.85	1.93
581	1.04	1.07	1.12	1.14	1.21	1.24	1.28

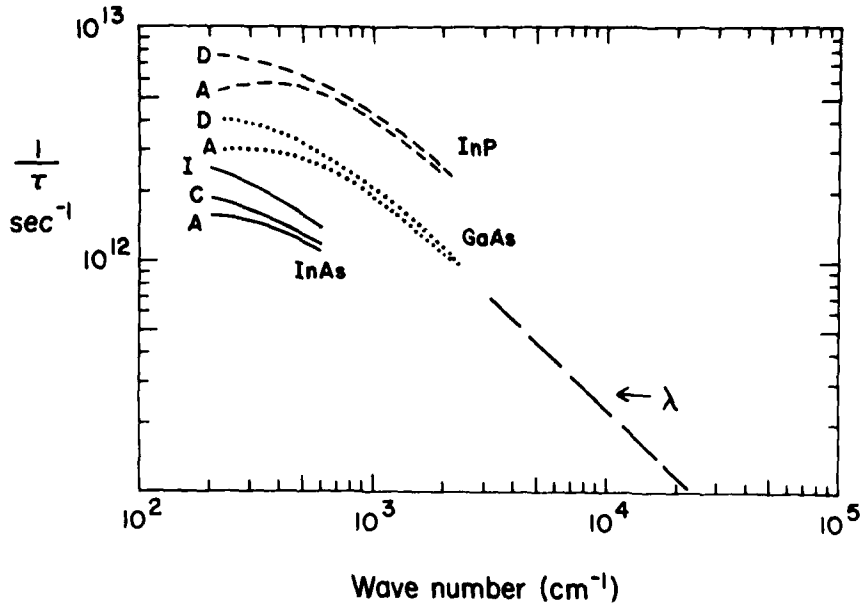

Figure 1. The frequency dependent electron scattering rate for samples of various carrier concentrations specified in table 1. Samples A include the contribution of polar scattering only. Other samples include the sum of polar plus impurity scattering.

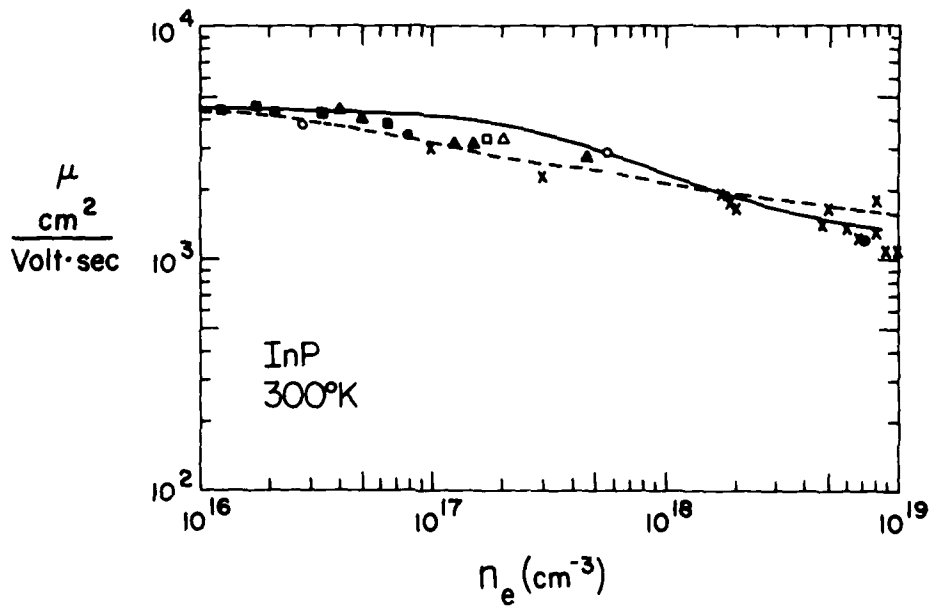

Figure 2. Theoretical results calculated here (solid line) compared with experimental results and an alternate theoretical calculation of the *dc* mobility (dashed line) from [27].

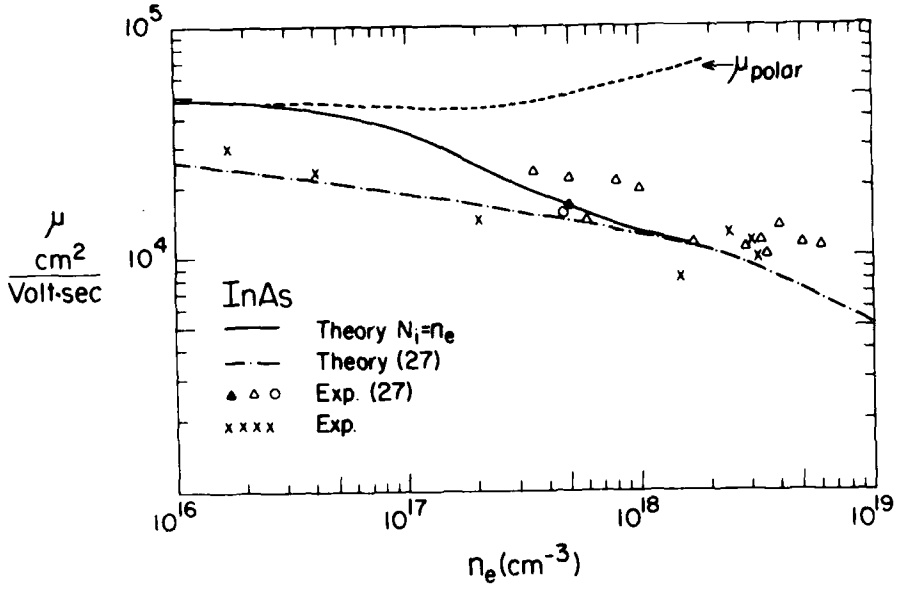

Figure 3. Mobility vs carrier concentration for InAs at 300°K. The polar mobility is calculated using the polar scattering rate in eq. (8).

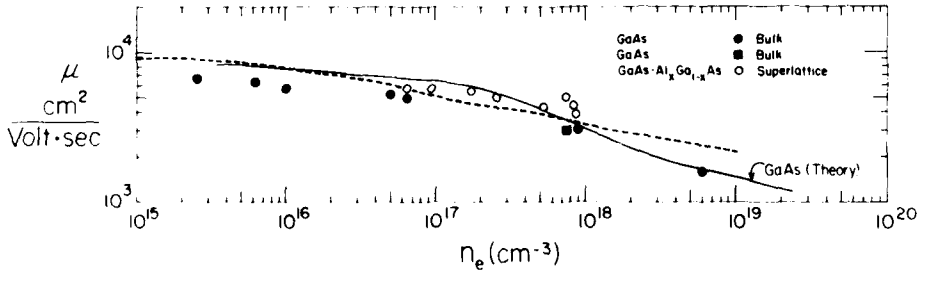

Figure 4. Mobility vs carrier concentration for GaAs calculated using the low frequency limit of the frequency dependent electron scattering rate. Polar and impurity scattering are included. The dashed line is an alternate calculation of the *dc* mobility and solid squares and circles are experimental results for bulk GaAs from [28].

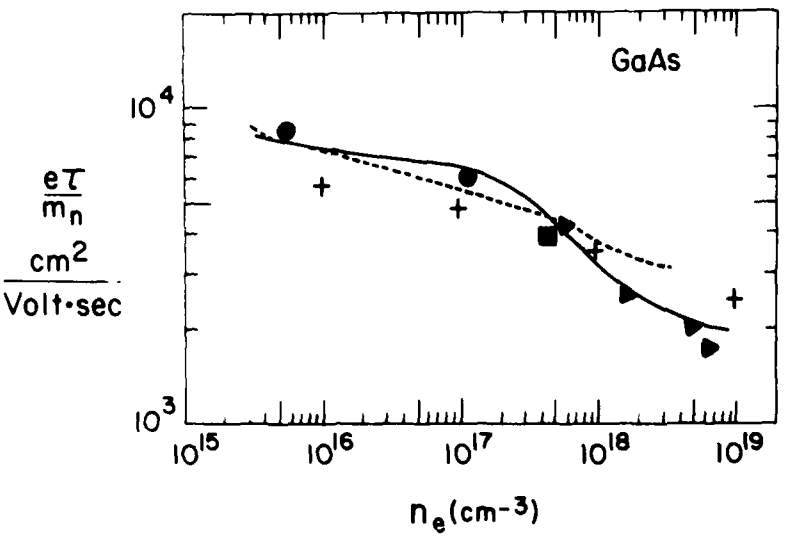

Figure 5. Theoretical results for GaAs (solid line) compared with experimental (solid geometrical figures) and alternate theoretical calculations (dashed line and ++++). Details are given in [18]. The experimental mobilities are the maximum obtained for a given carrier concentration.

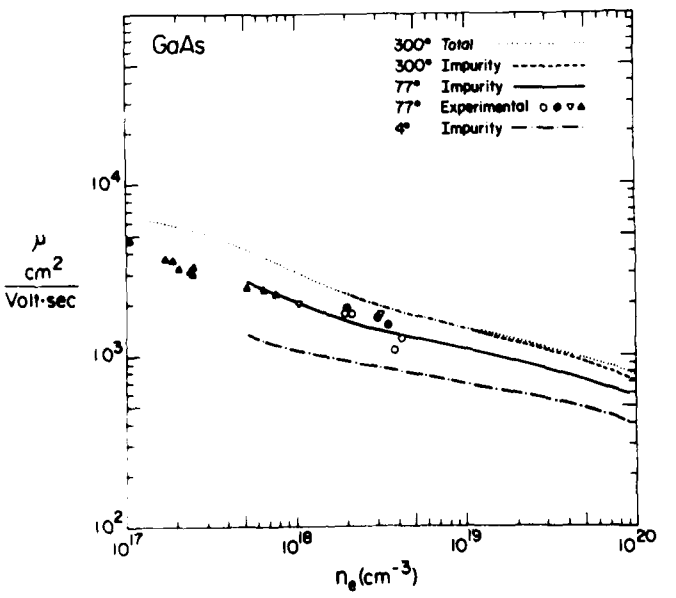

Figure 6. Temperature dependence of the mobility for GaAs calculated as discussed in the text. Experimental results are taken from [34].

INTERACTIONS OF INTENSE 2.7 μm PICOSECOND LASER PULSES WITH GERMANIUM

G. W. Bryant, A. Schmid, and P. Braunlich
Department of Physics
Washington State University
Pullman, Washington 99164

and

P. Kelly and D. Ritchie
Physics Department
National Research Council of Canada
Ottawa, Canada

Computer simulations of the generation and temporal evolution of hot plasmas in germanium during the passage of intense picosecond laser pulses have been begun. At 2.7μ two-photon absorption is the generating mechanism for carriers. Carrier heating from free-carrier absorption and energy transfer to the lattice through phonon-carrier collisions are described with an electron-hole band model similar to one previously used to describe plasma dynamics in germanium driven by one-photon absorption. Details of this model will be presented and the results available to date will be discussed

Key words: IR laser damage; Photoexcited carriers; Semiconductor plasma.

1. Introduction

Laser damage and laser annealing in semiconductors have recently lent a great deal of motivation to fundamental studies of the interaction of laser pulses with semiconductors such as Ge, Si, GaAs, etc. In addition to the understanding of free carrier kinetics and the interplay between heated carriers and the lattice background an analysis of the dynamic laser self-action has now become mandatory if a comprehensive insight into the intricate laser pulse - semiconductor processes is to be gained.

Laser self-action can best be described by recalling that the dielectric function, and in turn the refractive index, for each material is strongly dependent on the carrier distribution. Thus a change in this distribution due to the presence of an external field, due to changes in temperature or due to other influences will effectively change the optical properties of the material. Frequency shifts, self-focusing, self-defocusing changes in shape of laser pulses and possibly the whole phenomenon of laser damage in semiconductors may all lend themselves to explanations in terms of such dynamic refractive index changes. We present here a status report on an effort aimed at simulating such spatio-temporal changes in Ge which is exposed to 2.7 μm picosecond laser pulses. We will limit our discussion to temporal aspects only and will describe the entire spatial dynamics elsewhere. However, we will be able to address and answer an important question which has recently been raised. That is, Ge has been claimed to possess unusually high damage thresholds at 2.7 μm and 10.6 μm. We will comment on the possible cause for this effect.

2. Damage Criterium

From the outset we assume an idealized crystal. We disregard therefore any possible contribution to damage by inclusions or by other defects. We concentrate instead on heating of the phonon system which comprises an Einstein-type optical phonon system and a Debye-type acoustical phonon system. The two systems are coupled to each other and independently linked to the carrier systems, i.e. the photoexcited free carriers and holes. Each phonon system contributes to the temperature dependent mean square displacements of lattice constituents, $\langle u^2\rangle_{op}(T)$ and $\langle u^2\rangle_{ac}(T)$ respectively. If these two mean square displacements taken together become excessive (i.e. larger than the displacement sum at equilibrium melting temperature T_m)

$$\langle u^2\rangle_{ac}(T_{ac}) + \langle u^2\rangle_{op}(T_{op}) > \langle u^2\rangle_{ac}(T_m) + \langle u^2\rangle_{op}(T_m)$$

permanent lattice modifications are expected and damage is assumed to occur. Our purpose, is therefore, to perform calculations which permit monitoring of the temperatures in the two phonon systems during the passage of a laser pulse. Note that, according to our criterium, the required damage temperature has to exceed 5600°K in the optical phonon system alone if for some reason the acoustical phonon system should prove unable to significantly warm up during the pulse length of a picosecond pulse. Note also that the damaging temperature T_{op} calculated under these circumstances is still an approximation which will require further refinement. For example, we presently evaluate mean square displacements without accounting for anharmonic effects.

In order to calculate the phonon system temperatures and their change during the history of a laser pulse detailed information about electron-electron, electron-phonon and hole-phonon interactions in Ge is required. In the next section we will briefly review in form of a block diagram how the energy absorbed from the laser field ultimately ends up in the optical and acoustical phonon system. We will thereby specify some details of the different interactions.

3. Energy Transport

Photo-excitation in Ge at 2.7μ leads to the formation of electron-hole pairs via direct two-photon interband absorption. The transition rates for this process were evaluated in the recent work

by Bryant [1]. The dynamics of photoexcited electrons and holes in Ge has been studied in considerable detail by Elci, Scully, Smirl, and Matter [2]. Our present model uses their results modified to take account of the two separate phonon systems [3] and disregards Auger recombination for the time being. However, as our results will show, this simplification is no longer justified since appreciable heating at 2.7μ requires very high local free carrier concentrations, a condition under which Auger recombination is most effective. The next phase of program development will therefore include this effect as well. A further refinement, which is already part of the model, accounts without averaging for all the conduction band valleys and allows for single-photon hole transitions between different valence bands when the light and heavy hole bands are highly depleted.

In our block diagram (fig. 1) the sources of energy gain from the laser field are listed on top. In addition to two-photon absorption we consider free carrier absorption (FCA) and free hole absorption (FHA), which are both single photon absorption processes involving phonons for momentum conservation, and hole transitions to the split-off band. The last process does, of course, not generate any new holes but increases their energy instead.

The respective interband transitions are shown in figure 2. Excited carriers in the central conduction band valley are assumed to rapidly scatter into the side valleys (via electron-phonon scattering) where they thermalize into a quasi-Fermi distribution of temperature T_e. Note that scattering into the side valleys removes electrons from states which are the final states of the two-photon absorption process across the band gap and that the build-up of carriers in the side valleys thus regulates availability of those states and therefore the transition rate. Proper accounting of the availability of states demands as realistic a description of the bands as possible. Similarly, the light and heavy hole valence bands have to be treated as non-degenerate if hole transitions into the split-off band are to be treated correctly.

Phonon emission and absorption leads to carrier cooling by intravalley relaxation. Since the optical phonons have a stronger coupling to the heated carriers [3], this relaxation will bring about a slightly faster temperature rise in the optical phonon subsystem than in the acoustical one. Subsequently optical phonons decay into acoustical phonons with a characteristic, temperature independent time constant τ[4]. The temperature rise in the two systems is monitored in order to detect damage according to section 2.

The two temperature rises are given by

$$\frac{dT_{op}}{dt} = \frac{2}{c_v}\frac{du_{op}}{dt} - \left(\frac{\partial T_{op}}{\partial N_{op}}\right)\frac{N_{op}(T_{op}) - N_{op}(T_{ac})}{\tau}$$

and

$$\frac{dT_{ac}}{dt} = \frac{2}{c_v}\frac{du_{ac}}{dt} + \hbar\omega_o\frac{N_{op}(T_{op}) - N_{op}(T_{ac})}{\tau}$$

where optical and acoustical phonons have each been assigned half the contribution to the total specific heat c_v and where τ is the optical phonon decay lifetime, $N_{op}(T)$ the optical phonon number at temperature T and of uniform energy $\hbar\omega_o$, and du/dt the respective rate of change in energy density due to energy transfer during free carrier absorption and intravalley relaxation. These energy transfer rates depend on the carrier and hole density and respective energy distributions and therefore on the temperature of the electron and hole system. We will refrain from presenting the pertinent expressions here since they are rather involved and will be published when we have arrived at a comprehensive picture of the laser-semiconductor interaction. It suffices to say that the numerical procedure of modeling the temporal aspects of this interaction involves solving a set of five coupled differential equations each of which contains integrations over the carrier distributions in each valley and each valence band.

4. Results

We have tested the damaging properties of several 2.7μ laser pulses in the picosecond regime. Pulse lengths of 5, 10, and 20 psec were chosen at peak fluxes of 10^{28}, 10^{29}, and 10^{30} photons per cm^2 and sec, respectively. For reasons of operational simplicity the Gaussian temporal waveform of each pulse was truncated at the $1/e^3$ peak intensity points. Initial conditions for the carrier chemical potential and carrier temperature were determined by long hand and the dependence of the final results on the precise choice of these initial conditions was tested.

We present in figure 3 and 4 the free electron density N_e and free carrier energy density $\mathcal{E}$ per unit volume as both evolve during a 10^{28} photons/cm^2 sec peak flux, 20 psec pulse. Without an effective drain on the carriers, such as Auger recombination, one finds, as expected, a rapid increase in the carrier density in the early part of the pulse without any significant reduction in the latter part. A minute reduction which is noticeable only numerically and not on the graph of figure 3 accounts for two-photon stimulated emission which is included in our two-photon transition probability. The energy density $\mathcal{E}$ of the free carriers and holes shown in figure 4 exhibits similar behavior in the first half of the pulse. Along the trailing edge of the pulse the energy density diminishes first on account of the two phonon systems and stabilizes seemingly towards the end of the

[1] Figures in brackets indicate the literature references at the end of this paper.

pulse. This effect is a model artifact and can be explained in conjunction with figure 5. There the systems' temperatures are plotted for the free carrier and optical phonon systems as a function of time. The free carriers heat in accordance with the instantaneous availability of photons and of final states for transitions. The electron temperature follows therefore a modified Gaussian as one would expect for a temporal Gaussian intensity distribution in the laser pulse. However, since the temperature rise is accompanied by additional free carrier generation while the electron temperature decline is lacking a corresponding recombination process across the band gap, the available conduction band states rapidly fill up during carrier cooling, in the latter part of the pulse, thus keeping energy in the electron system which otherwise could be transferred in electron-phonon processes. This also explains why the optical phonon temperature rise proceeds at a less rapid rate in the late part of the pulse than earlier.

We also note that a 10^{28} photons/cm^2 sec peak flux, 20 psec pulse raises the optical phonon temperature merely to 552°K. Contrary to some earlier expectations [3] however, the acoustical phonon temperature rise does not lag behind the optical one and the two systems' temperatures agree to within less than 1% over the whole pulse length. The optical phonon temperature does therefore not have to rise to 5600°K in order for the damaging phase transition to take place.

It is tempting to compare these results with earlier work done at 1.06 μm [2]. While we find qualitatively plausible agreement comparison of numbers becomes difficult in light of the different experimental conditions chosen in each model. The work of reference 2 rests on the assumption of a square pulse, for instance, while the present work assumes a Gaussian temporal profile. Since the dynamic processes are nonlinear no simple scaling relation between the pulse shapes can be established. Our model calculations do, however, confirm that ideal Ge requires very high fluxes even at 2.7 μm for damage to occur. The flux regime of 10^{29} photons/cm^2 sec at which we predict damage to occur borders on fluxes which in much wider band gap materials, at larger photon energies and under physical processes quite different from the ones considered here also produce damage. These processes have been identified to be highly nonlinear and are thus requiring very high fluxes to come about. In contrast, free carrier generation at 2.7 μm in Ge is only a two-photon process and damage due to these carriers was intuitively expected to ensue at much lower fluxes. Our calculations show that for ideal Ge such expectations are unjustified.

In the next phase of our calculations several additional physical phenomena will be included into the model. Among them are Auger recombination of free carriers and band gap narrowing effects [5] as well as the dynamic dielectric constant which will allow a comprehensive spatio-temporal modeling of beam propagation.

This work was supported by AFOSR through Contract #F 49620-78-C-0095.

References

[1] Bryant, G. W., Phys. Rev. B 22, 1992 (1980).

[2] Elci, A., Scully, M. O., Smirl, A. L., and Matter, J. C., Phys. Rev. B 16, 191 (1977).

[3] Van Driel, H. M., Phys. Rev. B 19, 5928 (1979).

[4] Safran, S. and Lax, B. J. Phys. Chem. Solids 36, 753 (1975).

[5] Ferry, D. K., Phys. Rev. B 18, 7033 (1978).

Figures

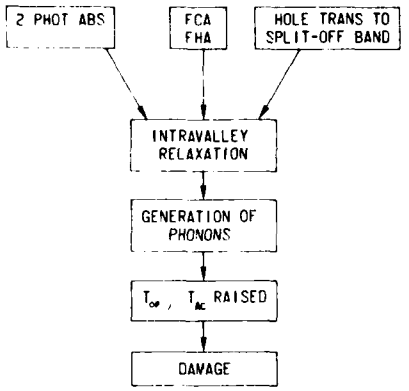

Figure 1. Block diagram illustrating the energy transfer in highly photo-excited Ge from the 2.7 μm photon field to the damage event.

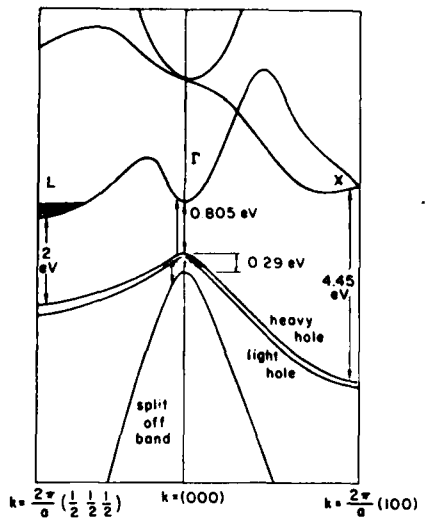

Figure 2. Band structure in germanium representing the excitation processes.

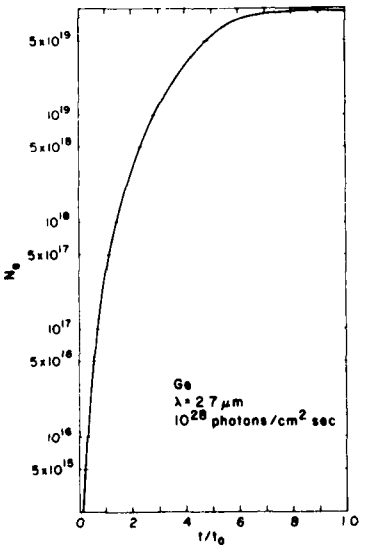

Figure 3. Electron density N_e cm^{-3} as a function of time normalized to the pulse length t_o for a peak flux of 10^{28} photons/ cm^2 sec.

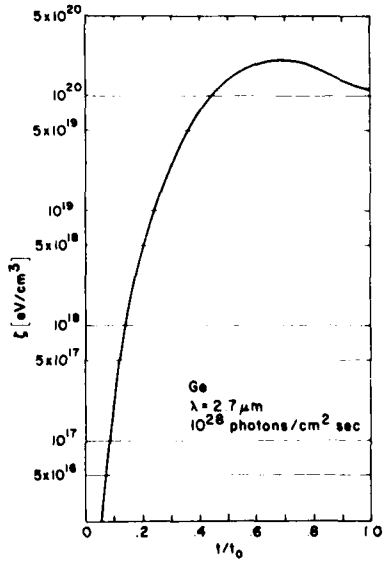

Figure 4. Variation of free carrier and hole energy density ξ with time normalized to pulse length t_o for a peak flux of 10^{28} photons/cm^2 sec.

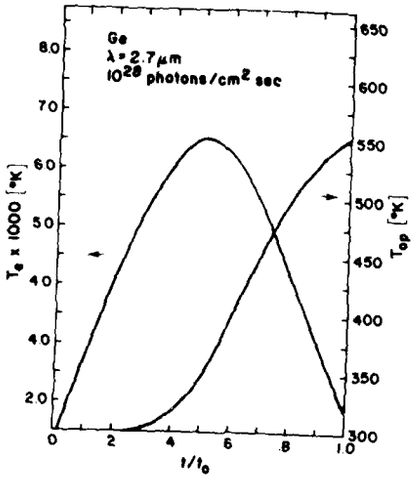

Figure 5. Variation of electron system temperature T_e (left vertical scale) and optical phonon temperature T_{op} (right vertical scale) with time normalized to pulse length t_o for same pulse as in figure 4.

The observation was made that the prediction of the frequency dependence is one of the desirable features of this theory.

BAND STRUCTURE CALCULATIONS OF THE TWO-PHOTON ABSORPTION COEFFICIENTS OF GaAs, InP, CdTe, and ZnSe

A. Vaidyanathan and A. H. Guenther
Air Force Weapons Laboratory
Kirtland Air Force Base, New Mexico 87117

and

S. S. Mitra
Department of Electrical Engineering
University of Rhode Island
Kingston, Rhode Island 02881

The two-photon absorption coefficients of crystalline GaAs, InP, CdTe and ZnSe at 1.064 μm and 0.694 μm are calculated by means of a new model which combines the elements of second order perturbation thoery and band structure calculations. A sufficient number of intermediate states are included to assure adequate convergence. This calculational procedure is shown to represent a significant improvement over currently available theoretical models, and the results are in good agreement with available experimental data.

Key words: Two-photon absorption; nonlinear absorption; band-structure; oscillator strength.

In the last two decades there have been numerous theoretical and experimental studies of the two-photon absorption (TPA) coefficients of crystalline solids [1-16][1]. In spite of these extensive investigations, a generally accepted quantitative description of two-photon absorption has not been achieved even for the simplest of semiconductors, as is evidenced by the unacceptably large disparity between theoretical estimates and the available experimental measurements. These differences stem largely from the simplifying models employed to describe the electronic band structure; approximate manner in which the oscillator strengths are estimated; and incorrect truncation of the summation over the intermediate states (see eq. (1) below). In an attempt to improve this situation we have calculated the two-photon absorption coefficients of several direct-gap zinc-blende type, crystalline semiconductors by first computing their electronic band structures and oscillator strengths throughout the first Brillouin zone by means of the empirical pseudopotential method, followed by a numerical evaluation of the two-photon transition probabilities employing second-order perturbation theory.

Within the context of second-order perturbation theory, the transition probability rate of an electron in a crystalline solid (with direct energy gap E_g) going from an initial valence band state $|v\vec{k}>$ to a final conduction band state $|c\vec{k}>$ by the simultaneous absorption of two-photons is given by:

$$W = \frac{2\pi}{\hbar} \int \frac{d^3\vec{k}}{(2\pi)^3} \left| \sum_n \frac{H_{vn}\, H_{nc}}{E_{vn}(\vec{k}) - \hbar\omega} \right|^2 \delta\left(E_{vc}(\vec{k}) - 2\hbar\omega\right), \qquad (1)$$

1. Figures in brackets indicate the literature references at the end of this paper.

where the photon energies are such that $2\hbar\omega \geq E_g > \hbar\omega$. In eq. (1), E_{ij}'s are the energy separation between states i and j at wave vector $\vec{k}$, the summation is over all intermediate states n, and the $\vec{k}$ integral extends over the entire first Brillouin zone. The interaction Hamiltonian H is of the form $H = e/mc\ \vec{A}\cdot\vec{P}$ where $\vec{A}$ is the vector potential of the radiation and $\vec{P}$ is the momentum operator. The two-photon absorption coefficient β is related to the two-photon transition probability rate W by the equation

$$\beta = \frac{4\hbar\omega W}{I^2} \tag{2}$$

where I is the intensity of the incident radiation. It is obvious from eq. (1) that to evaluate the two-photon transition probability, knowledge of the electronic energies and wavefunctions throughout the first Brillouin zone is needed. We obtain these at room temperature by performing empirical psuedopotential calculation (EPM), using the available pseudopotential form factors [17]. We used up to 35 plane waves at each $\vec{k}$ point and obtained the Bloch functions and eigen energies of the highest four valence bands the the lowest 31 conduction bands to an accuracy of approximately 0.1 eV near the Fermi level and to within 0.5 eV away from the Fermi level. (Each of these bands is doubly degenerate due to spin.) The reliability of the higher energy bands obtained in this calculation was checked by computing the conduction electron effective masses, which also involve sums over all the energy bands of the crystal. The results agreed with the experimentally known effective masses to within 10 percent. In order to numerically integrate eq. (1) we convert the delta function in energy to a delta function in wave vector by use of the following relation:

$$\delta\left(E_{vc}(\vec{k}) - 2\hbar\omega\right) = \sum_{\ell} \frac{\delta(\vec{k}-\vec{k}_\ell)}{\left|\vec{\nabla}_{\vec{k}}\, E_{vc}(\vec{k})\right|} \quad , \tag{3}$$

where $\vec{k}_\ell$ represents all values of $\vec{k}$ for which $E_{vc}(\vec{k}) = 2\hbar\omega$. The momentum matrix elements are calculated throughout the Brillouin zone by means of the relation

$$\left|P_{ij}\right|^2 = \left|< j\vec{k} \left| h\vec{\nabla}_{\vec{r}} \right| i\vec{k} >\right|^2 \tag{4}$$

where $|i\vec{k}>$ and $|j\vec{k}>$ are the Bloch functions obtained using the empirical pseudopotential method. In calculating W from eq. (1) we considered the transitions originating from the highest three valence bands, and included the intermediate states in all the 35 energy bands obtained in this calculation. The resulting two-photon absorption coefficient had a convergency of 0.0001 cm/MW.

The converged two-photon absorption coefficients of GaAs, InP, CdTe, and ZnSe at 1.064 and 0.694 μm at room temperature, obtained in this calculation, are reported in table 1 along with the results of other theoretical calculations based on second order perturbation theory, and selected experimental data to which the theories apply. Results using the models of Braunstein [1] and Basov [3] are seen to be one or two orders of magnitude smaller than our results. The biggest deficiency of the former two models, apart from the simplified band structure schemes employed, and the approximate manner in which the oscillator strengths are estimated, is the inaccurate manner in which the summation over the intermediate states in eq. (1) is truncated. Specifically, Braunstein considered only one higher conduction band for the intermediate state, while Basov considered only the intermediate states in the initial and final bands.

This calculation includes both of these intermediate states, and in addition those in all other valence and conduction bands. Furthermore, unlike the models of Braunstein and Basov the present calculation reported

herein fully takes into account the degeneracies of all the energy bands involved. Finally, while Braunstein considered only the highest single valence band for the initial electronic state, and Basov included the highest two valence bands, we have considered the highest three valence bands for the initial state whenever the transitions from these bands to the lowest conduction band are energetically possible. The model of Lee and Fan [4] takes into account the valence band degeneracies, and also considers excitonic effects. As a result, the TPA coefficients predicted by their model are significantly larger than those of Braunstein and Basov. However, in the present calculation we do not include excitonic effects, since these are known [2,4] to be small when the two-photon energy is quite a bit larger than the energy-gap, such as in the cases studied here. In spite of this, our results are considerably larger than those of Lee and Fan. This apparetnly arises from our use of more accurage energy bands and momentum matrix elements, which are obtained from detailed band structure calculations. In fact, Pidgeon [6] have recently shown that the nonparabolicity of the energy bands alone can dramatically increase the calculated TPA coefficients in semiconductors, especially away from the band edge.

Before making any comparison between the theoretical and experimental results, it is instructive to point out the following: The experimental results are known to be drastically affected by many factors: laser pulse duration, free carrier absorption, impurity type and concentration, spatial and temporal fluctuations of the laser pulse, sample temperature and thickness, experimental technique employed, etc. It is known [9,12] that in going from nanosecond pulses to picosecond pulses the TPA coefficient decreases by as much as three orders of magnitude, due to coherence effects such as self-induced transparency, etc. Whether the free carrier absorption is included or not in the analysis of a given set of nonlinear transmittance data has a serious influence on the values of the TPA coefficients deduced from the same data [14]. Large impurity concentrations can drastically reduce the TPA due to saturation effects [13]. At high laser intensities the TPA coefficients could considerably decrease due to the Stark shifts in the energy levels [15,16]. These considerations explain, in part, the large variations in the reported experimental data.

We will, therefore, take the following approach in comparing theories with experiments. We will restrict ourselves to the experimental data relating to nanosecond pulses, at room temperature, where coherence effects are usually absent. First, we will apply the various theoretical models to those crystals where the experimental data are unambiguous. Based on the success or failure of the different theories for reliable predictions of the nonlinear absorption coefficients in these crystals, we will be able to propose definite values for the TPA coefficients in crystals where there is a large disparity between the experimental data. Following this approach, we find that in the case of CdTe the result of the present calculation agrees well with the result of the only experiment [7] which reports the pulse duration to be in the nanosecond pulse regime. This experimental datum should be quite accurate since it was obtained using a laser calorimetric method, which had much greater sensitivity than nonlinear transmittance measurements. By contrast, the results of Braunstein and Basov formulas are orders of magnitude smaller. The same trend is noted in ZnSe also. In InP, our result is larger than the experimental data by a factor whose value is less than 1.5, while that of the Lee and Fan model is smaller than the experimental results by a factor between 2.5 and 3.

Based on these observations we make the following conclusions: The models for Braunstein and Basov grossly underestimate the TPA coefficients for reasons explained earlier. The model of Lee and Fan also underestimates them, albeit to a lesser degree, especially when the two-photon energy is significantly larger than the band-gap. This obviously arises from their use of approximate expressions for the electronic energies and oscillator strengths, which may not be accurate away from the band edge.

The present calculation overestimates the TPA coefficients, by a factor of approximately two. This probably arises due to our approximating the true electronic wavefunctions by the pseudo wavefunctions obtained with the EPM. Band structure calculations employing other methods such as OPW, APW, Green's function, etc. should shed more light on this situation. However, we conclude the results of the present calculation are significantly more reliable than those of earlier models, because of the use of more realistic energy bands and oscillator strengths and the inclusion of many intermediate states, resulting in good convergency. Finally, based on the above observations, we favor a value of the order of unity for the TPA coefficient of pure GaAs at 1.06μm, when free carrier absorption, coherence effects, etc. are absent, in close agreement with the experimental result of Arsenev [8].

Acknowledgement

This research was supported in part by an Air Force Systems Command National Research Council Postdoctoral Resident Research Associateship (A.V.).

References

[1] Braunstein, R., Phys. Rev. 125, 475 (1962); Braunstein, R., and Ockman, N., Phys. Rev. 134, A499 (1964).

[2] Loudon, R., Proc. Phys. Soc. 80, 952 (1962).

[3] Basov, N. G., Grasyuk, A. Z., Zubarev, I. G., Katulin, V. A., and Krokhin, O. N., Zh. Eksp. Theor. Fiz. 50, 551 (1966)(Sov. Phys. JETP 23, 366 (1966)).

[4] Lee, C. C. and Fan, H. Y., Appl. Phy. Lett. 20, 18 (1972); Lee, C. C. and Fan, H. Y., Phys. Rev. B 9, 3502 (1974).

[5] Vaidyanathan, A., Walker, T. W., Guenther, A. H., Mitra, S. S., and Narducci, L. M., Phys. Rev. B 21, 743 (1980); Vaidyanathan, A. and Guenther, A. H., Phys. Rev. B (to be published).

[6] Pidgeon, C. R., Wherrett, B. S., Johnston, A. M., Dempsey, J., and Miller, A., Phys. Rev. Lett. 42, 1785 (1979).

[7] Bass, M., Van Stryland, E. W., and Stewart, A. F., App. Phys. Lett. 34, 142 (1979).

[8] Arsenev, V. V., Dneproskii, V.S. Klyshko, D. N., and Penin, A. N. Zh. Eksp. Teor. Fiz. 56, (1969) (Sov. Phys. JETP 29, 413, (1969)).

[9] Grasyuk, A. Z., Zubarev, I. G., Lobko, V. V., Matveets, Yu A., Mirnov, A. B., and Shatberashvili, O. B., Zh. ETF Pis. Red. 17, 584 (1973) (Sov. Phys. JETP Lett. 17, 416 (1973)).

[10] Oksman, Ya., A., Semenov, A.A. Smirnov, V. N., and Smirnov, O. M., Fiz. Tekh. Poluprov. 6, 731 (1972) (Sov. Phy. Semicond. 6, 629 (1972)).

[11] Jayaraman, S. and Lee, C. H., Appl. Phys. Lett. 20, 392 (1972).

[12] Gvardzhaladze, T. L., Grasyuk, A. Z., and Kovalenko, V. A., Zh. Eksp. Teor. Fiz. 64, 446 (1973) (Sov. Phys. JETP 37, 227 (1973)).

[13] Miller, A., Johnston, A., Dempsey, J., Smith, J., Pidgeon, C. R., and Holah, G. D., J. Phys. C 12, 4839 (1979).

[14] Gibson, A. F., Hatch, C. B., Maggs, P. N. D., Tilley, D. R., and Walker, A. C., J. Phys. C 9, 3259 (1976).

[15] Keldysh, L. V., Zh. Eksp. Teor. Fiz. 47, 1945 (1964) (Sov. Phys. JETP 20, 1307 (1965)).

[16] Jones, M. D. and Reiss, H. R., Phys. Rev. B 16, 2466 (1977).

[17] Cohen, M. L. and Heine, V., in "Solid State Physics," ed. H. Ehrenreich, F. Seitz, and D. Turnbull (Academic, New York, 1970), vol. 24, p. 37.

Table 1. Comparison of theoretical and experimental two-photon absorption coefficients (in units of cm/MW) at room temperature.

Crystal	Wavelength (μm)	Theoretical				Experimental results obtained with nanosecond pulse
		Braunstein[a]	Basov[b]	Lee and Fan[c]	Present	
CdTe	1.064	0.007	0.028	----	0.201	0.13 ± 0.04[d]
ZnSe	0.694	0.002	0.009	----	0.081	0.04[e]
InP	1.064	0.008	0.038	0.096	0.351	0.26 ± 0.13[f]
GaAs	1.064	0.007	0.029	0.058	2.179	0.2 - 5.6[g]

a. Refs. 1 and 5
b. Refs. 3 and 5 --(These results are obtained by using the band effective masses, instead of the free electron mass in the expressions for the intraband momentum matrix elements, as in Ref. 3.)
c. Ref. 4
d. Ref. 7
e. Ref. 8
f. Ref. 4
g. Refs. 4 and 8-11

TWO-PHOTON ABSORPTION IN DIRECT-GAP CRYSTALS--AN ADDENDUM

A. Vaidyanathan and A. H. Guenther
Air Force Weapons Laboratory
Kirtland Air Force Base, New Mexico 87117

and

S. S. Mitra
Department of Electrical Engineering
University of Rhode Island
Kingston, Rhode Island 02881

An error made in an earlier paper by the authors regarding the appropriate effective masses to be used in calculations employing the Basov formulation is corrected. The new results for two-photon absorption coefficient obtained from the Basov formula now agree quite well with those computed using Keldysh's treatment. Furthermore, it is shown that improved agreement between theoretical and experimental two-photon absorption coefficients is obtained by including nonparabolocity and degeneracy of the energy bands in the calculations.

Key words: Two-photon absorption; band structure; oscillator strength; intraband-momentum matrix element; effective mass.

1. Introduction

In an earlier work [1][1] (referred to as I hereafter), the Keldysh [2], Braunstein [3], and Basov [4] formulas for two-photon absorption (TPA) in direct-gap crystals were critically compared with each other and with the experimental data. It was shown that the Keldysh and Braunstein formulas which describe allowed transitions yielded much better results than the Basov formula which describes forbidden transitions. That result was evidently the outcome of inadvertantly using the free-electron mass instead of the band effective mass in the expressions for the intraband-momentum matrix elements [5]. In this note we report the results of new calculations for the TPA coefficients of several zinc-blende-structure semiconductors using the correct mass in the Basov formula. These calculations have been further improved by including the effects of nonparabolocity and degeneracy of the energy bands as described by the Kane model [6].

2. Theory

2.1 Basov Formula

When, appropriately, the band effective masses are used in the expressions for the intraband-momentum matrix elements, instead of the free-electron mass [5], the Basov formula [1,4] takes the following form [compare with eq. (27) of I]:

$$\beta_B(\omega) = \frac{2^{7/2}\pi e^4 E_g (2\hbar\omega - E_g)^{3/2}}{3\varepsilon_\infty C^2 (\hbar\omega)^5 \left(m^*_{cv}\right)^{1/2}} \qquad (1)$$

Equation (1) is derived assuming all of the energy bands are quadratic functions of the wave vector $\vec{k}$. When one uses a more accurate nonparabolic

1. Figures in brackets indicate the literature references at the end of this paper.

expression for the interband energy difference E_{vc} of the form [6]

$$E_{vc}(\vec{k}) = E_g\left(1 + \frac{\hbar^2 k^2}{m^*_{vc} E_g}\right)^{1/2}, \qquad (2)$$

Basov's formula becomes

$$\beta_B^{np}(\omega) = \frac{2^3\pi e^4}{3\epsilon_\infty C^2} \frac{E_g^{3/2}}{(m^*_{cv})^{1/2}} \frac{1}{(\hbar\omega)^4}\left[\left(\frac{2\hbar\omega}{E_g}\right)^2 - 1\right]^{3/2} \qquad (3)$$

Equation (3) reduces to eq. (1) at the absorption edge, where $2\hbar\omega \simeq E_g$, as one would normally expect.

For the zinc-blende-type crystals studied in I, the highest valence band is triply degenerate [6] at the Brillouin-zone center in the absence of spin-orbit splitting. When the spin-orbit interaction is included and $\vec{k} \cdot \vec{p}$ perturbation applied [6], there results a heavy-hole band, a light-hole band, and a split-off band as shown in figure 1. For the laser wavelengths studied in I, the transitions from all three of these bands are energetically possible in the case of GaAs, InP, and ZnSe, while for InSb and CdTe only transitions from the heavy- and light-hole bands are energetically possible.

Using the band parameters listed in table 1 we carried out Basov-type calculations with aid of eq. (3) by including all possible two-photon transitions in CdTe, GaAs, InP, InSb, and ZnSe. The resulting TPA coefficients are reported in table 2 along with selected experimental data to which the theoretical estimates can be compared. Such calculations cannot be performed for the alkali halides due to the lack of reliable information regarding the relevant band-structure parameters.

2.2 Keldysh Formula

In the past, objections have been raised to the Keldysh formula based on parity considerations [15]. It has been stated that the Keldysh formula always predicts a frequency dependence of the form $(2\hbar\omega - E_g)^{1/2}$, which disagrees with the functional form $(2\hbar\omega - E_g)^{3/2}$ predicted by the second-order perturbation formulas for allowed-forbidden transitions. We note that if one expands the Dawson integral encountered in the Keldysh formula [2] in a series, the first term does yield the one-half power dependence corresponding to allowed-allowed transitions; however, the second and third terms yield three- and five-halves power dependences, respectively, corresponding to allowed-forbidden and forbidden-forbidden transitions. In fact, we can show that the second term of the series expansion of the Keldysh formula closely resembles the Basov formula at the TPA edge.

The second term of the series expansion of the exponential in the Dawson integral expressed by eq. (15) of I is

$$\frac{1}{3}\left(2\left\langle\frac{E_g}{\hbar\omega} + 1\right\rangle - \frac{2E_g}{\hbar\omega}\right)^{3/2}, \qquad (4)$$

where the notation $\langle\cdots\rangle$ means the integer part of the argument. Thus, the second term of the series expansion of the Keldysh formula, close to the TPA edge is [see eqs. (11)-(19) of I]

$$\beta_K^{\text{2nd term}}(2\hbar\omega \simeq E_g) = \frac{2^{5/2}\pi e^4 \exp(4)(2\hbar\omega - E_g)^{3/2}}{27\epsilon_\infty C^2(\hbar\omega)^2 E_g^2 (m^*_{vc})^{1/2}} \qquad (5)$$

From eqs. (5) and (1) [or (3)], for $2\hbar\omega \simeq E_g$, we obtain

$$\frac{\beta_K^{\text{2nd term}}}{\beta_B}\,(2\hbar\omega \simeq E_g) \simeq \frac{\exp(4)}{144} = 0.379. \qquad (6)$$

Thus, close to the TPA edge the second term of the Keldysh formula agrees with the Basov formula, not only in functional form, but also in absolute value to within a factor of three. This agreement must be considered good in view of the vast differences between the two theoretical approaches and the many approximations involved in them. The values of the TPA coefficients away from the absorption edge, obtained from the Keldysh formula by keeping all the terms in it, are in even closer agreement with the Basov results. This can be seen in table 2 where the results of the Keldysh formula including the effects of band degeneracies are compared with similar results obtained from the Basov formula. The Keldysh results are found to fall in between the Basov results with parabolic and nonparabolic energy bands, in all the crystals studied here except InSb. In InSb, the Keldysh results are somewhat larger than that of the Basov formula even in the nonparabolic model.

2.3 Braunstein Formula

The Braunstein [3] formula considers the next higher conduction band for the intermediate state. In zinc-blende-type crystals this band also consists of a heavy-mass band, a light-mass band, and a spin-orbit-split-off band [8]. When the degeneracies of the initial and intermediate states are taken into account, the Braunstein results obtained in I are increased by a factor between six and nine. However, the Braunstein formula suffers from the following drawback. It requires knowledge of the band parameters of the higher conduction bands, which in general are not accurately known either from theoretical calculations or experimental data. Thus, the Braunstein formula is generally not suitable for quantitatively reliable calculations and further discussion is omitted here.

3. Discussion

Before making any comparison between the theoretical and experimental results, it is instructive to point out the following: The experimental results are known to be seriously influenced by many factors: laser pulse duration, free-carrier absorption, sample purity (type and concentration of impurities), spatial and temporal fluctuations of the laser pulse, sample temperature and thickness, etc. For example, picosecond pulses are known to afford much smaller TPA coefficients than nanosecond pulses, due to coherence effects such as self-induced transparency, etc. [16] These considerations explain, in part, the large variations in the reported experimental data. The theoretical calculations discussed herein are for intrinsic two-photon absorption in pure crystals at room temperature. Hence, in comparing the theoretical predictions with experimental results we restrict ourselves to experimental data obtained with nanosecond pulses at room temperature, when coherence effects, etc., are usually absent or are of reduced influence. From table 2 it can be seen that the theoretical values somewhat underestimate the TPA coefficients. This is not surprising in view of the numerous approximations made in the theoretical calculations regarding the energy bands, oscillator strengths, intermediate states, etc., which may not be accurate, especially away from the band edge. Also, as pointed out earlier the experimental data are affected by many factors resulting in large spreads in the measured TPA coefficients.

These observations point out the need for more experiments using well-characterized lasers and crystals. On the theoretical side, more rigorous calculations that use reliable band structures and momentum matrix elements throughout the Brillouin zone and also include many intermediate states are highly desirable.

4. Conclusion

The effects of degeneracies and nonparabolocity of the energy bands on the two-photon absorption coefficients in direct-gap crystals are studied. The Basov results are found to be increased by as much as a factor of three due to the nonparabolocity of the energy bands. The Keldysh results for degenerate bands are shown to fall in between the corresponding Basov results with parabolic and nonparabolic energy bands, respectively. It is also noted that the theoretical values generally underestimate the experimental two-photon absorption coefficients. In order to achieve closer agreement between theoretical predictions and experimental data, one needs more experimental data obtained with well-characterized lasers and crystals, as well as theoretical values of the two-photon absorption coefficients obtained from rigorous band-structure calculations.

5. Acknowledgments

The authors wish to acknowledge enlightening discussions with Dr. C. R. Pidgeon of Heriot-Watt University. This research was supported in part by an Air Force Systems Command/National Research Council Post-Doctoral Resident Research Associateship (A.V.).

6. Note Added in Proof

The authors have recently carried out band-structure calculations of the two-photon absorption coefficients of GaAs, InP, CdTe and ZnSe, using the empirical pseudopotential method. Good agreement is noted between these results [17] and the experimental data.

7. References

[1] Vaidyanathan, A., Walker, T. W., Guenther, A. H., Mitra, S. S. and Narducci, L. M., NBS Spec. Pub. #568, 445 (1979); also Phys. Rev. B 21, 743 (1980).

[2] Keldysh, L. V., Zh. Eksp. Teor. Fiz. 47, 1945 (1964) [Sov. Phys. JETP 20, 1307 (1965)].

[3] Braunstein, R. and Ockman, N., Phys. Rev. 134, A499 (1964).

[4] Basov, N. G., Grasyuk, A. Z., Zubarev, I. G., Katulin, V. A. and Krokhin, O. On., Zh. Eksp. Teor. Fiz. 50, 551 (1966) [Sov. Phys.--JETP 23, 366 (1966)].

[5] Nguyen, Van-Tran, Strand, R. A. and Yafet, Y., Phys. Rev. Lett. 26, 1170 (1971).

[6] Kane, E. O., J. Phys. Chem. Solids 1, 249 (1957).

[7] See, for example, Hermann, C. and Weisbuch, C., Phys. Rev. B 15, 823 (1977) and references therein.

[8] Braunstein, R. and Kane, E. O. J. Phys. Chem. Solids 23, 1423 (1962).

[9] Cardona, M., J. Phys. Chem. Solids 24, 1543 (1963).

[10] Bass, M., Van Stryland, E. W. and Stewart, A. F., Appl. Phys. Lett. 34, 142 (1979); Ralston, J. M. and Chang, R. K., Opto-electronics 1, 182 (1969).

[11] Bosacchi, B., Bessey, J. S. and Jain, F. C., J. Appl. Phys. 49, 4609 (1978) and references therein.

[12] Lee, C. C. and Fan, H. Y., Phys. Rev. B 9, 3502 (1974); Appl. Phys. Lett. 20, 18 (1972).

[13] Miller, A., Johnston, A., Dempsey, J., Smith, J., Pidgeon, C. R. and Holah, G. D., J. Phys. C 12, 4839 (1979), and references therein.

[14] Arsenev, V. V., Dneproskii, V. A., Klyshko, D. N., and Penin, A. N., Zk. Eksp. Teor. Fiz., 56 760 (1969) [Sov. Phys.--JETP 29, 413 (1969)].

[15] Weiler, M. H., Phys. Rev. B 7, 5403 (1973).

[16] Grasyuk, A. Z., Zubarev, I. G., Lobko, V. A., Matveets, Yu. A., Mirnov, A. B., and Shatberashvili, O. B., Zh. Eksp. Teor. Fiz. Pis'ma Red. 17, 584 (1973) [Sov. Phys--JETP Lett. 17, 416 (1973)]Gvardzhaladze, T. L., Grasyuk, A. Z., and Kovalenko, V. A., Zh. Eksp. Teor. Fiz. 64, 446 (1973) [Sov. Phys.--JETP 37, 227 (1973)].

[17] Vaidyanathan, A., Guenther, A. H., and Mitra, S. S., NBS Spec. Publ.#(this volume).

Table 1. Values of band-structure parameters (refs. 7-9)

Crystal	Effective mass (units of free-electron mass)				Valence conduction band energy gap at 300 K (eV)	Spin-orbit splitting of valence bands (eV)	High-frequency dielectric constant
	Electron	Heavy hole	Light hole	Split-off hole			
CdTe	0.09	5	0.13	0.37	1.50	0.927	7.21
GaAs	0.0667	0.68	0.12	0.2	1.435	0.341	10.9
InP	0.0803	0.4	0.086	0.18	1.28	0.11	9.56
InSb	0.0139	0.25	0.012	0.12	0.18	0.81	15.68
ZnSe	0.17	0.6	0.25	0.67	2.58	0.45	5.9

Table 2. Comparison of experimental and theoretical two-photon absorption coefficients that include the effects of band degeneracies (in units of cm/MW).

Crystal	Wavelength (μm)	Theoretical (300 K) Basov (parabolic)	Basov (nonparabolic)	Keldysh (nonparabolic)	Experimental results with nanosecond pulses at room temperature	
CdTe	1.064	0.037	0.083	0.051	0.13 ± 0.04	[10]
GaAs	1.064	0.039	0.088	0.057	0.2 - 0.3 0.02 - 5.6	[10] [11]
InP	1.064	0.056	0.161	0.080	0.23 - 0.3 0.26 ± 0.13	[12] [12]
InSb	10.64	8.97	14.38	15.21	0.2 - 16	[13]
ZnSe	0.694	0.011	0.019	0.018	0.04	[14]

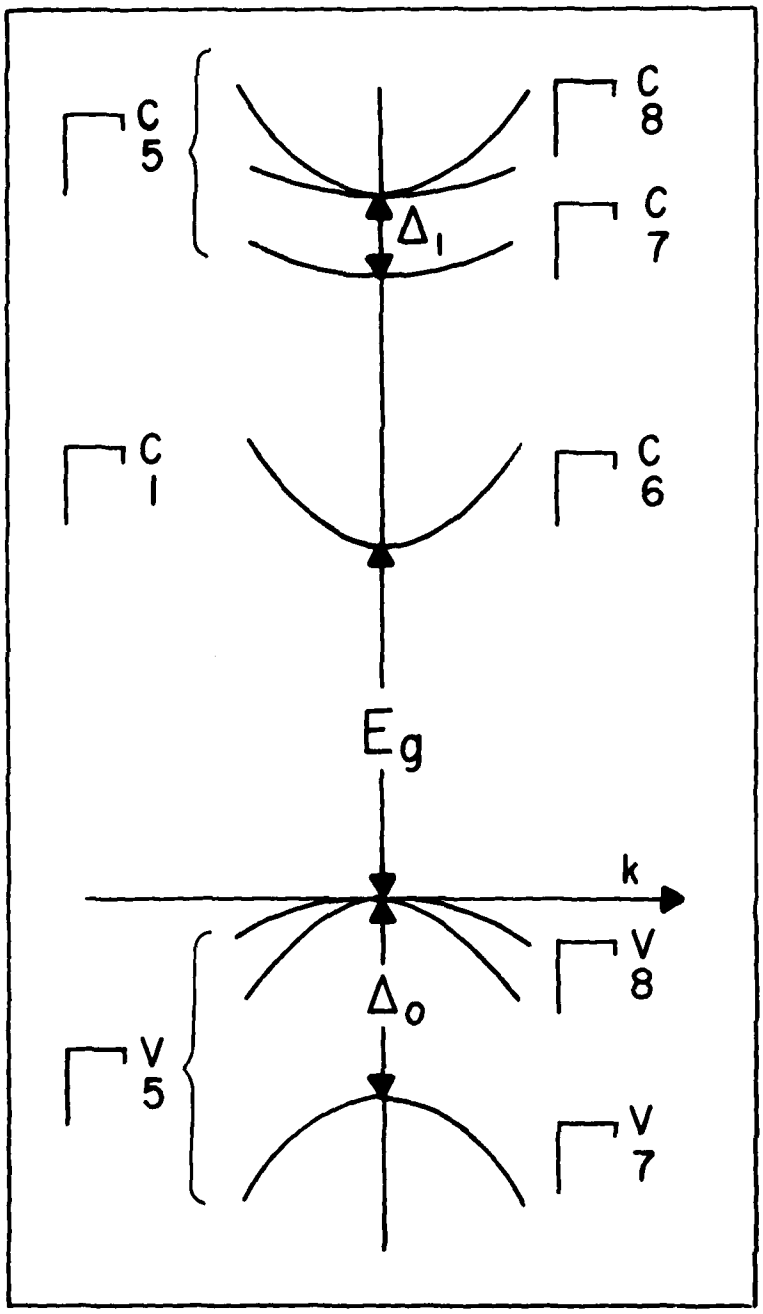

Figure 1. Schematic of the band structure of a typical zinc-blende-type semiconductor near the center of the Brillouin zone. E_g is the fundamental energy gap, while Δ_0 and Δ_1 are the spin-orbit splittings of the valence and conduction bands, respectively. Each of the bands is doubly degenerate due to spin.

THREE-PHOTON ABSORPTION IN DIRECT-GAP CRYSTALS

N. Judell and S. S. Mitra
Department of Electrical Engineering
University of Rhode Island
Kingston, Rhode Island 02881

and

A. Vaidyanathan* and A. H. Guenther
Air Force Weapons Laboratory
Kirtland Air Force Base
New Mexico 87117

Third-order time dependent perturbation theory is used to calculate the three-photon absorption coefficients of several direct-gap crystals. Both parabolic and nonparabolic energy band structures are employed. The intermediate states used in these calculations are the higher energy bands obtained from band structure calculations. The resulting three-photon absorption coefficients have the following frequency dependence. Initially the absorption coefficients increase with increasing energy, until a maximum is reached at a relatively low energy. On further increasing the photon energy the absorption coefficients decrease significantly. The behavior is qualitatively similar to the prediction of the Keldyoh formula, even though the magnitudes of the three-photon absorption coefficients obtained from the two calculations are different. The theoretical results for CdS at 1.06 μm agree well with the experimental data.

Key words: Non-linear optics; three-photon absorption; direct gap semiconductors.

1. Introduction

Multiphoton absorption processes in crystalline solids have been extensively studied in the last two decades [1], because of their varied applications in high-power laser technology and fundamental solid state physics. While there is an abundance of published literature relating to two-photon absorptions [2], the same is not true for third- and higher-order multiphoton absorptions. These highly nonlinear processes have been relatively less well studied both experimentally and theoretically. This is not surprising in view of the significantly smaller absorption coefficients [3] which make the experiments more difficult to perform, and the complexity of the equations describing these processes which makes the theoretical calculations more cumbersome.

Interest in three-photon absorption started when Ashkinadze et. al. [4], discovered nonlinear luminescence in single crystals of GaP excited by Nd:YAG laser at 77K. The minimum direct energy-gap of GaP at 77K is 2.9eV, making direct absorption of two Nd laser photon ($h\omega$ = 1.17eV) impossible. The observed luminescence was either due to the absorption of three photons with no phonon participation or due to a phonon assisted two-photon absorption. Since their experiment was incapable of distinguishing between these two processes, Ashkinadze et.al. calculated their theoretical probabilities by means of third-order time dependence perturbation theory in conjunction with a two-band model. Since then a number of workers [5-10] have theoretically and experimentally investigated direct three-photon absorption in CdS, GaP

*Now at Wright Aeronautical Laboratory - Materials Laboratory, Wright Patterson AFB, Ohio 45433.

and a few other crystals. In this paper we present new results for the three photon absorption (TPA) coefficients of CdS, GaAs, InSb, ZnSe and KCl with the aid of third-order perturbation theory in conjunction with parabolic and nonparabolic energy bands and k•p theory. The frequency dependence of the TPA coefficient is also discussed.

2. Theory

Third-order time dependent perturbation theory furnishes the following equation for the transition probability rate per unit volume of an electron in a valence band v going to a conduction band c by the simultaneous absorption of three photons, each of energy $\hbar\omega$ such that $3\hbar\omega > Eg > 2\hbar\omega$.

$$W_3 = \frac{2\pi}{\hbar} \int \frac{d^3k}{(2\pi)^3} \sum_n \sum_m \frac{H_{vm}H_{mn}H_{nc}\,\delta\{E_{vc}(\vec{k})-3\hbar\omega\}}{\{E_{mv}(\vec{k}) - \hbar\omega\}\{E_{mn}(\vec{k}) - 2\hbar\omega\}} \qquad (1)$$

In eq. (1) the H's are the interaction Hamiltonians taken to be of the form $H = (e/mc)\vec{A}\cdot\vec{p}$ where $\vec{A}$ and $\vec{p}$ are respectively the vector potential amplitude and the electron momentum operator. The indices m and n refer to the intermediate states, while E_{ij}'s are the energy differences between bands i and j.

Eq. (1) was first simplified by Bassani and Hassan [9] who assumed two higher conduction bands for the intermediate states (Figure 1), and assumed all the energy bands to be parabolic in k space. Yee [10] on the other hand, used a four-band model that consisted of one conduction band and three valence bands. In the folowing, we simplify eq. (1) by employing a four-band model, similar to that of Bassani and Hassan. However, our calculation differs from that of the above authors in two important aspects: (i) In addition to using the parabolic approximation for the energy bands, we also study the nonparabolic approximation. The effects of nonparabolicity are known to be important at high energies [11]. (ii) We estimate the interband momentum matrix elements from k•p theory [11], unlike Bassani and Hassan [9] who assumed all the interband momentum matrix elements to be equal to that between the highest valence band and the lowest conduction band.

The three-photon absorption coeffient α_3 is related to the transition probability W_3 by

$$\alpha_3 = 2W_3 \left(\frac{3\hbar\omega}{I^3}\right) \qquad (2)$$

where the factor of 2 arises from electron spin degeneracy. For parabolic energy bands of the form

$$E^p_{ij}(\vec{k}) = E_{ij}(o) + \frac{\hbar^2k^2}{2\mu^*_{ij}} \qquad (3)$$

Eqs. (1) and (2) give

$$\alpha^p_3(\omega) = \frac{24\pi^2e^6(2\mu^*_{vc})^{3/2}(3\hbar\omega-Eg)^{1/2}|G|^2}{\hbar^3\omega^5m^6c^3(\epsilon_\infty)^{3/2}} \qquad (4)$$

where

$$G = \frac{(1 + P_{mn})P_{vm}P_{mn}P_{nc}}{\{E_{mv}(o)-h\omega + \frac{\mu^*_{vc}}{\mu^*_{mv}}(3h\omega-Eg)\}\{E_{mn}(o)-2h\omega + \frac{\mu^*_{vc}}{\mu^*_{mn}}(3h\omega-Eg)\}} \qquad (5)$$

where the operator P_{mn} stands for interchange of subscripts m and n. Since the momentum matrix elements are in general complex, we write G as $r_1 e^{i\theta_1}$ + $r_2 e^{i\theta_2}$, and upon averaging over all directions, we find that $G^2 = r_1^2 + r_2^2$. Thus

$$|G|^2 = (1+P_{mn}) \left| \frac{P_{vm} P_{mn} P_{nc}}{\{E_{mn}(o)-\hbar\omega+ \frac{\mu^*_{vc}}{\mu^*_{mv}} (3\hbar\omega-Eg)\}\{E_{mn}(o)-2\hbar\omega+ \frac{\mu^*_{vc}}{\mu^*_{mn}} (3\hbar\omega-Eg)\}} \right| . \quad (6)$$

If in the place of eq. (3) one uses nonparabolic energy-momentum relationship of the form [13]

$$E^{np}_{ij}(\vec{k}) = E_{ij}(o) \left(1 + \frac{\hbar^2 k^2}{\mu^*_{ij}}\right)^{1/2} \quad (7)$$

then α_3 becomes

$$\alpha_3^{np}(\omega) = \frac{72\pi^2 e^6 (\mu^*_{vc})^{3/2}[(3\hbar\omega)^2 - E_g^2]^{1/2} |G|^2}{\hbar^2 \omega^4 m^6 c^3 \varepsilon_\infty^{3/2} E_g^{3/2}} \quad (8)$$

where

$$|G|^2 = (1+P_{mn}) \left| \frac{P_{vm} P_{mn} P_{nc}}{\left[E_{mv}(o)\left(1+ \frac{\mu^*_{vc}[(3\hbar\omega)^2-Eg^2]}{\mu^*_{mv} E_{mv}(o) Eg}\right)^{1/2} - \hbar\omega\right]\left[E_{mn}(o)\left(1+ \frac{\mu^*_{vc}[(3\hbar\omega)^2-Eg^2]}{\mu^*_{mn} E_{mn}(o) Eg}\right)^{1/2} - 2\hbar\omega\right]} \right|^2 \quad (9)$$

While the models of Bassani and Hassan, Yee and the present authors are based on third-order time dependent perturbation theory, a different approach to the multiphoton absorption problem was suggested by Keldysh [8]. He used first-order perturbation theory to calculate multiphoton absorption coefficients of arbitrary order, in a model that consisted of two non-parabolic energy bands. Keldysh model is closely related to the well-known tunneling effect and takes into account the Stark shifts in the energy bands as well as the intraband motion of the electrons.

3. Discussion

We calculated the TPA coefficients of CdS, GaAs, InSb, ZnSe and KCl from eqs. (4-9), by assuming that all the transitions are dipole allowed. In this case k•p theory gives the following expression for the interband momentum matrix elements [11]

$$|P_{ij}|^2 = \frac{E_{ij}(o) m^2}{4\mu^*_{ij}} . \quad (10)$$

The interband energy differences were obtained from diverse sources, while the effective masses of the higher conduction bands were assumed equal to that of the lowest conduction band, for the lack of better information.

In Table I we compare the results of the different theoretical calculations with available experimental data in the case of CdS. The result of the non-parabolic energy band model is found to be in good agreement with all of the experimental data, except the one of Ashkinadze et.al. whose sensitivity was rather low. The non-parabolic band result also agrees well with that of Bassani and Hassan. By contrast, the Keldysh prediction is about an order of magnitude smaller, while that of Yee is larger by approximately the same amount. In Table II the values of α_3 obtained in this work are compared with those from the Keldysh formula for GaAs, InSb, ZnSe and KCl. The values of photon energies were arbitrarily chosen corresponding to three-photon absorptions in these crystals. No comparison was made with experimental data due to the nonavailability of the latter.

The results of the third-order perturbation theory are again seen to be significantly larger than those of Keldysh. The effect of the non-parabolicity of the energy bands, in the model used here, is to increase the calculated values of α_3 by as much as a factor of two.

In Figure 2 we plot the frequency dependence of α_3 predicted by eqs. (4-9). It is found to exhibit a maximum at an energy slightly higher than one-third the band-gap energy. A similar variation is predicted by the Keldysh formula also. The physical origin of this behavior is not known at present, and should await further theoretical and experimental studies.

The authors thank Ms. Sheila Aaker for her deligent typing.

REFERENCES

[1] Bassani, F. in "Proceedings of the International School of Physics (Enrico Fermi) - Course LII", ed. E. Burstein (Academic, New York, 1972), p. 592.

[2] See, for example, Mahr, H., in "Quantium Electronics" ed., H. Rabin and C.L. Tang (Academic New York, 1975), part A, p. 285.

[3] Loudon, R. Proc. Phys. Soc. 80, 952 (1962).

[4] Ashkinadze, B.M., Bobrysheva, A.I., Vitin, E.V., Kovarskii, V.A., Lelyakov, A.V., Moscalenko, S.A. Pyshkin, S.L. and Radanksan, S.I., "Proc. of the 9th Intl. Conf. on the Phys. of Semiconductors, Moscow, 1968" (Nauka, Leningrad, 1968) Vol. I, p. 18.

[5] Penzkofer, A. and Falkenstein, W., Optics Commun. 16, 247 (1976).

[6] Jayaraman, S. and Lee, C.H., J. Appl. Phys. 44, 5480 (1973).

[7] Catalans, I.M., Cingolani, A. and Minafra, A., Phys. Rev. B 8, 1488 (1973).

[8] Keldysh, L.V., J. Eksp. Teor Fiz 47, 1945 (1964) (Sov. Phys. JETP, 20, 1307 (1965)).

[9] Bassani, F. and Hassan, A.R., Il Nuovo Cimento 7B, 313 (1972).

[10] Yee, J. Phys. Rev. B5, 449 (1972).

[11] Vaidyanethan, A., Mitra, S.S., Narducci, L.M., and Shatas, R.A., Solid State Commun. 21, 405 (1977); Pidgeon, C.R., Wherrett, B.S., Johnston, A.M., Dempsey, J. and Miller, A., Phys. Rev. Lett 42, 1785 (1979).

[12] See, for example, Callaway, J. "Quantum Theory of the Solid State"(Academic, New York, 1974), part A, p. 248; see also Narducci, L.M., Mitra, S.S., Shatas, R.A., Pfeiffer, P.A., and Vaidyanathan, A., Phys. Rev. B 14, 2508 (1976).

[13] Kane, E.O., J. Phys. Chem. Solids 1, 249 (1957).

TABLE I

Comparison of experimental and theoretical three-photon absorption coefficients of CdS at 1.064 μm in units of cm^3/GW^2

(Eg(300K) = 2.53eV, $\hbar\omega$ = 1.17eV)

Experimental	Theoretical	Source
$4 \times 10^{-4} - 4 \times 10^{-3}$		Ashkinadze et.al. [4]
$1.1 \pm 0.3 \times 10^{-2}$		Penzkofer and Folkenstein [5]
$(1.3 - 4) \times 10^{-2}$		Jayaraman and Lee [6]
5.7×10^{-2}		Catalano et.al. [7]
	1.8×10^{-3}	Present calculation (Keldysh model)
	8.2×10^{-3}	Present calculation(parabolic model)
	1.57×10^{-2}	Present calculation (non-parabolic model)
	2×10^{-2}	Bassani and Hassan [9]
	12.5	Yee [10]

TABLE II

Three-photon absorption coefficients of several direct-gap crystals

Crystals	Eg(300K) in eV	Photon energy in eV	Three-photon absorption coefficient in units of cm^3/GW^2		
			Parabolic model	Non-parabolic model	Keldysh model
GaAs	1.4	0.47	3.98×10^{-1}	3.98×10^{-1}	7.41×10^{-2}
		0.6	4.27×10^{-1}	5.89×10^{-1}	1.1×10^{-1}
InSb	0.18	0.07	7.76×10^{4}	9.12×10^{4}	2.82×10^{4}
ZnSe	2.58	0.87	1.0	1.0	2.82×10^{-3}
KCl	8.9	3.0	4.57×10^{-6}	4.68×10^{-6}	3.1×10^{-6}

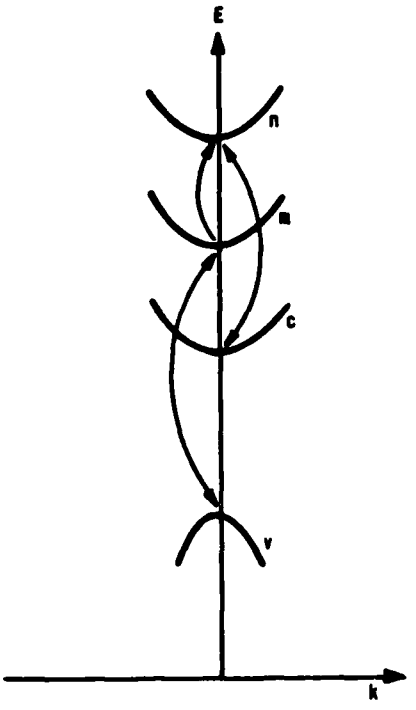

Fig. 1. Four band model of three photon absorption in a direct gap crystal.

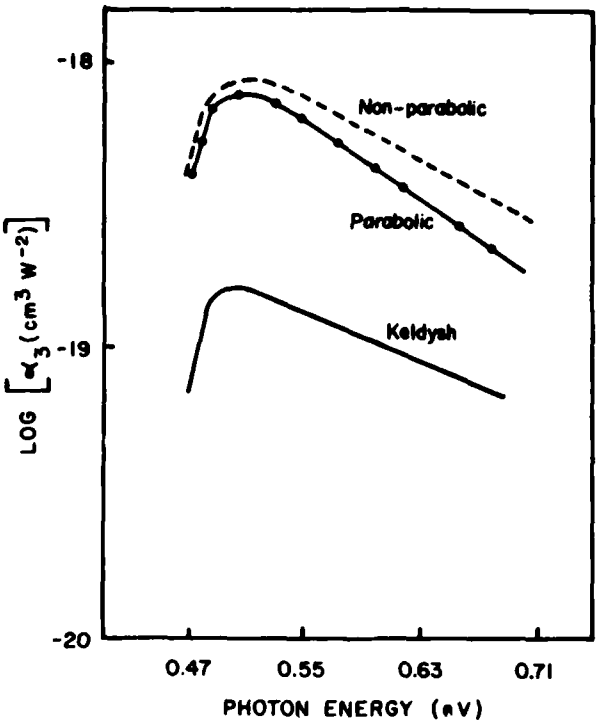

Fig. 2. Dispersion of α_3 of GaAs.

Discussion not recorded.

THEORY OF NONLINEAR BEAM PROPAGATION IN OPTICAL WAVEGUIDES

Bernard Bendow and Peter D. Gianino
Solid State Sciences Division, Rome Air Development Center
Hanscom AFB, MA 01731

and

Narkis Tzoar*
Department of Physics, City College of City University of New York
New York, New York 10031

We analyze the effect of transverse inhomogeneity on nonlinear beam propagation in a dielectric medium. Specifically, we consider the propagation of both CW beams and pulses in optical waveguides possessing a real nonlinear refractive index of the form $n=n_1(\vec{r},\omega) + n_2|E|^2$. The CW problem is treated within the paraxial approximation, for the case of a Gaussian beam incident on-axis. For powers lower than the homogeneous medium critical power, waveguiding dominates, and the beam focal parameter, although altered quantitatively, continues to vary sinusoidally as a function of distance as in the linear waveguide case, with a spectral period independent of the nonlinearity. Above the critical power, however, waveguiding is superceded and nonlinearity dominates. The beam becomes unstable, and displays oscillatory focussing in a fashion which is very similar to self-focussing in homogeneous media. Our pulse propagation studies employ a rather different starting point, based on the slowly varying envelope approximation and involving an averaging over the transverse coordinates. Our principal objective is to determine the conditions for undistorted pulse propagation, i.e., the existence of optical solitons. We obtain the equations governing the existence of solitons and find that they differ significantly from those for the homogeneous medium case. In particular, while "bright" soliton propagation is restricted to the anomolous dispersion regime in homogeneous media, in waveguides it is possible to propagate "bright" solitons in regimes of normal dispersion as well.

Key words: Nonlinear pulses, nonlinear propagation, waveguides, fiber optics, solitons, self-focussing.

1. Introduction

The transmission of intense light beams through optical waveguides is of interest for a wide variety of potential applications, among them: high bandwidth communications, integrated optics (phase conjugate devices, bistable devices), medical procedures (surgery, cauterization) and power transmission (all-optical systems, electrical hazard zone transmission). Both the spatial and temporal characteristics of intense light beams will be affected by the nonlinearity of the optical waveguide. In this paper we are concerned with effects stemming from the real part of the nonlinear refractive index on pulsed and CW beam propagation in optical fibers.

The inhomogeneous, multi-dimensional, nonlinear wave equation describing intense beam propagation in waveguides is not, in general, amenable to analytic solutions, nor is it well-suited to numerical methods of solution. In order to make this problem tractable, it is necessary to restrict consideration to specific models and/or to employ various simplifying approximations. The choice of the model and its treatment will be strongly influenced by physical considerations. In particular, in the CW beam problem we are concerned with spatial properties (transverse as well as longitudinal), but not with frequency dispersion. In the pulse propagation problem we need be concerned with nonlinear pulse distortion as well as frequency dispersion, while the variation in the transverse spatial properties may be less significant.

In the following we describe some of the principal features of both CW and pulsed nonlinear wave propagation in fiberguides and, where appropriate, indicate comparisons with homogeneous media.

2. CW Beam Propagation

The propagation in homogeneous media of nonlinear beams possessing Gaussian transverse spatial profiles has been treated previously utilizing the so-called paraxial approximation [1-4][1]. Correspondingly, the propagation of azimuthally symmetric linear beams in waveguides has been considered utilizing the paraxial approximation in conjunction with a parabolic transverse index variation [5]. We here combine the principal ingredients of these two treatments to obtain the propagation characteristics of CW Gaussian beams in nonlinear waveguides. Toward this end we choose the following simplified model for the dielectric function (z is the coordinate along the propagation axis and ρ is the transverse radial coordinate):

$$\epsilon(\rho,z,E) = \epsilon_0 - \epsilon_R \rho^2 + \epsilon_{NL} |E|^2 \qquad (1)$$

*Research supported by Solid State Sciences Division, Rome Air Development Center (AFSC) Under Contract No. F19628-79-C-0061.

[1] Figures in brackets indicate the literature references at the end of this paper.

In this model waveguiding is introduced through a quadratic variation in the transverse direction, while the nonlinearity is assumed to be proportional to the intensity (i.e., the square of the electric field intensity E). It is also possible to include longitudinal variations in the coefficients ϵ_0 and ϵ_R, but these will not be considered here.

The details of the application of the paraxial approximation to the scalar wave equation in conjunction with the model of eq. (1) will be given elsewhere [6]; only certain key results will be presented here. For an incident plane wave with frequency ω and wave number $k(=k_0\epsilon_0^{1/2}$, where $k_0=\omega/c)$, and a Gaussian spatial profile, one obtains the following expression for the electric field:

$$E = \frac{E_0}{f(z)} \exp[i(kz-\omega t)]$$

$$\times \exp\left(-\frac{\rho^2}{2\rho_0^2 f^2(z)}\right) \tag{2}$$

$$\times \exp\left[-ik\left(\frac{\rho^2}{2f(z)}\frac{df}{dz}+\phi(z)\right)\right]$$

where f and φ satisfy:

$$\frac{d^2f}{dz^2} = R_e^{-2} f^{-3} - \frac{\epsilon_R}{\epsilon_0} f \tag{3a}$$

$$\frac{d\phi}{dz} = -\frac{\rho_0^2}{f^2}\left(R_d^{-2}-\frac{1}{2}R_{NL}^{-2}\right) \tag{3b}$$

with

$$R_e^{-2} \equiv R_d^{-2} - R_{NL}^{-2}$$

$$R_d^2 = k^2\rho_0^4, \quad R_{NL}^2 = \frac{\rho_0^2\epsilon_0}{E_0^2\epsilon_{NL}} \tag{4}$$

Comparison of the above equations with those in the literature for homogeneous media indicate that to this level approximation, the expression for E is formally identical for both waveguides and homogeneous media. The modifications induced by the waveguide are contained entirely within the differential equation (3a) for the focal parameter f, namely, via the appearance of the $(\epsilon_R/\epsilon_0)f$ term. The nonlinearity, of course, is contained entirely within the R_{NL}^{-2} term in R_e^{-2}.

For the present purposes, we are primarily interested in obtaining the transverse spatial variation of the beam as a function of propagation distance z, which is determined by f(z). One finds that two different solutions for eq. (3a) depending on whether $R_e^2 > 0$ or $R_e^2 < 0$, i.e., on the relative size of the nonlinearity. When $R_e^2 > 0$ one obtains:

$$f^2 = 1/2\,[(1+C)+(1-C)\cos 2\zeta]$$

$$C=\frac{\epsilon_0}{\epsilon_R}R_e^{-2}; \quad \zeta = \left(\frac{\epsilon_R}{\epsilon_0}\right)^{1/2} z \,. \tag{5}$$

This solution represents waveguide-dominated propagation, in which the beam becomes "trapped" and oscillates with spatial period $\pi(\epsilon_0/\epsilon_R)^{1/2}$. Clearly, one obtains the exact same behavior as for the linear waveguide [5], except that R_d^{-2} is replaced with R_e^{-2} in the nonlinear case. Thus, at this level of approximation, waveguiding dominates diffraction, and the nonlinearity only modifies the oscillation amplitude but not its period. Note that when C=1, f becomes a constant. This occurs when the condition

$$\frac{k^2}{\rho_0^2}\left(\epsilon_R + \frac{\epsilon_{NL}E_0^2}{\rho_0^2}\right) = \frac{1}{\rho_0^4} \tag{6}$$

is satisfied. It can be shown that eq.(6) is equivalent to requiring $\rho_0=w_1$, *where* w_1 *is the spot size of the lowest order eigenmode of an effective wave equation at z=0, with the nonlinear term*

approximated by its expansion to order ρ^2(see [6] for details).

For the case where $R_e^2 < 0$ one obtains a singular, periodic, self-focussing type solution for f, namely:

$$f^2 = 1/2\ [(1-|C|) + (1+|C|)\cos 2\zeta\ ]$$

$$\text{for } 0 < \zeta > \zeta_F$$

$$f^2 = 1/2\ [(1-|C|) + (1+|C|)\cos 2(\zeta - j\,\zeta_F)$$

$$\text{for } j\,\zeta_F < \zeta < (j+2)\,\zeta_F \qquad (7)$$

where j is an odd integer. This solution indicates $f^2=1$ for even multiples of the dimensionless focal length ζ_F and $f^2=0$ for odd multiples of ζ_F, where

$$\zeta_F = 1/2\cos^{-1}\left(\frac{|C|-1}{|C|+1}\right),\quad z_F = \left(\frac{\varepsilon_0}{\varepsilon_R}\right)^{1/2}\zeta_F. \qquad (8)$$

The behavior indicated above is strictly analogous to that obtained in homogeneous media when the critical power, determined from the condition $R_e^{-2}=0$, is exceeded[1-4]. The main effect of the guide is to alter the functional form of f(from a quadratic dependence on z) and the focal length z_F.

Note that the self-focussing solution given above is not physically meaningful in the vicinity of focus (i.e., when $f \to 0$), in which case the present approximations break down. This problem is exactly the same as that encountered in the homogeneous medium case, which has been analyzed extensively in the literature. The interested reader is directed to refs. [1-4] and [7], for example.

One finds from the above development that the critical power P_c for self-focussing is indentical for a waveguide and a homogeneous medium, and is independent of the initial beam radius. Specifically, it is given by

$$P_c = \frac{c\lambda_0^2\,\varepsilon_0^{1/2}}{8(2\pi)^2\varepsilon_{NL}} \quad \text{(esu)} \qquad (9)$$

where λ_0 is the wavelength of the incident laser light in vacuo. At 1 um, for example, P_c typically ranges from 10Kw to 1Mw.

The above-described formalism may be applied to a calculation of the mode-mixing induced by nonlinearity in optical waveguides [6]. One can show, in general, that nonlinearity leads to an effective z-dependence of the refractive index, and thereby induces mode-mixing. Within the paraxial approximation, mode-mixing is averted only if C=1, in which case the beam waist remains constant as a function of z. The present formalism is capable, in principle, of incorporating z-dependences in the linear refractive index, and thereby treating propagation in waveguides possessing both longitudinal inhomogenity as well as nonlinearity. However, numerical methods are required to obtain solutions for f in the general case, in contrast to the analytic solutions available for uniform waveguides.

3. Nonlinear Pulse Propagation and Solitons

While for the case of CW beams one is primarily interested in transverse spatial characteristics, for the case of pulses one is primarily interested in changes in pulse width and shape as a function of propagation distance. For example, nonlinearity may distort pulses via self-phase modulation: i.e., a time-dependent phase is induced via the nonlinearity of the refractive index. In linear waveguides, on the other hand, pulse broadening is induced by material and waveguide dispersion [8]. We direct attention here to the search for special pulse solutions to the time-dependent nonlinear wave equation which propagate without distortion, refered to as solitary waves or "solitons" [9].

Regarding the search for solitons, several observations are in order: First, despite the vast literature on the subject, soliton-type solutions pertinent to the present case are known only for one-dimensional or quasi-one-dimensional nonlinear wave equations. Second, whatever approximations are introduced, they must properly account for pulse dispersion due to material and/or waveguide effects. Third, if the nonlinearity is sufficiently small then we may expect its principal effect will be on the longitudinal motion of the pulse. Indeed, the previous section provides guidance as to the scale of nonlinearity-induced modifications in transverse spatial properties, even indicating the possibility (for CW beams) of z-independent beam propagation.

We here present a very brief summary of the waveguide soliton problem; the reader interested in details is directed to refs. [10-13]. The dielectric function utilized is somewhat more general, accounting for frequency dependence and arbitrary spatial dependence of the linear term. For the present purposes we choose to work with the refractive index (square root of the dielectric function), which is taken as:

$$n(\vec{\rho},\omega,E) = n_1(\vec{\rho},\omega) + n_2|E|^2$$

$$n_1(\vec{\rho},\omega) = n_1(\omega)f(\vec{\rho}). \tag{10}$$

If one assumes a solution of Maxwell's equations of the form

$$E(\vec{r},t) = A(\vec{r},t)\exp[i(qz-\omega_0 t)] \tag{11}$$

where A is slowly varying in time, then one is able to obtain the following approximate wave equation:

$$\left[\frac{\partial^2}{\partial\vec{\rho}^2} + \frac{\partial^2}{\partial z^2} - q^2 + 2iq\frac{\partial}{\partial z} + f(\vec{\rho})k_0^2\right.$$

$$\left. + 2ia(\vec{\rho})\frac{\partial}{\partial t} - bf(\vec{\rho})\frac{\partial^2}{\partial t^2} + D|A(\vec{r},t)|^2\right] A(\vec{r},t) = 0 \tag{12}$$

where

$$b = k_0k_0'' + k_0'^2,\ a = k_0k_0'f,$$
$$D = 2(n_2/n_0)k_0^2,\ k(\omega) = (\omega/c)n_1(\omega), \tag{13}$$

the primes indicate derivatives with respect to ω, and the subscript "o" indicates evaluation at the pulse center frequency ω_0.

The principal approximation which is required to bring this multi-dimensional, nonlinear, dispersive and inhomogeneous equation into tractable form is the decoupling of the transverse and longitudinal motions [11]. One is then lead to assume that

$$A(\vec{r},t) = \phi(\vec{\rho})\,\theta(z,t) \tag{14}$$

and that the transverse inhomogeneity influences the propagation only by determining the form of $\phi(\vec{\rho})$. One may then average eq. (12) over the transverse direction to obtain

$$[d_1 - q^2 + \overline{f}k_0^2 + \frac{\partial^2}{\partial z^2} - b\overline{f}\frac{\partial^2}{\partial t^2} \tag{15}$$

$$+ d_2|\theta|^2 + 2i(q\frac{\partial}{\partial z} + \overline{a}\frac{\partial}{\partial t})]\,\theta(z,t) = 0$$

where

$$\overline{F} = \int d\vec{\rho}\,\phi F\phi\ ,\ d_1 = \int d\vec{\rho}\,\phi\frac{\partial^2}{\partial\vec{\rho}^2}\phi\ ,\ d_2 = D\int d\vec{\rho}\,\phi^4. \tag{16}$$

To solve eq. (15) we first look for solutions for which self-phase modulation is absent, i.e.,

$$(q\frac{\partial}{\partial z} + \overline{a}\frac{\partial}{\partial t})\theta = 0 \tag{17}$$

whence

$$\theta = \theta(\xi),\ \ \xi = t-(z/v),\ v = q/\overline{a}. \tag{18}$$

Thus θ represents a pulse envelope travelling with group velocity v; the remaining equation for θ admits single soliton solutions of the form

$$\theta = \theta_0\,\mathrm{sech}(\xi/\tau)\ \ \text{(bright soliton)}$$
$$\theta = \theta_0\tanh(\xi/\tau)\ \ \text{(dark soliton)} \tag{19}$$

where τ is the pulsewidth. Bright solitons represent pulses with intensity localized to a finite region of space, while dark solitons consist of an absence of intensity in a localized region of space. Since dark solitons require a constant signal-on condition for their transmission, they are obviously less desirable than bright solitons. The solutions in eq. (19) require the simultaneous satisfaction of two conditions:

$$q^2 = k_0^2\overline{f} + d_1 + 1/2\ d_2\,\theta_0^2,$$
$$\pm\,(\overline{a}^2/q^2 - b\overline{f})/\tau^2 = 1/2\ d_2\,\theta_0^2 \tag{20}$$

where the "+" is for bright solitons and "-" for dark. These equations represent the interdependence of the pulsewidth and amplitude for nonlinear pulses [14]. Soliton propagation can be achieved only when certain special conditions relating the two, such as eq. (20), are satisfied.

The most significant consequence of eq. (20) is the existence of bright solitons in waveguides in regimes of normal dispersion ($k_0'' > 0$). In the absence of the waveguide, $d_1 \to 0$ and $\bar{f} \to 1$. One finds, if $n_2 > 0$, bright solitons can exist only if $k_0'' < 0$, i.e., in regimes of anomalous dispersion. In contrast, it is easily demonstrated (see [11-13]) that for the waveguide case the conditions for the existence of bright solitons can in fact be satisfied for standard operating conditions and system parameters. Existence regions for solitons in step-index fused-silica waveguides, for example, are displayed graphically in ref. [12].

Interestingly, it is possible to achieve a condition of "zero-dispersion" in which a pulse of arbitrarily small amplitude may be propagated regardless of pulsewidth. This is realized for both bright and dark solitons when the condition

$$\left(1 + \frac{d_1}{k_0^2 \bar{f}}\right)\left(1 + \frac{k_0 k_0''}{k_0'^2}\right) = 1 \qquad (21)$$

is satisfied.

In order to provide a feeling for typical values resulting from eq. (20), consider the case of a step-index fused-silica fiberguide operating at 1μm. One finds [13] that for a bright soliton corresponding to the lowest order transverse mode in a guide with core radius ~ 5μm, that the pulse power density $P \sim 10^5 W/cm^2$ for a pulsewidth of $\tau \sim 1ns$.

It is possible to extend the present treatment to the case where the refractive index n_1 also possesses a slow longitudinal variation, $n_1 = n_1(\vec{\rho}, z, \omega)$. The principal result of the treatments given in refs. [13] and [15] is that for sufficiently weak longitudinal variation, only the soliton velocity is altered, but not its amplitude or shape. In general, the soliton velocity becomes time-dependent, as opposed to the constant value indicated above for the longitudinally uniform waveguide.

4. Concluding Remarks

In the above we have described some of the effects due to the real nonlinear refractive index of optical waveguides. In the case of CW beams, the nonlinearity induces only minor modifications in guided propagation below the homogeneous-medium critical power P_c. When $P > P_c$, however, waveguiding is superceded and self-focussing occurs; the focal distance and beam variation are modified by the presence of the waveguide.

For the pulse propagation case, one finds that waveguides are capable of supporting both bright and dark solitons under standard operating conditions. This contrasts with the homogeneous medium case, for which bright solitons exist only in regimes of anomolous dispersion.

Although only briefly mentioned here, the present formulations are well suited for the treatment of longitudinal waveguide variations, and for the analysis of mode-mixing in CW beam propagation.

References

[1] Akhmanov, S., Khokhlov, R., and Sukhorukov, A., Self-focussing, self-defocussing and self-modulation of laser beams, in Laser Handbook, Vol. 2, Arecchi, F., and Schultz-Dubois, E., eds (N. Holland, Amsterdam, 1972), and references therein.

[2] Svelto, O., Self-focussing, self-trapping and self-phase modulation of laser beams, in Progress in Optics XII, Wolf, E., ed. (N. Holland, Amsterdam, 1974).

[3] Sodha, M., Ghatak, A., and Tripathi, V. Self-focussing of laser beams in plasmas and semiconductors, in Progress in Optics XIII, Wolf, E., ed (N. Holland, Amsterdam 1976).

[4] Akhmanov, S., Sukhorukov, A. and Khokhlov, R., Self-focussing and self-trapping of intense light beams in a non-linear medium" Zh. Eksp. i Teor. Fiz. 50, 1537 (1966) [English transl.: Soviet Phys JETP 23, 1025 (1966)].

[5] Sodha, M., and Ghatak, A.K., Inhomogeneous Optical Waveguides (Plenum, NY, 1977), Secs. 3.1, 5.2 and 8.2.

[6] Bendow, B., Gianino, P.D., Tzoar, N., Theory of CW beam propagation in nonlinear optical waveguides, to be published.

[7] Tzoar, N., and Gersten, J.I., Calculation of the self-focussing of electro-magnetic radiation in semiconductors, Phys. Rev. B 4, 3540 (1971).

[8] Keck, D., in Fundamentals of Optical Fiber Communications, edited by Barnoski, M. (Academic, New York, 1976).

[9] Scott, A.C., Chu, F.Y.F. and McLaughlin, D.W., The Soliton: A new concept in applied science, Proc. IEEE 61, 1443-1483 (1973). An extensive list of references is contained in this review article.

[10] Hasegawa, A., and Tappert F., Transmission of stationary nonlinear optical pulses in dispersive dielectric fibers. I. anomalous dispersion, Appl. Phys. Lett. 23, 142-144 (1973): II. Normal dispersion, 23, 171-172 (1973).

[11] Jain, M., and Tzoar, N., Propagation of nonlinear optical pulses in inhomogeneous media, J. Appl. Phys. 49, 4649-4654 (1978).

[12] Jain, M., and Tzoar, N., Nonlinear pulse propagation in optical fibers, Opt. Lett. 3, 202-204 (1978).

[13] Bendow, B., Gianino, P.D., Tzoar, N. and Jain, M., Theory of nonlinear pulse propagation in optical waveguides, J. Opt. Soc. Am. 70, 539 (1980), and references therein.

[14] Whitham, G.B., Linear and Nonlinear Waves (Wiley, New York, 1974).

[15] Gianino, P.D., Bendow, B., Simplified formulae for solitons in media with slowly varying inhomogenity, Phys. Fluids 23, 220 (1979).

Discussion not recorded.

APPENDIX -- PARTICAPANTS

Joseph Abate
Laboratory for Laser Energetics
University of Rochester
250 East River Road
Rochester, New York 24623
(716) 275-5181

S. Aisenberg, President
Applied Science Laboratories
Gulf & Western Research
& Development Group
335 Bear Hill Road
Waltham, Massachusetts 02154
(617) 890-5100

Wayne Anderson
USAF Academy, CO 80840
(303) 472-2394

Robert Andrews
Univ. of Dayton Research Institute
AFWL/ARAO
Kirtland AFB, NM 87117
(505) 247-0512

Philip C. Archibald
Naval Weapons Center, Code 3818
China Lake, CA 93555
(714) 939-2869

Russell Austin
P. O. Box 132
Kelly, Wyoming
(307) 733-6638

E. Douglas Baird (L-506)
Lawrence Livermore National Laboratory
P. O. Box 808
Livermore, CA 94550
(415) 422-8156

William A. Barletta, L321
Lawrence Livermore National Laboratory
Livermore, CA 94550
(415) 422-6705

Michael K. Bartosewcz
Lockheed Missiles & Space Company, Inc
Electro-Optics Lab
3251 Hanover Street
Palo Alto, CA 94303
(415) 493-4411

Michael Bass
Center for Laser Studies
University of Southern California
University Park
Los Angeles, CA 90007
(213) 743-7994

W. T. Beauchamp
Optical Coating Laboratory Inc.
2789 Giffen Ave.
Santa Rosa, CA 95401
(707) 545-6440

Harold E. Bennett
Michelson Lab.
Naval Weapons Center, Code 38101
China Lake, CA 93555
(714) 939-2869 or 939-2970

Bernard Bendow
USAF/RADC
Hanscom AFB, Mass. 01731
(617) 861-3532

Jean M. Bennett
Code 38103 Michelson Lab.
Naval Weapons Center
China Lake, CA 93555
(714)939-2869

Jerry R. Bettis
USAF/USNA
C-3 Perry Circle
Annapolis, MD
(301) 267-7497 home
(301) 267-3878 office

John Bluege
United Technologies Research Center
Box 2691
West Palm Beach, FL
(305) 840-1369

Gordon H. Boultbee
Optical Coating Laboratory, Inc.
2789 Giffen Avenue
Santa Rosa, CA 95402
(707) 545-6440

Peter Braunlich
Department of Physics
Washington State University
Pullman, WA 99164
(509) 335-4946

Prof. Rubin Braunstein
Physics Department
University of Calif. at Los Angeles
(213) 825-1841

George Brost
Physics Department
Washington State University
Pullman, WA 99164

Dr. Paul Burgardt
Rockwell International
Rocky Flats, Box 464
Golden, CO 80401
(303) 497-4493

Dennis Burge
Naval Weapons Center
Physics Division, Code 3816
China Lake, CA 93555
(714) 939-2869

Charles Cason, Commander
U.S. Army Missile Command
DRSMI/RHS/CASON
Redstone Arsenal, AL 35802
(205) 876-8271 or AV 746-8271

Chalot
Laboratoires De Marcoussis
Centre De Recherches De La Compagnie
Generale d'Electricite
Route De Nozay
91460 Marcoussis, France
(1) 901-20-02

George E. Chamberlain
Div. 724.02
National Bureau of Standards
325 Broadway
Boulder, CO 80303

Jack Perry Chambers
II-VI Inc.
Saxonburg Blvd.
Saxonburg, PA 16056
(412) 352-4455

M. Clancy
Rockwell International Rocketdyne Division
6633 Canoga Avenue
Canoga Park, CA 91304

Joseph F. Connolly
CVD Incorporated
35 Industrial Parkway
Woburn, MA 01801
(617) 933-9243

Donald L. Decker, Code 3816
Naval Weapons Center
China Lake, CA 93555
(714) 939-3247

John A. Detrio
University of Dayton
Research Institute
300 College Park
Dayton, OH 45469
(513) 229-3527, 254-2641

T. M. Donovan
Naval Weapons Center
Code 3812
China Lake, CA 93555
(714) 446-2115

Clifton W. Draper
Western Electric Co.
P. O. Box 900
Princeton, NJ 08540
(609) 639-2527

Richard W. Dyer
W. J. Schafer Associates, Inc.
10 Lakeside Office Park
Wakefield, MA 01880
(617) 246-0450

D. F. Edwards
Los Alamos Scientific Laboratory
P. O. Box 1663
Los Alamos, NM

Edward A. Enemark
Optical Coating Lab., Inc.
2789 Giffen Avenue
Santa Rosa, CA 95402
(707) 545-6440

Albert Feldman
National Bureau of Standards
A251 Material Bldg.
Washington, DC 20234
(301) 921-3662

Nils C. Fernelius
Research Institute, University of Dayton
300 College Park Avenue
Dayton, OH 45469
(513) 254-2641

Giovanni Fiorenza
AFWL/KAFB
PSC 1, Box 4125
Kirtland Air Force Base, NM 87117
(505) 844-7368

Dennis Fischer
Coherent, Inc.
3210 Porter Drive
Palo Alto, CA 94304
(415) 493-2111 X401

Lawrence B. Fogdall
Boeing Co.
Mail Stop 2R-00
P.O. Box 3707
Seattle, Washington 98124
(206) 655-6711

Stephen Foltyn
Los Alamos Scientific Laboratory
P. O. Box 1663
Los Alamos, NM 87545
(505) 667-7314

Daniel Friart
CEA Lineil BP27
94190 Villeneuve
St Georges, France 5699660

William B. Gaumer
Northrop Corp., Electro-
Mechanical Division
500 E. Orangethrope Avenue
Anaheim, CA 92801
(714) 871-5000 X361

Alexander J. Glass
KMS Fusion Inc.
3941 Research Park Drive
P. O. Box 1778
Ann Arbor, Michigan 48106
(313) 769-1100

Ann Toby Glassman
Air Force Avionics Lab., AFWAL/AARI-1
E-O and Reconnaissance Branch
Reconnaissance & Weapon Delivery Division
Wright-Patterson A.F.B., OH 45433
(513) 255-5292

William T. Goosey Jr.
Eastman Kodak/Apparatus Division
901 Elmgrove Road
Rochester, NY 14650
(716) 726-6442

E. K. Gorton
Royal Sigbals Research Establishment
Andrews Road, Malvern Worchestershire
ENGLAND

George Graves
University of Dayton, Rm 162
Kettering Labs,300 College Park
Dayton, OH 45469
(513) 229-2517

Arthur H. Guenther
AFWL/CA
Kirtland AFB, NM 87117
(505) 844-9856

Marc von Gunten
Spectra-Physics, Mail Stop 4-30
1250 West Middlefield Road
Mountain View, CA 94042
(415) 961-2550 X3008

James Harvey
Univ. of Dayton Research Institute
AFWL/ARAO
Kirtland AFB, NM 87117
(505) 844-0512

W. C. Herrmann, Jr.
Optic Electronic Crop
117744 Pagemill Road
Dallas, TX
(214) 349-0190

Robert Hinebaugh
AGMC/MLLS, Newark Air Force Station
Newark, OH 43055
(614) 522-7473 or 7434

Robert Hofland, Jr.
Aerospace Corp.
P. O. Box 92957
Los Angeles, CA
(213) 648-6115

Nathan U. Holderman
UTRC
West Palm Beach, FL
(305) 840-1386

Samuel J. Holmes
Northrop Research & Technology Center
One Research Park
Palos Verdes Peninusla, CA 90274
(213) 377-4811 X314

Terry R. Holt
UDRI
Kirtland AFB, NM
(505) 247 0512

Thomas E. Honeycutt
CDR, US Army Missile Command
ATTN: DRSMI-RJS, Bldg. 8978
Redstone Arsenal, AL 35898
(205) 876-8274/8271

Alan K. Hopkins
AFWAL/MLPO (AF Materials Lab)
Wright-Patterson AFB, OH 45433
(513) 255-4474

Thomas W. Humpherys
US Air Force AFWL/ARAO
Kirtland AFB, NM 87117
(505) 844-1776

S. D. Jacobs
Laboratory for Laser Energetics
University of Rochester
250 East River Road
Rochester, NY 14623
(716) 275-4837

B. Jensen
Boston University
Department of Physics
111 Cummington Street
Boston, Mass. 02215
(617) 353-2610

Eric G. Johnson
Division 724.02
National Bureau of Standards
325 Broadway
Boulder, CO 80303

George Johnston
Univ. of Dayton Research Institute
AFWL/ARAO
Kirtland AFB, NM 87117
(505) 844-0512

Robert A. Kamper, Division 724
National Bureau of Standards
325 Broadway
Boulder, CO 80303
(303) 497-3535 or FTS 320-3535

Joon-Ho Kim
CVI Laser Corporation
200 Dorado Pl. S.E., P. O. Box 11308
Albuquerque, N.M. 87192
(505) 296-9541

Claude A. Klein
Raytheon/Research
Waltham, Mass. 02154
(617) 899-8400

Walter L. Knecht
AFWAL/MLPO
Wright Patterson AFB, OH 45433
(513) 255-4474

Nils Laegreid
Battelle Northwest Laboratory
P. O. Box 999
Richland, WA 99352
(509) 373-2417

Tony Lauderback
Litton Systems
5500 Canoga Ave.
Woodland Hills, CA
(213)887-2124

R. A. Lawton, Division 724.04
National Bureau of Standards
325 Broadway
Boulder, CO 80303

Thomas A. Leonard
University of Dayton, KL-102
Dayton, OH 45469

Terri Lichtenstein
Optical Coating Laboratory, Inc.
PO Box 1599
Santa Rosa, CA 95402

K. S. Lipton
Ferranti Ltd.
E.O.G.
S. Andrews Works
Robertson Avenue
Edinburgh, Scotland
031-337. 2442

Mike Lunt
Technical Optics Ltd.
Second Ave.
Onchan, Isle of Man
British Isles
44-624 4443

H. Angus Mcleod
Optial Sciences Center
University of Arizona
Tucson, AZ 85721
(602)626-3025

Mark Madigan
Optical Coating Laboratory, Inc.
2789 Giffen Ave.
Santa Rosa, CA 95401
(707)545-6440C.

Denton Marrs
Naval Weapons Center
Code 3817
China Lake, CA 93555
(714)939-2470

Dave K. Segawa
Hoya Optics USA, Inc.
2200 Sand Hill Road, Suite 200
Menlo Park, CA 94025

James M. McDavid
Univ. of Washington
Dept. of Electrical Engineering
FT-10
Seattle, WA 98195
(206) 543-2185, 543-2150

John K. McIver
Univ. of New Mexico
Dept. of Physics & Astronomy
800 Yale Blvd.
Albuquerque, NM 87131
(505) 277-5909

J. R. McNeil
New Mexico State Univ.
Las Cruces, NM
(505) 502-1315

David Milam
Livermore Labs.
PO Box 808
Livermore, CA 94550
(415) 422-5499

S. S. Mitra
Dept. of Electrical Engineering
University of Rhode Island
Kingston, RI 02881
(401) 792-2677

N. Kent Moncur
KMS Fusion, Inc.
PO Box 1567
3621 S. State Rd.
Ann Arbor, MI 48106
(313) 769-8500, ext. 381

Dennis Morelli
Optical Coating Laboratory, Inc.
2789 Giffen Ave.
Santa Rosa, CA 95401
(707) 545-6440

J. Mouchart
Laboratories de Marcoussis
Centre de Recherches
de la Compagnie Generale d'Electricite
Route de Nozay
91460 Marcoussis, France

Bill W. Mullins
USAF
AFWL/ARLO
Kirtland AFB, NM
(505) 844-7816

Narayan P. Murarka
IIT Research Inst.
10 W. 35th St.
Chicago, IL 60616
(312) 567-4533

Henry M. Musal, Jr.
Lockheed Research Lab.
3460 Hillview Ave.
B580, D5256
Palo Alto, CA 94304

Yoshiaru Namba
Osaka University
Yamada-Kami
Suita
Osaka 565, Japan

Roy D. Nelson
Rocketdyne
MS FA-42
6633 Canoga Ave.
Canoga Park, CA 91304
(213) 709-7197

Davis B. Nichols
Boeing Aerospace Co.
Mail Stop 88-46
PO Box 3999
Seattle, WA 98124
(206) 773-8938

N. Neuroth
Jenaer Glaswerk Schott & Gen.
Hattenbergstr. 10
6500 Mainz
West Germany
06131/66493

Brian E. Newnam
Los Alamos Scientific Lab.
PO Box 1663, MS 564
Los Alamos, NM 98545
(505) 667-3519, 667-7102

James L. Parham
US Army Missile Command
ATTN: DRSMI-EM
Redstone Arsenal, AL 35898
(205) 876-4933

AD-A106 548 NATIONAL BUREAU OF STANDARDS WASHINGTON DC F/G 20/5
LASER INDUCED DAMAGE IN OPTICAL MATERIALS: 1980.(U)
OCT 81 H E BENNETT, A J GLASS, A H GUENTHER
UNCLASSIFIED NBS-SP-620 NL

Alex Parker
MIT Lincoln Labs.
PO Box 73
Lexington, MA 02173
(617) 862-5500

W. T. Pawlewicz
Battelle Northwest Lab.
200-W Area/231-Z Bldg.
Richland, WA 99352
(509) 373-2537

Dr. Bruce Pierce
Univ. of Dayton Res. Inst.
AFWL/ARAO
Kirtland AFB, NM 87117
(505) 844-0512

James O. Porteus
Naval Weapons Center
Code 3817
China Lake, CA 93555
(714) 939-3827

Tim Pottenger
Hughes Aircraft
Bldg. 5, MS B107
Centinella & Teale Sts.
Culver City, CA
(213) 391-0711, x. 6410, x. 4592

Carl A. Preyer
Martin Marrietta Corp.
3654 S. Hudson St.
Denver, CO 80237
(303) 977-1500

Rudolf Protz
Messerschmitt-Bolkow-Blohm/AE101
PO Box 801149
D-8000 Munich 80
Fed. Rep. of Germany

Terry M. Quick
Lawrence Livermore Lab.
PO Box 808, L-369
Livermore, CA 94550
(415) 422-8005, FTS 532-8005

A Rauber
Fraunhofer-Institut fur
Angewandte Festkorperphysik
Eckerstrabe 4 . D-7800 Freiburg i. Br.
Germany
Telefon (0761)2714-1

Herman E. Reedy
II-VI Inc.
Saxonburg Blvd.
Saxonburg, PA 16056
(412) 352-1504

Mort Robinson
Hughes Research Labs.
Malibu, CA 90265
(213) 456-6411

Terry Roszhart
Perkin Elmer Corp.
100 Wooster Heights
Danbury, CT 06810
(203) 483-0371, x. 2625

Theodore T. Saito
FJSRL/NH
USAF Academy, CO 80840
(303) 472-6222

Aaron Sanders
724.02
National Bureau of Standards
325 Broadway
Boulder, CO 80303
(303) 497-5341

Raymond B. Schaefer
W. J. Schaefer Assoc. Inc.
10 Lakeside Office Park
Wakefield, MA 01880
(617) 246-0450

Paul Schall
The Aerospace Corp.
PO Box 92957
Los Angeles, CA 90009
(213) 648-7502

Ansgar Schmid
Physics Dept.
Washington State Univ.
Pullman, WA 98164
(509) 335-4672

Erik Schwendeman
CVI Laser Corp.
200 Dorado Pl. S.E.
PO Box 11308
Albuquerque, NM 87192
(505) 296-9541

Marion Scott
Univ. of Dayton Res. Inst.
AFWL/ARAO
Kirtland AFB, NM 87117
(505) 844-0512

Ian Seddon
Optical Coating Lab., Inc.
PO Box 1599
Santa Rosa, CA 95402

S. C. Seitel
Michelson Lab.
Code 3817, Naval Weapons Center
China Lake, CA 93555
(714) 939-2470 Ext. 225 or
FTS 729-4011

Philip Simpson
724.02
National Bureau of Standards
325 Broadway
Boulder, CO 80303
(303) 497-3789

James G. Sliney, Jr.
Aerojet ElectroSystems Co.
1100 W. Hollyvale St., PO Box 296
Azusa, CA 91702

M. J. Soileau
North Texas State University
Physics Department
Denton, TX 76203
(817) 788-2626 X225

Ralph Somers
Aerojet ElectroSystems Co.
PO Box 296
Azusa, CA 91702
(213) 334-6211

Marshall Sparks
Scientific Research Center
1640 Fifth Street, Suite 216
Santa Monica, CA 90401
(213) 394-0219

James L. Stanford
Naval Weapons Center, Code 3818
China Lake, CA 93555
(714) 939-3306

James L. Stapp
United States Air Force
AFWL/ARLO
Kirtland AFB, NM 87117
(505) 844-1704

Martin Stein
Applied Science Laboratories
335 Bear Hill Road
Waltham, Mass. 02154
(617) 890-5100

Alan F. Stewart
AFWL/ARAO, Kirtland AFB
Albuquerque, NM 87117
(505) 844-7368

Eric W. VanStryland
Physics Department
North Texas Stae University
Denton, TX 76203
(817) 788-2626

George W. Sutton, VP
Avco Everetrt Research Laboratory
Everett, Mass. 02149
(617) 389-3000

James E. Swain
Univ. of Calif., LLL
Livermore, CA
(415) 4212-5402

William C. Sweatt
University of New Mexico
Albuquerque, NM 87131
(505) 277-5148/5827

Paul A. Temple
Naval Weapons Center
China Lake, CA 93555
(714) 939-3247

Norman L. Thomas, L-461
Lawrence Livermore National Lab.
PO. Box 808
Livermore, CA 94550
(415) 422-0486

Scott J. Thomas
Los Alamos Scientific Lab.
L-9 MS 535
P.O. Box 1663
Los Alamos, NM 87544
(505) 667-3023 or 6952

Y. S. Touloukian
Cindas/Purdue Univ.
2595 Yeager Rd.
W. Lafayette, IN 47906
(317) 494-8486

N. Tzoar
City College
New York, NY 10031
(212) 690-6923 or 6832

A. Vaidyanathan
Air Force Materials Lab
AFWAL/MLPJ
Wright-Patterson AFB, OH 45433
(513) 255-6671

Eric W. Van Stryland
North Texas State University
Dept. of Physics, P.O. Box 5368
Denton, TX 76203
(817) 788-2626

Howard Volkin
Univ. of Dayton Research Institute
AFWL/ARAO
Kirtland AFB, NM 87117
(505) 844-0512

Marc VonGuten
Spectra-Physics
1250 West Middlefield
Mt. View, CA 94042
(415) 961-2550 Ext. 3008

Harshad Vara
Honeywell
Corporate Technology Center
10701 Lyndale Ave. S.
Bloomington, MN 55420
(612) 88704421

Rodger M. Walser
University of Texas
437 ENS
Austin, TX 78712
(512) 471-5733

Francis C. Wang
Lockheed Missiles & Space Co., Inc.
P. O. Box 1103, West Statin
Huntsville, AL 35807
(205) 1800 X272

Ronald W. Waynant
Naval Research Lab.
Code 6540
Washington, DC 20375
(202) 767-2813

T. A. Wiggins
AFWL/ARAO
Physics Dept.,Penn. State
University Park, PA 16802
Walter Wild
IIT Research Institute
10 West 35th Street
Chicago, IL 60616
(312) 567-4563

Charles B. Willingham
Raytheon Company Research Division
28 Seyon Street
Waltham, MA 02154
(617) 899-8400

Harry V. Winsor, USAF
Air Force Office of Scientific Research
AFOSR/NE
Bolling AFB, DC 20332
(202) 767-4931

G. Richard Wirtenson
Lawrence Livermore National Laboratory
P.O. Box 5508
Livermore, CA 94550
(415) 422-1332

Roger M. Wood
The General Electric Company Limited
Hirst Research Centre
East Lane, Wembley, Middlesex HA9 7PP
ENGLAND
01-904-1262 Ext. 205

Shin-Tson Wu
Center for Laser Studies
USC Center for Laser Studies
Los Angeles, CA 90007
(213) 743-6418

Matt Young, 724.02
National Bureau of Standards
325 Broadway
Boulder, CO 80303
(303) 497-3223

Robert Zimmerer
Scientech, Inc.
5649 Arapahoe
Boulder, CO 80303
(303) 497-3223

NBS-114A (REV. 2-8C)

U.S. DEPT. OF COMM. BIBLIOGRAPHIC DATA SHEET (See instructions)	1. PUBLICATION OR REPORT NO. NBS SP 620	2. Performing Organ. Report No. AD-A106 548	3. Publication Date October 1981

4. TITLE AND SUBTITLE

Laser Induced Damage in Optical Materials: 1980

5 Editors: Harold E. Bennett (NWC), Alexander J. Glass (LLL)
Arthur H. Guenther (AFWL), and Brian E. Newnam (LASL)

6. PERFORMING ORGANIZATION (If joint or other than NBS, see instructions)

NATIONAL BUREAU OF STANDARDS
DEPARTMENT OF COMMERCE
WASHINGTON, D.C. 20234

7. Contract/Grant No.

8. Type of Report & Period Covered
Final

9. SPONSORING ORGANIZATION NAME AND COMPLETE ADDRESS (Street, City, State, ZIP)

American Society for Testing and Materials
Office of Naval Research
Department of Energy
Defense Advanced Research Project Agency
Air Force Office of Scientific Research

10. SUPPLEMENTARY NOTES

Library of Congress Catalog Card Number: 81-600110

☐ Document describes a computer program; SF-185, FIPS Software Summary, is attached.

11. ABSTRACT (A 200-word or less factual summary of most significant information. If document includes a significant bibliography or literature survey, mention it here)

The Twelfth Annual Symposium on Optical Materials for High Power Lasers (Boulder Damage Symposium) was held at the National Bureau of Standards in Boulder, Colorado, September 30--October 1,1980. The Symposium was held under the auspices of ASTM Committee F-1, Subcommittee on Laser Standards, with the joint sponsorship of NBS, the Defense Advanced Research Project Agency, the Department of Energy, the Office of Naval Research, and the Air Force Office of Scientific Research. Over 150 scientists attended the Symposium, including representatives of the United Kingdom, France, Japan, and West Germany. The Symposium was divided into sessions concerning Materials and Measurements, Mirrors and Surfaces, Thin Films, and finally Fundamental Mechanisms. ~~As in previous years,~~ the emphasis of the papers presented at the Symposium was directed toward new frontiers and new developments. Particular emphasis was given to materials for high power systems. The wavelength range of prime interest was from 10.6 (μm) to the uv region. Highlights included surface characterization, thin film-substrate boundaries, and advances in fundamental laser-matter threshold interactions and mechanisms. The scaling of damage thresholds with pulse duration, focal area, and wavelength was discussed in detail. Harold E. Bennett of the Naval Weapons Center, Alexander J. Glass of the Lawrence Livermore Laboratories, Arthur H. Guenther of the Air Force Weapons Laboratory, and Brian E. Newnam of the Los Alamos Scientific Laboratory were co-chairmen of the Symposium. The Thirteenth Annual Symposium is scheduled for November 17-18, 1981 at the National Bureau of Standards, Boulder, Colorado.

12. KEY WORDS (Six to twelve entries; alphabetical order; capitalize only proper names; and separate key words by semicolons)

laser damage; laser interaction; optical components; optical fabrication; optical materials and properties; thin film coatings.

13. AVAILABILITY

☒ Unlimited
☐ For Official Distribution. Do Not Release to NTIS
☒ Order From Superintendent of Documents, U.S. Government Printing Office, Washington, D.C. 20402.
☐ Order From National Technical Information Service (NTIS), Springfield, VA. 22161

14. NO. OF PRINTED PAGES
483

15. Price
$9.50

USCOMM-DC 6043-P80

★U.S. GOVERNMENT PRINTING OFFICE: 1981-340-997/1803

NBS TECHNICAL PUBLICATIONS

PERIODICALS

JOURNAL OF RESEARCH—The Journal of Research of the National Bureau of Standards reports NBS research and development in those disciplines of the physical and engineering sciences in which the Bureau is active. These include physics, chemistry, engineering, mathematics, and computer sciences. Papers cover a broad range of subjects, with major emphasis on measurement methodology and the basic technology underlying standardization. Also included from time to time are survey articles on topics closely related to the Bureau's technical and scientific programs. As a special service to subscribers each issue contains complete citations to all recent Bureau publications in both NBS and non-NBS media. Issued six times a year. Annual subscription: domestic $13; foreign $16.25. Single copy, $3 domestic; $3.75 foreign.

NOTE: The Journal was formerly published in two sections: Section A "Physics and Chemistry" and Section B "Mathematical Sciences."

DIMENSIONS/NBS—This monthly magazine is published to inform scientists, engineers, business and industry leaders, teachers, students, and consumers of the latest advances in science and technology, with primary emphasis on work at NBS. The magazine highlights and reviews such issues as energy research, fire protection, building technology, metric conversion, pollution abatement, health and safety, and consumer product performance. In addition, it reports the results of Bureau programs in measurement standards and techniques, properties of matter and materials, engineering standards and services, instrumentation, and automatic data processing. Annual subscription: domestic $11; foreign $13.75.

NONPERIODICALS

Monographs—Major contributions to the technical literature on various subjects related to the Bureau's scientific and technical activities.

Handbooks—Recommended codes of engineering and industrial practice (including safety codes) developed in cooperation with interested industries, professional organizations, and regulatory bodies.

Special Publications—Include proceedings of conferences sponsored by NBS, NBS annual reports, and other special publications appropriate to this grouping such as wall charts, pocket cards, and bibliographies.

Applied Mathematics Series—Mathematical tables, manuals, and studies of special interest to physicists, engineers, chemists, biologists, mathematicians, computer programmers, and others engaged in scientific and technical work.

National Standard Reference Data Series—Provides quantitative data on the physical and chemical properties of materials, compiled from the world's literature and critically evaluated. Developed under a worldwide program coordinated by NBS under the authority of the National Standard Data Act (Public Law 90-396).

NOTE: The principal publication outlet for the foregoing data is the Journal of Physical and Chemical Reference Data (JPCRD) published quarterly for NBS by the American Chemical Society (ACS) and the American Institute of Physics (AIP). Subscriptions, reprints, and supplements available from ACS, 1155 Sixteenth St., NW, Washington, DC 20056.

Building Science Series—Disseminates technical information developed at the Bureau on building materials, components, systems, and whole structures. The series presents research results, test methods, and performance criteria related to the structural and environmental functions and the durability and safety characteristics of building elements and systems.

Technical Notes—Studies or reports which are complete in themselves but restrictive in their treatment of a subject. Analogous to monographs but not so comprehensive in scope or definitive in treatment of the subject area. Often serve as a vehicle for final reports of work performed at NBS under the sponsorship of other government agencies.

Voluntary Product Standards—Developed under procedures published by the Department of Commerce in Part 10, Title 15, of the Code of Federal Regulations. The standards establish nationally recognized requirements for products, and provide all concerned interests with a basis for common understanding of the characteristics of the products. NBS administers this program as a supplement to the activities of the private sector standardizing organizations.

Consumer Information Series—Practical information, based on NBS research and experience, covering areas of interest to the consumer. Easily understandable language and illustrations provide useful background knowledge for shopping in today's technological marketplace.

Order the **above** *NBS publications from: Superintendent of Documents, Government Printing Office, Washington, DC 20402.*

Order the **following** *NBS publications—FIPS and NBSIR's—from the National Technical Information Services, Springfield, VA 22161.*

Federal Information Processing Standards Publications (FIPS PUB)—Publications in this series collectively constitute the Federal Information Processing Standards Register. The Register serves as the official source of information in the Federal Government regarding standards issued by NBS pursuant to the Federal Property and Administrative Services Act of 1949 as amended, Public Law 89-306 (79 Stat. 1127), and as implemented by Executive Order 11717 (38 FR 12315, dated May 11, 1973) and Part 6 of Title 15 CFR (Code of Federal Regulations).

NBS Interagency Reports (NBSIR)—A special series of interim or final reports on work performed by NBS for outside sponsors (both government and non-government). In general, initial distribution is handled by the sponsor; public distribution is by the National Technical Information Services, Springfield, VA 22161, in paper copy or microfiche form.


DATE
FILME